frontiers | Research Topics

Prevention, mitigation, and relief of compound and chained natural hazards, volume II

Edited by
Chong Xu, Qi Yao, Xiangli He, Wenwen Qi, Sansar Raj Meena,
Wentao Yang and Liam Taylor

Published in
Frontiers in Earth Science

ISSN 1664-8714
ISBN 978-2-8325-6390-8
DOI 10.3389/978-2-8325-6390-8

About Frontiers

Frontiers is more than just an open access publisher of scholarly articles: it is a pioneering approach to the world of academia, radically improving the way scholarly research is managed. The grand vision of Frontiers is a world where all people have an equal opportunity to seek, share and generate knowledge. Frontiers provides immediate and permanent online open access to all its publications, but this alone is not enough to realize our grand goals.

Frontiers journal series

The Frontiers journal series is a multi-tier and interdisciplinary set of open-access, online journals, promising a paradigm shift from the current review, selection and dissemination processes in academic publishing. All Frontiers journals are driven by researchers for researchers; therefore, they constitute a service to the scholarly community. At the same time, the *Frontiers journal series* operates on a revolutionary invention, the tiered publishing system, initially addressing specific communities of scholars, and gradually climbing up to broader public understanding, thus serving the interests of the lay society, too.

Dedication to quality

Each Frontiers article is a landmark of the highest quality, thanks to genuinely collaborative interactions between authors and review editors, who include some of the world's best academicians. Research must be certified by peers before entering a stream of knowledge that may eventually reach the public - and shape society; therefore, Frontiers only applies the most rigorous and unbiased reviews. Frontiers revolutionizes research publishing by freely delivering the most outstanding research, evaluated with no bias from both the academic and social point of view. By applying the most advanced information technologies, Frontiers is catapulting scholarly publishing into a new generation.

What are Frontiers Research Topics?

Frontiers Research Topics are very popular trademarks of the *Frontiers journals series*: they are collections of at least ten articles, all centered on a particular subject. With their unique mix of varied contributions from Original Research to Review Articles, Frontiers Research Topics unify the most influential researchers, the latest key findings and historical advances in a hot research area.

Find out more on how to host your own Frontiers Research Topic or contribute to one as an author by contacting the Frontiers editorial office: frontiersin.org/about/contact

Prevention, mitigation, and relief of compound and chained natural hazards, volume II

Topic editors
Chong Xu — National Institute of Natural Hazards, Ministry of Emergency Management, China
Qi Yao — Institute of Earthquake Forecasting, China Earthquake Administration, China
Xiangli He — National Institute of Natural Hazards, Ministry of Emergency Management, China
Wenwen Qi — National Institute of Natural Hazards, Ministry of Emergency Management, China
Sansar Raj Meena — University of Padua, Italy
Wentao Yang — University of Leeds, United Kingdom
Liam Taylor — University of Leeds, United Kingdom

Citation
Xu, C., Yao, Q., He, X., Qi, W., Meena, S. R., Yang, W., Taylor, L., eds. (2025). *Prevention, mitigation, and relief of compound and chained natural hazards, volume II*. Lausanne: Frontiers Media SA. doi: 10.3389/978-2-8325-6390-8

Table of contents

frontiers | Frontiers in Earth Science

TYPE Editorial
PUBLISHED 15 May 2025
DOI 10.3389/feart.2025.1622457

Check for updates

OPEN ACCESS

EDITED AND REVIEWED BY
Gordon Woo,
Risk Management Solutions, United Kingdom

*CORRESPONDENCE
Chong Xu,
✉ xc11111111@126.com

RECEIVED 03 May 2025
ACCEPTED 09 May 2025
PUBLISHED 15 May 2025

CITATION
Xu C, Yao Q, He X, Qi W, Meena SR, Yang W and Taylor L (2025) Editorial: Prevention, mitigation, and relief of compound and chained natural hazards, volume II.
Front. Earth Sci. 13:1622457.
doi: 10.3389/feart.2025.1622457

Editorial: Prevention, mitigation, and relief of compound and chained natural hazards, volume II

Chong Xu[1,2,3]*, Qi Yao[4], Xiangli He[1,2], Wenwen Qi[1,2], Sansar Raj Meena[5], Wentao Yang[6] and Liam Taylor[7]

[1]National Institute of Natural Hazards, Ministry of Emergency Management of China, Beijing, China, [2]Key Laboratory of Compound and Chained Natural Hazards Dynamics, Ministry of Emergency Management, Beijing, China, [3]School of Geology and Mining Engineering, Xinjiang University, Urumqi, China, [4]Institute of Earthquake Forecasting, China Earthquake Administration, Beijing, China, [5]Department of Geosciences, School of Sciences, University of Padua, Padua, Italy, [6]School of Soil and Water Conservation, Beijing Forestry University, Beijing, China, [7]School of Geography, University of Leeds, Leeds, United Kingdom

KEYWORDS

compound and chained hazards, earthquake-induced geohazards, machine learning, landslide mapping and inventory, hydro-geomechanical coupling, natural hazards

Editorial on the Research Topic
Prevention, mitigation, and relief of compound and chained natural hazards, volume II

Introduction

In the face of global climate change and intensifying environmental variability, the frequency, magnitude, and complexity of natural hazards have significantly increased (Masson-Delmotte et al., 2021; Xu and Xu, 2021; Huang et al., 2023; Gao et al., 2024; Wang et al., 2025; Wu et al., 2025; Xu et al., 2025). These events rarely occur in isolation. Instead, they interact spatially and temporally, generating compound and chained disasters that amplify impacts across interconnected systems (Pescaroli and Alexander, 2015; Gill and Malamud, 2017; Zscheischler et al., 2018; Van Wyk de Vries, 2025). This presents unprecedented challenges to disaster risk science and emergency management.

Building upon the success of the first volume of this Research Topic, which focused on earthquake-related hazard chains and geohazards (Xu et al., 2024), the second volume expands its scope to encompass a broader array of hazard interactions, covering geophysical, hydrological, and anthropogenic domains. It directly responds to the original call for papers, which emphasized five core themes: (1) formation and evolution mechanisms of compound and chained hazards, (2) multi-hazard model building and chain-breaking strategies, (3) source detection and database construction, (4) intelligent early warning and risk assessment technologies, and (5) emergency equipment and post-disaster recovery.

This editorial provides a structured synthesis of the 14 accepted contributions in Volume II. The articles are grouped thematically and highlight emerging research frontiers including artificial intelligence (AI), high-resolution geospatial analysis, integrated physical and empirical modeling, and intelligent sensing technologies for real-time hazard monitoring.

Mechanisms and models of earthquake-triggered chained hazards

Earthquakes remain key initiators of cascading hazard sequences such as landslides, ground ruptures, and surface deformation (Keefer, 1984; Xu et al., 2014; Zhao et al., 2023; Li et al., 2024; Yu et al., 2024; Zhang et al., 2024; Huang et al., 2025). Liu et al. developed empirical relationships between Arias Intensity (AI) and peak ground acceleration (PGA) for western China, uncovering region-specific differences influenced by local site conditions and providing a new framework for energy-based seismic hazard metrics. Lu et al. compared a logistic regression-based data-driven model Xu et al. (2019) and a physics-based Newmark model to evaluate coseismic landslides after the 2022 Ms 6.8 Luding earthquake. Results show that the logistic model achieved higher accuracy and efficiency in emergency contexts. Wang et al. evaluated the predictive impact of lithology and precipitation in machine-learning models of earthquake-induced landslides. Surprisingly, they found these commonly used factors negatively affect model performance due to spatial clustering and data resolution issues. Hu and Ren proposed a probabilistic displacement hazard model for distributed surface ruptures along strike-slip faults in the Tibetan Plateau. Their work enables engineers to assess fault displacement risk for linear infrastructure exposed to large-magnitude events. Together, these studies deepen our understanding of chained seismic hazards and underscore the critical need for regionally adaptive, data-informed modeling strategies.

Smart monitoring and early warning of mining-induced geohazards

Mining operations represent hotspots for compound geological risks due to induced stress fields, water infiltration, and roof instability (Wang et al., 2018; Ma et al., 2022). Zhang et al. developed a comprehensive early warning method for coal mine roof and floor cracking and water inrush, using microseismic monitoring of source parameters such as apparent stress and energy. Their tri-dimensional model of fracture depth, intensity, and risk represents a significant advancement in real-time hazard forecasting. Sun et al. applied abrasive jet-based hydraulic fracturing technology for gently inclined hard roof treatment. Field results confirmed effective crack generation and reduced stress concentration, highlighting a safer alternative to traditional blasting. Hou et al. analyzed surface subsidence and crack development across super-long working faces. Their findings offer new insights into asymmetric settlement curves and secondary subsidence effects, vital for infrastructure protection over mining zones. These contributions collectively reinforce the value of multi-sensor integration and mechanistic insight for mining hazard mitigation.

Hydro-Geomechanical coupling and ground deformation dynamics

Groundwater level fluctuations and geologic structures play crucial roles in land subsidence and rebound phenomena (Chaussard et al., 2014; Jeanne et al., 2019). Liu and Bai investigated land deformation in Beijing's Chaobai River plain using InSAR and borehole extensometers. They discovered a previously undocumented uplift zone driven by managed aquifer recharge (MAR), controlled by fault permeability and lithologic variation—a paradigm shift in subsidence control theory. This work illustrates the evolving complexity of hydro-mechanical feedback loops in anthropogenic hazard settings.

Landslide inventories, mapping, and spatial distribution analysis

Reliable landslide inventories are foundational for hazard zoning and regional risk assessment (Guzzetti et al., 2012; Xu, 2015; Shao and Xu, 2022; Feng et al., 2024; Shao et al., 2024). Xue et al. compiled 3,979 landslide relics in Zhenxiong County, Yunnan using human-machine interactive visual interpretation. They identified four high-density landslide zones, emphasizing terrain incision and hydrological development. Wang and Xu built a database of 5,517 landslides in Minhe County, Qinghai, revealing the dominance of slope angle (15°–25°), elevation (2000–2,100 m), and proximity to rivers (0–2 km) in governing spatial susceptibility. Such granular spatial datasets are key to advancing machine-learning-based susceptibility mapping and chain hazard simulations.

Monitoring, reinforcement, and failure simulation in complex geological settings

Hazard dynamics in karst, loess, and liquefiable sites require specialized monitoring and engineering solutions (Zhao et al., 2012; Koseki et al., 2015; Lian et al., 2020). Wu Liang et al. used MEMS sensors in a series of slope model experiments to monitor internal displacements with high accuracy (<6% error), suggesting a promising alternative to traditional PIV methods in deep slope stability monitoring. Wu Yi et al. conducted six model tests on geotextile reinforcement of karst subgrades. They found that tensile membrane effects significantly reduced displacement—up to 66% under static loads—offering theoretical and design support for infrastructure in karst-prone zones. Peng et al. performed fully coupled dynamic effective stress analysis on liquefiable interlayers under bidirectional ground motion. Their results confirm that near-field vertical seismic components significantly increase ground settlement, reshaping our understanding of site response mechanisms. Zhao et al. simulated a loess landslide event in Shaanxi Province using discrete and finite element models to quantify impact damage on housing. The findings offer a blueprint for quantitative vulnerability assessment in loess terrain, a critical step in pre-disaster planning.

Conclusion and outlook: toward data-driven, intelligent multi-hazard resilience

While the contributions in this volume provide valuable insights into specific aspects of compound and chained natural hazards—particularly in the contexts of earthquake-induced geohazards, mining-related instabilities, and site-specific deformation phenomena—they only partially address the full breadth of challenges outlined in the original call for papers. Research gaps remain in areas such as meteorological hazard interactions, hydrological-ecological feedbacks, and transboundary disaster chains. Nevertheless, the application of machine learning, microseismic monitoring, geospatial mapping, and physical modeling across these case studies reflects a promising step forward in hazard assessment and scenario-based analysis.

We recognize that a comprehensive understanding of multi-hazard dynamics requires sustained and interdisciplinary efforts. To that end, we are continuing this Research Topic in future volumes, and we sincerely welcome further contributions that address broader hazard types, integrative modeling approaches, and proactive mitigation strategies. We invite researchers from around the world to join us in advancing science-based solutions for reducing the risks and cascading impacts of natural hazards.

Author contributions

CX: Funding acquisition, Writing – review and editing, Writing – original draft, Conceptualization. QY: Writing – review and editing. XH: Writing – review and editing. WQ: Writing – review and editing. SM: Writing – review and editing. WY: Writing – review and editing. LT: Writing – review and editing.

Funding

The author(s) declare that financial support was received for the research and/or publication of this article. This study was supported by the National Institute of Natural Hazards, Ministry of Emergency Management of China (2023-JBKY-57) and Chongqing Water Resources Bureau, China (CQS24C00836).

Acknowledgments

We sincerely thank all the authors for their submissions to this Research Topic, all the reviewers for their valuable comments and suggestions, and the staff of *Frontiers in Earth Science* for their strong support in all phases of the realization of this Research Topic.

Conflict of interest

The authors declare that the research was conducted in the absence of any commercial or financial relationships that could be construed as a potential conflict of interest.

The author(s) declared that they were an editorial board member of Frontiers, at the time of submission. This had no impact on the peer review process and the final decision.

Generative AI statement

The author(s) declare that no Generative AI was used in the creation of this manuscript.

Publisher's note

References

Chaussard, E., Bürgmann, R., Shirzaei, M., Fielding, E. J., and Baker, B. (2014). Predictability of hydraulic head changes and characterization of aquifer-system and fault properties from InSAR-derived ground deformation. *J. Geophys. Res. Solid Earth* 119 (8), 6572–6590. doi:10.1002/2014jb011266

Feng, L., Xu, C., Tian, Y., Li, L., Sun, J., Huang, Y., et al. (2024). Landslides of China's qinling. *Geosci. Data J.* 11 (4), 725–741. doi:10.1002/gdj3.246

Gao, H., Xu, C., Xie, C., Ma, J., and Xiao, Z. (2024). Landslides triggered by the July 2023 extreme rainstorm in the Haihe river basin, China. *Landslides* 21 (11), 2885–2890. doi:10.1007/s10346-024-02322-9

Gill, J. C., and Malamud, B. D. (2017). Anthropogenic processes, natural hazards, and interactions in a multi-hazard framework. *Earth-Science Rev.* 166, 246–269. doi:10.1016/j.earscirev.2017.01.002

Guzzetti, F., Mondini, A. C., Cardinali, M., Fiorucci, F., Santangelo, M., and Chang, K.-T. (2012). Landslide inventory maps: new tools for an old problem. *Earth-Science Rev.* 112 (1-2), 42–66. doi:10.1016/j.earscirev.2012.02.001

Huang, Y., Xu, C., He, X., Cheng, J., Xu, X., and Tian, Y. (2025). Landslides induced by the 2023 Jishishan Ms6.2 earthquake (NW China): spatial distribution characteristics and implication for the seismogenic fault. *npj Nat. Hazards* 2 (1), 14. doi:10.1038/s44304-025-00064-9

Huang, Y., Xu, C., Zhang, X., Li, L., and Xu, X. (2023). Research in the field of natural hazards based on Bibliometric analysis. *Nat. Hazards Rev.* 24 (2), 04023012. doi:10.1061/nhrefo.nheng-1739

Jeanne, P., Farr, T. G., Rutqvist, J., and Vasco, D. W. (2019). Role of agricultural activity on land subsidence in the San Joaquin Valley, California. *J. Hydrol.* 569, 462–469. doi:10.1016/j.jhydrol.2018.11.077

Keefer, D. K. (1984). Landslides caused by earthquakes. *Geol. Soc. Am. Bull.* 95 (4), 406–421. doi:10.1130/0016-7606(1984)95<406:lcbe>2.0.co;2

Koseki, J., Wakamatsu, K., Sawada, S., and Matsushita, K. (2015). Liquefaction-induced damage to houses and its countermeasures at minami-kurihashi in kuki city during the 2011 tohoku earthquake, Japan. *Soil Dyn. Earthq. Eng.* 79, 391–400. doi:10.1016/j.soildyn.2015.07.014

Li, Y., Zhang, Z., and Chen, X. (2024). Developing a rapid assessment framework for China earthquake disaster losses: insights from physical simulations of the Yangbi earthquake. *npj Nat. Hazards* 1 (1), 37–39. doi:10.1038/s44304-024-00037-4

Lian, B., Peng, J., Zhan, H., Huang, Q., Wang, X., and Hu, S. (2020). Formation mechanism analysis of irrigation-induced retrogressive loess landslides. *Catena* 195, 104441. doi:10.1016/j.catena.2019.104441

Ma, D., Duan, H., Zhang, J., and Bai, H. (2022). A state-of-the-art review on rock seepage mechanism of water inrush disaster in coal mines. *Int. J. Coal Sci. Technol.* 9 (1), 50. doi:10.1007/s40789-022-00525-w

Masson-Delmotte, V., Zhai, P., Pirani, A., Connors, S. L., and Péan, C. (2021). Climate change 2021: the physical science basis. *Intergov. Panel Clim. Change IPCC.* doi:10.1017/9781009157896

Pescaroli, G., and Alexander, V. (2015). A definition of cascading disasters and cascading effects: going beyond the "toppling dominos" metaphor. *Planet@ risk* 3 (1), 58–67. Available online at: https://discovery.ucl.ac.uk/id/eprint/1465510/.

Shao, X., Ma, S., Xu, C., Xie, C., Li, T., Huang, Y., et al. (2024). Landslides triggered by the 2022 Ms. 6.8 Luding strike-slip earthquake: an update. *Eng. Geol.* 335, 107536. doi:10.1016/j.enggeo.2024.107536

Shao, X., and Xu, C. (2022). Earthquake-induced landslides susceptibility assessment: a review of the state-of-the-art. *Nat. Hazards Res.* 2 (3), 172–182. doi:10.1016/j.nhres.2022.03.002

Van Wyk de Vries, M. (2025). All hazards are multihazards, few of them are natural. *npj Nat. Hazards* 2 (1), 18. doi:10.1038/s44304-025-00071-w

Wang, C., Zhang, C., Zhao, X., Liao, L., and Zhang, S. (2018). Dynamic structural evolution of overlying strata during shallow coal seam longwall mining. *Int. J. Rock Mech. Min. Sci.* 103, 20–32. doi:10.1016/j.ijrmms.2018.01.014

Wang, Q., Xu, C., Ma, J., Huang, Y., Zhang, S., and Gao, H. (2025). Preliminary analysis of the July 30, 2024, Wayanad landslide disaster in India: causes and impacts. *Nat. Hazards Res.* doi:10.1016/j.nhres.2025.04.005

Wu, S., Xu, C., Ma, J., and Gao, H. (2025). Escalating risks and impacts of Rainfall-induced geohazards. *Nat. Hazards Res.* doi:10.1016/j.nhres.2025.03.003

Xu, C. (2015). Preparation of earthquake-triggered landslide inventory maps using remote sensing and GIS technologies: principles and case studies. *Geosci. Front.* 6 (6), 825–836. doi:10.1016/j.gsf.2014.03.004

Xu, C., Xu, X., Yao, X., and Dai, F. (2014). Three (nearly) complete inventories of landslides triggered by the May 12, 2008 Wenchuan Mw 7.9 earthquake of China and their spatial distribution statistical analysis. *Landslides* 11 (3), 441–461. doi:10.1007/s10346-013-0404-6

Xu, C., Xu, X., Zhou, B., and Shen, L. (2019). Probability of coseismic landslides: a new generation of earthquake-triggered landslide hazard model. *J. Eng. Geol.* 27 (5), 1121–1129. doi:10.13544/j.cnki.jeg.2019084

Xu, C., Yao, Q., He, X., Qi, W., Meena, S. R., Yang, W., et al. (2024). Editorial: Prevention, mitigation, and relief of compound and chained natural hazards. *Front. Earth Sci.* 12, 1462471. doi:10.3389/feart.2024.1462471

Xu, X., Wang, S., Cheng, J., and Wu, X. (2025). Shaking the Tibetan Plateau: insights from the Mw 7.1 Dingri earthquake and its implications for active fault mapping and disaster mitigation. *npj Nat. Hazards* 2 (1), 16. doi:10.1038/s44304-025-00074-7

Xu, X., and Xu, C. (2021). Natural Hazards Research: an eternal subject of human survival and development. *Nat. Hazards Res.* 1 (1), 1–3. doi:10.1016/j.nhres.2020.12.003

Yu, X., Hu, X., Song, Y., Xu, S., Li, X., Song, X., et al. (2024). Intelligent assessment of building damage of 2023 Turkey-Syria Earthquake by multiple remote sensing approaches. *npj Nat. Hazards* 1 (1), 3. doi:10.1038/s44304-024-00003-0

Zhang, Z., Zeng, R., Zhao, S., Wei, Z., Meng, X., Long, Z., et al. (2024). 2023 Jishishan Earthquake-triggered river terrace landslide enabled by tectonic and human activities. *npj Nat. Hazards* 1 (1), 29. doi:10.1038/s44304-024-00029-4

Zhao, B., Su, L., Xu, Q., Li, W., Xu, C., and Wang, Y. (2023). A review of recent earthquake-induced landslides on the Tibetan Plateau. *Earth-Science Rev.* 244, 104534. doi:10.1016/j.earscirev.2023.104534

Zhao, H., Ma, F., and Guo, J. (2012). Regularity and formation mechanism of large-scale abrupt karst collapse in southern China in the first half of 2010. *Nat. Hazards* 60, 1037–1054. doi:10.1007/s11069-011-9888-3

Zscheischler, J., Westra, S., Van Den Hurk, B. J., Seneviratne, S. I., Ward, P. J., Pitman, A., et al. (2018). Future climate risk from compound events. *Nat. Clim. change* 8 (6), 469–477. doi:10.1038/s41558-018-0156-3

frontiers | Frontiers in Earth Science

TYPE Original Research
PUBLISHED 15 July 2024
DOI 10.3389/feart.2024.1434194

EDITED BY
Chong Xu,
Ministry of Emergency Management, China

REVIEWED BY
Zongchao Li,
China Earthquake Administration, China
Jiangwei Zhang,
Hebei GEO University, China

*CORRESPONDENCE
Jia Mei Liu,
✉ ljm19870918@126.com

RECEIVED 17 May 2024
ACCEPTED 24 June 2024
PUBLISHED 15 July 2024

CITATION
Liu JM, Zhang B and Zhao XD (2024), Empirical relationships between Arias Intensity and peak ground acceleration for western China.
Front. Earth Sci. 12:1434194.
doi: 10.3389/feart.2024.1434194

Empirical relationships between Arias Intensity and peak ground acceleration for western China

Jia Mei Liu[1,2]*, Bin Zhang[3] and Xu Dong Zhao[1,2]

[1]Key Laboratory of Active Tectonics and Geological Safety, Ministry of Natural Resources, Institute of Geomechanics, Chinese Academy of Geological Sciences, Beijing, China, [2]Observation and Research Station of Geological Disaster in Baoji, Ministry of Natural Resources, Baoji, Shaanxi, China, [3]Institute of Earthquake Forecasting, China Earthquake Administration, Beijing, China

There is little available attenuation relationship for Arias Intensity (AI) in China. Empirical relationships between AI and peak ground acceleration (PGA) provide another option for predicting AI. We establish empirical relationships for AI and PGA for western China, utilizing 3,169 horizontal and 979 vertical strong motion records with PGA $\geq$0.01 g from 274 earthquakes (M_S 4.0–8.0), originating in eight provinces in southwest (Yunnan, Sichuan) and northwest China (Gansu, Shaanxi, Ningxia, Qinghai, Inner Mongolia, and Xinjiang). The influences of M_S epicenter distance, and site conditions indicators V_{S30}, generic site classes (*i.e.*, rock and soil) are explored. The results show that the logarithm of AI increases linearly with the increase of the logarithm of PGA and M_S, and decreases with the logarithm of V_{S30}. However, the influence of site conditions on AI-PAG relationships can't be recognized by the simple generic rock and soil site classes. The epicenter distance has little effect on the AI-PAG relationships. Empirical relationships are developed to estimate horizontal or vertical AI as a function of PGA (basic model), PGA and M_S (model 2) for southwest, northwest, and western China, using all the records. Empirical relationships for AI as a function of PGA, M_S, and V_{S30} (model 1) are established using the 2,248 horizontal (70.9% of the total) and 670 vertical (68.4% of the total) records with V_{S30} between 148 and 841m/s. The notable disparity between model 1 of the southwest and northwest regions is chiefly attributed to local site conditions, indicating that the AI-PGA correlation is region-dependent. These findings enable one way of estimating AI for western China and will contribute to a better understanding of AI attenuation.

KEYWORDS

Arias intensity, peak ground acceleration, conditional model for Arias intensity, empirical correlations, western China

1 Introduction

As a mandatory national standard that is currently in force, the national seismic hazard maps of China (GB 18306–2015) employed the attenuation relationships for peak ground acceleration (PGA) developed using the transform method (Yu and Wang, 2007). This is mainly due to the lack of strong motion recordings and sparse distribution of strong ground motion stations, which limits the establishment of attenuation relations through regression analysis. Benefiting from the National Strong Motion Observation Network System (NSMONS) of China, which has been in formal operation since 2008, a large number of high quality strong motion recordings have been obtained in the past decade

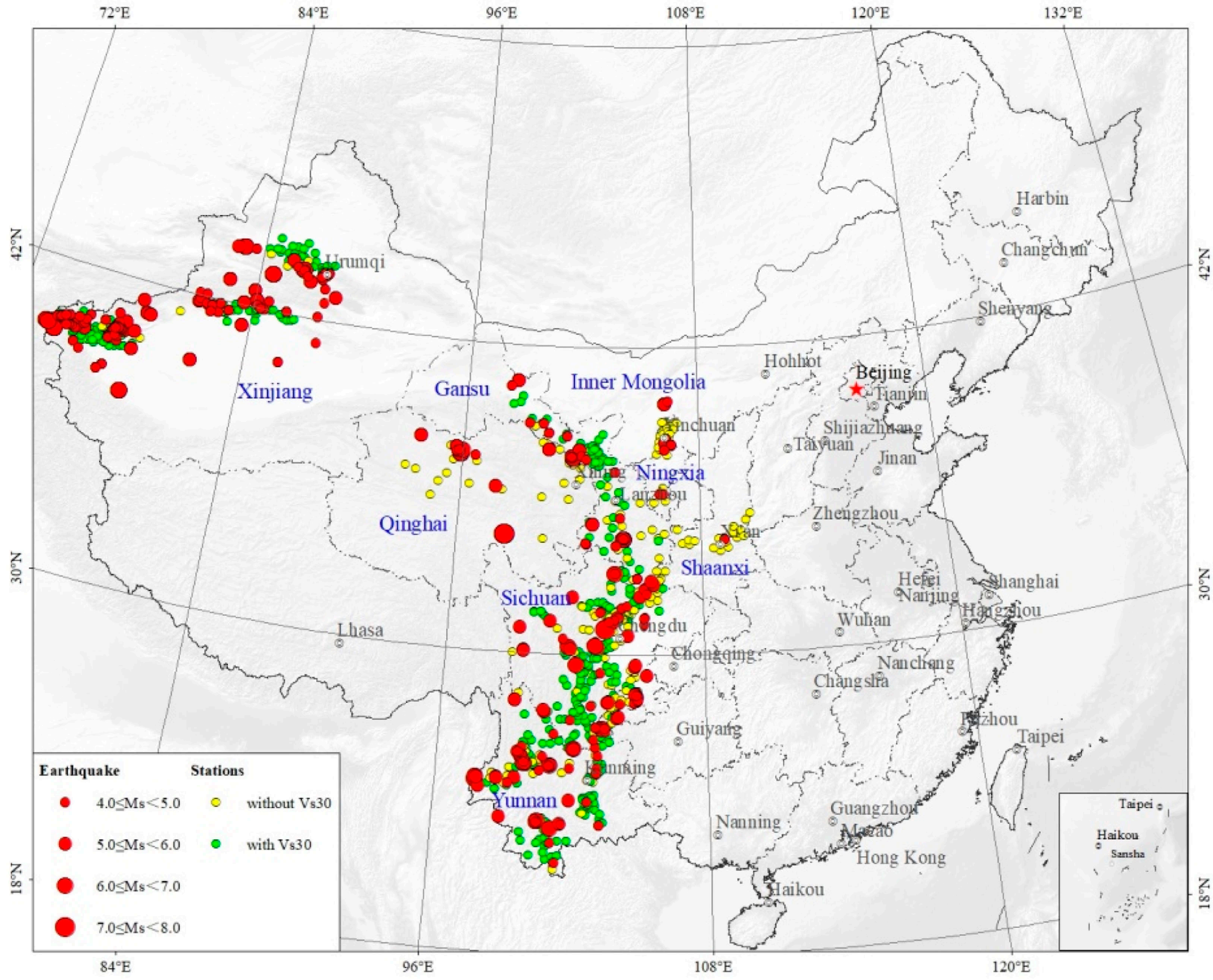

FIGURE 1
Earthquakes and strong-motion stations selected for this study.

or so (Ji et al., 2017; Xie et al., 2022). In recent years, the China Earthquake Administration has proposed the Next-Generation Attenuation project. As part of a broader effort to update national seismic hazard maps of China, this project aims to develop ground motion prediction equations (GMPEs) that incorporate broadband and multiple ground motion intensity parameter, such as PGA, peak ground velocity (PGV), peak ground displacement (PGD), response spectral and AI (Arias, 1970; Chousianitis et al., 2016; Zach et al., 2017).

For some widely used parameters in China, such as PGA, PGV, 5% damped response spectrum, some researchers (Li et al., 2020a; Zhang et al., 2021; Zhang et al. 2022; Zhang et al. 2023) investigated the influences of magnitude, rupture distance, fault types, site amplification and hanging-wall scaling on ground motions, and developed GMPEs for southwest China and capital circle region of China. These models incorporate parameters such as magnitude, geometric attenuation, anelastic attenuation, hanging-wall effect, and linear/nonlinear site response terms to improve the accuracy of ground motion predictions. However, in the case of AI, there is very little available attenuation relationship for this intensity measure in China (Liu et al., 2018). Lee et al. (2012) developed a regional AI attenuation relationship for Taiwan considering V_{S30} (the equivalent shear-wave velocity of soil layers within a depth of 30 m underground). Liu and Ren (2022) developed the AI attenuation relationship for the Sichuan-Yunnan region. Their functional forms were modified from that of Travasarou et al. (2003), which was derived from a point-source model. Before we propose the AI attenuation relation for the next-generation national seismic hazard maps of China, the applicability of existing AI attenuation models still needs further investigation. Moreover, for the region with limited strong ground motions, predicting AI through the relationships between AI and other seismic parameters is another option (Liu et al., 2015; Ji et al., 2021; Macedo et al., 2022). Moreover, correlations of AI and other intensity measures enable an easily ground motion selection and vector hazard analysis (Wang and Du, 2013; Bradley, 2015; Tao et al., 2020; Cheng et al., 2021).

In this study, we developed empirical AI-PGA relationships for western China based on our global empirical relationships (Liu

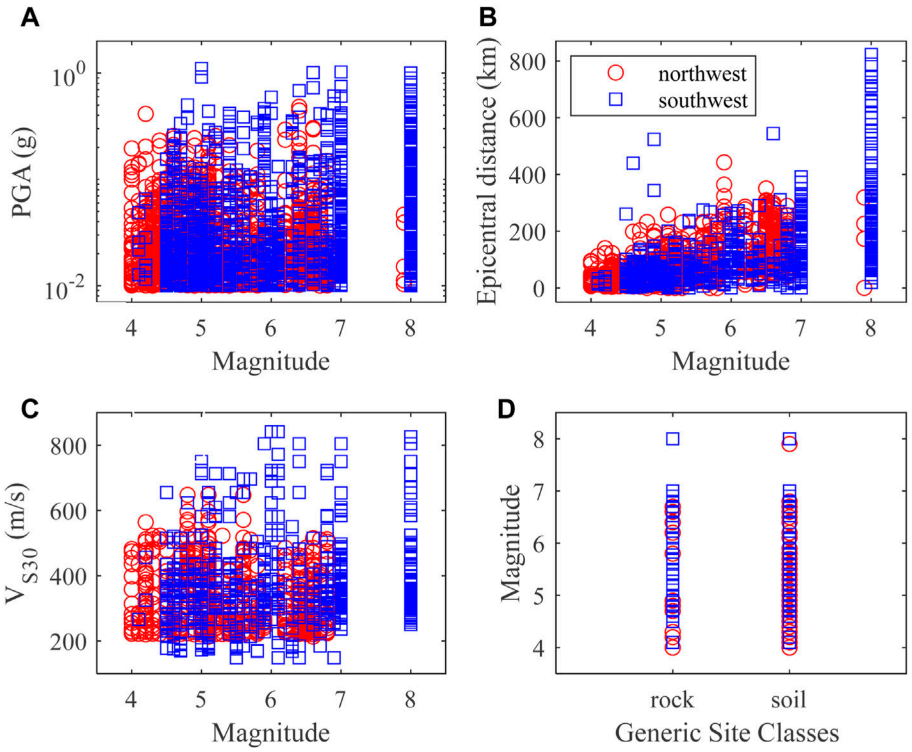

FIGURE 2
Distribution of strong-motion data used in this study: **(A)** magnitude and PGA, **(B)** magnitude and epicentral distance, **(C)** magnitude and V_{S30}, and **(D)** generic site class and magnitude.

TABLE 1 Numbers of earthquakes and records for different magnitude ranges.

Magnitude	Number of earthquakes			Number of horizontal records			Number of horizontal records with V_{S30}			Number of vertical records			Number of vertical records with V_{S30}		
	N	S	A	N	S	A	N	S	A	N	S	A	N	S	A
4≤Ms<4.5	55	15	70	275	11	286	157	6	163	70	3	73	39	3	42
4.5≤Ms<5	42	52	94	275	403	678	196	258	454	89	130	219	63	130	193
5≤Ms<5.5	29	26	55	303	352	655	263	218	481	87	120	207	69	120	189
5.5≤Ms<6	11	15	26	212	181	393	166	118	284	45	68	113	36	68	104
6≤Ms<6.5	6	7	13	168	187	355	151	135	286	50	53	103	47	53	100
6.5≤Ms<7	8	6	14	269	134	403	209	106	315	57	44	101	40	44	84
7≤Ms<7.5	0	0	0	0	155	155	0	111	111	0	59	59	0	59	59
7.5≤Ms	1	1	2	6	238	244	0	154	154	1	103	104	0	103	103

N, S and A represent northwest, southwest, and all west China areas.

et al., 2016). Our analysis involves 3,169 horizontal and 979 vertical strong motion records from 274 earthquakes with surface wave magnitude (M_S) ranging from 4.0 to 8.0. We examine the influences of earthquake magnitude and epicenter distance, as well as the dependencies on local site conditions using V_{S30} and generic site classes such as rock and soil. Finally, we develop models to predict AI as a function of PGA, PGA and M_S, PGA, M_S, and V_{S30} for southwest, northwest, and western China, encompassing both

TABLE 2 Regression coefficients for the horizontal and vertical AI and PGA relationships (Eq. 1).

Model parameter	Horizontal						Vertical					
	Northwest		Southwest		All west		Northwest		Southwest		All west	
	Value	SE	Value	SE	Value	SE	Value	SE	Value	SE	Value	SE
a	0.400	0.038	0.548	0.026	0.503	0.023	0.405	0.068	0.432	0.037	0.418	0.033
b	1.619	0.019	1.662	0.012	1.646	0.011	1.601	0.038	1.608	0.020	1.597	0.019
c	0.271	0.016	0.272	0.018	0.275	0.014	0.286	0.013	0.270	0.020	0.282	0.013
d	−0.790	0.052	−0.198	0.039	−0.468	0.032	−0.589	0.090	−0.196	0.064	−0.341	0.056
σ^{b}	0.187	-	0.169	-	0.186	-	0.186	-	0.156	-	0.173	-
τ^{c}	0.048	-	0.092	-	0.071	-	0	-	0.090	-	0.057	-
$\sigma_T{}^{d}$	0.196	-	0.195	-	0.201	-	0.186	-	0.186	-	0.187	-

[a] a, b, c, d are the regression coefficients of equation 1; SE, means the standard error of coefficients.
[b] Intraevent Sigma.
[c] Interevent Sigma.
[d] Total Sigma.

TABLE 3 Regression coefficients for the horizontal and vertical AI and PGA relationships (Eq. 2).

Model parameter	Horizontal						Vertical					
	Northwest		Southwest		All west		Northwest		Southwest		All west	
	Value	SE	Value	SE	Value	SE	Value	SE	Value	SE	Value	SE
a	0.567	0.034	0.560	0.023	0.566	0.021	0.502	0.063	0.439	0.032	0.455	0.030
b	1.626	0.017	1.659	0.011	1.641	0.010	1.607	0.035	1.597	0.018	1.590	0.016
c	0.260	0.017	0.272	0.016	0.262	0.013	0.248	0.021	0.273	0.018	0.255	0.014
σ^{b}	0.206	-	0.181	-	0.197	-	0.188	-	0.165	-	0.180	-
τ^{c}	0.065	-	0.088	-	0.076	-	0.056	-	0.086	-	0.075	-
$\sigma_T{}^{d}$	0.219	-	0.203	-	0.213	-	0.204	-	0.190	-	0.200	-

[a] a,b, c are the regression coefficients of equation 1; SE, means the standard error of coefficients.
[b] Intraevent Sigma.
[c] Interevent Sigma.
[d] Total Sigma.

TABLE 4 Regression coefficients for the horizontal and vertical AI and PGA relationships (Eq. 3).

Model parameter	Horizontal			Vertical		
	Northwest	Southwest	All west	Northwest	Southwest	All west
a	0.309	0.985	0.797	0.220	0.815	0.707
b	1.565	1.936	1.837	1.536	1.822	1.784
$\sigma_T{}^{a}$	0.317	0.388	0.365	0.298	0.408	0.374

a and b are the regression coefficients of Eq. 3 obtained through the least-squares estimation.
[a] Total Sigma.

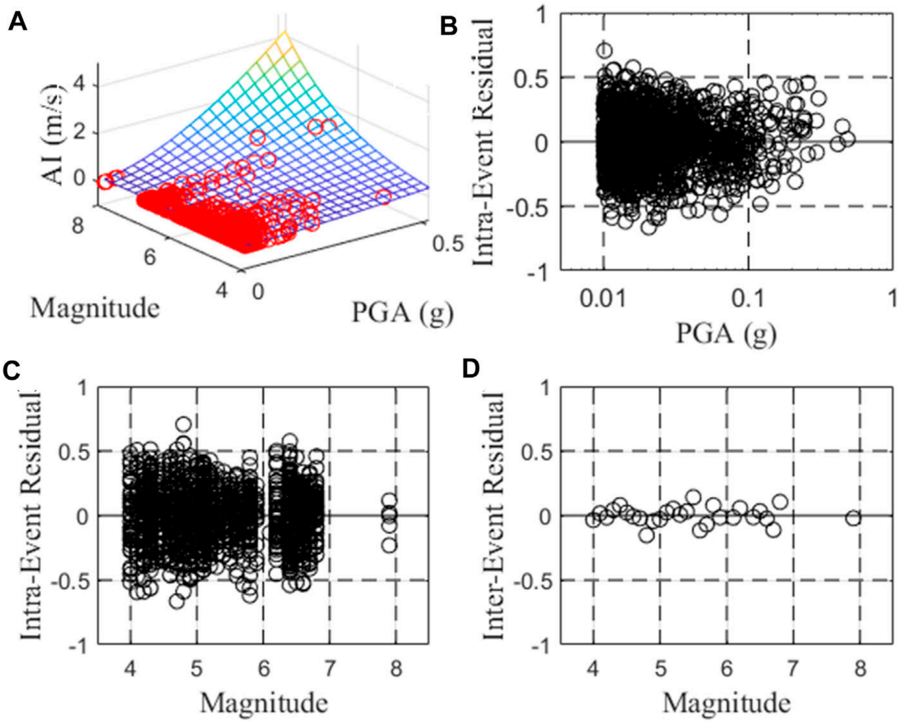

FIGURE 3
Comparison between the observed data of northwest China with model 2 **(A)**, and Intraevent residuals of model 1 against **(B)** PGA, **(C)** V_{S30}, and **(D)** Interevent residual against magnitude.

horizontal and vertical components. We investigate the region-dependent of AI-PGA correlation by comparing our southwest and northwest models with previous models, and discusse the potential reasons. These findings provide a methodology for estimating AI from PGA in western China, and contribute to a deeper understanding of the attenuation characteristics of AI in China overall.

2 Strong ground motion and empirical model

2.1 Strong ground motion dataset

The database used for this study comprises accelerograms from over 800 strong motion stations of NSMONS in western China. These records capture earthquakes that occurred in eight provinces of southwest (Yunnan, Sichuan) and northwest China (Gansu, Shaanxi, Ningxia, Qinghai, Inner Mongolia and Xinjiang), contributing nearly 71% earthquakes throughout China from 2009 to now, as documented by the unified earthquake cataloging of China Seismographic Network operated by the China Earthquake Networks Center (CENC). To mitigate the influence of site response, topographic and structural effects on ground motion, records from vertical arrays, topographical arrays, and structural arrays are excluded, with stations deployed at free field ground sites considered. The strong motion records are processed using the method of Zhang et al. (2022), with each horizontal component treated independently. For engineering purposes, we select strong motion data from stations with PGA larger than 0.01 g. By applying these selection criteria, there are finally 3,169 horizontal and 979 vertical strong motion records recorded by 646 strong motion stations. The currently available site information for all these stations is generic site classes (rock and soil) as listed in strong-motion record data files. Ji et al. (2017, 2022) provided site classification for about 170 stations using an empirical H/V spectral ratio method. Xie et al. (2022) developed a soil profile database of geotechnical soil profiles and shear-wave velocity logs, and site parameters for 678 stations in western China (Yunnan, Sichuan, Gansu, and Xinjiang). Unfortunately, there are still many stations without plausible site classification and V_{S30} value due to the lake of borehole logs or shear wave velocities profiles (Ren et al., 2023). Based on their research, we obtain V_{S30} for 406 stations, and assign V_{S30} to 2,248 horizontal (70.9% of the total) and 670 vertical (68.4% of the total) strong-motion records.

These strong-motion records are recorded in 274 earthquakes with magnitude ranging from 4.0 to 8.0. Surface wave magnitude (M_S) is provided for majority of the earthquakes, while local magnitude (M_L) is used for only 15 earthquakes (13 with $4.1 \le M_L \le 4.9$, 1 with $M_L=6.2$, and 1 with $M_L=6.6$) when M_S is unavailable. According to the review of Li et al. (2014), the MS and M_L measurements are consistent, with the empirical equation by Li et al. (2016) indicating a difference between estimated MS from ML and measured MS of less than 0.1 for these few data. Consequently, we believe that the mixed usage of MS and ML has negligible influence on the final empirical relationships between AI and PGA.

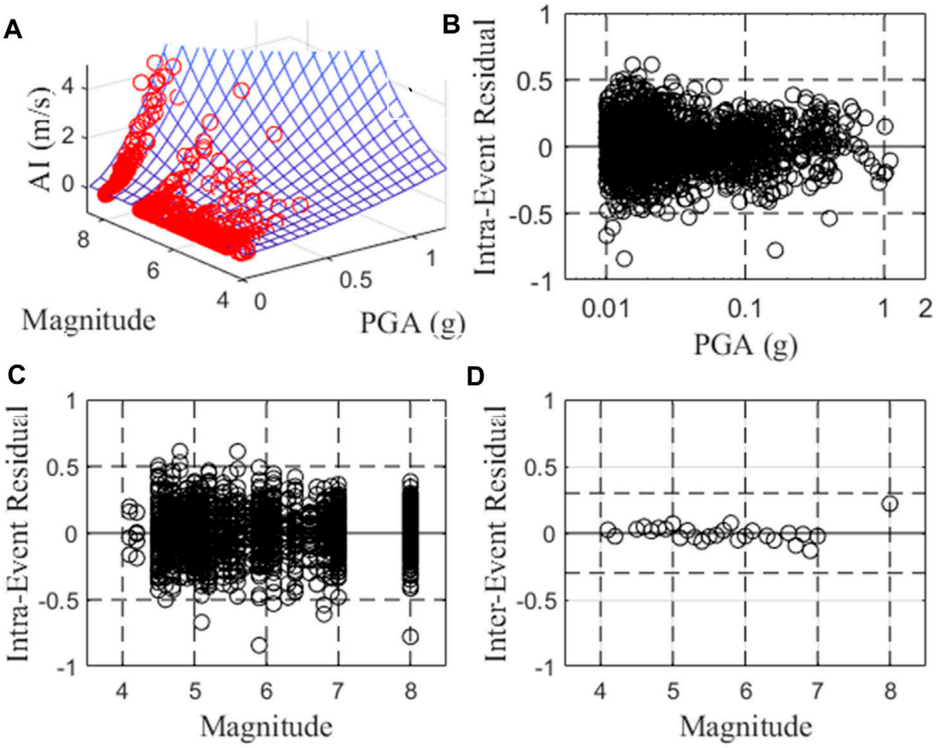

FIGURE 4
Comparison between the observed data of southwest China with model 2 **(A)**, and Intraevent residuals of model 1 against **(B)** PGA, **(C)** V_{S30}, and **(D)** Interevent residual against magnitude.

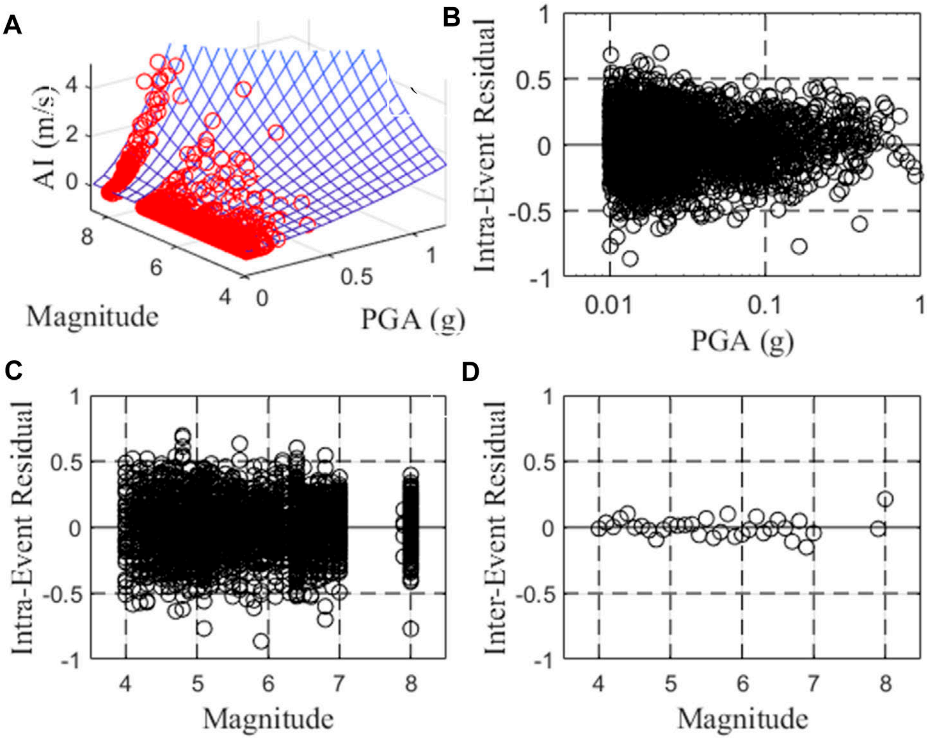

FIGURE 5
Comparison between the observed data of all west China with model 2 **(A)**, and Intraevent residuals of model 1 against **(B)** PGA, **(C)** V_{S30}, and **(D)** Interevent residual against magnitude.

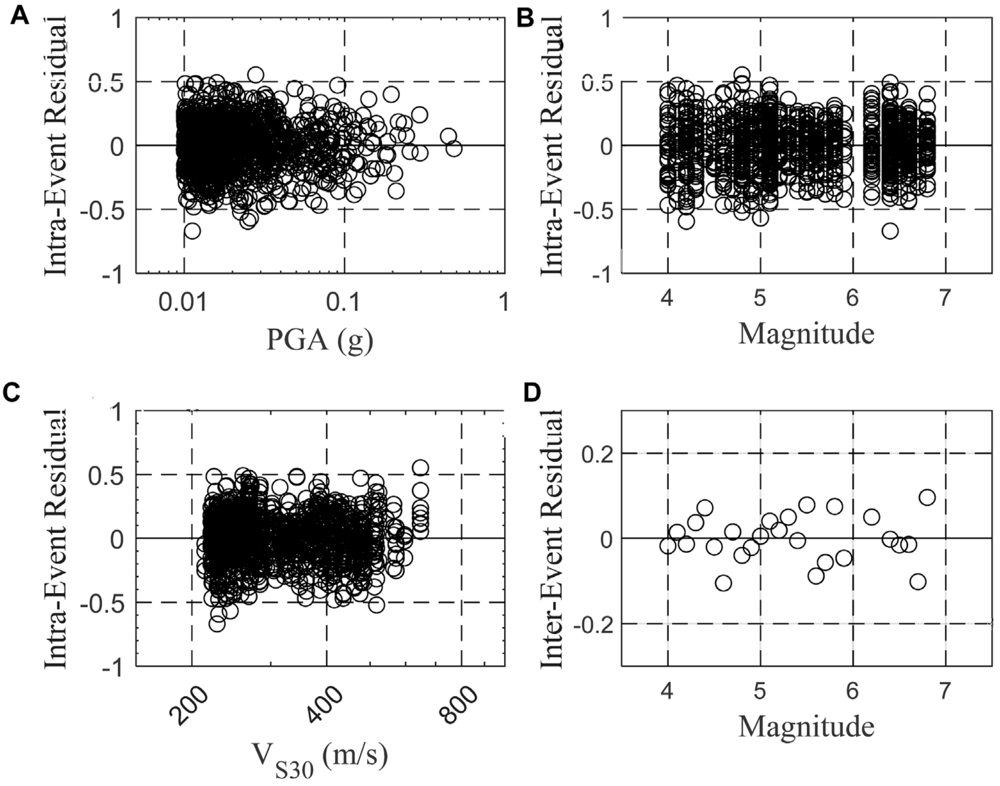

FIGURE 6
Intraevent residuals of model 1 for northwest China against **(A)** PGA,**(B)** magnitude, **(C)** V_{S30}, and **(D)** Interevent residual against magnitude.

The spatial distribution of these earthquakes and strong-motion stations is shown in Figure 1. The data distribution with respect to PGA, magnitude, epicentral distance, V_{S30} and generic site class are illustrated in Figure 2. Numbers of earthquakes and records for different magnitude ranges are listed is Table 1. For the complete list of the earthquake catalogue used, see Supplementary Tables S1, S2 in the electronic supplement to this article.

2.2 Model of empirical relationships

In previous study (Liu et al., 2016), we proposed global empirical AI-PGA relationships as a function of moment magnitude M_w, and V_{S30}. We concluded that AI-PGA relationship was not significantly affected by focal mechanism and fault distance. These global empirical relationships represented a significant advancement by incorporating such important features as magnitude and V_{S30} and enable an improved way of estimating AI from PGA. Its function was described as Eq. 1 (referred as model 1)

$$\log(AI) = a + b\log(PGA) + c(M_S - 6) + d\log(Vs30/500) \tag{1}$$

in which AI is Arias intensity in unit of m/s, and PGA is and peak ground acceleration in unit of g (1g = 9.8 m/s^2), M_S is the surface wave magnitude, V_{S30} is in unit of m/s, a, b, c and d are regression parameters.

In this paper, we also investigate the influence of epicentral distance using our data. We confirm that considering epicentral distance is unnecessary due to the absence of any biased residual. Eq. 1 is utilized for the dataset that included V_{S30} values. For the data without V_{S30} values, we test the usage of the generic site class (rock or soil) instead of V_{S30} by taking them as dummy variables. However, it did not yield statistically significant results. Consequently, Eq. 2 (referred to as model 2) is employed for the entire dataset.

$$\log(AI) = a + b\log(PGA) + c(M_S - 6) \tag{2}$$

in which AI and PGA are Arias intensity and peak ground acceleration in unit of m/s and g (1g = 9.8 m/s^2), M_S is the surface wave magnitude, a, b and c are regression parameters.

In order to facilitate a comprehensive comparison with previous models, we also establish a basic model that relates AI and PGA, represented by Eq. 3:

$$\log(AI) = a + b\log(PGA) \tag{3}$$

where AI and PGA are Arias intensity and peak ground acceleration in unit of m/s and g (1g = 9.8 m/s^2), a and b are regression parameters. This basic model is also widely recognized by the PGA *versus* the Arias intensity graph from series of data (Lenti and Martino, 2010; 2013).

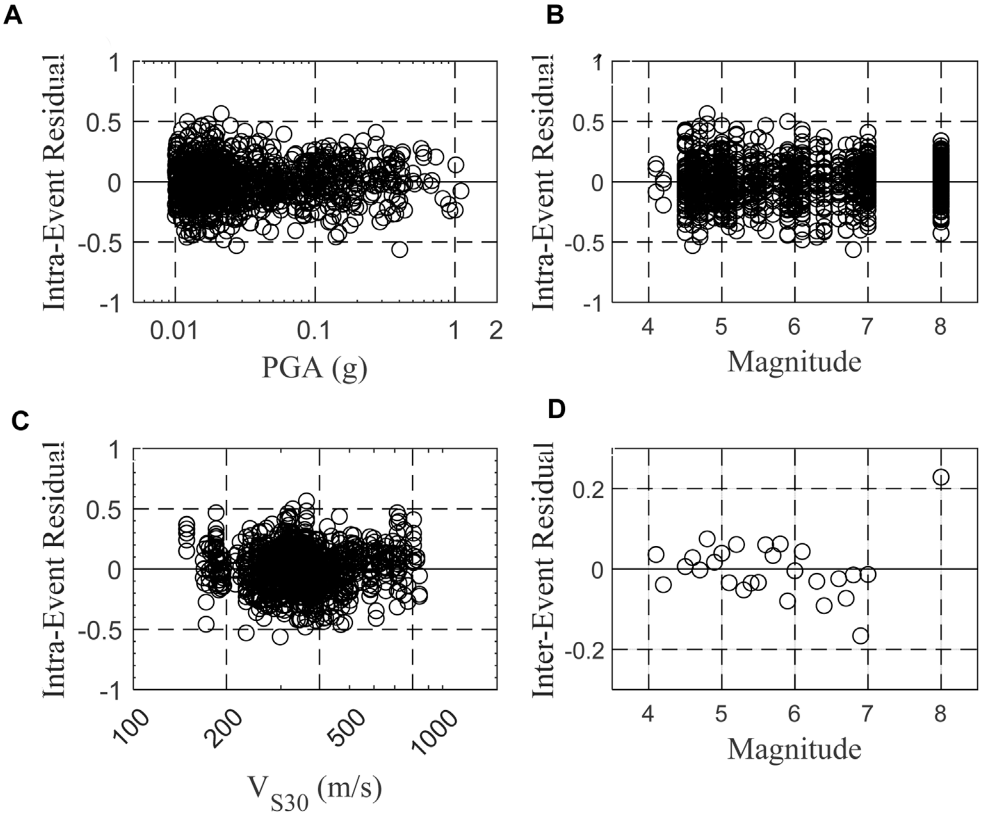

FIGURE 7
Intraevent residuals of model 1 for southwest China against **(A)** PGA,**(B)** magnitude, **(C)** V$_{S30}$, and **(D)** Interevent residual against magnitude.

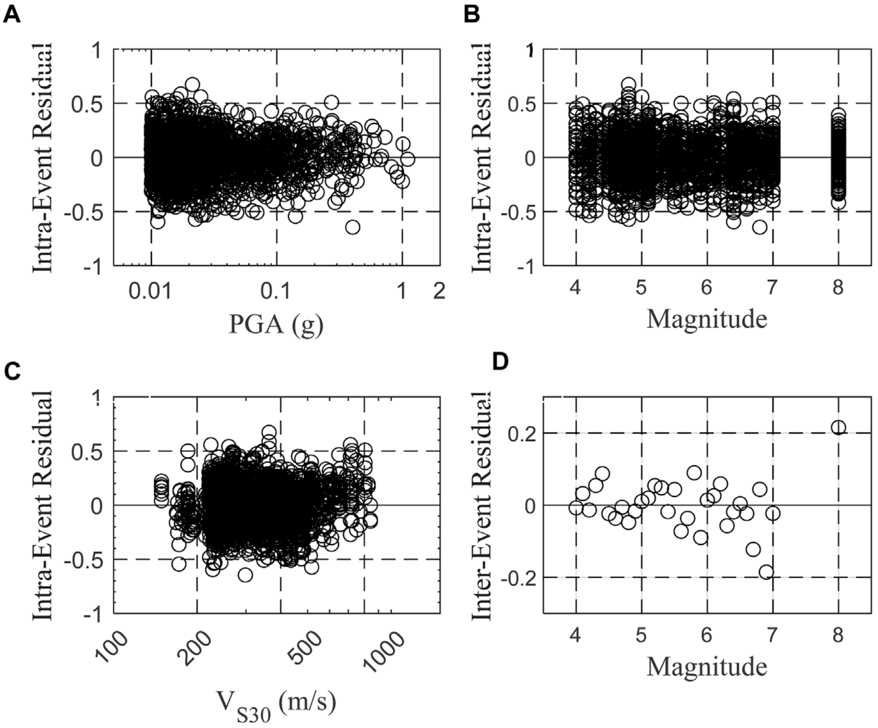

FIGURE 8
Intraevent residuals of model 1 for all west China against **(A)** PGA, **(B)** magnitude, **(C)** V$_{S30}$, and **(D)** Interevent residual against magnitude.

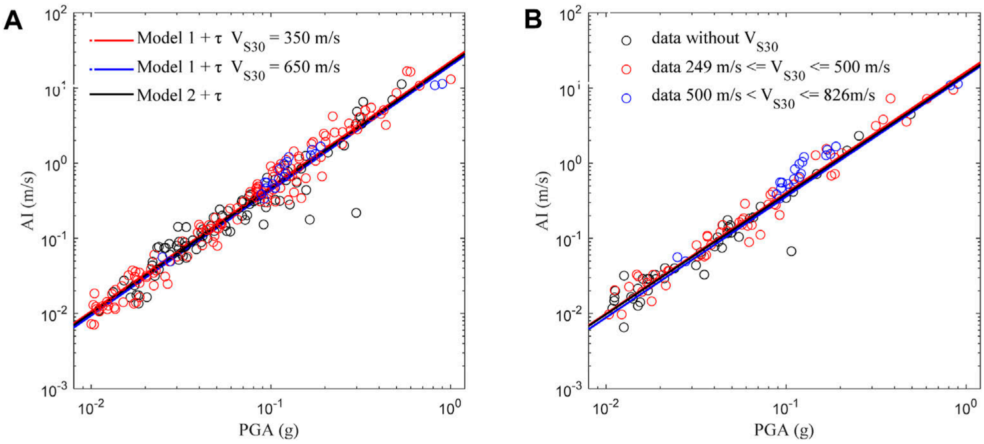

FIGURE 9
Comparison between the observed horizontal **(A)** and vertical **(B)** AI-PGA correlation during the Wenchuan earthquake for model 1 and 2.

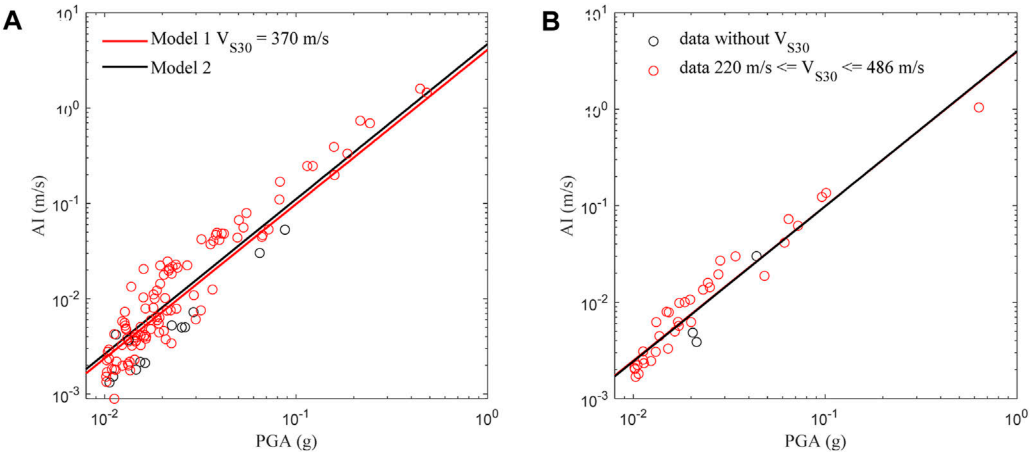

FIGURE 10
Comparison between the observed horizontal **(A)** and vertical **(B)** AI-PGA correlation during the Gashi and Menyuan Ms 6.4 earthquakes for model 1 and 2.

3 Development of correlation relationship

3.1 Empirical relationships of AI and PGA for west China

Using the dataset mentioned above, we develop empirical relationships of AI and PGA for southwest, northwest, and western China, considering both the horizontal and vertical components. These relationships are represented by model 1, model 2, and the basic model. The regression coefficients for model 1 and 2 are obtained through the mix-effect model (Lee et al., 2012), and are presented in Tables 2, 3, respectively. The coefficients for the basic model are determined using the least square method, and are shown in Table 4. The linear equation of the basic model can well explain the logarithm of AI linearly increases with the increase of the logarithm of PGA. However, there are noticeable discrepancies in the intercept (the parameter a in Table 4) and slope (the parameter b in Table 4) among the basic models for the southwest, northwest, and western regions. This discrepancy primarily arises from the lack of consideration for earthquake magnitude. By incorporating earthquake magnitude into the analysis (as demonstrated in Table 3), the regression coefficients a, b, and c of model 2 for the southwest, northwest, and western regions exhibit relatively close values within the same horizontal or vertical group. Without consideration the influence of V_{S30}, the estimated horizontal/vertical AI values are about 182%/177% higher for every one-unit increase in magnitude in northwest China, and about 187%/187% higher in southwest China for a given PGA value. In respect to all western China, the estimated horizontal/vertical AI values are roughly 183%/180% higher for every one-unit increase in magnitude. The goodness-of-fit to the observed data is well demonstrated across the entire range of PGA and magnitude, as is illustrated in Figures 3–5 (only horizontal results are shown here for simplicity).

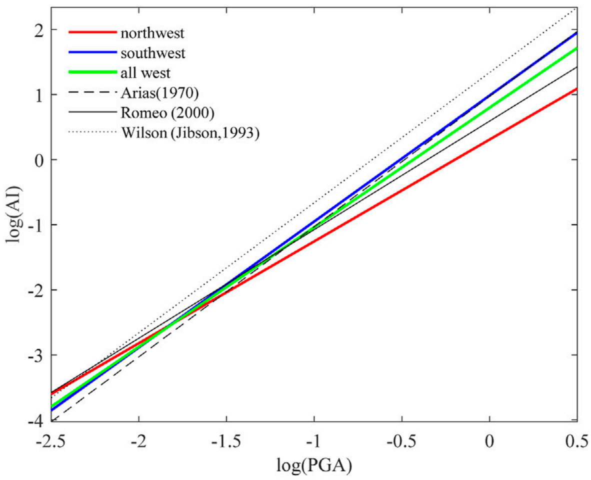

FIGURE 11
Comparison of the basic model for the northwest, southwest and all west China with existing models.

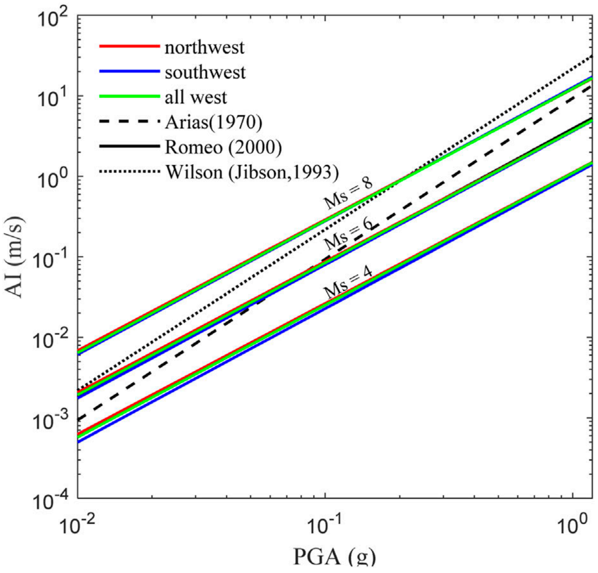

FIGURE 12
Comparison of model 2 for the northwest, southwest and all west China for selected magnitudes (Ms = 4, 6 and 8) with existing models.

The unbiased residuals (data minus model values), as functions of PGA and magnitude, indicate that our models provide a good fit. Furthermore, the addition of earthquake magnitude to the models reduces the standard deviation from over 0.3 to approximately 0.20 log unit, as compared to the basic model. This decrease in the standard deviation of model 2 further affirms the significant influence of earthquake magnitude on the AI-PGA correlation. AI not only increases with increasing PGA but also the increases of magnitude.

For the model with V_{S30} (model 1), the results reveal that the AI-PGA correlation is significantly affected by earthquake magnitude and site parameter V_{S30}. Compared with model 2, the inclusion of V_{S30} reduces the model standard deviation by approximately 0.01 log unit (Table 2). Given the fixed PGA and V_{S30} value, the estimated horizontal/vertical AI values are about 187%/193% higher for one-unit increase in magnitude in northwest China, approximately 187%/186% higher in southwest China, and roughly 188%/191% higher in all western China. Likewise, with the fixed PGA and earthquake magnitude, the estimated horizontal/vertical AI values are about 32%/43% (northwest), 75%/75% (southwest) and 51%/61% (all west) lower for a site with a V_{S30} value of 180 m/s compared to a site with a V_{S30} value of 760 m/s. To evaluate any potential bias in the regression, the residuals are plotted against PGA, magnitude and V_{S30} in Figure 6 (northwest China), Figure 7 (southwest China) and Figure 8 (all west China), respectively. Only the horizontal results are displayed here. Overall, no discernible trend is observed in the residuals as a function of PGA, magnitude, or V_{S30}, suggesting that there is no bias present in the regression. Consequently, these findings demonstrate that AI not only increases with increasing PGA and increasing magnitude but also displays an increase with decreasing V_{S30}.

3.2 Evaluation and comparison with previous models

The goodness-of-fit of the empirical relationships to the data is further demonstrated through the actual data plots. As an example, we can examine the case of the M_S8.0 Wenchuan earthquake that occurred on 12 May 2008 in Sichuan (Figure 9). In Figures 7D, 8D, the intraevent residuals are seen to be close to zero, indicating a good fit, while the interevent residual of Wenchuan earthquake appears relatively large at around 0.2. According to the V_{S30} values of the Wenchuan data, we subdivide the Wenchuan data into two groups: data with V_{S30} values between 249 m/s and 500 m/s, and data with V_{S30} values between 500 m/s and 826 m/s. We plot the prediction of model 1 for southwest China plus its variability of interevent residual with mean V_{S30} values as V_{S30} = 350 m/s and 650 m/s for these two V_{S30} bins. There is slight difference between these two sub-data. The estimated AI from a site with a V_{S30} value of 650 m/s is approximately 80% of that from a site with a V_{S30} value of 350 m/s for Wenchuan earthquake. We can see that this slight difference can be recognized by our model 1. Both model 1 and model 2 provide a good fit with the observations.

The data of the Ms6.4 Gashi earthquake that occurred on 19 January 2020, in Xinjiang, and the Ms6.4 Menyuan earthquake that occurred on 21 January 2016, in Qinghai are plotted together in Figure 10. The V_{S30} values for the Gashi and Menyuan data fall within the range of 220 m/s to 486 m/s, with the exception of three records from the 65PKY strong motion station (with V_{S30} values being 512 m/s) in the Gashi earthquake. The prediction of model 1 using a mean V_{S30} value of 370 m/s is provided. We can see that the logarithms of the observed AI and PGA exhibit a very good linear correlation, with nearly all the data points falling between the predicted lines. This indicates a agreement between the observed data and the predictions from model 1.

In order to assess the effectiveness of our models, we compare our models with previous studies (Arias, 1970; Jibson, 1993; Romeo, 2000, Liu et al., 2016). Except our NGA models, these models are established mostly using horizontal ground motion data sets

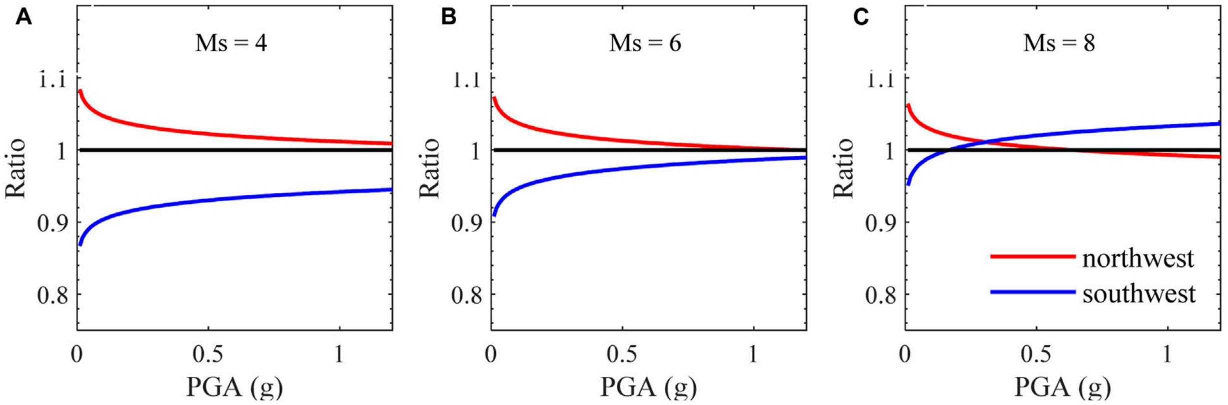

FIGURE 13
Ratios of model 2 for the northwest and southwest to all west China *versus* PGA. See the text for more detail for the definition of the ratio. **(A)** Ms = 4.0. **(B)** Ms = 6.0. **(C)** Ms = 8.0.

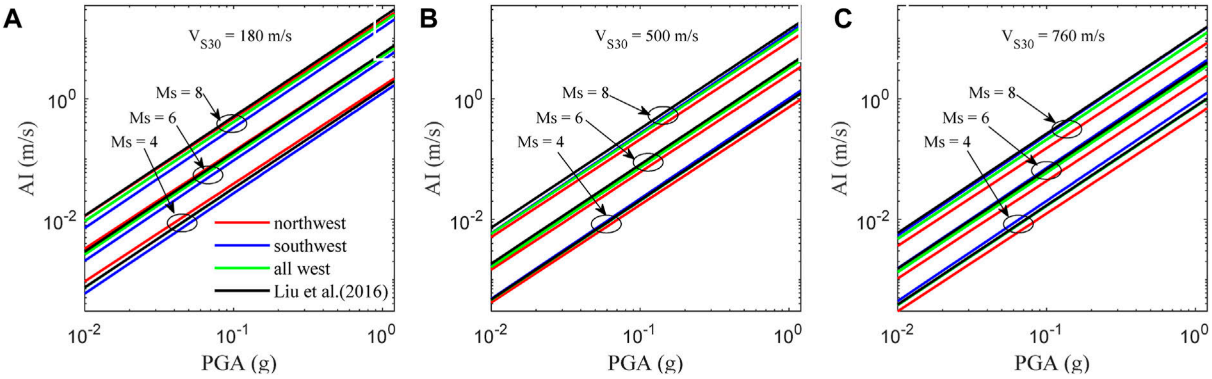

FIGURE 14
Comparison of model 1 for the northwest, southwest, and all west China or selected magnitudes (Ms = 4, 6 and 8) with the NGA model for **(A)** V_{S30} = 300 m/s, **(B)** V_{S30} = 500 m/s, and V_{S30} = 760 m/s.

from different earthquakes, and they did not take into account the influence of earthquake magnitude. So our comparison is focused on horizontal models. Without considering earthquake magnitude, the slope of the regression lines of the basic model (quantified by parameter b in Eq. 3) exhibits significant variation (Figure 11). This can also explain the large discrepancy among our northwest, southwest, and all western models. When we divide the data as sub-data with different magnitudes and consider the magnitude effect on AI-PGA correlation by model 2, we observe a remarkable consistency in the values of parameters b and c in our regression formula (Eq. 2) across earthquakes of varying magnitudes and regions. The differences between these parameter values are nearly within 0.03, as evidenced in Table 3. This consistency is also shown in Figure 12, where the horizontal model lines for the northwest, southwest, and western China regions appear almost parallel.

We future analyze the variability between model 2 for northwest and southwest China. The ratio (defined as the prediction of model 2 for northwest or southwest China divided by the prediction of model 2 for all west China) with respect to PGA is plotted in Figure 13. For northwest China, the mean ratios are 1.023, 1.014, and 1.005 for Ms = 4.0, 6.0 and 8.0, respectively. For northwest China, the mean ratios are 0.928, 0.972, and 0.987 accordingly. Consequently, the means ratios of northwest to southwest are approximately 1.102, 1.043, and 0.987 for model 2 with Ms = 4.0, 6.0 and 8.0, respectively. These results reveal that the AI-PGA correlation is region-dependent to some extent, as evidenced by the slightly discrepancy between model 2 of northwest and southwest China.

In this study, our model 1 for northwest, southwest, and all western China utilizes the same function form as our NGA model (Liu et al., 2016). Here, we make a future comparison between our relationships with our NGA relationships (Figure 14, horizontal component only). The result confirms that AI is not only increases with increasing PGA, but also increases with increasing earthquake magnitude and decreasing V_{S30}. These tendencies are consistent across all these four relationships, but are different in details. The ratio (defined as the prediction of model 1 divided by the prediction of NGA model) with respect to PGA is plotted in Figure 15. Given the fixed V_{S30} values, the mean ratios of northwest, southwest, and all west China are generally decrease with the increase of earthquake

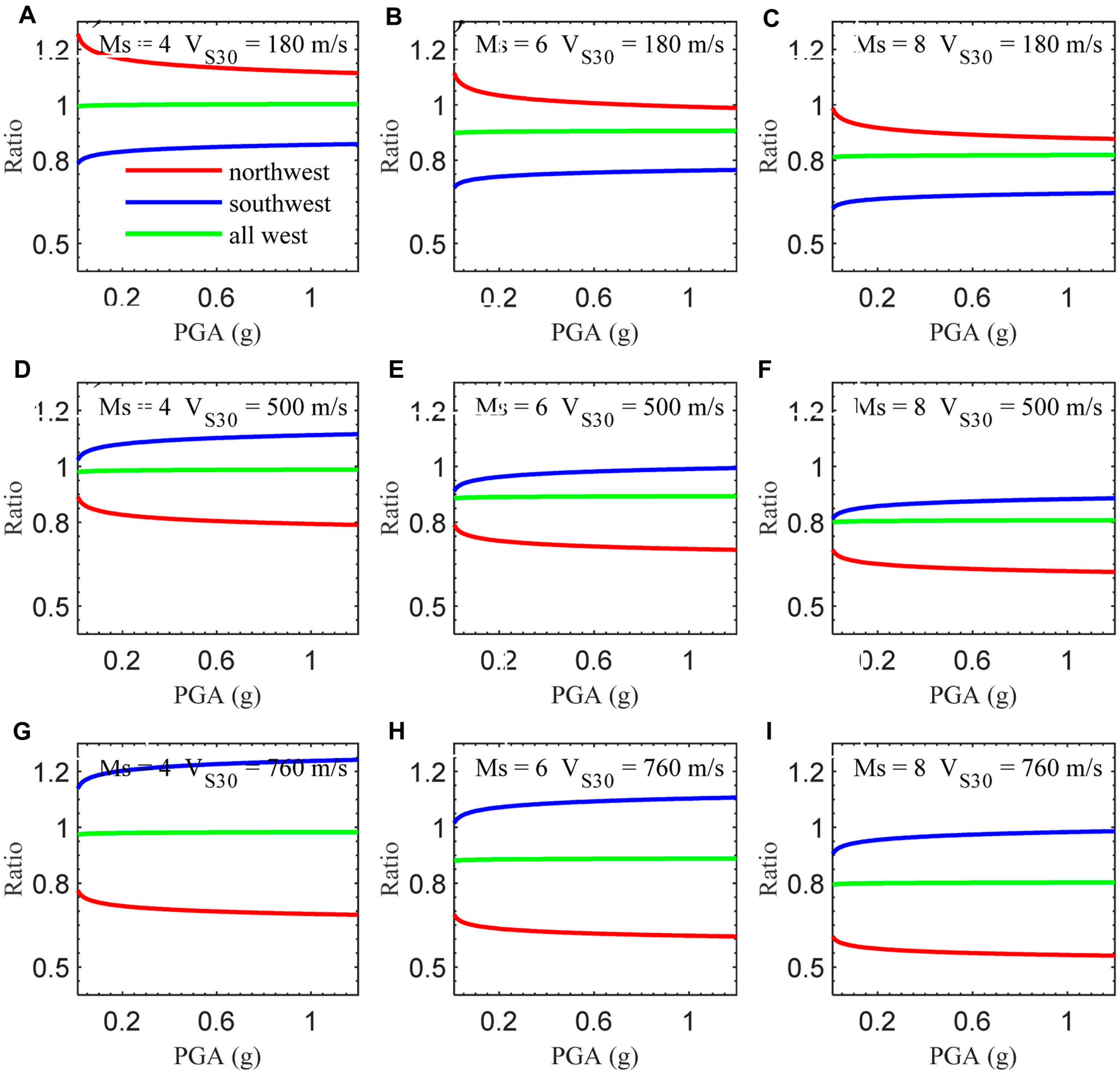

FIGURE 15
Ratios of model 1 for the northwest, southwest, and all west China to the NGA model *versus* PGA. See the text for more detail for the definition of the ratio. **(A)** Ms = 4.0 and V_{S30} = 180 m/s. **(B)** Ms = 6.0 and V_{S30} = 180 m/s. **(C)** Ms = 8.0 and VS30 = 180 m/s. **(D)** Ms = 4.0 and V_{S30} = 500 m/s. **(E)** Ms = 6.0 and V_{S30} = 500 m/s. **(F)** Ms = 8.0 and V_{S30} = 500 m/s. **(G)** Ms = 4.0 and V_{S30} = 760 m/s. **(H)** Ms = 6.0 and VS30 = 760 m/s. **(I)** Ms = 8.0 and V_{S30} = 760 m/s.

magnitude from Ms = 4.0 to 6.0, and 8.0, and the difference among these three regions remain relatively constant. Take V_{S30} =180 m/s as an example, the mean ratios for northwest, southwest, and all western China are 1.142, 0.844, and 1.001, respectively, for Ms = 4.0. For Ms = 6.0, these values become1.013, 0.752, and 0.905. For Ms = 8.0, the mean ratios are 0.899, 0.670, and 0.817. But the value of mean ratio northwest divided by that of southwest keeps remains 1.35. Conversely, when we fix the earthquake magnitude, the changes in mean ratios of northwest and southwest China exhibit a reversed trend adjustment. Take Ms = 6.0 as an example. The mean ratios for northwest shift from 1.013 (V_{S30} = 180 m/s) to 0.892 (V_{S30} = 500 m/s) and 0.625 (V_{S30} = 760 m/s), indicating a decreasing trend. In contrast, the mean ratios for southwest change from 0.752 (V_{S30} = 180 m/s) to 0.977 (V_{S30} = 500 m/s) and 1.088 (V_{S30} = 760 m/s), indicating an increasing trend.

4 Conclusion

In this paper, based on our previous empirical relation models between AI and PGA using the NGA database, we develop empirical relationships between AI and PGA for western China. This effort focuses on strong motion records with PGA ≥0.01g, obtained from eight provinces in southwest China (Yunnan, Sichuan) and northwest China (Gansu, Shaanxi, Ningxia, Qinghai, Inner Mongolia, and Xinjiang). This large set of data consists of

3,169 horizontal and 979 vertical strong motion records from 274 earthquakes with surface wave magnitude (M_S) ranging from 4.0 to 8.0. All the records are classed into generic site classes (rock and soil), and V_{S30} values are assigned to 2,248 horizontal (70.9% of the total) and 670 vertical (68.4% of the total) records. Empirical relationships are developed to estimate AI as a function of PGA (basic model), PGA and M_S (model 2), PGA, M_S, and V_{S30} (model 1) for the southwest, northwest, and west China, both for horizontal and vertical components. The results confirm that the logarithm of AI increases linearly with the increase of the logarithm of PGA and M_S, and decreases with the logarithm of V_{S30}. However, the influence of site conditions on AI-PAG relationships cannot be recognized by the simple generic rock and soil site classes. The epicenter distance has little effect on the AI-PAG relationships. Furthermore, the significant difference between the model 1 of southwest and northwest reveals that the AI-PGA correlation is region-dependent, which is chiefly attributed to local site conditions. The empirical AI-PGA relationships presented in this paper enable one way of estimating AI from PGA for western China. It will also contribute to a better understanding of the proposal of AI attenuation equations, which is one of the objectives of the next-generation seismic zonation map of China.

5 Discussion

In recent years, numerous GMPEs have been developed for PGA and AI (Boore et al., 2014; Zach et al., 2017; Du and Wang, 2017; Farhadi and Pezeshk, 2020; Bahrampouri et al., 2021; Davatgari-Tafreshi and Bora, 2023; Hu et al., 2023). These studies implicitly suggest that attenuation characteristic of PGA and AI, such as the magnitude-scaling effects and site effects are different (Campbell and Bozorgnia, 2012). Similarly, our proposed models demonstrate a significant dependence of AI-PGA correlation on earthquake magnitude and the V_{S30} value of the site. The distributions of the residuals of model 2 against magnitude and the residuals of model 1 against magnitude and V_{S30} exhibit no observable trend or change, indicating the absence of bias in our relationships. Notably, the model standard deviation decreases by 0.1 and 0.01 log unit in sequence, starting from the basic model to model 2 and model 1. This reduction signifies that our relationships can effectively identify the discrepancies in AI-PGA correlation across different earthquakes and site conditions, representing a significant advancement.

However, it is worth noting that the AI-PGA correlation does exhibit a certain degree of region-dependent. As we can see from Table 3, the values of parameters b and c in Eq. 2 tend to be consistent for earthquakes of different magnitudes and different regions, with their differences almost within 0.03. In Figure 13, the mean predicted value for northwest China from model 2 is about 110.0%, 104.3% and 98.7% of that for southwest China, for M_S = 4.0, 6.0 and 8.0, respectively. It shows that there is a slightly discrepancy between model 2 of northwest and southwest China. With regard to model 1, the discrepancy between northwest China and southwest China can be up to 30%–40% as illustrated in Figure 15. As listed in Table 2, the difference in the values of parameter b between the northwest and southwest is 0.043, while the difference in the values of parameter c is 0.001. The values of parameter d for the northwest and southwest China are −0.790 and −0.198, respectively. This discrepancy in parameter d plays a significant role in determining the difference between the models. The V_{S30} term, expressed as $d\log(Vs30/500)$ in Eq. 1, is plotted against V_{S30} for model 1 of northwest, southwest China, and the NGA model (Liu et al., 2016). It shows that the V_{S30} term of model 1 for northwest China has the highest descent rate against V_{S30}, while that of southwest China has the lowest descent rate against V_{S30} (Figure 16). This discrepancy helps to explain the above mentioned reverse trend adjustment observed in the mean ratios of northwest and southwest China to the NGA model for V_{S30} values of 180 m/s, 500 m/s, and 760 m/s, given a fixed magnitude.

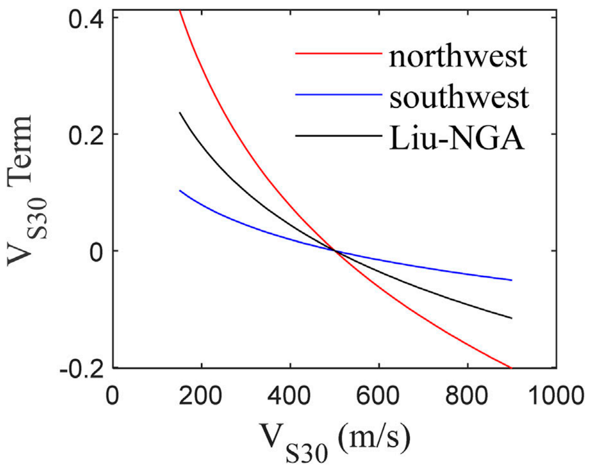

FIGURE 16
Variation of the V_{S30} term of model 1 for northwest, southwest China, and the NGA model against V_{S30}.

This means that the region-dependent of AI-PGA correlation is primarily attributed to the local site conditions, represented by V_{S30} in this study. The research conducted by Li et al. (2020b) indicated that geotechnical types and soil depths have significant effects on the reliability of the relationship between shear wave velocity and buried depth. Though V_{S30} provides unambiguous definitions of site classes, there might still be high uncertainties associated with determining soil type by V_{S30}. For the strong motion stations located in the plateau basin of northwest China or ravine region of southwest China, even if they have the same V_{S30} values, the soil depths in the northwest basin region (which belongs to a sedimentary environment) may be greater than those in the ravine region of southwest China (which is predominantly dominated by downward cutting erosion). This could potentially explain why the influence of site conditions on AI-PGA relationships cannot be adequately captured by the currently available rough and simplistic rock and soil site classes.

Data availability statement

The datasets presented in this article are not readily available because The strong-motion data used in this research are provided by the Strong Motion observation Center, Institute of Engineering Mechanics, China Earthquake Administration. Please contact them to apply for use. Requests to access the datasets should be directed to csmnc@iem.ac.cn.

Author contributions

JL: Conceptualization, Formal Analysis, Funding acquisition, Investigation, Methodology, Software, Writing–original draft, Writing–review and editing. BZ: Data curation, Writing–original draft, Writing–review and editing. XZ: Data curation, Writing–original draft, Writing–review and editing.

Funding

The author(s) declare that financial support was received for the research, authorship, and/or publication of this article. This study was supported by the by the National Key R&D Program of China (Grants Nos. 2022YFC3003503, 2022YFC3004302), China Geological Survey Project (Grants No. DD20221738), and the scientific research project (Grants No. 86) of Institute of Geomechanics.

Acknowledgments

We thank Professor Yefei Ren, Ruizhi Wen, and their research team for the verification of the strong motion records.

Conflict of interest

The authors declare that the research was conducted in the absence of any commercial or financial relationships that could be construed as a potential conflict of interest.

Publisher's note

Supplementary material

The Supplementary Material for this article can be found online at: https://www.frontiersin.org/articles/10.3389/feart.2024.1434194/full#supplementary-material

References

Arias, A. (1970). "A measure of earthquake intensity," in *Seismic design for nuclear power plants*. Editor R. J. Hansen (Cambridge, Massachusetts: MIT Press), 438–483.

Bahrampouri, M., Rodriguez-Marek, A., and Green, R. A. (2021). Ground motion prediction equations for Arias Intensity using the Kik-net database. *Earthq. Spectra* 37 (1), 428–448. doi:10.1177/8755293020938815

Boore, D. M., Stewart, J. P., Seyhan, E., and Atkinson, G. M. (2014). NGA-West2 equations for predicting PGA, PGV, and 5% damped PSA for shallow crustal earthquakes. *Earthq. Spectra* 30 (3), 1057–1085. doi:10.1193/070113eqs184m

Bradley, B. A. (2015). Correlation of Arias intensity with amplitude, duration and cumulative intensity measures. *Soil Dyn. Earthq. Eng.* 78, 89–98. doi:10.1016/j.soildyn.2015.07.009

Campbell, K. W., and Bozorgnia, Y. (2012). A comparison of ground motion prediction equations for Arias intensity and cumulative absolute velocity developed using a consistent database and functional form. *Earthq. Spectra* 28 (3), 931–941. doi:10.1193/1.4000067

Cheng, Y., Liu, T., Wang, J., and Ning, C. L. (2021). Empirical correlations of spectral input energy with peak amplitude, cumulative, and duration intensity measures. *Bull. Seismol. Soc. Am.* 112, 978–991. doi:10.1785/0120210164

Chousianitis, K., Gaudio, V. D., Sabatakakis, N., Kavoura, K., Drakatos, G., Bathrellos, G. D., et al. (2016). Assessment of earthquake-induced landslide hazard in Greece: from Arias intensity to spatial distribution of slope resistance demand. *Bull. Seismol. Soc. Am.* 106 (1), 174–188. doi:10.1785/0120150172

Davatgari-Tafreshi, M., and Bora, S. S. (2023). Empirical ground-motion models (GMMs) and associated correlations for cumulative absolute velocity, Arias intensity, and significant durations calibrated on Iranian strong motion database. *Bull. Earthq. Eng.* 21, 4139–4166. doi:10.1007/s10518-023-01708-9

Du, W., and Wang, G. (2017). Prediction equations for ground-motion significant durations using the NGA-west2 database. *Bull. Seismol. Soc. Am.* 107 (1), 319–333. doi:10.1785/0120150352

Farhadi, A., and Pezeshk, S. (2020). A referenced empirical ground-motion model for Arias intensity and cumulative absolute velocity based on the NGA-East database. *Bull. Seismol. Soc. Am.* 110 (2), 508–518. doi:10.1785/0120190267

Hu, J. J., Hu, L., Jin, C. Y., Wang, Z. W., Ding, Y. T., and Tang, C. (2023). Offshore ground motion models for Arias intensity and cumulative absolute velocity in the Japan trench area. *J. Earthq. Eng.* 27 (14), 4005–4023. doi:10.1080/13632469.2022.2155732

Ji, K., Ren, Y., and Wen, R. (2021). Empirical correlations between generalized ground-motion intensity measures for earthquakes in China. *Bull. Seismol. Soc. Am.* 111 (1), 274–294. doi:10.1785/0120200179

Ji, K., Ren, Y. F., and Wen, R. Z. (2017). Site classification for National Strong Motion Observation Network System (NSMONS) stations in China using an empirical H/V spectral ratio method. *J. Asian Earth Sci.* 147, 79–94. doi:10.1016/j.jseaes.2017.07.032

Ji, K., Ren, Y. F., Wen, R. Z., Zhu, C. B., Liu, Y., and Zhou, B. F. (2022). HVSR-based site classification approach using general regression neural network (GRNN): case study for China strong motion stations. *J. Earthq. Eng.* 26 (16), 8423–8445. doi:10.1080/13632469.2021.1991520

Jibson, R. W. (1993). Predicting earthquake-induced landslide displacements using Newmark's sliding block analysis. *Transp. Res. Rec.*, 9–17.

Lee, C. T., Hsieh, B. S., Sung, C. H., and Lin, P. S. (2012). Regional Arias intensity attenuation relationship for Taiwan considering V_{S30}. *Bull. Seismol. Soc. Am.* 102 (1), 129–142. doi:10.1785/0120100268

Lenti, L., and Martino, S. (2010). New procedure for deriving multifrequential dynamic equivalent signals (LEMA_DES): a test-study based on Italian accelerometric records. *Bull. Earthq. Eng.* 8, 813–846. doi:10.1007/s10518-009-9169-7

Lenti, L., and Martino, S. (2013). A parametric numerical study of the interaction between seismic waves and landslides for the evaluation of the susceptibility to seismically induced displacements. *Bull. Seismol. Soc. Am.* 103 (1), 33–56. doi:10.1785/0120120019

Li, M., Li, X. J., and L, J. H. (2016). Empirical relationships of earthquake magnitudes for local regions considering the active tectonic boundary areas. *Acta Seismol. Sin.* 38 (2), 157–166. doi:10.11939/jass.2016.02.001

Li, Y. Z., Ying, N., and Li, X. H. (2014). Review of the conversional relationship for different magnitude scales. China. *Earthq. Eng. J.* 36 (1), 80–87. (in Chinese with English abstract). doi:10.3969/i.issn.1000-0844.2014.01.0080

Li, M., Yang, L. G., Chen, H. P., Sheng, T. Q., and Agency, Z. E. (2020b). Relationship between shear wave velocity and soil depth of typical soil layers in Hangzhou area, Technol. *Earthq. Disaster Prev.* 15 (1), 77–88. (in Chinese with English abstract). doi:10.11899/zzfy20200108

Li, Xi. L., Zhai, C. H., Wen, W. P., and Xie, L. L. (2020a). Ground motion prediction model for horizontal PGA, 5% damped response spectrum in sichuan-yunnan region of China. *J. Earthq. Eng.* 24 (11), 1829–1866. doi:10.1080/13632469.2018.1485600

Liu, J. M., Gao, M. T., and Xie, J. J. (2015). Spatial variability and attenuation of Arias intensity during the 1999 chi-chi Mw 7.6 earthquake, taiwan. *Bull. Seismol. Soc. Am.* 105, 1768–1778. doi:10.1785/0120140157

Liu, J. M., Wang, T., Shi, J. S., Xin, P., and Wu, S. R. (2018). The influence of different Newmark displacement models on seismic landslide hazard assessment: a case study of Tianshui area, China. *J. Geomech.* 24 (1), 87–95. (in Chinese with English abstract). doi:10.12090/j.issn.1006-6616.2018.24.01.010

Liu, J. M., Wang, T., Wu, S. R., and Gao, M. T. (2016). New empirical relationships between Arias intensity and peak ground acceleration. *Bull. Seismol. Soc. Am.* 106 (5), 2168–2176. doi:10.1785/0120150366

Liu, P., and Ren, T. J. (2022). Arias intensity attenuation relationship in Sichuan–Yunnan region, China. *Bull. Earthq. Eng.* 20 (12), 6377–6406. doi:10.1007/s10518-022-01467-z

Macedo, J., Liu, C., and Abrahamson, N. A. (2022). On the interpretation of conditional ground-motion models. *Bull. Seismol. Soc. Am.* 112 (5), 2580–2586. doi:10.1785/0120220006

Ren, Y., Zhang, Y., Ji, K., Wen, R., Kishida, T., and Yao, X. (2023). Site classification scheme based on geological age and genesis for Xinjiang and the Capital Metropolitan areas of China. *Earthq. Spectra* 40, 174–199. doi:10.1177/87552930231213363

Romeo, R. (2000). Seismically induced landslide displacements: a predictive model. *Eng. Geol.* 58, 337–351. doi:10.1016/s0013-7952(00)00042-9

Tao, D., Ma, Q., Li, S., Xie, Z., Lin, D., and Li, S. (2020). Support vector regression for the relationships between ground motion parameters and macroseismic intensity in the Sichuan–Yunnan region. *Appl. Sci.* 10 (9), 3086. doi:10.3390/app10093086

Travasarou, T., Bray, J. D., and Abrahamson, N. A. (2003). Empirical attenuation relationship for Arias intensity. *Eng. Struct. Dynam* 32, 1133–1155. doi:10.1002/eqe.270

Wang, G., and Du, W. (2013). Spatial cross-correlation models for vector intensity measures (PGA, Ia, PGV, and SAs) considering regional site conditions. *Bull. Seismol. Soc. Am.* 103 (6), 3189–3204. doi:10.1785/0120130061

Xie, J. J., Li, X. J., Wen, Z. P., Jia, L., An, Z., Cui, J. W., et al. (2022). Soil profile database and site classification for national strong-motion stations in western China. *Seismol. Res. Lett.* 93 (3), 1930–1942. doi:10.1785/0220210271

Yu, Y. X., and Wang, S. Y. (2006). Attenuation relationship for horizontal peak ground acceleration and response spectrum in eastern and western China, Technol. *Earthq. Disaster Prev.* 1 (3), 207–217. (in Chinese with English abstract). doi:10.3969/j.issn.1673-5722.2006.03.005

Zach, B., Shideh, D., Abbie, L., Keith, P., Zan, K., and Brendon, B. (2017). Ground motion prediction equations for Arias intensity, cumulative absolute velocity, and peak incremental ground velocity for rock sites in different tectonic environments. *Bull. Seismol. Soc. Am.* 107 (5), 2293–2309. doi:10.1785/0120160388

Zhang, B., Li, X. J., Yu, Y. X., Sun, J. Z., Rong, M. S., and Chen, S. (2023). A new ground-motion model to predict horizontal PGA, PGV, and spectral acceleration for small-to-moderate earthquakes in the capital circle region of China. *J. Asian Earth Sci.* 257, 105853. doi:10.1016/j.jseaes.2023.105853

Zhang, B., Yu, Y. X., Li, X. J., and Wang, Y. (2022). Ground motion prediction equation for the average horizontal component of PGA, PGV, and 5% damped acceleration response spectra at periods ranging from 0.033 to 8.0s in southwest China. *Soil Dyn. Earthq. Eng.* 159, 107297. doi:10.1016/j.soildyn.2022.107297

Zhang, B., Yu, Y. X., Li, X. J., Wang, Y. S., and Rong, M. S. (2021). Ground motion attenuation relationship of horizontal component of PGV and PGD in southwest China. *Chin. J. Geophys.* 64 (8), 2733–2748. (in Chinese with English abstract). doi:10.6038/cjg2021O0445

frontiers | Frontiers in Earth Science

TYPE Original Research
PUBLISHED 24 July 2024
DOI 10.3389/feart.2024.1436970

OPEN ACCESS

EDITED BY
Chong Xu,
Ministry of Emergency Management, China

REVIEWED BY
Huajin Li,
Chengdu University, China
Dan Ma,
China University of Mining and Technology, China

*CORRESPONDENCE
Bin Gong,
✉ bin.gong@brunel.ac.uk

†These authors have contributed equally to this work

RECEIVED 22 May 2024
ACCEPTED 01 July 2024
PUBLISHED 24 July 2024

CITATION
Zhang S, Wei X, Tang L, Duan W, Gong B, Mu C and Zhang S (2024), Study on the early warning of cracking and water inrush risk of coal mine roof and floor.
Front. Earth Sci. 12:1436970.
doi: 10.3389/feart.2024.1436970

Study on the early warning of cracking and water inrush risk of coal mine roof and floor

Shichao Zhang[1,2†], Xiuqi Wei[3†], Liming Tang[4], Wenshuo Duan[5], Bin Gong[6]*, Chaomin Mu[1,7] and Shujin Zhang[8]

[1]Institute of Energy, Hefei Comprehensive National Science Center, Hefei, China, [2]School of Public Safety and Emergency Management, Anhui University of Science and Technology, Huainan, China, [3]Anhui Zhibo Photoelectric Technology Co., Ltd., Hefei, China, [4]School of Environment and Civil Engineering, Chengdu University of Technology, Chengdu, China, [5]School of Infrastructure Engineering, Dalian University of Technology, Dalian, China, [6]College of Engineering, Design and Physical Sciences, Brunel University London, Uxbridge, United Kingdom, [7]School of Safety Science and Engineering, Anhui University of Science and Technology, Huainan, China, [8]Guizhou Mine Safety Scientific Research Institute Co., Ltd., Guiyang, China

Microseismic monitoring has proven to be an effective approach for detecting and preempting water inrush incidents within mining operations. However, challenges persist, particularly in terms of relying on a singular early warning index and the complexities involved in quantification. In response to these obstacles, a dedicated investigation was undertaken against the backdrop of mining activities at the 11,023 working face of Paner Coal Mine. Primarily, a novel methodology for categorizing the roof and floor into distinct zones was established based on the vertical distribution of microseismic events. Furthermore, this study delves into the dynamic evolution of key source parameters, such as microseismic energy, apparent stress, and apparent volume, amidst mining disturbances, enabling a comprehensive evaluation of the risk associated with roof and floor cracking, as well as potential water inrush incidents. A groundbreaking approach to early warning was proposed, operating on three pivotal dimensions: the depth of fractures, the intensity of fractures, and the likelihood of water inrush. Through rigorous validation during mining operations at the 11,023 working face, the efficacy was substantiated. Ultimately, the achievements offer invaluable insights and practical guidance for the advancement and implementation of water inrush early warning systems in coal mining contexts.

KEYWORDS

coal mine, water inrush, early warning, microseismic monitoring, periodic pressure

1 Introduction

Water inrush is a common geological disaster in coal mines. During the process of mining, it is caused by the combined action of disturbed stress and water pressure, leading to the failure of surrounding rocks and the sudden inrush of a large amount of groundwater into the mine (Yin et al., 2022; Li et al., 2024). The water inrush disaster brings extremely heavy economic losses and casualties to coal mining. In recent years, with the exhaustion of shallow coal resources and the increase of mining intensity, coal mine water disasters have become more severe. The incubation of coal mine water inrush is affected by many factors and is a complex process involving the gestation, development and formation of water channels. Researchers have carried out in-depth research on the mechanism of water inrush and reinforcement technology (Kang et al., 2023; Ren et al., 2023; Wang et al., 2023). Zhang (2005) revealed that reduction of confinement due to mining is a major cause of water-conducting failure in the floor strata. Ding et al. (2014) pointed out that high-intensity mining of water-rich coal seams can lead to changes in stratum behavior, such as roof caving and water inrush. Zhang et al. (2017) verified the role of stress fields and seepage fields in the formation of water channels through physical experiments. Mining-induced fractures in the surrounding rock of a coal mine roof connect and extend upward to form these water channels (Sun et al., 2022). Based on a large number of cases of water inrush in karst tunnels, Li et al. (2016) proposed that the main factors affecting water inrush are karst hydrogeology and engineering disturbance. Li et al. (2021a) proposed a logistic regression model to describe the effects of compressive stress and grain size distribution on permeability and nonlinear flow characteristics of fractured rock mass. Ma et al. (2022a), Ma et al. (2022b) conducted one-dimensional radial seepage test and numerical simulation to study the process and law of water channel formation in fault rock until water inrush. In summary, water inrush is closely related to the redistribution of stress fields caused by excavation, cracking damage to surrounding rocks.

It can be seen that micro-fractures are an important precursor feature of water inrush disasters (Zhang et al., 2023; Liu et al., 2024; Shen, 2024; Zhang et al., 2024). Therefore, to monitor and forecast coal mine water inrush disasters, in addition to monitoring water flow, temperature, and pressure, it is crucial to understand the essential mechanism and precursor patterns of micro-fractures for developing analytical and forecasting methods (Li et al., 2021b; Feng et al., 2022; Gong et al., 2022; Feng et al., 2023a; Gong et al., 2024). Microseismic monitoring technology has been proved to be an effective method for coal mine water inrush monitoring and early warning (Chen et al., 2023; Wang et al., 2024). It can accurately locate the spatial position of water inrush channels, and real-time monitor the occurrence and expansion of rock bursting and micro-damage. For example, Liu et al. (2023) used a microseismic monitoring system to accurately predict and locate the water inrush path in a coal mine. Tu et al. (2021) proposed an improved microseismic monitoring technology scheme for locating the spatial position of water inrush channels in tunnel construction. Wang et al. (2021) constructed a comprehensive intelligent early warning recognition model for coal mine water inrush based on analysis of multiple precursor factors using long-term monitoring data. Ma et al. (2021) used microseismic monitoring, theoretical calculation and numerical simulation methods to analyze the failure characteristics of coal seam floor, providing reference for preventing underground water inrush disasters. Yu et al. (2022) proposed the use of mixed frequency microseismic waveform recognition to identify potential water hazards and achieve early warning. Yin et al. (2023) introduced a data-driven method that combines machine learning and deep learning models to analyze microseismic events, improving the accuracy and effectiveness of water inrush prediction. However, the precursor early warning of water inrush based on microseismic monitoring faces challenges in quantifying warning indicators. Water inrush is an occasional disaster, making it difficult to determine the threshold values of disaster warning indicators based on normal microseismic activity characteristics.

In addition, the division of three zones at the roof and floor of coal mines is also conducive to risk assessment and prediction of water inrush. Jing et al. (2006) emphasized the role of geological features such as collapsing rocks and rock layer separation, as well as the impact of overlying strata movements, on the formation of water inrush. Qiu et al. (2022) highlighted the weakening effect of faults on the key stratum, leading to multiple separation layers and increased water-conducting fractures. Wu et al. (2022) simulated the nonlinear water inrush process by solving the Darcy-Brinkman flow equation for the host rock and the fault zone based on the concept of "Three Zones" fault structure. Wei et al. (2010) predicted the risk of water inrush in the water-bearing strata of the coal seam floor based on the "lower three zones" theory. Building on the three-zone theory, Cheng et al. (2017) proposed a more detailed zoning method based on the elevation distribution of microseisms. It can be seen that microseismic monitoring results can help divide three zones and cracking depth at roof and floor, assisting in dynamic early warning of water inrush risks. The division of the three zones is mainly from the perspective of microseismic spatial distribution and disturbance range of roof and floor to assist water inrush early warning. Together, they used the microseismic location results to measure the failure depth of the roof and floor.

To address the issues and shortcomings in water inrush warning, this study was conducted against the background of the 11,023 working face mining in Paner Coal Mine. The roof and floor three-zone classification criteria were established based on the spatial distribution of microseismic activities during initial back mining. The evolution patterns of microseismic events in the roof and floor under mining disturbance were analyzed. On this basis, a comprehensive warning method for roof and floor cracking and water inrush risk was established and applied for verification. The research results can provide references for the research and application of coal mine water inrush warning.

2 Engineering background

2.1 Working face overview

The 11,023 working face of Paner Coal Mine is located in the eastern mining area, Panji District, Huainan City, Anhui Province. The designed length of the upper gate road is 580 m, the lower gate road is 760 m, the cutting length is 130 m, and the working face elevation is −442.8 to −474.1 m. The working face is arranged along the strike, with a mining direction length of 605 m, an inclined width of 125 m, an area of 75,625 m^2, and it employs the retreat longwall mining method and fully mechanized top coal caving mining process. The entire caving method is used to manage the roof. The third coal seam thickness in the excavation block of the 11,023 working face ranges from 4.0 to 5.8 m, with an average thickness of 5.0 m. The coal seam angle is 3–15°, with an average of 9°. The overlying fourth coal seam at −350 to −400 m stage has been mined. The underlying 11,221 working face has been connected. The plan view of the 11,023 working face is shown in Figure 1.

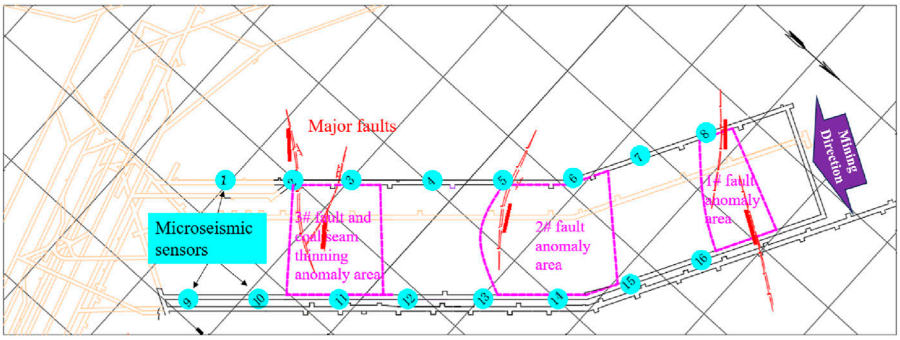

FIGURE 1
Plan view of the 11,023 working face.

2.2 Geological survey

Within the mining block of the working face, the immediate roof consists of dark gray mudstone with a thickness of approximately 1.1–12.0 m and an average thickness of 7.0 m. The compressive strength ranges from 22.2 to 35.1 MPa. The old roof is composed of medium-fine sandstone with a thickness of 7.9–17.0 m and an average thickness of 12.0 m. The direct floor is mudstone with a thickness of 1.0–2.0 m and an average thickness of 1.5 m. The average distance between the third coal seam and the underlying first coal seam is 1.5 m, and the distance from the first coal bottom to the C_3I limestone roof is 13.20–19.37 m. Details are provided in Table 1. Based on the above information, the roof of the third coal seam is composed of mudstone, sandstone, and medium-fine sandstone. The lithology varies greatly, the thickness is extremely unstable, mostly mud-calcium cemented, and a small amount is silica-cemented. It belongs to an unstable to moderately stable roof, and the overlying rock lithology is classified as medium-hard to soft and weak types. According to the drilling and geological data analysis of the 11,023 bottom extraction roadway, the working face is located in the southern wing of the Panji anticline, and the geological structure is relatively complex. There are 21 faults in the mining area, with a maximum fault drop of 5 m, including three faults with a drop greater than 3 m.

2.3 Threat of water hazards

Based on mining data, surface drilling, geophysical data, and the analysis of the results of surface area management projects, there are no collapsed columns or water-conducting faults within the scope of the working face. The main factors affecting the advance of the working face are water from Taiyuan Group limestone karst, water from sandstone fractures in the roof, and fault water. The Taiyuan Formation limestone can be divided into three groups from top to bottom, namely, Group C_3I, Group C_3II, and Group C_3III, with each group containing 3-6 layers of limestone. They are all weakly water-rich. The bottom of 11,023 working face is 12.2–32.0 m away from Group C_3I limestone, with an average distance of 20.7 m. During excavation, the direct source of water supply is the karst water from Group C_3I limestone in the floor, which is the main threat of water damage during the mining period.

According to exploration data, Group C_3I limestone includes four layers of limestone, with C_3 I^1 and C_3I^2 as thin layers without water, and C_3I^{3upper} and C_3I^{3lower} as thicker layers with slight water content. The thickness of Group C_3I is 16.9–43.1 m with an average of 32.5 m, and the total thickness of limestone is 11.4–23.1 m with an average of 16.1 m. Two pumping tests and one water injection test were conducted within the mining area for Group C_3I limestone, with unit water inflow Q = 0.000009–0.0003L/(s.m), permeability coefficient K = 0.000021–0.0013 m/d, weak water richness, and poor water conductivity; the mineralization degree is 2.104–2.980 g/L, and the water quality is Cl-HCO3-K+Na type with a temperature range of 38°C–42°C.

3 Fiber optic microseismic monitoring system

When cracks occur, propagate, and friction within rocks, the cumulative energy is released in the form of stress waves, generating microseismic events that propagate in the form of P-waves and S-waves. The microseismic monitoring system uses seismic detectors or acceleration sensors to convert received waveforms into electrical signals, which are then transformed into data signals through a data acquisition system. With specialized data processing software, the system can accurately determine the time, location, and magnitude (space-time strength) of microseismic events in three-dimensional space. This enables qualitative and quantitative evaluations of the extent, stability, and development trends of rock damage activities.

3.1 Basic principles and monitoring mechanism

The adopted fiber optic microseismic monitoring system is based on Michelson fiber optic vibration monitoring technology, providing high-precision and intelligent monitoring of rock microfractures. The fiber optic microseismic monitoring instrument, with advantages such as high sensitivity, wide frequency response, and large dynamic range, meets the monitoring requirements for a broad frequency band of coal and rock fracture vibrations from low seismic to high seismic frequencies. The fiber

TABLE 1 Coal seam roof and floor conditions.

Roof/Floor	Thickness (m)	Rock type
Old roof	7.9–17.0	Medium-fine sandstone: Gray, thick-layered, medium-fine grain structure, parallel bedding, primarily composed of quartz with small amounts of feldspar and muscovite, visible mudstone interlayers, brittle, hard
3rd coal seam	4.0–5.8	Coal: Black, blocky to powdery, semi-dull to semi-bright type
Parting rock	1.0–2.0	Mudstone: Dark gray, blocky, dominated by muddy structure, visible plant-induced fragments, fragmented in nature
1st coal seam	2.0–4.8	Coal: Black, blocky to powdery, semi-dull to semi-bright type
Direct floor	0.8–2.2	Mudstone: Dark gray, blocky, dominated by muddy structure, containing small amounts of sandy components, visible plant-induced fragments, unevenly developed coal seams, fragmented in nature

optic microseismic monitoring system in this project consists of one host unit of a 16-channel mine explosion-proof and intrinsically safe fiber optic microseismic monitoring device, 16 sensors, one set of ground collection servers, and supporting microseismic collection and processing software systems, all connected by armored fiber optics, as shown in Figure 2.

(1) The mine explosion-proof and intrinsically safe fiber optic microseismic monitoring device host is divided into three main components: fiber optic laser module, signal acquisition and demodulation module, and data acquisition module. The host creates a fiber optic microseismic monitoring array through a wavelength division multiplexing network using the light generated by the fiber optic laser module. The microseismic vibrations collected by the fiber optic sensors are converted into analog signals by the signal acquisition and demodulation module, then transformed into digital signals by the data acquisition module before being sent to the data processing and analysis warning center for further analysis.

(2) The fiber optic acceleration sensor uses a polarization-independent fiber optic Michelson interferometer based on a push-pull structure. Under the action of microvibrations generated by rock fractures, the mass block stretches or compresses the elastic body, causing deformation in the fiber wound around the elastic body, creating interference phase difference. The change in optical phase shift is proportional to acceleration. Through backend phase demodulation technology, the acceleration signal is restored, achieving microseismic acceleration monitoring.

3.2 Microseismic monitoring scheme

Considering the geological conditions of the 11,023 working face and ensuring the accuracy of event location, a total of 16 microseismic monitoring points were deployed in the 11,023 working face network, as shown by the cyan dot in Figure 1. Eight microseismic monitoring points were arranged in the upper gate road with a distance of approximately 80 m between adjacent points, and eight were arranged in the lower gate road with a distance of about 85 m between adjacent points. This spatial arrangement provided comprehensive monitoring of the 11,023 working face in all directions. The first microseismic monitoring point in the upper gate road was approximately 95 m from the cutting head, while the first point in the lower gate road was about 145 m from the cutting head. The collection station located in the return airway and connected to the surface through fiber optics for signal transmission to the ground server and storage. The layout scheme of the microseismic monitoring system network is shown in Figure 3. The detectors adopted the single-axis highly sensitive acceleration sensors, which needed to be placed at the tail of the support anchor rod (anchor rod length 2.5 m) with the help of connecting joints.

3.3 Data processing approach

Once microseismic waveforms are collected, the system uses a recursive STA/LTA algorithm for initial screening. Waveforms triggered by four or more channels within 0.4 s are marked as suspected events and saved. Suspected events contain both microseismic signals (as shown in Figure 4A) and a significant amount of construction noise and interference signals, such as drilling, human movement, drainage pumps, etc. (as shown in Figure 4B). Noise signals are identified and removed through signal analysis. After picking the arrival times of microseismic P waves, the simplex method is used for location. Based on feedback from location results, the software calculates theoretical P wave arrival times for correcting and optimizing arrival time picking and location errors.

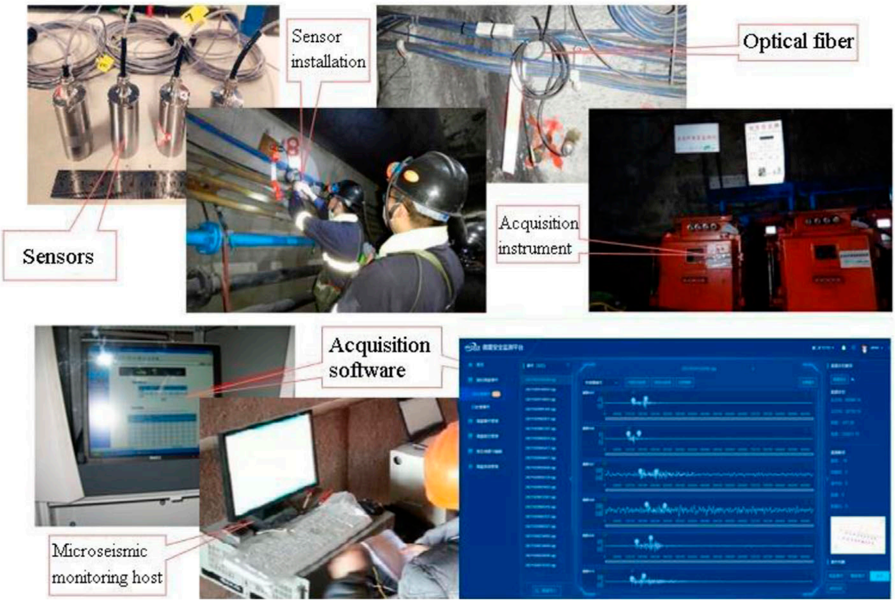

FIGURE 2
Fiber optic microseismic monitoring system.

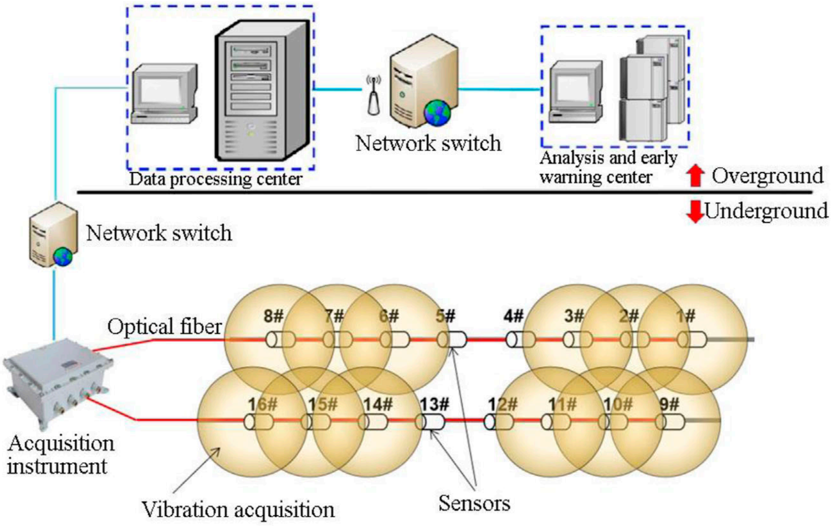

FIGURE 3
The layout scheme of microseismic monitoring system on the 11,023 working face.

3.4 Solution of source parameters

After microseismic event location, source parameters can be solved, focusing on seismic moment, energy, apparent stress, and apparent volume, and energy density.

3.4.1 Seismic moment

The seismic moment numerically equals the work done during the source tension or faulting process, causing corresponding non-elastic deformation. It is a scalar quantity. A larger seismic moment indicates more severe damage to the source area. The seismic moment can be estimated using Eq. 1 (Aki, 1968):

$$M = \frac{4\pi\rho {v_{P,S}}^{3} R\Omega_{P,S}}{F_{P,S}} \tag{1}$$

where ρ is the density of the source rock, v is the P-wave or S-wave velocity, R is the source distance, Ω is the low-frequency displacement amplitude, and F is the root mean square of the far-field displacement pattern mapped onto the source sphere for P-waves ($F_P = 0.516$), and for S-waves ($F_S = 0.632$).

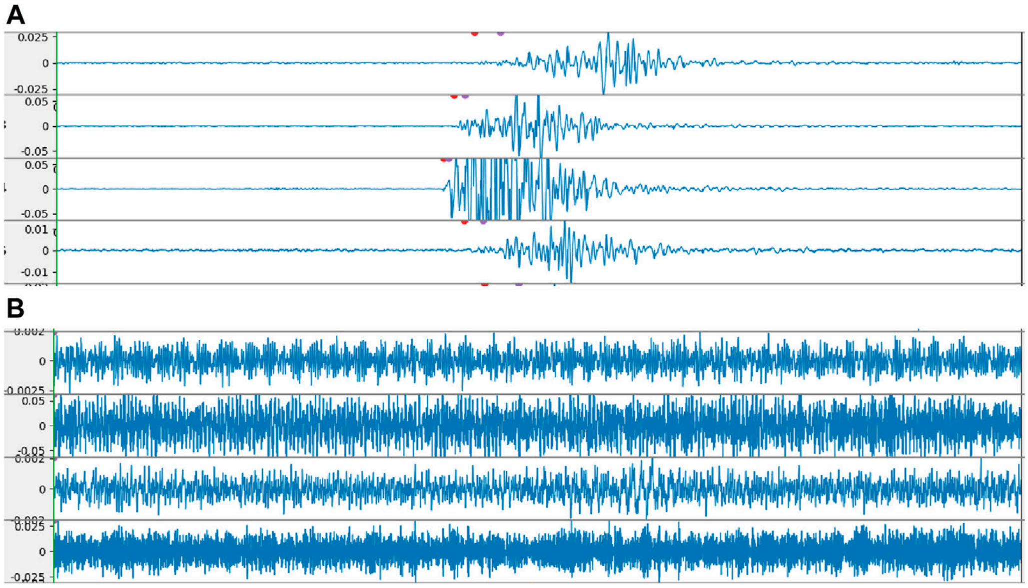

FIGURE 4
Typical waveforms: **(A)** rock fracture waveform and **(B)** noise waveform.

3.4.2 Energy

Microseismic radiation energy (referred to as energy) is the energy of stress waves radiated outward during the rock fracture process. In the time domain, the radiated seismic energy of P-waves or S-waves is proportional to the integral of squared velocity signal, represented by Eq. 2 (Snoke, 1987):

$$E = 4\pi\rho v_{\mathrm{P,S}} R^2 S_{V2} \tag{2}$$

where S_{V2} is the integral of the square of the velocity spectrum.

3.4.3 Apparent stress

The apparent stress represents the stress level at the source, expressed by Eq. 3 (Wyss and Brune, 1968; Wyss and Brune, 1971):

$$\sigma_{\mathrm{A}} = \frac{\mu E}{M} = \frac{\xi}{2}(\sigma_0 + \sigma_1) \tag{3}$$

where μ is the rigidity of the rock mass, ξ represents the seismic efficiency, σ_0 stands for the initial stress, σ_1 is the residual stress. The larger the apparent stress of the microseism, the greater the energy released in the process of achieving the same non-elastic deformation.

3.4.4 Apparent volume

The apparent volume measures the volume of rock body that undergoes the corresponding non-elastic strain under the effect of apparent stress, and the calculation formula is as follows:

$$V_{\mathrm{A}} = \frac{M}{2\sigma_{\mathrm{A}}} = \frac{M^2}{2\mu E} \tag{4}$$

In Eq. 4, the physical unit of the apparent volume is m^3, so it is convenient to accumulate and can also be analyzed in the form of a heat map.

4 Spatial microseismic distribution and division of three zones

The rock failure of the roof and floor and the evolution of water-conducting fractures caused by mining in the working face are essentially the macroscopic manifestations of micro-fracture behaviors such as the expansion of the original cracks and the formation of new cracks. Based on the spatial clustering properties of microseismic events, the depth of the concentrated region of micro-fracturing is regarded as the depth of roof and floor damage. Therefore, it is reasonable to associate the spatial distribution of microseismic events with the distribution of geological layers to determine the depth of floor damage.

4.1 Spatial microseismic distribution

Based on the analysis of microseismic data from 11,023 working face from October to November 2022, spatial analysis of the microseismic events was conducted. Figure 5 represents the statistical count of microseismic events changing with elevation. It can be seen that microseismic events during different time periods show similar distribution characteristics in terms of elevation. Most of the microseismic events are distributed within the range of 0–30 m in the floor and 0–20 m in the roof. There are more microseismic events in the floor than in the roof, indicating that the floor is affected by mining activities resulting in more extensive damage.

Additionally, the variation in the degree of microseismic event clustering in the roof and floor can be observed. There are notable turning points in the number of microseismic events within the 30–40 m range of the floor and the 20–30 m range of the roof. This indicates that the failure depth of the floor is not completely stratified according to the geological structure. Consequently, it is

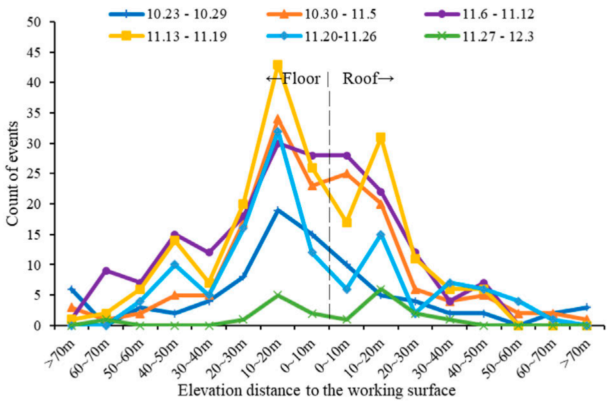

FIGURE 5
The distribution of microseismic events on elevation in different time ranges.

necessary to determine the depth of roof and floor damage based on the vertical distribution of microseismic events to dynamically assess the damage situation.

Figure 6 shows the distribution of microseismic events in the horizontal direction. It can be seen that during October and November, microseismic events were mainly distributed within a range of 100 m in front of the working face. The quantity and energy of the events increased near the 1# fault anomaly area, mainly due to the mining activities that disrupted the static equilibrium of the fault structure, causing the fault to release a large amount of energy and inducing a great deal of microseismic activity. Early roadway sides also saw microseismic activity, mainly due to mining disturbance-caused stress changes in the surrounding rock, plus the extension of the 1# fault anomaly area from the working face to beyond. The rock on the outer side of the roadway is prone to fragmentation.

4.2 Division of the roof three zones

After the roof of a coal mining face collapses, the rock layers above progressively fall, layer by layer, until the collapsed gangue comes into contact with the overlying rock layers. This zone of collapse and damage is known as the roof caved zone. After the free fall of the roof rock, the rock layers above the collapse zone continue to sink and bend. When this bending exceeds the strength of the rock layers, tensile fractures and eventual breakage occur. This process develops layer by layer upwards until the overall sinking and bending of the overlying rock layers ceases. This part is referred to as the fractured zone.

Based on the range of microseismic activity in the roof, an analysis of the damage height of the roof rock layers is conducted. Since the distribution of microseismic events' height may not necessarily conform to the statistical distribution in Figure 5, using the turning point of the statistical distribution as the basis for dividing the three zones may not reflect the actual situation. Therefore, the height of the caved zone is inferred from the height of 80% of the microseismic events. The data analysis infers the height of the caved zone to be about 31.72 m. The height of the fractured zone is inferred from the height of the maximum distance between the microseismic event and the roof. The inferred height of the fractured zone is about 44.52 m according to data analysis.

According to the geological conditions of the 11,023 working face. The heights of the caved zone and fractured zone of the roof are calculated using empirical formulas from the *Regulations on the Preservation of Roof Pillars of Buildings, Water Bodies, Railways and Main Wells and the Mining Procedure of Pressurized Coal* (short for *Regulations*) and the *Standards for Hydro-geological Geological Survey in the Mining Area* (short for *Standards*). The calculations are compared with the heights of the caved zone and fractured zone of the roof inferred from the microseismic monitoring, as shown in Table 2. It can be seen that compared with the empirical formulas, the caved zone height inferred by microseismic monitoring is higher, and the fractured zone height is in good agreement.

4.3 Division of floor three zones

Due to the effect of mining pressure, the floor rock strata are continuously damaged, and the layer zone with significantly changed water conductivity is called the floor damaged zone. The floor water-blocking zone is the part where the rock layer at the bottom of the coal seam maintains its integrity and original waterproof performance. This zone is located between the floor damaged zone and the confined water uplift zone. This zone plays a role in preventing the connection between the floor damaged zone and the confined water uplift zone. Since the Floor Direct Water-bearing Layer of 3 Coal is a weak water-bearing layer, the confined water uplift zone can be ignored. According to the range of microseismic activity in the floor, the depth of floor damaged is analyzed. Using the depth where 80% of the microseismic events are concentrated to infer the height of the floor damaged zone, the data analysis infers that the floor damaged zone is about 33.94 m below the coal seam floor; using the deepest depth of the microseismic events from the floor to infer the height of floor water-blocking zone, according to the data analysis, the height of the water-blocking zone is about 54.68 m.

According to the geological conditions of the 11,023 working face, the height of the floor damaged zone of the floor is calculated using the empirical formulas from the *Regulations* and the *Standards*. The calculation results of the floor damaged zone height and the water-blocking zone height are compared with the results inferred from the microseismic monitoring, as shown in Table 3. It can be seen that compared with the empirical formula, the height of the floor damaged zone inferred by microseismic monitoring is higher. There is no empirical formula for predicting the height of floor water-blocking zone.

5 Microseismic evolution under the action of mining disturbance

The formation of water-conducting fractures in coal mine surrounding rock under mining activities is an evolutionary process of stress and strain, inevitably accompanied by rock fracturing, crack expansion, and other rock mechanics phenomena, leading to microseismic events. Studying the evolution of microseismic

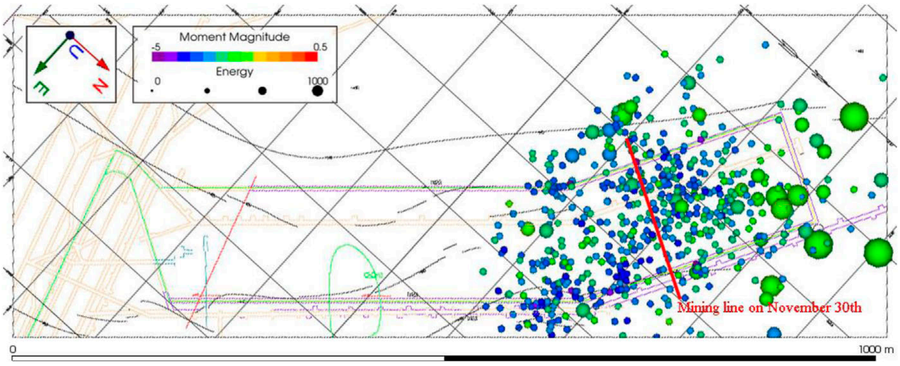

FIGURE 6
The distribution of microseismic events in the horizontal direction.

TABLE 2 Inferred heights of roof caved zone and fractured zone from empirical formulas and microseismic monitoring.

Method	Roof caved zone height (m)	Roof fractured zone height (m)
Empirical formula in *Regulations*	9.56–13.96	37.50–48.70
Empirical formula in *Standards*	18.00	47.32–57.52
Inferred from microseismic monitoring	31.72	44.52

TABLE 3 Inferred heights of the floor damaged zone and water-blocking zone from empirical formulas and microseismic monitoring.

Method	Floor damaged zone height (m)	Floor water-blocking zone height (m)
Empirical formula in *Regulations*	13.96–15.78	
Empirical formula from *Standards*	14.62	
Inferred from microseismic monitoring	33.94	54.68

parameters under the action of mining disturbance can be used to evaluate the formation of water-conducting channels and the risk of water inrush.

5.1 Correlation between construction footage and micro-fractures

The correlation between the cumulative energy of daily microseismic events, the cumulative number of events, and the daily footage in November is statistically summarised, as shown in Figure 7. It can be seen that the mining speed was relatively high at the beginning of November. Correspondingly, the number of microseismic events was also higher. As the mining speed decreased, the degree of mining disturbance reduced, and the number of microseismic events also showed a downward trend. Overall, there is a certain positive correlation between the two.

Similarly, the daily cumulative energy of the microseismic events on the 11,023 working face is positively related to the mining speed. Since the energy release size during the surrounding rock destruction mainly depends on the original geostress field and the coal rock geological conditions, the defects like joints, structural planes, and other adverse geological bodies existing in the surrounding rock make different sections have certain differences in the stress field and geological conditions. Therefore, the fluctuation of cumulative energy is relatively more apparent. The advancement speed of the working face and the frequency and energy of the microseismic events caused by disturbances are somewhat related. When the mining speed is faster, the intensity of microseismic activity will increase, thereby increasing the risk of roof and floor fracturing and water inrush. Thus, the risk of roof and floor fracturing and water inrush can be reduced by reasonably controlling the mining speed of the working face.

By taking daily excavating progress, microseismic event counts, cumulative energy, apparent stress, and apparent volume as five parameters in November, their correlation coefficients are calculated and the resultant confusion matrix is acquired, as shown in Figure 8. The excavation progress has a low correlation coefficient with various source parameters. The number of microseismic events and the cumulative energy are significantly positively correlated, and the apparent stress and apparent volume are negatively correlated at a smaller degree. In short, these microseismic parameters characterize the evolution of rock micro-fractures under the influence of mining disturbance from different dimensions. Through the statistical analysis of the abnormal changes of these parameters, dynamic early warning of roof and floor fracturing and water inrush risks can be realized.

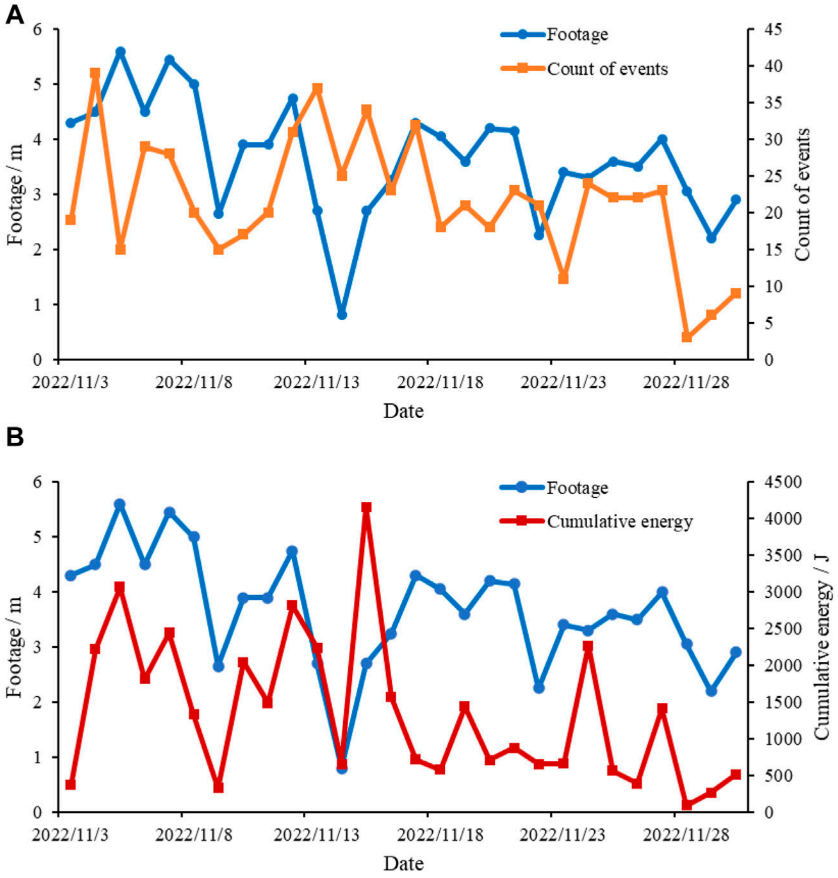

FIGURE 7
Changes of microseismic parameters under excavation disturbance in November. **(A)** Relationship between daily microseismic event count and daily footage, **(B)** Relationship between daily cumulative energy and daily footage.

5.2 Periodic changes in microseismic parameters

Figure 9 shows the variation curves of the daily average apparent stress and cumulative apparent volume of the roof microseismic events from October to November. It can be seen that the apparent stress and apparent volume are roughly negatively correlated. Moreover, the apparent stress and apparent volume generally show periodic changes. The time interval for the trough of the apparent volume is about 3 days.

Periodic pressure is a phenomenon that occurs when the mining face continues to advance and the span of roof exposure reaches a certain length, causing the roof to break and collapse along the coal wall. Influenced by the advancement of the working face, this collapse phenomenon often appears periodically. According to field records, the periodic pressure time interval of the initial mining face roof is about 4 days. Judging from the periodic changes of the microseismic event parameters above, the two have a good correspondence. Specifically, when periodic pressure occurs, the average microseismic apparent stress is often low, and the cumulative apparent volume is often high. Then the average apparent stress gradually increases and the apparent volume decreases. When the next periodic pressure event occurs, the apparent stress of a microseismic event drops again, and the cumulative apparent volume increases simultaneously.

According to the periodic changes in microseismic parameters, it can be considered that the rock mass has undergone a process of stress accumulation and stress release. As the working face advances, the roof continues to accumulate stress under its own weight and the load of the overlying rock layer, which is manifested as an increase in microseismic apparent stress. When the accumulated stress reaches a certain level, the accumulated stress starts to be released and the roof collapses as weight, manifested as an increase in microseismic apparent volume. With the release of stress, the apparent stress also starts to decrease. In summary, the apparent stress and apparent volume effectively reflect the stress-strain process in the rock mass under excavation disturbance. Apparent stress can serve as an indicator to measure the degree of stress accumulation in the rock mass, while the apparent volume can serve as an important index to quantify the extent of rock fracturing.

5.3 Microseismic energy distribution

The energy released during rock fracturing involves dissipative energy and elastic strain energy. Elastic strain energy is positively correlated with high stress, which is a necessary

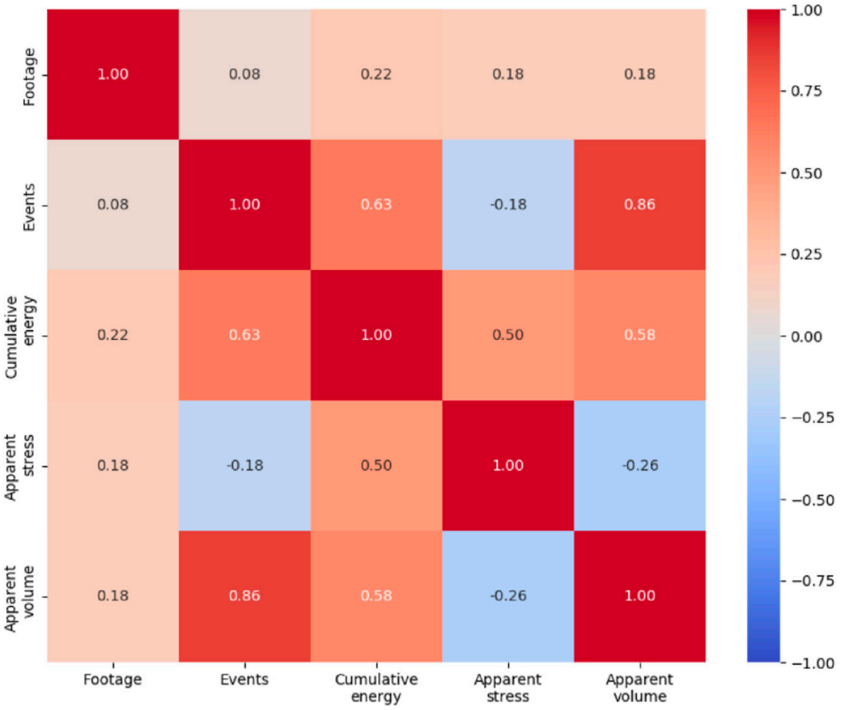

FIGURE 8
Confusion matrix of excavation footage and microseismic parameters.

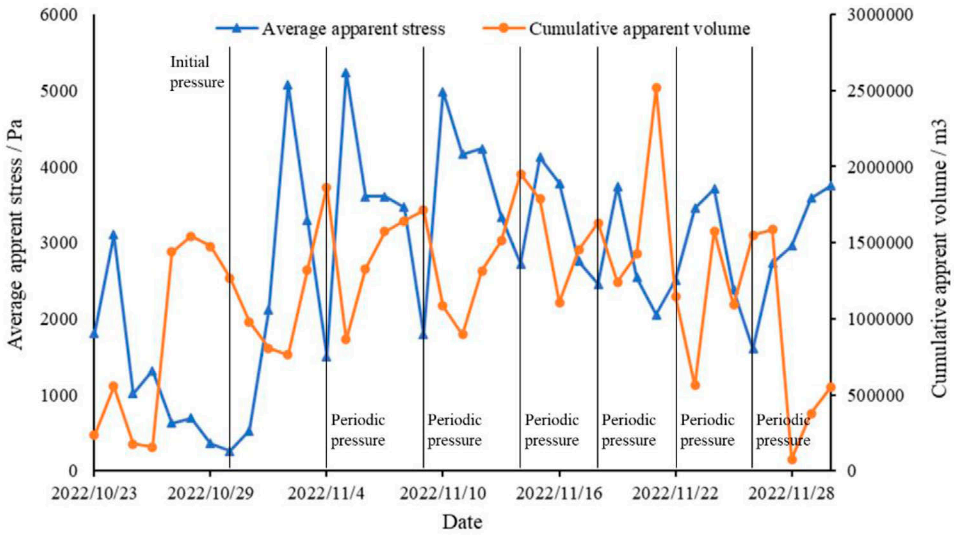

FIGURE 9
The daily average apparent stress and cumulative apparent volume of the roof microseismic events from October to November 2022.

condition for the fracturing and water permeability of the roof and floor. Therefore, the vertical distribution of microseismic energy obtained from monitoring can indirectly reflect the high-stress distribution necessary for the formation of water-conducting channels.

From October to November 2022, the maximum energy of a microseismic event on the mine floor was 6,655.89 J. The number of events in the energy ranges of 0J–100J, 100J–500J, 500J–1000J, and above 1000 J were 401, 58, 5, and 1, respectively, accounting for 86.24%, 12.47%, 1.08%, and 0.22% of the total. The energy

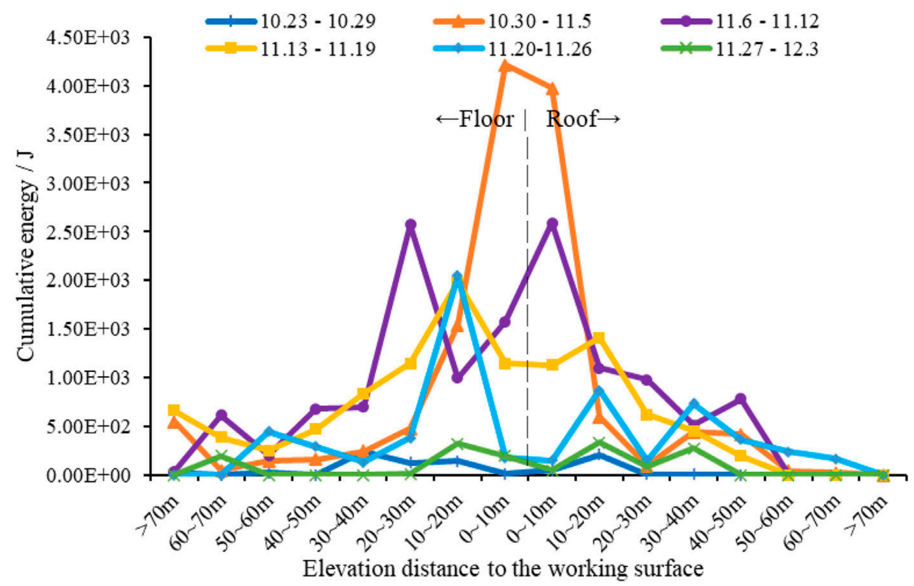

FIGURE 10
The distribution of cumulative energy on elevation in different time ranges.

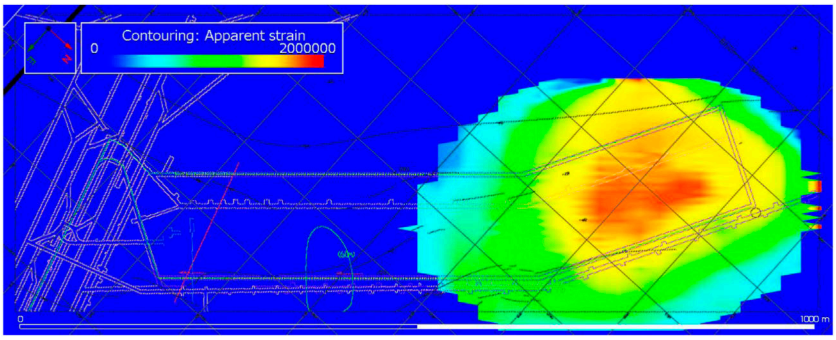

FIGURE 11
Cumulative apparent volume contour of the floor during October-November.

of microseismic events is low, indicating a lesser degree of rock fracturing. Vertically, high-energy events are mainly concentrated within 20 m of the mine floor (as shown in Figure 10). In the Carboniferous II group limestone and below, only scattered low-energy microseismic events were observed, with no deep aquifer microseismic events detected. No hidden water-conducting structures or weak areas were found in the monitored area of the working face floor, making it impossible to form water inrush channels.

5.4 Apparent volume and water inrush risk

Since apparent volume can quantify the degree of rock fracturing, it can be used to assess the development of water-conducting fracture zones in the mine floor and the risk of water inrush. Project the microseismic events of the mine floor onto a horizontal plane and divide the mining area into a grid of 30 × 160. Calculate the cumulative apparent volume of microseismic events in each grid. Based on the cumulative apparent volume in each grid, draw an apparent volume cloud map. By analyzing the apparent volume cloud map, the extent of non-elastic deformation of the mine floor and the potential locations of water-conducting fractures can be determined. Finally, the potential directions of extension of water-conducting channels can be identified based on areas with higher apparent volumes on the map.

The apparent volume cloud map of the mine floor from October to November is shown in Figure 11. It can be seen that the areas with higher apparent volumes overlap with the distribution of 1# fault anomaly area. The highest cumulative apparent volume is 204,514 m^3. According to hydrogeological

TABLE 4 The range of warning indicators for the depth of fractures.

Indicator: Height (m)	Roof caved zone	Roof fractured zone	Floor damaged zone	Floor water-blocking zone
Average	31.72	44.52	33.94	54.68
Standard deviation	10.75	14.25	8.87	13.32
Low level warning threshold	53.21	73.02	51.69	81.31
Medium level warning threshold	63.96	87.27	60.56	94.63
High level warning threshold	74.71	101.53	69.44	107.95

TABLE 5 The range of warning indicators for the intensity of fractures.

	Roof event count	Roof cumulative energy	Floor event count	Floor cumulative energy
Average	21.95	1,460.53	36.86	2060.14
Standard deviation	9.22	1,115.67	12.63	1,598.01
Low level warning threshold	40.39	3,691.87	62.12	5,256.15
Medium level warning threshold	49.62	4,807.54	74.75	6,854.16
High level warning threshold	58.84	5,923.21	87.38	8,452.16

TABLE 6 The range of warning indicators for the water inrush risk.

	The maximum cumulative apparent volume in each grid cell	The elevation of the maximum microseismic energy event
Average	122,231.20	−474.06
Standard deviation	39,700.23	17.94
Low level warning threshold	201,631.65	−509.93
Medium level warning threshold	241,331.88	−527.87
High level warning threshold	281,032.11	−545.81

conditions, this magnitude of cumulative apparent volume is insufficient to form fault water. In early warning practices, microseismic energy and apparent volume are often complementary parameters. For example, a large apparent volume may indicate a broad area of fracturing and deformation but does not necessarily mean that these areas are accompanied by a significant release of energy. On the other hand, high-energy microseismic activity may indicate a localized area undergoing severe damage, representing the manifestation of high stress. Therefore, using both indicators in combination can provide a more comprehensive assessment of the rock damage status and water inrush risk.

6 Comprehensive warning method of roof and floor cracking and water inrush risk

6.1 Early warning method

Due to the fact that microseismic activity is mainly concentrated in the range of 0–20 m on the roof and 0–40 m on the floor, and the microseismic energy is generally small, the risk of water inrush is relatively low, making it difficult to establish a microseismic index quantization early warning model based on traditional intelligent algorithms and established water inrush disasters. Therefore, this

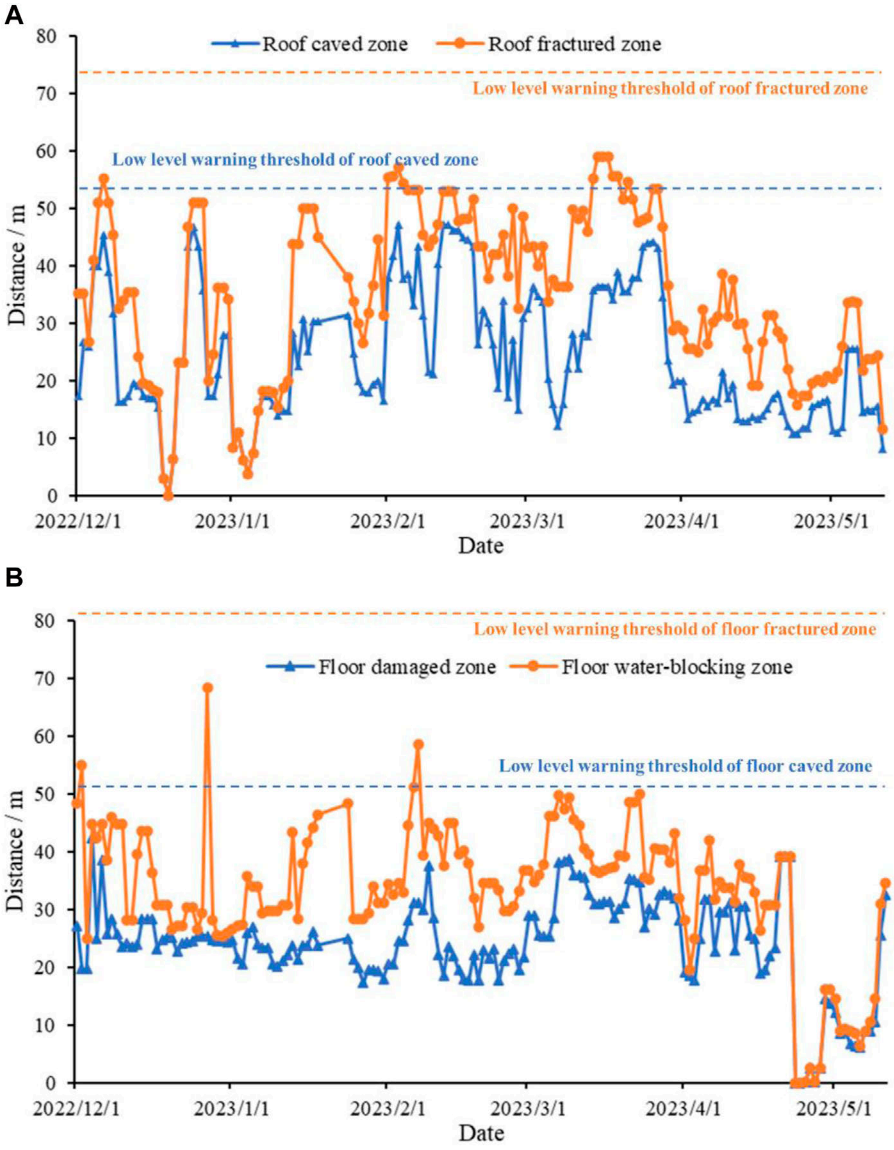

FIGURE 12
The fracture depth and warning results from December 2022 to May 2023. **(A)** Roof, **(B)** Floor.

study adopts an anomaly detection approach to establish an early warning model for water inrush risk based on anomaly judgment criteria. From the three dimensions of fracture depth, fracture strength, and water inrush risk, different discriminant indicators are used for early warning. Based on the results of previous microseismic monitoring, the distribution of each indicator is determined, and the expected value and standard deviation of each indicator under normal conditions are solved. Then, the double standard deviation is taken as the early warning threshold. That is, if the indicator deviates from the double standard deviation, it is considered abnormal and an early warning judgment is made. The greater the degree of deviation of the indicator, the higher the risk of cracking and water inrush. Therefore, every time a standard deviation is exceeded, the early warning level is raised one level.

During early warning, the size of the early warning indicator is calculated based on the current monitoring data, and the early warning level is determined. Finally, the comprehensive early warning results of the depth of fractures, the intensity of fractures, and the water inrush risk are provided, providing a reference for the prevention and control of water disasters. This comprehensive early warning method can be integrated with the microseismic data processing and positioning interface based on artificial intelligence to achieve automatic early warning and generate early warning reports automatically.

6.2 On-site performance

6.2.1 Quantification of early warning indicators based on initial mining monitoring data

6.2.1.1 The depth of fractures

The depth of fractures mainly depends on the vertical distribution of microseismic events in the 3 days before the warning.

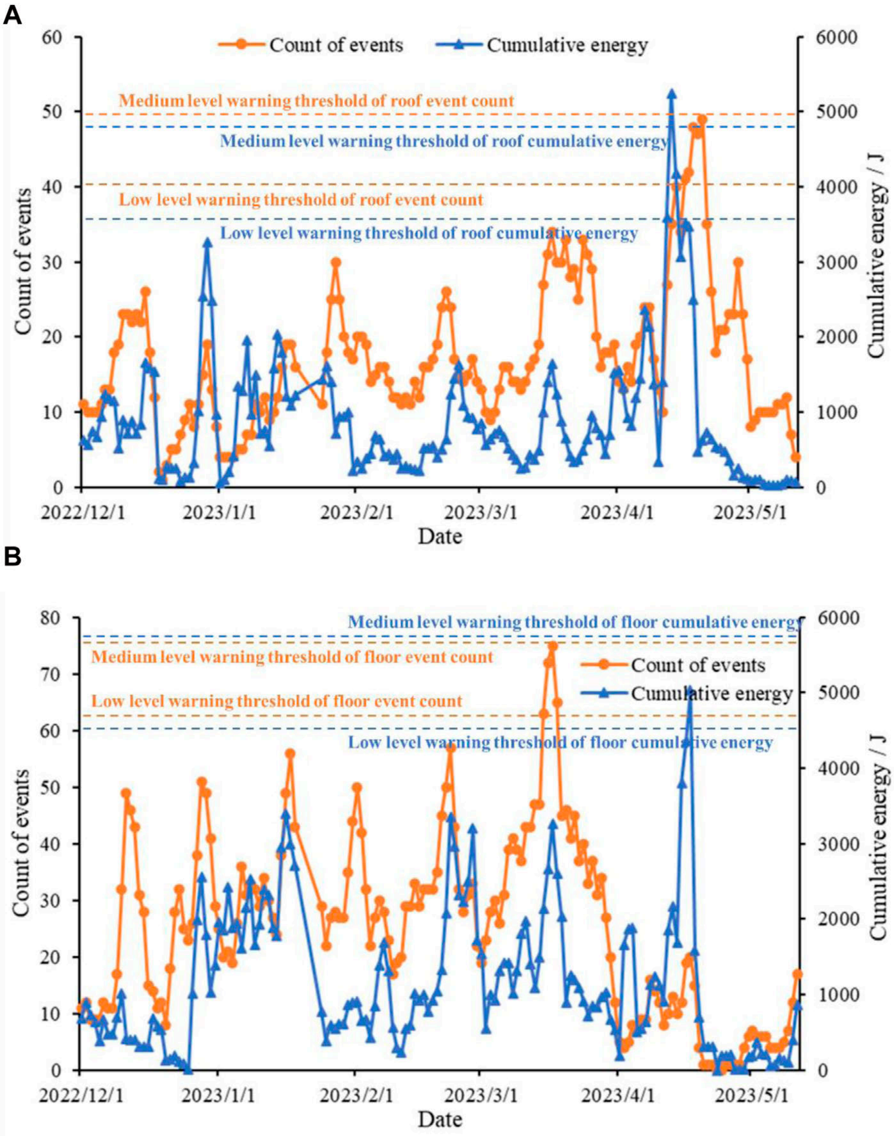

FIGURE 13
The fracture intensity and warning results from December 2022 to May 2023. **(A)** Roof, **(B)** Floor.

Following the stratification criteria determined in Section 4, the height at which 80% of the microseismic events are concentrated is used to infer the height of the roof caved zone and the floor damaged zone. The maximum distance between microseismic events and the roof and floor are used to infer the height of the roof fractured zone and the floor water-blocking zone. According to the statistical results of monitoring from October-November, the average height, standard deviation, and the range of warning indicators for the depth of fractures obtained from the warning criteria are shown in Table 4.

6.2.1.2 The intensity of fractures

The intensity of fractures is primarily determined based on the number of microseismic events and the cumulative energy in the roof and floor during the 3 days preceding the warning. According to the statistical results of the monitoring from October to November, the average number detected in the floor over three consecutive days was 36.86, the average cumulative energy was 2060.14 J, and the standard deviations were 12.63 and 1,598.01 J, respectively. For the roof, the average number of events was 21.95, the average cumulative energy was 1,460.53 J, and the standard deviations were 9.22 and 1,115.67 J, respectively. According to the warning criteria, the range of the intensity of fracture warning indicators are shown in Table 5. A warning is issued if any one of the event count or cumulative energy exceeds the warning indicator.

6.2.1.3 The water inrush risk

The water inrush risk is primarily based on the cumulative apparent volume cloud map of the floor in the 3 days preceding the warning moment. To simplify calculations, only the maximum cumulative apparent volume in each grid cell of the cloud map is taken as the warning indicator for assessing the risk of water inrush. According to the warning criteria, the range of warning indicators for the water inrush risk is shown in the table. As a useful supplement, the elevation of the daily maximum microseismic

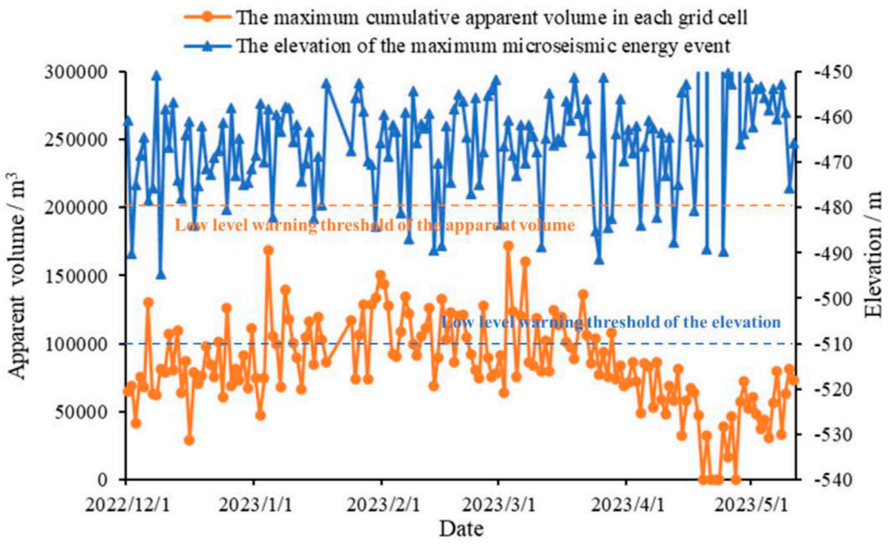

FIGURE 14
The water inrush risk and warning results from December 2022 to May 2023.

energy is also used as an indicator of water inrush risk warning, in order to quantify the depth of stress accumulation. According to the statistics of the monitoring results from October to November, the range of the warning indicator obtained is shown in Table 6.

6.2.2 Evaluation of early warning effect

The proposed early warning method was applied to the roof and floor cracking and water inrush warning for the 11,023 working face since December. During the application process, input parameters needed to update daily. Microseismic data were collected, input classification and arrival picking algorithms. The location and solution of the source parameters were carried out, and warning indicators were calculated and the warning level determined, finally giving the early warning result. The fracture depth and warning results from December to May are shown in Figure 12. After December 2022, as the mining face gradually moved away from 1# fault anomaly area, the roof fracture depth gradually decreased. Then, during February 2023, while crossing 2# fault anomaly area, the roof damage depth increased. Until April 2023, when the mining essentially crossed 3# fault and coal seam thinning anomaly area, as the mining speed slowed down, the depth of roof fractures decreased. In comparison, the change of depth was insignificant in the floor damaged zone and the floor water-blocking zone. As the warning indicators did not exceed the threshold, no fracture depth warning was triggered.

The fracture intensity and warning results from December to May are shown in Figure 13. Due to the slowdown of the mining pace in December 2022, the number of roof microseismic events was small. From February 2023, as the mining speed increased, the number of roof microseismic events increased, but the cumulative energy decreased. From March to April 2023, with a faster mining speed, and crossing 3# fault and coal seam thinning anomaly area, the disturbance caused the surrounding rock to fracture more, thus the number of roof microseismic events and cumulative energy reached their peaks. As the mining speed decreased in the late period, the number and energy of microseismic events also decreased. As the cumulative energy exceeded the threshold in mid-April, a low and medium level warning was triggered for roof fracture intensity. In comparison, the peak of floor microseismic events occurred in March, and the peak of cumulative energy occurred in April, overall being less influenced by geological conditions. As the warning indicators exceeded the threshold in March, a low-level warning was triggered for floor fracture intensity.

The water inrush risk and warning results from December to May are shown in Figure 14. Since December 2022, as the mining face gradually moved away from 1# fault anomaly area, the stress release of the working face slowed down, keeping the apparent volume low. From January to March 2023, as the face crossed 2# fault anomaly area, 3# fault and coal seam thinning anomaly area, the apparent volume returned to the level established by the warning indicators from October to November. After April, the apparent volume continuously decreased. In comparison, the elevation of the maximum microseismic energy event does not show any apparent anomalies. Since the warning indicators did not exceed the threshold, no warning was triggered for water inrush risk. In summary, the changes in microseismic activity, geological conditions, and early warning indicators during the mining period have a good correspondence, which demonstrates the effectiveness of the established early warning method.

7 Discussion

Based on the initial monitoring data from working face 11,023, the early warning method for water inrush proposed in this study has established a comprehensive early warning model. The characteristics of microseismic activity may vary for different projects, but remain self-similar within the same project. Figures 5, 10, as well as other figures, also demonstrate similar spatial and energy distribution characteristics of microseismic activity across different time periods. Therefore, it is reasonable to develop an early warning model based on the self-similar nature of microearthquakes.

However, due to variations in microseismic activity among different projects, the actual distribution characteristics of microseismic activity used to divide the three zones and establish a comprehensive early warning model may differ significantly from those observed in this case. For instance, at the Dongjiahe Coal Mine, most microearthquakes are concentrated in the roof area and occurrences within tens to hundreds of meters depth are not uncommon (Cheng et al., 2017). In such cases, appropriate adjustments should be made to the segmentation threshold of the comprehensive early warning model based on actual microseismic distribution and geological conditions.

Additionally, this study utilizes the standard deviation of microseismic distribution to establish the warning threshold. Depending on the degree of similarity of the specific problem, the distribution characteristics of key early warning indicators, and mathematical modeling skills, other types of early warning methods can also be considered (Feng et al., 2023b; Xiang et al., 2023; Cai et al., 2024).

8 Conclusion

This study focuses on assessing the cracking of both the roof and floor within the 11,023 working face of the Paner Coal Mine, particularly under the influence of mining disturbances and hydraulic pressure, while also evaluating the potential risk of water inrush incidents. Through meticulous analysis of the spatiotemporal distribution of microseismic events and an in-depth exploration of the interplay between key source parameters including energy, apparent stress, and apparent volume, and excavation disturbances, the research endeavors to gauge the extent of roof and floor cracking and the associated risk of water inrush. Moreover, the study pioneers the establishment of a comprehensive early warning methodology tailored to predict roof and floor fractures as well as anticipate water inrush risks. The conclusions can be drawn as follows:

1. It proposes to use the height at which 80% of microseismic events are concentrated to infer the height of the roof caved zone and the floor damaged zone; and to use the maximum distance between microseismic events and the roof and floor to infer the height of the roof fractured zone and the floor water-blocking zone. Compared to the three-zone height division based on empirical formulas, the three-zone division through microseismic monitoring can dynamically identify the current fractured zone height of the roof and floor of the working face, better predicting the impact of mining disturbances and hydraulic pressure on them.
2. The advancement speed of the working face has a certain correlation with the frequency and energy of microseismic events caused by disturbances. The periodic changes in average apparent stress and cumulative apparent volume correspond well with the roof pressure during back mining. Apparent stress can be used as an indicator to measure the degree of stress accumulation in the rock mass, while apparent volume is an important indicator for quantifying the degree of rock fracturing.
3. It proposes a comprehensive early warning method for roof and floor cracking and water inrush risk, considering three dimensions: the depth of fractures, the intensity of fractures, and the water inrush risk. Based on previous microseismic monitoring results, twice the standard deviation of each warning indicator is used as the warning threshold. The application and verification during the back mining period of the 11,023 working face show a good correspondence between microseismic activity, geological conditions, and the change in warning indicators, demonstrating the effectiveness of the established warning method.

Data availability statement

The raw data supporting the conclusions of this article will be made available by the authors, without undue reservation.

Author contributions

SoZ: Formal Analysis, Funding acquisition, Investigation, Writing–original draft. XW: Formal Analysis, Investigation, Writing–original draft. LT: Data curation, Investigation, Validation, Writing–review and editing. WD: Formal Analysis, Validation, Writing–review and editing. BG: Conceptualization, Methodology, Supervision, Writing–review and editing. CM: Formal Analysis, Project administration, Writing–review and editing. SnZ: Formal Analysis, Visualization, Writing–review and editing.

Funding

The author(s) declare that financial support was received for the research, authorship, and/or publication of this article. This research was funded by the Collaborative Innovation Project of Colleges and Universities in Anhui Province (Grant No. GXXT-2022-020); the Scientific Research Foundation for High-level Talents of Anhui University of Science and Technology (Grant No. 2023yjrc07); the University Natural Science Foundation of Anhui Province (Grant No. 2022AH030088); the Anhui Provincial Natural Science Foundation (Grant No. 2308085ME153); the Foundation of Joint National-Local Engineering Research Centre for Safe and Precise Coal Mining (Grant No. EC2022011); the National Natural Science Foundation of China (Grant No. 52227901); the Guizhou Provincial Key Technology R&D Program (Grant No. 2022-005).

Conflict of interest

Author XW was employed by Anhui Zhibo Photoelectric Technology Co., Ltd. Author SnZ was employed by Guizhou Mine Safety Scientific Research Institute Co., Ltd.

The remaining authors declare that the research was conducted in the absence of any commercial or financial relationships that could be construed as a potential conflict of interest.

Publisher's note

References

Aki, K. (1968). Seismic displacements near a fault. *J. Geophys. Res.* 73, 5359–5376. doi:10.1029/jb073i016p05359

Cai, W., Lan, F., Huang, X., Hao, J., Xia, W., Tang, R., et al. (2024). Generative probabilistic prediction of precipitation induced landslide deformation with variational autoencoder and gated recurrent unit. *Front. Earth Sci.* 12, 1394129. doi:10.3389/feart.2024.1394129

Chen, G., Liu, X., and Song, D. (2023). Research on *in situ* stress inversion of deep-buried tunnel based on pressure/tension axis mechanism and geological structure. *Deep Undergr. Sci. Eng.* 2 (1), 61–73. doi:10.1002/dug2.12025

Cheng, G., Ma, T., Tang, C., Liu, H., and Wang, S. (2017). A zoning model for coal mining-induced strata movement based on microseismic monitoring. *Int. J. Rock Mech. Min. Sci.* 94, 123–138. doi:10.1016/j.ijrmms.2017.03.001

Ding, H., Miao, X., Ju, F., Wang, X., and Wang, Q. (2014). Strata behavior investigation for high-intensity mining in the water-rich coal seam. *Int. J. Min. Sci. Technol.* 24 (3), 299–304. doi:10.1016/j.ijmst.2014.03.002

Feng, X., Gong, B., Cheng, X., Zhang, H., and Tang, C. (2022). Anisotropy and microcrack-induced failure precursor of shales under dynamic splitting. *Geomatics, Nat. Hazards Risk* 13, 2864–2889. doi:10.1080/19475705.2022.2137440

Feng, X., Gong, B., Liang, Z., Wang, S., Tang, C., Li, H., et al. (2023a). Study of the dynamic failure characteristics of anisotropic shales under impact Brazilian splitting. *Rock Mech. Rock Eng.* 57, 2213–2230. doi:10.1007/s00603-023-03673-w

Feng, Y., Yang, W., Wan, J., and Li, H. (2023b). Granular risk assessment of earthquake induced landslide via latent representations of stacked autoencoder. *Front. Environ. Sci.* 11. doi:10.3389/fenvs.2023.1308808

Gong, B., Liang, Z., and Liu, X. (2022). Nonlinear deformation and failure characteristics of horseshoe-shaped tunnel under varying principal stress direction. *Arabian J. Geosciences* 15, 475. doi:10.1007/s12517-022-09678-z

Gong, B., Zhao, T., Thusyanthan, I., and Tang, C. (2024). Modelling rock fracturing by a novel implicit continuous to discontinuous method. *Comput. Geotechnics* 166, 106035. doi:10.1016/j.compgeo.2023.106035

Jing, J., Shi, L., Li, Z., Liu, T., Wei, J., and Li, S. (2006). Mechanism of water-inrush from roof in Huafeng mine. *J. China. Univ. Min. Tech.* 35.

Kang, H., Li, W., Gao, F., and Yang, J. (2023). Grouting theories and technologies for the reinforcement of fractured rocks surrounding deep roadways. *Deep Undergr. Sci. Eng.* 2 (1), 2–19. doi:10.1002/dug2.12026

Li, G., Wang, K., Gong, B., Tao, Z., Du, K., and Tang, C. (2021a). A multi-temporal series high-accuracy numerical manifold method for transient thermoelastic fracture problems. *Int. J. Solids Struct.* 230-231, 111151. doi:10.1016/j.ijsolstr.2021.111151

Li, L., Tu, W., Shi, S., Chen, J., and Zhang, Y. (2016). Mechanism of water inrush in tunnel construction in karst area. *Geomatics, Nat. Hazards Risk* 7, 35–46. doi:10.1080/19475705.2016.1181342

Li, Q., Ma, D., Zhang, Y., Liu, Y., Ma, Y., and Hu, D. (2021b). Insights into controlling factors of pore structure and hydraulic properties of broken rock mass in a geothermal reservoir. *Lithosphere* 2021 (Special 5). doi:10.2113/2022/3887832

Li, W., Wang, Y., Ye, Z., Liu, Y. A., and Wang, L. (2024). Development of a mixed reality assisted escape system for underground mine-based on the mine water-inrush accident background. *Tunn. Undergr. Space Technol.* 143, 105471. doi:10.1016/j.tust.2023.105471

Liu, R., Zhi, G., Yang, S., and Xu, X. (2023). Investigation on mining-induced floor water inrush from column and its control based on microseismic monitoring. *Adv. Civ. Eng.* 5 (20), 3754079.

Liu, X., Zhang, X., Wang, L., Qu, F., Shao, A., Zhao, L., et al. (2024). Research progress and prospects of intelligent technology in underground mining of hard rock mines. *Green Smart Min. Eng.* 1 (1), 12–26. doi:10.1016/j.gsme.2024.03.007

Ma, D., Duan, H., and Zhang, J. (2022b). Solid grain migration on hydraulic properties of fault rocks in underground mining tunnel: radial seepage experiments and verification of permeability prediction. *Tunn. Undergr. Space Technol.* 126, 104525. doi:10.1016/j.tust.2022.104525

Ma, D., Duan, H., Zhang, J., Liu, X., and Li, Z. (2022a). Numerical simulation of water–silt inrush hazard of fault rock: a three-phase flow model. *Rock Mech. Rock Eng.* 55 (8), 5163–5182. doi:10.1007/s00603-022-02878-9

Ma, K., Sun, X. Y., Tang, C. A., Yuan, F. Z., Wang, S. J., and Chen, T. (2021). Floor water inrush analysis based on mechanical failure characters and microseismic monitoring. *Tunn. Undergr. Space Technol.* 108, 103698. doi:10.1016/j.tust.2020.103698

Qiu, Q., Zheng, L., Hong, L., Zhang, W., He, H., Zhao, C., et al. (2022). Water inrush mechanism of roof induced by the fault weakening effect in the coal mining. *Math. Problems Eng.* 2022, 5737738.

Ren, Z., Zhang, C., Wang, Y., Lan, S., and Liu, S. (2023). Stability analysis and grouting treatment of inclined shaft lining structure in water-rich strata: a case study. *Geohazard Mech.* 1 (4), 308–318. doi:10.1016/j.ghm.2023.11.002

Shen, W. Q. (2024). Effective yield strength of a saturated porous medium with a spheroidal meso-pore and spherical micro-pores. *Rock Mech. Bull.* 3 (1), 100097. doi:10.1016/j.rockmb.2023.100097

Snoke, J. A. (1987). Stable determination of (Brune) stress drops. *Bull. Seismol. Soc. Am.* 77 (2), 530–538.

Sun, D., Hou, X., Yang, T., Zhao, Y., Zhang, P., Yang, B., et al. (2022). Calibration of water inrush channel and numerical simulation of water inrush process in coal mine roof. *Front. Earth Sci.* 10, 931508. doi:10.3389/feart.2022.931508

Tu, W., Li, L., Cheng, S., Chen, D., Yuan, Y., and Chen, Y. (2021). Evolution mechanism, monitoring, and early warning method of water inrush in deep-buried long tunnel. *Geofluids* 2021, 1–6. doi:10.1155/2021/2023782

Wang, W., Yao, Q., Wang, A., Hudson-Edwards, K. A., Zheng, C., Yan, L., et al. (2023). Study of a damage constitutive model for water-bearing coal measures sedimentary rock with nonlinear deformation during compaction stage. *Geohazard Mech.* 1 (3), 244–254. doi:10.1016/j.ghm.2023.09.002

Wang, X., Xu, Z., Sun, Y., Zheng, J., Zhang, C., and Duan, Z. (2021). Construction of multi-factor identification model for real-time monitoring and early warning of mine water inrush. *Int. J. Min. Sci. Technol.* 31 (5), 853–866. doi:10.1016/j.ijmst.2021.07.012

Wang, Y., Chen, Q., Dai, B., and Wang, D. (2024). Guidance and review: advancing mining technology for enhanced production and supply of strategic minerals in China. *Green Smart Min. Eng.* 1 (1), 2–11. doi:10.1016/j.gsme.2024.03.005

Wei, J., Li, Z., Shi, L., Guan, Y., and Yin, H. (2010). Comprehensive evaluation of water-inrush risk from coal floors. *Min. Sci. Technol.* 20 (1), 121–125. doi:10.1016/s1674-5264(09)60172-1

Wu, J., Wang, X., Wu, L., Lu, Y. N., and Han, Y. H. (2022). Parametric study of water inrush in a tunnel crossing a fault based on the "three zones" fault structure. *KSCE J. Civ. Eng.* 26 (8), 3600–3619. doi:10.1007/s12205-022-1310-z

Wyss, M., and Brune, J. N. (1968). Seismic moment, stress, and source dimensions for earthquakes in the California-Nevada region. *J. Geophys. Res.* 73 (14), 4681–4694. doi:10.1029/jb073i014p04681

Wyss, M., and Brune, J. N. (1971). Regional variations of source properties in southern California estimated from the ratio of short-to long-period amplitudes. *Bull. Seismol. Soc. Am.* 61 (5), 1153–1167. doi:10.1785/bssa0610051153

Xiang, G., Jiang, T., Yang, Q., Cui, S., Zhu, L., He, Y., et al. (2023). The influence of vertical seismic acceleration on the triggering of landslides constrained by bedding faults under an inertial frame reference: the case of the daguangbao (DGB) landslide. *Appl. Sci.* 13 (23), 12911. doi:10.3390/app132312911

Yin, H., Wu, Q., Yin, S., Dong, S., Dai, Z., and Soltanian, M. Z. (2022). Predicting mine water inrush accidents based on water level anomalies of borehole groups using long short-term memory and isolation forest. *J. Hydrology* 616, 128813. doi:10.1016/j.jhydrol.2022.128813

Yin, H., Zhang, G., Wu, Q., Yin, S., Soltanian, M. R., Thanh, H. V., et al. (2023). A deep learning-based data-driven approach for predicting mining water inrush from coal seam floor using micro-seismic monitoring data. *IEEE Trans. Geoscience Remote Sens.* 61, 1–15. doi:10.1109/tgrs.2023.3300012

Yu, R., Qian, J., Liu, L., Zha, H., and Li, N. (2022). Microseismic precursors of coal mine water inrush characterized by different waveforms manifest as dry to wet fracturing. *Int. J. Environ. Res. Public Health* 19 (21), 14291. doi:10.3390/ijerph192114291

Zhang, C., Chen, Y., Ren, Z., and Wang, F. (2024). Compaction and seepage characteristics of broken coal and rock masses in coal mining: a review in laboratory tests. *Rock Mech. Bull.* 3 (2), 100102. doi:10.1016/j.rockmb.2024.100102

Zhang, J. (2005). Investigations of water inrushes from aquifers under coal seams. *Int. J. Rock Mech. Min. Sci.* 42 (3), 350–360. doi:10.1016/j.ijrmms.2004.11.010

Zhang, S., Guo, W., Li, Y., Sun, W., and Yin, D. (2017). Experimental simulation of fault water inrush channel evolution in a coal mine floor. *Mine Water Environ.* 36 (3), 443–451. doi:10.1007/s10230-017-0433-9

Zhang, Y., Zhang, W., Xia, H., Gong, B., Liu, F., Zhang, J., et al. (2023). Case study and risk assessment of water inrush disaster in Qingdao metro line 4. *Appl. Sci.* 13, 3384. doi:10.3390/app13063384

frontiers | Frontiers in Earth Science

TYPE Original Research
PUBLISHED 26 July 2024
DOI 10.3389/feart.2024.1434519

OPEN ACCESS

EDITED BY
Chong Xu,
Ministry of Emergency Management, China

REVIEWED BY
Yulong Cui,
Anhui University of Science and Technology, China
Siyuan Ma,
China Earthquake Administration, China
Kun Fang,
Hong Kong University of Science and Technology, Hong Kong SAR, China

*CORRESPONDENCE
Zhou Zhao,
✉ zhaozhou@xust.edu.cn

RECEIVED 18 May 2024
ACCEPTED 28 June 2024
PUBLISHED 26 July 2024

CITATION
Zhao Z, Zhang Y, Chen X, Wei J, Ma J, Tang H and Liu F (2024), Simulation and prediction of dynamic process of loess landslide and its impact damage to houses.
Front. Earth Sci. 12:1434519.
doi: 10.3389/feart.2024.1434519

Simulation and prediction of dynamic process of loess landslide and its impact damage to houses

Zhou Zhao*, Yuhan Zhang, Xing Chen, Jiangbo Wei, Jianquan Ma, Hao Tang and Fei Liu

College of Geology and Environment, Xi'an University of Science and Technology, Xi'an, China

The mountainous areas of the Loess Plateau in China are crisscrossed with ravines, fragile ecological environment, and frequent landslide hazards. Landslides often cause building collapses and casualties, seriously affecting the sustainability of economic and social development in the region. In order to study the damage of loess landslides to village and town buildings, the paper takes the Xingwang landslide in Fugu County, Shaanxi Province, China as an example, and uses discrete element method and finite element method to study the dynamic process of landslide and its damage to houses. Firstly, the geological characteristics of the landslide were identified by means of investigation, surveying, engineering exploration and geotechnical testing. Secondly, a three-dimensional numerical model of the landslide area was established by using the particle flow code system (PFC^{3D}). Finally, the entire movement process of the landslide was simulated, and the impact damage to houses induced from landslide was analyzed and predicted. The results show that the whole movement of the landslide lasted a total of 180 s, with a maximum average velocity of 2.01 m/s and a maximum average displacement of 73.7 m. The first and second rows of houses located at the foot of the landslide will suffer serious damage, with most bricks displacement ranging from 0.1 to 2.5 m and a maximum displacement of 10.3 m, posing a serious safety risk to the houses. Only a portion of the third row houses will be damaged, and the fourth row houses will not be threatened by landslide. By comparing with the prediction results of other methods and the current situation of buildings deformation, the results of this paper have a certain credibility. This study provides a numerical method for quantitative assessment of the risk and building damage for loess landslide, which can be used as a reference. It also provides technical support for formulating hazard prevention and reduction plans for the Xingwang landslide.

KEYWORDS

loess landslide, dynamic process, impact damage to houses, simulation and prediction, the discrete element method, the finite element method

1 Introduction

Landslides are a common geological hazard in mountainous areas of China, with strong destructiveness and huge harmfulness. Landslides on the Loess Plateau account for at least one-third of the total number of landslides in China (Ji et al., 2024), and more than 16,600 loess landslides have been developed in northern Shaanxi (Peng et al., 2016;

Peng et al., 2019), which have caused a large number of casualties and property losses, affecting the socio-economic development of urban areas. For example, the Sale Mountain loess landslide in 1983 resulted in 220 deaths (Yan et al., 2018), the Baqiao loess landslide occurred in 2011 with 32 deaths (Zhuang et al., 2015), and the Jiangliu loess landslide in 1984 buried large areas of farmland and houses (Liu and Kang, 1986). From the perspective of hazard consequences, the mobility of landslide and its impact performance on buildings are the key reasons for these casualties and losses. Therefore, the prediction study on the whole process of loess landslide movement and impact damage to houses of great practical significance for landslide risk prevention and reduction.

The landslide movement is a dynamic process with a time effect. Currently, research in this area mainly focuses on landslide velocity, displacement, influence range and other indicators (Wang et al., 2023; Wu et al., 2023; Xu et al., 2023). On the other hand, the prediction of damage caused by landslides impact to buildings needs to be based on the analysis of the landslide movement, so the study of landslide dynamic processes has always been a hot topic in the field of engineering geology. Considering the significant difficulties in accurately measuring the dynamic indicators of landslides during the sliding process, researchers have begun to use numerical simulation methods to study the motion characteristics in recent years (McDougall, 2006; Xiao and Lin, 2016; Li et al., 2019; Wang et al., 2020; Li et al., 2021; Chang et al., 2022; Song et al., 2023; Zhang et al., 2024), which not only reduces the cost but also visualizes the process of landslide movement and the physical law.

At present, in terms of numerical simulation of landslide dynamic processes, there are generally two types of models: finite element models and discrete element models. The former mainly relies on the continuum theory for the study of landslides dynamic characteristics, and the corresponding software system mainly includes DAN^{3D} (Delaney and Evans, 2015; Jordan and Oldrich, 2016; Gao et al., 2023), FLOW-3D (Zhang et al., 2022; Sabeti et al., 2024), MassMov^{2D} (Monia et al., 2014; Ma et al., 2021), etc. The latter mainly relies on the discontinuous theory and is commonly used to study the dynamic characteristics, energy evolution characteristics, and deformation characteristics of buildings during landslide movement, mainly includes PFC (Wei et al., 2019; Zhao et al., 2023; Li et al., 2021), UDEC (Luo et al., 2021; Zabuski and Marcato, 2020; Li et al., 2021), 3DEC (Wu and Hsieh, 2021; Mreyen et al., 2022) and so on. In contrast, finite element method has the advantages of simple modeling, convenient operation, and low computational complexity. However, it has limitations in analyzing the flow and deformation characteristics of granular materials and solving large deformations. In fact, the most commonly used PFC (particle flow code) in the discrete element method can treat the landslide as a body composed of several particles, and simulate the deformation and motion process of the landslide through the interaction between particles and walls. Compared with the continuous medium model, the PFC does not require the assumption of macroscopic continuity to solve the problems. It can better simulate the deformation, failure, and movement processes of loose rock and soil mass such as loess landslides, and monitor their changes in velocity, impact force, energy transfer, and other characteristics. Therefore, it is increasingly widely used in the study of the dynamic process of soil landslides (Tang et al., 2009; Lo et al., 2011; Hu et al., 2019; Chen, 2022; Zhao et al., 2023). In the research of houses damage induced from landslide, the existing cases have shown that the discrete element model can effectively simulate the dynamic process of masonry structure houses subjected to landslide, especially in simulating the deformation and cracking of masonry. However, it is difficult to express the continuous deformation of the wall (Zhao et al., 2023). The finite element model has obvious advantages in analyzing the continuous deformation and overall displacement of masonry, but it is difficult to express the failure characteristics such as masonry cracking (Luo et al., 2019; Luo et al., 2019).

In the mountainous areas of the Loess Plateau in China, village and town buildings are mostly single story houses with brick and concrete masonry structures. Analyzing and predicting the damage of these types of buildings induced from loess landslides has become a key aspect for landslide quantitative risk assessment. However, most of the available research results focus on the damage to buildings caused by accumulation layers or debris landslides, a few studies on loess landslides. The researchers of this manuscript have used discrete element method and finite element method to predict the dynamic process of a shallow accumulation layer landslide and its impact damage to brick-concrete buildings (Zhao et al., 2023), but whether these methods are also applicable to the scenario simulation of a loess landslide is a small task worthy of discussion. In view of this, the manuscript takes the Xingwang loess landslide as an example. Based on field investigation, UAV survey, geological exploration, and geotechnical test analysis, a three-dimensional numerical model of landslide was established by using PFC^{3D} discrete element program. The entire dynamic process of the landslide was simulated, and dynamic parameters such as velocity, displacement, and impact force were obtained. On this basis, discrete element model and finite element model are used respectively to simulate and predict the landslide damage of buildings. The relevant results have important reference significance for risk assessment and hazard prediction of loess landslides.

2 Materials

2.1 Landslide environment

The Xingwang landslide is located in the loess mountainous area in the southern part of Fugu County, Shaanxi Province, with geographical coordinates of 38° 59′37″N and 110° 44′16″E (Figure 1). The area belongs to the temperate continental monsoon semi-arid climate, with large temperature differences and variable climate. The rainfall in August is the largest, mostly rainstorm, which is easy to cause landslide occurs. Except for the Jurassic sandstone or mudstone exposed in some local valleys, most areas are covered by Quaternary loess, and the fault structures are not developed.

2.2 Landslide characteristics

The landslide is located on a loess slope northeast of Xingwang Village (Figure 2), with a total length of about 300 m, an average

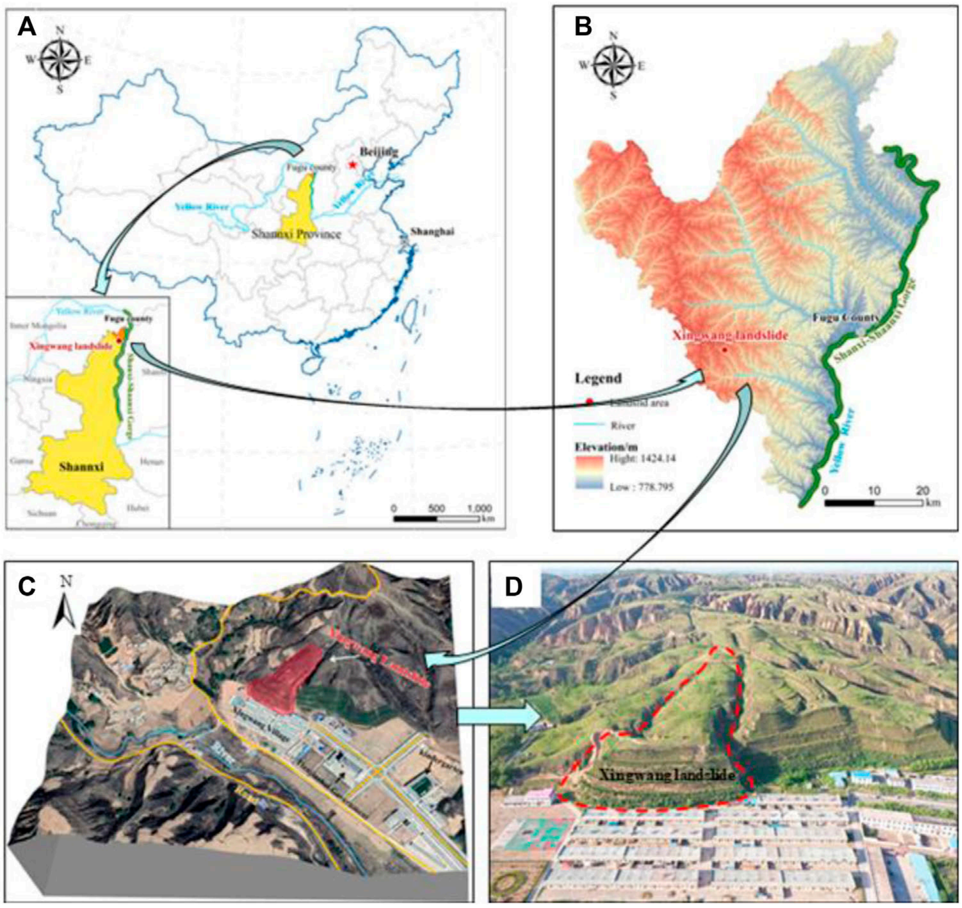

FIGURE 1
Location and image of Xingwang landslide: **(A)** and **(B)** Location of landslide; **(C)** Image of landslide area; **(D)** A photo of landslide area.

width of about 90 m, an average thickness of about 32 m, the height is about 38m, and the volume is about 4.37515 × 10^5 m^3. The main sliding direction is about 210°. The sliding body is tongue shaped on the plane, and due to the influence of engineering excavation, the front edge of the slope is steep with a slope of about 45°. The upper part of the slope is relatively flat, about 5°–10°, with gullies on both sides as the boundary (Figure 2A).

Over the past 10 years, two tensile cracks with a width of 5–10 cm and a length of about 12 m have appeared at the rear edge of the landslide (Figure 2B). Local collapse has occurred at the top of the steep slope at the front edge (Figure 2C), and the original retaining wall has undergone bulging deformation and cracking (Figure 2D). The horizontal ground at the foot of the slope has raised and cracked (Figures 2E, F). The first row of houses near the foot of the slope threatened by the landslide have also gradually deformed and cracked locally. All these signs of deformation indicate that the Xingwang landslide is in a stage of creep deformation.

Drilling data shows that the Xingwang landslide is a loess landslide, with the sliding body mainly composed of Quaternary loess (Figure 3).In addition; the sliding surface near the shear outlet exhibits an anti-tilting characteristic and intersects with the ground water level (Figure 3).

2.3 Buildings

At the foot of the landslide slope, there are four rows of buildings, each row of 13 houses, all of which are single-storey brick-concrete structures (as shown in Figure 1D). Each room is 7 m wide, 10 m long and 4 m high, with a foundation depth of 0.6 m. The roofs of the houses are 120 mm thick cast-in-place concrete floors, and the walls are 240 mm thick ordinary sintered brick walls. The cross-section size of the structure column and ring beam is 240 mm × 240 mm, and the built-in longitudinal reinforcement bar is made of 4 bars with the diameter of 12. The stirrup adopts the model diameter of 6 steel bars, and the encryption spacing is 150 mm. The hoop reinforcement is made of steel bars with a diameter of 6, with an increased spacing of 150 mm.

3 Modeling methology

3.1 Modeling based on PFC

3.1.1 Calibration of landslide soil mesoscopic parameters

The calibration of mesoscopic parameters in the PFC^{3D} determines the performance and accuracy of the landslide

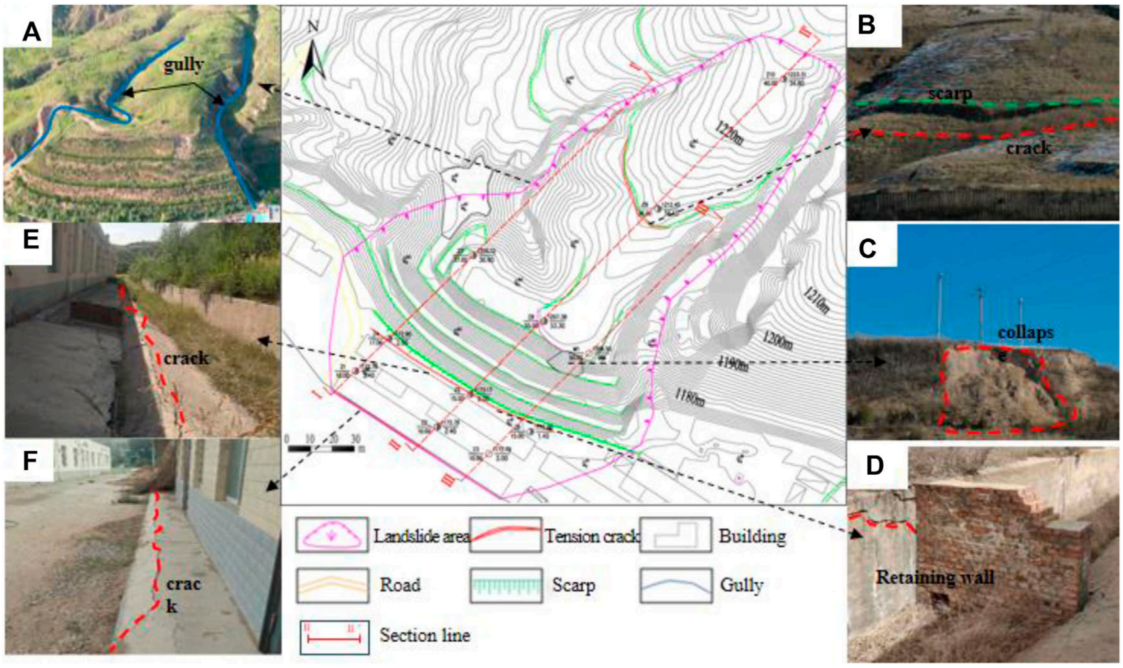

FIGURE 2
Details of the Xingwang landslide: **(A)** Gullies on both sides of the landslide; **(B)** scarp and cracks at the rear edge; **(C)** Collapse of the steep slope at the front edge; **(D)** Cracks at the retaining wall; **(E)** Cracks at the slope foot; **(F)** Cracks at the house floor.

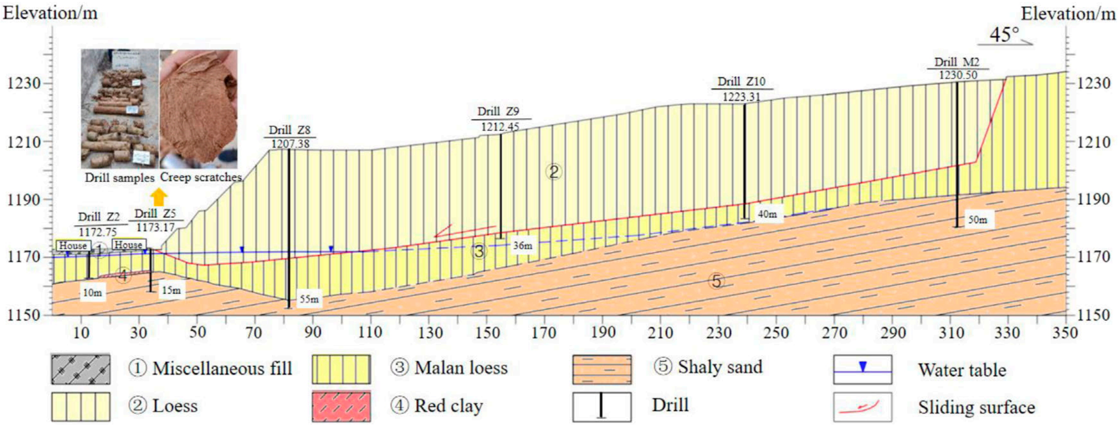

FIGURE 3
Geological profile of section II-II′ of Xingwang landslide. The location of the section is shown in Figure 2.

simulation, which is a key step in model construction, as well as characterizing the macroscopic mechanical properties of the landslide soils. The main mesoscopic parameters include particle density, particle size, normal stiffness, tangential stiffness, friction coefficient, etc. The inversion trial and error method is usually used to conduct numerical triaxial tests on soil mass with calibrated initial mesoscopic parameters of particles. When the test results are consistent with the physical and mechanical test results in laboratory, these mesoscopic parameters are applied to the construction of landslide numerical models (Wu et al., 2023).

In this paper, the corresponding stress-strain curves under different confining pressures were obtained through laboratory tests (Figure 4A), the Mohr's stress circle and Mohr's-Coulomb strength envelope were plotted (Figure 4B), and the macroscopic parameters of the landslide soil mass under saturated conditions were obtained - internal friction angle (13.2°) and cohesive force (11.8 kPa). Numerical triaxial tests were carried out in PFC3D (Figure 4C). After multiple calculations, when the macroscopic shear strength of soil mass obtained by numerical tests is consistent with that obtained by laboratory tests, the current microscopic parameters of particles can be used to build a landslide model (Table 1).

3.1.2 Calibration of houses parameters

For the buildings, considering that these houses are all single story and brick concrete structures, the RBlock module in PFC

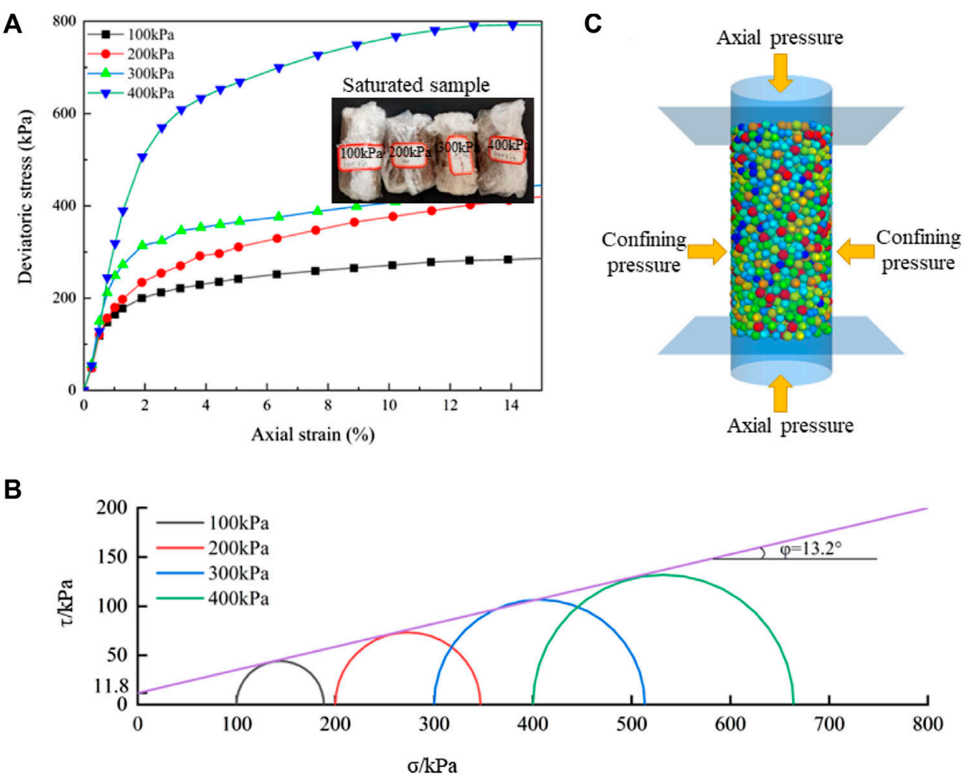

FIGURE 4
(A) Stress-strain curve; **(B)** Numerical simulation model of triaxial compression test; **(C)**. Mohr stress circle and Mohr-Coulomb strength envelope.

TABLE 1 Mesoscopic parameters of the landslide in PFC model.

Density (kg/m^3)	Rmin/Rmax	Kratio	Friction	pb_ten (Pa/m)	pb_coh (Pa/m)	pb_rmul
1580	0.3	1.0	0.28	7e5	5e5	0.5

TABLE 2 Parameters related to the brick house model.

Parameter	Value	Parameter	Value
Brick size (m)	0.24×0.12×0.06	Density (kg/m^3)	1850
Damp	0.7	Friction	0.65
Normal to tangential bond stiffness ratio	1.0	Deformation modulus (Pa)	1e8
Pb_ten (N/m)	3e6	Pb_coh (N/m)	6e3

software was chosen for building modeling, and the mortar material was replaced by the bonding between bricks. The parameters for modeling have been detailed in another research paper of the author (Zhao et al., 2023), and the relevant parameter values are shown in Table 2.

3.1.3 Model generation

The detailed technical scheme for constructing landslide models has been listed in in two other papers by the author (Zhao et al., 2023; Wei et al., 2019), and will not be elaborated here. The main steps include: Firstly, the DEM data of landslide area was obtained through field survey and UAV mapping, and the sliding surface DEM was generated in ArcGIS by analyzing the drill data. Then, integrate the above two DEM data to produce a complete landslide grid model. Finally, the grid model is imported into the PFC^{3D} system to complete the construction of the landslide three-dimensional numerical model. Considering the limitation of computer performance, 274,505 particles with size between 0.3 and 1.0 m were randomly generated to simulate the landslide body, of which 12 particles were used as monitoring particles (as shown

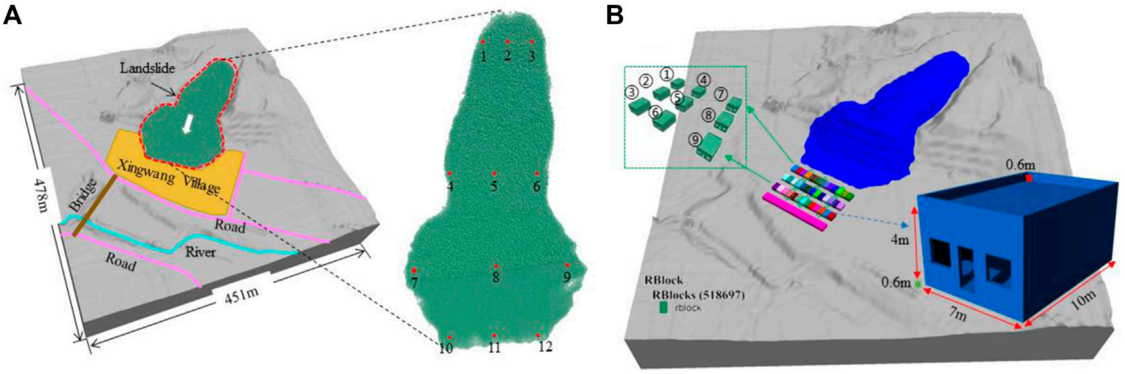

FIGURE 5
(A) Landslide model, the number represents the serial number of the monitored red particles; **(B)** Combined model of landslide and buildings, with houses in small windows specifically designed to analyze the impact damage of landslide.

TABLE 3 Main parameters of building materials.

Materials	Density (kg/m^3)	Elasticity modulus (MPa)	Poisson's ratio
Concrete	2.5×10^3	2.8×10^4	0.2
Reinforced bar	7.8×10^3	2.1×10^5	0.3
Masonry	1.8×10^3	2.2×10^3	0.15

TABLE 4 The parameters of houses numerical model.

Materials	Expansion Angle(°)	Eccentricity ratio	f_{bo}/f_{co}	K	Viscous parameter
Concrete	30	0.1	1.16	0.667	0.005
Masonry	15	0.1	1.16	0.667	0.005

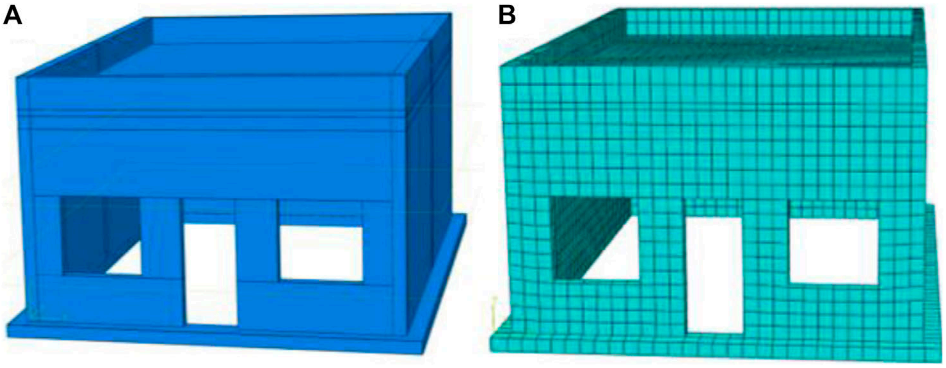

FIGURE 6
The model produced from ABAQUS: **(A)** solid model; **(B)** grid model.

in Figure 5A). And then, the combination model of landslide and buildings was established by using the RBlock module in PFC, combined with the UAV surveying information and the house characteristics shown in Table 2 (the model is shown in Figure 5B).

3.2 Modeling based on ABAQUS

In order to compare with the results of house damage based on discrete element model (PFC model), a house model of the same size is produced based on ABAQUS finite element program to simulate and predict the overall deformation and damage of the houses. Considering the limitation of calculation performance, this paper uses the integral modeling method in ABAQUS to simulate the house located on the main sliding section. In this study, according to the characteristics of buildings investigation, the concrete with strength grade of C25 is selected for building model. In terms of reinforcement, HRB400 was selected for longitudinal reinforcement and HRB335 for stirrup reinforcement. The blocks were selected as sintered ordinary bricks with grade MU10 strength, while the mortar was selected with grade M5 strength. The relevant parameters of the house model are shown in Table 3 and Table 4, and the model is shown in Figure 6.

4 Results and discussion

4.1 Simulation based on PFC

The simulation of the whole process of Xingwang landslide movement and impact damage to houses is shown in Figure 7.

4.1.1 Velocity and displacement

According to the analysis of the velocity and displacement curves of the monitored particles (as shown in Figure 8), the average peak velocity of the Xingwang landslide is 2.01 m/s, and the average maximum displacement reaches 73.7 m (Figure 9A), this happens to be the distance where the back wall of the fourth row house is located. Compared with the calculated results of the Empirical model, frictional model (Scheidegger,1973; Seng, 1989) and the Li model (Li and Wang, 1989), the maximum velocity and displacement at different reach positions in Figure 9A are both smaller than the calculated values (Table 5; Table 6). The displacement obtained from PFC model is close to the calculation results of empirical model and Li model, while Li models consider the slide conditions. Therefore, the blocking effect of the houses on landslide reduces the maximum displacement, and the influence on landslide velocity is particularly obvious. On the other hand, as a kind of granular material, the collision and friction between the particles of loess dissipate energy in the process of landslide movement, which reduces the kinetic energy, resulting in a decrease in the maximum velocity and displacement.

4.1.2 Impact force of landslide to houses

The impact force of landslide is a key index to evaluate the vulnerability of the elements at risk. By using PFC model, rigid walls are constructed at different positions of slope foot to monitor the impact force of landslide. Figure 9B shows the dynamic variation of the impact force on the rigid wall (8 m high and 60 m wide) at the first row of houses, and the maximum force is about 19 × 10^6 N. When the landslide stops moving, the impact force is constant at about 14.5 × 10^6 N. The results of landslide impact force change with time are basically consistent with those of Shen et al. (2018), Zhao et al. (2023).

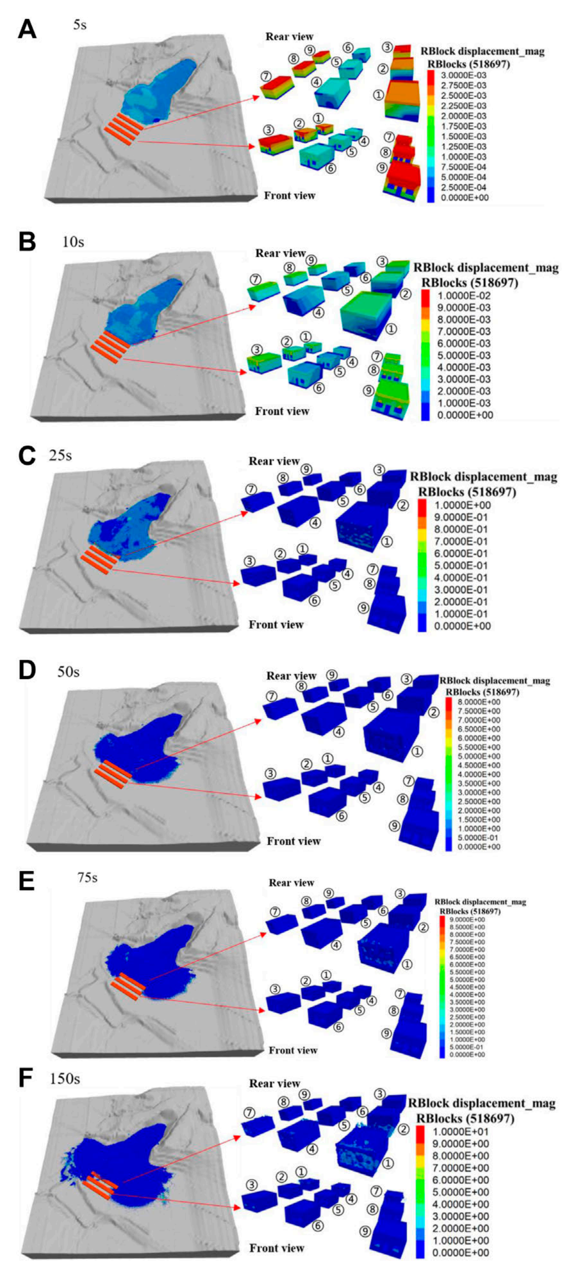

FIGURE 7
Cloud maps of landslide movement and houses displacement at different times. **(A–F)** correspond to the cloud maps of landslide and house displacement at times of 5 s, 10 s, 25 s, 50 s, 75 s, and 150 s, respectively.

Compared with the dry granular flow impact tests (Jiang et al., 2020), the normal impact force (F_n) calculation model is shown in Eq. 1.

$$F_n = \rho_d v^2 b h_0 + \frac{1}{2} k \rho_s g b {h_1}^2 \tag{1}$$

In Eq. 1, ρ_d is the dynamic density (kg·m^{-3}), v is the averaged velocity (m·s^{-1}), b is the chute width (m), h_0 is the thickness of the flowing layer (m), k is the earth pressure coefficient, ρ_s is the static density (kg·m^{-3}), g is gravitational acceleration (m·s^{-2}), and h_1 is depth measured vertically down from the front

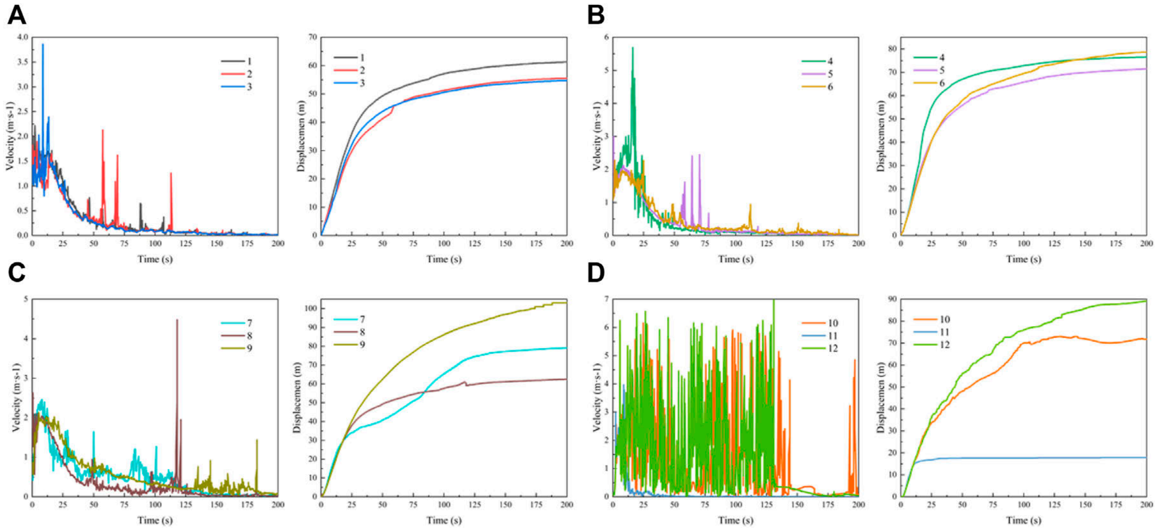

FIGURE 8
Velocity and displacement curves of the monitored particles: **(A)** Particle 1, 2, and 3; **(B)** Particle 4, 5, and 6; **(C)** Particle 7, 8, and 9; **(D)** Particle 10, 11, and 12. The monitored particles are shown in Figure 5A.

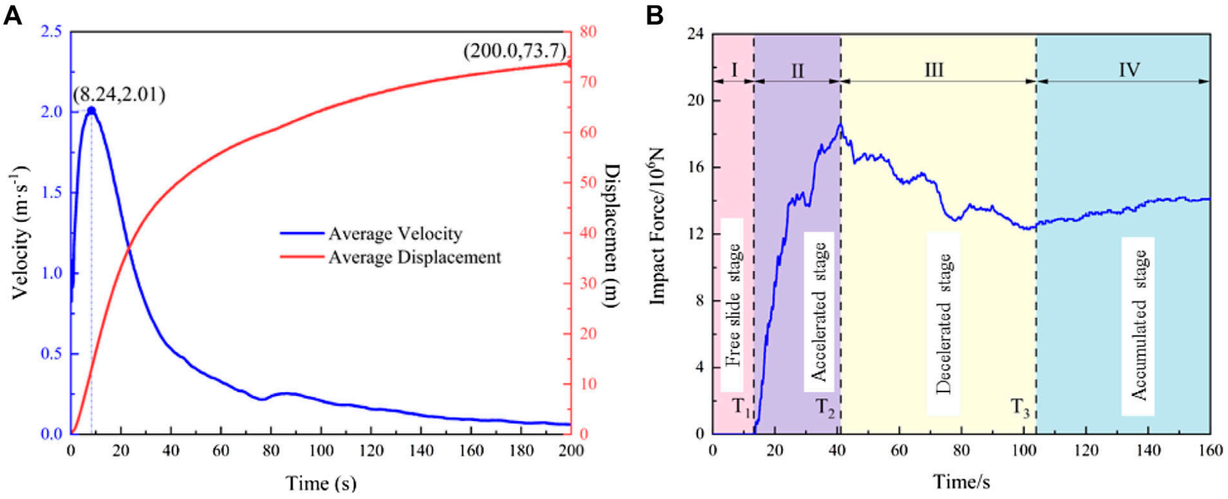

FIGURE 9
Average velocity, displacement and impact force curves of landslide: **(A)** Average velocity and displacement; **(B)** Impact force.

TABLE 5 List of landslide maximum displacement.

Method	Formula	Maximum displacement (m)
PFC model	——	73.7
Empirical formula	L=2H	76
Xieson formula	$\lg(H/L) = 0.1\text{-}0.094 \lg V$	102.33
Li Baoxiong formula	$L=n\times H/\tan Ø$	79.4

Here: H is the total vertical height of the path of the landslide, taking 38 m; V is landslide volume, taking 4.37515 × 105 m3; L is maximum displacement (m); Ø is the internal friction angle of loess, taking 13.2°; n is the coefficient of sliding out conditions for landslide, taking 0.49.

of the free surface (m). According to Eq. 1, for the Xingwang landslide, k is equal to 1 (Ashwood and Hungr, 2016), ρ_d and ρ_s are 1580 kg.m^{-3}, g equals 9.81 m.s^{-2}, b is a unit width of 60 m, h_0 = 1.0 m, h_1 = 8.0 m. Thus, F_n = 29.8 × 10^6 N. Obviously, the computational model is larger than the impact force in the PFC model due to the failure to consider the bonding strength between particles.

4.1.3 Damage of buildings

This study selects three houses from each row of the buildings in front of the slope for analysis the damage induced from landslide (1 house in the east, 1 house in the middle, and 1 house in the west, as shown in Figure 5B). From the simulation of building damage (as shown in Figure 7), the landslide began to impact the first row of houses after 10 s of movement (Figure 7B), and the deformation

TABLE 6 List of landslide velocity at different displacement.

Method	Formula	Displacement (m)								
		10	20	30	50	70	80	90	100	102.33
		Velocity (m/s)								
PFC method	——	1.9	1.8	1.6	0.5	0.3	0.0	0.0	0.0	0.0
Scheidegger formula	$v=\sqrt{2g(H-f\times l)}$	13.1	12.4	11.6	9.6	7.8	6.4	4.8	2.1	0.5

Here: *H is the total vertical height of the path of the landslide, taking 38 m;; l* represents the distance where the landslide reaches in horizontal direction, which is composed of the horizontal length of the landslide body (295 m) and its displacement (here we take 10 m, 20 m, 30 m, 50 m, 70 m, 80 m, 90 m, and 100 m and 102.33 m, respectively); *f* is the friction coefficient of landslide, expressed as the total vertical height *H* divided by the maximum *l*; *v* is the velocity at different displacements.

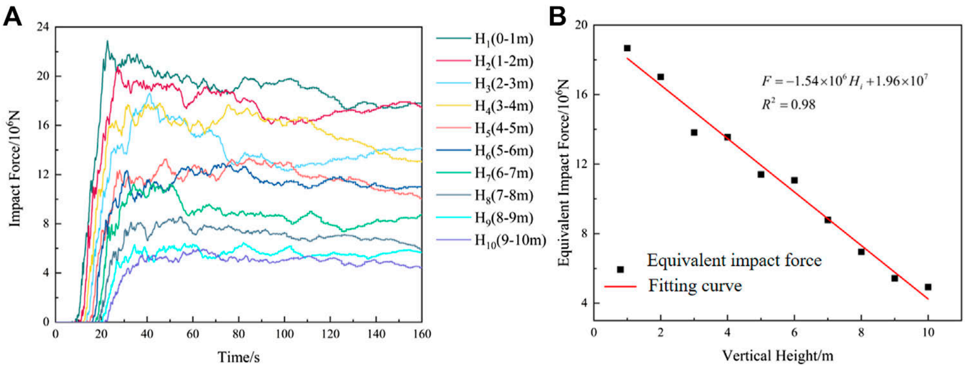

FIGURE 10
Characteristics of landslide impact force in height direction: **(A)** curves of dynamic impact force at different heights; **(B)** the fitting curve of equivalent impact force and height.

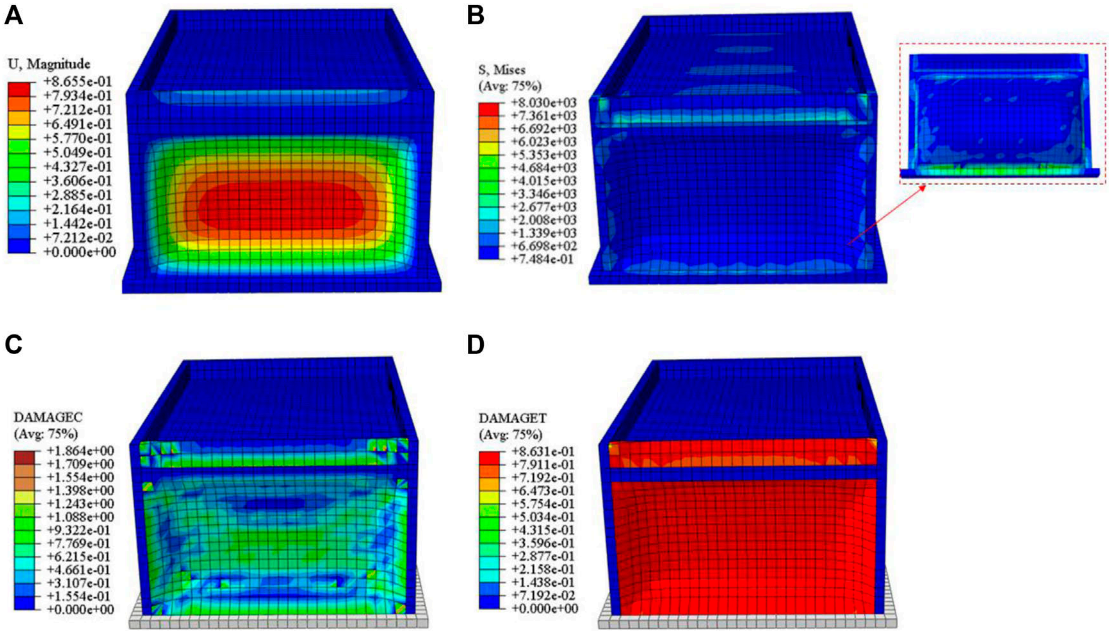

FIGURE 11
Cloud maps of house damage based on finite element model: **(A)** Displacement cloud map; **(B)** Stress cloud map, right red box (inset): stress distribution inside the impacted wall; **(C)** compression damage cloud map; **(D)** Tensile damage cloud map.

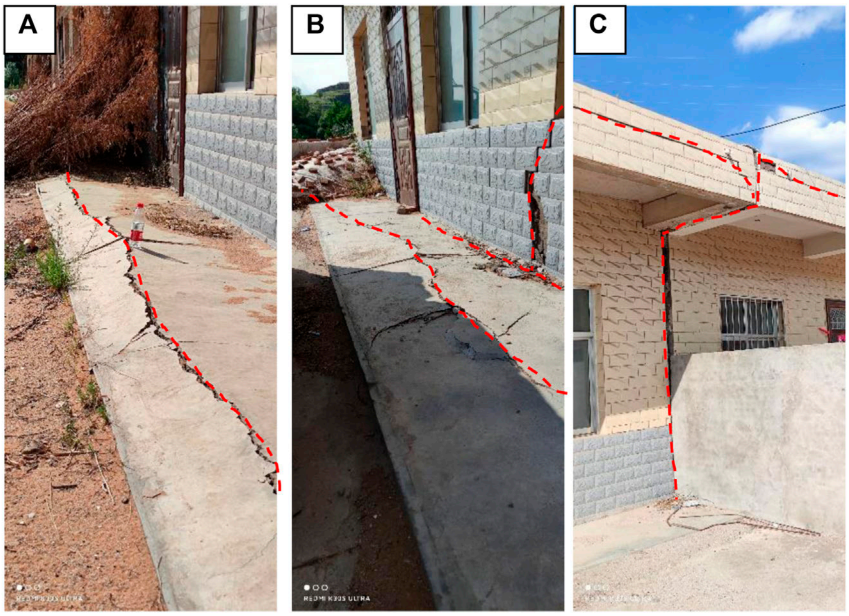

FIGURE 12
Actual deformation and damage of houses: **(A)** and **(B)** The shear cracks at the foot of the wall; **(B)** and **(C)** The tensile cracks at the roof and structural columns.

of the wall gradually expanded from the foot to the top, but there was no significant displacement at this time. After 25 s, the impact strength of the landslide gradually increased, and the deformation of the first row of house walls intensified, causing the bricks are sunken inward (Figure 7C). After 50 s, the first row of houses is completely buried, and the maximum displacement of some bricks reached 8.2 m, while the foot of the second row of houses began to deform (Figure 7D). At 75 s, the landslide soil flooded into the first row of houses, and the deformation of the second row of houses intensified (Figure 7E). After 150 s, the sliding motion gradually stops. At this time, the first and second rows of houses at the foot of the slope were severely damaged, with some bricks reaching a maximum displacement of 10.3 m, and most of the brick displacement was distributed between 0.1 and 2.5 m. The third row of houses is not as severely damaged as the first two rows, with only part of the brick detached from the wall at the window area and some landslide soil pouring into the houses (Figure 7F).

4.2 Simulation based on ABAQUS

In order to compare with the house damage prediction simulated by discrete element model, the finite element system ABAQUS is used to construct a new house model (Figure 6). Firstly, we need to analyze the distribution characteristics of landslide impact force at different heights to determine the load of the wall per unit area. Because the impact force in Figure 9B is a dynamic force, we need to convert it into an equivalent impact force by using Eqs 2, 3.

$$E = \int_{T1}^{T3} f(t)dt = S \tag{2}$$

$$F = \frac{E}{\Delta T} = \frac{S}{T_3 - T_1} \tag{3}$$

where: T_1 is the time when the landslide starts to move (s); T_3 is the time when the landslide stops moving (s); E is landslide impulse (N·s); S is the area under the impact force curve (N·s); $f(t)$ is to monitor the horizontal impact force (N); F is the equivalent impact force (N). The impact forces at different heights of rigid walls in Figure 9B are shown in Figure 10A. According to Eqs 1, 2, the fitting curves of the equivalent impact force of landslide at different heights of the wall are shown in Figure 10B. The linear relationship between the equivalent impact force and the height is: $F = - 1.54 \times 10^6 \times H_i + 1.96 \times 10^7$ ($R^2 = 0.98$) and the horizontal load is $p = -17111.11 \times H_i + 217{,}778$, with the maximum impact load being 2.18×10^5Pa. The results demonstrate that the equivalent impact force increases with the height of the wall. Then, we apply the horizontal load to the house model in Figure 6, and the result of house damage is shown in Figure 11.

The simulation results show that the wall moves towards the interior of the room after being impacted by the landslide, with a maximum displacement of 0.87 m (Figure 11A), and a maximum stress of 8.03 Mpa at the foot of the wall (Figure 11B). A large area of compressive and tensile damage occurs around the wall impacted by the landslide (Figures 11C, D), which is completely consistent with the deformation and failure characteristics of the houses at the foot of the Xingwang landslide (Figure 12). Due to the integral modeling method, the simulation results cannot display the collapse situation of the house. However, from the displacement cloud map, stress cloud map, compression and tensile damage cloud map of the wall impacted by landslide, it can be seen that the house located in the first row at the foot of the slope will inevitably collapse and be damaged.

5 Conclusion

Based on the above research, the dynamic process of the Xingwang loess landslide was simulated using the discrete element method, with a focus on predicting the consequences of landslide damage to buildings using both discrete element and finite element models. Through comparative analysis, the following conclusions can be drawn.

(1) According to the results of discrete element simulation, most of the displacements of wall bricks are between 0.1 and 2.5 m, and the maximum is 10.3 m. The finite element model reveals the displacement, stress and strain characteristics of the building under the landslide impact. The maximum displacement of the building is 0.87 m, the stress around the wall is the most concentrated, and the deformation and damage are the most obvious, which is basically consistent with the field investigation.

(2) From the simulation results, the Xingwang landslide will cause serious damage to the houses at the foot of the slope, and there is a greater safety risk. Measures such as monitoring, early warning and engineering treatment should be taken to reduce the occurrence of landslide accidents and ensure the safety of residents' lives and property.

(3) The research shows that the discrete element method is suitable for the simulation of the dynamic process of loess landslide, and can accurately predict the dynamic indexes such as the velocity and displacement of landslide, but it is not perfect in the analysis of the overall damage of houses. The finite element model can well simulate the deformation and failure characteristics of masonry structure and the whole buildings, but the loading force is static force, and how to simulate the dynamic impact process of landslide on the buildings is still worthy of further study.

(4) This study improves the necessary reference for loess landslide risk assessment using discrete element method and the finite element method, especially the quantitative prediction of vulnerability for the buildings. However, there are some limitations in the study of this paper. For example, it fails to establish a full simulation model for all buildings due to the limitation of calculation performance. These deficiencies are also the focus of our next research.

Data availability statement

The original contributions presented in the study are included in the article/Supplementary Material, further inquiries can be directed to the corresponding author.

Author contributions

ZZ: Investigation, Methodology, Project administration, Validation, Writing–original draft, Writing–review and editing. YZ: Software, Writing–original draft. XC: Software, Writing–review and editing. JW: Software, Writing–review and editing. JM: Investigation, Writing–review and editing. HT: Investigation, Writing–review and editing. FL: Investigation, Writing–review and editing.

Funding

The author(s) declare that financial support was received for the research, authorship, and/or publication of this article. This work was supported by the Scientific Research Project of Geological Research Institute for Coal Green Mining, Xi'an University of Science and Technology (MTy2019-22).

Conflict of interest

The authors declare that the research was conducted in the absence of any commercial or financial relationships that could be construed as a potential conflict of interest.

Publisher's note

References

Ashwood, W., and Hungr, O. (2016). Estimating total resisting force in flexible barrier im-pacted by a granular avalanche using physical and numerical modeling. *Can. Geotechnical J.* 53 (10), 1700–1717. doi:10.1139/cgj-2015-0481

Chang, W., Xu, Q., Dong, X., Zhuang, Y., Xing, A., Wang, Q., et al. (2022). Dynamic process analysis of the Xinmo landslide via seismic signal and numerical simulation. *Landslides* 19 (6), 1463–1478. doi:10.1007/s10346-022-01876-w

Chen, X. (2022). Prediction study of movement characteristics and impact intensity of accumulation landslide of southern Shaanxi-Taking Fenghuang Street landslide in Ningqiang County as an example. Thesis. China: XI'an University of Science and Technology.

Delaney, K., and Evans, S. (2015). The 2000 Yigong landslide (Tibetan Plateau), rockslide-dammed lake and outburst flood: review, remote sensing analysis, and process modelling. *Geomorphology* 246, 377–393. doi:10.1016/j.geomorph.2015.06.020

Gao, Y., Li, B., Gao, H., Gao, S., Wang, M., and Liu, X. (2023). Risk assessment of the Sedongpu high-altitude and ultra-long-runout landslide in the lower Yarlung Zangbo River, China. *Bull. Eng. Geol. Environ.* 82 (9), 360. doi:10.1007/s10064-023-03374-2

Hu, X., Fan, X., and Tang, J. (2019). Accumulation characteristics and energy conversion of high-speed and long-distance landslide on the basis of DEM: a case study of Sanxicun landslide. *J. Geomech.* 25 (4), 527–553. doi:10.12090/j.issn.1006-6616.2019.25.04.051

Ji, Q., Liang, Y., Xie, F., Yu, Z., and Wang, Y. (2024). Automatic and efficient detection of loess landslides based on deep learning. *Sustainability* 16 (3), 1238. doi:10.3390/su16031238

Jiang, Y. J., Fan, X. Y., Su, L. J., Xiao, S. Y., Sui, J., Zhang, R. X., et al. (2020). Experimental validation of a new semi-empirical impact force model of the dry granular flow impact against a rigid barrier. *Landslides* 18 (4), 1387–1402. doi:10.1007/s10346-020-01555-8

Jordan, A., and Oldrich, H. (2016). Dynamic simulation of the motion of partially-coherent landslides. *Eng. Geol.* 205, 1–11. doi:10.1016/j.enggeo.2016.02.006

Li, B., Zhu, Y., Qi, F., and Yuan, Z. (2021). Failure of an under-dip shale slope and its response under excavation conditions. *J. Eng. Res.* 9 (1), 63–72. doi:10.36909/jer.v9i1.8111

Li, B. X., and Wang, D. K. (1989). A new theory of space forecast for loess landslides. *J. Gansu Sci.* 10 (3), 57–58. doi:10.16468/j.cnki.issn1004-0366.1998.03.014

Li, D., Zheng, D., Wu, H., Shen, Y., and Nian, T. (2021). Numerical simulation on the longitudinal breach process of landslide dams using an improved coupled DEM-CFD method. *Front. EARTH Sci.* 9, 673249. doi:10.3389/feart.2021.673249

Li, P., Shen, W., Hou, X., and Li, T. (2019). Numerical simulation of the propagation process of a rapid flow-like landslide considering bed entrainment: a case study. *Eng. Geol.* 263, 105287. doi:10.1016/j.enggeo.2019.105287

Liu, Z. Y., and Kang, W. L. (1986). Mechanism analysis of high-speed sliding of Jiangliu landslide in Jingyang County. *Soil Water Conservation China* 1986 (02), 19–21. doi:10.14123/j.cnki.swcc.1986.02.006

Lo, C. M., Lin, M. L., Tang, C. L., and Hu, J. C. (2011). A kinematic model of the Hsiaolin landslide calibrated to the morphology of the landslide deposit. *Eng. Geol.* 123 (1–2), 22–39. doi:10.1016/j.enggeo.2011.07.002

Luo, H., Zhang, L., Wang, H., and He, J. (2021). Process of building collapse caused by the Po Shan Road landslide in Hong Kong on 18 June 1972. *Landslides* 18, 3769–3780. doi:10.1007/s10346-021-01745-y

Luo, H., Zhang, L., and Zhang, L. (2019). Progressive failure of buildings under landslide impact. *Landslides* 16, 1327–1340. doi:10.1007/s10346-019-01164-0

Luo, J., Pei, X., Evans, S., and Huang, R. (2019). Mechanics of the earthquake-induced hongshiyan landslide in the 2014 Mw 6.2 ludian earthquake, yunnan, China. *Eng. Geol.* 251, 197–213. doi:10.1016/j.enggeo.2018.11.011

Ma, S., Xu, C., Shao, X., Xu, X., and Liu, A. (2021). A large old landslide in sichuan Province, China: surface displacement monitoring and potential instability assessment. *Remote Sens.* 13 (13), 2552. doi:10.3390/rs13132552

McDougall, S. (2006). A new continuum dynamic model for the analysis of extremely rapid landslide motion across complex three-dimensional terrain. Thesis. CA: The University of British Columbia.

Monia, E. M., Massimiliano, C., and Claudia, M. (2014). r.massmov: an open-source landslide model for dynamic early warning systems. *Natrual Hazards* 70, 1153–1179. doi:10.1007/s11069-013-0867-8

Mreyen, A., Donati, D., Elmo, D., Donze, F., and Havenith, H. (2022). Dynamic numerical modelling of co-seismic landslides using the 3D distinct element method: insights from the Balta rockslide (Romania). *Eng. Geol.* 307, 106774–106790. doi:10.1016/j.enggeo.2022.106774

Peng, J., Wang, S., Wang, Q., Zhuang, J., Huang, W., Zhu, X., et al. (2019). Distribution and genetic types of loess landslides in China. *J. Asian Earth Sci.* 170, 329–350. doi:10.1016/j.jseaes.2018.11.015

Peng, J., Wu, D., Duan, Z., Tang, D., Cheng, Y., Che, W., et al. (2016). Disaster characteristics and destructive mechanism of typical loess landslide cases triggered by human engineering activities. *J. Southwest Jiaot. Univ.* 51 (05), 971–980. doi:10.3969/j.issn.0258-2724.2016.05.021

Sabeti, R., Heidarzadeh, M., Romano, A., Ojeda, G., and Lara, J. (2024). Three-dimensional simulations of subaerial landslide-generated waves: comparing OpenFOAM and FLOW-3D HYDRO models. *Pure Appl. Geophys.* 181, 1075–1093. doi:10.1007/s00024-024-03443-x

Scheidegger, A. E. (1973). On the prediction of the reach and velocity of catastrophic landslides. *Rock Mech.* 5 (4), 65–236. doi:10.1016/0148-9062(74)91709-4

Seng, X. K. (1989). Translated by Wang N. Q. Geomorphologic prediction of landslide movement distance. *Railw. Geol. Subgrade* 3, 42–~47.

Shen, W., Zhao, T., Zhao, J., Dai, F., and Zhou, G. (2018). Quantifying the impact of dry debris flow against a rigid barrier by DEM analyses. *Eng. Geol.* 241, 86–96. doi:10.1016/j.enggeo.2018.05.011

Song, K., Ruan, D., Lyu, H., Han, L., and Huang, H. (2023). Material point method-based simulation and dynamic characteristic analysis of instability-induced landslide movement: a case study of the Yanguan landslide in the Three Gorges Reservoir area. *Coal Geol. Explor.* 51 (7), 140–150. doi:10.12363/issn.1001-1986.22.11.0897

Tang, C. L., Hu, J. C., Lin, M. L., Angelier, J., Lu, C. Y., Chan, Y. C., et al. (2009). The Tsaoling landslide triggered by the Chi-Chi earthquake, Taiwan: insights from a discrete element simulation. *Eng. Geol.* 106 (1-2), 1–19. doi:10.1016/j.enggeo.2009.02.011

Wang, G., Gong, W., Xing, L., and Li, B. (2023). Model tests of run-out and deposition process of landslide debris considering influence of deposition zone width. *J. Eng. Geol.* 31 (5), 1637–1647. doi:10.13544/j.cnki.jeg.2022-0117

Wang, H., Liu, S., Xu, W., Yan, L., Qu, X., and Xie, W. (2020). Numerical investigation on the sliding process and deposit feature of an earthquake-induced landslide: a case study. *Landslides* 17 (1), 2671–2682. doi:10.1007/s10346-020-01446-y

Wei, J., Zhao, Z., Xu, C., and Wen, Q. (2019). Numerical investigation of landslide kinetics for the recent Mabian landslide (Sichuan, China). *Landslides* 16 (7), 2287–2298. doi:10.1007/s10346-019-01237-0

Wu, F., Sun, W., Li, X., Guan, Y., and Dong, M. (2023). Material point method-based simulation of dynamic process of soil landslides considering pore fluid pressure. *Int. J. Numer. Anal. Methods Geomechanics* 47 (13), 2385–2404. doi:10.1002/nag.3581

Wu, J., and Hsieh, P. (2021). Simulating the postfailure behavior of the seismically-triggered Chiu-fen-erh-Shan landslide using 3DEC. *Eng. Geol.* 287, 106113. doi:10.1016/j.enggeo.2021.106113

Wu, M., Hu, A., Zhou, S., Mao, X., and Fei, W. (2023). Research on calibration method of microscopic parameters of siltstone based on gray theory. *Sci. Rep.* 13, 15802. doi:10.1038/s41598-023-43008-x

Xiao, H., and Lin, P. (2016). Numerical modeling and experimentation of the dam-overtopping process of landslide-generated waves in an idealized mountainous reservoir. *J. Hydraulic Eng.* 142 (12), 04016059. doi:10.1061/(ASCE)HY.1943-7900.0001203

Xu, Y., Fan, X., Yang, W., and Wang, J. (2023). Analysis of motion process and dynamic parameters of high-speed and long-distance landslide in shuicheng, guizhou Province. *J. Disaster Prev. Mitig. Eng.* 43 (5), 987–998. doi:10.13409/j.cnki.jdpme.20220109002

Yan, Y. Z., Liu, G., Yang, X. Y., and Huang, D. (2018). Process simulation of the Sale Mountain landslide based on continuum-based discrete element method. *J. Lanzhou Univ. Nat. Sci.* 54 (06), 744–752. doi:10.13885/j.issn.0455-2059.2018.06.005

Zabuski, L., and Marcato, G. (2020). Analysis of potential landslide processes in the passo della Morte (carnian alps, Italy). *Geol. Q.* 64 (3), 681–691. doi:10.7306/gq.1552

Zhang, C., Ma, M., Shan, W., and Guo, Y. (2024). Process and numerical simulation of landslide sliding caused by permafrost degradation and seasonal precipitation. *Nat. Hazards* 120 (6), 5429–5458. doi:10.1007/s11069-024-06433-3

Zhang, S., Huang, X., Cheng, Y., and Shen, B. (2022). Near and far field division of landslide surge and analysis of water wave characteristics. *J. Changjiang River Sci. Res. Inst.* 39 (5), 76–82. doi:10.11988/ckyyb.20201283

Zhao, Z. (2013). Study on landslide risk management of county region in southern mountainous area of Shaanxi Province. Thesis. China: XI'an University of Science and Technology.

Zhao, Z., Chen, X., Wei, J., Ma, J., and Ye, W. (2023). Numerical study on landslide dynamic process and its impact damage prediction to brick-concrete buildings, a case from Fenghuang street landslide in Shaanxi, China. *Front. Earth Sci.* 10, 1004710. doi:10.3389/feart.2022.1004710

Zhuang, J. Q., Peng, J. B., Li, T. L., and Wang, F. W. (2015). *J. Eng. Geol.* 23 (04), 747–754. doi:10.13544/j.cnki.jeg.2015.04.024

Frontiers in Earth Science

TYPE Original Research
PUBLISHED 20 August 2024
DOI 10.3389/feart.2024.1429421

EDITED BY
Wentao Yang,
University of Leeds, United Kingdom

REVIEWED BY
Maria Francesca Ferrario,
University of Insubria, Italy
Kun He,
Southwest Jiaotong University, China

*CORRESPONDENCE
Siyuan Ma,
✉ masiyuan@ies.ac.cn

RECEIVED 08 May 2024
ACCEPTED 07 August 2024
PUBLISHED 20 August 2024

CITATION
Lu Y, Ma S and Xia C (2024) Application of different earthquake-induced landslide hazard assessment models on the 2022 Ms 6.8 luding earthquake.
Front. Earth Sci. 12:1429421.
doi: 10.3389/feart.2024.1429421

Application of different earthquake-induced landslide hazard assessment models on the 2022 Ms 6.8 luding earthquake

Yao Lu[1,2], Siyuan Ma[3,4]* and Chaoxu Xia[3,4]

[1]Shanxi Earthquake Administration, Taiyuan, China, [2]National Continental Rift Valley Dynamics Observatory of Taiyuan, Taiyuan, Shanxi, China, [3]Institute of Geology, China Earthquake Administration, Beijing, China, [4]Key Laboratory of Seismic and Volcanic Hazards, Institute of Geology, China Earthquake Administration, Beijing, China

Following the earthquake, prompt evaluation of the distribution of coseismic landslides and estimation of potential disaster losses are crucial for emergency response and resettlement planning. The Luding earthquake of 2022 offers a valuable opportunity to conduct a rapid assessment of coseismic landslides using various models. In this study, we utilize the Logistic Regression (LR)-based Xu_{2019} model, a new-generation model developed in China, alongside the Newmark model to perform the rapid hazard assessment of coseismic landslides. Assessing the accuracy and applicability of these two models based on the coseismic landslides from the Luding earthquake, we find that within intensity area of IX, the high probability area identified by the Newmark model aligns closely with the actual distribution of landslides. However, the Newmark model's prediction is overestimated in the intensity area of VIII. For the Xu_{2019} model, the prediction results are in good agreement with the distribution of actual landslides. Most landslides are located in high probability areas, such as Detuo town, Wandong, and Xingfu villages, indicating that the model has a higher prediction accuracy. Overall, two models have good practical utility in emergency hazard assessment of coseismic landslides. However, the Newmark model requires multi-input parameters and the assignment of these parameters will increase the uncertainty and subjectivity in the practical application of the modeling assessment.

KEYWORDS

2022 Ms6.8 luding earthquake, coseismic landslide, emergency assessment, newmark model, logistic regression (LR) model

1 Introduction

Powerful earthquakes often trigger numerous seismic geological disasters in mountainous regions. The casualties and property losses resulting from these catastrophes significantly contribute to the overall earthquake risk (Gorum et al., 2013; Fan et al., 2019; Havenith et al., 2022). Earthquake-induced landslides are significant secondary geological disasters, often occurring during or shortly after an earthquake (Keefer, 1984; Xu et al., 2016; Shao et al., 2023a). They are characterized by their large quantity and scale, wide distribution, complex mechanisms, resulting in severe casualties and economic losses, and prolonged post-earthquake effects (He et al., 2023; He et al., 2024).

Rapid and precise acquisition of the spatial distribution and potential hazard assessment of coseismic landslides following an earthquake is crucial for emergency rescue and resettlement planning (Tanyas et al., 2019a; Tanyas et al., 2019b; Nowicki Jessee et al., 2019). Currently, the coseismic landslide hazard assessment methods included the machine learning methods (Shao et al., 2019; Ma et al., 2020; Huang et al., 2022; Shao and Xu, 2022; Wang et al., 2023) and the Newmark method based on mechanics mechanism (Chen et al., 2014; Jin et al., 2018; Liu et al., 2018; Huang et al., 2020). Machine learning methods face a challenge: they require detailed co-seismic landslide data for model training. However, visually interpreting earthquake-induced landslides is difficult and time-consuming due to issues such as collecting and processing satellite or aerial images, cloud cover, and the slow speed of manually identifying massive landslides (Robinson et al., 2017). As a result, the assessment results based on data-driven methods frequently lag behind the actual emergency response, rendering them ineffective for the prevention and mitigation of seismic landslides (Nowicki et al., 2014; He et al., 2021).

In recent years, near-real-time assessment models of coseismic landslides based on data-driven approaches have emerged as powerful tools for quickly estimating the spatial location of landslides (Kritikos et al., 2015; Xu et al., 2019; He et al., 2021). The goal of these models is to create a near real-time prediction model of seismic landslides at a large regional scale (global or national) by utilizing the existing landslide inventories and machine learning methods. The model can then be applied in a sudden earthquake event by combining with the ground motion, and topographic and geological data of the quake-affected area (Tanyas et al., 2019a; Nowicki Jessee et al., 2019). For example, Nowicki et al. (2014) used the logistic regression (LR) method to create a globally applicable near real-time assessment model with a 1 km resolution based on four global coseismic landslide databases. Subsequently, Nowicki Jessee et al. (2019) updated the existing coseismic landslide inventories and established a new evaluation model based on the 23 earthquake events. Tanyas et al. (2019a) established a global slope unit-based model for the near real-time prediction of earthquake-induced landslides based on seven influencing variables and 25 coseismic landslide inventories around the world. Allstadt et al. (2018) chose the 2016 Mw 7.8 New Zealand earthquake as a test case to assess the performance and applicability of three globally published near-real-time models. The evaluation results show that the global empirical model for near-real-time assessment of coseismic landslides has great potential in emergency assessment. Meanwhile, Xu et al. (2019) introduced a real probability prediction method for coseismic landslides using the Bayesian probability method and LR model. They established a new generation earthquake landslide hazard model in China based on nine real earthquake cases. These studies suggest that data-driven near-real-time prediction models have promising prospects and significant potential for rapidly assessing regional earthquake-induced landslides.

The physically-based Newmark displacement method fully considers the mechanism of earthquake-induced landslides. It utilizes slope instability results and seismic displacement to quantitatively classify the hazard level of coseismic landslides. This method is widely used globally for rapidly assessing earthquake-induced landslides (Jibson, 2011; Wang et al., 2018). This method has also been applied to the emergency assessment of coseismic landslides in many regions, such as the 1979 ML 5.7 Coyote lake earthquake (Wilson and Keefer, 1983), 1994 Mw6.7 Northridge earthquake (Jibson et al., 2000), 2008 Mw7.9 Wenchuan earthquake (Godt et al., 2008), 2013 Mw6.7Lushan earthquake (Ma and Xu, 2019b; Jin et al., 2019), 2014 Mw6.1 Ludian earthquake (Chen et al., 2018), 2015 Mw7.9 Nepal earthquake (Gallen et al., 2017), 2017 Mw7.0 Jiuzhaigou earthquake (Yue et al., 2018), 2017 Ms 6.9 Milin earthquake (Du et al., 2022), 2021Mw7.4 Maduo earthquake (Wei and Chen, 2022). These cases demonstrate the reliability and timeliness of the physically-based Newmark model in emergency assessments of regional earthquake-induced landslides.

Overall, although both methods are widely used in the rapid assessment of earthquake-induced landslides, there is still a lack of quantitative comparative analysis regarding the applicability of data-driven models and the Newmark model in rapid emergency assessment of coseismic landslides, especially in the Sichuan and Yunnan area with frequent earthquake. On 5 September 2022, an Ms6.8 earthquake struck Luding County, Ganzi Tibetan Autonomous Prefecture, Sichuan Province, with an epicenter reported at 102.08 E, 29.59 N and a focal depth of 16 km by the China Earthquake Networks Center (CENC). The earthquake-produced shaking by the China Earthquake Administration (CEA) assigned a maximum seismic intensity of IX on the Mercalli scale, which is determined by the degree of damage to buildings during an earthquake, instrumentally measured ground motion, engineering damage, human perception, and other macroscopic phenomena. As of September 13, the earthquake had resulted in 93 deaths and 25 individuals missing. Otherwise, this event triggered massive coseismic landslides, mainly including shallow debris flows, collapses, topples and a few large-scale debris slides (Zhao et al., 2022; Dai et al., 2023; Yang et al., 2023). Many residential houses and roads were destroyed, resulting in greater personnel and property losses. Among them, casualties directly caused by building's collapses account for about 20%, and more than 80% are related to earthquake-induced landslides (Fan et al., 2022), which provides an excellent opportunity for us to carry out different evaluation models in the regional rapid assessment of earthquake-induced landslides.

This study utilized the Xu_{2019} model, a new generation Chinese seismic landslide hazard model, along with a simplified Newmark model to perform a rapid emergency assessment of landslides triggered by the 2022 Ms6.8 Luding earthquake. Then, Based on the coseismic landslide inventory derived from the visual interpretation of pre and post-quake Planet images with 3 m resolution, a detailed quantitative analysis of the emergency evaluation results was performed to investigate the applicability of the two models in this earthquake event. This study is expected to be useful for rapid emergency response, optimizing emergency deployment, and improving emergency rescue efficiency for a single earthquake event.

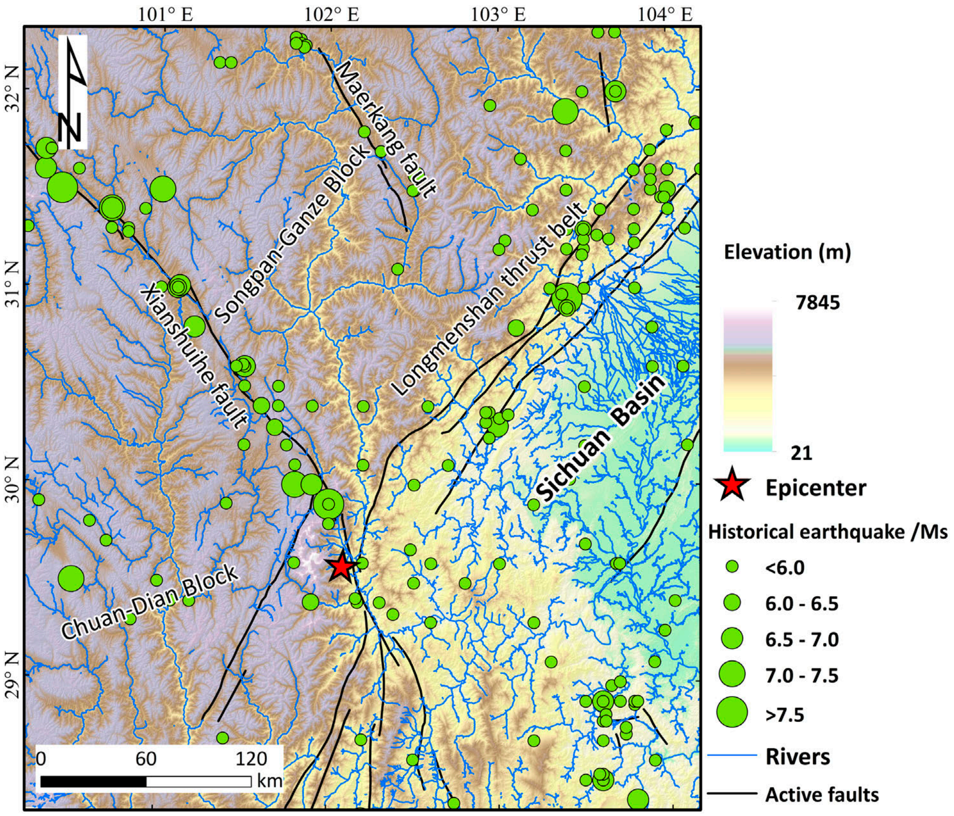

FIGURE 1
Map showing the active faults, historical earthquakes and topography distribution near the Xianshuihe fault. The active fault lines are from Deng (2007).

2 Study area

The Xianshuihe fault is an active and large-scale strike-slip fault zone that controls the relative movement and extrusion of sub-plates. This occurs against the backdrop of continued southeastward squeezing of crustal materials at the southeast margin of the Tibetan Plateau due to the convergence of the India-Eurasia plate (Tapponnier et al., 2001). The Xianshuihe fault is situated at the boundary between the Songpan-Ganze block and the Chuan-Dian block on the eastern margin of the Tibetan Plateau. It intersects with the Longmenshan fault and the Anninghe fault, forming the well-known “Y-shaped” fault zone in western Sichuan (Figure 1). Stretching 350 km from the northwest of Donggu to the south of Moxi, the fault has a strike ranging from about 130° to 148° (Bai et al., 2018). The 2022 Ms 6.8 Luding earthquake happened close to the Moxi fault in the southeastern segment of the Xianshuihe fault zone. Since 1700, there have been 17 earthquakes with a magnitude of seven or higher along the Xianshuihe fault zone, with nine of them occurring in the middle segment of the fault (Figure 1).

The Luding area is situated in the Hengduan Mountains on the southeastern edge of the Tibetan Plateau, characterized by alpine and canyon landforms. The Dadu River flows through the region from north to south, featuring a significant drop in elevation. The epicenter of the Luding earthquake, at 102.08°E, 29.59°N, is located in the Hailuogou Glacier Forest Park of Gongga Mountain, standing at 7,556 m above sea level with an altitude difference of 6,570 m. The study area experiences a typical subtropical monsoon climate, with an average annual temperature of 15.5 C and annual rainfall of 664.4 mm. The formation lithology in the area is mainly Quaternary alluvial proluvial deposits (Qh^{2apl}) and fluvioglacial deposits (Qp^{3-lgfl}), Permian dolomite, middle Devonian limestone and magmatic rock (Figure 2). The extensive tectonic activity and weathering in this region have led to the development of rock mass joints and fragmentation, creating favorable conditions for landslides to occur (Li et al., 2022).

3 Method and data

3.1 Coseismic landslide inventory of 2022 luding earthquake

The coseismic landslide database relies on visual interpretation of satellite images taken before and after the earthquake (Shao et al., 2024). The post-earthquake images are Planet images with a resolution of 3 m, collected from September 8 to 30 December 2022. In order to verify that any landslides present before the earthquake were not mistaken for coseismic landslides, the pre-quake Planet images in July and August of the study area were acquired. The results reveal that the earthquake triggered approximately 12,600 landslides with a total landslide area of 36.0 km^2 in areas above VIII intensity zones on the Mercalli scale. The largest landslide area

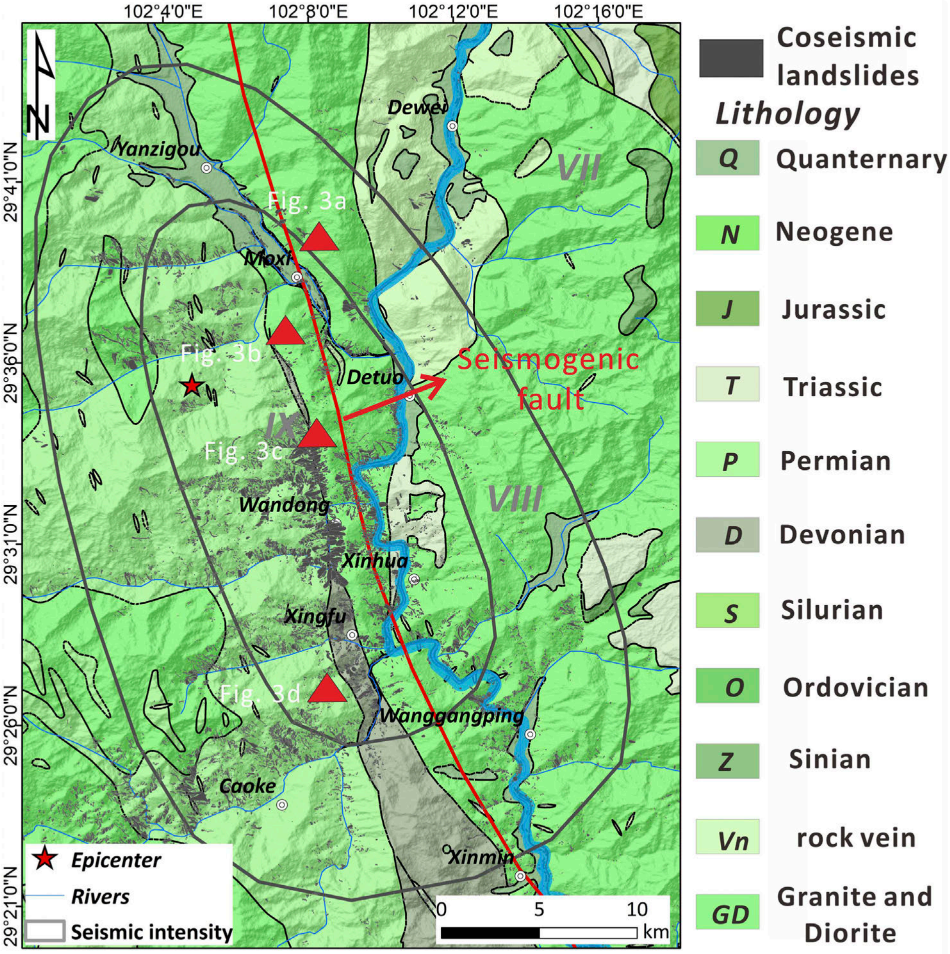

FIGURE 2
Geological map of the study area; the red line is the seismogenic fault of luding earthquake event; the coseismic landslide inventory of this event is obtained from Shao et al. (2024).

measures 120,000 m^2, while the smallest is 65 m^2, with an average area of 2,700 m^2 (Figure 2). Coseismic landslides are mainly found on both sides of the Moxi fault and the Dadu River and concentrated in intensity IX areas like Moxi, Detuo, and Wanggangping town (Figure 2). Among them, Wandong village is the most affected area by landslides in this earthquake. Field photos illustrating the development of coseismic landslides in the landslide-prone areas of this earthquake event are shown in Figure 3.

3.2 Newmark method

The Newmark displacement method was initially introduced by Newmark (1965) for analyzing the stability of dams under earthquake conditions. It posits that the instability of the dam is influenced by the deformation resulting from the earthquake rather than the minimum safety factor. This method considers that the permanent displacement is caused by constantly accumulated displacement along the most dangerous sliding surface after the instantaneous instability of the sliding body under the ground action. In this method, the critical (or yield) acceleration (ac) of the potential sliding body is determined by the pseudo-static method, and the permanent displacement can be calculated by quadratic integration of the portion of the ground motion acceleration time history that exceeds the ac.

The cumulative displacement based on the Newmark model is calculated in three steps including slope safety factor (Fs), critical acceleration (ac), and permanent displacement:

(1) Through geometric properties of the slope (thickness of rock and soil mass (t), saturation degree of rock and soil mass (m), the inclination angle of the sliding surface (α) and mechanical properties of rock and soil mass (effective cohesion (c'), internal friction angle (φ), the weight of rock and soil (γ) and groundwater weight (γ_w)), we can obtain the slope safety factor (Fs) by Equation 1.

$$Fs = \frac{c'}{\gamma t sin\alpha} + \frac{tan\,\varphi}{tan\,\alpha} - \frac{m\gamma_w\,tan\,\varphi}{\gamma\,tan\,\alpha} \quad (1)$$

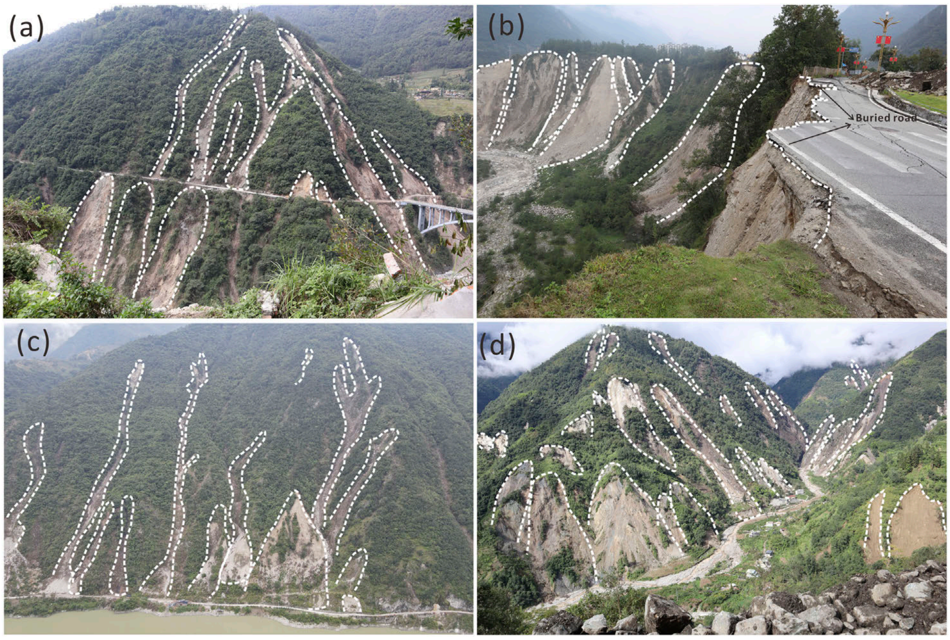

FIGURE 3
The field photos of coseismic landslides triggered by the Luding earthquake event; **(A)** Shallow debris flows in the west of Hailuogou Bridge; **(B)** Group-occurring collapses near Moxi Platform; **(C)** Shallow landslides near Detuo town; **(D)** Shallow landslides and collapses near Xingfu village.

(2) Using the infinite slope method, we can derive the ac from the above Fs (Equation 2).

$$a_c = (Fs - 1)gsin\alpha \tag{2}$$

where g is the gravitational acceleration, α is the inclination angle of the sliding surface, which is approximated by the slope angle.

(3) The Newmark displacement (Dn) of the study area can be determined using a simplified Newmark equation (Equation 3). In this study, we selected the empirical Newmark equation, derived from a dataset of 2,270 strong-motion records from 30 earthquakes worldwide (Jibson, 2007).

$$logDn = 0.215 + log\left[\left(1 - \frac{ac}{PGA}\right)^{2.341} \times \left(\frac{ac}{PGA}\right)^{-1.438}\right] \tag{3}$$

The probability of slope failure (Pf) in the study area can be calculated based on the spatial distribution of the Newmark displacement (Dn). This calculation is performed using the failure probability curve, which is fitted using data from the 2008 Wenchuan earthquake-induced landslide inventory (Ma and Xu , 2019b) (Equation 4). This formula enables the estimation of the instability probability of earthquake-induced landslides in the Wenchuan and surrounding areas

$$P(f) = 0.1005\left[1 - \exp\left(-0.2217Dn^{0.6511}\right)\right] \tag{4}$$

where $p(f)$ represents the probability of failure (Pf); Dn is the calculated Newmark displacement.

3.3 Logistic regression method

The logistic regression (LR) model is a regression analysis used when the dependent variable is a binary categorical variable. It's widely employed as a nonlinear multivariate statistical model in landslide hazard assessment. Moreover, it's the preferred method for establishing near-real-time prediction models of earthquake-induced landslides (Tanyas et al., 2019a; Nowicki Jessee et al., 2019; Shao et al., 2020). The LR model transforms the dependent variable into a binary categorical variable, where landslide occurrence is denoted by one and non-occurrence by 0. The relationship between the probability of landslide occurrence and potential influencing factors can be expressed as (Equations 5, 6):

$$Z = \beta_0 + \beta_1\chi_1 + \beta_2\chi_2 + \beta_3\chi_3 \cdots \beta_i\chi_i \tag{5}$$

$$P = 1/\left(1 + e^{-Z}\right) \tag{6}$$

Among them, p represents the occurrence probability of landslide. Z represents the sum of the linear weights after the independent variables are superimposed; χ_3 represents the independent variable, and βi is the regression coefficient.

This study utilizes the Xu_{2019} model, a new seismic landslide hazard model, as the near real-time evaluation tool for coseismic landslides (Xu et al., 2019). The model utilizes nine earthquake-induced landslide inventories from various regions in China as training samples. It incorporates 13 influencing factors, including elevation, relative elevation, slope angle, and aspect, to develop a near real-time evaluation model for coseismic landslides using the LR method. This model enables rapid assessment of coseismic landslides following individual earthquake events based on the actual distribution of Peak Ground Acceleration (PGA). Further details about the model are available in the previous study by Xu et al. (2019).

3.4 Data

The elevation data utilized in this study is derived from the ALOS PALSAR Digital Elevation Model (DEM), with a resolution of 12.5 m, obtained from the Alaska Satellite Facility (https://vertex.daac.asf.alaska.edu). The slope gradient across the study area was calculated based on this DEM data. As illustrated in Figure 4A, the spatial distribution of slope angles shows steeper slopes in the western region and gentler slopes in the eastern region. For the ground motion data, we utilized the Peak Ground Acceleration (PGA) map provided by the Xuanmei Fan team from Chengdu University of Technology. This map was generated by interpolating strong motion records collected within 100 km from the epicenter of the earthquake in Sichuan. According to Fan et al. (2022), the seismic stations recorded a maximum PGA value of 644.4 cm/s^2, with the corresponding station located approximately 20 km away from the epicenter. The PGA distribution map indicates that areas with higher PGA values are situated to the south of the epicenter, while the northern areas exhibit relatively lower PGA values (https://mp.weixin.qq.com/s/I7lHKb6c7GeJ-Z83T9rJqw).

Based on 1:200,000 geological maps published by the China Geological Survey (http://dcc.cgs.gov.cn/), the lithology of the study area was classified into engineering geological rock types, drawing upon previous studies (Zhang et al., 2017; Ma and Xu, 2019b; Wang et al., 2021), and considering the classification of rock masses engineering GB/T 50,218–2014 (Ministry of Water Resources of the People's Republic of China, 2014). Consequently, the lithology of the study area was divided into five categories: hard rock, relatively hard rock, soft rock, weak rock, and loose rock groups, with corresponding mechanical parameters assigned for each rock group (see Table 1). It is noteworthy that granite and intrusive dikes in this area are significantly affected by tectonic activity, leading to highly developed joints and fissures in the rock mass, resulting in the actual strength of the rock mass being notably lower than that of the rock itself. Based on previous studies (Ma and Xu , 2019a; Ma et al., 2020; Wang et al., 2021), appropriate adjustments were made to the mechanical values of the hard rock group, with a reduction coefficient set at 0.8. Considering that the majority of landslides triggered by this earthquake event are shallow disrupted landslides, it is assumed that the sliding depth of the landslide (t) is 3 m, and the saturation degree of the rock mass (m) is 0, based on previous studies (Dreyfus et al., 2013; Ma and Xu , 2019b).

4 Result

According to Formulas 1, 2 in the above-mentioned Newmark model and the corresponding terrain data and mechanical parameters of rock mass, we can calculate the ac distribution results of the study area (Figure 5A). The ac is used to characterize coseismic landslide susceptibility. In general, the higher the ac, the less prone to slope failure in ground motion. The lower the ac, the more unstable the slope and the easier the slope is to lose stability in ground motion (Chen et al., 2014). The results show that the majority of the areas with lower ac values are located in the steep slopes (that is, slopes greater than 50°, and the ac values in these areas, i.e., red area are generally less than 0.15 (Figure 5A). The ac value of the study area is relatively small in most areas on the west side of the seismogenic fault, while the ac value in the east side of the seismogenic fault is large. By combining the Newmark model and the corresponding PGA distribution (Figure 4B), the Dn value of the Luding earthquake can be calculated. The result shows that the majority of the areas with large Dn values are concentrated on both sides of the valley. In particular, the concentrated areas with large Dn value (that is, the blue area) are distributed in the north of the Luding epicenter such as the nearby area of Detuo town, the western area of Wandong village and Xingfu village (Figure 5B).

Combined with the above Dn distribution result, the estimation of failure probability of the Newmark model can be calculated by the probability curve of slope failure (Figure 6A). As for the LR model, we can also use the Xu$_{2019}$ model to calculate the probability map of this event through the PGA distribution (Figure 6B). The results indicate that most landslides are mainly distributed along both sides of the seismogenic fault, especially concentrated within a 5 km range on either side of the fault. The Newmark model's high probability areas align reasonably well with actual landslide distributions in seismic intensity IX zones, primarily situated along both sides of the Dadu River, indicating areas of elevated failure likelihood. However, in regions with seismic intensity VIII, the Newmark model tends to overestimate landslide occurrences. Specifically, it predicts high failure probabilities in the northwest and southern areas of the epicenter, but the actual landslide distribution in these areas is relatively sparse. Conversely, the LR model demonstrates a strong agreement between its prediction results and the observed landslide distribution, with the majority of landslides occurring in high-probability areas. Several landslide abundance areas such as Detuo town, Wandong village, and Xingfu village have high predicted probability which demonstrates that the model has high predictive accuracy.

To compare the spatial distribution of slope failure probability with actual landslides, we selected Wandong Village, the area most affected by landslides in this earthquake. Figure 7 displays a locally enlarged area showing the estimated failure probability calculated by different prediction models near Wandong Village. Overall, the predictions of both models align well with the actual landslide distribution in this area. For the Newmark model, high-probability areas are concentrated on both sides of the Dadu River, which corresponds to the actual landslide distribution in this area (Figure 7A). Conversely, the Xu$_{2019}$ model indicates that the majority of landslides are distributed in regions with middle to high probabilities of instability, with only sporadic landslides occurring in areas of low probability (Figure 7B)

To quantitatively analyze the prediction results of the two models, we divided the study area into grids measuring 1 km by 1 km, and then calculated the predicted landslide area and the actual area under each grid (Figure 8). We computed the actual landslide area for each grid, revealing that the majority of landslides are concentrated in areas with a seismic intensity of IX (Figure 8A). Particularly, most landslides occur along both sides of the Dadu River, with few coseismic landslides observed in regions with a

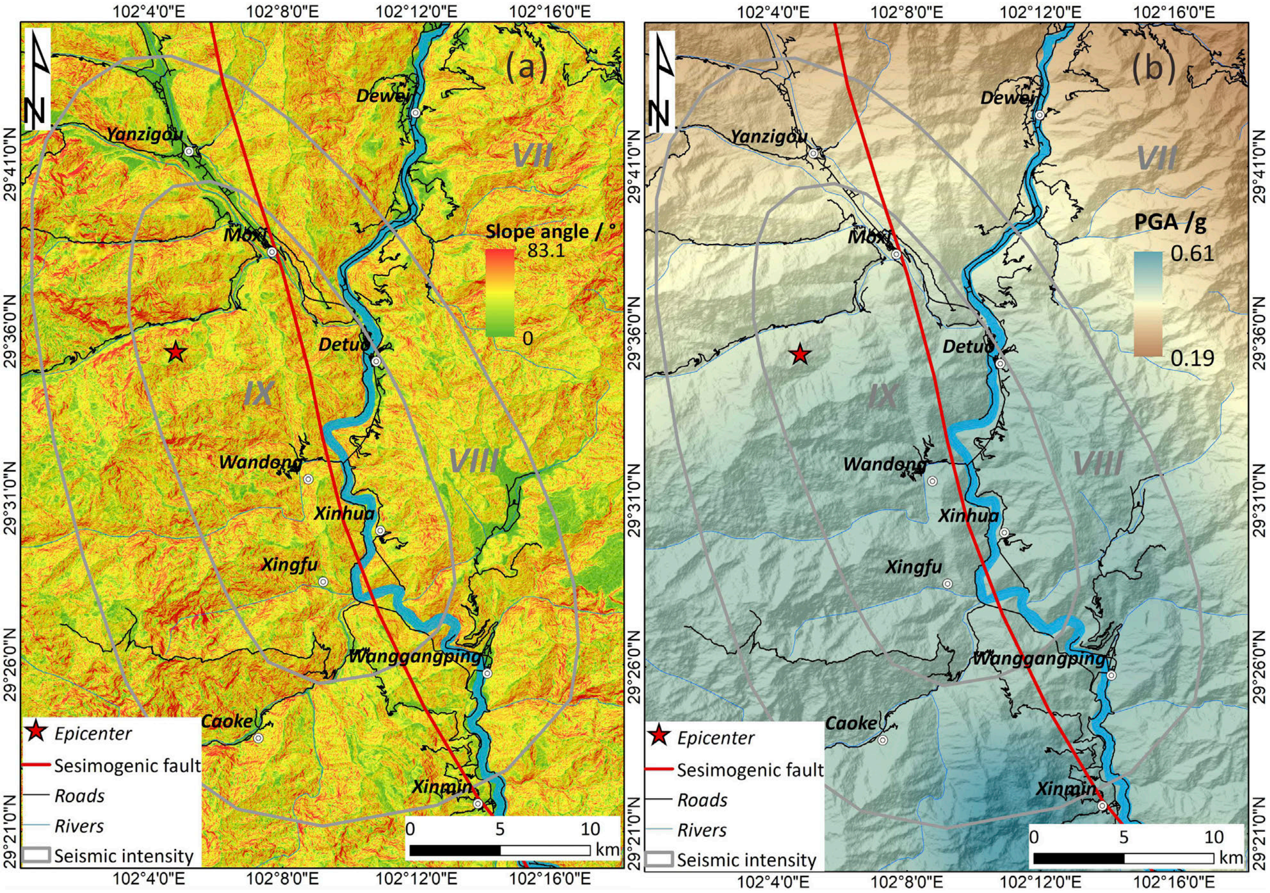

FIGURE 4
Map showing the distribution of slope angle and ground motion (PGA); **(A)** The spatial distribution of slope angle; **(B)** The spatial distribution of PGA (g) is obtained by open peak ground acceleration (PGA) distribution maps published by Xuanmei Fan team of the Chengdu University of Technology.

TABLE 1 Classification of engineering geological lithology formations for Luding earthquake.

Rock groups	Lithology	Weight (kN/m^3)	Internal friction angle (°)	Cohesion, (Kpa)
Loose rock group	Quaternary alluvial proluvial deposits (Qh2apl) and fluvioglacial deposits (Qp3-lgfl)	20	18	15
Weak rock group	Middle lower jurassic mudstone mixed with thin quartz sandstone of Ziliujing formation; middle silurian mudstone mixed with argillaceous siltstone of luoreping formation	23	25	25
Soft rock group	Lower sinian rhyolite; upper ordovician shale of wufeng formation; upper ordovician argillaceous limestone of baota formation	25	28	30
Relatively hard rock group	Upper triassic grey quartz sandstone of xujiahe formation; middle devonian limestone; permian dolomite	27	32	35
Hard rock group	Yajiageng plagioclase granite; detuo migmatite granite; moxi diorite; intrusive dyke	30	32	32

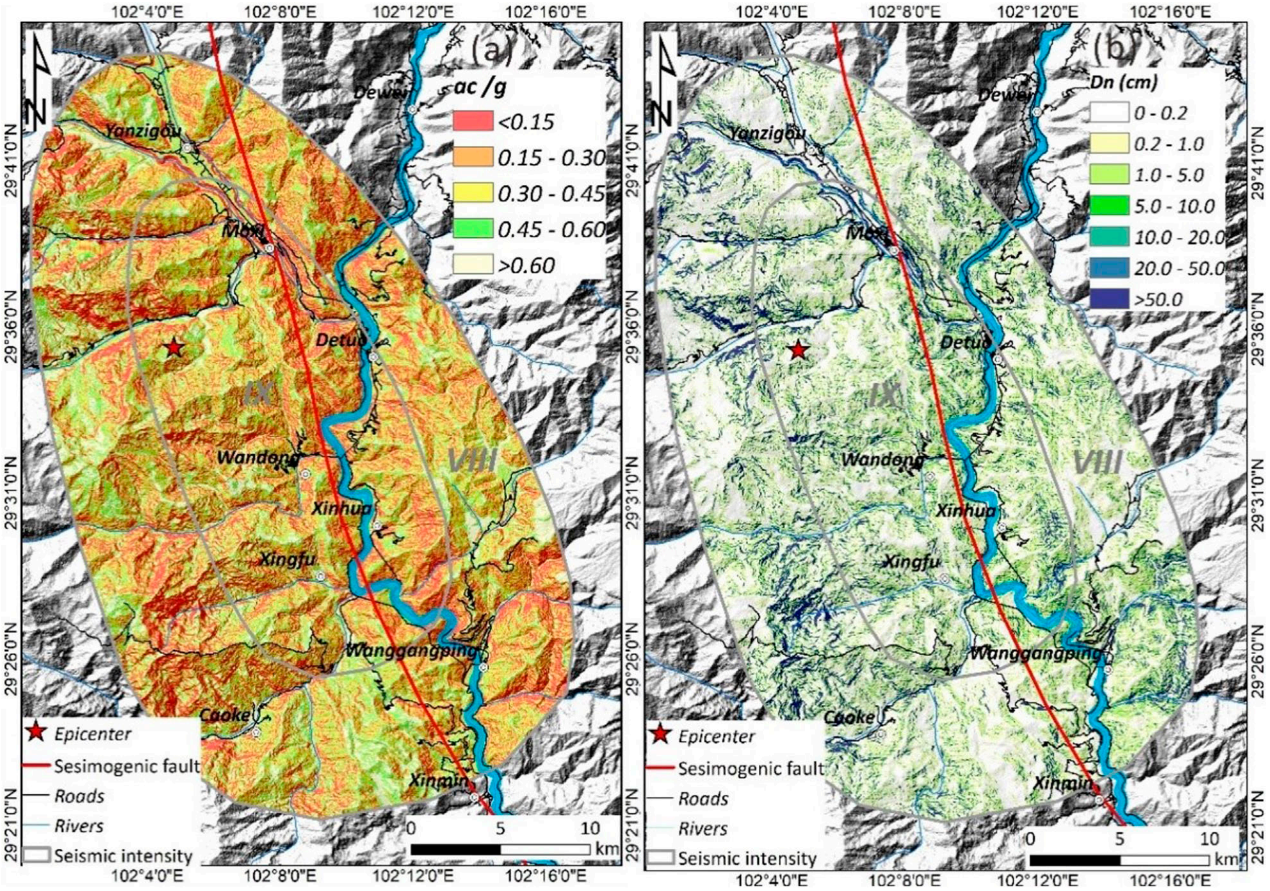

FIGURE 5
Map showing the distribution of ac and Dn of this Lushan earthquake; **(A)** Critical acceleration (ac); **(B)** Newmark displacement (Dn).

seismic intensity of VIII. The total coseismic landslide area is 36.0 km^2, with the largest landslide area within a single grid of 0.5 km^2, located near Xingfu Village (Figure 8A). Figure 8B displays the predicted landslide area for each grid using the Newmark model. The results indicate that the maximum landslide area within a single grid is 0.045 km^2, with the total predicted area by the Newmark model estimated at 8.57 km^2. Notably, the predicted results in the northwest and southern areas of the epicenter are significantly overestimated. Figure 8C presents the predicted landslide area for each grid using the Xu$_{2019}$ model. The predicted areas with high values are largely consistent with the distribution of landslide-prone areas. For example, the areas surrounding Detuo town, Wandong, and Xingfu village have highly developed landslides, and the prediction results indicate that these areas are also high-hazard areas. The total predicted landslide area of the Xu$_{2019}$ model is 8.17 km^2 and the maximum landslide area of a single grid is 0.047 km^2.

Additionally, the modeling accuracy is assessed using the ROC curve. The receiver operating characteristic (ROC) curve provides a comprehensive measure of continuous sensitivity and specificity variables (Swets, 1988). The evaluation criteria are as follows: AUC = 0.5 indicates a stochastic model; AUC between 0.5 and 0.7 suggests low accuracy; AUC between 0.7 and 0.9 indicates high accuracy; AUC > 0.9 indicates very high accuracy (Brenning, 2005). For this study, ~12,600 landslides within seismic intensity VIII are utilized as landsliding positive samples. Non-sliding negative samples consist of ~12,600 randomly selected points outside the buffer zone of landsliding samples (buffer radius = 100 m), resulting in a total of ~25,200 sample points. Based on the SPSS software, the prediction accuracy of different models is calculated based on these sample points. The prediction results reveal that the Xu2019-based model demonstrates significantly higher accuracy than the Newmark model, with a prediction accuracy of 0.76, whereas the Newmark model exhibits relatively lower accuracy, at only 0.63 (Figure 9).

5 Discussion

Timing is critical during the post-earthquake emergency response phase. Swift emergency assessments can promptly identify high-risk areas of coseismic landslides, laying the groundwork for optimizing emergency deployment (Robinson et al., 2017; Ma et al., 2020). In recent years, few achievements have emerged in the construction of near-real-time assessment models based on the abundant earthquake-induced landslides data, but the application and accuracy of these models in actual quake events are rare. Allstadt et al. (2018) compared three globally near-real-time prediction models and calculated the predicted landslide area of the

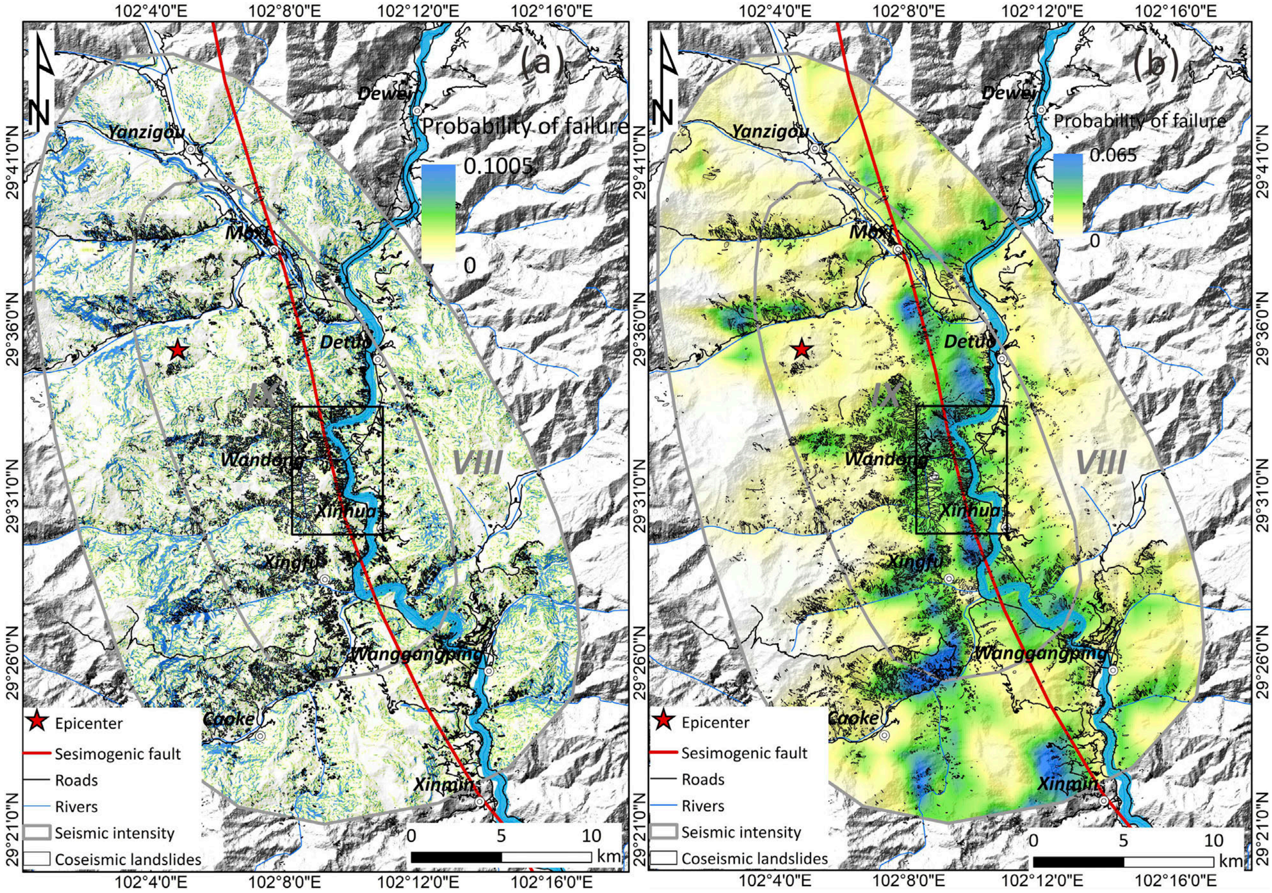

FIGURE 6
Estimation of slope failure probability calculated by different prediction models; **(A)** Newmark model; **(B)** Xu_{2019} model.

2016 Kaikoura earthquake by constantly updating PGA distribution results published by the USGS at different times. The results indicate a significant overestimation of the actual landslide distribution, with the predicted landslide area being 6.5–55 times larger than the observed area. To address these issues, a new seismic landslide hazard model of Xu_{2019} model, was developed using the Bayesian probability method and the LR model, and subsequently applied to the Luding earthquake. The result shows that the Xu_{2019} model can more accurately predict the spatial location of coseismic landslides, with most high-susceptibility areas distributed on both sides of the seismogenic fault. However, there are still some deviations in local areas. For example, the model underestimates the occurrence of coseismic landslides in the northwest region, where coseismic landslides are most developed. Conversely, for the southwest region on the left side of the seismogenic fault, the predicted results are overestimated. We believe the possible reasons for this phenomenon are, firstly, the base data resolution of Xu_{2019} model is 100 m, which affects the model's prediction accuracy to some extent, causing spatial prediction errors at local scales. Secondly, the nine earthquake cases selected for Xu_{2019} model are events that triggered landslides in China and neighboring areas since 1999, occurring in regions with varying topography and geological conditions. Only three of these cases are located in the Sichuan region, which may weaken the applicability of the Xu_{2019} model in the Luding earthquake, Sichuan province (Xu et al., 2019). Additionally, due to the relatively sparse seismic station records in the region, the interpolated PGA distribution might be lower than the actual situation, which is another potential reason for the underestimation of the predicted area. Otherwise, it is important to note that the total landslide area predicted by the Xu_{2019} model is lower than the landslide area triggered by the Luding earthquake. We believe that the main reason for this phenomenon is the unique high mountain and canyon terrain of the Luding region. Furthermore, the earthquake is located at the Y-shaped junction of three major active tectonic faults, and the rock and soil masses are relatively fractured, making this area prone to landsliding. Therefore, compared to earthquakes of similar magnitude, the Luding earthquake has a more pronounced ability to trigger landslides (Shao et al., 2024).

Emergency hazard assessment using the Newmark model involves multiple parameters, such as terrain, geotechnical mechanics, groundwater, and ground motion. However, there are numerous uncertainties associated with these parameters, both in their inherent nature and in the process of obtaining them (Wang et al., 2015; Bojadjieva et al., 2018). To achieve more precise predicted displacement, the Newmark method requires clear physical and mechanical properties of rocks, as well as accurate

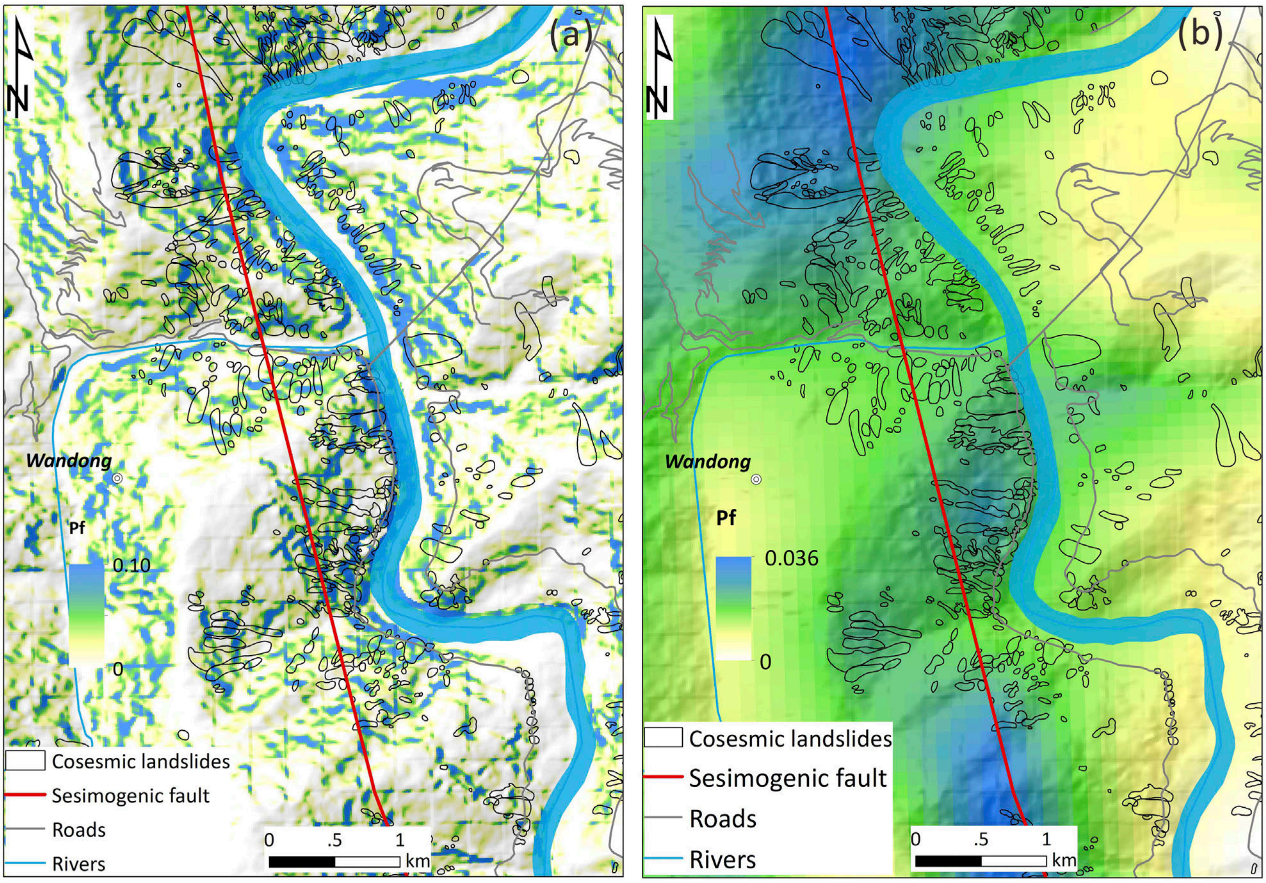

FIGURE 7
Locally enlarged area of estimated slope failure probability calculated by different prediction models; **(A)** Newmark model; **(B)** Xu2019 model.

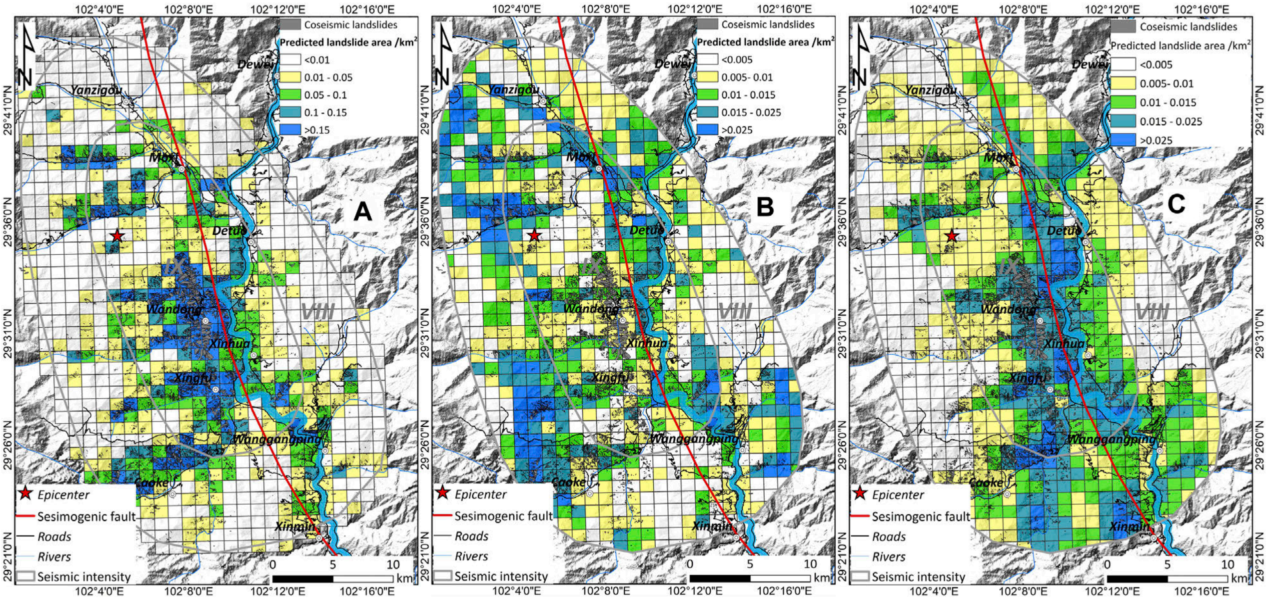

FIGURE 8
Map showing the distribution of predicted landslide area and actual landslide area (fishnet is 1 km ∗ 1 km); **(A)** Actual landslide area; **(B)** Newmark model; **(C)** Xu_{2019} model.

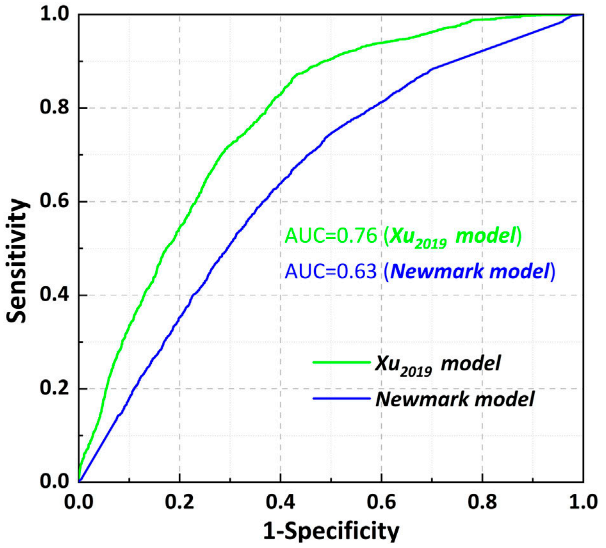

FIGURE 9
ROC curves and AUC values calculated by different models.

ground motion parameters (Dreyfus et al., 2013). Therefore, for the Newmark model, the set of input parameters may be the key point to affect the evaluation results, especially the assignment of rock mass parameters. The combination of different lithology is required in the process of engineering geological rock groups. Although this simplified treatment is easier to calculate, it may obliterate the spatial difference in rock mass strength distributions (Wang et al., 2015). Moreover, the rock mass in the source area of coseismic landslides predominantly consists of weathered jointed-cracked rock mass, exhibiting mechanical properties that deviate from typical rocks. Consequently, empirical or measured rock strength parameters may inadequately represent the strength characteristics of the *in-situ* rock mass. This discrepancy can lead to assignment results that diverge from the actual conditions during the stage of mechanical parameter assignment, ultimately resulting in significant disparities between the predicted and actual landslide distributions (Wang et al., 2015).

From the predicted results of the Newmark model, we can observe that the area with high instability probability has a certain degree of agreement with the actual landslide distribution. Most source areas of the coseismic landslides are located in the area on both sides of the Dadu River, of which this area is also a high hazard area. However, in the region with a seismic intensity of VIII, the prediction results based on the Newmark model are overestimated. According to the actual distribution of the coseismic landslides, there are few landslides in this area. However, this area is predicted to be a high-hazard area based on the Newmark model. We believe that this phenomenon is caused by an underestimation of the mechanical parameters of the rock during the combination of different lithology in engineering rock group groups. Furthermore, it should be noted that the PGA map used in this study is based on the interpolation of ground motion records by strong motion instruments within 100 km from the epicenter which are provided by the Sichuan earthquake administration. While the PGA result can roughly characterize the distribution of ground motion in this earthquake event, it does not account for the site effect of ground motion propagation, specifically ignoring local topography, slope structure, and the propagation direction of seismic waves. Therefore, As a result, we may be unable to obtain accurate seismic motion information and underestimate seismic amplitude in the middle and upper parts of the mountain which result in predicted landslide displacement being less than the actual situation (Wang et al., 2015; Li and Su, 2021).

Prompt and accurate identification and prediction of landslide risk areas following earthquakes can effectively guide the deployment of rescue personnel and allocation of resources, thereby minimizing casualties and property losses (Shao et al., 2023b). In comparing two models, the Xu_{2019} model demonstrates better capability in identifying high landslide hazard areas, aligning well with hazard levels and distribution characteristics of Luding-induced landslides. This can provide decision-makers with scientific guidance for deploying emergency rescue teams and assessing property and casualty impacts. In contrast, the Newmark model exhibits deviations between predicted and actual landslide distributions, potentially leading to misjudgments in coseismic landslide hazard assessment. Furthermore, both models underestimated the landslide area for the Luding earthquake and consequently underestimates its destructive impact and complicating rescue resource deployment, but the Xu_{2019} model effectively distinguishes between low and high landslide hazard areas that can offer valuable insights for emergency response and rapid risk assessment.

6 Conclusion

The aim of this study is to conduct a quantitative analysis of different assessment models in the rapid emergency evaluation of coseismic landslides triggered by the 2022 Ms 6.8 Luding earthquake. The data-driven Xu2019 model and the physically-based Newmark model are selected for this purpose. Using the coseismic landslide inventory of this event, the applicability and accuracy of these two models are discussed. The findings reveal that the Newmark model predicts high probability areas that somewhat align with the actual landslide distribution, primarily concentrated on both sides of the Dadu River where failure probability is high. However, the Newmark model tends to overestimate landslide occurrence in regions with a seismic intensity of VIII. Conversely, the LR model closely matches the actual landslide distribution, indicating high prediction accuracy. To assess model accuracy, the ROC curve is employed. Results indicate that the Xu_{2019} model outperforms the Newmark model, achieving a prediction accuracy of 0.76 compared to 0.63 for the Newmark model. Both models demonstrate good timeliness in rapid hazard assessment of earthquake-induced landslides. However, while the Newmark model theoretically considers the occurrence mechanism of seismic landslides and has broader applicability, it requires multiple input parameters, leading to increased uncertainty and subjective factors in practical application.

Overall, compared to the Newmark model, the Xu_{2019} model has a higher predictive capability. However, since the Xu_{2019} model is primarily trained on the earthquake-induced landslide database from the Sichuan-Yunnan region, its applicability to other regions still needs further validation. Therefore, establishing a high-precision geospatial database of basic geomechanical parameters is crucial to improving the accuracy of the Newmark model in emergency evaluation. For the Xu_{2019} model, continual enrichment of earthquake-induced landslide inventories in mainland China can lead to the development of a near-real-time model tailored to the area, enhancing forecast accuracy in emergency assessments of coseismic landslides.

Data availability statement

The raw data supporting the conclusions of this article will be made available by the authors, without undue reservation.

Author contributions

YL: Writing–original draft. SM: Conceptualization, Data curation, Supervision, Validation, Visualization, Writing–review and editing. CX: Data curation, Writing–review and editing.

Funding

The author(s) declare that financial support was received for the research, authorship, and/or publication of this article. This research was supported by the National Natural Science Foundation of China (Grant No. 42207532).

Acknowledgments

We are grateful to thank the strong earthquake-induced geological disasters research team led by Professor Xuanmei Fan of Chengdu University of Technology for sharing the PGA map of the 2022 Ms6.8 Luding earthquake. In addition, we also thank team of Professor Chong Xu for sharing the cosiesimic landslide inventory of this earthquake event at the first time. We appreciate the constructive feedback provided by the two reviewers, which has been helpful in improving the quality of our manuscript.

Conflict of interest

The authors declare that the research was conducted in the absence of any commercial or financial relationships that could be construed as a potential conflict of interest.

Publisher's note

References

Allstadt, K. E., Jibson, R. W., Thompson, E. M., Massey, C. I., Wald, D. J., Godt, J. W., et al. (2018). Improving near-real-time coseismic landslide models: lessons learned from the 2016 Kaikōura, New Zealand, Earthquake. *Bull. Seismol. Soc. Am.* 108, 1649–1664. doi:10.1785/0120170297

Bai, M., Chevalier, M. L., Pan, J., Replumaz, A., Leloup, P. H., Métois, M., et al. (2018). Southeastward increase of the late Quaternary slip-rate of the Xianshuihe fault, eastern Tibet. Geodynamic and seismic hazard implications. *Earth Planet. Sci. Lett.* 485, 19–31. doi:10.1016/j.epsl.2017.12.045

Bojadjieva, J., Sheshov, V., and Christophe, B. (2018). Hazard and risk assessment of earthquake-induced landslides—case study. *Landslides* 15, 161–171. doi:10.1007/s10346-017-0905-9

Brenning, A. (2005). Spatial prediction models for landslide hazards: review, comparison and evaluation. *Nat. Hazards and Earth Syst. Sci.* 5, 853–862. doi:10.5194/nhess-5-853-2005

Chen, X., Liu, C., and Wang, M. (2018). A method for quick assessment of earthquake-triggered landslide hazards: a case study of the Mw6.1 2014 Ludian, China earthquake. *Bull. Eng. Geol. Environ.* 78, 2449–2458. doi:10.1007/s10064-018-1313-7

Chen, X. L., Liu, C. G., Yu, L., and Lin, C. X. (2014). Critical acceleration as a criterion in seismic landslide susceptibility assessment. *Geomorphology* 217, 15–22. doi:10.1016/j.geomorph.2014.04.011

Dai, L., Fan, X., Wang, X., Fang, C., Zou, C., Tang, X., et al. (2023). Coseismic landslides triggered by the 2022 Luding Ms6.8 earthquake, China. *Landslides* 20, 1277–1292. doi:10.1007/s10346-023-02061-3

Deng, Q. D. (2007). *Chinese active tectonic map*. Beijing: Seismological Press.

Dreyfus, D. K., Rathje, E. M., and Jibson, R. W. (2013). The influence of different simplified sliding-block models and input parameters on regional predictions of seismic landslides triggered by the Northridge earthquake. *Eng. Geol.* 163, 41–54. doi:10.1016/j.enggeo.2013.05.015

Du, G., Zhang, Y., Zou, L., Yang, Z., Yuan, Y., and Ren, S. (2022). Co-seismic landslide hazard assessment of the 2017 Ms 6.9 Milin earthquake, Tibet, China, combining the logistic regression–information value and Newmark displacement models. *Bull. Eng. Geol. Environ.* 81, 446. doi:10.1007/s10064-022-02901-x

Fan, X., Scaringi, G., Korup, O., West, A. J., van Westen, C. J., Tanyas, H., et al. (2019). Earthquake-induced chains of geologic hazards: patterns, mechanisms, and impacts. *Rev. Geophys.* 57, 421–503. doi:10.1029/2018rg000626

Fan, X., Wang, X., Dai, L., Fang, C., Deng, Y., Zou, C., et al. (2022). Characteristics and spatial distribution pattern of Ms 6.8 Luding earthquake occurred on September 5, 2022. *J. Eng. Geol.* (In Chinese).

Gallen, S. F., Clark, M. K., Godt, J. W., Roback, K., and Niemi, N. A. (2017). Application and evaluation of a rapid response earthquake-triggered landslide model to the 25 April 2015 Mw 7.8 Gorkha earthquake, Nepal. *Tectonophysics* 714-715, 173–187. doi:10.1016/j.tecto.2016.10.031

Godt, J. W., Sener, B. ., Verdin, K. L., and Wald, D. J. (2008). "Rapid assessment of earthquake-induced landsliding," in Proceedings of the first world landslide forum, Tokyo, Japan, November 18–21.

Gorum, T., van Westen, C. J., Korup, O., van der Meijde, M., Fan, X., and van der Meer, F. D. (2013). Complex rupture mechanism and topography control symmetry of mass-wasting pattern, 2010 Haiti earthquake. *Geomorphology* 184, 127–138. doi:10.1016/j.geomorph.2012.11.027

Havenith, H. B., Guerrier, K., Schlögel, R., Braun, A., Ulysse, S., Mreyen, A. S., et al. (2022). Earthquake-induced landslides in Haiti: analysis of seismotectonic and possible climatic influences. *Nat. Hazards Earth Syst. Sci.* 22, 3361–3384. doi:10.5194/nhess-22-3361-2022

He, K., Lombardo, L., Chang, L., Sadhasivam, N., Hu, X., Fang, Z., et al. (2024). Investigating earthquake legacy effect on hillslope deformation using InSAR-derived time series. *Earth Surf. Process. Landforms* 49, 980–990. doi:10.1002/esp.5746

He, K., Tanyas, H., Chang, L., Hu, X., Luo, G., and Lombardo, L. (2023). Modelling InSAR-derived hillslope velocities with multivariate statistics: a first attempt to generate interpretable predictions. *Remote Sens. Environ.* 289, 113518. doi:10.1016/j.rse.2023.113518

He, Q., Wang, M., and Liu, K. (2021). Rapidly assessing earthquake-induced landslide susceptibility on a global scale using random forest. *Geomorphology* 391, 107889. doi:10.1016/j.geomorph.2021.107889

Huang, D., Wang, G., Du, C., Jin, F., Feng, K., and Chen, Z. (2020). An integrated SEM-Newmark model for physics-based regional coseismic landslide assessment. *Soil Dyn. Earthq. Eng.* 132, 106066. doi:10.1016/j.soildyn.2020.106066

Huang, Y., Xu, C., Zhang, X., and Li, L. (2022). Bibliometric analysis of landslide research based on the WOS database. *Nat. Hazards Res.* 2, 49–61. doi:10.1016/j.nhres.2022.02.001

Jibson, R. W. (2007). Regression models for estimating coseismic landslide displacement. *Eng. Geol.* 91, 209–218. doi:10.1016/j.enggeo.2007.01.013

Jibson, R. W. (2011). Methods for assessing the stability of slopes during earthquakes—a retrospective. *Eng. Geol.* 122, 43–50. doi:10.1016/j.enggeo.2010.09.017

Jibson, R. W., Harp, E. L., and Michael, J. A. (2000). A method for producing digital probabilistic seismic landslide hazard maps: an example from the Los Angeles, California, area. *Eng. Geol.* 58, 271–289. doi:10.1016/s0013-7952(00)00039-9

Jin, J., Wang, Y., Gao, D., Yuan, R. M., and Yang, X. Y. (2018). New evaluation models of Newmark displacement for southwest China. *Bull. Seismol. Soc. Am.* 108, 2221–2236. doi:10.1785/0120170349

Jin, K. P., Yao, L. K., Cheng, Q. G., and Xing, A. G. (2019). Seismic landslides hazard zoning based on the modified Newmark model: a case study from the Lushan earthquake, China. *Nat. Hazards* 99, 493–509. doi:10.1007/s11069-019-03754-6

Keefer, D. K. (1984). Landslides caused by earthquakes. *Geol. Soc. Am. Bull.* 95, 406–421. doi:10.1130/0016-7606(1984)95<406:lcbe>2.0.co;2

Kritikos, T., Robinson, T. R., and Davies, T. R. H. (2015). Regional coseismic landslide hazard assessment without historical landslide inventories: a new approach. *J. Geophys. Res. Earth Surf.* 120, 711–729. doi:10.1002/2014jf003224

Li, C., and Su, L. (2021). Influence of critical acceleration model on assessments of potential earthquake–induced landslide hazards in Shimian County, Sichuan Province, China. *Landslides* 18, 1659–1674. doi:10.1007/s10346-020-01578-1

Li, W., Chen, J., Lu, H., Shan, Y., Li, Z., Chen, B., et al. (2022). Emergency analysis of the impact of the luding Ms 6.8 earthquake on Hailuogou Glacier. *Geomatics Inf. Sci. Wuhan Univ.* (In Chinese).

Liu, J., Shi, J., Wang, T., and Wu, S. (2018). Seismic landslide hazard assessment in the Tianshui area, China, based on scenario earthquakes. *Bull. Eng. Geol. Environ.* 77, 1263–1272. doi:10.1007/s10064-016-0998-8

Ma, S., and Xu, C. (2019a). Applicability of two Newmark models in the assessment of coseismic landslide hazard and estimation of slope-failure probability: an example of the 2008 wenchuan Mw 7.9 earthquake affected area. *J. Earth Sci.* 30, 1020–1030. doi:10.1007/s12583-019-0874-0

Ma, S., Xu, C., and Shao, X. (2020). Spatial prediction strategy for landslides triggered by large earthquakes oriented to emergency response, mid-term resettlement and later reconstruction. *Int. J. Disaster Risk Reduct.* 43, 101362. doi:10.1016/j.ijdrr.2019.101362

Ma, S. Y., and Xu, C. (2019b). Assessment of co-seismic landslide hazard using the Newmark model and statistical analyses: a case study of the 2013 Lushan, China, Mw6.6 earthquake. *Nat. Hazards* 96, 389–412. doi:10.1007/s11069-018-3548-9

Ministry of Water Resources of the People's Republic of China (2014). *Standrad for engineering classification of rock masses GB/T 50218-2014*. Beijing: Standards Press of China.

Newmark, N. M. (1965). Effects of earthquakes on dams and embankments. *Géotechnique* 15, 139–160. doi:10.1680/geot.1965.15.2.139

Nowicki, M. A., Wald, D. J., Hamburger, M. W., Hearne, M., and Thompson, E. M. (2014). Development of a globally applicable model for near real-time prediction of seismically induced landslides. *Eng. Geol.* 173, 54–65. doi:10.1016/j.enggeo.2014.02.002

Nowicki Jessee, M. A., Hamburger, M. W., Allstadt, K., Wald, D. J., Robeson, S. M., Tanyas, H., et al. (2019). A global empirical model for near-real-time assessment of seismically induced landslides. *J. Geophys. Res. Earth Surf.* 123, 1835–1859. doi:10.1029/2017jf004494

Robinson, T. R., Rosser, N. J., Densmore, A. L., Williams, J. G., Kincey, M. E., Benjamin, J., et al. (2017). Rapid post-earthquake modelling of coseismic landslide intensity and distribution for emergency response decision support. *Nat. Hazards Earth Syst. Sci.* 17, 1521–1540. doi:10.5194/nhess-17-1521-2017

Shao, X., Ma, S., and Xu, C. (2023a). Distribution and characteristics of shallow landslides triggered by the 2018 Mw 7.5 Palu earthquake, Indonesia. *Landslides* 20, 157–175. doi:10.1007/s10346-022-01972-x

Shao, X., Ma, S., and Xu, C. (2023b). Hazard assessment modeling and software development of earthquake-triggered landslides in the Sichuan–Yunnan area, China. *Geosci. Model Dev.* 16, 5113–5129. doi:10.5194/gmd-16-5113-2023

Shao, X., Ma, S., Xu, C., Xie, C., Li, T., Huang, Y., et al. (2024). Landslides triggered by the 2022 Ms. 6.8 Luding strike-slip earthquake: an update. *Eng. Geol.* 335, 107536. doi:10.1016/j.enggeo.2024.107536

Shao, X., Ma, S., Xu, C., Zhang, P., Wen, B., Tian, Y., et al. (2019). Planet image-based inventorying and machine learning-based susceptibility mapping for the landslides triggered by the 2018 Mw6.6 Tomakomai, Japan Earthquake. *Remote Sens.* 11, 978. doi:10.3390/rs11080978

Shao, X., Ma, S., Xu, C., and Zhou, Q. (2020). Effects of sampling intensity and non-slide/slide sample ratio on the occurrence probability of coseismic landslides. *Geomorphology* 363, 107222. doi:10.1016/j.geomorph.2020.107222

Shao, X., and Xu, C. (2022). *Earthquake-induced landslides susceptibility assessment: a review of the state-of-the-art. Natural Hazards Research* 2, 172–182.

Swets, J. A. (1988). Measuring the accuracy of diagnostic systems. *Science* 240, 1285–1293. doi:10.1126/science.3287615

Tanyas, H., Rossi, M., Alvioli, M., van Westen, C. J., and Marchesini, I. (2019a). A global slope unit-based method for the near real-time prediction of earthquake-induced landslides. *Geomorphology* 327, 126–146. doi:10.1016/j.geomorph.2018.10.022

Tanyas, H., Westen, C. J., Persello, C., and Alvioli, M. (2019b). Rapid prediction of the magnitude scale of landslide events triggered by an earthquake. *Landslides* 16, 676.

Tapponnier, P., Zhiqin, X., Roger, F., Meyer, B., Arnaud, N., Wittlinger, G., et al. (2001). Oblique stepwise rise and growth of the Tibet plateau. *Science* 294, 1671–1677. doi:10.1126/science.105978

Wang, L., Xiao, T., Liu, S., Zhang, W., Yang, B., and Chen, L. (2023). Quantification of model uncertainty and variability for landslide displacement prediction based on Monte Carlo simulation. *Gondwana Res.* 123, 27–40. doi:10.1016/j.gr.2023.03.006

Wang, T., Liu, J., Li, Z., Xin, P., Shi, J., and Wu, S. (2021). Seismic landslide hazard assessment of China and its impact on national territory spatial planning. *Geol. China* 48, 21–39.

Wang, T., Wu, S., Shi, J., and Xin, P. (2015). Concepts and mechanical assessment method for seismic landslide hazard: a review. *J. Eng. Geol.* 23, 93–104.

Wang, T., Wu, S. R., Shi, J. S., Xin, P., and Wu, L. Z. (2018). Assessment of the effects of historical strong earthquakes on large-scale landslide groupings in the Wei River midstream. *Eng. Geol.* 235, 11–19. doi:10.1016/j.enggeo.2018.01.020

Wei, Y., and Chen, X. (2022). Applicability of different seismic landslide risk assessment methods: a case study of Maduo Ms 7.4 earthquake. *Sesimology Geol.* 44, 590–603.

Wilson, R. C., and Keefer, D. K. (1983). Dynamic analysis of a slope failure from the 6 August 1979 Coyote lake, California, earthquake. *Bull. Deismological Soc. Am.* 73, 863–877. doi:10.1785/bssa0730030863

Xu, C., Xu, X., Tian, Y., Shen, L., Yao, Q., Huang, X., et al. (2016). Two comparable earthquakes produced greatly different coseismic landslides:The 2015 Gorkha,Nepal and 2008 Wenchuan,China events. *J. Earth Sci.* 27, 1008–1015. doi:10.1007/s12583-016-0684-6

Xu, C., Xu, X., Zhou, B., and Shen, L. (2019). Probability of coseismic landslides: a new generation of earthquake-triggered landslide hazard model. *J. Eng. Geol.* 27, 1122.

Yang, Z., Pang, B., Dong, W., and Li, D. (2023). Spatial pattern and intensity mapping of coseismic landslides triggered by the 2022 luding earthquake in China. *Remote Sens.* 15, 1323. doi:10.3390/rs15051323

Yue, X., Wu, S., Yin, Y., Gao, J., and Zheng, J. (2018). Risk identification of seismic landslides by joint Newmark and RockFall analyst models: a case study of roads affected by the Jiuzhaigou earthquake. *Int. J. Disaster Risk Sci.* 9, 392–406. doi:10.1007/s13753-018-0182-9

Zhang, Y.-s., Yang, Z.-h., Guo, C.-b., Wang, T., Wang, D.-h., and Du, G.-l. (2017). Predicting landslide scenes under potential earthquake scenarios in the Xianshuihe fault zone, Southwest China. *J. Mt. Sci.* 14, 1262–1278. doi:10.1007/s11629-017-4363-6

Zhao, B., Hu, K., Yang, Z., Liu, Q., Zou, Q., Chen, H., et al. (2022). Geomorphic and tectonic controls of landslides induced by the 2022 Luding earthquake. *J. Mt. Sci.* 19, 3323–3345. doi:10.1007/s11629-022-7732-8

frontiers | Frontiers in Earth Science

TYPE Original Research
PUBLISHED 11 October 2024
DOI 10.3389/feart.2024.1469772

Check for updates

OPEN ACCESS

EDITED BY
Chong Xu,
Ministry of Emergency Management, China

REVIEWED BY
Bing Bai,
Beijing Jiaotong University, China
Jiewei Zhan,
Chang'an University, China
Yuandong Huang,
Ministry of Emergency Management, China
Jiansheng Chen,
Hohai University, China

*CORRESPONDENCE
Shao-Min Liu,
✉ liusm2023@126.com
Ming-Zhou Bai,
✉ 279459260@qq.com

RECEIVED 24 July 2024
ACCEPTED 27 September 2024
PUBLISHED 11 October 2024

CITATION
Liu S-M and Bai M-Z (2024) Groundwater level rise and geological structure influences on land deformation dynamics: insights from managed aquifer recharge operations in Beijing, China.
Front. Earth Sci. 12:1469772.
doi: 10.3389/feart.2024.1469772

Groundwater level rise and geological structure influences on land deformation dynamics: insights from managed aquifer recharge operations in Beijing, China

Shao-Min Liu[1,2,3]* and Ming-Zhou Bai[1,2]*

[1]School of Civil Engineering, Beijing Jiaotong University, Beijing, China, [2]Beijing Urban Rail Transit Safety and Disaster Prevention Engineering and Technology Research Center, Beijing, China, [3]Beijing Institute of Geology and Mineral Exploration, Beijing, China

Managed Aquifer Recharge (MAR) has been implemented in the upper alluvial plain of the Chaobai River, significantly affecting the groundwater level and causing it to rise. However, the effects of the MAR on land subsidence,remain largely unknown. To elucidate the effects of MAR on land subsidence, a comprehensive analysis was undertaken, integrating interferometric synthetic aperture radar (InSAR) data, extensometer measurements, and groundwater level observations.Our analysis revealed a discernible land rebound phenomenon, with rates escalating from 2.3 mm/a in 2015 to 20 mm/a in 2021. This rebound extends southwestward, following a dispersion pattern that aligns with pre-existing fault structures, suggesting their controlling influence. The groundwater level changes caused by the MAR can cause land rebound, especially near fault footwalls. However,low permeability in fault zones hinders groundwater flow in the hanging wall resulting in slight land deformation. Lithology also affects rebound, with sandy soils showing more significant land rebound, while low-sand areas exhibit limited or delayed rebound. These findings offer crucial insights into the interplay between MAR, groundwater dynamics, and land subsidence in the studied region. They provide a foundation for informed decision-making in groundwater replenishment strategies and precise subsidence prevention and control measures. Future research should maintain a vigilant monitoring of the long-term consequences of MAR on land subsidence to ensure sustainable regional development.

KEYWORDS

land rebound, pre-existing fault, low permeability, aquifer recharge, Beijing

1 Introduction

The groundwater over-exploitation has change the original stress state in the aquifer system, resulting in a decrease in pore pressure and an increase in the effective stress (Lofgren, 1968). When the stress exceeds the preconsolidation stress that the soil has previously endured, inelastic consolidation occurs in the clay layer and as the deformation gradually increases, land subsidence begins to form (Holzer,

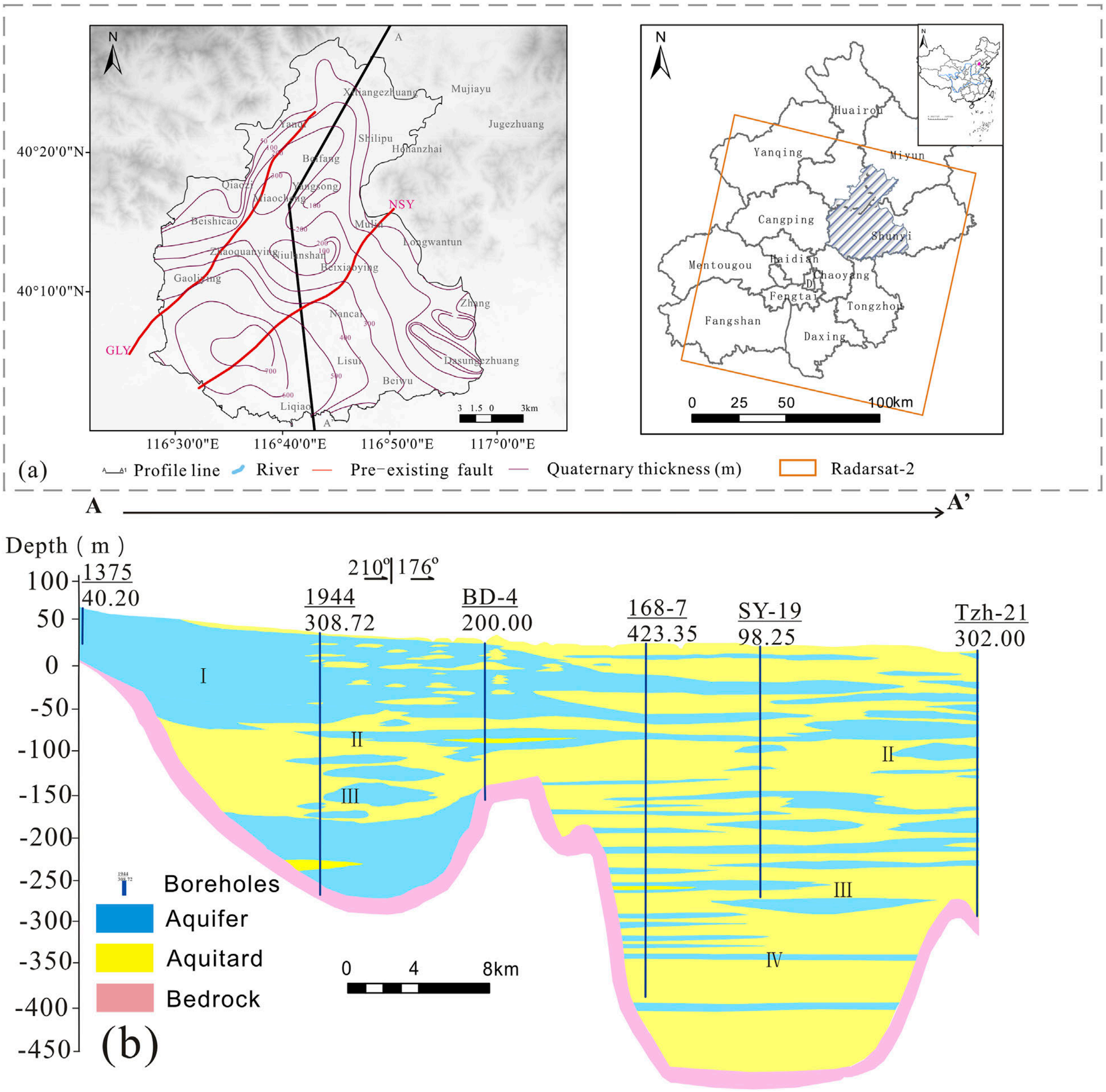

FIGURE 1
Location and geology of the study area: **(A)** The distribution and descriptions of the Quaternary sediments and preexisting faults in the study area. **(B)** Hydrogeological cross-section A–A1 (the location is displayed in **(A)**. The I-Phreatic aquifers, the II-The first confined aquifers, the III-The second confined aquifer, and the IV-The third confined aquifer.

1981; Galloway and Burbey, 2011). Land subsidence poses a significant threat in the world (Bagheri-Gavkosh et al., 2021; Negahdary, 2022; Ao et al., 2024), According to UNESCO International Initiative on Land Subsidence Working Group, land subsidence is projected to affect 19% of the global population by 2040 (Herrera-García et al., 2021).

A variety of groundwater management strategies, which are based on water allocation, are being implemented to mitigate the land subsidence (Roose and Starks, 2006; Calderhead et al., 2012; Zhu et al., 2020). These strategies have resulted in a shift in the groundwater level from a decline to a rise, and some regions found the land subsidence relief and, even land rebound (Castellazzi et al., 2021; Tang et al., 2022). The state of land deformation was intricate in the region with pre-existing fault (Parker et al., 2021; Zhao et al., 2021). Many research found that the pre-existing faults serve as boundaries for land deformation and control the developed of the land deformation (Burbey, 2002; Hu et al., 2019; Salehi Moteahd et al., 2019). Unfortunately, the effect mechanism of pre-existing faults on the land deformation was relatively weak, which restrict scientific replenishment of regional groundwater.

TABLE 1 The monitoring layers of extensometers and groundwater wells in J1 extensometer station.

Extensometers	F1	F3	F5	F7
Monitoring depth (m)	35.4	64.5	102	148.49
Groundwater wells	D1	D3	D5	D7
Monitoring depth (m)	31	63.4	91.3	146.8

The study area, situated in the northern region of Beijing, has been affected by severe land subsidence, with maximum cumulative settlement above 80 cm (1955–2014). The pre-existing in the study area has resulted in rapid formation of uneven subsidence and earth fissures. Since 2015, the MAR has been operational, and land rebound appeared in some area, offering a valuable opportunity to gain a better understanding of this mechanism. Here, RadarSAT-2 SAR data in the study area from 2015 to 2021 is utilized to present the promising effects of the MAR on land subsidence. The effect mechanism of geological structure on the land deformation is analysed.

2 Description of the study area

2.1 Geological setting

The study area is in the upper and middle part of the Chaobai River’s alluvial fan, which was formed in the Pleistocene by the alluvial-diluvial action of the Chaobai and Wenyu Rivers (Lei et al., 2022a). The geological environment in this area is highly complex due to the heterogeneous distribution of alluvial deposits (Wei, 2008). The thickness of the Quaternary deposits varies between 50 m in the northeastern region and extends up to 1,100 m in the southwestern region, change from an coarse sand in the piedmont areas to fine clay in the floodplain zones (Zhu et al., 2020).

Two buried geological faults are located: the northern section of the Gaoliying (GLY) fault (Figure 1A) and the northern section of the Shunyi (NSY) fault (Figure 1A). The GLY fault is a tension normal fault with a length of 40 km, a strike of 70°–80°, and a SE trend (Wei, 2008). The GLY fault has experienced multiple periods of activity since the Cretaceous Period and has been very active since the Cenozoic in controlling the Palaeocene, Neoproterozoic, and Quaternary deposits (Wei, 2008). The average activity rates of the Early Pleistocene, Middle Pleistocene, Late Pleistocene and Holocene faults were 0.07 mm/a, 0.04 mm/a, 0.23 mm/a and 0.10 mm/a, respectively (Zhang et al., 2016).

The NSY fault is a tension normal fault with a length of 40 km, a strike of 40° and a SE trend (Wei, 2008). According to the measurements and geochronological results, the average activity rates of the Early Pleistocene, Middle Pleistocene, Late Pleistocene and Holocene faults were 0.23 mm/a, 0.03 mm/a, 0.29 mm/a and 0.51 mm/a, respectively (Qi et al., 2020).

2.2 Hydrogeological setting and manged aquifer recharge

The aquifers in the study area can be divided into four groups (Figure 1B). Phreatic aquifers (PAs), the first confined aquifers (FCAs), the second confined aquifer (SCA), and the third confined aquifer (TCA). Phreatic aquifers (PAs) originated in the Holocene and late Pleistocene and are widely distributed in the study area with thicknesses varying from 40 m to 50 m. Medium-coarse sands with gravel were deposited along the PA layers. The PA is supplied by atmospheric precipitation, infiltration from agricultural irrigation and river water, and its own abundant groundwater resources. The first confined aquifers (FCAs) were formed in the mid-Pleistocene, with depths ranging from 80 to 120 m. The second confined aquifer (SCA) is mainly distributed in the middle of the alluvial fan. Its layers were formed in the lower Pleistocene. The bottom depth of this group ranges from 150 to 180 m. The third confined aquifer (TCA) is distributed south of Mapo village. It was formed in the Lower Pleistocene, and the bedrock comprises the bottom of this group.

The MAR commenced in 2015, with recharge operations conducted annually from April to June. By the end of 2020, a total of 501, 508, 900 cubic meters of groundwater had been recharged. The South-to-North Water Diversion water, after being released through the Lishishan Diversion Gate on the Jingmi Diversion Canal, flows through the Xiaozhong River, Mangniu River, and Huaihe River before entering the upstream groundwater recharge site at the Chaobai River Niulanshan Rubber Dam (Lei et al., 2022a).

3 Data set

In this paper, The InSAR data, extensometer data and groundwater level data have been gathered. Those multi-source monitoring datasets were used to analyze the changes of the land deformation in the study area before and after the MAR, and the effects of the pre-exising fault, and lithology on land deformation under the background of groundwater level rise were also studied.

3.1 Interferometric synthetic aperture radar (InSAR) data

Since its launch in 2007, the Radarsat-2 satellite has been in operation. With a revisit period of 24 days, it employs a C-band Synthetic Aperture Radar (SAR) featuring a 56 mm wavelength. The satellite boasts a spatial resolution of 30 m, making the data it collects ideal for monitoring regional subsidence (Ng et al., 2017; Samsonov et al., 2017).

In this study, 70 scenes of the Radarsat-2 dataset in W1 mode between October 2014 and October 2021 were collected to acquire the regional subsidence of the study area. Persistent scatterer InSAR (PS-InSAR) technology was adopted to process the SAR dataset and extract subsidence information. The basic principle of the PS-InSAR technique is to use several SAR images of the same area to find permanent scatterers (such as buildings, bridges, roads, etc.,) that are not subject to temporal and spatial baseline deconvolution and atmospheric effects by statistically

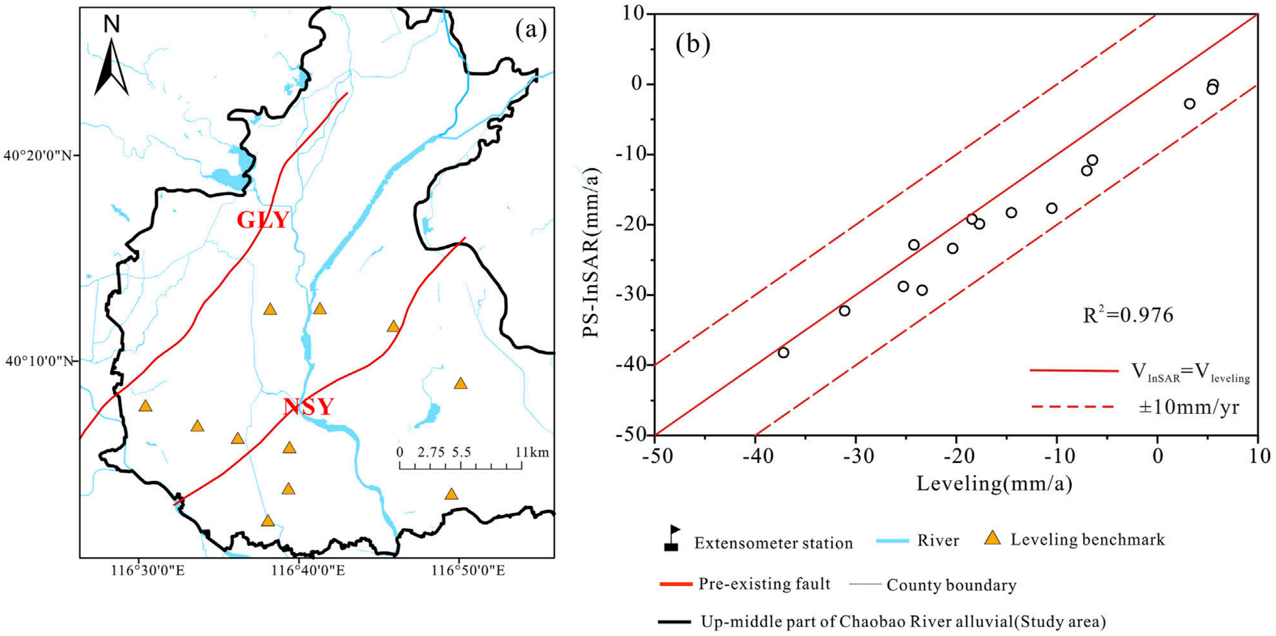

FIGURE 2
The location of the study sites **(A)** and comparisons of the PS-derived land subsidence rates and levelling measurement rates **(B)**. The orange triangle indicates the levelling benchmark used in this study. The black triangle indicates the extensometer monitoring stations.

analysing the magnitude information of the images and then to separate the errors from the differential interference phases one by one using the network formed by connecting these PS points and the spatiotemporal characteristics of each phase component (Ferretti et al., 2001). Using the network of these PS points and the spatial and temporal characteristics of each phase component, the errors are separated from the differential interference phase one by one, and the surface deformation phase of each PS point is finally obtained (Ferretti et al., 2001). It can overcome the factors of spatial and temporal incoherence and atmospheric delay in conventional differential interferometry and thus obtain continuous and reliable surface deformation information (Ferretti et al., 2001). The accuracy of the annual average deformation rate obtained by the PS-InSAR method can reach the millimetre level (Lei et al., 2022b). The data were processed via the following steps:

The master image is determined based on information such as the spatial and temporal baseline, the Doppler shift and the number of datasets. The remote sensing images are then cropped according to the extent of the study area to determine the processing area of the remote sensing images. The coordinate mapping relationship between the master image and all SAR imagery in the distance and azimuth directions is calculated, and the mapping relationship is used to perform coordinate mapping on all SAR imagery. Then, the image is resampled to a new image to align all the SAR images to the master image. The 30 m resolution SRTM data are resampled into the SAR image coordinate system, and an amplitude image is generated from the reference SRTM data. The aligned images were then subjected to differential interferometry to obtain N differential interferograms, with each image element of each differential interferogram containing five components. To avoid calculation errors caused by low coherence points, the high coherence points in the differential interferograms were selected for calculation. In this paper, the amplitude deviation index is used for screening, and the time series amplitude extreme deviation values are obtained by calculating the mean and standard deviation of the PS points in each period and the ratio of the two. The threshold value of the amplitude deviation index is set to filter the PS points, and then the Delaunay triangulation network is used to construct the point network of the PS point analysis. Once the PS points are selected, strong reflection points with zero phase components of deformation and elevation, high coherence and stable reflection characteristics are selected as the reference points. Then, the phase distributions of all other pixels are calculated based on the current reference points, and the phase values are improved based on the above phase distribution. The surface deformation of the study area and the physical and statistical properties of the components of the interferometric phase are used to establish an entangled phase function model with the elevation error, linear deformation, thermal deformation and other factor parameters. The atmospheric phase is analysed according to the pixel network using the phase difference relationship between adjacent permanent scattering targets, and the function model is solved based on the inverse residuals algorithm. The phase of the elevation error, linear deformation and other contributing factors of each pixel is solved, the phase of nonlinear deformation and incoherent noise in the residuals is decomposed, and finally, the entangled phase values of atmospheric delay components such as the elevation difference and linear deformation rate are accurately calculated. The above steps were completed using the SARPROZ tool.

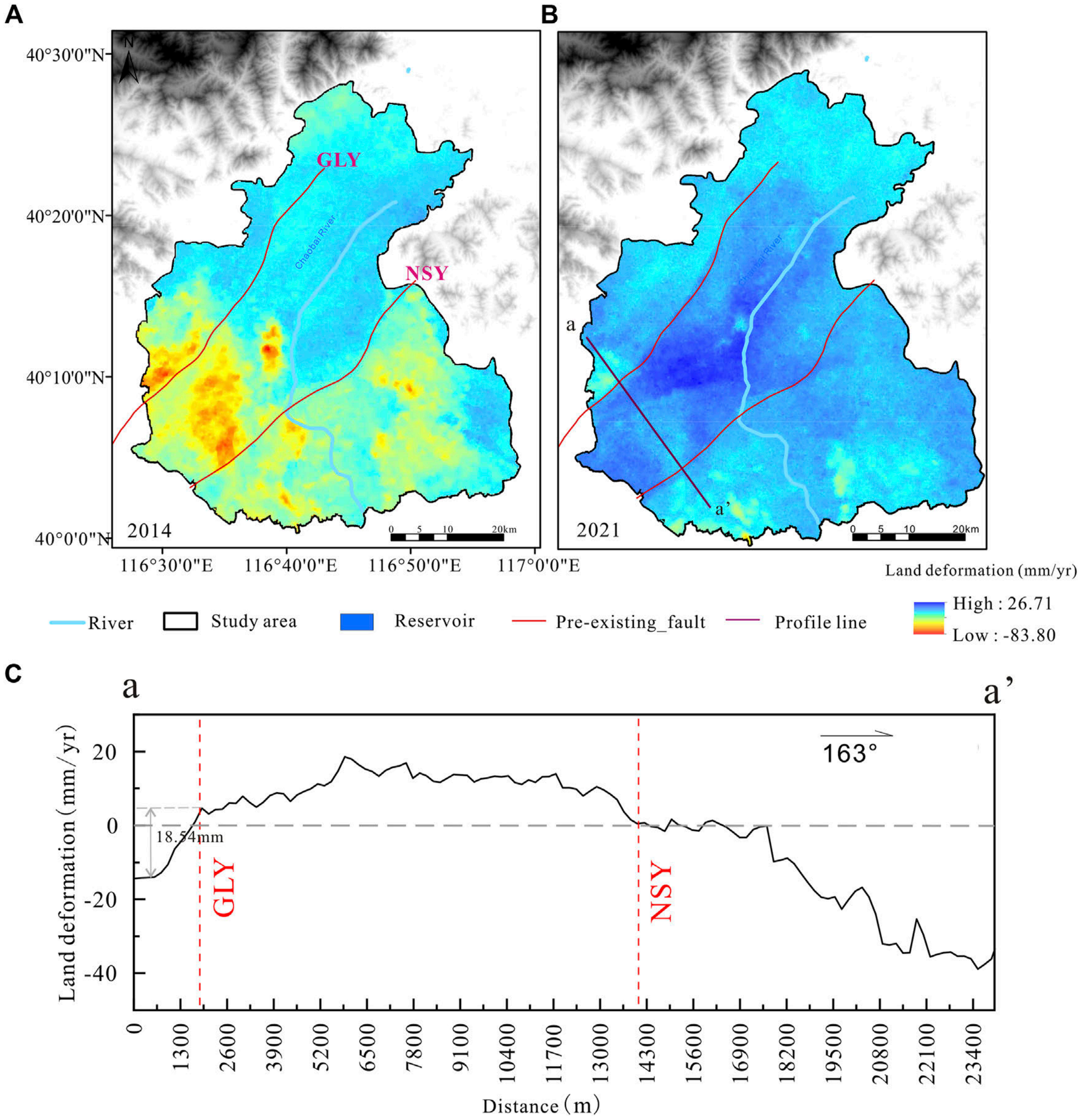

FIGURE 3
Maps of land displacements (vertical magnitude in mm) in 2014 and 2021 and the profile cross the pre-exising faults.

3.2 *In-situ* deformation data

The J1 land subsidence monitoring station is equipped with extensometers of varying depths. Data from these extensometers, spanning from 2004 to 2021, have been selected for analysis to discern the characteristics of soil deformation and to explore the correlation between the deformation of stratified soil layers and groundwater levels. The extensometer data at varying depths can be analyzed by deducting the cumulative deformation of the underlying layer from the total deformation. The monitoring layers of the extensometers and the corresponding groundwater wells at the monitoring station are detailed in Table 1. The geographical location of the monitoring station is depicted in Figure 1.

3.3 Groundwater level data

Data collected from monitoring wells in groundwater level directly reflect the hydraulic parameters of the aquifer. In this study, GWL was collected from 53 monitoring wells. The data is gathered on a monthly basis by the Beijing Institute of Geo-Environmental Monitoring from 2014 to 2021. In addition, time series analysis was conducted using data from 6 observation wells at both sides of the NSY fault. W1, W2, S1, S2, S3 and S4 wells. The depths of the wells are 111 m, 102 m, 60 m, 50 m, 80 m, and 102 m, respectively. In this study, the groundwater level refers to the elevation of groundwater, and the calculation method is to subtract the groundwater depth from the surface elevation.

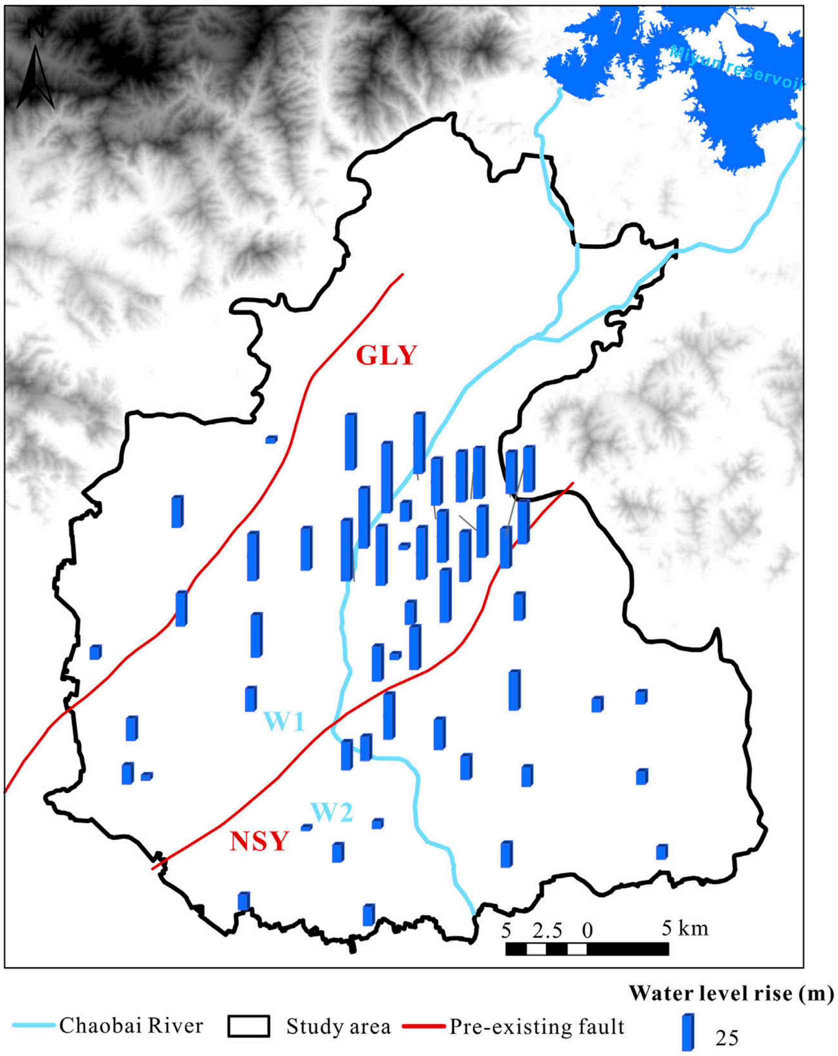

FIGURE 4
Distribution of groundwater level changes in 53 wells from 2015 to 2021.

4 Result and discussion

4.1 Accuracy assessment

Fifteen levelling benchmarks evenly distributed across the study regions were measured to verify the reliability of the PS-InSAR processing results (Figure 2A). Owing to the absence of permanent scatterers (PS) at the reference points, the average displacement of PS points within a 100-m buffer zone surrounding these leveling points was employed as the land deformation value in the reference point during the calibration process.

As shown in Figure 2B, a cross-comparison levelling result in 2014 and 2021 and the PS-InSAR data was obtained via linear regression analysis. The assessment results reveal that the PS-InSAR data matched the levelling results, and the error ranged from 1 to 7.5 mm. The R-squared value was 0.976. The comparison validated the PS-InSAR data, and the data could be used for further analysis of the spatial pattern of land deformation.

4.2 Spatial pattern of land deformation

As depicted in Figure 3, a comparison of the velocity maps from 2014 to 2021 reveals that both land subsidence relief have been observed within the study area. The deformation values higher than 0 indicate uplift, while the values lower than 0 indicate land subsidence.

Significant land subsidence has been detected in the southern region of the study area, with a maximum deformation rate of −83.8 mm/yr. Conversely, in 2021, widespread uplift was documented in the Shunyi district, with rates varying between +10 and +20 mm/yr (Figure 3). The PS (Persistent Scatterer) data within the land subsidence funnel indicate subsidence rates exceeding −50 mm/yr in 2014. By 2021, the region experienced land uplift at a rate as high as +5 cm/yr. The maximum land rebound was observed in the region around 2021, amounting to ten percent of the land subsidence recorded in 2014.

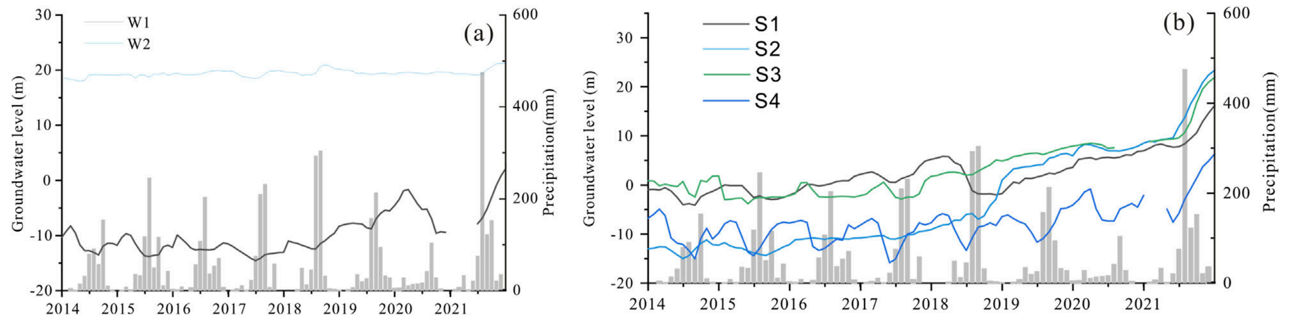

FIGURE 5
Time series of groundwater levels on both sides of the NSY fault. See the well locations of **(A)** in the Figure 4 and **(B)** in the Figure 6.

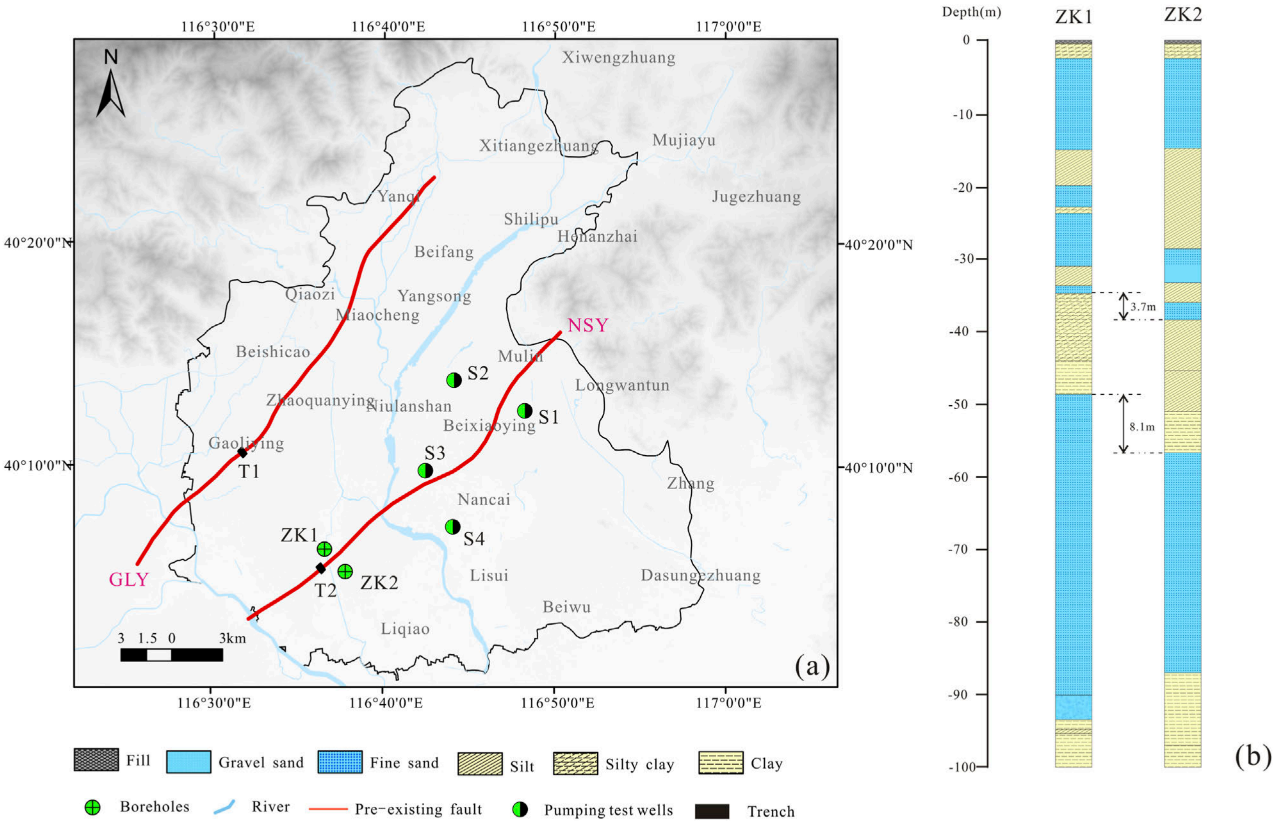

FIGURE 6
(A) The locations of the boreholes, the trenching, and the pumping test well. **(B)** The geological cross-section of the NSY fault.

Interesting, the visible uplift zone, the rebound rate above 20 mm/yr, is dominated spreading in a fan area striking approximately NE-SW. By jointly preexisting faults and land deformation driven by the InSAR, the uplift zone is mainly developed in the depression bounded by the GLY fault in the northwest and the NSY fault in the southeast.

For further reveal the effect of pre-existing fault on the land deformation, We drew a profile a-a (marked as the brown dashed line in Figure 3B) perpendicular to the pre-existing fault. We plotted the trend of vertical displacement (black line) and the gradient of subsidence (brown line) based on the points (600 points total) within the profile. As shown in Figure 3C, the deformation rate reveals an decreasing trend at the hangingwall of NSY and footwall of GLY. The maximum value of the vertical displacementis 38.89 mm. A visible land rebound area were generated at the foot wall of NSY, with a maximum rebound of 18.54 mm. The deformation rate exhibits a distinct uneven changes crossing the GLY Fault and NSY fault, with a maximum uneven deformation of 18.7 mm.

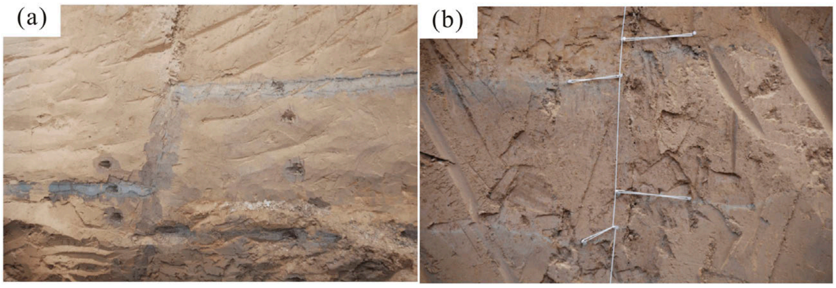

FIGURE 7
Trench profile of the preexisting fault. **(A)** Trench profile excavated perpendicular to the GLY fault in Xiwanglu town. **(B)** Trench profile excavated perpendicular to the NSY fault Shunyi petroleum company.

TABLE 2 Results of the pumping test on both sides of the NSY fault. See Figure 6A for a map of the pumping test well locations.

Piezometer	Piezometer end depth(m)	Average saturated hydraulic conductivity value (m/d)
S1	22.6	276.21
S2	21.5	402
S3	49.91	62.5
S4	47.69	38.55

4.3 Influences of groundwater on the spatial extent of land rebound

Previous studies have shown that land uplift could result from the expansion of the granular skeleton due to the increase in pore pressure associated with recovery of the groundwater level (Waltham, 2002; Wang et al., 2017). This phenomenon is referred to as elastic or poroelastic rebound (Chen et al., 2007). Therefore, we consider the change in groundwater levels on both sides of the preexisting faults to likely be triggering factors that influence the spatial extent of land rebound.

53 automatically monitored wells were used to investigate the groundwater level changes from 2014 to 2021 at both sides of the preexisting faults. As shown in Figure. During the MAR operation, Groundwater levels exhibited a relative increase at 90% of the monitoring well sites. Groundwater levels in the footwall of the NSY fault have been observed to rise, with a peak increase of nearly 50 m. In contrast, the groundwater levels at the hanging wall of the NSY fault exhibited a relatively minor upward trend. As the distance from the fault increased, no discernible changes in groundwater levels was observed.

To further examine groundwater level changes at both sides of the preexisting fault, The monitoring wells, located at at both sides of the fault, was selected. The location of the wells are shown in Figures 4, 6 respectively. The groundwater level exhibited significant difference on either side of the NSY fault. For instance, monitoring well 3 showed an visible increase in response to the MAR with 10.71 increase after the MAR operation in 2018. While W1 record seasonal variations associated with changes in precipitation throughout the observation period Figure 5A.

A similar finding was made by Lapperre et al. (2022) for the Peel Boundary Fault. They concluded that this effect may caused by low normal permeability of the preexisting fault zone. Previous studies have shown that the most direct cause of the low permeability around the fault zone is because of fault throwing, which can juxtapose low-permeability confining units against well-permeability aquifers (Lapperre et al., 2019; Zhao et al., 2021).

The geological section of the NSY fault at a depth of 0–100 m was revealed by drilling. As shown in Fig, notable stratigraphic dislocation begins at a depth of 35 m, and the vertical throw of the strata gradually increases, displaying a juxtapose of low-permeability confining units against well-permeability aquifers (Figure 6). The geophysical prospecting profiles also show that the stratigraphic dislocation propagates downward into the sediments and may extend to depths of more than 100 m (Qi et al., 2020).

The earth fissure trenches reveal the shallow characteristics of pre-existing faults. There is a clear vertical offset of strata within the trench's range, resulting in the development of a clay smear along the fault zone that cuts through the clay beds (Figure 7).

Based on the results of the trenching and geological section analysis, significant stratigraphic displacement and distinct fault surfaces were observed. The results indicates that the NSY Fault displays pronounced brittle fault characteristics. As shown in Fig, under the effect of the MAR, the water level rise was occurred in the foot wall of NSY fault Figure 5B. The juxtapose of low-permeability confining units against well-permeability aquifers caused by the throwing lead to a gradual decrease in the hydraulic conductivity of the fault zone. An obvious reduction in the permeability of half the magnitude in the hanging wall of the NSY fault zone compared to the aquifer in the footwall of the NSY fault zone was found (Table 2).

As shown in Figure 8B The presence of a low-permeability layer diminishes the hydraulic connection between the hanging wall and footwall of the NSY fault, the groundwater in the deep aquifers located in the footwall of the NSY fault have to circumvent the aquiclude by moving upward and downward through aquifers situated above and below it,resulting in reduced water transmission from the MAR to the hanging wall of the NSY fault, as compared to

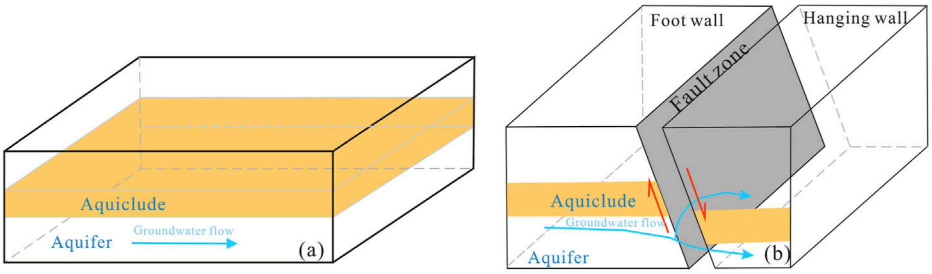

FIGURE 8
Conceptual model of groundwater flow dynamics **(A)** Natural groundwater flow patterns. **(B)** Groundwater flow behavior across pre-existing fault.

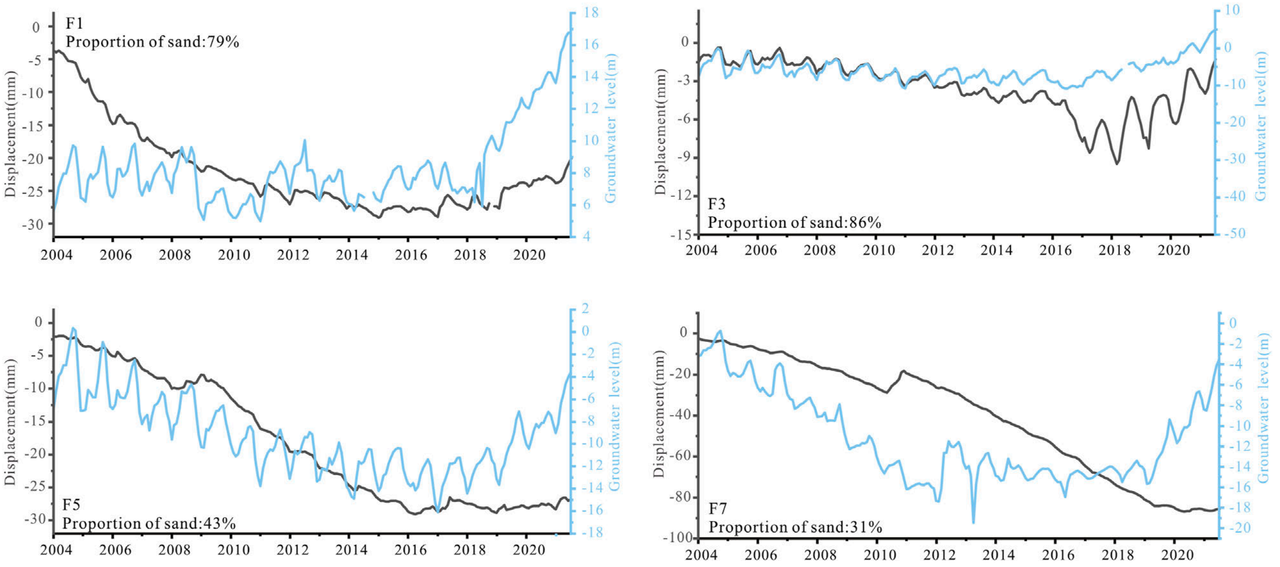

FIGURE 9
Time series curve of the relationship between cumulative layer deformation and groundwater level at extensometer station. F1, F3, F5, and F7 represent the monitoring data captured at various depth levels. See Figure 2A for a map of the monitoring station locations.

the natural state Figure 8A. Consequently, this results in a hysteresis effect or a lack of groundwater level rise in response to the MAR.

According to the principle of effectiveness, MAR leads to an obvious rebound of the aquifers located at the footwall of the NSY fault. On the other hand, due to the sluggish recharge of water from the footwall to the hangingwall aquifers, there was few rebound in contrast to the deformation observed in the footwall of the NSY fault.

4.4 Influences of lithology on the spatial extent of land rebound

Ground surface deformation is a result of the total deformation of deep soil layers (Liu et al., 2019; Zhang et al., 2015). It can be inferred that the spatial variation may be caused by the complex loading and unloading in deep soil deformation caused by the groundwater level rise. To better understand the relationship between the groundwater level and the deep soil deformation, the deformation of the soil layer measured at extensometer station, located at the foot wall of the NSY fault, is plotted in Figure 9.

As shown in Figure 9, the land rebound responds differently to a rise in groundwater level. Land rebound can be broadly grouped into two deformation modes.

Firstly, as the groundwater level rises, the deformation of the aquifer is closely related to the change in the groundwater level and exhibited the soil rebound. Secondly, the deformation of the aquifer is no closely related to the change in the groundwater level. The relieve of soil compaction was found during the monitoring period following the rise in water levels. Based on the boreholes data, the former mainly occurred in the soil with higher proportion of sand layer, while the latter mainly occurred in the soil with higher proportion of the clay layer.

We made comparisons of the lithology at both sides of the NSY fault to assess the effect of the lithology on the land rebound. As shown in Figure 10, The fairly high proportion of sand layer, suggested that this area may occurred significant elastic or poroelastic rebound in soil during the groundwater level rise. In

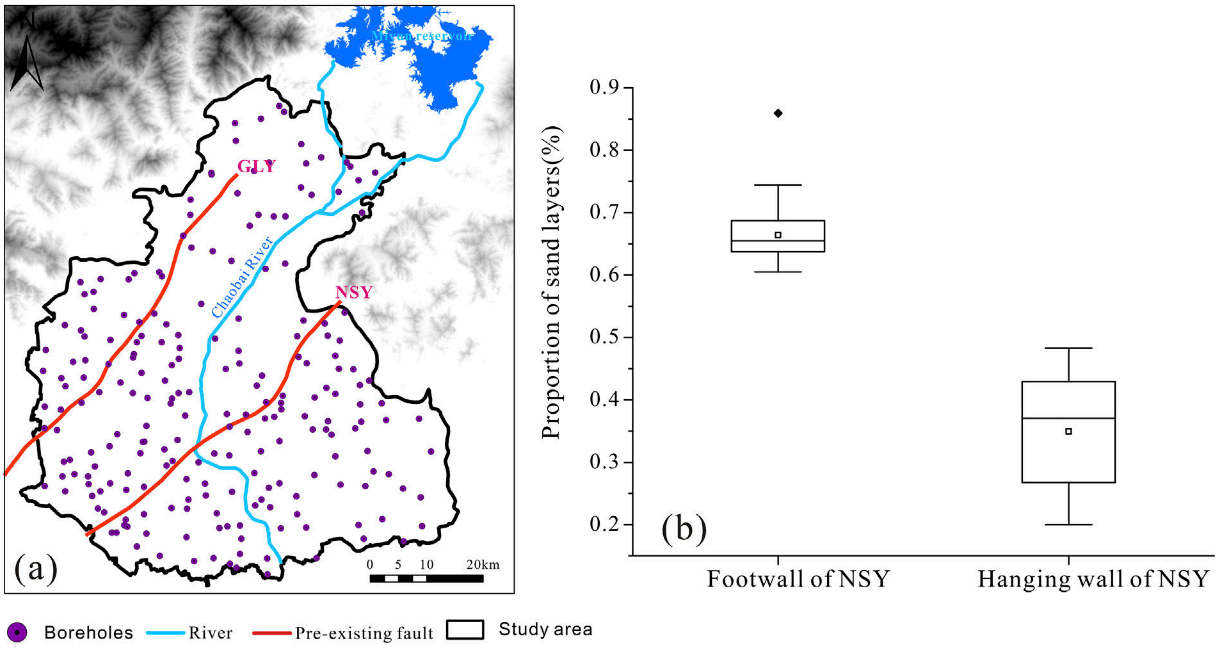

FIGURE 10
Lithology at both sides of pre-existing faults **(A)** Borehole locations **(B)** Proportion of sand layers on both sides of pre-existing faults.

contrast, lower proportion of sand layer was identified in hanging wall of NSY fault. The information indicates that this area can not experience the rebound immediately when the groundwater level rise.

5 Conclusion

In summary, the most important new insight from our analysis is that MRP is an effective measure for controlling land subsidence. A certain deceleration of the process of land subsidence has been detected in the MRP area.

The InSAR reveal a significant shift from land subsidence to land uplift in the study area between 2014 and 2021. The uplift zones, particularly those exceeding 20 mm/yr, exhibit a fan-shaped pattern striking approximately NE-SW, closely mirroring the preexisting fault.

The study highlights the influence of groundwater level changes on land rebound. The MAR process led to a noticeable rise in groundwater levels, particularly at the footwall of the faults. The low permeability across the fault zone weakened the hydraulic connection between the hanging wall and footwall, further inhibiting groundwater flow and land deformation in the hanging wall.

The study underscores the significance of lithology in determining the spatial extent of land rebound. Soils with a higher proportion of sand layers were found to exhibit more pronounced rebound in response to groundwater level rise. Conversely, areas with lower sand content, such as the hanging wall of the NSY fault, demonstrated delayed or limited rebound.

Data availability statement

The original contributions presented in the study are included in the article/supplementary material, further inquiries can be directed to the corresponding authors.

Author contributions

SL: Conceptualization, Data curation, Formal Analysis,Investigation, Methodology, Software, Writing–original draft,Writing–review and editing. MB: Conceptualization, Data curation, Funding acquisition, Resources, Supervision, Validation,Writing–review and editing.

Funding

The author(s) declare financial support was received for the research, authorship, and/or publication of this article. This research is supported by the Natural Science Foundation of China (Grant No. 42172311), Beijing Natural Science Foundation (Grant No. 8242018).

Acknowledgments

We greatly thank the editors, as well as the reviewers for their helpful or valuable comments on the paper.

Conflict of interest

The authors declare that the research was conducted in the absence of any commercial or financial relationships that could be construed as a potential conflict of interest.

The reviewer BB declared a shared affiliation with the authors to the handling editor at time of review.

Publisher's note

References

Ao, Z., Hu, X., Tao, S., Hu, X., Wang, G., Li, M., et al. (2024). A national-scale assessment of land subsidence in China's major cities. *Science* 384, 301–306. doi:10.1126/science.adl4366

Bagheri-Gavkosh, M., Hosseini, S. M., Ataie-Ashtiani, B., Sohani, Y., Ebrahimian, H., Morovat, F., et al. (2021). Land subsidence: a global challenge. *Sci. Total Environ.* 778, 146193. doi:10.1016/j.scitotenv.2021.146193

Burbey, T. J. (2002). The influence of faults in basin-fill deposits on land subsidence, Las Vegas Valley, Nevada, USA. *Hydrogeology J.* 10, 525–538. doi:10.1007/s10040-002-0215-7

Calderhead, A. I., Martel, R., Garfias, J., Rivera, A., and Therrien, R. (2012). Sustainable management for minimizing land subsidence of an over-pumped volcanic aquifer system: tools for policy design. *Water Resour. Manag.* 26, 1847–1864. doi:10.1007/s11269-012-9990-7

Castellazzi, P., Garfias, J., and Martel, R. (2021). Assessing the efficiency of mitigation measures to reduce groundwater depletion and related land subsidence in Querétaro (Central Mexico) from decadal InSAR observations. *Int. J. Appl. Earth Observation Geoinformation* 105, 102632. doi:10.1016/j.jag.2021.102632

Chen, C. T., Hu, J. C., Lu, C. Y., Lee, J. C., and Chan, Y. C. (2007). Thirty-year land elevation change from subsidence to uplift following the termination of groundwater pumping and its geological implications in the Metropolitan Taipei Basin, Northern Taiwan. *Eng. Geol.* 95, 30–47. doi:10.1016/j.enggeo.2007.09.001

Ferretti, A., Prati, C., and Rocca, F. (2001). Permanent scatterers in SAR interferometry. *IEEE Trans. geoscience remote Sens.* 39 (1), 8–20. doi:10.1109/36.898661

Galloway, D. L., and Burbey, T. J. (2011). Review: regional land subsidence accompanying groundwater extraction. *Hydrogeology J.* 19 (8), 1459–1486. doi:10.1007/s10040-011-0775-5

Herrera-García, G., Ezquerro, P., Tomás, R., Béjar-Pizarro, M., López-Vinielles, J., Rossi, M., et al. (2021). Mapping the global threat of land subsidence. *Science* 371, 34–36. doi:10.1126/science.abb8549

Holzer, T. L. (1981). Preconsolidation stress of aquifer systems in areas of induced land subsidence. *Water Resour. Res.* 17 (3), 693–703. doi:10.1029/WR017i003p00693

Hu, L., Dai, K., Xing, C., Li, Z., Tomás, R., Clark, B., et al. (2019). Land subsidence in Beijing and its relationship with geological faults revealed by Sentinel-1 InSAR observations. *Int. J. Appl. Earth Observation Geoinformation* 82, 101886. doi:10.1016/j.jag.2019.05.019

Lapperre, R. E., Bense, V. F., Kasse, C., and van Balen, R. T. (2022). Temporal and spatial variability of cross-fault groundwater-level differences: the impact of fault-induced permeability reduction, precipitation and evapotranspiration. *Hydrogeol. J.* 30, 1233–1257. doi:10.1007/s10040-022-02465-w

Lapperre, R. E., Kasse, C., Bense, V. F., Woolderink, H. A. G., and Van Balen, R. T. (2019). An overview of fault zone permeabilities and groundwater level steps in the Roer Valley Rift System. *Neth. J. Geosciences* 98, e5. doi:10.1017/njg.2019.4

Lei, K., Ma, F., Chen, B., Luo, Y., Cui, W., Zhao, L., et al. (2022a). Effects of South-to-North water diversion Project on groundwater and land subsidence in Beijing, China. *Bull. Eng. Geol. Environ.* 82, 18. doi:10.1007/s10064-022-03021-2

Lei, K., Ma, F., Chen, B., Luo, Y., Cui, W., Zhou, Y., et al. (2022b). Characteristics of land-subsidence evolution and soil deformation before and after the Water Diversion Project in Beijing, China. *Hydrogeology J.* 30, 1111–1134. doi:10.1007/s10040-022-02489-2

Liu, Y., Li, J., and Fang, Z. N. (2019). Groundwater level change management on control of land subsidence supported by borehole extensometer compaction measurements in the houston-galveston region, Texas. *Geosciences* 9, 223. doi:10.3390/geosciences9050223

Lofgren, B. E. (1968). *Analysis of stresses causing land subsidence*. US: Geological survey research, B219–B225.

Negahdary, M. (2022). Shrinking aquifers and land subsidence in Iran. *Science* 376 (6599), 1279. doi:10.1126/science.add1263

Ng, A. H. M., Ge, L., Du, Z., Wang, S., and Ma, C. (2017). Satellite radar interferometry for monitoring subsidence induced by longwall mining activity using Radarsat-2, Sentinel-1 and ALOS-2 data. *Int. J. of App. Earth Observation and Geoinformation* 61, 92–103.

Parker, A. L., Pigois, J. P., Filmer, M. S., Featherstone, W. E., Timms, N. E., and Penna, N. T. (2021). Land uplift linked to managed aquifer recharge in the Perth Basin, Australia. *Int. J. Appl. Earth Obs. Geoinf* 105, 102637. doi:10.1016/j.jag.2021.102637

Qi, B., Pan, Z., Feng, C., Tan, C., Zhang, P., Meng, J., et al. (2020). Application of comprehensive geophysical-drilling exploration to detect the buried Shunyi active fault belt in Beijing. *Acta Geol. Sin.* 94, 1315–1329. doi:10.19762/j.cnki.dizhixuebao.2020002

Roose, D., and Starks, D. (2006). "The California state water Project - asset management and condition assessment," in Proceedings of the Operations Management Conference, Sacramento, California, 1–13. doi:10.1061/40875(212)1

Salehi Moteahd, F., Hafezi Moghaddas, N., Lashkaripour, G. R., and Dehghani, M. (2019). Geological parameters affected land subsidence in Mashhad plain, north-east of Iran. *Environ. Earth Sci.* 78, 405–412. doi:10.1007/s12665-019-8413-y

Samsonov, S. V., Feng, W., and Fialko, Y. (2017). Subsidence at cerro prieto geothermal field and postseismic slip along the Indiviso fault from 2011 to 2016 RADARSAT-2 DInSAR time series analysis. *Geophysical Research Letters* 44, 2716–2724.

Tang, W., Zhao, X., Motagh, M., Bi, G., Li, J., Chen, M., et al. (2022). Land subsidence and rebound in the Taiyuan basin, northern China, in the context of inter-basin water transfer and groundwater management. *Remote Sens. Environ.* 269, 112792. doi:10.1016/j.rse.2021.112792

Waltham, T. (2002). Sinking cities. *Geol. Today* 18 (3), 95–100. doi:10.1046/j.1365-2451.2002.00341.x

Wang, G. y., Zhu, J. Q., You, G., Yu, J., Gong, X. L., Li, W., et al. (2017). Land rebound after banning deep groundwater extraction in Changzhou, China. *Eng. Geol.* 229, 13–20. doi:10.1016/j.enggeo.2017.09.006

Wei, W. (2008). *3D geological survey based on multiparameter of geological body in Beijing plain*. Beijing, China: Beijing Geology and Mineral Resources Exploration and Development Bureau.

Zhang, L., He, J., Bai, L., Cai, X., Wang, J., and Yang, T. (2016). The response relationship between the variation characteristics of deposition rate of Quaternary depression basin on the northern margin of Beijing depression and the activity of Shunyi fault. *Geol. China* 43, 511–519. doi:10.12029/gc20160212

Zhang, Y., Wu, J., Xue, Y., Wang, Z., Yao, Y., Yan, X., et al. (2015). Land subsidence and uplift due to long-term groundwater extraction and artificial recharge in Shanghai, China. *Hydrogeol. J.* 23, 1851–1866. doi:10.1007/s10040-015-1302-x

Zhao, L., Li, Y., Luo, Y., Liu, J., Cui, W., Zhang, Y., et al. (2021). An extension-dominant 9-km-long ground failure along a buried geological fault on the eastern Beijing Plain, China. *Eng. Geol.* 289, 106168. doi:10.1016/j.enggeo.2021.106168

Zhu, L., Gong, H., Chen, Y., Wang, S., Ke, Y., Guo, G., et al. (2020). Effects of Water Diversion Project on groundwater system and land subsidence in Beijing, China. *Eng. Geol.* 276, 105763. doi:10.1016/j.enggeo.2020.105763

frontiers | Frontiers in Earth Science

TYPE Original Research
PUBLISHED 28 October 2024
DOI 10.3389/feart.2024.1431203

OPEN ACCESS

EDITED BY
Hans-Balder Havenith,
University of Liège, Belgium

REVIEWED BY
Haijun Qiu,
Northwest University, China
Jian Fang,
Central China Normal University, China
Yajun Li,
Lanzhou University, China

*CORRESPONDENCE
Wentao Yang,
✉ yang_wentao@bjfu.edu.cn

†These authors share first authorship

RECEIVED 11 May 2024
ACCEPTED 18 September 2024
PUBLISHED 28 October 2024

CITATION
Wang H, Wu W, Yang W and Liu M (2024) Examining the contribution of lithology and precipitation to the performance of earthquake-induced landslide hazard prediction.
Front. Earth Sci. 12:1431203.
doi: 10.3389/feart.2024.1431203

Examining the contribution of lithology and precipitation to the performance of earthquake-induced landslide hazard prediction

Hui Wang[1]†, Wei Wu[2]†, Wentao Yang[1]* and Meiyu Liu[2]

[1]School of Soil and Water Conservation, Beijing Forestry University, Beijing, China, [2]National Disaster Reduction Center of China, Ministry of Emergency Management, Beijing, China

Earthquake-induced landslides (EQIL) are one of the most catastrophic geological hazards. Immediate and swift evaluation of EQIL hazard in the aftermath of an earthquake is critically important and of substantial practical value for disaster reduction. The selection of influencing factor layers is crucial when using machine learning methods to predict EQIL hazard. As important input factors for EQIL hazard models, lithology and precipitation are extensively employed in forecasting EQIL hazard. However, few work explored whether these layers can improve the accuracy of EQIL hazard predictions. With Random Forest (RF) models, we employed a traditional and a state-of-the-art sampling strategy to assess EQIL modelling with and without lithology and precipitation data for the 2022 Luding earthquake in China. First, by excluding both factors, we used eight other influencing factors (land use, slope aspect, slope, elevation, distance to faults, distance to rivers, NDVI, and peak ground acceleration) to generate a landslide hazard map. Second, lithology and precipitation were separately added to the original EQIL hazard models. The results indicate that neither lithology nor precipitation have positive effects on the prediction of EQIL for both sampling strategies. The high-risk areas (or low-risk areas) tend to cluster within certain lithology types or precipitation ranges, which significantly affects the accuracy of the hazard map. Additionally, the model with the state-of-the-art sampling strategy deteriorates more than the model with the traditional sampling strategy. We believe this is very likely due to the strong spatial clustering of negative sample points caused by the latest sampling strategy. Our findings will contribute to the assessment of post-earthquake landslide hazards and the advancement of emergency disaster mitigation efforts.

KEYWORDS

earthquake-induced landslide, hazard prediction, lithology, precipitation, luding

1 Introduction

Earthquake-induced landslides pose significant threats to human life and property. EQIL hazard maps, indicating the likelihood of landslides in areas affected post-earthquake, are critical for enabling decision-makers to implement emergency responses. Thus, accurately predicting and mapping the hazard of earthquake-induced landslides is indispensable (Jibson et al., 2000; Marano et al., 2010; Raspini et al., 2017). Despite considerable research efforts, the accuracy of EQIL hazard maps frequently falls short, leading to a substantial number of areas being misjudged or their risk levels exaggerated (Dreyfus et al., 2013; Allstadt et al., 2018). This situation hampers decision-makers' ability to devise accurate emergency response strategies, thus making the creation of high-quality EQIL hazard maps a particularly challenging task.

Machine learning methods are currently the mainstream approach for creating EQIL hazard maps (Shao and Xu, 2022). In machine learning approaches, selecting the influencing factors for co-seismic landslides is a critical step that directly impacts the outcomes of predictions. During the selection of influencing factors, lithology factors and mean annual precipitation are widely used by researchers (Shao et al., 2022; Aditian et al., 2018; Pyakurel et al., 2024; Li et al., 2024; Khaliq et al., 2023; Nefeslioglu et al., 2008). Especially, lithology factors are recognized as one of the landslide-triggering factors considered in any landslide susceptibility assessment using data-driven methods, a fact well acknowledged in the field (Guzzetti et al., 1996; Van Westen et al., 2006; Blahut et al., 2010). But whether these factors positively impact the precision of EQIL hazard prediction results has seldom been explored.

The classification of lithology is usually conducted through stratigraphic ages, with rocks from various epochs exhibiting distinct physical properties (Gallen et al., 2015). These differences contribute to varying levels of landslide susceptibility. Although there is a strong correlation between lithology and EQIL hazard, lithology layers come in a wide variety and often have lower resolution, with significant differences in lithology across different regions. Therefore, lithology factors may not always play a beneficial role in predicting EQIL hazards. Precipitation increases pore water pressure and reduces the shear resistance of soil and rock layers, thereby leading to landslides (Aditian et al., 2018). Precipitation data (such as mean annual precipitation) is also a significant factor affecting landslide occurrence. However, the resolution of mean annual precipitation layers is coarse, at 0.1°, and regional differences are significant. Whether using mean annual precipitation layers can effectively enhance the accuracy of EQIL predictions merits further investigation.

To address these issues, this study utilized high-quality landslide inventories from eight earthquake events in China to create two sets of positive and negative sample points datasets for machine learning, employing both traditional and contemporary non-landslide point sampling strategies. Utilizing the Random Forest model, eight influencing factors were selected: "land use," "slope aspect," "slope," "elevation," "distance to fault lines," "distance to rivers," "NDVI," and "peak ground acceleration." These were used to predict the EQIL hazard for the VII degree area affected by the 2022 Luding earthquake. The prediction results were validated against the interpreted landslide inventory for this earthquake, exploring the accuracy of the prediction outcomes from the two sampling strategies. Subsequently, lithology factors and mean annual precipitation were added to the aforementioned eight influencing factors, while keeping the machine learning model and sample datasets unchanged. This allowed for an exploration of how the inclusion of lithology or precipitation factors affects the differences in prediction outcomes. The novelty of this study lies in its demonstration of how lithology and mean annual precipitation impact the accuracy of EQIL hazard predictions. It shows that both factors have a significant effect on prediction accuracy. Avoiding these factors can notably enhance the precision of EQIL hazard forecasts.

2 Study area

The study area selected for this research encompasses the VII degree zone affected by the 6.8 magnitude Luding earthquake in 2022 (Figure 1), situated at the southeastern edge of the Tibetan Plateau, covering the southern part of Luding County and the northern part of Shimian County in Ganzi Prefecture. The earthquake's epicenter was located near the Moxi Fault, close to the Gongga Mountain Hailuogou Glacier Forest Park, along the southeastern edge of the Tibetan Plateau within the Xianshuihe fault zone. The Xianshuihe fault zone is one of the highly active and large-scale boundary strike-slip fault zones, positioned at the eastern edge of the Tibetan Plateau, where the Bayan Har block meets the Sichuan-Yunnan block. It intersects with the Longmenshan Fault Zone and the Anning River Fault Zone, forming the famous "Y-shaped" fault zone in western Sichuan (Wang et al., 2015).

This earthquake triggered at least 5,007 landslides, with preliminary spatial distribution analysis indicating that the landslides were concentrated in areas of VIII and IX earthquake intensity. There is a clear connection between the coseismic fault and the distribution of landslides, with the landslides primarily clustered around both sides of the causative fault. Notably, there are more landslides on the northeast side compared to the southwest side (Huang et al., 2023).

3 Materials and methods

3.1 Landslide inventories

We obtained open access lists of high-quality earthquake landslides from publicly available research, as follows: the 2008 Wenchuan earthquake (Xu et al., 2014a), the 2010 Yushu earthquake (Xu et al., 2013), the 2013 Lushan earthquake (Xu et al., 2015), the 2013 Minxian earthquake (Xu et al., 2014b), the 2014 Ludian earthquake (Wu et al., 2020), the 2017 Jiuzhaigou earthquake (Xu et al., 2018), the 2017 Milin earthquake (Hu et al., 2019), the 2022 Lushan earthquake (Shao et al., 2022), and the 2022 Luding earthquake (Huang et al., 2023). High-quality landslide inventories from the first eight earthquakes were used to create the training samples. The landslide inventory from the 2022 Luding earthquake was used to validate the EQIL hazard prediction results for the Luding study area.

3.2 Identifying influencing factors for EQIL

The occurrence of landslides is influenced by a variety of factors, and scientifically selecting these factors is crucial for

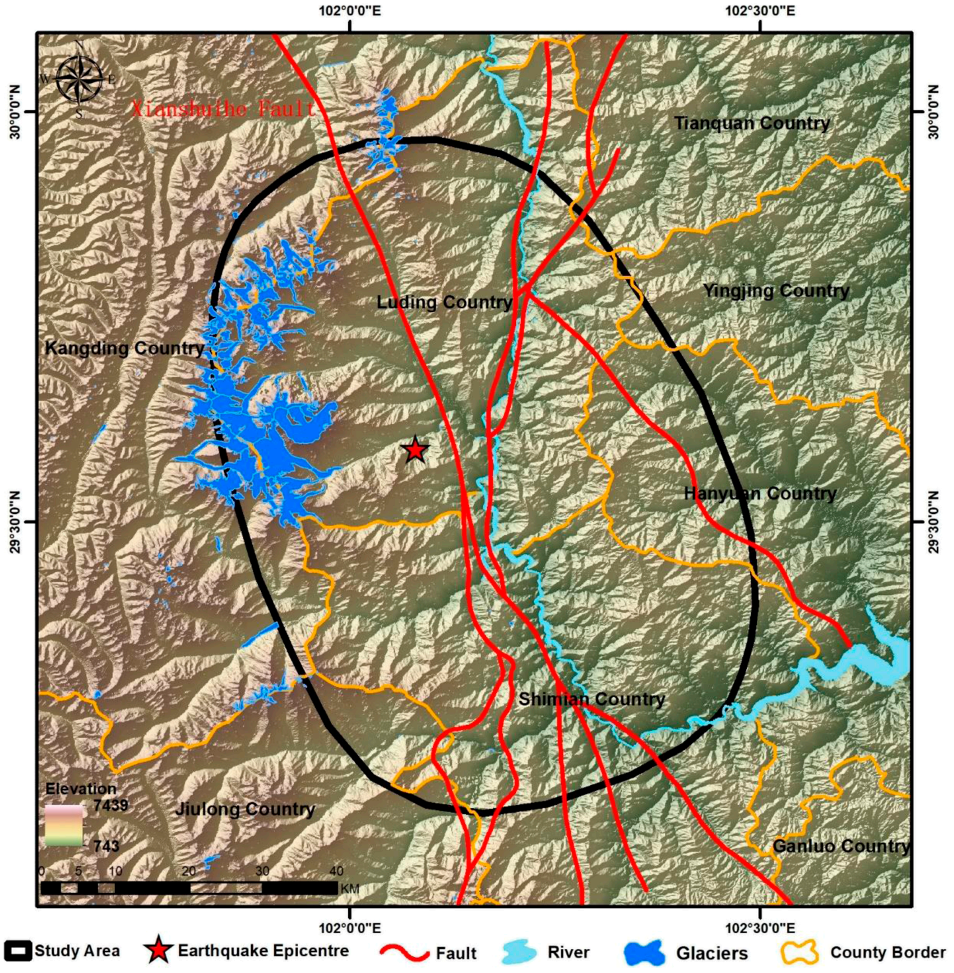

FIGURE 1
Overview of the study area for the Ms 6.8 Luding Earthquake in 2022.

conducting studies on regional landslide risk assessment. To investigate the impact of lithology and mean annual precipitation on the precision of EQIL hazard prediction, we selected ten potential factors that could cause landslides. This selection was made after a comprehensive process that included field observations, collection of available data, review of relevant literature, and numerous tests (Fan et al., 2021; Chen et al., 2017; Pham et al., 2017; Tien et al., 2016; Youssef et al., 2016). The factors are elevation, slope aspect, slope, land use, mean annual precipitation (MAP), lithology, distance to faults, distance to rivers, NDVI, and peak ground acceleration (PGA) during earthquakes. The data sources for these factors can be seen in Table 1.

It is noteworthy that, in the case of the 2022 Luding earthquake event, there was some discrepancy between the epicenter location and peak ground acceleration provided by the USGS and the results of field investigations. Therefore, we estimated and mapped the peak ground acceleration raster for the study area based on intensity zones provided by the China Earthquake Administration. Examples of influencing factor layers focused on the study area are shown in Figure 2.

3.3 Creation of machine learning training sample points

3.3.1 Creation of positive sample points

In this study, the landslide inventories from the eight selected earthquake events are all represented as landslide polygon layers. Centroids of the landslide polygons were generated using ArcMap version 10.8. Given that many landslide polygons are of irregular shapes, some centroids did not fall within their respective polygons (Qiu et al., 2024). Therefore, using ArcMap, all centroids located within the landslide polygons were selected to serve as landslide points (positive sample points).

3.3.2 Creation of negative sample points

In traditional landslide hazard assessments, the sampling ratio of positive (landslide) to negative (non-landslide) sample points is 1:1 (Hong et al., 2020). Zhu et al. (2017) proposed a method in areas with landslide polygons where every seismic zone is filled with a sampling grid at 100 m intervals. If a grid cell contains a landslide point, or if 30% of the grid cell is covered

TABLE 1 Sources and resolution of data layers for influencing factors.

Provider	Spatial resolution	Source
SRTM	30 m	http://Ipdaac.usgs.gov/
SRTM	30 m	Derived from the SRTM30 DEM
SRTM	30 m	Derived from the SRTM30 DEM
Wuhan University	30 m	10.5821/zenodo.4417809
USGS	30 m	http://earthquake.usgs.gov/earthquakes/search/
NASA GPM	0.1°	http://gpm.nasa.gov/
Ye et al. (2017)	1:2,500,000	http://doi.org/10.12029/gc2017Z103
Ye et al. (2017)	1:2,500,001	http://doi.org/10.12029/gc2017Z103
OSM	30 m	http://www.openstreetmap.org
Sentinel-2	30 m	http://dataspace.copernicus.eu/

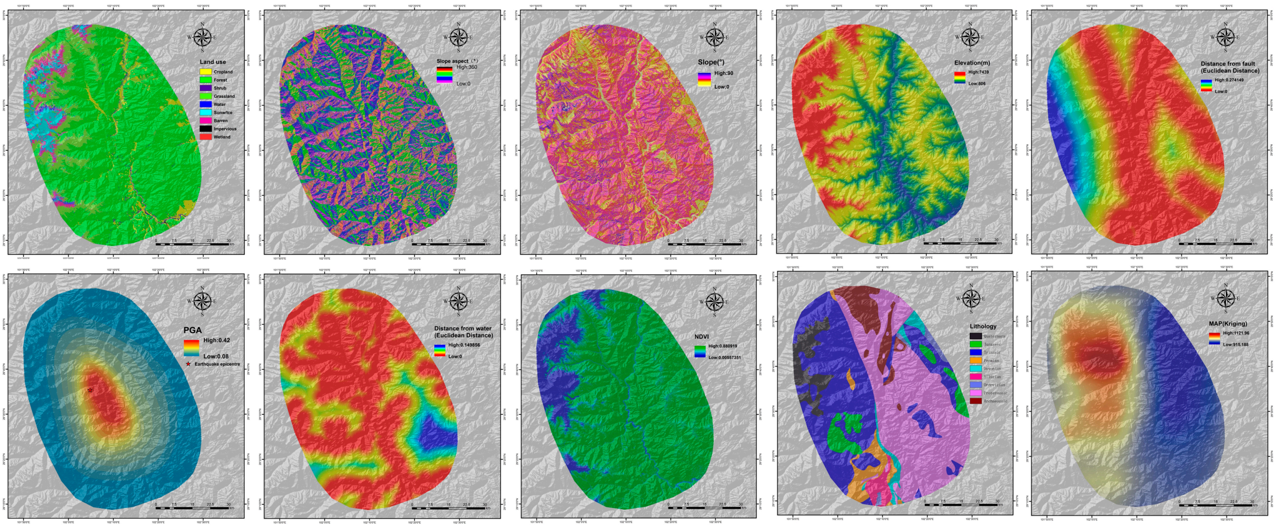

FIGURE 2
EQIL influencing factor layers in the study area.

by landslide polygons, that cell is marked as a landslide grid. Then, non-landslide points are randomly selected from areas not marked as landslide grids. In seismic zones where the landslide inventory consists of point data, non-landslide points are generated using the range of point buffers, ultimately balancing the total number of landslide and non-landslide points at a one-to-one ratio. M. A. Nowicki Jessee also utilized this method for global sampling of positive and negative sample points for EQIL (Nowicki et al., 2018). Huang and colleagues concluded that an unequal number of positive and negative sample points affects model performance and adopted a 1:1 ratio for sampling positive and negative sample points (Huang and Zhao, 2018; Tien et al., 2012). Currently, in studies concerning landslide hazard, traditional methods predominantly utilize a sampling ratio of 1:1 for positive and negative samples.

However, some studies have proposed alternative negative sample sampling strategies that achieved results superior to the traditional approach. Shao and colleagues argued that the conventional 1:1 sampling method might exaggerate the proportion of landslide samples in the study area, thereby diminishing model performance. They introduced logistic regression models constructed with different sampling intensities and non-landslide/landslide sampling ratios, applying their method to the Lushan earthquake (Shao et al., 2020). Yang H. et al., (2023) predicted landslide susceptibility using an uncertain positive/negative sample ratio method, while Pourghasemi and colleagues explored three different ratios to identify the most suitable ratio for model training, finding that a 1:2 ratio of positive to negative samples yielded the best results (Pourghasemi et al., 2020). After multiple trials of different ratios of positive to negative samples, Sun and colleagues opted for a 1:5 ratio, randomly selecting negative sample points within the study area (Sun et al., 2023). These studies suggest that the 1:1 sampling strategy might not be the most appropriate choice for selecting negative sample points.

Regarding the scope of negative sample point sampling, traditional methods often lack detailed descriptions. He and others suggested randomly sampling negative sample points within the range provided by the USGS ShakeMap (He et al., 2021). Many references simply state “selection within the study area,” where the study area is usually a range delineated by the authors or the boundaries of a province, city, or county (Wu et al., 2023; Heo et al., 2023; Hu et al., 2021).

In the absence of a clear standard for the range of negative sample point sampling and the ratio of positive to negative sample points, Yang H. et al., (2023) proposed a heterogeneous negative sample sampling strategy, which achieved commendable results in the inversion of the Wenchuan earthquake. It significantly reduced the areas overestimated for EQIL hazard, though this study was not applied to predictions in areas without historical EQIL landslide inventories. In order to fully consider the characteristic differences between the landslide surface in the historical landslide inventory and its surrounding non-landslide surface, we improved the negative sample point sampling strategy of Yang et al., in order to generate more high-quality negative sample points around the landslide surface, and put them into the EQIL hazard prediction in areas without historical earthquake landslide inventory.

3.3.2.1 Creation of negative sample points using the improved heterogeneous sampling strategy

Using ArcGIS, a 2 km ∗ 2 km grid (fishnet) is generated for the landslide inventory, retaining grids that contain positive sample points. Within each grid, the landslide area (a), non-landslide area (b), and the number of landslide points (c) are calculated. The number of negative sample points to be sampled in each grid (d) is then calculated using the formula $\left(\mathrm{d} = \frac{b}{a} \times c\right)$. Corresponding numbers (d) of random points are generated within each grid as negative sample points. Given that all rasters used in this study have a resolution of 30 m × 30 m, the aim is to sample as many high-quality negative sample points as possible to cover non-landslide areas surrounding the landslide zones. To prevent negative sample points from falling within the same grid as landslide areas, causing errors, and to avoid duplication of multiple negative sample points in the same grid, the negative sample points must adhere to the following rules: 1. Negative sample points should be more than 43 m away from landslide polygons (the length of the diagonal of a 30 m × 30 m grid). 2. The distance between each non-landslide point should be more than 50 m.

3.3.2.2 Creation of negative sample points using the traditional strategy

To conduct comparative studies and investigate the impact of lithology and mean annual precipitation on the accuracy of the traditional negative sample point sampling strategy, we also need to create negative sample points generated by the traditional strategy. In the traditional approach, the ratio of positive to negative sample points is set at 1:1. Thus, within the aforementioned grid (fishing net) scope, we generate a number of negative sample points equal to the number of positive sample points. Other than the difference in the number of negative sample points, all other rules remain the same.

3.4 Random forest model

Random Forest is a powerful machine learning model known for its exceptional performance in several areas. First, it excels in handling large datasets. Thanks to the parallel nature of Random Forest, it can efficiently process data containing millions of samples without leading to overfitting. This makes it highly advantageous for applications in big data environments. Secondly, Random Forest boasts remarkable robustness. It tolerates outliers and noisy data well due to its foundation on ensemble learning from multiple decision trees. By aggregating the outcomes of various trees, Random Forest minimizes the impact of individual tree errors on the overall model, thereby enhancing the model’s robustness. Furthermore, Random Forest can effectively assess the importance of features. This capability is incredibly useful as it aids in identifying which features play critical roles in prediction. This contributes to feature selection, simplifying the model and improving its interpretability. Increasingly, studies have demonstrated the efficacy of Random Forest models in landslide susceptibility research.

4 Results

4.1 Results of positive and negative sample point creation

Sample points were created for the historical earthquake events using both the traditional strategy and the improved heterogeneous sampling strategy. The numbers of positive sample points and negative sample points created by the two strategies are presented in Table 2. Figure 3 illustrates the sample point creation results using the 2017 Jiuzhaigou EQIL inventory as an example. Figure 3A shows the landslide polygon inventory, Figure 3B displays the positive sample points, Figure 3C represents the negative sample points generated by the traditional strategy (Strategy 1), and Figure 3D depicts the negative sample points generated by the improved heterogeneous sampling strategy (Strategy 2).

4.2 EQIL hazard prediction using eight influencing factors under two sampling strategies

This section utilizes two sampling strategies and employs eight influencing factors: “land use,” “slope aspect,” “slope,” “elevation,” “distance to faults,” “distance to rivers,” “NDVI,” and “peak ground acceleration.” These are used for predicting the EQIL hazard in the VII degree area affected by the 2022 Luding earthquake. The accuracy and precision of the prediction results are validated using the interpreted landslide inventory from this earthquake event.

TABLE 2 Number of landslide inventories, positive samples, and negative samples for eight historical earthquake events.

	Mw	UTC	Landslide polygons	Positive sample	Negative samples (strategy 1)	Negative samples (strategy 2)
Wenchuan, china	7.9	2008.05.12	197,481	196,037	196,037	1,760,754
Yushu, China	6.9	2010.04.13	2036	1872	1872	73,637
Minxian, China	5.9	2013.07.21	2,330	2,137	2,137	15,284
Lushan, China	6.6	2013.04.20	15,546	14,943	14,943	108,996
Ludian, China	6.2	2014.08.03	1,024	1,016	1,016	17,066
Jiuzhaigou, China	6.5	2017.08.08	4,834	4,248	4,248	19,656
Milin, China	6.4	2017.11.17	766	684	684	21,108
Lushan, CHina	5.8	2022.06.01	2,352	2,334	2,334	22,297
sum	~	~	226,369	223,271	223,271	2,038,798

4.2.1 Modeling results of the two sampling strategies

The Random Forest model can directly output the contribution of influencing factors. The contributions of the eight influencing factors under the two sampling strategies are presented in Figure 4.

The EQIL hazard prediction results under the two sampling strategies are shown in Figure 5.

4.2.2 Validation of prediction results

4.2.2.1 ROC curve

The ROC curve and AUC value are utilized to assess the performance of the models. The samples were randomly divided into two subsets, with 70% serving as the training data and the remaining 30% used for validation. The Random Forest models were then applied to their respective validation datasets to estimate the probability of landslides. These predicted probabilities of landslides were compared against their known labels to determine the predictive capability of the models. The Area Under the Curve (AUC) was calculated for this purpose. As shown in Figure 6, both strategies achieved high AUC values. The traditional strategy's AUC (0.8909) was slightly higher than that of the improved heterogeneous strategy (0.8816), indicating that the models constructed from datasets prepared by both strategies performed well.

4.2.2.2 Validation against the interpreted landslide inventory

Earthquake-induced landslides are universally acknowledged as stochastic events (36), making it impossible for EQIL landslide hazard predictions to achieve 100% accuracy. As illustrated in Figure 7, by selecting areas near the epicenter with a dense concentration of landslide inventories for comparison, it is clear that the spatial distribution of medium to high hazard levels in both prediction results closely matches the spatial distribution of the interpreted landslide inventory. The vast majority of landslide areas fall within the regions predicted to have medium or higher hazard levels, demonstrating the reliability of both prediction outcomes.

We selected six densely landslide-populated areas, each measuring 4 km by 6 km (as shown in Figure 8), for a closer comparison of the two prediction results. This comparison clearly reveals that all landslide areas fall within the predicted regions of medium or higher risk. However, in both sets of results, there are sections within the medium to high hazard areas where no landslides occurred. Therefore, we quantified the number of non-landslide grid cells within the areas classified as medium or higher hazard for each region, with the results presented in Table 3.

It is evident that the improved heterogeneous sampling strategy (Strategy 2) resulted in fewer areas classified as medium or higher hazard on non-landslide surfaces compared to the traditional sampling strategy (Strategy 1). This demonstrates that the actual predictive performance of the improved negative sample point heterogeneous sampling strategy surpasses that of the traditional negative sample point sampling strategy, with a performance improvement of approximately 30% in areas prone to landslides.

4.3 EQIL hazard prediction with the addition of lithology factors

In this section, the set of influencing factors is expanded. Building upon the previously utilized eight influencing factors, lithology factors are added, making a total of nine influencing factors. The lithology layer is categorized into 14 classes based on stratigraphic age. This section explores the EQIL hazard prediction results under the two strategies with the inclusion of lithology factors, comparing the differences with predictions made without using lithology factors.

4.3.1 Prediction results after adding lithology factors using the traditional sampling strategy

The contributions of the nine influencing factors and the ROC curve of the model are presented in Figure 9. It can be seen from the contribution table that the contribution of

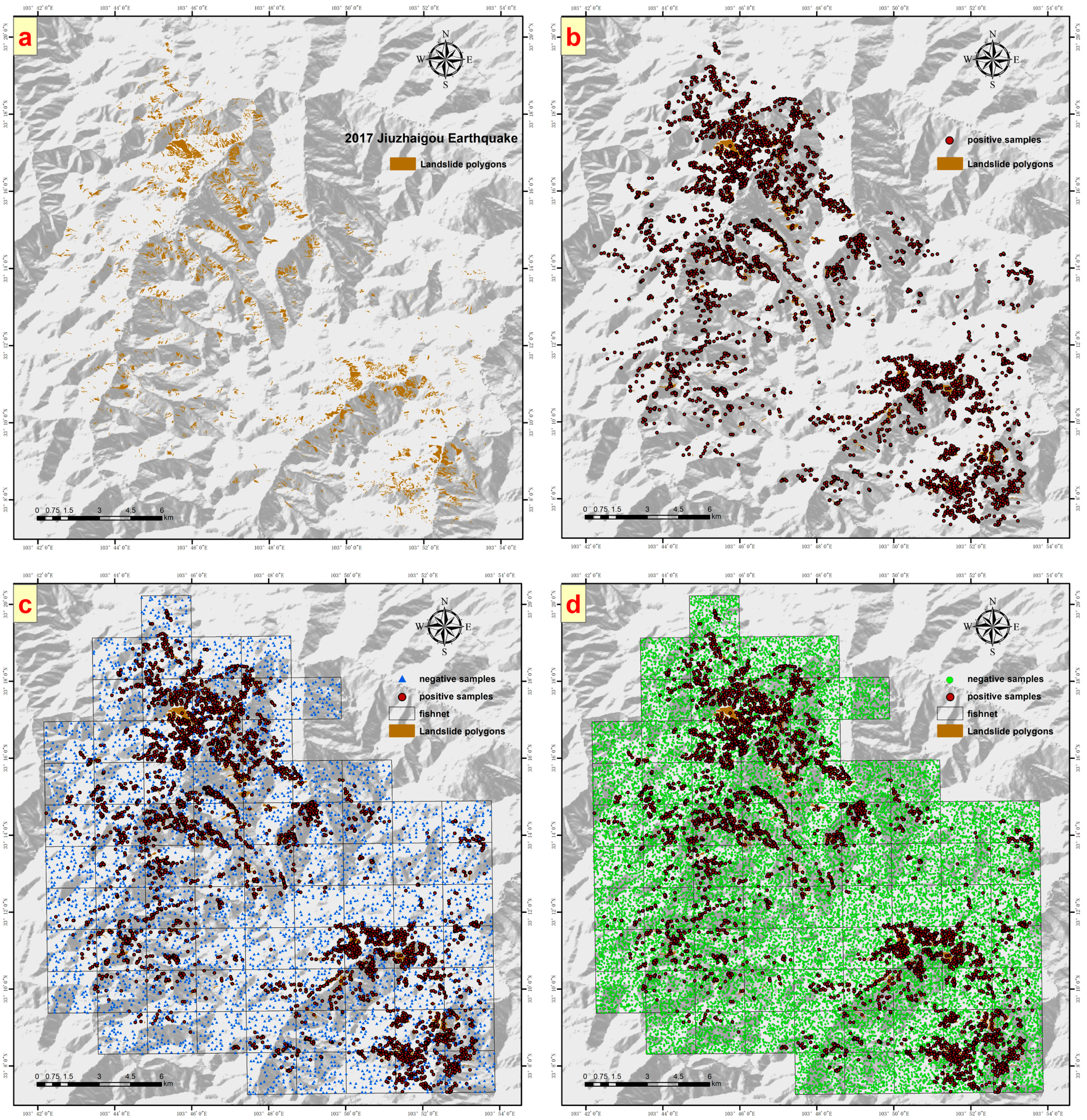

FIGURE 3
Using the 2017 Jiuzhaigou Earthquake Landslide Inventory as an Example, **(A)** shows the landslide inventory polygons, **(B)** displays the created positive sample points, **(C)** illustrates the negative sample points generated by Strategy 1, and **(D)** shows the negative sample points generated by Strategy 2.

lithology factors is about 10%. The trends in contributions from other factors remain essentially consistent with those observed when lithology factors were not included. This indicates that the addition of lithology factors does have a certain impact on the prediction results. The ROC curve reveals that the AUC value of the model constructed with lithology factors is 0.9104, slightly higher than the AUC value of 0.8909 when lithology factors were not used. Based solely on the ROC curve, the modeling results incorporating lithology factors appear superior. However, this conclusion is drawn purely from the model construction perspective and requires further comparative analysis with actual prediction effectiveness.

Figure 10 sequentially presents the results without using lithology factors from earlier sections, the current prediction results, and the lithology factor layer. Overall, a significant segmentation phenomenon in the current prediction results is clearly visible. By comparing with the lithology factor layer, it is observed that the boundaries of the apparent segmented blocks in these results align with the boundaries of different lithology classifications within the lithology layer. This demonstrates that, despite lithology factors contributing only about 10%, they have a significant impact on the actual prediction effectiveness. We selected areas where the differences between the two sets of results are most pronounced, marked with blue boxes. Within these blue-boxed areas, regions classified as “Archaeozoic” exhibit a wide range of relatively higher hazard levels compared to the results without lithology factors. We zoom into these blue-boxed areas for a closer comparison with the landslide inventory from this earthquake to explore whether the addition of these medium to high hazard regions is justified, as shown in Figure 11.

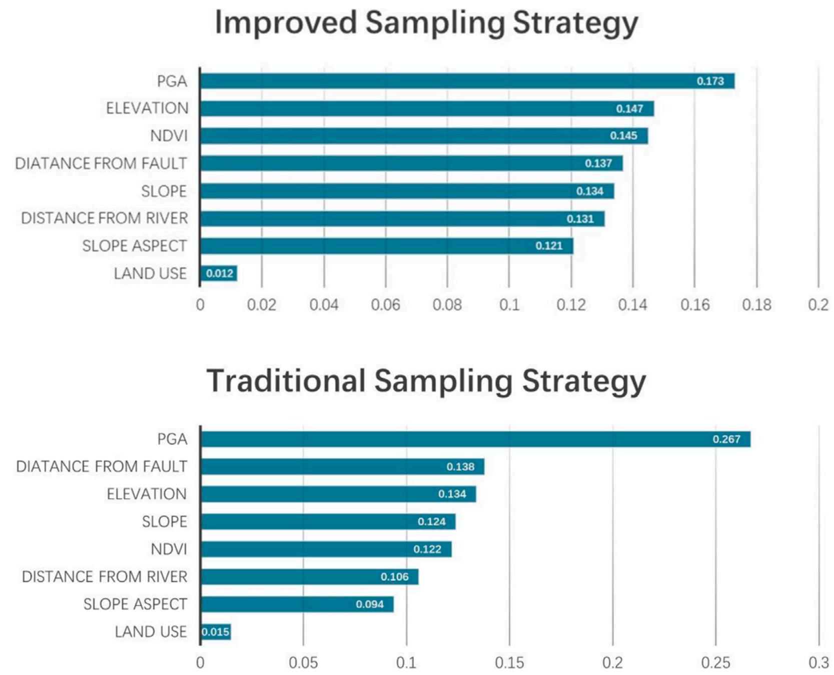

FIGURE 4
Contribution of eight influencing factors under two strategies.

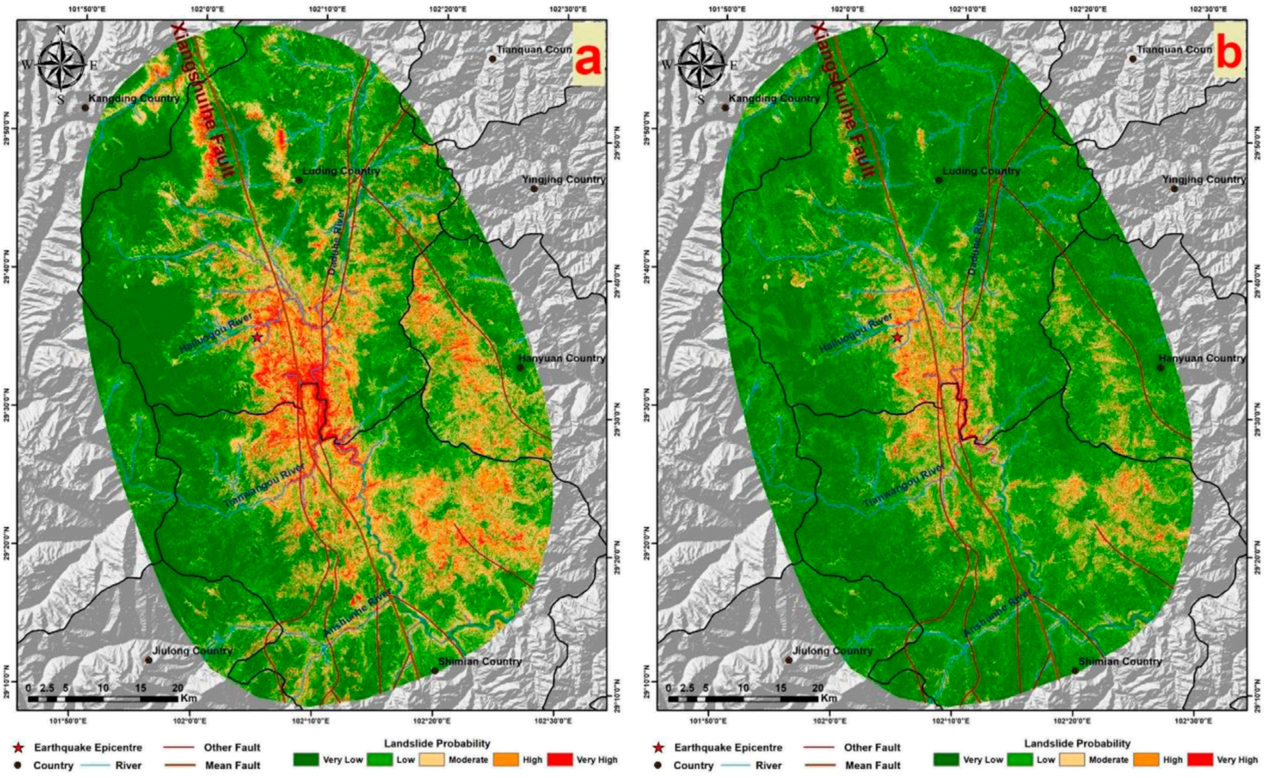

FIGURE 5
(A) shows the prediction results using the traditional strategy, and **(B)** displays the prediction results using the improved heterogeneous strategy.

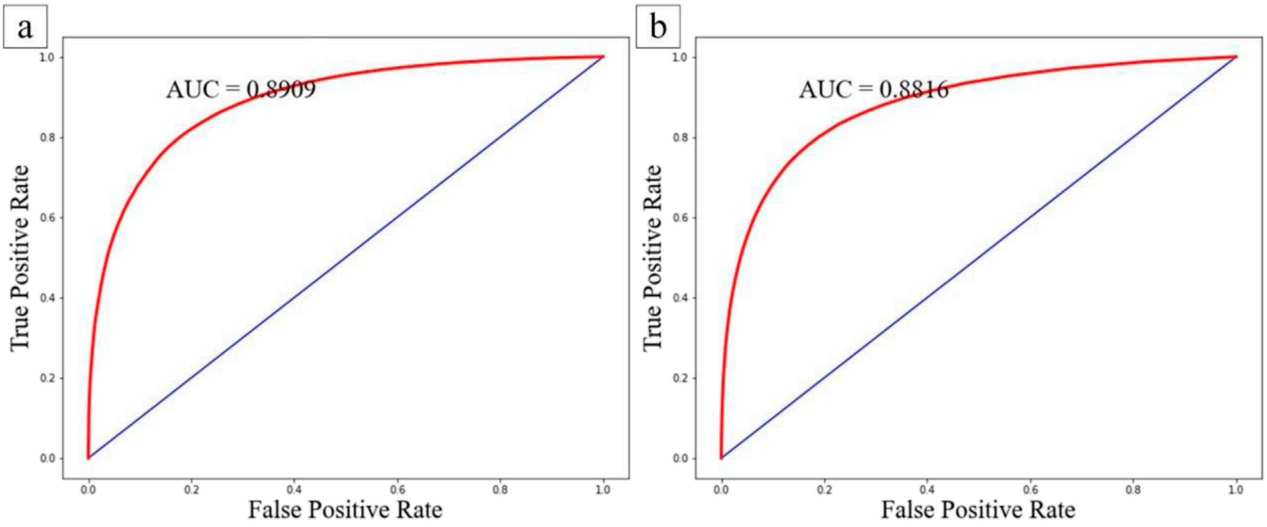

FIGURE 6
ROC Curves for the Training Sets of the Two Strategies. **(A)** Shows the ROC curve for the traditional strategy, and **(B)** displays the ROC curve for the improved heterogeneous sampling strategy.

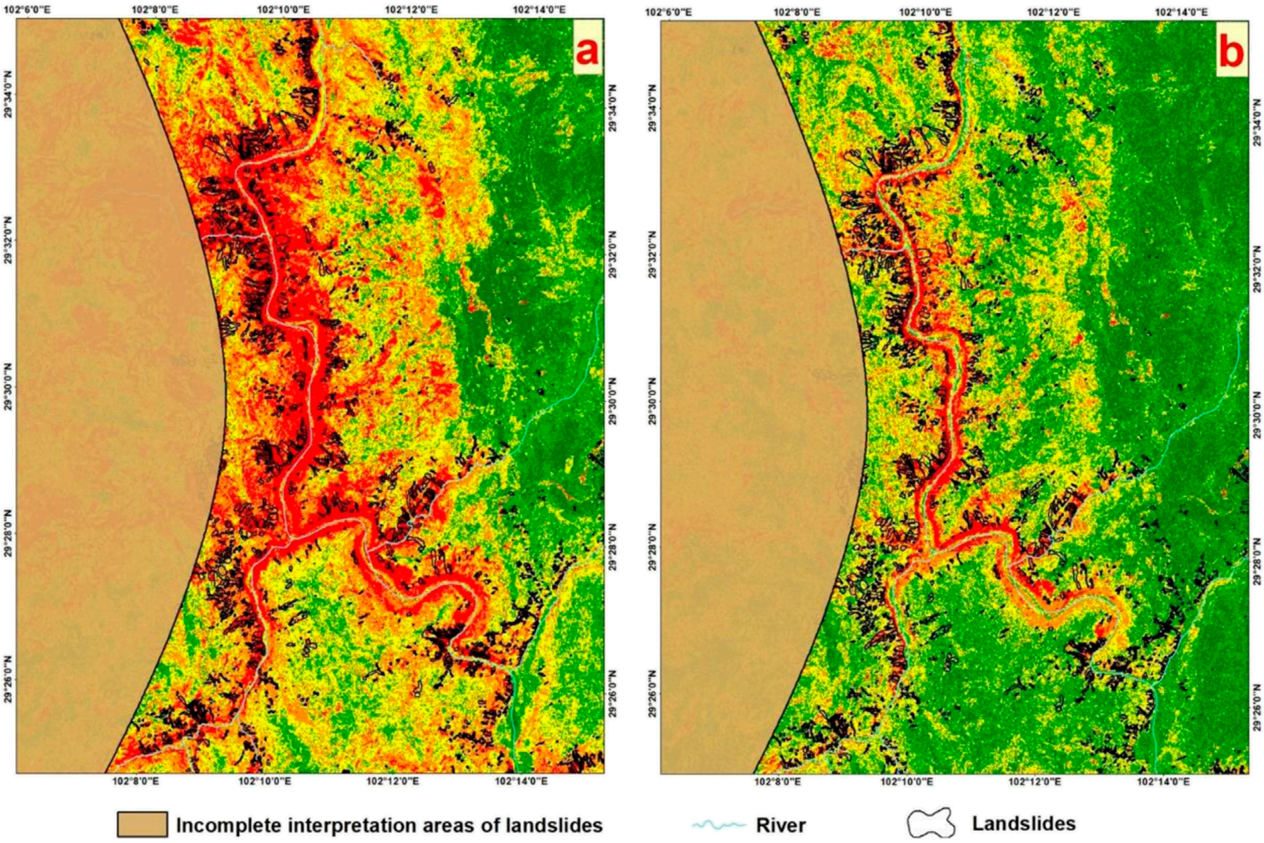

FIGURE 7
Epicentral Area and Interpreted Landslide Inventory Maps for the Two Prediction Outcomes. **(A)** Represents the epicentral area using the traditional strategy, and **(B)** shows the epicentral area with the improved heterogeneous sampling strategy.

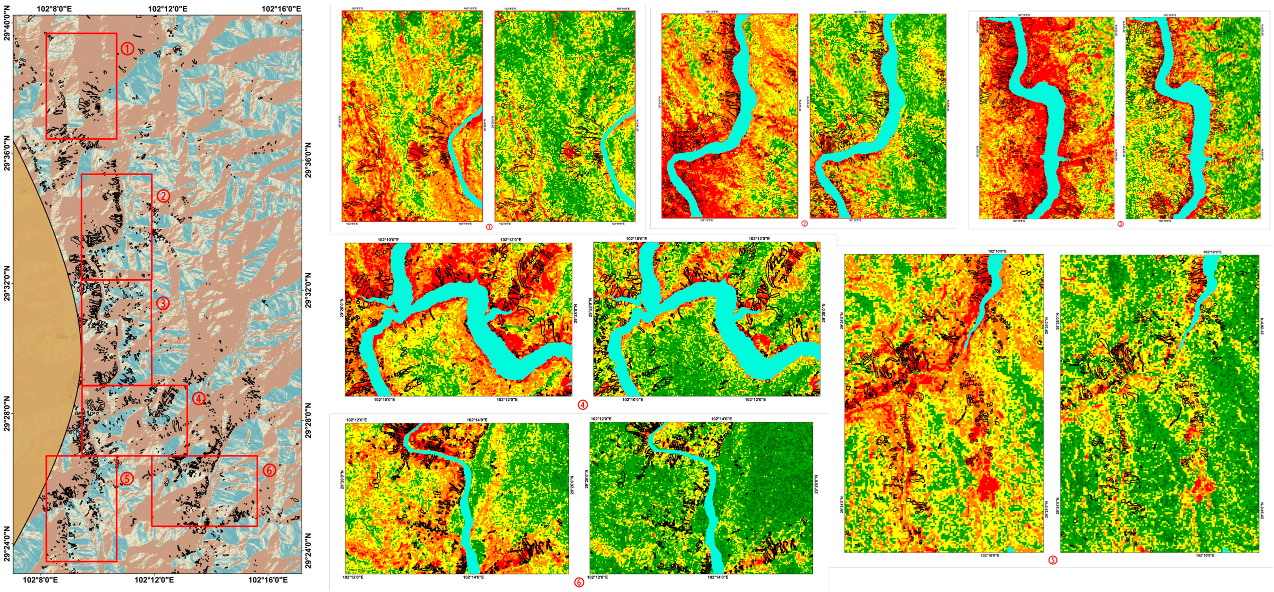

FIGURE 8
Selected six area locations and comparison of results for each area using the two strategies.

TABLE 3 Verification grid number results for six areas.

Number	Strategy 1	Strategy 2	Number of grids on non-slip surfaces	Percentage of high-hazard areas in strategy 1 non-landslide surfaces (%)	Percentage of high-hazard areas in strategy 2 non-landslide surfaces (%)
1	20,877	13,083	25,576	81.63	51.15
2	23,048	15,098	25,029	92.09	60.32
3	22,610	16,440	23,972	94.32	68.58
4	22,532	15,766	24,341	92.57	64.77
5	20,394	10,780	25,341	80.48	42.54
6	17,976	6,749	25,161	71.44	26.82

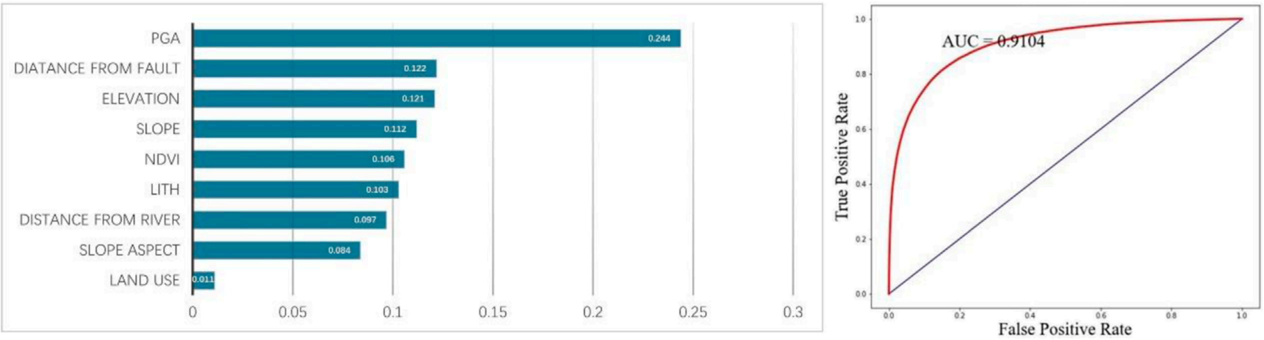

FIGURE 9
Contributions table and ROC curve for the traditional strategy using lithology factors.

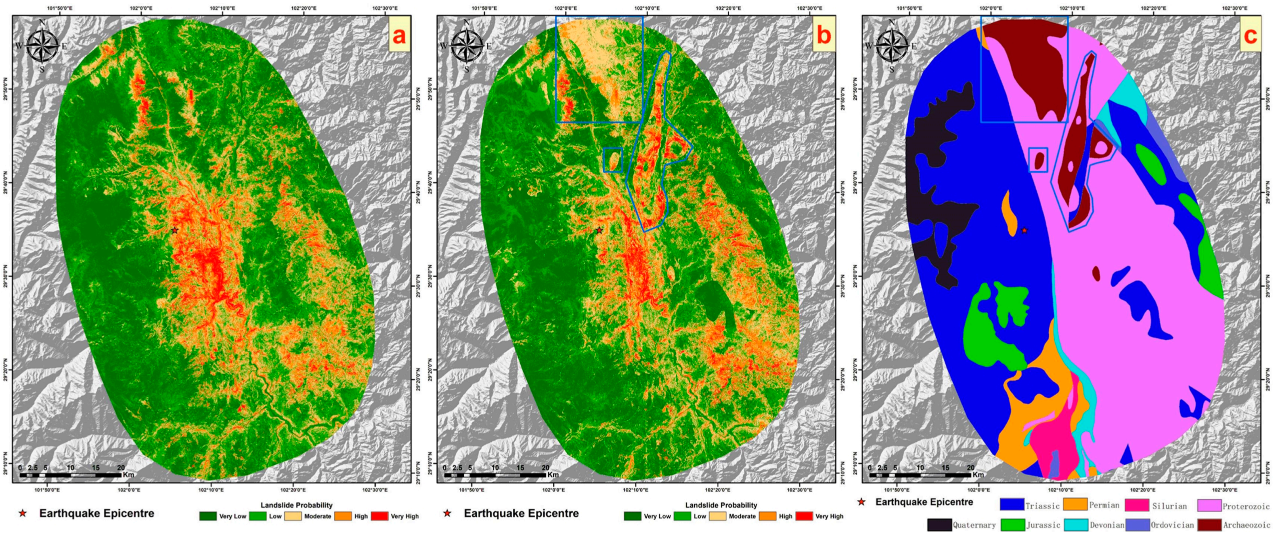

FIGURE 10
(A) shows the results using the eight factors from earlier sections, **(B)** displays the current results, and **(C)** illustrates the lithology factor layer.

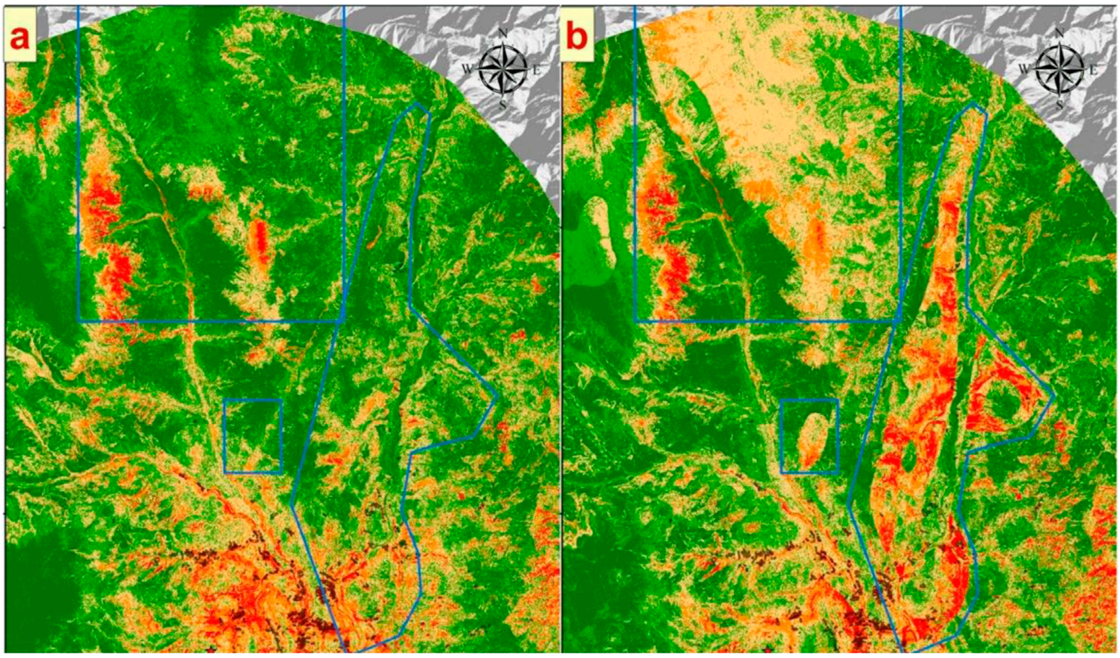

FIGURE 11
Enlarged comparison of the blue areas in Figure 10. **(A)** Figure 10A's detail view, and **(B)** Figure 10B's detail view.

It is evident that in both images, landslide areas are located within regions classified as medium or higher hazard. However, the prediction results utilizing lithology factors contain more mistakenly predicted medium to high hazard areas compared to those without lithology factors. Therefore, we can conclude that under the traditional sampling strategy, employing lithology factors does not enhance the precision of predictions. On the contrary, it affects the original prediction outcomes, resulting in a significant number of incorrectly predicted areas.

4.3.2 EQIL hazard prediction results with the addition of lithology factors under the improved heterogeneous sampling strategy

The contributions of the nine influencing factors and the ROC curve of the model are presented in Figure 12.

The contribution table shows that under the improved sampling strategy, the contribution of lithology factors is lower than that under the traditional strategy (about 10%), accounting for only about 6%. The ROC curve indicates that incorporating lithology

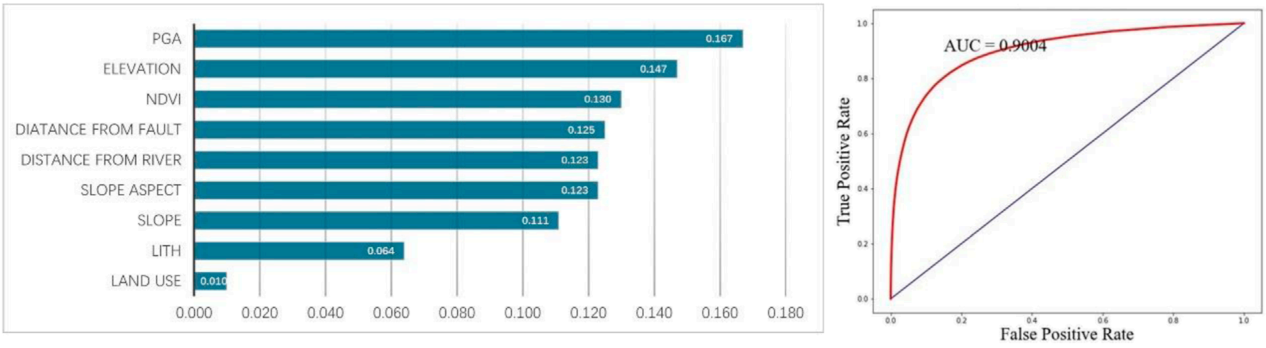

FIGURE 12
Contributions of various factors and ROC curve with the addition of lithology factors using the improved heterogeneous strategy.

factors under the improved strategy results in a higher AUC value compared to not using them. Similar to the traditional sampling strategy, the inclusion of lithology factors improves the model's simulation effect. Moving on to an analysis of the actual prediction results, Figure 13 compares the outcomes without using lithology factors under the improved strategy, the current results, and the outcomes with lithology factors under the traditional strategy. Under the improved heterogeneous sampling strategy, the overall prediction results exhibit a more pronounced difference compared to the results obtained without incorporating lithology factors. As previously demonstrated, the improved heterogeneous sampling strategy enhances prediction accuracy, reduces areas of medium to high hazard, and increases the proportion of low hazard areas predicted. Therefore, after adding lithology factors, the segmentation phenomenon becomes more marked compared to using the strategy without lithology factor. Within the blue-boxed areas in Figure 13, regions classified as "Archaeozoic" lithology also show a significant number of areas where the hazard level has been mistakenly overestimated, compared to predictions made without lithology factors.

As the previous article verified, the prediction results without lithology factors under the two sampling strategies are reliable. However, the two sets of results with lithology factors added in this chapter have large errors. The use of lithology factors will lead to excessively high hazard levels in some lithology areas in the study area. From this, we can conclude that lithology has a negative effect on the prediction of EQIL hazard. On the contrary, not using lithology factors will have a better prediction effect.

4.4 EQIL hazard prediction including precipitation factors

Having explored the EQIL hazard prediction with the addition of lithology factors previously, this section investigates the EQIL hazard prediction incorporating precipitation factors. Similarly, the analysis employs the eight influencing factors plus the mean annual precipitation, making a total of nine factors. The hazard predictions are conducted using the two sampling strategies, with a comparative validation to verify the accuracy of the prediction results.

4.4.1 Prediction results after adding precipitation factors using the traditional sampling strategy

The contributions of the nine factors, the ROC curve, and the prediction results are shown in Figure 14, and the prediction results are illustrated in Figure 15.

From the contribution table, it is noticeable that the contribution of the mean annual precipitation factor is second only to peak ground acceleration, with a contribution significantly higher than other influencing factors, at about 19%. This indicates that the mean annual precipitation factor has a substantial impact on predicting landslide hazard. The ROC curve reveals a higher AUC value (0.9216) after incorporating the mean annual precipitation factor, but the actual prediction performance requires further comparative research. The comparison and validation against the landslide inventory are shown in Figure 16. Sequentially, Figure 16 presents the prediction results using the eight factors under the traditional sampling strategy, the current prediction results, and the mean annual precipitation layer. Given the high contribution of mean annual precipitation, there's a strong consistency between the prediction effect graph and the distribution trend of mean annual precipitation. Compared to the results without using precipitation factors, the lower part of the map shows lower hazard levels, while the upper part shows higher hazard levels. Considering the landslide inventory for this earthquake event, many landslide areas in the lower part of the current prediction results are underestimated in terms of hazard level, whereas the upper part has many medium to high hazard areas without landslides occurring, leading to severe underestimation and overestimation of hazard levels. Under the traditional sampling strategy, despite the superior AUC value with precipitation factors, the prediction results were poorer, failing to enhance prediction accuracy and resulting in numerous incorrectly predicted areas.

4.4.2 Prediction results after adding precipitation factors under the improved heterogeneous sampling strategy

The contributions of the nine influencing factors and the ROC curve of the model are presented in Figure 17, and the results are illustrated in Figure 18. Under the heterogeneous sampling strategy, the mean annual precipitation contributes more significantly than the peak ground acceleration, approximately 20% compared to

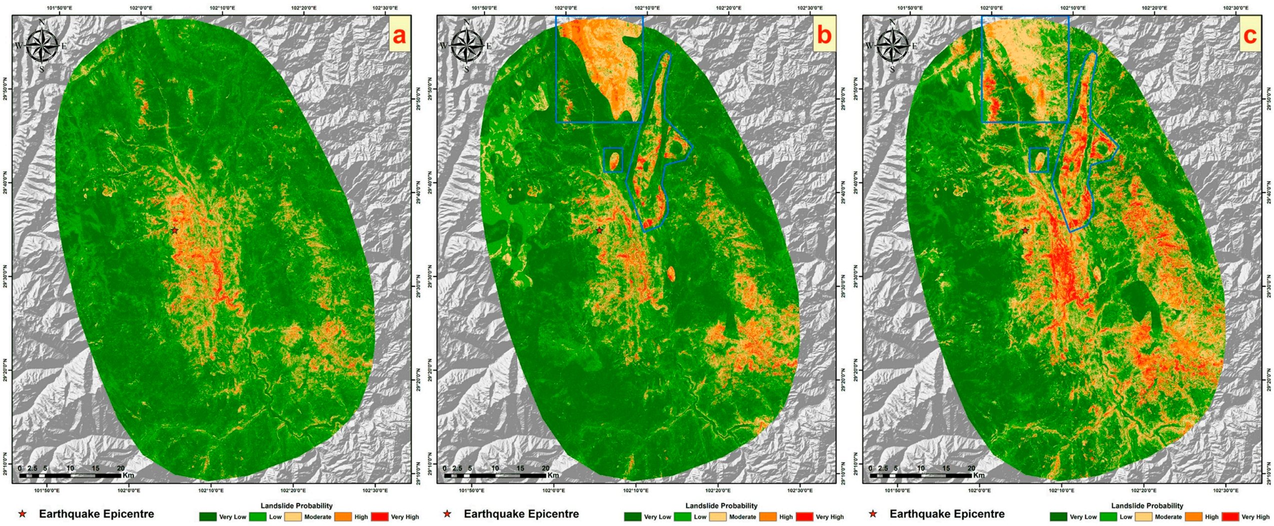

FIGURE 13
(A) shows the results of the eight factors using the improved heterogeneous strategy from earlier sections, **(B)** displays the current results, and **(C)** illustrates the results of adding lithological factors using the traditional strategy from earlier sections.

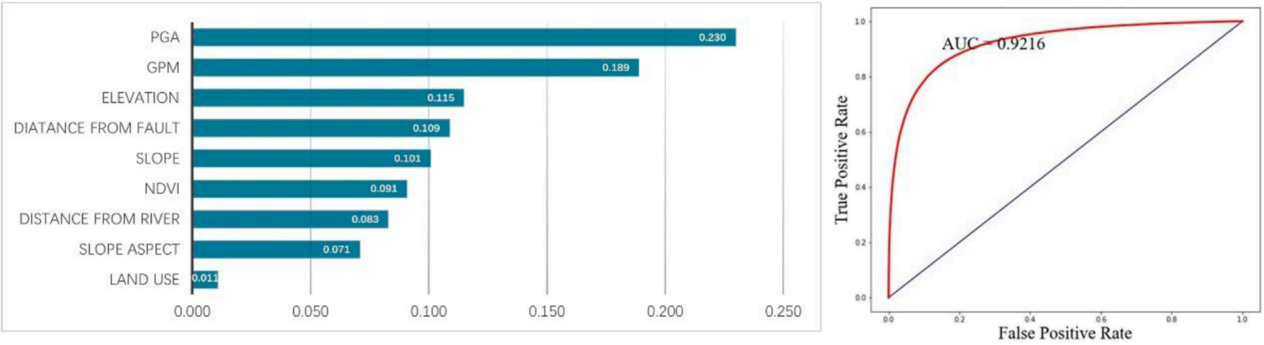

FIGURE 14
Contributions of various factors and ROC curve with the addition of mean annual precipitation using the traditional strategy.

about 14% for the latter. This indicates an unrealistic dominant role of mean annual precipitation, given that our study focuses on landslides triggered by earthquakes, where seismic factors (peak ground acceleration) should logically have the highest contribution. Despite a higher AUC value with the inclusion of precipitation factors, the actual outcomes, as shown in Figure 19, present some concerns. Comparing previous results without precipitation factors and the current prediction outcomes, the current results exhibit a more pronounced segmentation phenomenon. In the prediction map, lower hazard levels are assigned to landslide areas in the lower part of the layer, while higher hazard levels are attributed to non-landslide areas in the upper part. This leads to a more distinct regional segmentation than seen with the traditional sampling strategy predictions, aligning closely with the mean annual precipitation layer. It is evident from the map that areas with higher annual precipitation generally have higher EQIL hazard levels, and areas with lower annual precipitation have lower EQIL hazard levels, which is unreasonable.

Based on the prediction results using mean annual precipitation factors under both the traditional sampling strategy and the improved heterogeneous sampling strategy, we can conclude that using the annual average precipitation factor will have a significant negative effect on the prediction results, not favorably for enhancing the precision of earthquake-induced landslide hazard predictions.

5 Discussion

In landslide susceptibility mapping, the quality of input data decisively influences the quality of landslide susceptibility assessment (Pradhan, 2013; Pradhan et al., 2014; Kalantar et al., 2018). Hence, the sampling of training sample points and the selection of influencing factors are critical steps that determine the quality of input data. During the process of negative sample sampling, the improved heterogeneous sampling strategy can generate a large number of non-landslide points around landslide

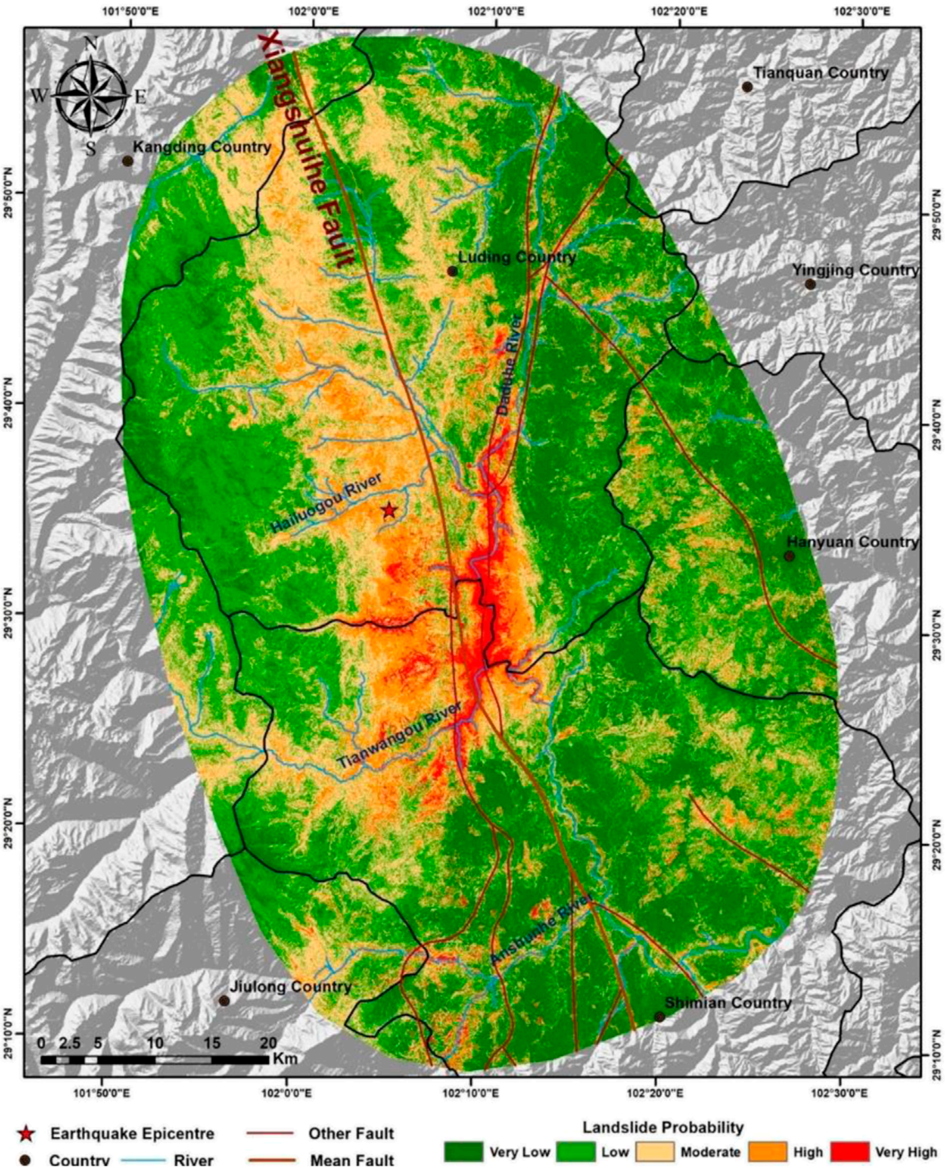

FIGURE 15
Result map with the addition of mean annual precipitation using the traditional strategy.

areas. There are fewer non-landslide points in densely landslide-affected areas and more in sparsely affected areas. This strategy enables a focused differentiation between the characteristics of historical co-seismic landslide areas and surrounding non-landslide areas. In existing studies, nearly all EQIL hazard maps overestimate the hazard level of the seismic area, especially giving excessively high hazard ratings to the epicentral region (Dreyfus et al., 2013; Allstadt et al., 2018). This study demonstrates that the improved heterogeneous sampling strategy can more accurately predict the spatial location of EQIL occurrences, reducing the overestimated hazard areas around the epicenter. This proves the strategy to be reasonable and advanced, making the investigation into the effectiveness of using lithology and precipitation factors under this strategy and the traditional strategy highly persuasive.

Lithology factors and mean annual precipitation are important influencing factors for the occurrence of EQIL (Duman et al., 2006; Yalcin, 2008; Ercanoglu and Temiz, 2011; Nefeslioglu et al., 2012; Das et al., 2013; Nefeslioglu et al., 2008). However, the results of this study indicate that under both sampling strategies, the use of lithology and mean annual precipitation factors has an adverse impact on EQIL hazard prediction. We believe this is closely related to the model training sample dataset. Initially, the training samples for EQIL hazard prediction following an earthquake event should be created using the historical EQIL inventory from the location of that earthquake. However, in reality, historical landslide inventories from the same location area are scarce. To address this issue, we considered creating a large sample dataset using high-quality landslide inventories from eight historical earthquake events in China, aiming to identify the patterns of EQIL occurrence

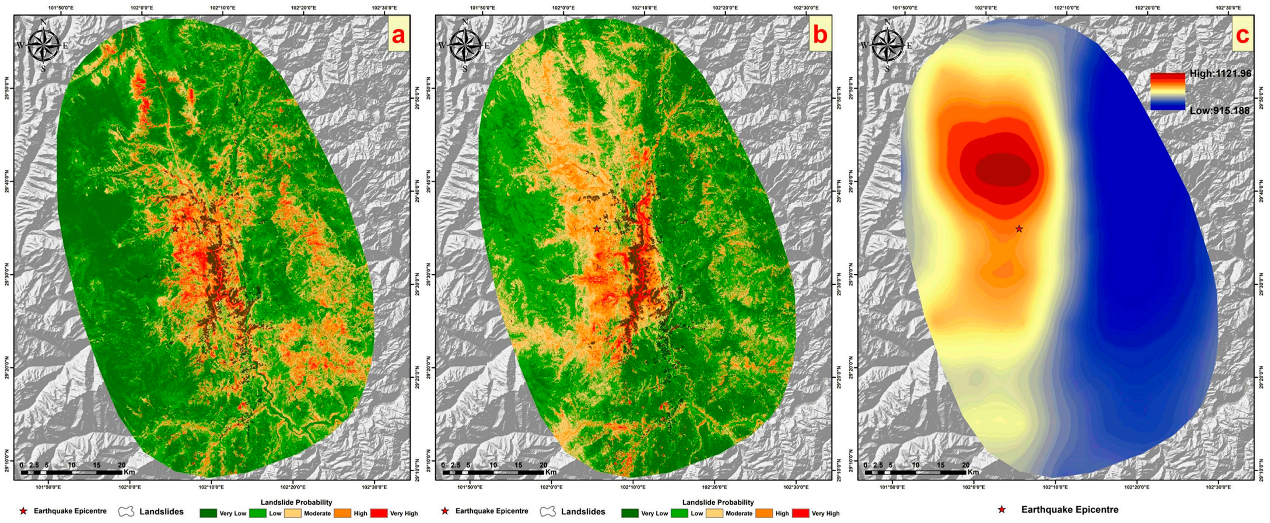

FIGURE 16
Comparison using the landslide inventory. **(A)** Shows the results of the eight factors under the traditional strategy from earlier sections, **(B)** displays the current results, and **(C)** illustrates the Mean Annual Precipitation layer.

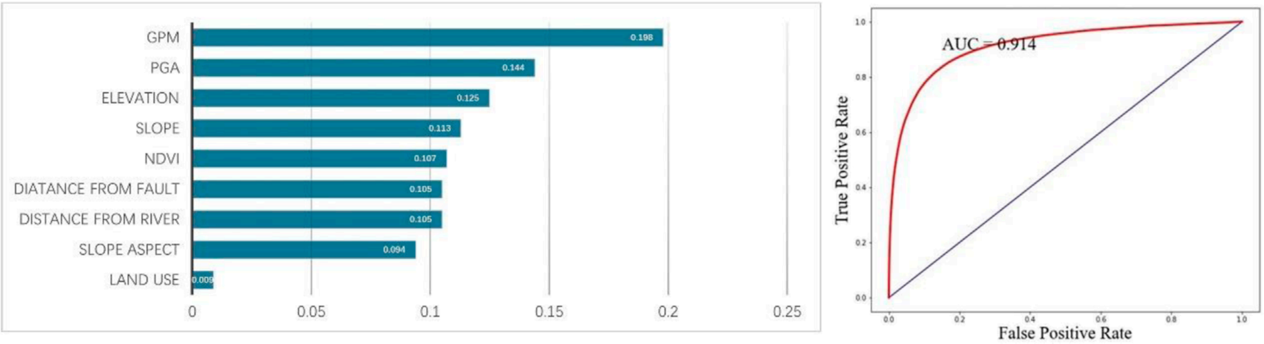

FIGURE 17
Contributions of various factors and ROC curve with the addition of mean annual precipitation using the improved heterogeneous strategy.

through machine learning and then apply these insights to EQIL hazard prediction after an earthquake event. These eight historical earthquake landslide inventories are distributed across different regions in Southwest China, where there is a significant variation in lithology and mean annual precipitation across regions. This variation is likely a reason for the poor performance of lithology and mean annual precipitation factors. It is possible that certain lithologies or ranges of annual precipitation have a large number of historical earthquake landslide samples (or non-landslide samples), leading to a higher (or lower) hazard level being predicted for these lithologies or precipitation ranges in the prediction area, thus resulting in poor performance when using lithology and mean annual precipitation factors.

Secondly, the resolution of lithology and mean annual precipitation layers is relatively low, resulting in significant segmentation. The scale of lithology data is 1:2,500,000, which corresponds to a spatial resolution of approximately 660 m. After classifying lithology by geological age, the segmentation phenomenon becomes pronounced. If mispredictions occur, it can easily lead to hazard levels being generally overestimated or underestimated within certain lithology regions. In such cases, the segmentation phenomenon in prediction results is inevitable unless higher precision lithology data are used, a more detailed lithology classification method is applied, or lithology factors are not utilized at all. The resolution of mean annual precipitation is 0.1°, and even after interpolation to a 30 m resolution grid, the variability between different regions remains significant. The impact of layer resolution differences on lithology and mean annual precipitation factors cannot be overlooked.

Furthermore, the two sampling strategies used in this study generate non-landslide sample points in areas near landslide samples, emphasizing the differences in characteristics between landslide and surrounding non-landslide areas, thereby achieving better prediction results. However, this approach also results in a strong clustering of non-landslide sample points, especially with the improved heterogeneous sampling strategy, which produces ten

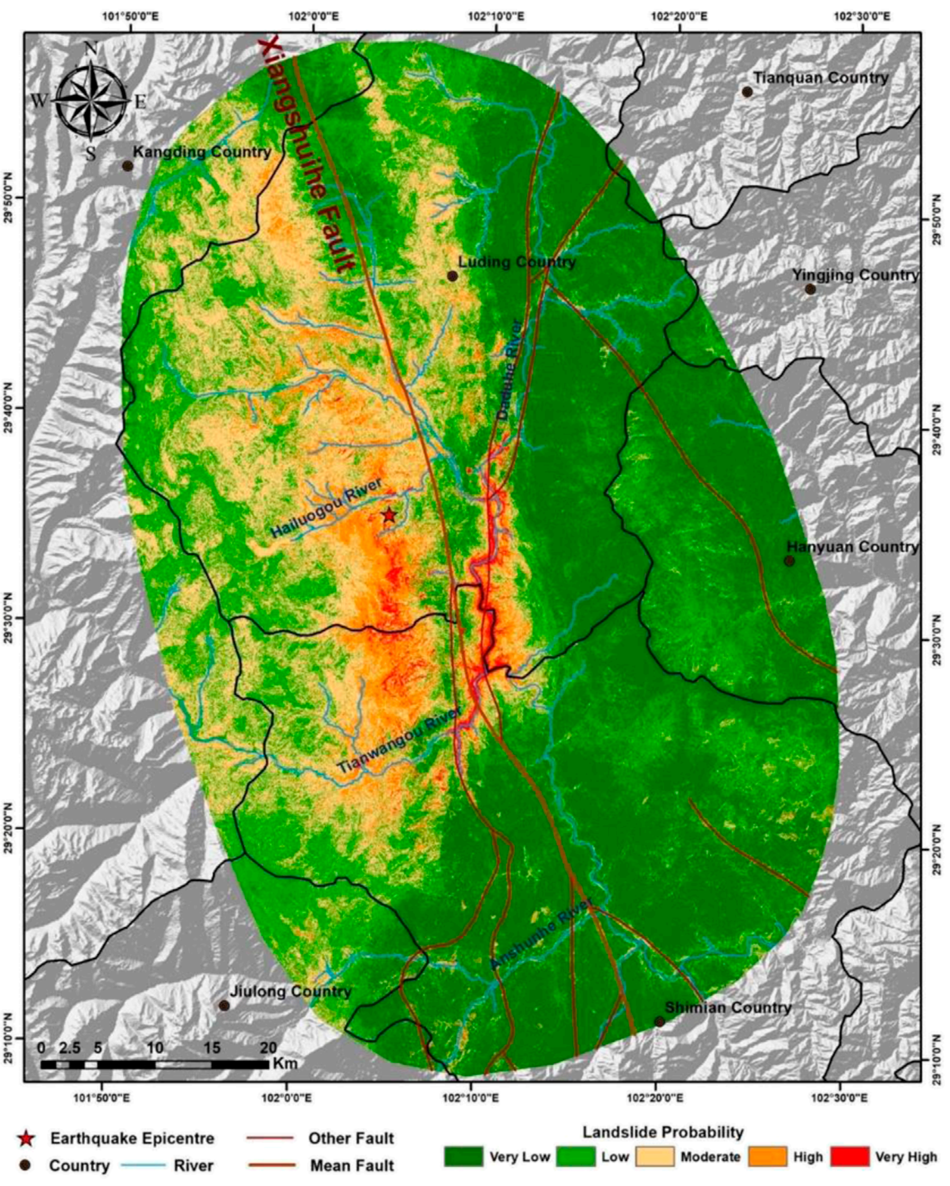

FIGURE 18
Result map with the addition of mean annual precipitation using the improved heterogeneous strategy.

times as many negative sample points as the traditional strategy, leading to even greater clustering. This could explain why, in the experiments described earlier, the use of lithology or precipitation factors led to a more pronounced segmentation phenomenon with the heterogeneous sampling strategy compared to the traditional strategy. Coupled with the regional differences and lower resolution of lithology and mean annual precipitation factors, this might cause negative sample points to cluster around certain lithology types and precipitation ranges, resulting in these areas being assigned lower hazard levels and affecting the accuracy of the prediction results.

To verify this hypothesis, we analyzed the number of positive and negative sample points located within each lithology classification in the study area under the traditional sampling strategy, as shown in Table 4.

It was observed that the number of landslide sample points in the "Archaeozoic" lithology category is about three times the number of non-landslide sample points. This disproportion could lead to the "Archaeozoic" lithology areas in the study region generally being assigned a higher EQIL hazard level, resulting in erroneous predictions.

Finally, although lithology and precipitation factors are important, why are the results without using these two factors so reliable? We believe that the other influencing factors used may have a certain degree of correlation with these two factors. Topography can influence precipitation distribution patterns through its impact on large-scale weather systems, atmospheric flows, and the microphysics of clouds (Wu et al., 2005; Beniston, 2006; Liu et al., 2024; Yang, D. et al., 2023). Elevation, slope aspect, and slope gradient have been shown to have strong correlations

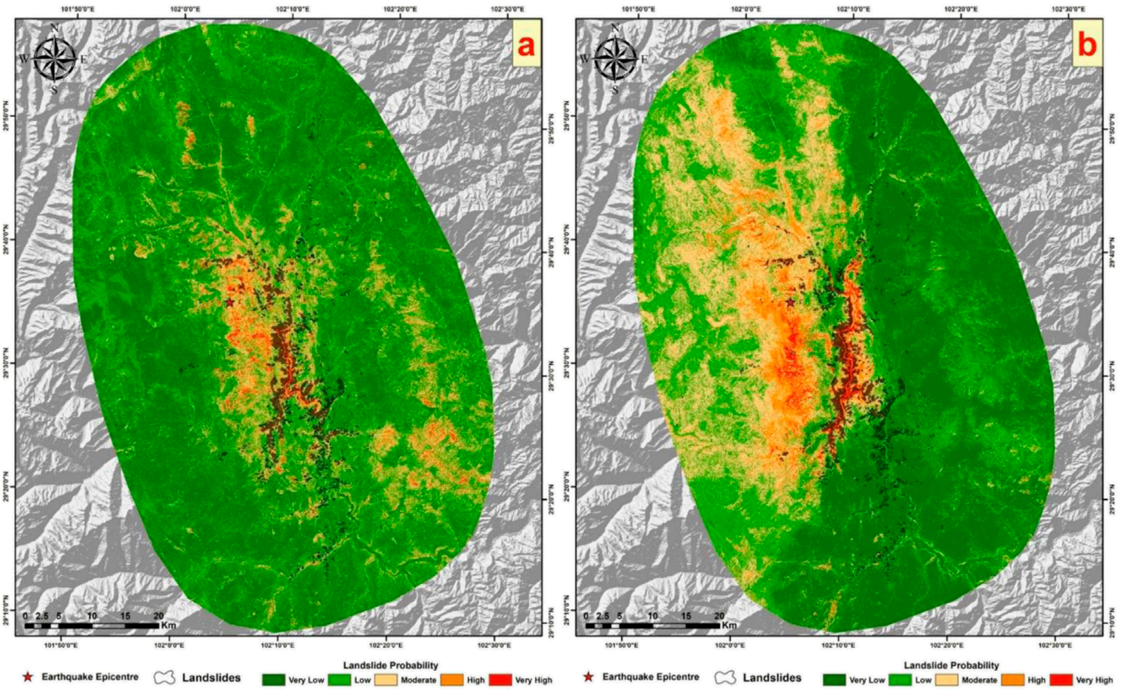

FIGURE 19
(A) shows the result map using eight factors with the improved heterogeneous strategy from earlier sections, and **(B)** displays the current result map.

TABLE 4 Number of positive and negative sample points in each lithology classification.

	Positive samples	Negative samples
Quaternary	205	1704
Jurassic	2,411	13,069
Triassic	27,761	56,202
Permian	10,616	12,741
Devonian	25,389	34,389
Silurian	29,334	40,092
Ordovician	2,202	2,241
Proterozoic	92,710	40,045
Archaeozoic	13,723	3,127

with precipitation (Liu et al., 2018; Zhang et al., 2014). Distance to rivers and proximity to seas also share a strong correlation with precipitation levels (Zheng et al., 2017). The Normalized Difference Vegetation (NDVI) is used to assess the condition of surface vegetation. The relationship between precipitation and NDVI is dynamic, influenced by various factors, including geographical location, season, soil type, and vegetation type. To a certain extent, there is a strong correlation between NDVI and precipitation (Ding et al., 2007; Kawabata et al., 2001). The link between landslides and lithology considers the geological strength index and cohesion of rocks (Gallen et al., 2015). Although rocks from different geological ages can have significant differences in shear strength, but the actual strength of rock is affected by many factors (Gallen et al., 2015; Li et al., 2020; Schmidt and Montgomery, 1995; Hoek and Brown, 1980; Ye et al., 2024). It is difficult to characterize shear strength on global and regional scales (Dreyfus et al., 2013). However, environmental factors are very likely to affect the strength of near-surface rocks (Gallen et al., 2015), and there is a certain correlation between environmental factors and lithology. Factors such as slope aspect, slope gradient, elevation, land use, distance to rivers, and the NDVI all affect environmental conditions to some extent, thereby affecting rock strength. In summary, although lithology and precipitation factors were not directly used, employing other factors may have indirectly considered these two factors as well.

6 Uncertainties and prospects

This study employs traditional and novel negative sample sampling strategies to create sample points from historical earthquake-induced landslides and investigates the impact of lithology factors and mean annual precipitation on the accuracy of earthquake-induced landslide hazard predictions. This is of significant importance for future research on the influencing factors and precision of earthquake-induced landslide hazard predictions. However, there are still some limitations that need to be further improved and explored.

We improved the latest EQIL negative sample point sampling strategy proposed by Yang, H. et al., (2023). However, the 2 km × 2 km grid for negative sample points may not be suitable for all EQIL inventories used in this study. Therefore, in the future, grids of appropriate sizes can be customized for each earthquake event's landslide inventory, considering factors such as the range of the landslide inventory and the area of landslide polygons. Moreover, the approach is not limited to grids; methods such as buffer zones can also be used to define the sampling range for non-landslide points.

This study found a significant discrepancy between the ROC curves of machine learning methods and the actual prediction outcomes, indicating that ROC curves can be misleading. A higher AUC value does not necessarily equate to better prediction results. Future efforts should focus on evaluating models based on actual outcomes or developing more sophisticated methods to assess model quality.

Lithology and precipitation factors are considered significant influencing factors for EQIL. However, this study found that their impact on the accuracy of actual predictions was poor. Future research should explore how to improve these two factors to make them more effectively applicable to EQIL prediction, such as enhancing the precision of lithology and mean annual precipitation layers or using alternative layers that can represent lithology and precipitation more accurately.

This study utilized sample points created from eight historical EQIL inventories. In the future, more high-quality EQIL lists can be added to improve the sample point data, allowing for the selection of influencing factors that are more suitable for the dataset to construct the model. The broader the coverage of sample points, the wider the prediction range can be, leading to higher prediction accuracy. The more appropriate the influencing factors, the better the prediction outcomes will be.

This study exclusively employed the Random Forest model for modeling and did not engage in a series of studies with other machine learning models. Therefore, the effectiveness of the methodologies and datasets used in this research when applied to other machine learning models remains uncertain.

7 Conclusion

This study exploring the impact of lithology factors, classified by geological age, and mean annual precipitation on the accuracy of earthquake-induced landslide hazard predictions. The use of lithology and mean annual precipitation factors was found to reduce the accuracy of the predictions. Without these two factors, both strategies demonstrated good predictive performance, with the improved heterogeneous sampling strategy showing an approximate 30% improvement in predictive performance in the epicentral region compared to the traditional strategy. In summary, lithology factors classified by geological age and mean annual precipitation factors have a significant negative impact on EQIL hazard predictions. They are not suitable for EQIL hazard prediction. This research holds significant implications for the selection of influencing factors and the precision of future earthquake-induced landslide hazard predictions.

Data availability statement

The original contributions presented in the study are included in the article/supplementary material, further inquiries can be directed to the corresponding authors.

Author contributions

HW: Data curation, Formal Analysis, Investigation, Methodology, Software, Writing–original draft, Writing–review and editing. WW: Resources, Supervision, Visualization, Writing–review and editing. WY: Supervision, Writing–review and editing. ML: Resources, Writing–review and editing.

Funding

The author(s) declare that financial support was received for the research, authorship, and/or publication of this article. This project is funded by the National Key R&D Program “Design and Development Technology of Multi-Agency Multi-Hazard Comprehensive Risk Prevention Service Product System” (Project No. 2018YFC1508901).

Conflict of interest

The authors declare that the research was conducted in the absence of any commercial or financial relationships that could be construed as a potential conflict of interest.

Publisher's note

References

Aditian, A., Kubota, T., and Shinohara, Y. (2018). Comparison of GIS-based landslide susceptibility models using frequency ratio, logistic regression, and artificial neural network in a tertiary region of Ambon, Indonesia. *Geomorphology* 318, 101–111. doi:10.1016/j.geomorph.2018.06.006

Allstadt, K. E., Jibson, R. W., Thompson, E. M., Massey, C. I., Wald, D. J., Godt, J. W., et al. (2018). Improving near-real-time coseismic landslide models: lessons learned from the 2016 Kaikōura, New Zealand, earthquake. *Bull. Seismol. Soc. Am.* 108 (3B), 1649–1664. doi:10.1785/0120170297

Beniston, M. (2006). Mountain weather and climate: a general overview and a focus on climatic change in the Alps. *Hydrobiologia* 562, 3–16. doi:10.1007/s10750-005-1802-0

Blahut, J., Van Westen, C. J., and Sterlacchini, S. (2010). Analysis of landslide inventories for accurate prediction of debris-flow source areas. *Geomorphology* 119 (1-2), 36–51. doi:10.1016/j.geomorph.2010.02.017

Chen, W., Panahi, M., and Pourghasemi, H. R. (2017). Performance evaluation of GIS-based new ensemble data mining techniques of adaptive neuro-fuzzy inference system (ANFIS) with genetic algorithm (GA), differential evolution (DE), and particle swarm optimization (PSO) for landslide spatial modelling. *Catena* 157, 310–324. doi:10.1016/j.catena.2017.05.034

Das, H. O., Sonmez, H., Gokceoglu, C., and Nefeslioglu, H. A. (2013). Influence of seismic acceleration on landslide susceptibility maps: a case study from NE Turkey (the Kelkit Valley). *Landslides* 10, 433–454. doi:10.1007/s10346-012-0342-8

Ding, M., Zhang, Y., Liu, L., Zhang, W., Wang, Z., and Bai, W. (2007). The relationship between NDVI and precipitation on the Tibetan Plateau. *J. Geogr. Sci.* 17, 259–268. doi:10.1007/s11442-007-0259-7

Dreyfus, D., Rathje, E. M., and Jibson, R. W. (2013). The influence of different simplified sliding-block models and input parameters on regional predictions of seismic landslides triggered by the Northridge earthquake. *Eng. Geol.* 163, 41–54. doi:10.1016/j.enggeo.2013.05.015

Duman, T. Y., Can, T., Gokceoglu, C., Nefeslioglu, H. A., and Sonmez, H. (2006). Application of logistic regression for landslide susceptibility zoning of Cekmece Area, Istanbul, Turkey. *Environ. Geol.* 51, 241–256. doi:10.1007/s00254-006-0322-1

Ercanoglu, M., and Temiz, F. A. (2011). Application of logistic regression and fuzzy operators to landslide susceptibility assessment in Azdavay (Kastamonu, Turkey). *Environ. Earth Sci.* 64, 949–964. doi:10.1007/s12665-011-0912-4

Fan, X., Yunus, A. P., Scaringi, G., Catani, F., Siva Subramanian, S., Xu, Q., et al. (2021). Rapidly evolving controls of landslides after a strong earthquake and implications for hazard assessments. *Geophys. Res. Lett.* 48 (1), e2020GL090509. doi:10.1029/2020gl090509

Gallen, S. F., Clark, M. K., and Godt, J. W. (2015). Coseismic landslides reveal near-surface rock strength in a high-relief, tectonically active setting. *Geology* 43 (1), 11–14. doi:10.1130/g36080.1

Guzzetti, F., Cardinali, M., and Reichenbach, P. (1996). The influence of structural setting and lithology on landslide type and pattern. *Environ. and Eng. Geoscience* 2 (4), 531–555. doi:10.2113/gseegeosci.ii.4.531

He, Q., Wang, M., and Liu, K. (2021). Rapidly assessing earthquake-induced landslide susceptibility on a global scale using random forest. *Geomorphology* 391, 107889. doi:10.1016/j.geomorph.2021.107889

Heo, S., Park, S., and Lee, D. K. (2023). Multi-hazard exposure mapping under climate crisis using random forest algorithm for the Kalimantan Islands, Indonesia. *Sci. Rep.* 13 (1), 13472. doi:10.1038/s41598-023-40106-8

Hoek, E., and Brown, E. T. (1980). Empirical strength criterion for rock masses. *J. geotechnical Eng. Div.* 106 (9), 1013–1035. doi:10.1061/ajgeb6.0001029

Hong, H., Tsangaratos, P., Ilia, I., Loupasakis, C., and Wang, Y. (2020). Introducing a novel multi-layer perceptron network based on stochastic gradient descent optimized by a meta-heuristic algorithm for landslide susceptibility mapping. *Sci. total Environ.* 742, 140549. doi:10.1016/j.scitotenv.2020.140549

Hu, K., Zhang, X., You, Y., Hu, X., Liu, W., and Li, Y. (2019). Landslides and dammed lakes triggered by the 2017 Ms6. 9 Milin earthquake in the Tsangpo gorge. *Landslides* 16, 993–1001. doi:10.1007/s10346-019-01168-w

Hu, X., Mei, H., Zhang, H., Li, Y., and Li, M. (2021). Performance evaluation of ensemble learning techniques for landslide susceptibility mapping at the Jinping county, Southwest China. *Nat. Hazards* 105, 1663–1689. doi:10.1007/s11069-020-04371-4

Huang, Y., Xie, C., Li, T., Xu, C., He, X., Shao, X., et al. (2023). An open-accessed inventory of landslides triggered by the MS 6.8 Luding earthquake, China on September 5, 2022. *Earthq. Res. Adv.* 3 (1), 100181. doi:10.1016/j.eqrea.2022.100181

Huang, Y., and Zhao, L. (2018). Review on landslide susceptibility mapping using support vector machines. *Catena* 165, 520–529. doi:10.1016/j.catena.2018.03.003

Jibson, R. W., Harp, E. L., and Michael, J. A. (2000). A method for producing digital probabilistic seismic landslide hazard maps. *Eng. Geol.* 58 (3-4), 271–289. doi:10.1016/s0013-7952(00)00039-9

Kalantar, B., Pradhan, B., Naghibi, S. A., Motevalli, A., and Mansor, S. (2018). Assessment of the effects of training data selection on the landslide susceptibility mapping: a comparison between support vector machine (SVM), logistic regression (LR) and artificial neural networks (ANN). *Geomatics, Nat. Hazards Risk* 9 (1), 49–69. doi:10.1080/19475705.2017.1407368

Kawabata, A., Ichii, K., and Yamaguchi, Y. (2001). Global monitoring of interannual changes in vegetation activities using NDVI and its relationships to temperature and precipitation. *Int. J. remote Sens.* 22 (7), 1377–1382. doi:10.1080/01431160119381

Khaliq, A. H., Basharat, M., Riaz, M. T., Tayyib Riaz, M., Wani, S., Al-Ansari, N., et al. (2023). Spatiotemporal landslide susceptibility mapping using machine learning models: a case study from district Hattian Bala, NW Himalaya, Pakistan. *Ain Shams Eng. J.* 14 (3), 101907. doi:10.1016/j.asej.2022.101907

Li, B., Ye, X., Dou, Z., Zhao, Z., Li, Y., and Yang, Q. (2020). Shear strength of rock fractures under dry, surface wet and saturated conditions. *Rock Mech. Rock Eng.* 53, 2605–2622. doi:10.1007/s00603-020-02061-y

Li, Y., Ming, D., Zhang, L., Niu, Y., and Chen, Y. (2024). Seismic landslide susceptibility assessment using newmark displacement based on a dual-channel convolutional neural network. *Remote Sens.* 16 (3), 566. doi:10.3390/rs16030566

Liu, W., Zhang, Q., Fu, Z., Chen, X., and Li, H. (2018). Analysis and estimation of geographical and topographic influencing factors for precipitation distribution over complex terrains: a case of the Northeast slope of the Qinghai–Tibet plateau. *Atmosphere* 9 (9), 349. doi:10.3390/atmos9090349

Liu, Y., Qiu, H., Kamp, U., Wang, N., Wang, J., Huang, C., et al. (2024). Higher temperature sensitivity of retrogressive thaw slump activity in the Arctic compared to the Third Pole. *Sci. Total Environ.* 914, 170007. doi:10.1016/j.scitotenv.2024.170007

Marano, K. D., Wald, D. J., and Allen, T. I. (2010). Global earthquake casualties due to secondary effects: a quantitative analysis for improving rapid loss analyses. *Nat. hazards* 52, 319–328. doi:10.1007/s11069-009-9372-5

Nefeslioglu, H. A., Duman, T. Y., and Durmaz, S. (2008). Landslide susceptibility mapping for a part of tectonic kelkit valley (eastern black sea region of Turkey). *Geomorphology* 94 (3-4), 401–418. doi:10.1016/j.geomorph.2006.10.036

Nefeslioglu, H. A., San, B. T., Gokceoglu, C., and Duman, T. (2012). An assessment on the use of Terra ASTER L3A data in landslide susceptibility mapping. *Int. J. Appl. earth observation geoinformation* 14 (1), 40–60. doi:10.1016/j.jag.2011.08.005

Nowicki Jessee, M. A., Hamburger, M. W., Allstadt, K., Wald, D. J., Robeson, S. M., Tanyas, H., et al. (2018). A global empirical model for near-real-time assessment of seismically induced landslides. *J. Geophys. Res. Earth Surf.* 123 (8), 1835–1859. doi:10.1029/2017jf004494

Pham, B. T., Tien Bui, D., Pourghasemi, H. R., Indra, P., and Dholakia, M. B. (2017). Landslide susceptibility assesssment in the Uttarakhand area (India) using GIS: a comparison study of prediction capability of naïve bayes, multilayer perceptron neural networks, and functional trees methods. *Theor. Appl. Climatol.* 128, 255–273. doi:10.1007/s00704-015-1702-9

Pourghasemi, H. R., Kornejady, A., Kerle, N., and Shabani, F. (2020). Investigating the effects of different landslide positioning techniques, landslide partitioning approaches, and presence-absence balances on landslide susceptibility mapping. *Catena* 187, 104364. doi:10.1016/j.catena.2019.104364

Pradhan, B. (2013). A comparative study on the predictive ability of the decision tree, support vector machine and neuro-fuzzy models in landslide susceptibility mapping using GIS. *Comput. and Geosciences* 51, 350–365. doi:10.1016/j.cageo.2012.08.023

Pradhan, B., Abokharima, M. H., Jebur, M. N., and Tehrany, M. S. (2014). Land subsidence susceptibility mapping at Kinta Valley (Malaysia) using the evidential belief function model in GIS. *Nat. hazards* 73, 1019–1042. doi:10.1007/s11069-014-1128-1

Pyakurel, A., Kc, D., and Dahal, B. K. (2024). Enhancing co-seismic landslide susceptibility, building exposure, and risk analysis through machine learning. *Sci. Rep.* 14 (1), 5902. doi:10.1038/s41598-024-54898-w

Qiu, H., Su, L., Tang, B., Yang, D., Ullah, M., Zhu, Y., et al. (2024). The effect of location and geometric properties of landslides caused by rainstorms and earthquakes. *Earth Surf. Process. Landforms* 49 (7), 2067–2079. doi:10.1002/esp.5816

Raspini, F., Bardi, F., Bianchini, S., Ciampalini, A., Del Ventisette, C., Farina, P., et al. (2017). The contribution of satellite SAR-derived displacement measurements in landslide risk management practices. *Nat. hazards* 86, 327–351. doi:10.1007/s11069-016-2691-4

Schmidt, K. M., and Montgomery, D. R. (1995). Limits to relief. *Science* 270 (5236), 617–620. doi:10.1126/science.270.5236.617

Shao, X., Ma, S., Xu, C., and Zhou, Q. (2020). Effects of sampling intensity and non-slide/slide sample ratio on the occurrence probability of coseismic landslides. *Geomorphology* 363, 107222. doi:10.1016/j.geomorph.2020.107222

Shao, X., and Xu, C. (2022). Earthquake-induced landslides susceptibility assessment: a review of the state-of-the-art. *Nat. Hazards Res.* 2 (3), 172–182. doi:10.1016/j.nhres.2022.03.002

Shao, X., Xu, C., and Ma, S. (2022). Preliminary analysis of coseismic landslides induced by the 1 June 2022 Ms 6.1 Lushan Earthquake, China. *Sustainability* 14 (24), 16554. doi:10.3390/su142416554

Sun, D., Gu, Q., Wen, H., Xu, J., Zhang, Y., Shi, S., et al. (2023). Assessment of landslide susceptibility along mountain highways based on different machine learning algorithms and mapping units by hybrid factors screening and sample optimization. *Gondwana Res.* 123, 89–106. doi:10.1016/j.gr.2022.07.013

Tien Bui, D., Pradhan, B., Lofman, O., and Revhaug, I. (2012). Landslide susceptibility assessment in vietnam using support vector machines, decision tree, and Naive Bayes Models. *Math. problems Eng.* 2012 (1), 974638. doi:10.1155/2012/974638

Tien Bui, D., Tuan, T. A., Klempe, H., Pradhan, B., and Revhaug, I. (2016). Spatial prediction models for shallow landslide hazards: a comparative assessment of the efficacy of support vector machines, artificial neural networks, kernel logistic regression, and logistic model tree. *Landslides* 13, 361–378. doi:10.1007/s10346-015-0557-6

Van Westen, C. J., Van Asch, T. W. J., and Soeters, R. (2006). Landslide hazard and risk zonation—why is it still so difficult? *Bull. Eng. Geol. Environ.* 65, 167–184. doi:10.1007/s10064-005-0023-0

Wang, M. J., Li, T. B., Meng, L. B., and Tang, H. (2015). Back analysis of stress field in the intersection region of Y shaped fault, Sichuan. *J. Railw. Sci. Eng.* 12 (5), 1088–1095. doi:10.19713/j.cnki.43-1423/u.2015.05.016

Wu, G. X., Wang, J., and Liu, X. (2005). Numerical modeling of the influence of Eurasian orography on the atmospheric circulation in different seasons. *Acta Meteorol. Sin.* 63 (5), 603–612.

Wu, W., Guo, S., and Shao, Z. (2023). Landslide risk evaluation and its causative factors in typical mountain environment of China: a case study of Yunfu City. *Ecol. Indic.* 154, 110821. doi:10.1016/j.ecolind.2023.110821

Wu, W., Xu, C., Wang, X., Tian, Y., and Deng, F. (2020). Landslides triggered by the 3 August 2014 Ludian (China) M w 6.2 earthquake: an updated inventory and analysis of their spatial distribution. *J. Earth Sci.* 31, 853–866. doi:10.1007/s12583-020-1297-7

Xu, C., Wang, S. Y., Xu, X. W., Zhang, H., Tian, Y. Y., Ma, S. Y., et al. (2018). A panorama of landslides triggered by the 8 August 2017 Jiuzhaigou, Sichuan M S 7.0 earthquake. *Seismol. Geol.* 40 (1), 232–260. doi:10.3969/j.issn.0253-4967.2018.01.010

Xu, C., Xu, X., and Shyu, J. B. H. (2015). Database and spatial distribution of landslides triggered by the Lushan, China Mw 6.6 earthquake of 20 April 2013. *Geomorphology* 248, 77–92. doi:10.1016/j.geomorph.2015.07.002

Xu, C., Xu, X., Shyu, J. B. H., Zheng, W., and Min, W. (2014b). Landslides triggered by the 22 July 2013 Minxian–Zhangxian, China, Mw 5.9 earthquake: inventory compiling and spatial distribution analysis. *J. Asian Earth Sci.* 92, 125–142. doi:10.1016/j.jseaes.2014.06.014

Xu, C., Xu, X., Yao, X., and Dai, F. (2014a). Three (nearly) complete inventories of landslides triggered by the May 12, 2008 Wenchuan Mw 7.9 earthquake of China and their spatial distribution statistical analysis. *Landslides* 11, 441–461. doi:10.1007/s10346-013-0404-6

Xu, C., Xu, X., and Yu, G. (2013). Landslides triggered by slipping-fault-generated earthquake on a plateau: an example of the 14 April 2010, Ms 7.1, Yushu, China earthquake. *Landslides* 10, 421–431. doi:10.1007/s10346-012-0340-x

Yalcin, A. (2008). GIS-based landslide susceptibility mapping using analytical hierarchy process and bivariate statistics in Ardesen (Turkey): comparisons of results and confirmations. *catena* 72 (1), 1–12. doi:10.1016/j.catena.2007.01.003

Yang, C., Liu, L. L., Huang, F., and Wang, X. M. (2023). Machine learning-based landslide susceptibility assessment with optimized ratio of landslide to non-landslide samples. *Gondwana Res.* 123, 198–216. doi:10.1016/j.gr.2022.05.012

Yang, D., Qiu, H., Ye, B., Liu, Y., Zhang, J., and Zhu, Y. (2023). Distribution and recurrence of warming-induced retrogressive thaw slumps on the Central Qinghai-Tibet plateau. *J. Geophys. Res. Earth Surf.* 128 (8), e2022JF007047. doi:10.1029/2022jf007047

Yang, H., Shi, P., Quincey, D., Qi, W., and Yang, W. (2023). A heterogeneous sampling strategy to model earthquake-triggered landslides. *Int. J. Disaster Risk Sci.* 14 (4), 636–648. doi:10.1007/s13753-023-00489-8

Ye, B., Qiu, H., Tang, B., Liu, Y., Liu, Z., Jiang, X., et al. (2024). Creep deformation monitoring of landslides in a reservoir area. *J. Hydrology* 632, 130905. doi:10.1016/j.jhydrol.2024.130905

Youssef, A. M., Pourghasemi, H. R., El-Haddad, B. A., and Dhahry, B. K. (2016). Landslide susceptibility maps using different probabilistic and bivariate statistical models and comparison of their performance at Wadi Itwad Basin, Asir Region, Saudi Arabia. *Bull. Eng. Geol. Environ.* 75, 63–87. doi:10.1007/s10064-015-0734-9

Zhang, K., Pan, S., Cao, L., Wang, Y., Zhao, Y., and Zhang, W. (2014). Spatial distribution and temporal trends in precipitation extremes over the Hengduan Mountains region, China, from 1961 to 2012. *Quat. Int.* 349, 346–356. doi:10.1016/j.quaint.2014.04.050

Zheng, Y., He, Y., and Chen, X. (2017). Spatiotemporal pattern of precipitation concentration and its possible causes in the Pearl River basin, China. *J. Clean. Prod.* 161, 1020–1031. doi:10.1016/j.jclepro.2017.06.156

Zhu, J., Baise, L. G., and Thompson, E. M. (2017). An updated geospatial liquefaction model for global application. *Bull. Seismol. Soc. Am.* 107 (3), 1365–1385. doi:10.1785/0120160198

frontiers | Frontiers in Earth Science

TYPE Original Research
PUBLISHED 30 October 2024
DOI 10.3389/feart.2024.1485210

Check for updates

OPEN ACCESS

EDITED BY
Xiangli He,
Ministry of Emergency Management, China

REVIEWED BY
Mohammad Azarafza,
University of Tabriz, Iran
Cun Zhang,
China University of Mining and Technology, China

*CORRESPONDENCE
Ruda Sun,
✉ tssunruda@163.com

RECEIVED 23 August 2024
ACCEPTED 07 October 2024
PUBLISHED 30 October 2024

CITATION
Sun R, Zhao Z, Yang W and Li H (2024) Research and application of hydraulic fracturing axial roof cutting technology for gently inclined hard roof based on abrasive jet.
Front. Earth Sci. 12:1485210.
doi: 10.3389/feart.2024.1485210

Research and application of hydraulic fracturing axial roof cutting technology for gently inclined hard roof based on abrasive jet

Ruda Sun[1,2]*, Zhipeng Zhao[3], Wei Yang[3] and Hongping Li[3]

[1]CCTEG Coal Mining Research Institute, Beijing, China, [2]Coal Mining and Designing Department, Tiandi Science and Technology Co., Ltd., Beijing, China, [3]Xinjiang Energy Co., Ltd., CHN Energy, Erumqi, China

In order to explore a new method and mode of gently inclined hard roof treatment, the hydraulic fracturing axial roof cutting technology based on abrasive jet is introduced, and the key technical parameters of abrasive jet axial cutting and fracturing are determined based on indoor experiments and field industrial experiments. Taking the mining of working face under the condition of hard roof in Kuangou Coal Mine as the background, the implementation process and the effect of mining process are tested by means of water pressure gauge, drilling peep and observation well water level observation, microseismic monitoring, support fracture monitoring and coal stress monitoring. The research results show that the key technical parameters of slotting and fracturing are mastered in the axial cutting test of abrasive jet. Wherein the kerf depth is 200 m, the kerf length is 300 m, the kerf pressure is 40–50 mpa, the fracturing pressure is 50–55 mpa, and the fracturing time is 20–30 min. After grooving fracturing, the cracks in the roof strata are effectively generated and expanded, which destroys the integrity of the roof, and the fracturing radius is 10–20 m. During the mining period, compared with the tradi-tional blasting technology, the concentrated area of microseismic events was shifted from 80 m in front of the working face to 130 m after the combined treatment of abrasive jet axial roof cutting and blasting, and the microseismic energy release was mainly small energy events. After the application of abrasive jet axial roof cutting and scour prevention technology in hard roof, the periodic weighting step is obviously reduced, the influence range of mining stress and stress concentration coefficient are obviously reduced, the activity intensity and dynamic load effect of surrounding rock are obviously weakened. The research results provide a basis for effective prevention and control of rockburst disasters under the condition of hard roof.

KEYWORDS

hard roof, rockburst, hydraulic fracturing, pressure relief regulation, axial fracture cutting and fracturing of abrasive jet

1 Introduction

With the increasing depth of coal mining, rockburst accidents occur frequently. According to statistics, there are more than 170 rockburst mines in China. Hard roof is one of the main disaster-causing factors of rock burst or strong ground pressure during coal mining. Its hard roof has the characteristics of good integrity, high strength and strong ability to bear overlying load, which provides high static load and strong dynamic load for the occurrence of rock burst (Pan et al., 2003; Pan et al., 2012).

At present, the methods of blasting roof breaking and hydraulic fracturing are widely used at home and abroad to weaken the hard roof. In view of the large-area hanging roof of the working face during the initial mining under the condition of hard roof, Zhao (2021) put forward the cooperative anti-scour mechanism of deep-hole roof pre-splitting blasting. Kuangou Coal Mine has been seriously affected by hard roof for a long time. A systematic study was carried out on the reasonable control height of hard roof in close-distance coal seam in Kuangou Coal Mine, and the key technical parameters of roof blasting presplitting were optimized, which effectively reduced the activity intensity of hard roof and the stress concentration of coal body. The combined method of directional long-distance drilling and blasting roof cutting was used to effectively relieve the pressure of the hard roof (Zhang et al., 2019; Jia et al., 2022; Jia et al., 2024). As an effective method to weaken the hard roof and relieve the pressure of sur-rounding rock, hydraulic fracturing technology has been widely used in the prevention and control of rock burst of hard roof (Junzhe et al., 2020). On the basis of scaling analysis, Ali Naghi Dehghan and others scaled the laboratory experimental parameters to simulate the hy-draulic fracturing process under field conditions (Dehghan, 2020). Some scholars use numerical simula-tion and rock mechanics test methods to analyze the influence of natural fractures on hy-draulic fracturing aperture and fracture propagation geometry (Cruz et al., 2018; Liu et al., 2014). Qingyuan He et al. obtained that the homogeneity of rock mass significantly affects the propagation distance of hydraulic fracture from its starting point in its predetermined direction before reorienta-tion (He et al., 2017). Shuai Heng et al. developed a two-dimensional numerical model of hydraulic fracturing to clarify the evolution of hydraulic fractures and their non-planar behavior at the level (Heng et al., 2019). Based on the finite-discrete method, Mingyang Wu et al. mastered that when the elastic modulus of discrete embedded blocks and the number of discrete embedded cracks reach a certain level, the propagation of hydraulic cracks will suddenly change (Wu et al., 2021). Mingqi Qin and others studied the mechanism of hydraulic frac-turing of layered rock mass based on the hydraulic fracturing model of surrounding dy-namics (Qin et al., 2021). Ayaka Abe et al. studied the formation law of fracture network when hydrau-lic fractures and pre-existing fractures interact through laboratory-scale hydraulic frac-turing experiments (Abe et al., 2021). Arash Dahi Taleghani and others discussed the linear elastic fracture mechanics, cohesive element method and continuous damage mechanics tech-niques for understanding the interaction between hydraulic fractures and natural frac-tures (Taleghani et al., 2016). Amir Ghaderi and others combine the extended finite element method (XFEM) with the discrete element method (DEM) to identify the propagation of hydraulic fractures in porous media containing natural fracture blocks (Ghaderi et al., 2018). Ali Naghi Dehghan et al. con-ducted laboratory experiments on the size synthetic rock samples, and grasped the influ-ence of the pre-dip angle and strike of fractures on the propagation behavior and geometry of hydraulic fractures (Dehghan et al., 2018). Kang et al. (2023) developed a complete set of technology and equipment for hydraulic fracturing in underground areas of coal mines, focusing on the propagation law of hydraulic cracks at different scales. Junfeng et al. (2023) put forward the method of hydraulic fracturing “artificial liberation layer” to relieve pressure and prevent rockburst in the area of thick hard roof where the overlying coal seam caused dis-aster, and Mengshan mining area introduced hydraulic fracturing technology to explore a new mode of rockburst control (Weng et al., 2019). In addition, relevant scholars have studied the impact of land settlement caused by tunnel excavation and the coordination of cable-soil deformation under different anchoring conditions. It provides conditions for the safe conduct of the project site (Junfeng et al., 2021; Wu et al., 2020; Irani et al., 2022).

With the rapid development of high-pressure abrasive water jet technology in recent years, Junfeng et al. (2021) obtained the variation law of fracture characteristic index values such as rock failure depth, width and erosion volume under different hydraulic parameters through laboratory tests. Xia et al. (2020) developed a new technology of axial top-cutting fracturing with abrasive jet in hole and hydraulic reaming and cutting in coal seam, and further developed the hydraulic fracturing technology and technology. Domestic scholars (Feng, 2012; Li et al., 2009) established the empirical model of cutting depth and surface roughness in smooth area of abrasive water jet machining hard and brittle materials, and put forward the pressure relief mechanism of high-pressure water jet grooving coal seam. In addition, in other aspects of research on rock burst, some scholars have analyzed the precursor characteristics of rock burst, and introduced loading and unloading response ratios to study the reasonable advancement speed of their working faces (Feng et al., 2022; Lai et al., 2022).

The research results of the above scholars have made effective research on the preven-tion and control of blasting pressure relief, hydraulic fracturing and pressure relief of hard roof. However, there is relatively little research on the application of pressure relief prevention and control of abrasive jet. In view of this, this paper takes the mining of I010206 working face in Kuangou Coal Mine as the research object, and carries out the determina-tion of key technical parameters of axial roof cutting with abrasive jet. Using this technology, the pre-splitting engineering practice of combining abrasive jet with blasting is carried out, and the effect is tested. It is verified that the axial cutting technology of hard roof abrasive jet can achieve the effect of conventional blasting treatment in hard roof. The purpose of this paper is to lay a foundation for comprehensive application in the practice of rock burst prevention and control of hard roof in Kuangou Coal Mine.

2 Engineering background

2.1 General situation of working face

Kuangou Coal Mine is located in Hutubi County, Xinjiang, China. The mine mainly mines B4-1 coal seam, B2 coal seam and B1 coal seam. Now it is mined to I010206 working face of B2 coal seam, with an average thickness of 10.5 m, which belongs to extra-thick coal seam. Before expansion, the inclined length is 85 m, after expansion, the inclined length is 137.8 m, the

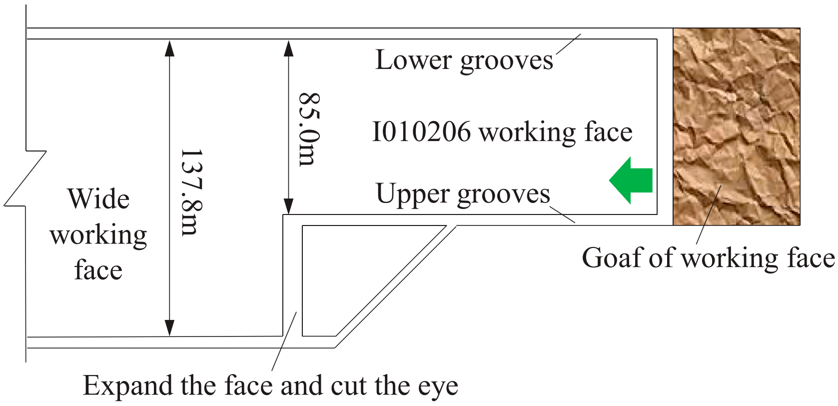

FIGURE 1
The layout of I010206 working face.

recoverable strike length is 1,672 m, the average inclination angle of working face is 14, and the average buried depth is 434 m. The width of I010206 working face is ir-regular during mining, and the layout of I010206 working face is shown in Figure 1. I010206 working face of B2 coal seam adopts comprehensive mechanized top-coal caving mining technology, with a mining thickness of 3.2 m and a caving thickness of 7.3 m, with a mining-caving ratio of about 1: 2.4.

According to the analysis of borehole data in Kuangou Coal Mine, there are multiple sandstone roofs within 50 m above the coal seam. The lithology statistics of B2 coal seam and its roof are shown in Table 1. There are 13.59 m thick medium-grained sandstone and 12.51 m thick fine-grained sandstone in the roof of coal seam. Among them, 13.59 m me-dium-grained sandstone is a sub-critical stratum, with uniaxial compressive strength of 115.25 MPa, uniaxial tensile strength of 7.48 MPa, elastic modulus of 31.65 GPa and Pois-son's ratio of 0.24.

TABLE 1 Statistical table of lithology of B2 coal seam and its roof.

Serial number	Rock character	Thickness/m
1	B4-1 coal seam	3.93
2	Mudstone	7.99
3	Fine grained sandstone	5.29
4	B3 coal seam	2.35
5	Siltstone	6.16
6	Fine grained sandstone	12.51
7	Medium grained sandstone	13.59
8	Fine grained sandstone	0.69
9	Mudstone	2.15
10	B2 coal seam	11.11

2.2 The strata behavior of previous working face mining in B2 coal seam

After I010203 working face of B2 coal seam is mined, I010206 working face is mined. During the mining period of I010203 working face in the past, rock burst and many mine earthquakes occurred. Taking the large energy appearance of mine earthquake on 8 March 2018 as an example, the source distribution of mine earthquake and its roadway defor-mation are drawn as shown in Figure 2. During the mining of I010203 working face in B2 coal seam, a mine earthquake occurred at the side of coal pillar in the lower gateway. The energy of mine earthquake is 9.7 × 106 J, and the source is at the side roof of coal pillar in the lower gateway of I010203, as shown in Figure 2A. The mine earthquake was accompanied by loud noise, which caused floor heave and net pocket at the bottom of roadway in the area of 148–198 m ahead of the working face in the lower gateway of I010203. The floor heave of the roadway where the mine earthquake occurred is about 20 cm, and the local top coal sinks about 30 cm, as shown in Figure 2B.

2.3 I010206 working face impact risk analysis

This paper comprehensively analyzes the main geological factors and mining tech-nology factors that affect the risk of rock burst in I010206 working face of Kuangou Coal Mine. The main geological factors include physical properties of coal and rock, buried depth, hard rock stratum, faults, local fold areas and so on. The main mining factors are overlying structure, section coal pillar, roof activity, liberated layer, bottom coal, roadway crossing and so on. The comprehensive index method is used to carry out the impact risk assessment, and the multi-factor coupling method is used to draw the results of impact risk area division as shown in Figure 3.

B2 coal seam and its floor have weak impact tendency, and B2 coal seam roof has strong impact tendency. As can be seen from Figure 3, when I010206 working face is advancing, the danger-ous area along the gateway on the working face changes from a medium impact dangerous

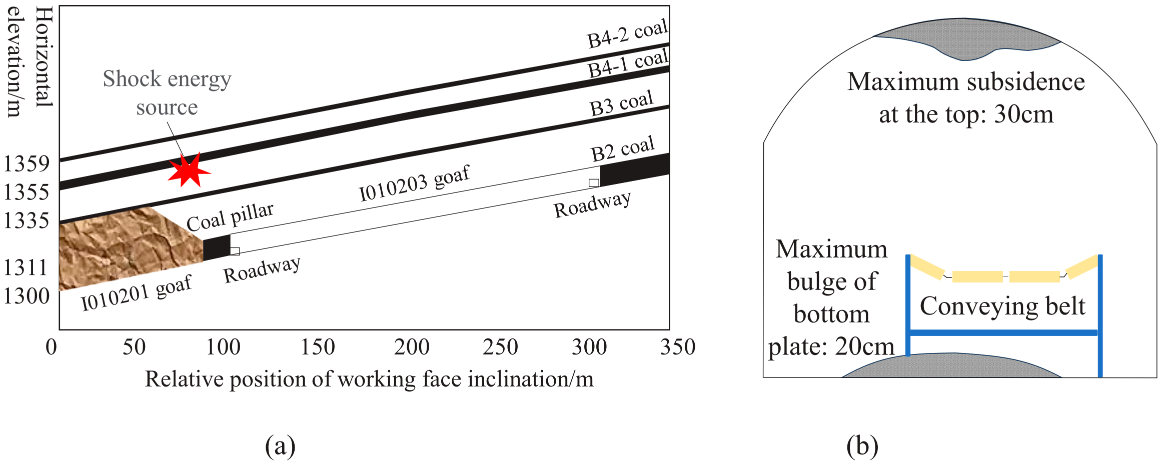

FIGURE 2
The source distribution of mine earthquake and its roadway deformation. **(A)** Focal location of mine earthquake; **(B)** Roadway deformation caused by mine earthquake.

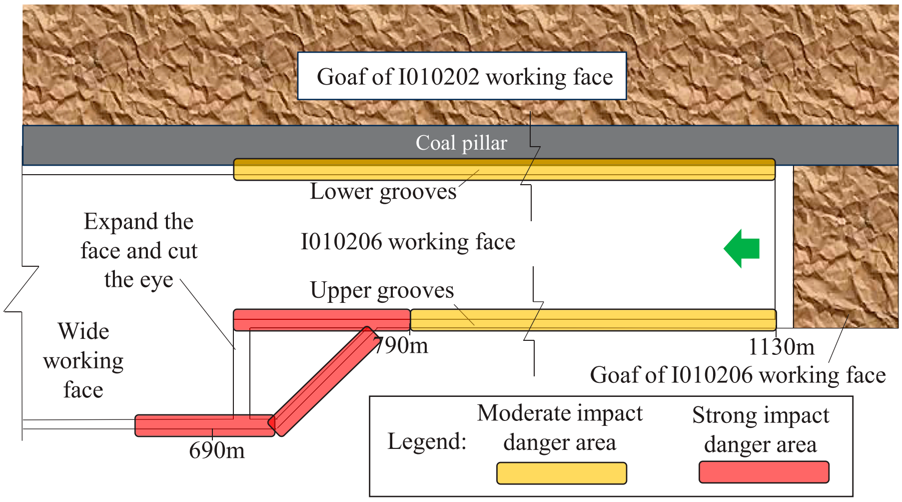

FIGURE 3
Division result of impact danger zone.

area to a strong impact dangerous area near the wide working face. Among them, the range of 790–1,130 m in the upper gateway is a medium impact danger zone, and the range of 690–790 m is a strong impact danger zone. In the mining process of the working face, the lower gateway area is a medium impact danger area.

3 Principle and technology of axial top cutting with frosted jet

3.1 Principle of axial roof cutting with abrasive water jet to prevent impact

The technology of axial cutting of hard roof with abrasive jet is to drill holes in the roof, and the initial cracks with a depth of 300–500 mm are formed on the wall of the hole with abrasive jet technology. Fracturing is carried out along the cutting direction, so that a fracture network dominated by axial cracks is formed in the hard roof, and a cluster frac-ture network along the strike or inclination is formed. Under the action of mine pressure, the technology of directional cutting off the roof is realized (Wu et al., 2020).

According to the related theory of rock burst, the energy sources of rock burst are mainly static load of foundation and additional dynamic load. When the combined action of dynamic and static loads reaches the critical condition of rockburst, rockburst will occur, and the conditions for rockburst can be expressed as Equation 1:

$$\sigma_j + \sigma_d \geq \sigma_{b\,min} \tag{1}$$

In the formula, σ_j is the static load in coal and rock mass; σ_d is the dynamic load in-duced impact in coal and rock mass; $\sigma_{b\min}$ is the critical stress when rock burst occurs.

The technology of axial roof cutting with abrasive jet can reduce the bending elastic energy caused by roof hanging and the dynamic load caused by roof fracture. At the same time, the goaf fully collapses, which plays a supporting role for the roof, thus reducing the compressive elastic energy of coal and the dynamic load caused by roof collapse.

3.2 Construction technology of axial topcutting technology with scrubbed water jet

The construction technology mainly includes "drilling-slotting-fracturing" three links, and the schematic diagram of the frosted jet construction technology is shown in Figure 4. Firstly, a drilling rig, a matching drill bit and a drill pipe are used to drill a hole with a certain aperture in the roadway roof. Secondly, connect the hole sealer with the abrasive jet device and send it to the preset position of drilling, start the water jet system and adjust it to the jet mode. Operate the drilling rig to retreat the drill pipe at a uniform speed, and form prefabricated cracks on both sides of the drilling axis. Finally, turn off the abrasive pump, adjust the high-pressure pump to hole sealing mode, and inject high-pressure water into the hole sealer to seal the upper and lower hole sealers of the crack. Switch the water jet system to fracturing mode, and the high-pressure water continues to expand along the crack tip.

When the pump pressure drops suddenly or the fracturing time reaches the design time, turn off the high-pressure pump, relieve the pressure with the hole sealer, and com-plete the fracturing work in this section. Start the drilling rig and operate the drill pipe to move the ejector to the next slot position, and construct the next section according to the above method.

4 Experimental study on main technical parameters of axial topcutting of grinding jet

4.1 Design of experimental scheme for axial topcutting of scrubbing jet

The purpose of "slotting" technology in abrasive jet axial cutting technology is to prefabricate slotting and provide guidance for "fracturing." According to the theoretical research foundation and field engineering experience of the research group at present, combined with the laboratory test results, equipment capacity and operational safety, the kerf radius and kerf length that meet the engineering needs are comprehensively set to be 200 mm and 300 mm for this kerf test analysis.

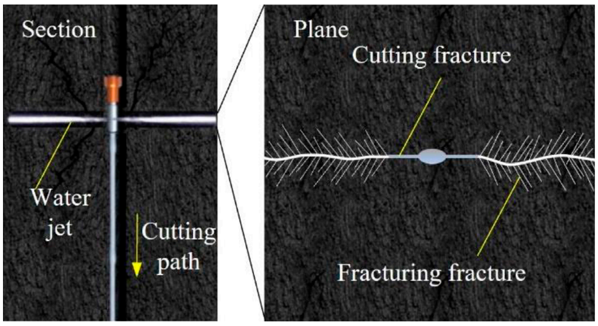

FIGURE 4
The schematic diagram of the frosted jet construction technology.

The layout of slotting test scheme is shown in Figure 5. On I010206 working face, the gateway is 300 m ahead of the working face to avoid the influence of mining. Slotting is carried out from hole *B* to hole *A*, and hole *A* is observation well, so as to determine lithol-ogy, adjust fracturing position and test the effect. When the kerf radius is 200 mm, the rela-tionship between kerf pressure and kerf time is determined, and the kerf is planned to be carried out in hole B in four sections to hole A with a spacing of 200 mm. This time, two schemes are designed to carry out slotting test analysis. In Scheme 1, the slotting direction is *B*→*A*, the slotting pressure is 40 MPa, so that the slotting hole can be slotted with the 200 mm rock stratum in observation well, and the slotting length is 300 mm. Record the slotting time and sand consumption, and move the slotting downwards. In Scheme 2, the kerf pressure is changed to 50 MPa, and other kerf parameters are consistent with Scheme 1.

The layout of fracturing test scheme is shown in Figure 6. There are 4 boreholes in the fracturing test, among which *E* and *H* boreholes are observation well, and *F* boreholes and *I* boreholes are slotting and fracturing boreholes. After the cutting and fracturing of the F hole and I hole, the internal conditions of the *E* hole and the *H* hole are detected, and the fracturing test results are analyzed accordingly. Using the determined parameters of abrasive kerf, the fracturing experiment after abrasive jet is further carried out to determine the fracturing radius.

In the first scheme, the cutting direction is *F*→*E*, the cutting radius is 200 mm, the cutting length is 300 mm, the sand consumption is 25 kg, and the fracturing pressure is 50 MPa. Based on this, the feasibility of 5 m fracturing radius is analyzed. In the second scheme, the cutting direction is *F*→*E* and the fracturing pressure is 60 MPa. Based on this, the feasibility of 5 m fracturing radius is analyzed. In the third scheme, the cutting direc-tion is *I*→*H*, and the fracturing pressure is 60 MPa. Based on this, the feasibility of 10 m fracturing radius is analyzed. The remaining parameters of Scheme 2 and Scheme 3 are consistent with those of Scheme 3.

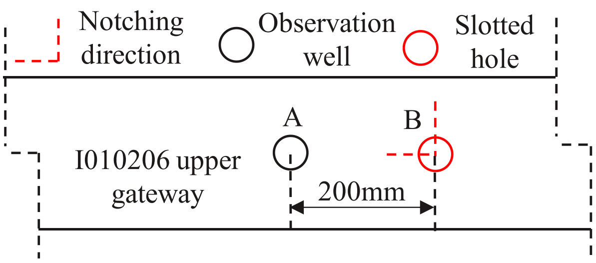

FIGURE 5
The layout of slotting test scheme.

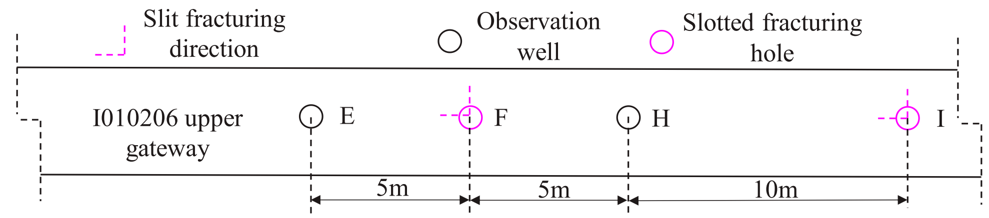

FIGURE 6
The layout of fracturing test scheme.

TABLE 2 Statistical table of slit test results.

Scheme serial number	Slotting directio	Kerf radius/n	Slotting pressure	Sand consum	Slotting time/mi
Scheme 1	*B*→*A*	200	40	25	1.5
Scheme 2	*A*→*B*	200	50	25	1

4.2 Analysis of experimental results of axial topcutting of scrubbing jet

During the slotting test, slotting was conducted from the position of hole *B* at 17 m to the direction of hole A at a distance of 200 mm. The pressure of water injection pump was 40 MPa, the amount of sand added was 25 kg, the slotting length was 300 mm, the slotting duration was 1.5 min, the rock stratum at a distance of 200 mm between holes *A* and *B* was cut, and water came out from hole *A*. From the 15 m position of hole *B*, cut the seam in the direction of hole *A* with an interval of 200 mm. The water injection pump gives a pressure of 50 MPa, the sand addition is 25 kg, the length of the seam is 300 mm, and the length of the seam is 1 min. Cut through the rock strata with an interval of 200 mm between holes *A* and *B*, and the water comes out of hole *A*.

The main parameters such as kerf radius, kerf pressure, kerf time and sand consump-tion are determined through experiments, as shown in Table 2.

Based on the experimental study of fracturing radius parameters of two sections of hole *F* with 5 m, the fracturing radius of two sections with 5 m was successfully completed. Its kerf length is 300 mm, kerf radius is 200 mm, and kerf pressure is 40–55 MPa. The frac-turing parameters include fracture initiation pressure of 50–55 MPa, fracturing time of 10–12 min and fracturing radius of 5 m.

According to the experimental study on the parameters of fracturing radius of *I* hole in four stages of 10 m, the fracturing radius of 10 m for three times was successfully com-pleted. Its kerf length is 500 mm, kerf radius is 200 mm, and kerf pressure is 40–55 MPa. The fracturing parameters include fracture initiation pressure of 55–60 MPa, fracturing time of 10–20 min and fracturing radius of 10–20 m. The test results are shown in Table 3.

TABLE 3 Fracturing test results.

Scheme serial number	Slotting directio	Fracturi position	Fracturi pressure	Fracturi time/mi	Fracturi radius/n
Scheme 1	*F*→*E*	25	50	12	5
Scheme 2	*F*→*E*	20	55	10	5
	I→*H*	28	55	12	10.3
Scheme 3	*I*→*H*	25	55	20	10.3
	I→*H*	19	60	24	10
	I→*H*	15	60	34	Without water

As the kerf radius increases from 5 to 10 m, the fracturing pressure increases accordingly. The results show that higher pressure is needed to overcome the fracture strength and friction of rock in order to reach a longer crack propagation radius, thus promoting the crack to extend further. At the same time, when the fracturing pressure is 55 MPa, the fracturing time to reach the fracturing radius of 5 and 10.3 m is 10 and 24 min respectively. The fracturing time is significantly prolonged with the increase of fracture radius, which reflects the gradual accumulation and release of energy in the process of fracture propagation and the longer time required for a larger fracture volume to form stably. Through industrial experimental study, the main parameters of kerf depth of 200 m and kerf length of 300 m are determined as follows: kerf pressure of 40–50 MPa, sand con-sumption of 25 kg and kerf time of 1–1.5 min. By determining the main parameters of kerf, the fracturing pressure is 50–55 MPa with a kerf radius of 5 m and the fracturing time is 10–12 min, and the fracturing pressure is 55–60 MPa with a kerf radius of 10 m and the frac-turing time is 20–24 min.

5 Practice of axial top cutting and scour prevention of frosted jet

5.1 I010206 partition scour prevention scheme for working face

In the process of mine production, roof control measures are taken to prevent scour. According to the impact risk evaluation results of the working face, that is, area I, with a mileage of

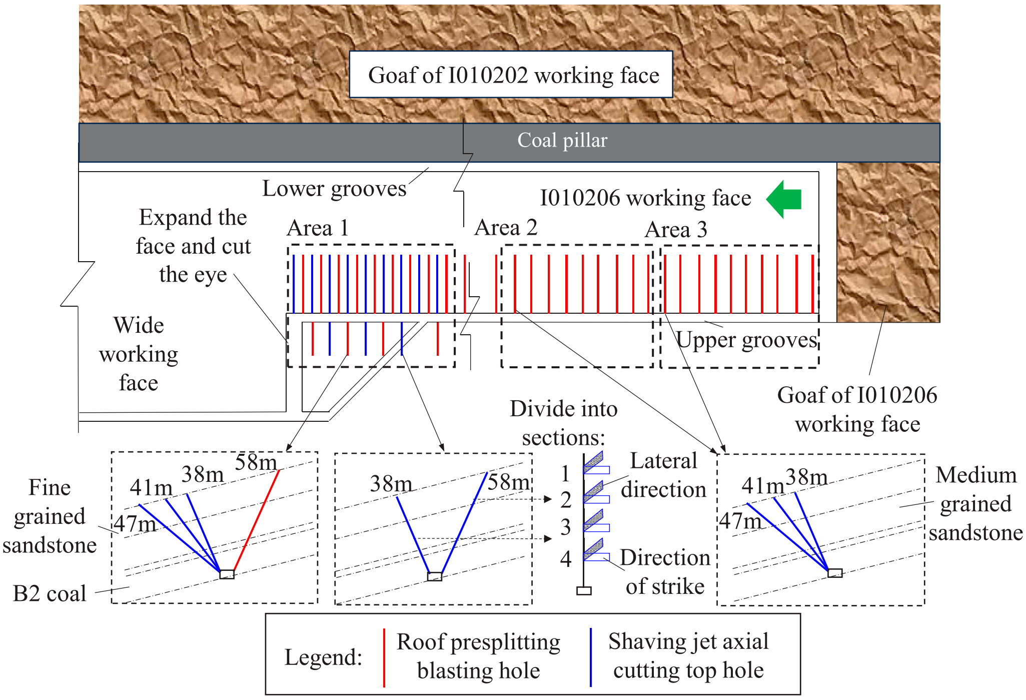

FIGURE 7
The layout of the upper partition scour prevention scheme of I010206 working face.

690–790 m, is a strong impact risk area, area II, with a mileage of 930–1,030 m, is a medium impact risk area, and area III, with a mileage of 1030–1,130 m, is a medium impact risk area. The area I mainly adopts the methods of axial cutting and blasting presplitting of frosted jet to control the roof, while the area II and area III adopt the traditional blasting presplitting method to control the roof. The layout of the upper partition scour prevention scheme of I010206 working face is shown in Figure 7.

According to the results of field test parameters, the designed kerf pressure is 50–55 MPa, kerf time is 3–5 min, sand content is 25 kg, and kerf length is 300–500 mm. The cutting direction is strike direction to cut off the connection with goaf, and the inclined direction is tangent to the lateral roof. The fracturing pressure used this time is 50–65 MPa, the fracturing time is 15–20 min, and each hole is designed to be divided into four sections.

The main parameters of roof blasting presplitting in area I are that four holes are fan-shaped perpendicular to the center line of roadway. The drilling length is 47, 41, 38, and 58 m respectively, the inclination angles are 39, 52, 66 and 65 respectively, and the charge density is 2.75 kg/m. The main parameters of roof blasting presplitting in areas II and III are fan-shaped with three holes perpendicular to the center line of the roadway. The drilling length is 47, 41, and 38 m respectively, the inclination angles are 39, 52 and 66 respectively, and the charge density is 2.75 kg/m. Three-stage emulsion explosive, instant detonator and forward charging are used, and the connection mode is parallel connection in the hole and series connection outside the hole.

5.2 Implementation process of axial topcutting project of scrubbing jet

During the implementation of axial roof cutting by abrasive jet, the data of hydraulic pressure gauge and the on-site slotting and fracturing process are used for control. The typical abrasive jet curve is taken to analyze the implementation process, and its sectional slotting and fracturing curves are shown in Figure 8. Through the monitoring data of hydraulic pressure instrument, it can be clearly seen that the single-stage process includes three processes: pipeline testing and pressure testing, slotting and fracturing. The main purpose of pipeline testing and pressure testing is to check whether the pipeline is normal and to judge the primary fracture of rock stratum. The cutting and fracturing process is controlled on site according to the main design parameters and the field observation of water production, and 4 stages of fracturing are designed for each hole. The operation process of other sections is mainly the process of circular cutting, judging primary cracks and fracturing. Then, enter the circulation of the next hole.

After the completion of the process, the drilling peep is used to observe the propagation of kerf and fracturing cracks in the hole, and the kerf and fracture can be displayed intuitively through the peep. Through strict on-site supervision, on-site monitoring and observation, the application of abrasive jet axial roof cutting technology in hard roof control and scour prevention of I010206 working face was completed.

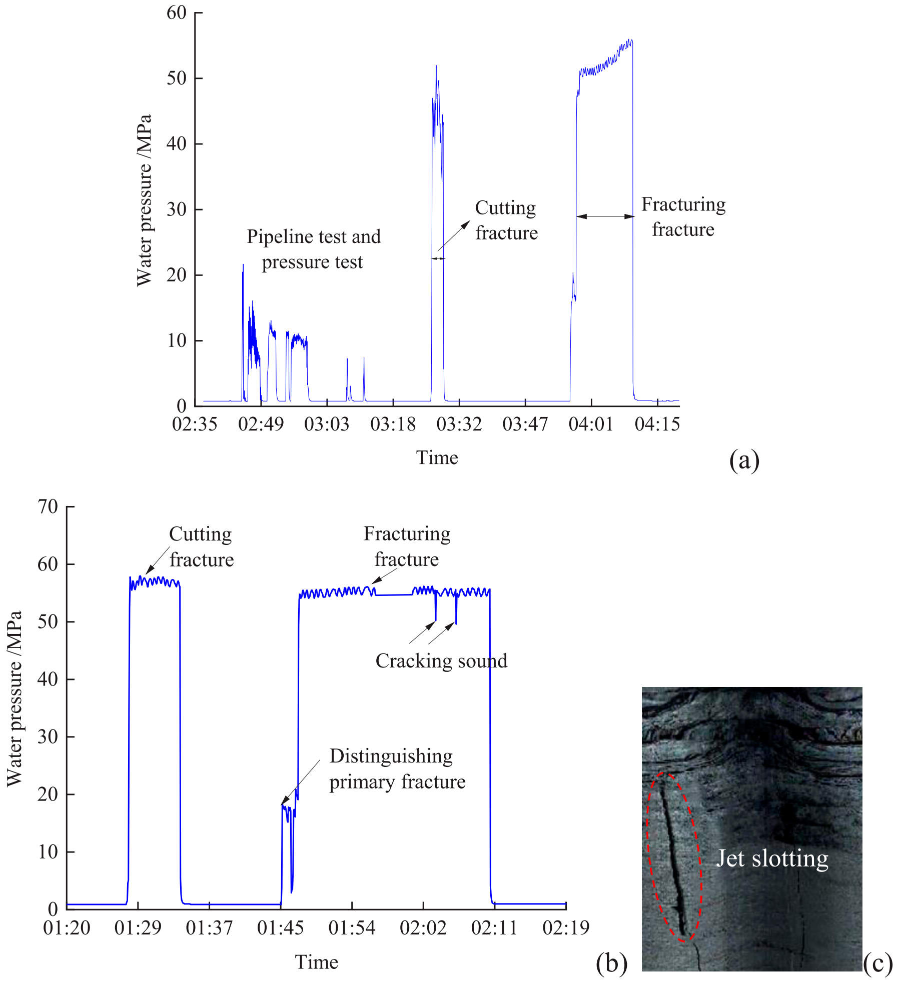

FIGURE 8
Sectional slotting and fracturing curve. **(A)** typical curve of the first section of a hole; **(B)** typical curve of other sections of a hole; **(C)** fracture hole peep diagram.

5.3 Inspection of scour prevention effect in mining process of working face

Microseismic monitoring can monitor the time, space and energy of coal and rock fracture events during mining. Therefore, firstly, the anti-scour effect of mining face is an-alyzed through microseismic monitoring and analysis.

The microseismic monitoring results of different zones are shown in Figure 9. The results of microseismic monitoring show that the distribution range of microseismic events in area I is mainly 200 m ahead of the working face, and the peak distribution area is 130 m ahead of the working face. The distribution range of microseismic events in Area II is mainly 200 m ahead of the working face, and the peak distribution area is 80 m ahead of the working face. The distribution range of microseismic events in area I is mainly 200 m ahead of the working face, and the peak area of concentrated distribution is 80 m ahead of the working face.

According to the monitoring results of microseisms, the statistical table of average en-ergy-cumulative frequency of microseisms in different areas is summarized as shown in Table 4. The average released energy of area I is 137.64 J, which is about 10% lower than that of area II and 52.4% lower than that of area III. There were 1998 microseismic events in area I, which was about 20% higher than that in area II and 34.5% higher than that in area III. Compared with the traditional blasting presplitting area, the concentrated distribution of microseismic events in the roof combination presplitting area I shifts to the front away from the working face, which makes the rock activity far away from the stope operation area. The safety of operators in the mining influence range is increased. Advance promotes the energy release of surrounding rock, and releases it with small energy. It reduces the ac-tivity intensity of surrounding rock and weakens the dynamic load effect of impact danger.

5.4 Support pressure monitoring and analysis

The greater the periodic weighting step of roof strata, the stronger the dynamic load, and the higher the possibility of

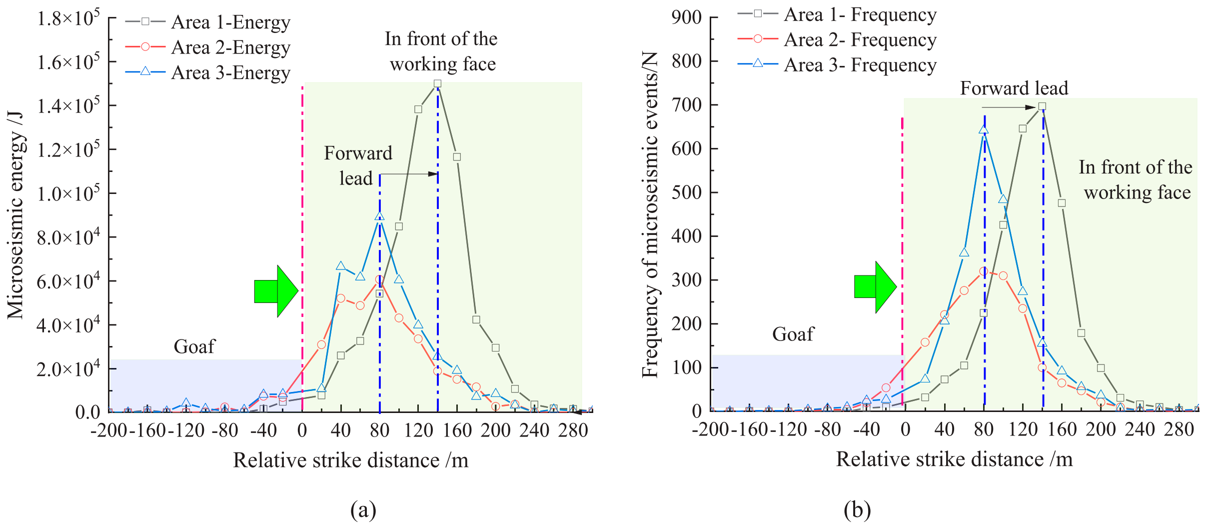

(a) (b)

FIGURE 9
The microseismic monitoring results of different zones. **(A)** comparison of energy advance distribution of microseismic events; **(B)** comparison of frequency advance distribution of microseismic events.

TABLE 4 The statistical table of average energy-cumulative frequency of microseisms in different areas is summarized.

Location	Average energy of microseisms/J	Cumulative frequency of microseisms/N
Area 1	137.64	1,998
Area 2	152.97	1,667
Area 3	289.56	1,485

inducing impact danger. According to the monitoring re-sults of the support pressure, the comparison chart of periodic weighting is drawn as shown in Figure 10. In the process of working face mining, combined with the field caving observation, it shows that the hard roof can collapse in time. The combination of axial roof cutting with abrasive jet and blasting presplitting can effectively weaken the intact hard rock stratum of the roof and avoid large-scale rock stratum collapse. Compared with the blasting area only, the weighting step under the combined mode of axial cutting of abra-sive jet and blasting presplitting is reduced. The optimization of pressure relief mode effectively improves the working condition of hydraulic support, and the periodic weighting step is reduced from 12.0~19.2 m to 8.0~14.4 m, which provides a new method for the treatment of hard roof erosion in the later stage of mine. The average periodic weighting step is reduced from 15.84 to 11.20 m, with a reduction rate of 29.29%.

Strong rock movement is the main cause of impact danger during initial mining, and the cloud map of support pressure distribution in working face is shown in Figure 11. In the process of working face mining, combined with field caving observation, it shows that the hard roof can collapse in time, and the axial cutting of abrasive jet can effectively weaken the complete hard rock layer of the roof. Thus, large-scale rock caving is avoided, and the expanded non-abrasive jet area is larger, which effectively improves the working conditions of the hydraulic support. Therefore, the effect of the roof on the coal wall of the working face in the axial roof cutting area of the abrasive jet is obviously improved, which realizes the effect of the first roof caving compared with the traditional blasting, and provides an effective new method for the treatment of the hard roof in the later stage of the mine.

5.5 Measurement and analysis of coal body stress

In order to further control the impact hazard, through the measurement of coal stress, the static load control effect and stress level of the working face after taking measures are analyzed. Because area I is a dangerous area of strong impact, it is treated by increasing the axial cutting top hole of frosted jet because of the distance between the pre-splitting holes of area II and area III measures. On the other hand, the layout distance of pre-splitting holes in single-sided square and double-sided square area blasting is the same as that in area I, only in the axial cutting of frosted jet and blasting pre-splitting mode.

For this reason, a comparative analysis is made between the area I with combined pressure relief and the measured area of static load of coal with one-sided square and double-sided square with blasting presplitting. The measured results of coal stress moni-toring are shown in Figure 12. The significant influence range of coal static load in area I is 20 m, the peak value is 8–10 m, and the stress concentration factor is 1.68. The significant influence range of static load on one side square area is 45 m, the peak value is 8–10 m in the leading face, and the stress concentration factor is 2. The significant influence range of static load in the double-sided square

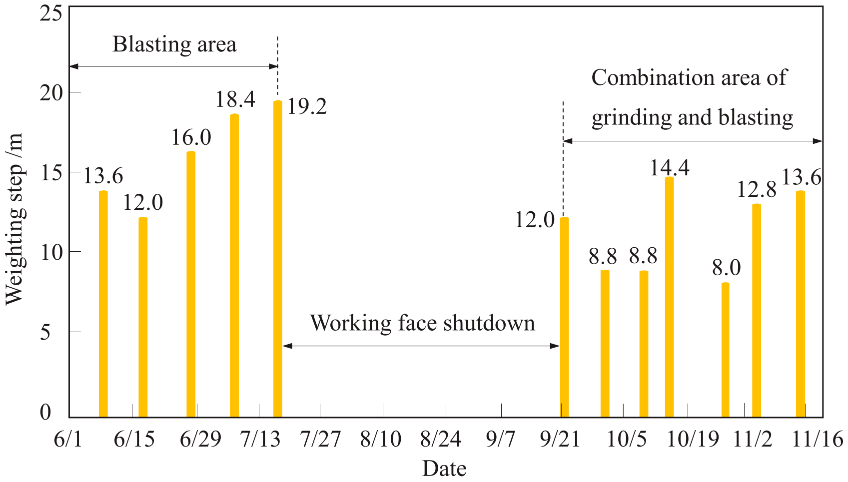

FIGURE 10
The comparison chart of periodic weighting.

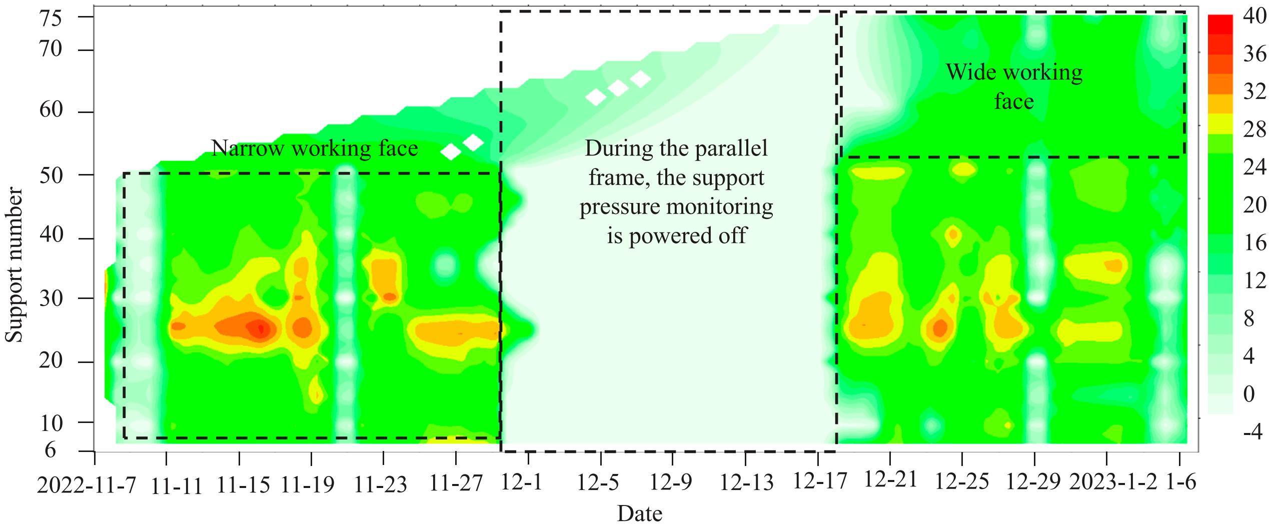

FIGURE 11
The cloud map of support pressure distribution in working face.

area is 80 m in the leading face, the peak value is 8–10 m in the leading face, and the stress concentration factor is 4.4. Compared with the traditional blasting pre-splitting area, the influence range of the leading abutment pres-sure in the blasting combined pre-splitting area is greatly reduced, and the stress concen-tration factor is obviously reduced, thus achieving a good effect of coal static load control in the combined pre-splitting area.

The stress change curve of coal before and after fracturing is shown in Figure 13. After the width of the working face increases, the coal stress curve is measured at the 5 m posi-tion of the upper trough leading working face. After the axial cutting of the frosted jet, the stress concentration of the coal body gets a rapid response, and the stress of the coal body has an obvious stress drop, reaching 2.9 MPa. After the axial cutting of the frosted jet, the stress concentration of the coal body gets a rapid response, and the stress of the coal body drops obviously, and the maximum reduction of the stress reaches 2.9 MPa, with a decrease of about 41.85%. During the mining period of face expansion, the stress concentration of coal has been significantly improved. Under the influence of mining, the stress concentration of coal body in the axial cutting area of frosted jet does not increase again, which has a good effect of pressure relief of coal body.

Based on the combination of frosted jet axial roof cutting and roof deep-hole pre-splitting blasting, the prevention and control of rock burst in I010206 working face is car-ried out. The construction management and control of the new technology of frosted jet axial roof cutting and the analysis of anti-scour effect in the mining process are realized. The anti-scour practice shows that the control effect of dynamic and static load is good, the strong impact dangerous area mentioned above is safely pushed over and the mine safety production is realized.

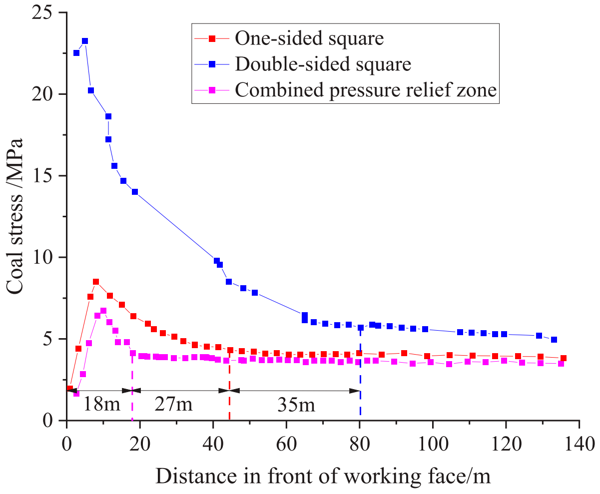

FIGURE 12
The measured results of coal stress monitoring.

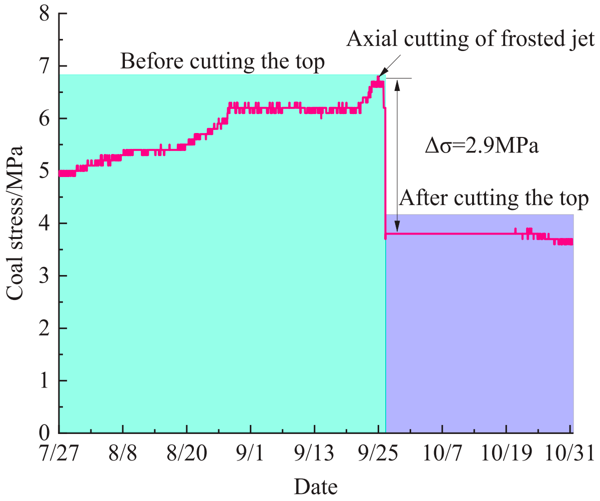

FIGURE 13
The stress change curve of coal before and after fracturing.

6 Conclusion

(1) The main contents of this paper are as follows: (1) through the analysis of hard roof frosted jet axial cutting and anti-scour test, the key technical parameters of hard roof frosted jet axial cutting suitable for Kuangou Coal Mine are determined. The slotting test results show that the slotting depth is 200 m, the slotting length is 300 m, the slotting pres-sure is 40–50 MPa, the sand consumption is 25 kg, and the slotting time is 1–1.5 min. The fracturing pressure of 50–60 MPa and the fracturing time of 20–24 min are obtained by axial topping of frosted water jet.

(2) After the implementation of the new technology of frosted jet axial roof cutting, the cracks in the roof strata are produced and expanded effectively after slotting and fractur-ing, and the cracks break during the fracturing period, and the crack extends in the range of 10–20 m, which destroys the integrity of the roof. The periodic pressure step distance de-creased obviously, the pressure step distance decreased from 12.0 ~ 19.2 m to 8.0 ~ 14.4 m, the influence range of mining stress and stress concentration factor decreased obviously, and the activity strength and dynamic load effect of surrounding rock decreased obvious-ly.

(3) Compared with the traditional blasting roof cutting technology, after the combined treatment of frosted jet axial cutting and blasting, the concentration area of microseismic events during mining is transferred from 80 to 130 m. After the axial cutting of the frosted jet, the stress concentration of the coal body gets a rapid response, and the stress of the coal body has an obvious stress drop, reaching 2.9 MPa. The energy release of microearthquakes is mainly small energy events, which achieves a good anti-erosion effect.

Data availability statement

The raw data supporting the conclusions of this article will be made available by the authors, without undue reservation.

Author contributions

RS: Methodology, Writing–original draft, Funding acquisition, Project administration, Resources, Software, Supervision, Validation, Visualization. ZZ: Conceptualization, Writing–review and editing. WY: Data curation, Writing–original draft. HL: Formal Analysis, Investigation, Writing–original draft.

Funding

The author(s) declare that financial support was received for the research, authorship, and/or publication of this article. This work was supported by the National Natural Science Foundation of China [grant number 51874231].

Conflict of interest

Author RS was employed by Tiandi Science and Technology Co., Ltd. Authors ZZ, WY, and HL were employed by Xinjiang Energy Co., Ltd., CHN Energy.

Publisher's note

References

Abe, A., Kim, T. W., and Home, P. A. (2021). Laboratory hydraulic stimulation experiments to investigate the interaction between newly formed and preexisting fractures. *Int. J. Rock Mech. Min. Sci.* 141, 104665. doi:10.1016/j.ijrmms.2021.104665

Cruz, F., Roehl, D., and Vargas, E. A. V. (2018). An XFEM element to model intersections between hydraulic and natural fractures in porous rocks. *Int. J. Rock Mech. Min. Sci.* 112, 385–397. doi:10.1016/j.ijrmms.2018.10.001

Dehghan, A. N., Goshtasbi, K., Ahangari, K., and Jin, Y. (2018). The effect of natural fracture dip and strike on hydraulic fracture propagation. *Int. J. Rock Mech. and Min. Sci.* 171, 422–430. doi:10.1016/j.ijrmms.2015.02.001

Dehghan, A. N. (2020). An experimental investigation into the influence of pre-existingnatural fracture on the behavior and length of propagatinghydraulic fracture. *Eng. Fract. Mech.* 107330 (240), 107330–107414. doi:10.1016/j.engfracmech.2020.107330

Feng, C., Chong, J., Xingping, L., Jianqiang, C., Suilin, Z., and Shifeng, H. (2022). Study on advancing rate of steeply inclined extra-thick coal seam in rock burst mine based on loading-unloading response ratio. *J. China Coal Soc.* 47 (2), 745–761.

Feng, X. C. (2012). *Study on the Theory and experiment of hard-brittle materials with high-pressure AWJ cutting*. Harbin, Heilongjiang: Harbin University of Science and Technology.

Ghaderi, A., Shakib, J. T., and Nik, M. A. S. (2018). The distinct element method (DEM) and the extended finite element method (XFEM) application for analysis of interaction between hydraulic and natural fractures. *J. Petroleum Sci. Eng.* 171, 422–430. doi:10.1016/j.petrol.2018.06.083

He, Q. Y., Suorineni, F. T., Ma, T. H., and Oh, J. (2017). Effect of discontinuity stress shadows on hydraulic fracture re-orientation. *ternational J. Rock Mech. and Min. Sci.* 91, 179–194. doi:10.1016/j.ijrmms.2016.11.021

Heng, S., Liu, X., Li, X. Z., Zhang, X., and Yang, C. (2019). Experimental and numerical study on the non-planar propagation of hydraulic fractures in shale. *J. Petroleum Sci. Eng.* 179, 410–426. doi:10.1016/j.petrol.2019.04.054

Irani, A. E., Azadi, A., Nikbakht, M., Azarafza, M., Hajialilue Bonab, M., and Behrooz Sarand, F. (2022). GIS-based settlement risk assessment and its effect on surface structures: a case study for the tabriz metro-line 1. *Geotech. Geol. Eng.* 40, 5081–5102. doi:10.1007/s10706-022-02201-x

Jia, C., Lai, X. P., Cui, F., Zhang, S., Sun, J., and Tian, M. (2022). Mechanism of rock burst and its dynamic control measures in extra-thick coal seam mining from below the residual coal seam to below the gob. *Lithosphere* 2022, 17. doi:10.2113/2022/8179501

Jia, C., Lai, X. P., Cui, F., Xu, H., Zhang, S., Li, Y., et al. (2024). Mining Pressure distribution lawand disaster prevention of isolated island working face under the condition of hard “umbrella arch”. *Rock Mech. Rock Eng.* 57, 8323–8341. doi:10.1007/s00603-024-03961-z

Junfeng, P., Wentao, M., Shaohong, L., and Jiaming, G. (2021). A prevention technology of rock burst based on directional presplitting of water jet prefabricated slot in hard roof. *Chin. J. Rock Mech. Eng.* 40 (8), 1591–1602. doi:10.13722/j.cnki.jrme.2020.1056

Junfeng, P., Hongpu, K., Yaodong, Y., Xiaohui, M., Wentao, M., Chuang, L., et al. (2023). The method, mechanism and application of preventing rock burst by artificial liberation layer of roof. *J. China Coal Soc.* 48 (02), 636–648.

Junzhe, Y., Kaige, Z., Zhenrong, W., and Naiyong, P. (2020). Technology of weakening and danger-breaking dynamic disasters by hard roof. *J. China Coal Soc.* 45 (10), 3371–3379. doi:10.13225/j.cnki.jccs.2020.0599

Hongpu, K., Yanjun, F., Zhen, Z., Kaikai, Z., and Peng, W. (2023). Hydraulic fracturing technology with directional boreholes for strata control in underground coal mines and its application. *Coal Sci. Technol.* 51 (01), 31–44. doi:10.13199/j.cnki.cst.2022-2004

Lai, X. P., Jia, C., Cui, F., Chen, J., Zhou, Y., Feng, G., et al. (2022). Microseismic energy distribution and impact risk analysis of complex heterogeneous spatial evolution of extra-thick layered strata. *Scieitific Rep.* 12, 10832. doi:10.1038/s41598-022-14538-7

Li, Z. H., Pan, Y. S., Zhang, X., Yin, L. L., Xia, Y. X., Ju, W. J., et al. (2009). Mechanism of releasing pressure by high-pressure water jet applied to cutting coal seam. *J. Liaoning Tech. Univ. Sci.* 28 (1), 43–45.

Liu, Z. Y., Chen, M., and Zhang, G. Q. (2014). Analysis of the influence of a natural fracture network on hydraulic fracture propagation in carbonate formations. *Rock Mech. Rock Eng.* 47, 575–587. doi:10.1007/s00603-013-0414-7

Pan, Y. S., Li, Z. H., and Zhang, M. T. (2003). Distribution type mechanism and prevention of rock brust in China. *Chin. J. Rock Mech. Eng.* 22 (11), 1844–1851.

Pan, J. F., Ning, Y., Mao, D. B., Lan, H., Du, T., and Peng, Y. (2012). Theory of rockburst start-up during coal mining. *Chin. J. Rock Mech. Eng.* 31 (3), 586–596.

Qin, M., Yang, D., Chen, W., and Yang, S. (2021). Hydraulic fracturing model of a layered rock mass based on peridynamics. *Eng. Fract. Mech.* 258, 108088. doi:10.1016/j.engfracmech.2021.108088

Taleghani, A. D., Gonzalez, M., and Shojaei, A. (2016). Overview of numerical models for interactions between hydraulic fractures and natural fractures: challenges and limitations. *Comput. Geotechnics* 71, 361–368. doi:10.1016/j.compgeo.2015.09.009

Weng, M. Y., Hao, Y. H., and Xie, J. H. (2019). Study on “drilling cutting-fracturing” integrated energy dissipation technology for hard coal rock mass. *Coal Sci. Technol.* 47 (8), 84–88.

Wu, H., Zhu, H. H., Zhang, C. C., Zhou, G. Y., Zhu, B., Zhang, W., et al. (2020). Strain integration-based soil shear displacement measurement using high-resolution strain sensing technology. *Measurement* 166, 108210. doi:10.1016/j.measurement.2020.108210

Wu, M. Y., Wang, W. S., Song, Z. L., Liu, B., and Feng, C. (2021). Exploring the influence of heterogeneity on hydraulic fracturing based on the combined finite-discrete method. *Eng. Fract. Mech.* 252, 107835. doi:10.1016/j.engfracmech.2021.107835

Xia, Y. X., Ju, W. J., Su, S. J., Lu, Q., Ding, G. L., Su, B., et al. (2020). Experimental study on hydraulic reaming of gutters in coal seam with impact pressure. *J. Min. Strata Control Eng.* 2 (1), 84–91.

Zhang, C. J., Du, T. T., Li, H. P., and Jia, B. B. (2019). Research on rock burst prevention of high static coal seam in hard roof working face. *Coal Sci. Technol.* 47 (3), 112–119.

Zhao, S. K. (2021). Mechanism and application of force-structure cooperative prevention and control on rockburst with deep hole roof pre-blasting. *J. China Coal Soc.* 46 (11), 3419–3432.

frontiers | Frontiers in Earth Science

TYPE Original Research
PUBLISHED 22 November 2024
DOI 10.3389/feart.2024.1489096

OPEN ACCESS

EDITED BY
Wentao Yang,
University of Leeds, United Kingdom

REVIEWED BY
Nurhan Ecemis,
Izmir Institute of Technology, Türkiye
Longwei Chen,
Institute of Engineering Mechanics, China Earthquake Administration, China
Jinhang Liang,
Beijing Forestry University, China

*CORRESPONDENCE
Xiao-Bo Peng,
✉ xiaobo_peng@163.com
Ling-Yu Xu,
✉ lyxu@njtech.edu.cn

RECEIVED 03 September 2024
ACCEPTED 07 November 2024
PUBLISHED 22 November 2024

CITATION
Peng X-B, Gao Y, Xue Y-Y, Tao X-S and Xu L-Y (2024) Dynamic effective stress analysis of a site with liquefiable interlayer: considering vertical and horizontal ground motion. *Front. Earth Sci.* 12:1489096. doi: 10.3389/feart.2024.1489096

Dynamic effective stress analysis of a site with liquefiable interlayer: considering vertical and horizontal ground motion

Xiao-Bo Peng[1]*, Yuan Gao[2], Ying-Ying Xue[1], Xiao-San Tao[1] and Ling-Yu Xu[2]*

[1]Jiangsu Earthquake Risk Prevention Center, Earthquake Administration of Jiangsu Province, Nanjing, China, [2]Institute of Geotechnical Engineering, Nanjing Tech University, Nanjing, China

This study uses a fully coupled dynamic effective stress analysis method to evaluate the seismic response of a site containing silty sand which is a liquefiable interlayer. A generalized plasticity model is employed to describe the liquefaction behavior of silty sand under seismic action, and a nonlinear constitutive model is used to account for the nonlinear and hysteretic characteristics of non-liquefiable soils. The parameters of constitutive model were calibrated from the shear wave velocity and results of resonant column tests on different soils in a borehole. The results indicated that (1) A new spike with a period of approximately 1 s was observed at the top of the liquefiable interlayer compared to that at the bottom of the interlayer, reflecting a common seismic response characteristic induced by the rise in the excess pore water pressure (EPWP); (2) The low-frequency input motion caused higher EPWP within the liquefiable interlayer and more ground settlement at the consolidation stage; (3) The increase in either peak horizontal acceleration or peak vertical acceleration of input motions resulted in higher increase in the EPWP and ground surface settlement. Moreover, the vertical seismic component in near-field earthquakes has much more significant effect on the ground settlement in liquefiable sites than that in far-field earthquakes.

KEYWORDS

biot theory, liquefaction, nonlinear constitutive model, resonant column tests, spectral acceleration

1 Introduction

Earthquakes, as a powerful dynamic force of nature, pose a significant threat to human society and engineering structures, especially at liquefiable sites, where earthquake-induced ground damage is particularly severe (Fan et al., 2023; Sui et al., 2024). The destruction of soil structure and the sharp rise in excess pore water pressure EPWP lead to soil liquefaction during earthquakes, which in turn causes significant ground settlement and lateral spreading, severely damaging buildings, bridges, roads, and other infrastructure. Therefore, it is of great theoretical and practical importance to conduct in-depth analysis on the liquefaction effects of sites induced by earthquakes.

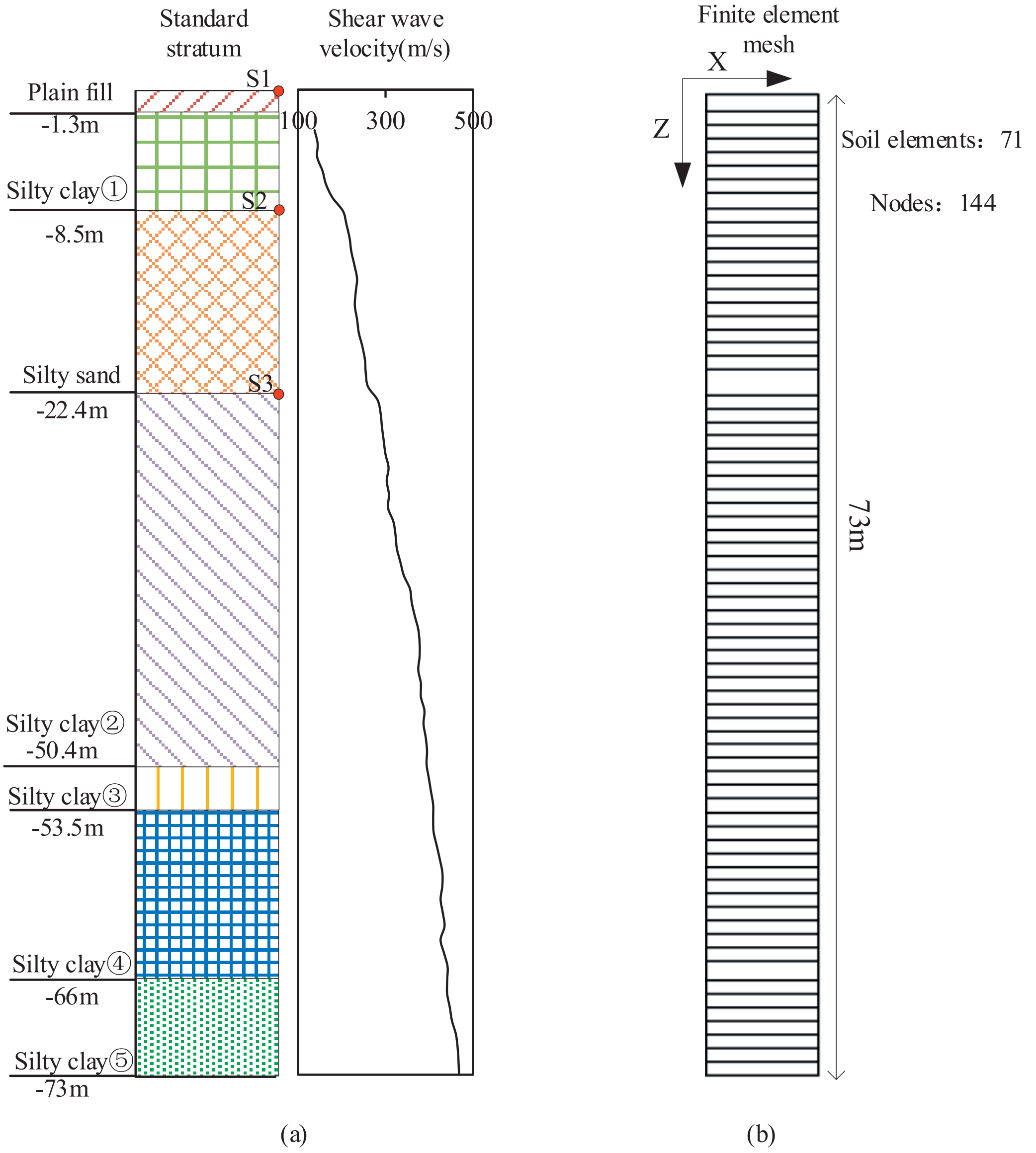

FIGURE 1
WX-03 borehole: **(A)** distribution of the shear velocity of soil layers and **(B)** finite element mesh.

The seismic response characteristics of liquefiable sites are a well-established yet challenging topic in geotechnical earthquake engineering. Scholars have extensively investigated seismic response characteristics of liquefiable sites through physical model tests, theoretical analysis, numerical simulation, and field seismic record analysis. Jia and Wang (2013) showed that interlayer thickness significantly affects liquefaction resistance of layered sand. Ecemis (2021) found that the thickness of the silt seam plays a crucial role in determining the liquefaction resistance of stratified sand deposits located beneath it. Cubrinovski et al. (2019) emphasizes the necessity of considering the system response of liquefying soils when assessing the occurrence and severity of liquefaction-induced damage. Xiu et al. (2020) noted that the powdery sand interlayer can effectively impede the transmission of pore water pressure within layered sand. Adampira and Derakhshandi (2020) experimentally found that site liquefaction is more severe when the liquefiable interlayer is thicker and shallower, leading to more attenuation of peak ground motion and greater ground settlement. Shen et al. (2022) discovered that the dilatancy of liquefied soil can significantly amplify the peak horizontal acceleration in liquefiable layers. Yao and Lin (2023) conducted numerical studies revealing that the location of liquefiable interlayers significantly impacts the internal force response of subway station structures. Youd and Carter (2005) recorded accelerations at liquefiable sites and found that soil softening or liquefaction has little effect on short-period response spectral accelerations but can significantly amplify long-period spectral accelerations. Sun and Yuan (2004) demonstrated that liquefaction can extend the predominant period of acceleration response spectra, amplifying long-period spectral accelerations while slightly suppressing short-period spectral accelerations.

TABLE 1 Parameters of PZ III model for the silty sand interlayer.

	Descriptions (unit)	Silty sand interlayer
M_{fc}	Failure line constant	1.028
M_{gc}	Critical state line constant	1.89
α_f	Yield constant	0.45
α_g	Plastic flow constant	0.45
K_{evo}	Bulk modulus constant	165
G_{eso}	Shear modulus constant	300
m_v	Exponent of bulk modulus	0.5
m_s	Exponent of shear modulus	0.5
β_0	Soil softening constant	10
β_1	Soil softening constant	0.135
H_0	Loading plastic modulus constant	1,450
H_{U0}	Unloading plastic modulus (kPa)	12,000
γ_R	Reloading plastic modulus constant	12
γ_U	Unloading plastic modulus constant	10

Therefore, site liquefaction may have more severe adverse effects on long-period and highly flexible structures (Sun et al., 2014). However, most existing studies focus on unidirectional seismic excitation, with relatively few studies on the response of liquefiable sites under both vertical and horizontal seismic excitations.

Horizontal seismic motions are often accompanied by vertical seismic motions during actual earthquakes. Considering combined effects of vertical and horizontal input motions can help provide a more comprehensive understanding of the seismic response of liquefiable sites, offering a more scientific basis for seismic risk assessment of engineering structures. Yang et al. (2002) found that the peak horizontal ground acceleration and frequency content of spectral accelerations depend on the intensity of the input motions and the nonlinearity of soils, while the input motion intensity has minimal effect on the amplification factor of vertical ground motions. Tsai and Liu (2017) proposed a method for equivalent nonlinear analysis of soil considering vertical seismic motion, emphasizing the importance of soil nonlinearity on vertical seismic wave propagation. Song et al. (2024) found that vertical seismic components greatly increase the influence of the approach bridge on the lateral displacement and internal forces of piles in liquefiable sites. Chen et al. (2018) investigated the impact of vertical seismic motion on the transient liquefaction of the seabed, finding that increasing the hydraulic coefficient of the surface soil can effectively inhibit seabed liquefaction. Xu et al. (2021a) numerically investigated the effect of vertical seismic motion on the settlement of pile groups, showing that vertical seismic motion significantly increases the settlement of pile groups in liquefied sites. Tsaparli et al. (2016) found that vertical input motion could increase liquefaction depth and post-liquefaction ground settlement. Thus, the dynamic response of liquefiable sites under combined horizontal and vertical input motions is more complex than that under unidirectional horizontal input motion alone. However, existing research has rarely considered the impact of the frequency of horizontal and vertical input motions on the dynamic response of liquefiable sites, particularly under conditions where liquefiable interlayers are present.

To address these issues, we thoroughly investigated a typical borehole with a liquefiable interlayer in the Yangtze River Delta Plain region of China. A fully coupled dynamic effective stress analysis method was adopted to evaluate the seismic response of a site containing a liquefiable interlayer. A generalized plasticity model is employed to describe the liquefaction behavior of silty sand under seismic action, and a nonlinear constitutive model is used to account for the nonlinear and hysteretic characteristics of non-liquefiable soils. The parameters of constitutive model were calibrated from the shear wave velocity and results of resonant column tests on different soils in the borehole. The effect of peak horizontal acceleration, frequency content, and peak vertical acceleration of input motions on the seismic response of the liquefiable site was discussed.

2 Finite element model

2.1 Site conditions

Figure 1 shows the borehole WX-03 with the distribution of shear wave velocity of different soils. In the finite element model, the total thickness of soil layers is taken as 73 m. In this study, the instrument employed in the field test was the ZD16 hole excitation wave tester, which utilizes a single-hole method to measure the wave velocity of the soil layers. This approach allows for the direct determination of the shear wave velocity in various soil layers. Following the" GB50011-2010 Code for Seismic Design of Buildings", the equivalent shear wave velocity (V_{se}) was confirmed as 185 m/s by averaging the values obtained from five measurements. Accordingly, this site is classified as a type III. According to the site investigation, the averaged actual standard penetration test (SPT) blow count is 7, which is below the critical SPT blow count range of 11–13, as calculated according to GB50011-2010. Therefore, the silty sand (i.e., third layer) located between the silty clay layers is deemed to be potentially liquefiable. The borehole is located near Jiangyin City in the Yangtze River Delta Plain region of China, and its representativeness and uniqueness lie in the presence of a liquefiable silt interlayer, as shown in Figure 1.

2.2 Governing equation

In the seismic analysis, the solid and fluid phases of the soil are modeled using Biot's theory with the u-p formulation (Biot, 1956; Zienkiewicz et al., 1999) and the governing equations are given by Equations 1, 2, respectively:

$$\mathbf{M\ddot{u}} + \mathbf{C\dot{u}} + \mathbf{Ku} - \mathbf{Qp} = \mathbf{f^u} \tag{1}$$

$$\mathbf{Q\dot{u}} + \mathbf{S\dot{p}} + \mathbf{Hp} = \mathbf{f^p} \tag{2}$$

TABLE 2 Model parameters of non-liquefiable soils at WX-03 borehole.

Soil type	Thickness (m)	V_s (m/s)	Density (g/cm^3)	G_0 (MPa)	Poisson's ratio(υ)	c(kP$_a$)	φ(°)	p' (kPa)	*b*	*n*	R_f
Plain fill	1.3	135	1.4	25.5	0.33	7	22	5.9	10,630	2.0	1.42
Silty clay①	7.2	144	2.14	44.4	0.33	36	10.9	39.8	8,060	1.6	1.49
Silty clay②	28	365	1.95	256.7	0.33	28	12.4	494.2	5,915	1.7	0.59
Silty clay③	3.1	409	2.09	349.9	0.33	38	12.7	693.8	4,641	1.7	0.51
Silty clay④	12.5	432	2.12	395.3	0.33	58	16.1	798.9	4,095	1.7	0.61
Silty clay⑤	7	461	2.09	445.2	0.33	56	15.7	915.7	4,096	1.7	0.56

TABLE 3 Key influence factors considered in parametric studies.

	Case	*PHA*(g)	*PVA/PHA*	Input motions
1	Kobe-0.3-0.00	0.3	0.00	Kobe
2	Kobe-0.4-0.00	0.4	0.00	Kobe
3	Kobe-0.5-0.00	0.5	0.00	Kobe
4	Kobe-0.5-0.37	0.5	0.37	Kobe
5	Kobe-0.5-0.67	0.5	0.67	Kobe
6	Nahanni-0.5-0.00	0.5	0.00	Nahanni
7	Nahanni-0.5-0.37	0.5	0.37	Nahanni
8	Nahanni-0.5-0.67	0.5	0.67	Nahanni
9	Liuan-0.5-0.00	0.5	0.00	Liuan
10	Liuan-0.5-0.37	0.5	0.37	Liuan
11	Liuan-0.5-0.67	0.5	0.67	Liuan

where **M** is the mass matrix, u, is the displacement vertor, **C** is Rayleigh damping matrix, **K** is the stiffness matrix, **Q** is the coupled matrix, **p** is the pore water pressure vector, **H** is the seepage matrix, S is the compression matrix, and $\mathbf{f}^u$ and $\mathbf{f}^p$ are the external load vectors. Note that a single dot and two dots above a variable represents the first and second derivative of that variable with respect to time, respectively. The u-p formulation is solved by the UWLC program, a fully coupled dynamic effective stress finite element analysis software, which is adopted in this study (Forum 8 Co. Ltd, 2005; Xu et al., 2013; Xu et al., 2019; Xue et al., 2023).

Soil damping plays a critical role in the dissipation of seismic energy and significantly affects the seismic response of the ground. In the study, soil damping was modeled by incorporating Rayleigh damping at small-strain level and by material damping characterized by constitutive models at large-strain level.

2.3 Constitutive modeling of soils

2.3.1 Generalized plasticity model for silty sand interlayer

To simulate earthquake-induced liquefaction of the silty sand interlayer in the WX-03 borehole, this study employed a modified generalized plasticity model, Pastor-Zienkiewicz III (PZ III) model, to represent the silty sand interlayer. The generalized plasticity model used in the study was specifically chosen because it can handle complex behaviors, such as cyclic loading and liquefaction in silty soils. This model accounts for the plastic strain accumulation during seismic events, which is crucial in accurately capturing the buildup of EPWP (Pastor et al., 1990; Xue et al., 2023; Xu et al., 2023). The generalized plasticity model is originally proposed by Zienkiewic et al. (1999) and modified by Cai et al. (2002) and calculates the stress increment (d$\boldsymbol{\sigma}$) using strain increment (d$\boldsymbol{\varepsilon}$) through an elasto-plastic matrix $\mathbf{D}_{ep}$. The d$\boldsymbol{\varepsilon}$ and $\mathbf{D}_{ep}$ are given by Equations 3, 4, respectively:

$$d\boldsymbol{\sigma} = \mathbf{D}_{ep} d\boldsymbol{\varepsilon} \tag{3}$$

$$\mathbf{D}_{ep} = \mathbf{D}_e - \frac{\mathbf{D}_e \mathbf{n}_{gL/U} \mathbf{n}^T \mathbf{D}_e}{H_{L/U} + \mathbf{n}^T \mathbf{D}_e \mathbf{n}_{gL/U}} \tag{4}$$

where $\mathbf{D_e}$ is the elastic matrix, $H_{L/U}$ is the plastic modulus, **n** is the loading direction vectors, and $\mathbf{n}_{gL/U}$ is the plastic flow direction vector. The subscripts L and U indicate loading and unloading, respectively. Detailed information about the model is referred to the literature (Cai et al., 2002; Xu et al., 2023).

The parameters of the PZ III model were calibrated using the liquefaction resistance (R_L), which is estimated based on the shear wave velocity (Amoly et al., 2016):

$$R_L = 0.68 \times 10^{-5} \times V_{s1}^2 \tag{5}$$

where

$$V_{s1} = V_s (p'_0 / P_a)^{-0.25} \tag{6}$$

V_s and p'_0 are the shear velocity and the effective mean stress. These values were taken at the midpoint of the silty sand interlayer, where V_s= 233.5 m/s and p'_0 =106 kPa, resulting in R_L=0.357. R_L was defined as the cyclic stress ratio (*CSR*) needed to produce 2.5%

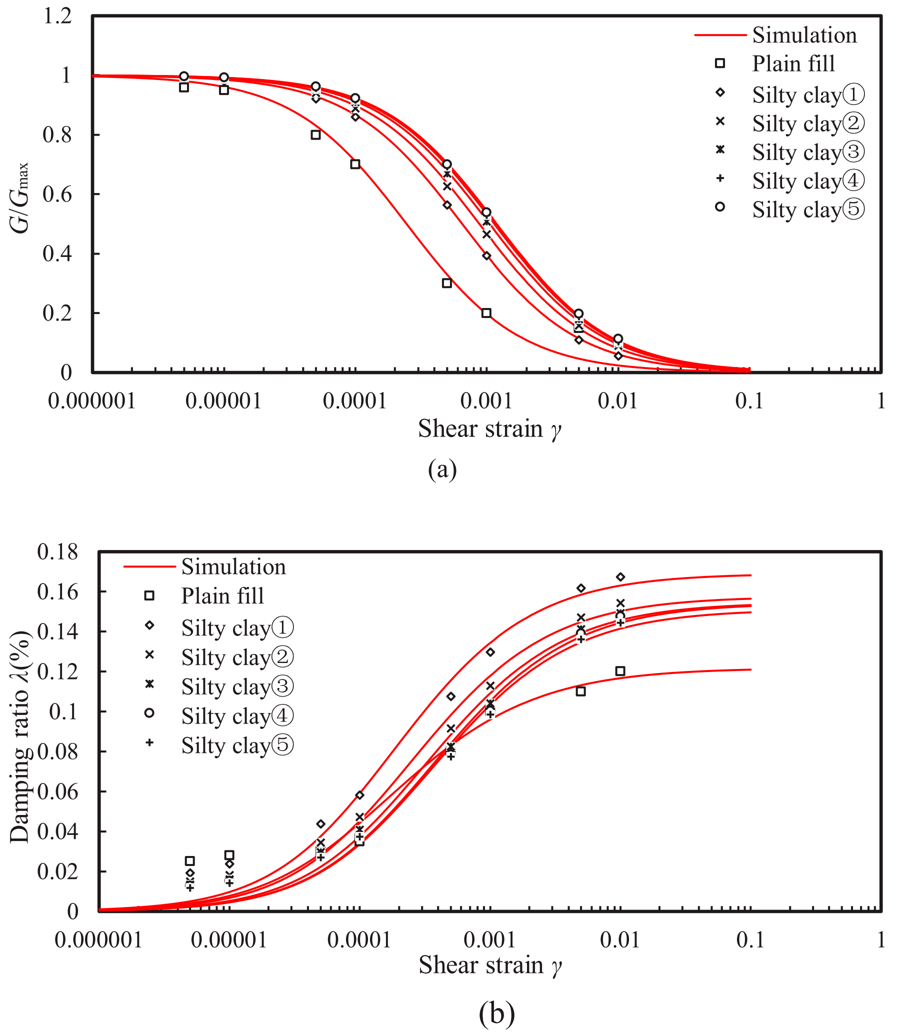

FIGURE 2
Comparison between the measurements and model simulations: **(A)** the $G/G_{max} \sim \gamma$ relationship and **(B)** $\lambda \sim \gamma$ relationship.

single-amplitude axial strain over 20 cycles (Amoly et al., 2016). Equations 5, 6 applied to sandy soils with shear wave velocities ranging from 120 to 250 m/s. According to Amoly et al. (2016), the R_L value derived from this formula tends to be greater than the value calculated using the method proposed by Andrus and Stoke (2000). Table 1 presents the parameters of PZ III model for the silty sand interlayer.

The generation and dissipation of EPWP were modeled using a fully coupled dynamic effective stress approach together with the generalized plasticity constitutive model, which simultaneously solves the equations of motion and fluid flow in the soil. The numerical model has been validated through various laboratory tests and model tests in the literature (Pastor et al., 1990; Xu et al., 2023).

2.3.2 Nonlinear constitutive model for non-liquefiable soils

The Wakai and Ugai (2004) model was employed to model dynamic characteristics of non-liquefiable soils in this study. The backbone and hysteresis curves of the model are given by Equations 7, 8 respectively:

$$\tau = \frac{G_0 \gamma}{1 + G_0 \gamma / \tau_f} \tag{7}$$

$$\tau = \frac{a\gamma^n + G_0 \gamma}{1 + b\gamma} \tag{8}$$

where τ and γ represent shear stress and shear strain, respectively, G_0 is the initial shear modulus and was calculated from the shear wave velocity, b and n are two model constants, a is the internal variable, G_0 and τ_f were given by Equations 9, 10, respectively:

$$G_0 = G_{0,r} P_a \left(\frac{p'}{P_a} \right)^m \tag{9}$$

$$\tau_f = \frac{\sqrt{3}}{2} \left(c \cos \varphi + p' \sin \varphi \right) \left(\cos \Theta - \frac{\sin \Theta \sin \varphi}{\sqrt{3}} \right) / R_f \tag{10}$$

where p' is the mean effective stress, P_a is the standard atmospheric pressure, Θ is Lode angle, and $G_{0,r}$, m, and R_f are model constants.

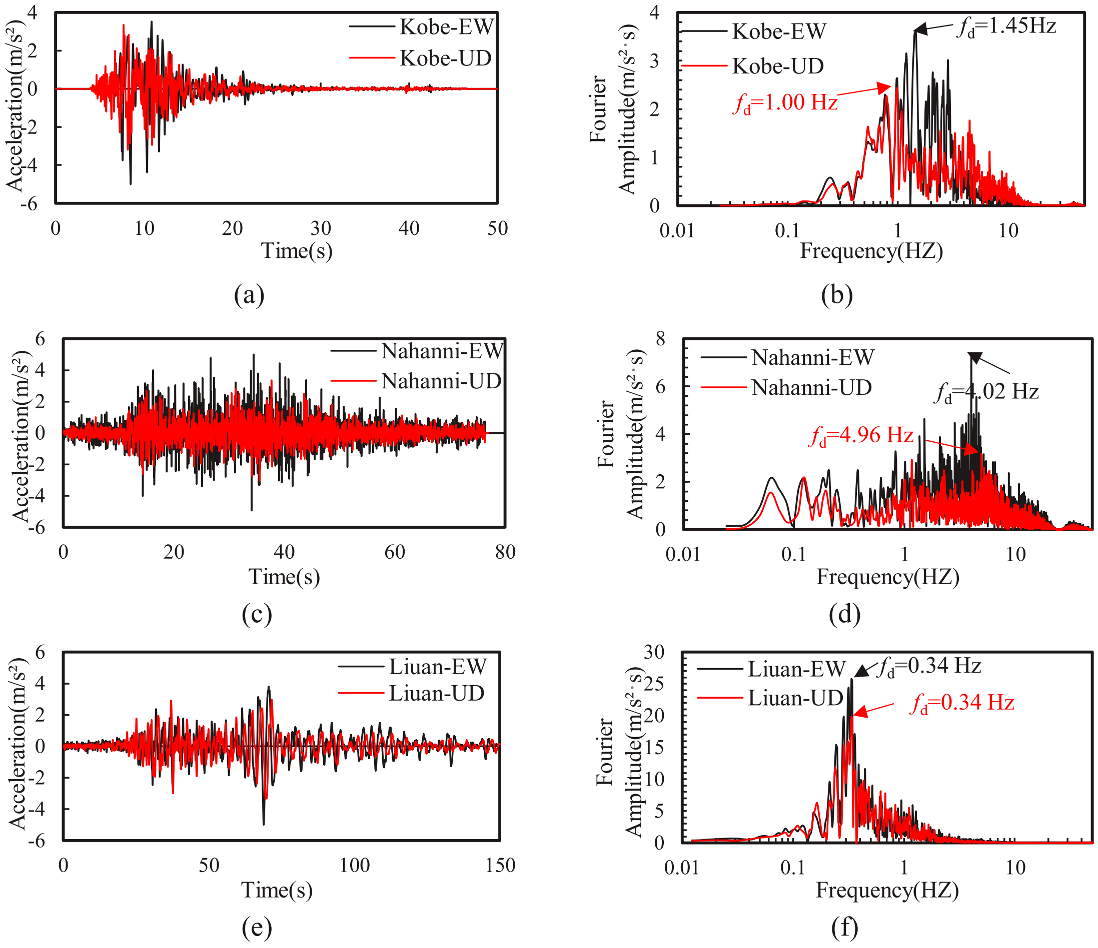

FIGURE 3
Time history of Fourier amplitude of the horizontal (EW) and vertical (UD) input motions: **(A)** Kobe, **(C)** Nahanni, and **(E)** Liuan input motions; **(B)** Kobe **(D)** Nahanni **(F)** Liuan Fourier amplitudes.

To accurately calibrate the parameters of the Wakai and Ugai (2004) model, this study used the GZZ-50 type resonant column apparatus to conduct element tests on different soils at WX-03 borehole, obtaining the shear modulus and damping curves of soils. Resonant column tests were conducted on samples with diameter of 5.0 cm and height of 10.0 cm. The test procedure is detailed in (ASTM, 2015). The Wakai and Ugai (2004) model parameters were then inversely determined using the UWLC model parameter calibration program. As shown in Figure 2, the model's simulation results corresponded well with the measurements. Table 2 gives model parameters of non-liquefiable soils at WX-03 borehole.

Note that P-wave velocity is indeed a crucial parameter in seismic analysis, especially when vertical ground shaking is involved. However, the calculation process typically focuses on the seismic effects of vertically propagating S-waves, and P-wave testing is generally more challenging than S-wave testing (Zhubayev and Ghose, 2012). Thus, only the shear wave velocity was measured in this study. In the finite element analysis, the soil was assumed to be isotropic, so the shear modulus derived from shear wave velocity results and Poisson's ratio, were used to calculate Young's modulus in the constitutive model for dynamic analysis under vertical seismic loading.

2.4 Boundary conditions

Static analysis is required before the dynamic analysis. The initial displacement and strain from the static analysis are reset to zero before starting the dynamic analysis. The purpose of the static analysis is to provide the initial stress for the dynamic analysis. In the static analysis, the lateral boundaries are fixed in the horizontal direction but are free to move in the vertical direction. In the dynamic analysis, the two lateral boundaries use the Multi-Point Constraints (MPC) boundary condition. The bottom boundary of the model is fixed in both static and dynamic analyses.

3 Results and discussions

To consider the impact of the spectral characteristics of input ground motions on site seismic response, this study selected three

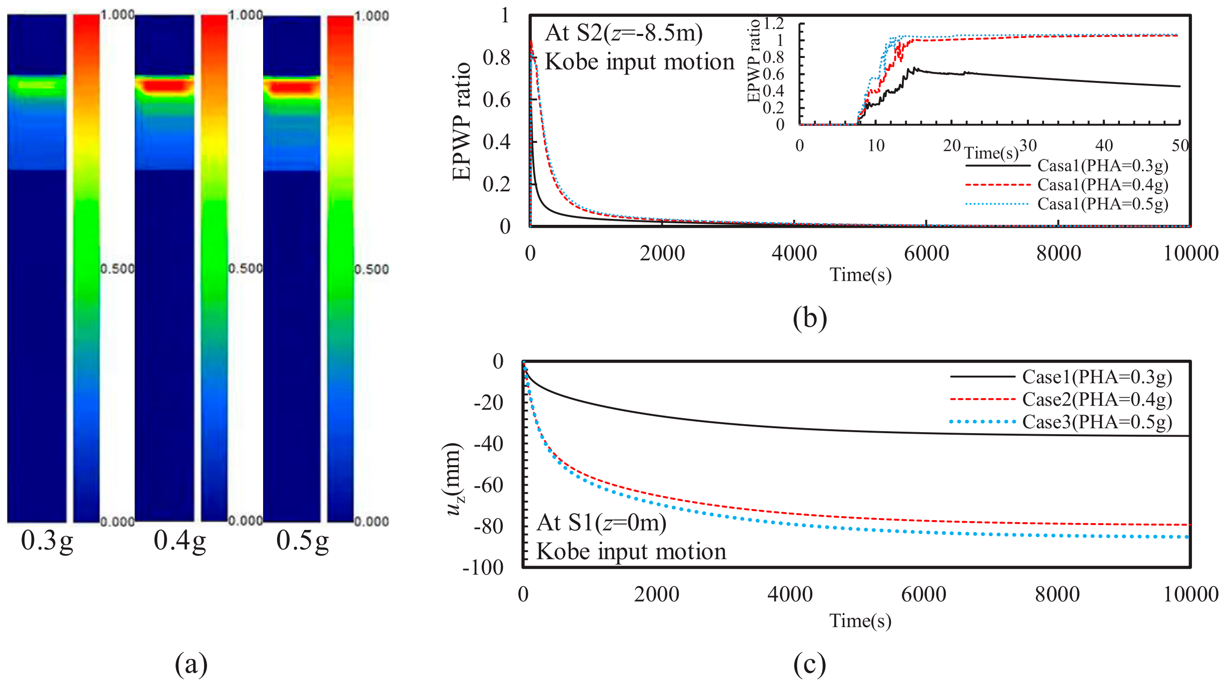

FIGURE 4
Effect of *PHA* on the **(A)** distribution of EPWP ratio after earthquake, **(B)** time history of EPWP ratio **(C)** and vertical displacement (u_z).

(i.e., Liu'an, Kobe, and Nahanni) seismic input ground motions with distinct spectral differences. Figure 3 shows the horizontal accelerations and Fourier amplitude for these three input motions with peak horizontal acceleration (*PHA*) of 0.5 g. It can be observed that the Kobe input motion has a uniform frequency distribution, indicating that its energy is evenly distributed across different frequency components. The Nahanni input motion is rich in high-frequency components, suggesting that it has stronger energy in the higher frequency range, which may significantly impact on the short-period response of structures. The Liu'an input motion is richer in low frequencies, which may have a greater impact on the long-period response of structures. The predominant frequencies (f_d) corresponding to the Liu'an, Kobe, and Nahanni input motions are 0.34 Hz, 1.45 Hz, and 4.02 Hz, respectively. Liuan wave is considered far-field seismic input motion, whereas Kobe and Nahanni waves are classified as near-field seismic input motions.

This study also considers the variation of *PHA* and peak vertical acceleration (*PVA*), with *PHA* ranging from 0.3g to 0.5 g. According to GB 50011-2010, 2016 and American Society of Civil Engineers, 2017, the general peak vertical ground motion is approximately 2/3 of the peak horizontal ground motion, thus, the ratio of *PVA* to *PHA* varies from 0 to 0.67. The vertical accelerations and corresponding Fourier amplitude of for *PVA*/*PHA* = 0.67 are also plotted in Figure 3. This study focuses on investigating the effects of the input motion frequency, *PHA*, and *PVA* on the site response at typical points, including the horizontal acceleration and acceleration response spectra, excess pore water pressure, and ground settlement.

In Sections 3.1, 3.2, we focus solely on the impact of horizontal ground excitation, setting *PVA* = 0. In Section 3.3, we examined the effects of vertical ground excitation, considering scenarios where both horizontal and vertical ground shaking occur simultaneously, with peak acceleration ratios of *PVA*/*PHA* = 0, 0.37, and 0.67. Table 3 gives the key influence factors considered in parametric studies.

3.1 Effect of *PHA*

Figure 4A shows the effect of *PHA* on the distribution of EPWP in the silty sand interlayer after the Kobe input motion. It can be seen that when *PHA* = 0.3g, the EPWP ratio in the entire silt interlayer was less than unity, indicating that liquefaction did not occur. Note that the EPWP ratio was defined as the ratio of EPWP to the initial effective vertical stress. Additionally, the peak value of the EPWP ratio in the silty sand interlayer also increased as the *PHA* increases. Particularly, when *PHA* = 0.4g, the EPWP ratio at the top of the silty sand interlayer reached unity, indicating that liquefaction has occurred (see Figure 4B). Moreover, when *PHA* increases from 0.4 g to 0.5 g, the liquefaction depth increased by approximately 7.4% in the silty sand interlayer.

A consolidation analysis was performed on the liquefiable site after earthquake, showing that the EPWP ratio decreased gradually with the time due to pore pressure dissipation under various *PHA*s (see Figure 4B). In the consolidation phase, the dissipation of EPWP relies on the magnitude of the EPWP following the earthquake; therefore, the settlement during this phase is mainly affected by the residual EPWP. The results indicate that the EPWP in the silty sand interlayer can completely dissipate after 10,000 s. Furthermore, *PHA* significantly affected the dissipation rate of the EPWP. In the case that liquefaction did not occur (*PHA* = 0.3 g), the EPWP ratio dropped to around 0.1 after approximately 212 s. In

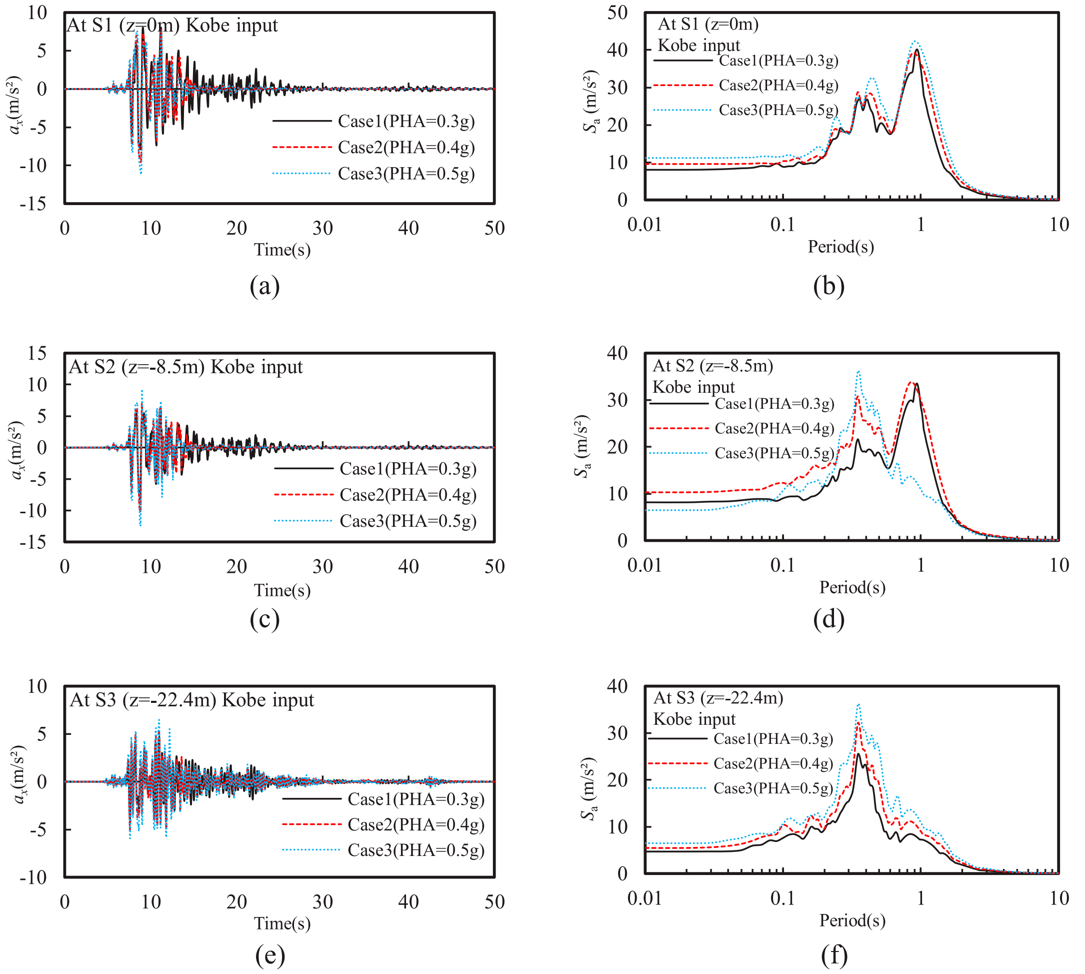

FIGURE 5
Effect of *PHA* on the time history of horizontal acceleration and spectral acceleration at different depths: **(A)** a_x and **(B)** S_a at $z = 0$ m; **(C)** a_x and **(D)** S_a at $z = -8.5$ m; **(E)** a_x and **(F)** S_a at $z = -22.4$ m.

contrast, the EPWP ratio took about 667 s to decrease to 0.1 when liquefaction occurred. Additionally, the *PHA* did not significantly impact the pore pressure dissipation rate after the silty sand interlayer liquefied. Moreover, the ground settlement induced by the earthquake increases with the peak ground motion (see Figure 4C). When the liquefaction did not occur at silty sand interlayer (*PHA* = 0.3 g), the maximum ground settlement was about 36.2 mm. However, the ground settlement increased by 119% at *PHA* = 0.4g and 135% at *PHA* = 0.5g, indicating that the EPWP associated to the liquefaction greatly affected the ground settlement. Thus, the residual EPWP, particularly after seismic events, can result in prolonged settlement due to the slow dissipation of excess pressures. This may lead to ongoing ground subsidence long after the earthquake, which poses a risk to long-term stability of underground structures.

Figure 5 shows the effect of *PHA* on the acceleration time histories and Fourier amplitude at typical points, including S1, S2, and S3 representing the point at the ground surface, the top and bottom of the silty sand interlayer, respectively. Overall, the peak horizontal acceleration at the top of the silty sand interlayer was greater than that at the bottom, indicating that even though the EPWP in the silty sand interlayer developed during the earthquake, the peak horizontal acceleration was still significantly amplified for various *PHA*s. As the *PHA* increased, the ratio of the peak horizontal acceleration at the top of the silty sand interlayer to that at the ground surface gradually increased. Especially, the peak horizontal acceleration at the top of the silty sand interlayer was much greater that that at the ground surface when *PHA* = 0.5 g. This is primarily because the silty sand interlayer exhibited significant cyclic mobility after liquefaction, which in turn leads to larger peak horizontal acceleration at this point. Moreover, the acceleration at the top of the silty sand interlayer becomes very small after liquefaction, at 14.7 s when *PHA* = 0.4 g and after 14.1 s at *PHA* = 0.5 g.

Figure 5 further illustrates that the spectral acceleration peak generally increased as *PHA* increased. Notably, the spectral acceleration the top of the silty sand interlayer and the ground surface exhibited largest spikes centered around a 1-s period, indicating that the rise in EPWP decreases high-frequency

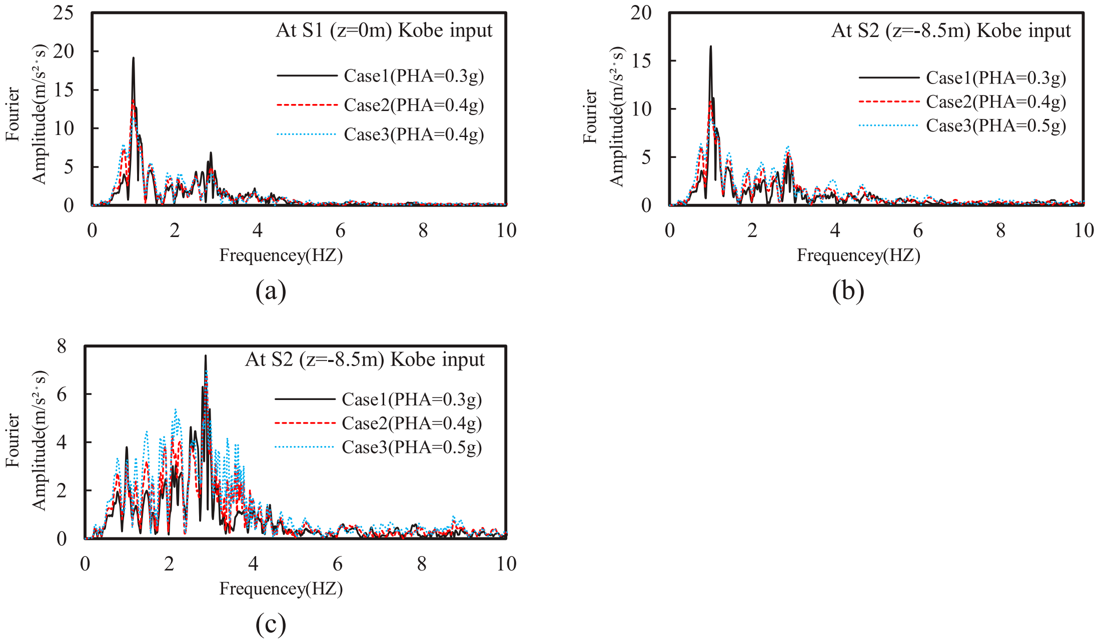

FIGURE 6
Effect of *PHA* on Fourier amplitude of horizontal acceleration at different depths: **(A)** z = 0 m; **(B)** z = −8.5 m; **(C)** z = −22.4 m.

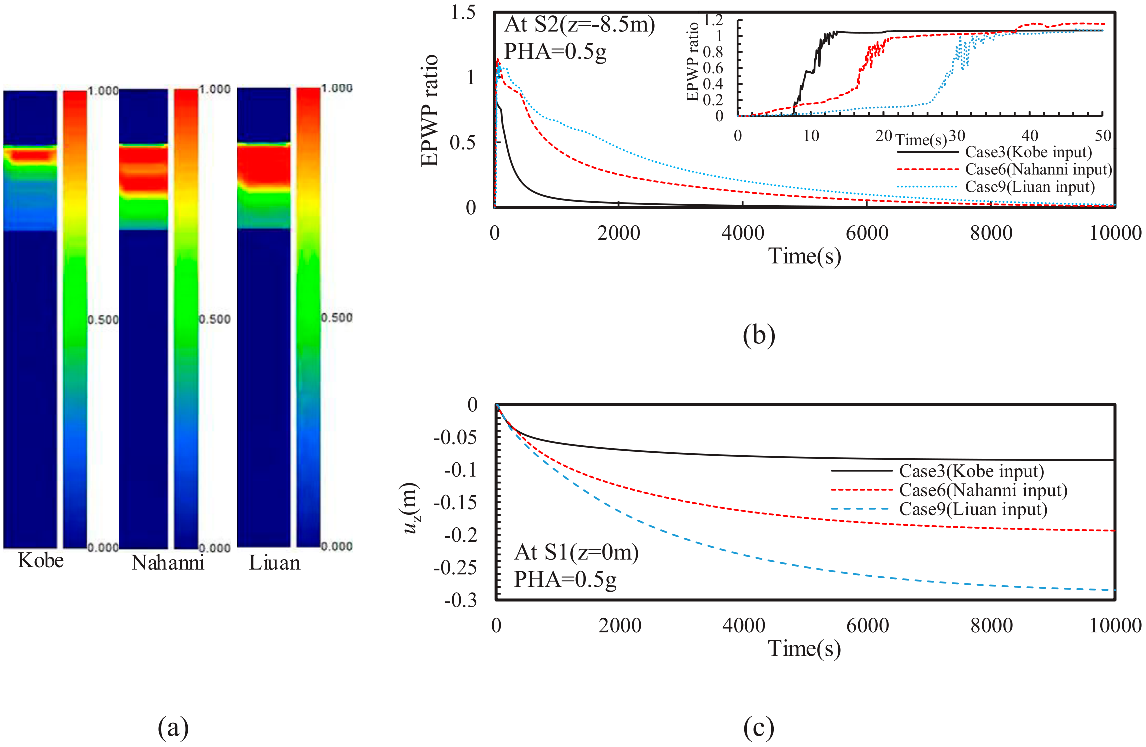

FIGURE 7
Effect of input motion frequency on the **(A)** distribution of EPWP ratio after earthquake, **(B)** time history of EPWP ratio **(C)** and vertical displacement (u_z)

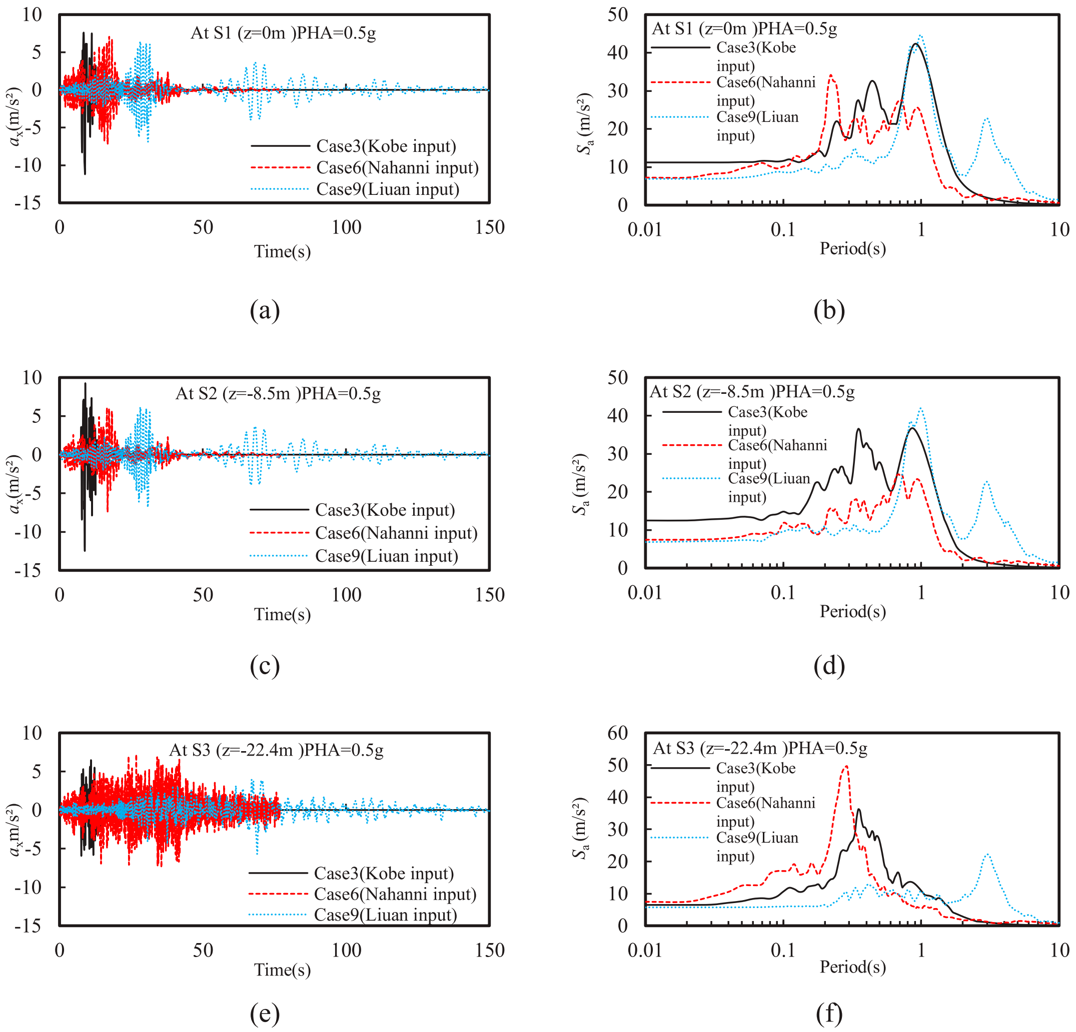

FIGURE 8
Effect of input motion frequency on the time history of horizontal acceleration and spectral acceleration at different depths: **(A)** ax and **(B)** Sa at z = 0 m; **(C)** ax and **(D)** Sa at z = −8.5 m; **(E)** ax and **(F)** Sa at z = −22.4 m.

components of seismic input motions while amplifying the low-frequency components. The Fourier amplitude also shows the largest spike at 1 Hz, and the Fourier amplitudes surrounding this spike gradually increased as the *PHA* increased (see Figure 6).

It is concluded that the increase in *PHA* results in a rise in EPWP within the silty sand interlayer, an increase in ground surface settlement, and a significant acceleration amplification at the top of the silty sand interlayer. These results demonstrate that *PHA* significantly impacts dynamic responses of ground containing liquefiable interlayers, and the presence of liquefiable interlayers may amplify the propagation effect of seismic input motions, resulting in more intense responses at the ground surface and in structures. These findings are important for understanding seismic liquefaction phenomena, assessing earthquake risks, and designing seismic mitigation measures in the case of the ground containing liquefiable interlayer.

3.2 Effect of input motion frequency

Figure 7 shows that liquefaction occurred in the silty sand interlayer under different input motions with identical *PHA* of 0.5 g. Moreover, the liquefaction depth was significantly greater under Nahanni and Liuan input motions compared to that under Kobe input motion. This is because the former two motions have richer low-frequency components; as shown in Figure 3, the Fourier amplitude within 1 Hz for these two motions is significantly greater than that of the latter. Additionally, the liquefaction depth caused by the Nahanni input motion was about 9.1% greater than that under the Liuan input motion. This was mainly due to the richer high-frequency components of the Nahanni motion, which can generate higher oscillatory EPWP in deeper soil layers. However, the Liuan input motion, which is rich in lower frequencies, resulted in higher residual EPWP in the silty sand interlayer. This further caused

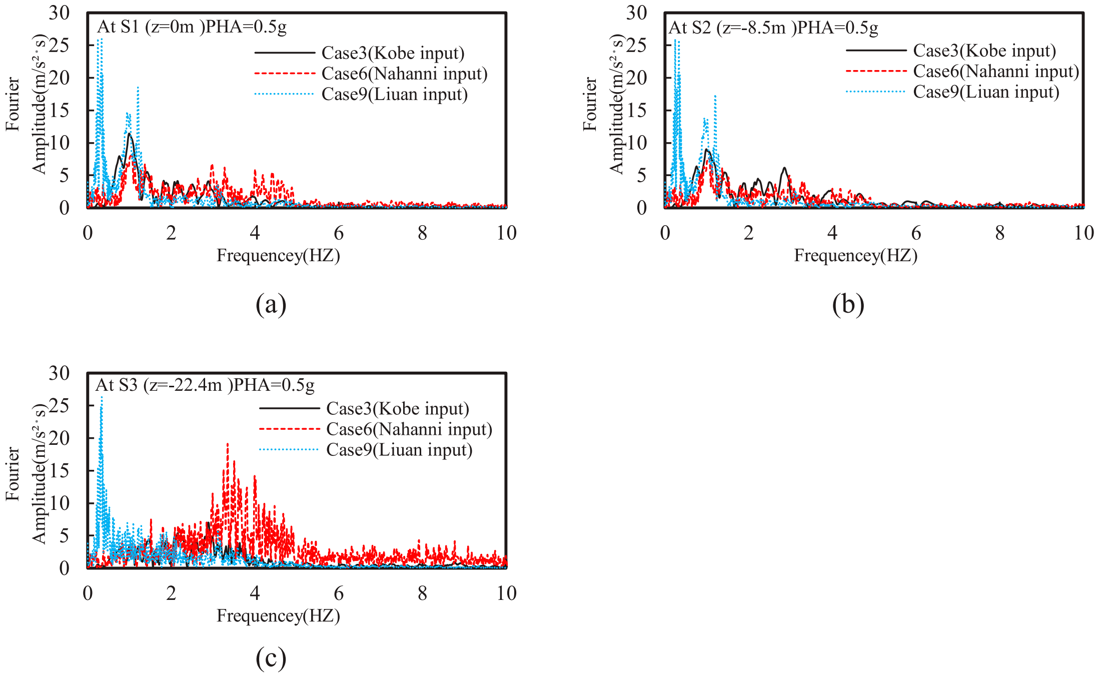

(a)

(b)

(c)

FIGURE 9
Effect of input motion frequency on Fourier amplitude of horizontal acceleration at different depths: **(A)** z = 0 m; **(B)** z = −8.5 m; **(C)** z = −22.4 m.

the slowest dissipation rate of EPWP at the top of the silty sand interlayer and the greatest ground settlement at the consolidation stage. Moreover, the maximum ground settlement under the Kobe input motion is only about 29.9% of that under Liuan input motion, primarily because the overall EPWP was lowest in the silty sand interlayer under Kobe input motion.

Figure 8 shows that the frequency content of input motions had a minimal impact on the peak horizontal acceleration at the bottom of the silty sand interlayer. However, the peak horizontal accelerations at the ground surface and the top of the silty sand interlayer under Kobe input motion were significantly higher than those under Nahanni and Liuan input motions. This is mainly because the liquefaction of the silty sand interlayer occurred after the peak of Kobe input motions, but the liquefaction occurred before the peak of Nahanni and Liuan ground motions. Moreover, a new spike with a period of approximately 1 s was observed at the top of the silty sand interlayer compared to that at the bottom of the silty sand interlayer (see Figures 8D–F). This reflects a common seismic response characteristic induced by the rise in EPWP within the silty sand interlayer. Moreover, a spike was observed at around 3 s in the spectral acceleration at both top and bottom of the silty sand interlayer, and the spectral acceleration with $T > 2$ s is not affected by the generation of EPWP in the silty sand interlayer.

Figure 9 further shows that Fourier amplitude of the high-frequency components (i.e., frequency larger than 3 Hz) significantly decreased after the Nahanni input motion passed through the silty sand interlayer. In contrast, there was a notable increase in the amplitude around 1 Hz at the top of the silty sand interlayer, which corresponds to the peak spectral acceleration observed at $T = 1$ s.

3.3 Effect of *PVA*

Figure 10A shows the effect of *PVA* on the distribution of EPWP ratio after earthquake. In this comparison, the *PVA*/*PHA* varies from 0 to 0.67. It can be observed that the liquefaction depth increased as *PVA* increased. This is because the increase in *PVA* resulted in higher EPWP within the silty sand interlayer, especially causing significant oscillations of EPWP (see Figure 10B), which is consistent with results reported in the existing literature (Xu et al., 2021b). Additionally, the lowest dissipation rate of EPWP was observed at *PVA/PHA* = 0.67, further indicating that higher *PVA* induces greater residual EPWP in the silty sand interlayer. The numerical results also confirms that the ground settlement increased with increasing *PVA*, as also reported by Tsaparli et al. (2016). This study further investigated the impact of input motion frequency on the maximum ground settlement under both horizontal and vertical input motions. As the *PVA/PHA* increased from 0 to 0.67, the maximum ground settlement under Nahanni input motion increased by 28%, followed by 22% under Kobe input motion, and 4% under Liuan input motion (see Figure 10C). This indicates that the vertical seismic component in near-field earthquakes has much more significant effect on the ground settlement in liquefiable sites than that in far-field earthquakes. Thus, the adverse effect of vertical seismic motion with combination of the input motion frequency should be carefully considered in practical engineering. As shown in Figure 12, the vertical seismic motion had minimal effect on the horizontal seismic response of liquefiable sites, including the acceleration time history and spectral acceleration. A new spike with a period of approximately 1 s was observed at the top of the silty sand interlayer compared to that at the bottom of the silty sand interlayer, reflecting

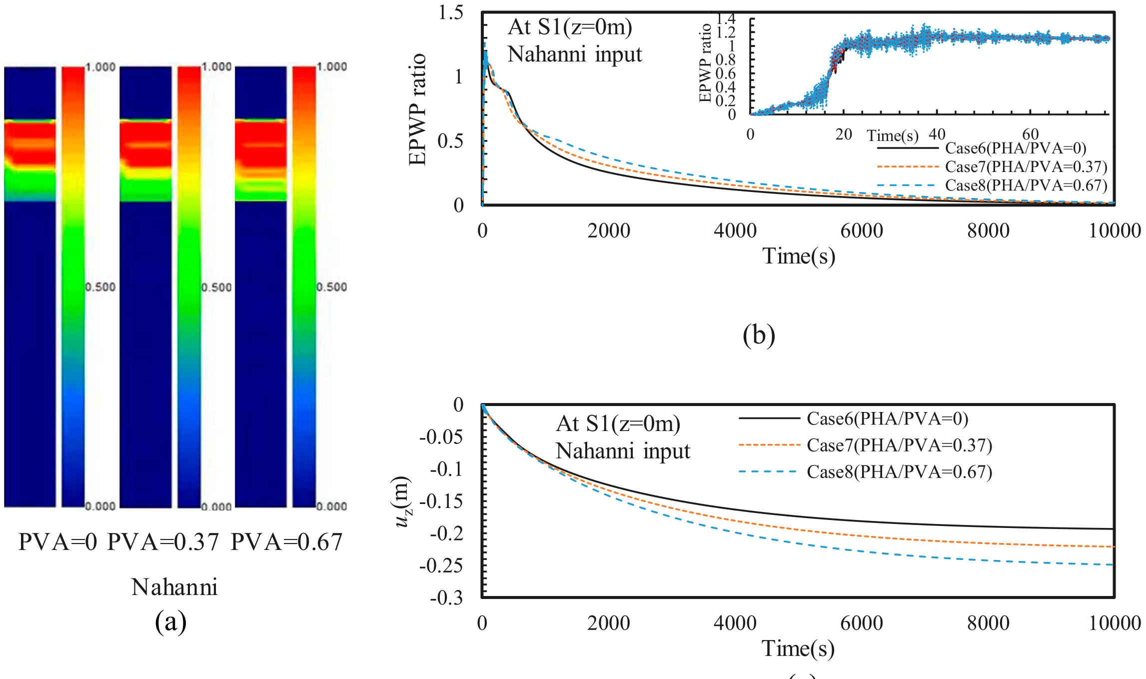

(a)

(b)

(c)

FIGURE 10
Effect of *PVA* on the **(A)** distribution of EPWP ratio after earthquake, **(B)** time history of EPWP ratio **(C)** and vertical displacement (u_z).

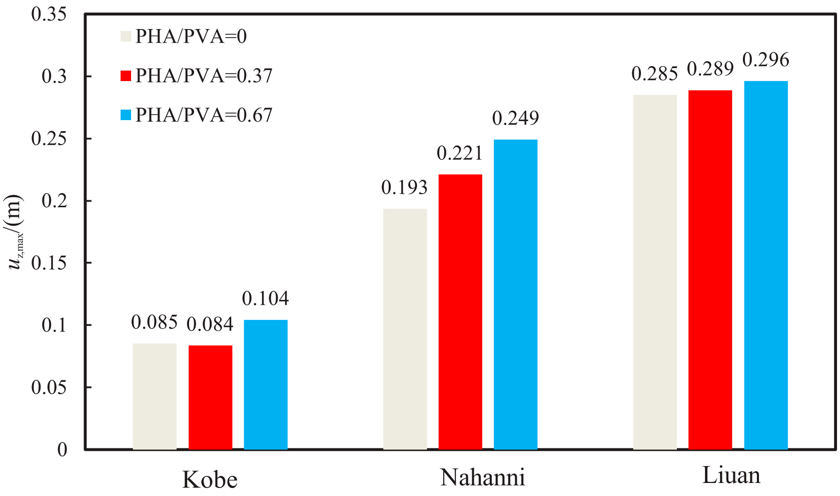

FIGURE 11
Effect of *PVA* on the maximum ground settlement for various input motions.

a common seismic response characteristic induced by the rise in EPWP within the silty sand interlayer. Moreover, a spike was observed at around 3 s in the spectral acceleration at both top and bottom of the silty sand interlayer, and the spectral acceleration with $T > 2$ s is not affected by the generation of EPWP in the silty sand interlayer.

In summary, the interaction between vertical and horizontal ground motions can significantly affect the seismic response of liquefiable soils. In our study, the vertical ground motion influences the generation of excess pore water pressure, while the horizontal motion contributes to shearing and displacement of the soil layers. The interaction is particularly important in near-field seismic events where vertical acceleration can amplify the liquefaction potential. Moreover, we recommend that engineers consider both horizontal and vertical seismic components when designing foundations for structures in liquefiable areas. In particular, structures in regions with rich low-frequency seismic input, such as near-field earthquake zones, should be designed to accommodate increased ground

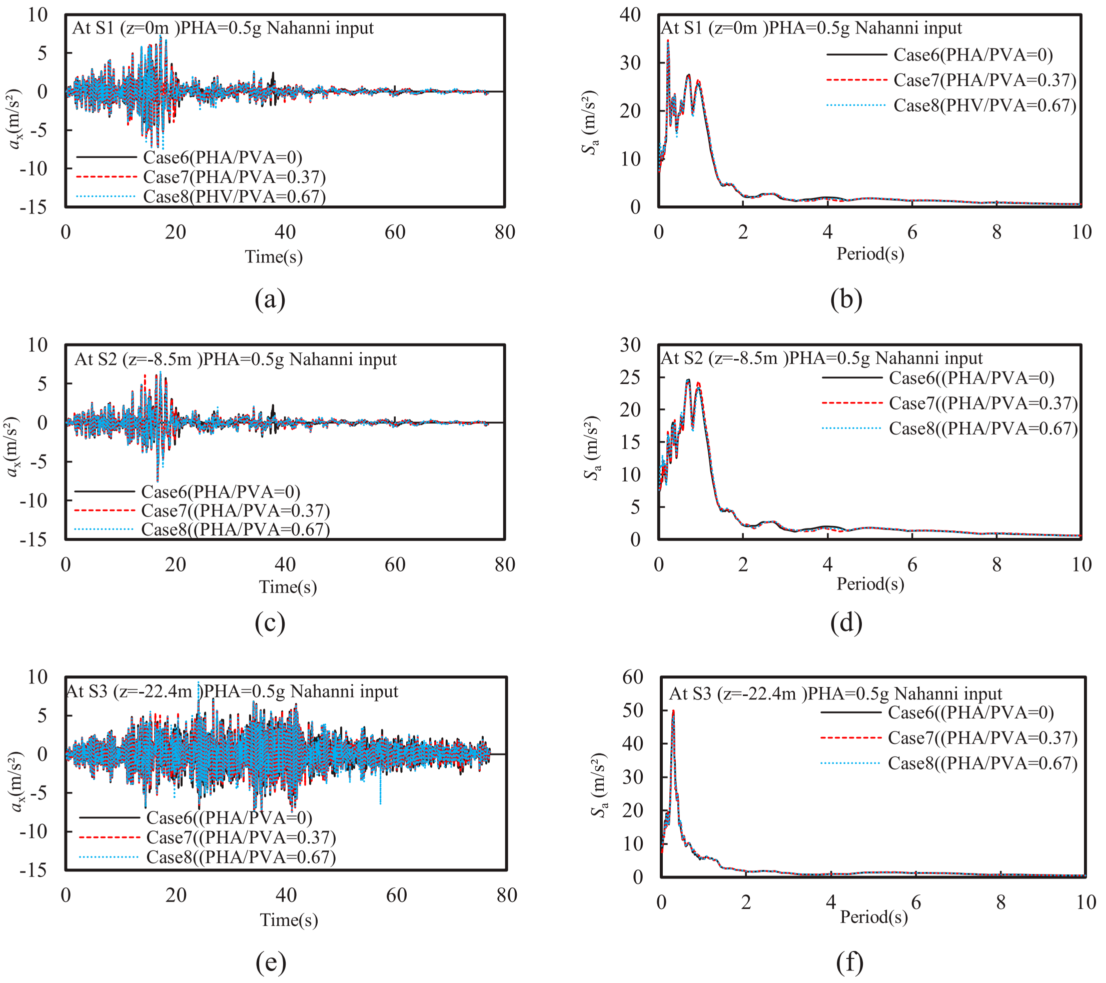

FIGURE 12
Effect of *PVA* on the time history of horizontal acceleration and spectral acceleration at different depths: **(A)** a_x and **(B)** S_a at $z = 0$ m; **(C)** a_x and **(D)** S_a at $z = -8.5$ m; **(E)** a_x and **(F)** S_a at $z = -22.4$.

settlement and the potential for deeper liquefaction. Additionally, the use of ground improvement techniques, such as soil compaction or drainage systems, may be necessary to reduce the risk of long-term settlement.

4 Conclusion

A typical borehole with a liquefiable interlayer in the Yangtze River Delta Plain region of China was thoroughly and numerically investigated in this study, the following conclusions were obtained.

- The increase in *PHA* leads to a rise in EPWP within the silty sand interlayer, an increase in ground settlement, and a significant acceleration amplification at the top of the silty sand interlayer. The acceleration at the ground surface becomes very small after liquefaction of the silty sand interlayer.
- The liquefaction depth was significantly greater under Nahanni and Liuan input motions compared to that under Kobe input motion. This is because the former two motions have richer low-frequency components.
- The Liuan input motion, which is rich in lower frequencies, resulted in higher residual EPWP in the silty sand interlayer. This further caused the slowest dissipation rate of EPWP at the top of the silty sand interlayer and the greatest ground settlement at the consolidation stage.
- The ground settlement generally increased with increasing *PVA*. As the *PVA/PHA* increased from 0 to 0.67, the maximum ground settlement under Nahanni input motion increased by 28%, followed by 22% under Kobe input motion, and 4% under Liuan input motion. This indicates that the vertical seismic component in near-field earthquakes has much more significant effect on the ground settlement in liquefiable sites than that in far-field earthquakes.

The findings are particularly relevant for sites with similar soil compositions, such as those with liquefiable interlayers. However, the methodology, including the fully coupled dynamic analysis and the use of generalized plasticity models, can be applied to other regions with different soil conditions by recalibrating the model parameters based on local soil characteristics.

Data availability statement

The raw data supporting the conclusions of this article will be made available by the authors, without undue reservation.

Author contributions

X-BP: Conceptualization, Funding acquisition, Writing–original draft. YG: Software, Writing–original draft. Y-YX: Data curation, Writing–original draft. X-ST: Methodology, Writing–review and editing. L-YX: Funding acquisition, Methodology, Writing–original draft.

Funding

The author(s) declare that financial support was received for the research, authorship, and/or publication of this article. This work was supported by Jiangsu Earthquake Administration Scenario Earthquake Construction and Application Innovation Team (Grant No. 2022-03) and the National Natural Science Foundation of China (Grant No. 52378345).

Conflict of interest

The authors declare that the research was conducted in the absence of any commercial or financial relationships that could be construed as a potential conflict of interest.

Publisher's note

References

Adampira, M., and Derakhshandi, M. (2020). Influence of a layered liquefiable soil on seismic site response using physical modeling and numerical simulation. *Eng. Geol.* 266, 105462. doi:10.1016/j.enggeo.2019.105462

American Society of Civil Engineers (2017). Minimum design loads and associated criteria for buildings and other structures. *Am. Soc. Civ. Eng.* doi:10.1061/9780784414248

Amoly, R. S., Ishihara, K., and Bilsel, H. (2016). The relation between liquefaction resistance and shear wave velocity for new and old deposits. *Soils Found.* 56 (3), 506–519. doi:10.1016/j.sandf.2016.04.016

Andrus, R. D., and Stokoe, K. H. (2000). Liquefaction resistance of soils from shear-wave velocity. *J. geotechnical geoenvironmental Eng.* 126 (11), 1015–1025. doi:10.1061/(asce)1090-0241(2000)126:11(1015)

Astm, A. (2015). *D4015–15: standard test methods for modulus and damping of soils by fixed-base resonant column devices.* West Conshohocken: ASTM international.

Biot, M. A. (1956). Theory of propagation of elastic waves in a fluid-saturated porous solid. II. Higher frequency range. *J. Acoust. Soc. Am.* 28 (2), 179–191. doi:10.1121/1.1908241

Cai, F., Hagiwara, T., Imamura, S., and Ugai, K. (2002). "2D Fully coupled liquefaction analysis of sand ground under tank," in *Proceedings of the 11th Japan earthquake engineering symposium*, 819–824. doi:10.1093/treephys/22.12.819

Chen, W. Y., Wang, Z. H., Chen, G. X., Jeng, D. S., Wu, M., and Zhao, H. Y. (2018). Effect of vertical seismic motion on the dynamic response and instantaneous liquefaction in a two-layer porous seabed. *Comput. Geotechnics* 99, 165–176. doi:10.1016/j.compgeo.2018.03.005

Cubrinovski, M., Rhodes, A., Ntritsos, N., and Van Ballegooy, S. (2019). System response of liquefiable deposits. *Soil Dyn. Earthq. Eng.* 124, 212–229. doi:10.1016/j.soildyn.2018.05.013

Ecemis, N. (2021). Experimental and numerical modeling on the liquefaction potential and ground settlement of silt-interlayered stratified sands. *Soil Dyn. Earthq. Eng.* 144, 106691. doi:10.1016/j.soildyn.2021.106691

Fan, H. F., Wang, Y. Z., Chen, G. X., Chen, W. Y., Zhao, K., and Zhu, S. D. (2023). Nonlinear seismic response analysis of layered seabed considering seawater-seabed coupling effects. *Front. Mar. Sci.* 10, 1270721. doi:10.3389/fmars.2023.1270721

Forum 8 Co Ltd (2005). "Finite element fully coupled dynamic effective stress analysis program (UWLC)," in *Electrical manual 2005. Product Info: dynamic effective stress analysis for ground(UWLC)*. forum8.co.jp).

GB 50011-2010 (2016). *Code for seismic Design of buildings*. Beijing: China Architecture and Building Press.

Jia, M. C., and Wang, B. Y. (2013). Liquefaction testing of stratified sands interlayered with silt. *Appl. Mech. Mater.* 256, 116–119. doi:10.4028/www.scientific.net/amm.256-259.116

Pastor, M., Zienkiewicz, O. C., and Chan, A. (1990). Generalized plasticity and the modelling of soil behaviour. *Int. J. Numer. Anal. Methods Geomech.* 14 (3), 151–190. doi:10.1002/nag.1610140302

Shen, Y., Zhong, Z., Li, L., Du, X., and El Naggar, M. H. (2022). Seismic response of shield tunnel structure embedded in soil deposit with liquefiable interlayer. *Comput. Geotechnics* 152, 105015. doi:10.1016/j.compgeo.2022.105015

Song, C. X., Tang, X. W., Zhang, C. P., and Wang, K. (2024). Investigating the influence of an approach bridge on a pile-supported wharf at a liquefiable site under horizontal and vertical seismic excitations. *Soil Dyn. Earthq. Eng.* 185, 108872. doi:10.1016/j.soildyn.2024.108872

Sui, T., Yang, M., Peng, L., Chen, J., Zhang, C., and Zheng, J. (2024). Wave-induced residual response and liquefaction of a nonhomogeneous layered seabed. *Front. Mar. Sci.* 11, 1360641. doi:10.3389/fmars.2024.1360641

Sun, R., and Yuan, X. M. (2004). Effect of soil liquefaction on response spectrum of surface acceleration. *World Earthq. Eng.* 20 (3), 33–38.

Sun, R., Zhao, Q., and Yuan, X. (2014). Comparison between acceleration response spectra on liquefaction and non-liquefaction sites. *Rock Soil Mech.* 35, 299–305. doi:10.16285/j.rsm.2014.s1.021

Tsai, C. C., and Liu, H. W. (2017). Site response analysis of vertical ground motion in consideration of soil nonlinearity. *Soil Dyn. Earthq. Eng.* 102, 124–136. doi:10.1016/j.soildyn.2017.08.024

Tsaparli, V., Kontoe, S., Taborda, D. M., and Potts, D. M. (2016). Vertical ground motion and its effects on liquefaction resistance of fully saturated sand deposits. *Proc. R. Soc. A Math. Phys. Eng. Sci.* 472 (2192), 20160434. doi:10.1098/rspa.2016.0434

Wakai, A., and Ugai, K. (2004). A simple constitutive model for the seismic analysis of slopes and its applications. *Soils found.* 44 (4), 83–97

Xiu, Z., Wang, S., Ji, Y., Wang, F., and Ren, F. (2020). Experimental investigation on liquefaction and post-liquefaction deformation of stratified saturated sand under cyclic loading. *Bull. Eng. Geol. Environ.* 79, 2313–2324. doi:10.1007/s10064-019-01696-8

Xu, L. Y., Cai, F., Wang, G. X., Ugai, K., Wakai, A., Yang, Q. Q., et al. (2013). Numerical assessment of liquefaction mitigation effects on residential houses: case histories of the 2007 Niigata Chuetsu-offshore earthquake. *Soil dynam. Earthq. Eng.* 53, 196–209. doi:10.1016/j.soildyn.2013.07.008

Xu, L. Y., Cai, F., Zhang, J. Z., Pan, D. D., Wu, Q., and Chen, G. X. (2021b). Evaluation of grain size and content of nonplastic fines on undrained behavior of sandy soils. *Mar. Georesources and Geotechnol.* 39 (10), 1215–1229. doi:10.1080/1064119X.2020.1821847

Xu, L. Y., Chen, W. Y., Cai, F., Song, Z., Pan, J. M., and Chen, G. X. (2023). Response of soil–pile–superstructure–quay wall system to lateral displacement under horizontal and vertical earthquake excitations. *Bull. Earthq. Eng.* 21 (2), 1173–1202. doi:10.1007/s10518-022-01572-z

Xu, L. Y., Song, C. X., Chen, W. Y., Cai, F., Li, Y. Y., and Chen, G. X. (2021a). Liquefaction-induced settlement of the pile group under vertical and horizontal ground motions. *Soil Dyn. Earthq. Eng.* 144, 106709. doi:10.1016/j.soildyn.2021.106709

Xu, L. Y., Zhang, J. Z., Cai, F., Chen, W. Y., and Xue, Y. Y. (2019). Constitutive modeling the undrained behaviors of sands with non-plastic fines under monotonic and cyclic loading. *Soil dynam. Earthq. Eng.* 123, 413–424. doi:10.1016/j.soildyn.2019.05.021

Xue, Y. Y., Wang, X. G., and Cai, F. (2023). Effect of inclined pile on seismic response of bridge abutments undergoing liquefaction—induced lateral displacement: case study of Nishikawa bridge in the 2011 Great East Japan earthquake. *Front. Mater.* 10, 1185210. doi:10.3389/fmats.2023.1185210

Yang, J., Sato, T., Savidis, S., and Li, X. S. (2002). Horizontal and vertical components of earthquake ground motions at liquefiable sites. *Soil Dyn. Earthq. Eng.* 22 (3), 229–240. doi:10.1016/S0267-7261(02)00010-6

Yao, J., and Lin, Y. (2023). Influence analysis of liquefiable interlayer on seismic response of underground station structure. *Appl. Sci.* 13 (16), 9210. doi:10.3390/app13169210

Youd, T. L., and Carter, B. L. (2005). Influence of soil softening and liquefaction on spectral acceleration. *J. Geotechnical Geoenvironmental Eng.* 131 (7), 811–825. doi:10.1061/(ASCE)1090-0241(2005)131:7(811)

Zienkiewic, Z. O. C., Chan, A. H. C., Pastor, M., Schrefler, B. A., and Shiomi, T. (1999). *Computational geotechnics with special reference to earthquake engineering.* Sussex, United Kingdom: John Wiley & Sons Ltd.

Zienkiewicz, O. C., Chan, A. H. C., Pastor, M., Schreffer, B. A., and Shiomi, T. (1999). *Computational geomechanics with special reference to earthquake engineering.* Chichester, England: Wiley

Zhubayev, A., and Ghose, R. (2012). Contrasting behavior between dispersive seismic velocity and attenuation: advantages in subsoil characterization. *J. Acoust. Soc. Am.* 131 (2), EL170–EL176. doi:10.1121/1.3678692

Frontiers in Earth Science

TYPE Original Research
PUBLISHED 19 December 2024
DOI 10.3389/feart.2024.1514086

OPEN ACCESS

EDITED BY
Qi Yao,
China Earthquake Administration, China

REVIEWED BY
Guihua Chen,
China Earthquake Administration, China
Zhonghai Wu,
Chinese Academy of Geologi-cal Sciences (CAGS), China

*CORRESPONDENCE
Junjie Ren,
renjunjie@gmail.com,
renjunjie@cugb.edu.cn

RECEIVED 20 October 2024
ACCEPTED 02 December 2024
PUBLISHED 19 December 2024

CITATION
Hu F and Ren J (2024) Displacement hazard from distributed ruptures of strike-slip faults in the Tibetan plateau.
Front. Earth Sci. 12:1514086.
doi: 10.3389/feart.2024.1514086

Displacement hazard from distributed ruptures of strike-slip faults in the Tibetan plateau

Fangbo Hu[1,2] and Junjie Ren[3,4,5]*

[1]School of Emergency Management Science and Engineering, University of Chinese Academy of Sciences, Beijing, China, [2]National Institute of Natural Hazards, Ministry of Emergency Management of China (MEMC), Beijing, China, [3]School of Earth Sciences and Resources, China University of Geosciences, Beijing, China, [4]Key Laboratory of Compound and Chained Natural Hazards Dynamics, MEMC, Beijing, China, [5]Key Laboratory of Intraplate Volcanoes and Earthquakes (China University of Geosciences, Beijing), Ministry of Education, Beijing, China

Large strike-slip earthquakes are generally characterized by long surface rupture zones and relatively concentrated displacement distribution. The displacements on main seismogenic faults have been well studied and assessed by numerous empirical relations. Detailed mapping of the deformation zone of strike-slip earthquakes in the past decades indicates that distributed ruptures beyond the main faults have controlled the width of surface deformation zones and influenced the distribution of damages and earthquake-induced geological disasters. Therefore, the displacement hazard assessment from distributed surface rupture along strike-slip faults is urgent for disaster prevention and mitigation and the seismic safety of linear engineering. The Tibetan Plateau is marked by a series of strike-slip faults accompanied by lateral extrusion of material due to the Cenozoic collision of the Indian and Eurasian plates. In this study, we collected the surface rupture data of five strike-slip earthquakes in the Tibetan Plateau during the past decades, including the 1997 Mani (M_W 7.5), 2010 Yushu (M_W 6.9), 2014 Yutian (M_W 6.9), 2021 Maduo (M_W 7.4), and 2022 Menyuan (M_W 6.6) earthquakes. Then, we preprocess the original data to form the standardized dataset after removing the fractures due to non-tectonic factors such as landslides, gravity instability under seismic ground motion, and so on. Based on the standardized dataset, the surface rupture displacements generated by strike-slip faults are incorporated into a probabilistic displacement hazard analysis framework, and a probability model of the surface rupture displacement distribution is established for the Tibetan Plateau. This model estimates the probability per unit area of finding a distributed rupture that allows a displacement that exceeds a displacement threshold at a given distance from the principal fault. This study not only provides a framework for the probabilistic displacement hazard of distributed ruptures from strike-slip faults but also supports the seismic hazard assessment of linear engineering crossing strike-slip faults in the Tibetan Plateau.

KEYWORDS

distributed rupture, strike-slip fault, probabilistic displacement hazard, Tibetan plateau, displacement threshold

1 Introduction

Large strike-slip earthquakes are marked generally by long surface ruptures and relatively narrow deformation zones (Xu et al., 2006; Choi et al., 2018; Antoine et al., 2022; Nurminen et al., 2022). The displacement on a strike-slip fault is always estimated by empirical relations between magnitude and coseismic displacement based on surface rupture measurements of large earthquake cases (Wells and Coppersmith, 1994; Cheng et al., 2020; Shaw, 2023). However, detailed mapping of surface ruptures of recent strike-slip earthquakes demonstrates that the coseismic displacement of surface ruptures occurs on the main fault plane and associated secondary structures (e.g., Antoine et al., 2022; Liu-Zeng et al., 2024). The displacement on the secondary structures is commonly accommodated by the distributed ruptures in a wide zone (Figure 1). In some cases, the role of distributed displacement is more than that on the main fault (Antoine et al., 2022; Liu-Zeng et al., 2024). This type of distributed displacement caused a wider surface rupture zone and affected the distribution of coseismic damages and earthquake-triggered geological hazards. It is urgent to assess the distributed displacement hazard of strike-slip faults for seismic safety of large linear engineering and seismic disaster prevention and mitigation.

Increasing studies in the past 20 years have been conducted on evaluating the displacement from active strike-slip faults (Lee and Trifunac, 1995; Peter, 2010; Inoue et al., 2020; Nurminen et al., 2020; Visage et al., 2023). A Probabilistic fault displacement hazard analysis (PFDHA) framework was first proposed based on permanent fault displacements and the classical probabilistic seismic hazard analysis was applied to assess the seismic risk of the Yucca Mountain nuclear waste disposal project in the United States (Youngs et al., 2003). When more attention focused on the distribution of surface displacement, six types of regression curves were used to fit the coseismic surface slip distribution of historical earthquakes and the spatial distribution pattern of surface displacement of large earthquakes along their seismogenic fault strike were explored (Wesnousky, 2006; Wesnousky, 2008). Since many related studies had been carried out in America, researchers tried to conduct similar method in other regions, using the actual seismic data in Japan with the PFDHA method to establish a surface-rupturing fault displacement prediction model which is applicable to Japan (Takao et al., 2013). But these studies do not consider the effect of distributed ruptures on the spatial distribution of coseismic displacement along a strike-slip fault. A unified method for calculating on-fault and off-fault displacement was presented based on fault sections with different geometry and structures. The off-fault displacement is similar to distributed displacement and may include some deformation that does not generate surface ruptures (Antoine et al., 2022). In addition, the distribution curve of coseismic displacements perpendicular to the fault strike is inconsistent with the specific coseismic offset data of large earthquakes (Petersen et al., 2011). Further work tried to mainly focus on distributed ruptures, the distance from the main fault was taken into account in a probability model to predict the displacement distribution of distributed rupture crossing the fault traces using surface rupture data from five strike-slip earthquakes in northern America. These five earthquakes span a range of magnitudes between M_W 6.4 and 7.3, four of which are from M_W 7.1 to 7.3 (Rodriguez Padilla and Oskin, 2023). However, the applicability of this model to strike-slip faults in other areas is unknown.

In western China, the increasing seismic potential of many strike-slip faults poses a high risk of the displacement of linear engineers across active faults. Especially the 2022 Menyuan earthquake (M_W 6.6) offset the railway tunnel (Li et al., 2023), stimulating the displacement hazard of distributed ruptures along strike-slip faults. The probability of permanent displacement was estimated across faults of the second line of West-East natural gas transmission pipeline by using the potential focal region parameters of China's ground motion parameter zoning map (Zhao et al., 2008). Based on the surface-rupturing data of strike-slip faults in China, both parabolic and elliptic prediction equations related to surface displacement and surface rupture length were presented. Similarly, the permanent displacement risk curve of surface-rupturing zones of the Zemuhe active fault zone was obtained combined with the practical application of PFDHA method (Jin, 2019). However, these earlier studies only use the uniform models and do not consider the

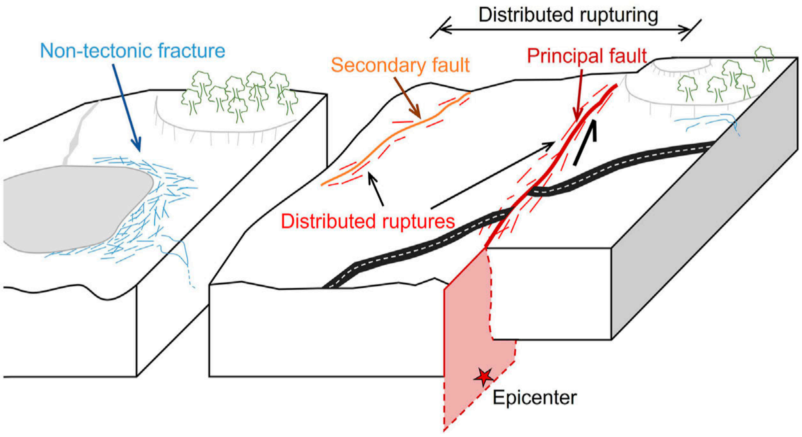

FIGURE 1
Schematic diagram of surface rupture patterns caused by a large strike-slip earthquake.

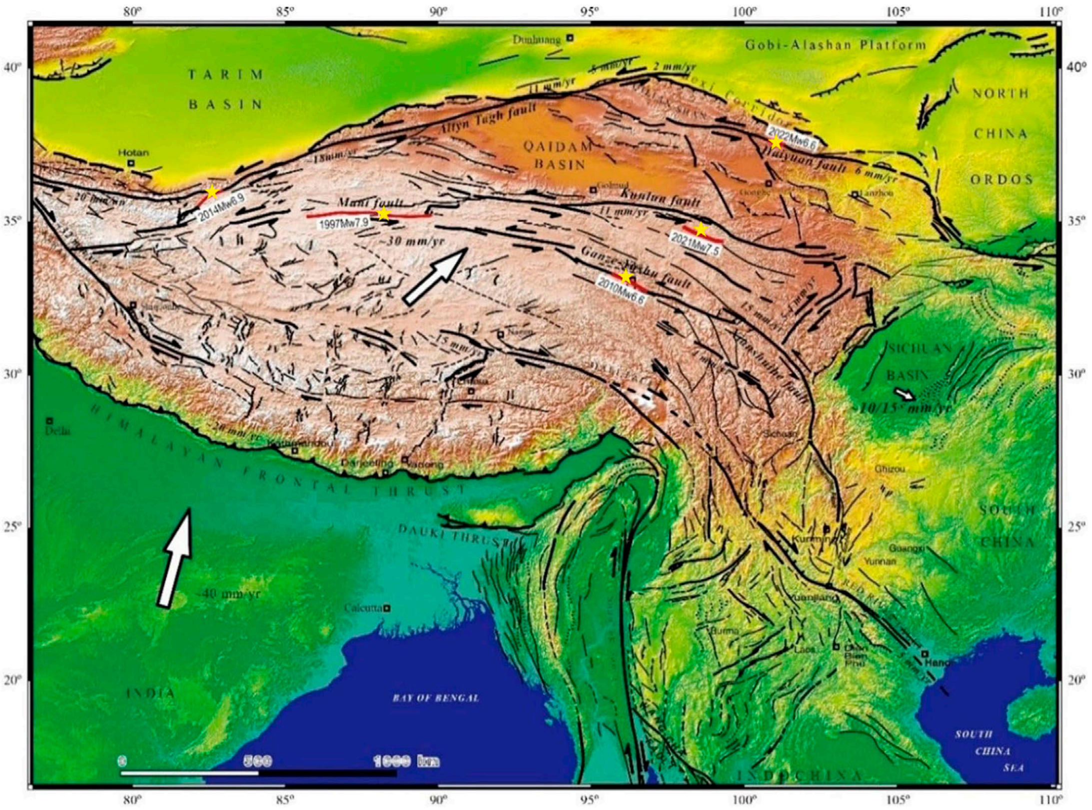

FIGURE 2
Active faults of the Tibetan Plateau and the recent well-studied surface-rupturing strike-slip earthquakes. Adapted from Tapponnier et al. (2001). Yellow stars represent the epicenters of the five earthquakes used in this study. Red lines show the surface rupture zones of the five earthquakes used in this study.

application of these models in China. Also, the distributed ruptures along a strike-slip fault are not taken into account.

In the Tibetan Plateau, several large earthquakes along large strike-slip faults have been well studied, and associated detailed surface ruptures have been mapped (Figure 2) (Li et al., 2012; Ren and Zhang, 2019; Yuan et al., 2021; Ren et al., 2022; Li et al., 2023; Liu-Zeng et al., 2024), providing an opportunity to construct the model of displacement hazard of distributed ruptures from strike-slip faults in China. In this study, we collected the recent surface rupture data of five strike-slip earthquakes in the Tibetan Plateau and built the probability model to predict the displacement hazard of distributed rupture crossing the fault trace when a certain magnitude occurs. This study not only proposes a workflow for the probabilistic displacement hazard of distributed ruptures from strike-slip faults but also supports the seismic hazard assessment of linear engineering crossing strike-slip faults in the Tibetan Plateau.

2 Tectonic setting of the Tibetan plateau

The Tibetan Plateau, controlled by the Cenozoic Indian-Eurasian collision, forms the most intense area of tectonic activity in China. Accompanied by the uplift of the plateau, the material began to the outward extrusion and produced many large strike-slip faults, such as the Kunlun, Altyn Tagh, Haiyuan, Ganze-Yushu-Xianshuihe faults (Molnar and Tapponnier, 1978; Xu et al., 2005; Ren et al., 2013). These faults undergo the late Quaternary slip rate of ~5–10 mm/yr and have ruptured in serval large earthquakes in the past 20 years (Kirby et al., 2007; Ren et al., 2013; Yao et al., 2019).

We choose five strike-slip earthquakes in the northern Tibetan Plateau: the 1997 Mani (M_W 7.5), 2010 Yushu (M_W 6.9), 2014 Yutian (M_W 6.9), 2021 Maduo (M_W 7.4), and 2022 Menyuan (M_W 6.6) earthquakes (Figure 2) (Table 1). The original datasets are mainly obtained by scanning published papers or from relevant experts and researchers. When the specific methods collecting raw data may vary from person to person, field measurement and optical image correlation are usually chosen in current studies. In addition to the basic data of the five earthquakes in TableX, since they happened in different regions and seasons along with other possible factors, the actual geological and structural characteristics and the surface condition of every earthquake are significantly different, resulting in different surface fractures.

The 1997 Mani earthquake ruptured the left-lateral Mani fault, a possible westernmost segment of the Kunlun fault (Shan et al., 2006; Ren and Zhang, 2019). This earthquake occurred in November 1997 when the temperature was below freezing point and the epicentral area was covered by permafrost. The rupture zone of the Baixue Lake section is located in the lacustrine plain and passes through

TABLE 1 The basic characteristic information of the five earthquakes in our study.

Eq_name	Eq_date	M_W	Length/km	Maximum offset/m	Average offset/m
Mani	1997.11.8	7.5	~170	~7	~5–6
Yushu	2010.4.14	6.9	~65	~2.4	~1.3
Yutian	2014.2.12	6.9	~37	~0.84–0.9	~0.39–0.52
Maduo	2021.5.22	7.4	~151	~3.6	~0.35
Menyuan	2022.1.8	6.6	~27	~3.7	~1.0–1.5

a series of large-scale ice water alluvial fans, and the Chaoyang-Shuangduan Lake section created a fault-plug pond formed by seismic steep ridges blocking the flow of melting ice and snow (Ren and Zhang, 2019).

The 2010 Yushu earthquake occurred on the Yushu segment of the Ganz-Yushu fault (Li et al., 2012; Sun et al., 2012). Located in the alpine region at a high altitude, Longbao Lake and the surrounding water were frozen during this earthquake, leading to a unique surface rupture trace in such frozen regions: ice cracks. The ice fissure zone is distributed in a planar shape and large scale, accompanied by sand liquefaction, showing a normal component dipping the Longbao Lake (Sun et al., 2012).

The 2014 Yutian earthquake mainly ruptured the left-lateral strike-slip Altyn Tagh fault (ATF) system with normal-slip (Li et al., 2016; Yuan et al., 2021). The earthquake vibrations near the Xiaoerkule Lake caused the instability of the diluvial fan, and the landslide and graben system formed after the slide of the salty lake's shoreline due to gravity, which belongs to the associated shallow deformation. This earthquake was located in the inner flow area of the Tibetan Plateau, in the middle of the rupture zone a thick loose sedimentary cover was formed based on the lake, which would magnify the seismic rupture in the shallow surface and enlarge the surface rupture width (Yuan et al., 2021).

The 2021 Maduo earthquake mainly ruptured the left-lateral strike-slip fault with a partly normal slip, the southeastern branch of the Kunlun fault zone, the Jiangcuo fault (Ren et al., 2022). This earthquake ruptured across a long-range area with complex landform, including many valleys, lakes, wetlands, grasslands, mountains and some sand dunes, etc (Pan et al., 2021; Ren et al., 2022). In the rupture section across Mustan Bridge, north of Huanghe Township and the valley of Yellow River, as the rupture zone is mainly distributed along the valley, a large number of tensile fractures parallel to the river channel are formed due to slope instability, accompanied by sandblasting water and sand liquefaction (Liu-Zeng et al., 2024).

The 2022 Menyuan earthquake mainly ruptured the left-lateral strike-slip fault with a slight thrust component, the middle segment of Qilian-Haiyuan fault (Xue et al., 2022; Li et al., 2023). This earthquake happened in winter when the Liuhuanggou River was frozen, causing the ice river surface and flood plain to break in the nature of thrust with the phenomenon of tension cracks on the bank slope and slope slide under the effect of gravity from slope instability on the right bank of the river, which may amplify the actual left-lateral offsets (Li et al., 2023).

With the continuous development of western China, a large number of pipeline projects have been built or are being built in the Tibetan Plateau region. The damages of strike-slip faulting can be found in these five earthquakes selected in this study: Maduo earthquake caused the serious collapse of Mustan Bridge as part of the Gongyu Expressway, which is a major traffic route (Ren et al., 2022); The dislocation of the Lanzhou-Urumqi High-speed Railway's Daliang Tunnel caused by Menyuan earthquake directly disrupted the traffic in this section for up to 18 months (Li et al., 2023); Yushu earthquake caused serious damage to the national and provincial trunk roads and transportation infrastructure in the Yushu area, with an affected area of 20,000 square kilometers (Li et al., 2012). Therefore, predicting the distribution of surface rupture caused by strike-slip earthquakes in the Tibetan Plateau region can help maintain the safety of transportation arteries in the region and provide reference for avoidance locations for transportation arteries currently being built or planned to be built in the region, in order to reduce potential damage in the future.

3 The rupture displacement probability model

Rodriguez Padilla and Oskin (2023) proposed a mathematical approach to estimate fault displacement based on data from detailed surface-ruptures strike-slip earthquakes:

$$P(S > S_0|x, M_W) = P(rupture|x)P(S > S_0|x, rupture, M_W). \quad (1)$$

Equation 1 shows the probability per unit area of finding a distributed rupture that accommodates a displacement that exceeds a displacement threshold at a given distance from the principal fault. The equation is produced by the joint probability of two parts: the former $P(rupture|x)$ is the probability of rupture occurring per unit area at a distance x from the fault; The latter $P(S > S_0|x, rupture, M_W)$ is the probability of finding a displacement that exceeds the threshold at a given distance from the fault for a given earthquake magnitude, given the presence of a rupture. In the following paragraphs, the process of establishing these two parts will be carried out separately before being combined into the final equation (Rodriguez Padilla and Oskin, 2023).

$P(rupture|x)$ can be calculated by studying the spatial distribution of the rupture density, which can be given by the inverse power law (e.g., Padilla et al., 2022):

$$V(x) = V_0\left(\frac{x + x_{fr}}{x_{fr}}\right)^{-\gamma}. \tag{2}$$

In which V_0 is the rupture density at the origin in number of ruptures per unit area ($1\,m^2$), x_{fr} is a normalized factor which is related to the uncertainty of the location of the principal fault trace in meters, the exponent γ is the slope of the decay of rupture density with distance for values of $x \gg d$ in log-log space or scaling exponent. $V(x)$ is the probability of a rupture occurrence per unit $1\,m^2$.

With reference to the inverse power law used in Equation 2, we try to analyze the relationship between the displacement measurements and the distance to the principal fault trace:

$$\lambda(x) = \beta\left(\frac{x + x_S}{x_S}\right)^{-n}. \tag{3}$$

In which λ is the mean of the displacement at every distance bin, β is the average displacement at the origin, x is the location away from the principal fault in meters, x_S is a normalized factor which we set as $1\,m$ in this equation, and n is the slope of the relationship between mean displacement and distance in log-log space or scaling exponent.

To deeply understand the meanings of above parameters, we put them back in actual situation to help with this. The parameter V_0 describes the amount of the surface ruptures per unit area on the principal fault trace, so as the parameter β which describes the average displacement value on the principal fault trace. These two parameters are used to describe the surface-ruptures and the displacement on the principal fault. Unlike V_0 and β, the parameter γ and n are both the slope of the best-fitting curve in log-log space which can describe the state of decay.

By comparing several distribution functions, it is found that the population of displacement measurements can be better described by exponential distributions, and the distribution can be described as follows:

$$f(S|x) = \frac{1}{\lambda}e^{\frac{-S}{\lambda}}. \tag{4}$$

Combining Equations 3, 4 yields:

$$f(S|x) = \frac{1}{\beta}\left(\frac{x + x_S}{x_S}\right)^{n} e^{-\frac{S}{\beta}\left(\frac{x+x_S}{x_S}\right)^n}. \tag{5}$$

This equation is a probability density function (PDF) of displacement measurements with distance x from the principal fault trace. To solve the probability of finding a displacement that exceeds S_0 with a given earthquake magnitude:

$$\begin{aligned} P(S > S_0|x, rupture, M_W) &= \int_{S_0}^{S_{max}} \frac{1}{\beta}\left(\frac{x + x_S}{x_S}\right)^{n} e^{-\frac{S}{\beta}\left(\frac{x+x_S}{x_S}\right)^n} dS \\ &= -e^{-\frac{S}{\beta}\left(\frac{x+x_S}{x_S}\right)^n}\Big|_{S_0}^{S_{max}} \end{aligned} \tag{6}$$

Since the model focuses on the displacements on the distributed ruptures which do not tend to be of large value, the evaluation limits the threshold $S_0 \ll S_{max}$ to appropriately predict the probability of distributed displacements above the threshold S_0. Completing the integration of Equation 6 with this application can yield:

$$P(S > S_0|x, rupture, M_W) = e^{\frac{-S_0}{\beta}\left(\frac{x+x_S}{x_S}\right)^n}. \tag{7}$$

Combining Equations 2, 7 yields the final model:

$$P(S > S_0|x, M_W) = V_0\left(\frac{x + x_{fr}}{x_{fr}}\right)^{-\gamma} e^{\frac{-S_0}{\beta}\left(\frac{x+x_S}{x_S}\right)^n}. \tag{8}$$

This model is presented to calculate the probability per unit area of finding a distributed rupture that accommodates a displacement that exceeds a displacement threshold at a given distance from the principal fault (Rodriguez Padilla and Oskin, 2023). This probability model can quantify the displacement hazard of surface ruptures and estimate the expected displacement distribution caused by strike-slip faults, to provide reference data for the design, evaluation, and maintenance of engineering structures and lifelines located near or across strike-slip faults.

The entire probability model involves the calculation of multiple unknown parameters, which will all influence the final results. Therefore, after clarifying the model-building process, a brief analysis of the characteristics of each parameter is needed, and then the expected results of the theoretical model should be summarized as a reference for further research.

The origin rupture density V_0 and the origin average displacement β reflect the rupture and displacement conditions along each principal fault trace of the earthquake, and further affect the establishment of their respective models. A larger V_0 and β will result in higher $P(S > S_0)$ at the same location. The influence of parameter V_0 on $P(S > S_0)$ is greater than that of parameter β when $S_0 = 0.01, 0.1$ m, the probability curve with a larger V_0 gradually dissociates above other curves with the increase of distance x; When the threshold S_0 is large, the influence of parameter β on $P(S > S_0)$ becomes prominent, which actually reflects the magnitude dependence of parameter β: the small magnitude earthquake event tend to have a small β, and its probability curve gradually dissociates below other curves with the increase of distance x.

For the magnitude dependence of parameter β, the equation was proposed between moment magnitude M_W and mean displacement β to explore the empirical relationship between them (Wells and Coppersmith, 1994):

$$log_{10}(\beta) = bM_W - a, \tag{9}$$

where parameters a and b are regression coefficients derived from the best fit of the data using the least square method, and all fitted data used are strike-slip earthquakes. When $S_0 = 0.5$ m, the $P(S > S_0)$ of the smallest magnitude earthquake is significantly smaller than that of other earthquakes. In other words, for strike-slip earthquakes with smaller magnitude, the probability of large rupture occurring at a certain distance from the fault will be significantly lower than that of earthquakes with larger magnitude, which also matches our prediction about the characteristics of the surface rupture displacement distribution for strike-slip earthquakes.

According to the definition, the values of the exponents γ and n obtained by fitting are affected by the rupture density and average displacement of each earthquake respectively, but there is a reasonable range of values. After obtaining the respective parameters and models of each earthquake, a theoretical model is established. The parameters of the theoretical model are obtained by combining all the seismic data used and fitting through Equations 2, 3, and the range of the exponents γ and n obtained by the joint fitting will be affected by all the seismic data used.

The reasonable outputs of theoretical model should also be summarized after the analysis of the characteristics of each parameter. The reasonable results obtained after the establishment of the theoretical model are consistent. The rupture density curve from the fit of Equation 2 shows a downward trend, with certain fluctuations at the end; The scatter-fitting curve of displacement measurements from Equation 3 also showed a downward trend, and the scatters concentrated around the best fitting curve with a little isolated from the entirety.

Then comes to the final model output by Equation 8, it can be seen from the curve that the theoretical $P(S > S_0)$ decreases with the increase of fault-perpendicular distance, and the slope keeps increasing. Set with the input of moment magnitude $M_W = 7$ and threshold $S_0 = 0.1$ m, $P(S > S_0)$ has dropped to about 1/1,000 when the distance reaches about 100 m, and at 1,000 m it has dropped to less than 1/1,000, reaching a relatively small risk probability value. Such results indicate that there is a very low probability for the surface ruptures in the area far away from the principal rupture trace to accommodate a large value of displacement.

In this study, we introduce the approach of Rodriguez Padilla and Oskin (2023) to the surface rupture dataset of large strike-slip earthquakes in the Tibetan Plateau and then build the displacement probability distribution model. By analyzing the model building process and output results of the theoretical model, we can summarize the reasonable results of the theoretical model and use it as a reference to guide the subsequent model-building work in China.

4 Data preprocessing

Detailed analysis of the surface rupture dataset indicates that the coseismic surface rupture zone of a large strike-slip earthquake consists primarily of principal ruptures along the main fault and secondary ruptures caused by the secondary fault or fault branch (Figure 1). In addition, minor fractures occurred outside of the main fault zone. These fractures are related to non-tectonic factors such as landslides, and gravity instability under seismic ground motion (Liu-Zeng et al., 2024). These minor fractures are generally located in the local environment and are not directly produced by fault displacement. Therefore, we should remove these minor fractures, and only tectonic ruptures are involved in our analysis.

After preliminary sorting of the five original earthquake data (map documents and statistical tables of displacement measurements at the rupture), it is found that the original data will record the surface rupture traces with event particularity caused by the earthquake itself due to structural characteristics and some other causes (Li et al., 2012; Li et al., 2016; Ren and Zhang, 2019; Pan et al., 2021; Xue et al., 2022). Since the model is expected to be applied to a wide range of the Tibetan Plateau, to reduce the impact of non-tectonic factors (such as seismic motion) on the model results, we formulate criteria for the screening of the original data combined with the rupture characteristics of the five typical earthquakes on the Tibetan Plateau, hoping to get more consistent data to obtain a more uniform result and model.

For the convenience of data storage and search, we store all the data in a standardized format after data filtering. After comparing the data processing methods of standardized empirical databases that have been generated in recent years (e.g., Ancheta et al., 2013; Chiou et al., 2008; Nurminen et al., 2022), we chose to refer to the Fault Displacement Hazards Initiative (FDHI) database hosted and maintained by the Natural Hazards Risk and Resilience Research Center at the University of California, Los Angeles, to conduct standardized processing of surface rupture data form these five earthquakes in China (Sarmiento, 2021). The buildup of the model in this study mainly needs two parts of data: surface rupture maps and surface rupture displacement measurement, which are sorted into ESRI Shapefile (*.SHP format) and table form, respectively, after standardized processing.

Based on the original data collected from these five earthquakes, we first screened the surface rupture traces based on the following four criteria (Figure 3):

1. Through image comparison, the rupture traces around the water body are generally interpreted as resulting from the instability of the water body under seismic ground motion. These ruptures strike along the boundary of the water body and do not have a similar strike to the main fault. Such fractures are removed.
2. The ruptures associated with landsliding of a local topography that deviate significantly from the orientation of the main fault were eliminated. These ruptures are generally distributed around a landslide and do not have a uniform direction.
3. Remove the rupture traces originating from surface deformation in complex structural areas, such as large stepovers, the tips of a strike-slip fault, and so on.
4. Previous studies indicate that the tectonic-related coseismic deformation generated by a strike-slip fault is generally not distributed in the area too far away from the principal fault (Xu et al., 2006; Sun et al., 2012; Antoine et al., 2022.) Combining the original rupture traces of these five typical earthquakes, we opted to retain the rupture traces within 1 km from the principal fault and exclude those located beyond this distance.

After completing the standardized filtering of the original surface rupture traces maps, the displacement measurements located on the removed rupture traces are also deleted to ensure the uniformity of the data used. Then we unified the format of surface rupture displacement measurements according to that of FDHI (Sarmiento, 2021). Currently, the displacement measurements for each earthquake as recorded by various scholars are typically documented and reported separately in the original data, including horizontal slip and vertical component (e.g., Li et al., 2012; Li et al., 2016; Pan et al., 2021; Li et al., 2023). It is important to note that we focus on the horizontal slip of a strike-slip rupture and the influence of other factors causing vertical slip in a local area is not considered in this study. Therefore, all original displacement measurements should be classified before calculation and organized into a uniform representation of net horizontal slip.

After all original data have been preprocessed, we conduct the following work such as quantifying the fracture density and describing the variation in displacement measurements at the fracture point with the distance from the main fault. We integrated the FDHI database's definitions of principal rupture and the location of principal faults in each seismic event, and consequently, a

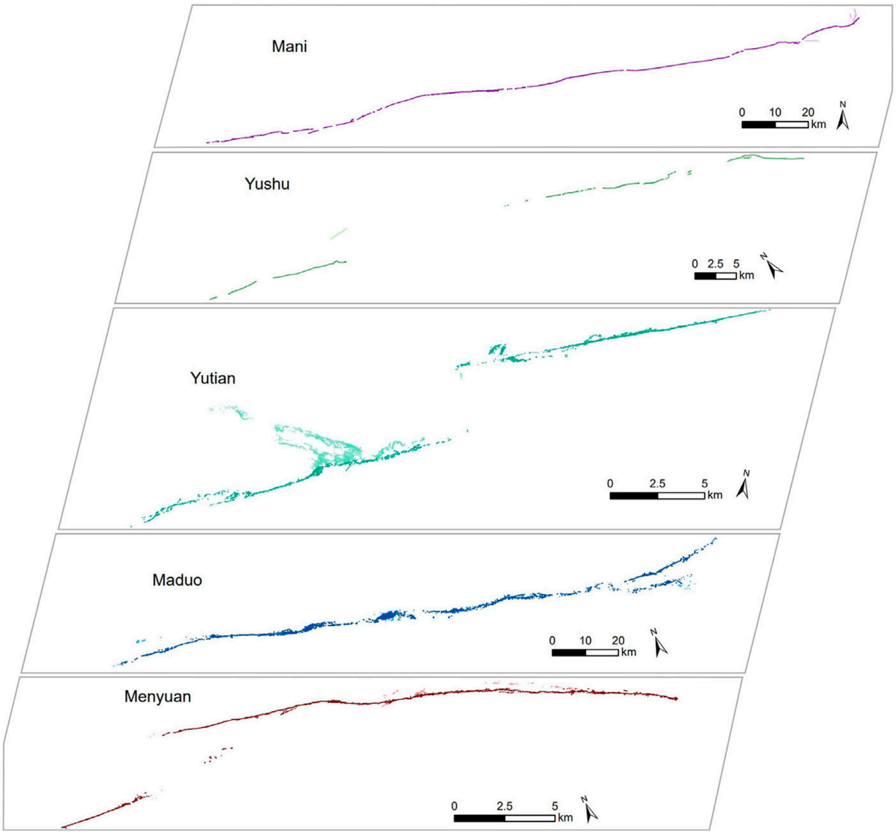

FIGURE 3
The mapped surface rupture traces of the Mani, Yushu, Yutian, Maduo, and Menyuan earthquakes. The traces in a light color are non-tectonic fractures, and the traces in a dark color are principal and secondary ruptures used in this study. The surface rupture data of Mani earthquake are from Ren and Zhang (2019). The data of Yushu earthquake are from Li et al. (2012), Sun et al. (2012). The data of Yutian earthquake are from Yuan et al. (2021). The data of Maduo earthquake are from Liu-Zeng et al. (2024), Pan et al. (2021), Ren et al. (2022), and the Menyuan data are from Li et al. (2023).

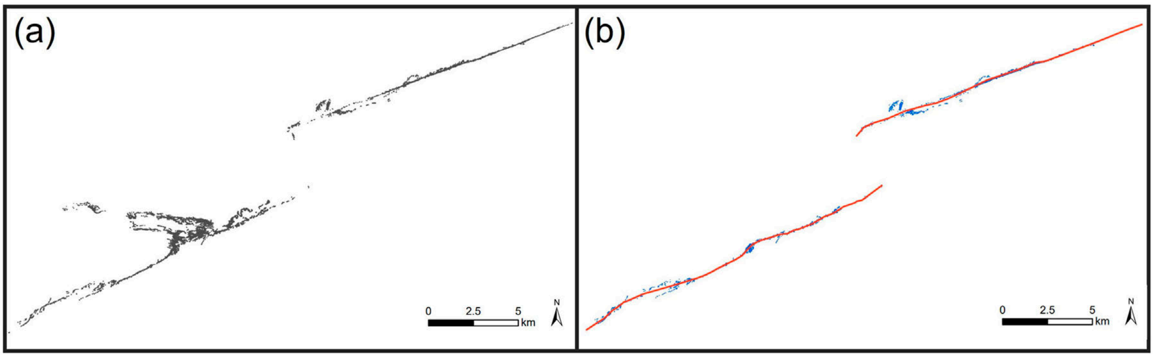

FIGURE 4
Preprocessing of the surface ruptures of the Yutian earthquake. **(A)** The original surface ruptures from high-resolution imagery and field observations. **(B)** The non-tectonic factures are removed after data preprocessing, and the main fault is highlighted in red.

simplified principal rupture trace was delineated (Figure 4). A singular, continuous fault trace was defined along the densely distributed and consistent principal ruptures. This approach can enhance the convenience of data processing in the subsequent model development by utilizing a limited number of rupture trace lines.

5 Results of rupture-displacement probability model

After pre-processing of the original surface rupture data of these five earthquakes, we built our model based on these data. Firstly,

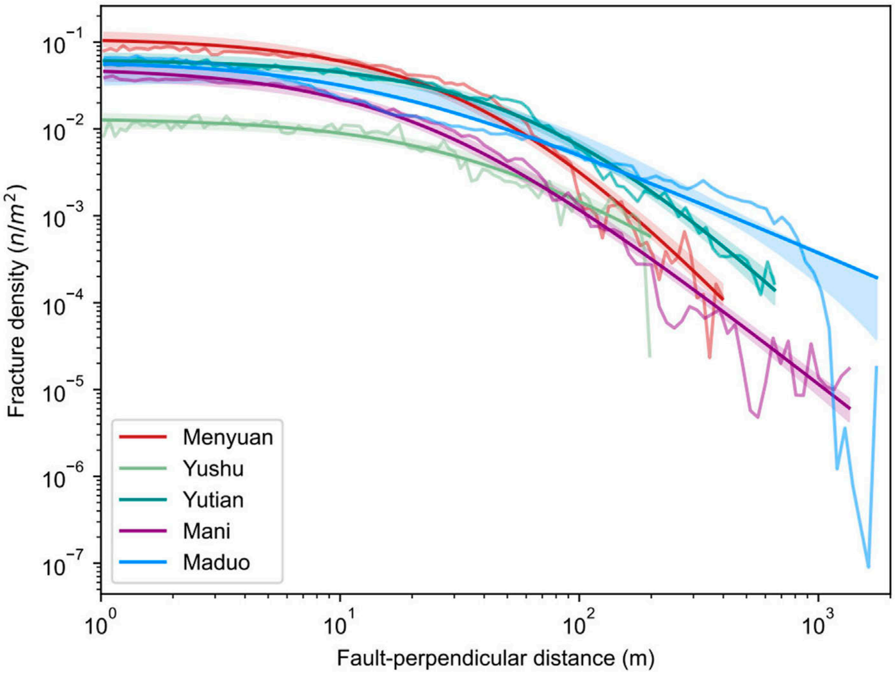

FIGURE 5
Rupture density distribution for the Mani, Yushu, Yutian, Maduo, and Menyuan earthquakes.

TABLE 2 Distribution of best-fit parameters for each event in Equation 2.

Parameter	Mani	Yushu	Yutian	Maduo	Menyuan
V_0	0.051	0.013	0.063	0.062	0.112
$X_{fr}(m)$	21.259	38.355	73.423	13.297	43.893
γ	2.169	1.722	2.665	1.179	2.999

the spatial distribution of surface rupture density is studied based on Equation 2. When all the rupture traces have been separated into segments at a 1 m interval, we calculated the smallest distance from each segment to the principal rupture trace, and fit the attenuation of surface rupture density for each earthquake based on these data (Figure 5).

When the surface rupture density distribution for each earthquake has been obtained, we fit each decay with an affine-invariant ensemble sampler for Markov chain Monte Carlo (Goodman and Weare, 2010; Foreman-Mackey et al., 2013), setting the prior ranges of the values of the three unknown parameters in Equation 2 to estimate the maximum-likelihood values by using the actual surface rupture data of each earthquake (Table 2).

We follow a similar method to estimate the attenuation of displacement distribution with the fault-perpendicular distance in Equation 3: With the smallest distance of each displacement measurement point to the principal rupture trace calculated, we calculate the attenuation of the surface rupture displacement measurements for each earthquake (Figure 6).

When the decay of displacement measurements with fault-perpendicular distance for each earthquake has been obtained, we set the prior ranges of the values of the two unknown parameters in Equation 3 to estimate the maximum-likelihood values by using the actual surface rupture data of each earthquake (Table 3). Then, we build the probability model for each of the five earthquakes after obtaining the parameters for the final model (Figure 7).

As the individual models are built, we fit the parameters of the general model based on all the surface rupture data from these five earthquakes according to the above method (Table 4). About the value of β, according to Equation 9 we give the input of M_W. Using the parameters in Table 3, we build the general model for the Tibetan Plateau and set different values of M_W, S_0 to observe the rationality of the results (Figure 8). In the establishment of the model, we imported the code into Jupyter Notebook, enabling end users to input the displacement threshold S_0 and earthquake moment magnitude M_W to obtain outputs for $P(S > S_0)$ (Figure 9).

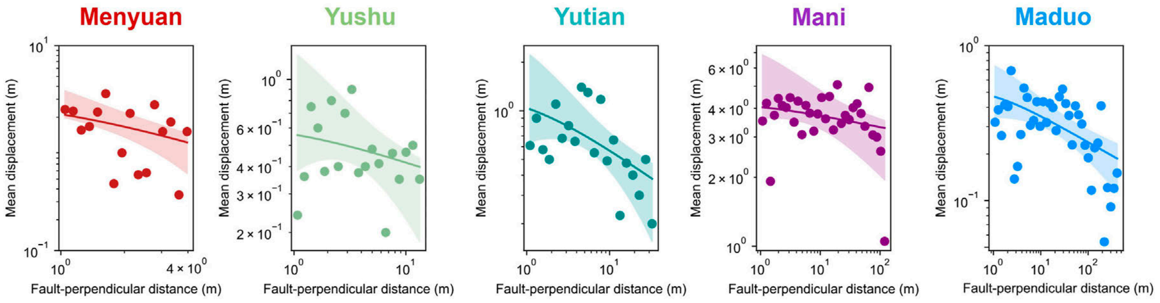

FIGURE 6
Distribution of displacement measurements for the Mani, Yushu, Yutian, Maduo, and Menyuan earthquakes.

TABLE 3 Distribution of best-fit parameters for each event in Equation 3.

Parameter	Mani	Yushu	Yutian	Maduo	Menyuan
$\beta(m)$	4.197	1.334	0.631	0.530	3.482
n	0.051	0.357	0.173	0.173	0.698

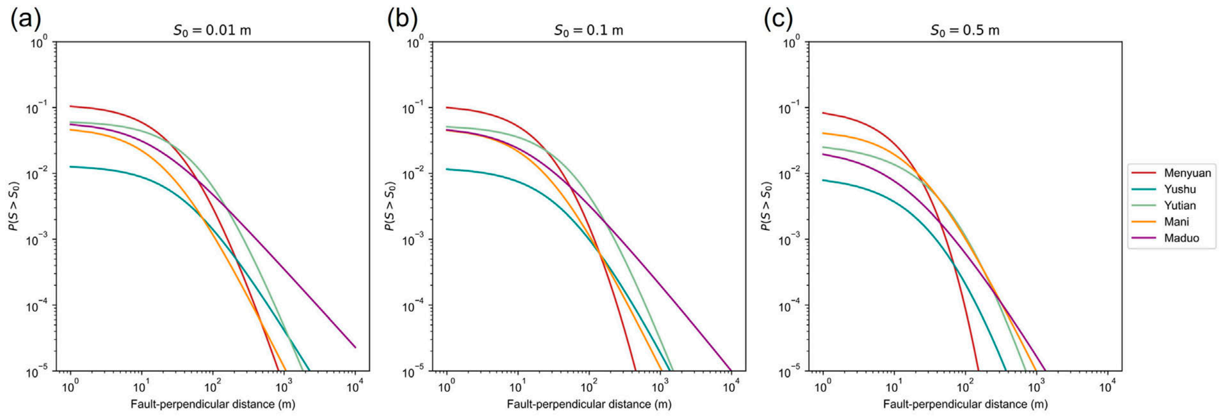

FIGURE 7
Curves representing the probability per square meter of finding a rupture hosting a displacement that exceeds threshold S_0 for the Mani, Yushu, Yutian, Maduo, and Menyuan earthquakes. These models generated by using Equation 5 show models for **(A)** $S_0 = 0.01$ m, **(B)** 0.1 m, and **(C)** 0.5 m, respectively.

TABLE 4 Distribution of best-fit parameters for general model in Equation 8.

Parameter	V_0	X_{fr}(m)	γ	β(m)	n
	0.045	33.933	1.803	M_W	0.291

6 Discussion

6.1 The effect of the data preprocessing on the model

As mentioned above, the original data of surface ruptures from field observations and high-revolutionary imagery include a large number of fractures related to non-tectonic factors. These non-tectonic fractures are distributed along a local environment and are not directly related to fault slip during the earthquake. Therefore, it is hard to be assessed by a general model. We compare the model result using the data before and after data preprocessing to address the role of data filtering.

The effect of the data-preprocessing work can be reflected in some results during the establishment of the general model. Before and after data filtering, the best-fitting rupture density attenuation for each of the five earthquakes demonstrates a downward trend, which aligns with expectations. Although the curves derived from the original data generally follow this downward trend, they exhibit several peaks and abrupt increases and decreases towards the end. Compared to the original data, these peaks correspond to fracture

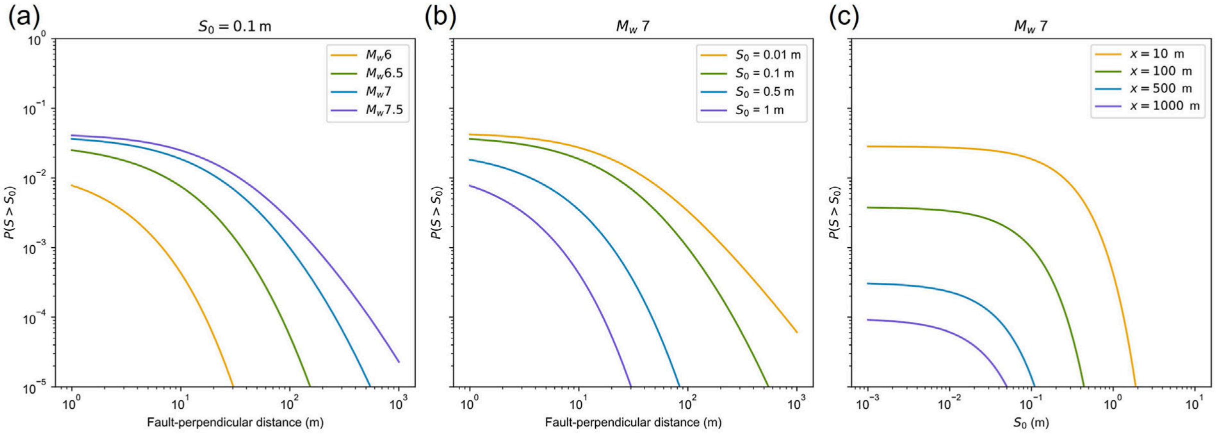

FIGURE 8
Curves showing the probability per unit area of finding a rupture accommodating a displacement that exceeds threshold S_0 for a surface-rupturing strike-slip earthquake. The models are generated by using Equation 5. **(A)** Models for M_W 6, 6.5, 7, and 7.5, in which $S_0 = 0.1m$. **(B)** Models for $S_0 = 0.01m, 0.1m, 0.5m$ and $1m$ for a M_W 7 event. **(C)** Probability *versus* displacement hazard curves for a M_W 7 event at distances of $10m, 100m, 1000m$, and $5000m$ from the fault.

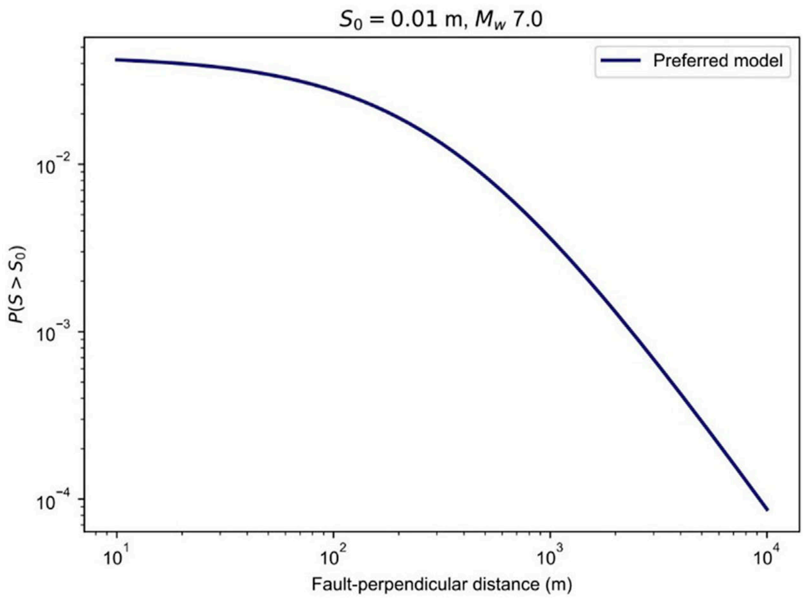

FIGURE 9
The general probabilistic fault displacement hazard analysis model expressing the probability of finding a rupture accommodating a displacement that exceeds threshold $S_0 = 0.01m$ for a surface-rupturing strike-slip earthquake of Mw 7.

traces far from the principal fault, where surface fractures at these distal locations are predominantly influenced by local complicated structures, stopovers, or seismic vibrations similar to the Yutian earthquake (Yuan et al., 2021). The comparative results indicate that the filter of the original surface rupture traces of the five earthquakes based on established criteria can, to some extent, remove the discrepancies in peak distributions at the end of the rupture density attenuation curve arising from individual variations (Figure 10). The differences in distribution are primarily reflected in the number of peaks and their respective locations.

Similar to the rupture density distribution, the best-fitting attenuation of displacement values also exhibits a decreasing trend, consistent with our expectation that surface rupture displacement values diminish with increasing distance from the principal fault. However, the distribution of the original actual displacement values markedly differs from that of the best-fitting case. The measurement and collection of original data primarily stem from field investigations, which can introduce measurement deviations. For instance, in the case of the Yushu earthquake, the displacement measurements show a small proximal value and a larger distal value,

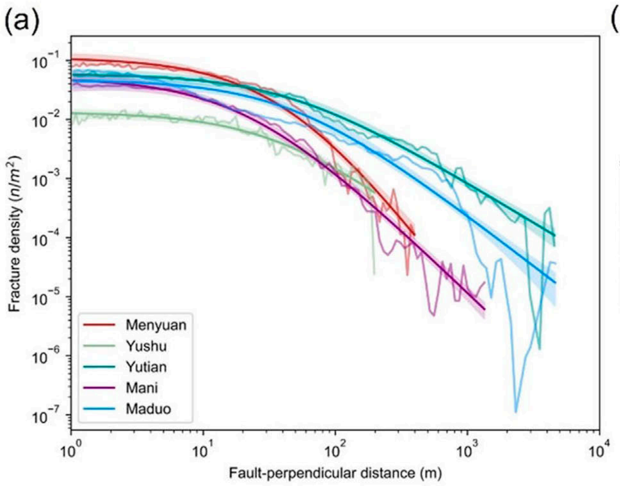

FIGURE 10
Comparison of rupture density before and after the data screening. **(A)** Before data screening. **(B)** After data screening.

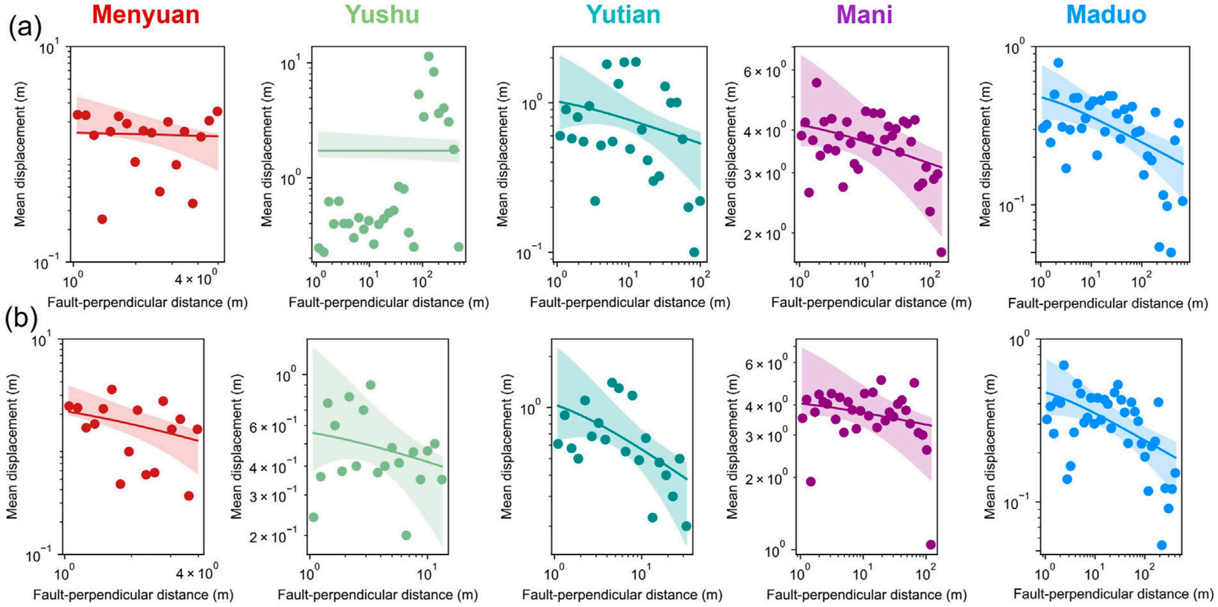

FIGURE 11
Comparison of the attenuation of the displacement distribution before and after the data screening. **(A)** Before data screening. **(B)** After data screening.

resulting in a lack of an obvious downward trend in the overall distribution (Figure 11). Consequently, the best-fitting situation approaches a horizontal line. The comparative results indicate that the selected displacement values, based on the established screening criteria, are generally too small near the principal fault or excessively large at greater distances. This suggests that the removal of these outliers can enhance the best-fitting results to some extent.

The comparative results demonstrate that screening the original seismic data according to established standards can improve the data quality. Upon completion of the screening process, the data consistency is initially enhanced through the organization of data formats, thereby increasing the efficiency of follow-up search and use. This enhancement is subsequently reflected in the model establishment, which exhibits more reasonable and consistent parameters and results, collectively validating the effectiveness of data filtering.

It should be pointed out here that the fitting curves of displacement values of Yutian, Yushu and Menyuan earthquakes were still not very good compared with that of Maduo and Mani earthquakes after the completion of data filtering, with the best-fitting curves tended to be horizontal which don't show the ideal downward trend (Figure 11). Combined with the establishment

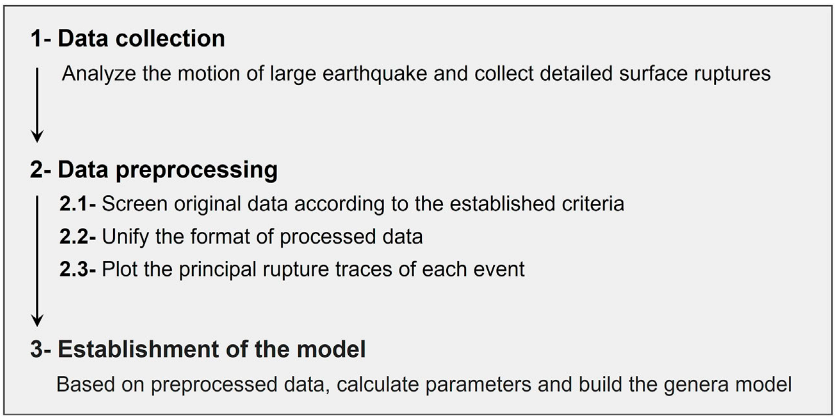

FIGURE 12
Overall workflow of the buildup of the model.

principles of Formula 3 and the analysis of the distribution characteristics of displacement values of the ideal curves, the displacement values in the original seismic data will have the most intuitive impact on the fitting situation: Since the original seismic datasets we used were all from the field investigation and measurement work of different experts and scholars, the specific measurement and sorting methods involved were different, and such differences could not be completely eliminated by our current work; Besides, the original datasets of these three earthquakes includes fewer displacement values, for which the removal of several values may cause more obvious impact on the best-fitting curve. Considering the above two characteristics of every original seismic dataset, we only to some extent improved the quality of the results after the completion of data filtering, improving the best-fitting curve from basically being horizontal to decay with a relatively slow decline trend.

Therefore, the data filtering work established in our study can improve the quality of the original seismic data to a certain extent, but the differences existing in the field investigation and measurement process of the original data cannot be completely removed through this work, and will finally remain in the best-fitting curve after filtering: Usually the most intuitive manifestation is that the displacement values are not completely in line with our prediction of the theoretical value, resulting in the attenuation trend of the best-fitting curve is too small. Our data filtering is mainly established to obtain relatively uniform datasets under certain criterion to make the results of theoretical model more consistent. For the specific situation of Yutian, Yushu and Menyuan earthquakes, the quality of the data is improved as much as possible on the basis of the above differences in the process of data-collection.

6.2 The general model

After the establishment of the general model, we provide a Jupyter Notebook that allows users to put a displacement threshold S_0 and earthquake moment magnitude M_W to obtain results of models in different conditions. Besides deriving the probability of significant damage in areas at varying distances from the principal fault by altering the distance x, we can extend our predictions from the distribution of surface ruptures in a specified region to the width of the rupture zone: In existing seismic fortification specifications for pipeline projects, avoidance width or fortification displacement is typically provided as a reference, with this displacement serving as a default for model outputs. By considering $P(S > S_0)$ set at 1/10000, we can ascertain the width of the surface rupture zone that has a defined probability of encountering displacements exceeding the fortification value, represented by the value of x. Compared with current models, our model not only predicts the displacement hazard from distributed ruptures of strike-slip faults, but also try to give a roughly referable fracture zone width, which corresponds to some existing fortification criterion for the avoidance width for engineering projects, providing more reference value.

We preprocessed raw data from five earthquakes to enhance data standardization and established a general probability model of the surface rupture displacement distribution of strike-slip earthquakes. The magnitudes of these five earthquakes range from Mw 6.6 to 7.5, covering a wide range of probable magnitudes of large strike-slip earthquakes, which lets our model fairly representative. The final model can be applicable for this magnitude range. If a large strike-slip fault with a potential of earthquake larger than Mw 7.5, the applicability of this model is unknown. Maybe more data from larger earthquakes like the 2001 Mw 7.8 Kunlunshan earthquake needs to be added to our database. In addition, the five earthquakes in this study are from the Tibetan Plateau. The general model could be applied in other regions with caution.

This study assumes that only horizontal displacement occurs on the strike-slip fault, without considering the effect of fault dip changes on surface rupture. Many factors may influence the distribution characteristics of surface ruptures on strike-slip faults: (1) variations in fault dip angles can affect the distribution of surface ruptures; (2) complicated fault geometry such as fault bend, and stepover may enhance the width of deformation zone (Visage et al., 2023); (3) the near-surface properties of covers above the fault tip, such as overburden thickness, geological characteristics, and consolidation, may influence the rupture pattern on the surface (Nurminen et al., 2020).

These factors may have influenced the surface ruptures of the five earthquakes used in this study. In the Yutian earthquake, the thicker loose sedimentary cover around the lake amplified the seismic rupture and rupture width at shallow depths (Yuan et al., 2021). In the Maduo earthquake, an extremely wide deformation zone in the epicentral region was probably related to a stepover covered by the sand layer in the upper reach of the Yellow River (Ren et al., 2022; Liu-Zeng et al., 2024). In future work, we will consider more factors in the establishment of a model and improve the applicability of the general model.

7 Conclusion

Based on a systematic analysis of surface ruptures from the five strike-slip earthquakes in the Tibetan Plateau in the past decades, we construct a general probabilistic model for displacement hazards associated with distributed ruptures from strike-slip faults. The following conclusions can be drawn:

(1) This study summarizes a workflow for building localized models of displacement hazard for active faults based on surface ruptures from large earthquake cases (Figure 12).
(2) Data preprocessing of the original surface rupture data is essential to enhancing the reliability of the general model. We set criteria to screen the original data to improve the consistency of our model's results to mainly make our model focused on the tectonic influence from strike-slip faults. We can add more actual seismic data and other possible factors in our future work to extend our research.
(3) The general probability model can be used to predict displacement hazard for distributed ruptures from surface-rupturing strike-slip faults with an earthquake potential of M_W 6.6–7.5 of the Tibetan Plateau.
(4) Current work has several limitations. Our model mainly focuses on the structural influence on the characteristics of surface ruptures for strike-slip faults with other factors removed during the data filtering, the range of our model's application will be limited. When applied to the events with other factors, the rationality of the results should be assessed. Besides, with the magnitudes of the five earthquakes ranging from Mw 6.6 to 7.5, when applied out of such range the rationality of the results should be assessed.

Data availability statement

The original contributions presented in the study are included in the article/supplementary material, further inquiries can be directed to the corresponding author.

Author contributions

FH: Data curation, Methodology, Software, Visualization, Writing–original draft. JR: Conceptualization, Funding acquisition, Supervision, Writing–review and editing.

Funding

The author(s) declare that financial support was received for the research, authorship, and/or publication of this article. This work was jointly supported by the National Natural Science Foundation of China (U2139201, 41941016).

Acknowledgments

We thank Zhikun JR, Zhaode Yuan, Kang Li, and Xinzhe Sun for the data collection of surface ruptures of large earthquakes. Special thanks are sent to Jia Cheng for useful discussions on the displacement hazard model.

Conflict of interest

The authors declare that the research was conducted in the absence of any commercial or financial relationships that could be construed as a potential conflict of interest.

Generative AI statement

The author(s) declare that no Generative AI was used in the creation of this manuscript.

Publisher's note

References

Ancheta, T. D., Darragh, R. B., Stewart, J. P., Seyhan, E., Silva, W. J., Chiou, B. S. J., et al. (2013). PEER NGA-west2 database. *PEER Rep.*

Antoine, S. L., Klinger, Y., Delorme, A., and Gold, R. D. (2022). Off-Fault deformation in regions of complex fault geometries: the 2013, M_w7.7, baluchistan rupture (Pakistan). *J. Geophys. Res. Solid Earth* 127 (11), e2022JB024480. doi:10.1029/2022JB024480

Cheng, J., Rong, Y., Magistrale, H., Chen, G., and Xu, X. (2020). Earthquake rupture scaling relations for mainland China. *Seismol. Res. Lett.* 91 (1), 248–261. doi:10.1785/0220190129

Chiou, B., Darragh, R., Gregor, N., and Silva, W. (2008). NGA project strong-motion database. *Earthq. Spectra* 24 (1), 23–44. doi:10.1193/1.2894831

Choi, J.-H., Klinger, Y., Ferry, M., Ritz, J.-F., Kurtz, R., Rizza, M., et al. (2018). Geologic inheritance and earthquake rupture processes: the 1905 M ≥ 8 tsetserleg-bulnay strike-slip earthquake sequence, Mongolia. *J. Geophys. Res. Solid Earth* 123 (2), 1925–1953. doi:10.1002/2017JB013962

Foreman-Mackey, D., Conley, A., Meierjurgen Farr, W., Hogg, D. W., Lang, D., Marshall, P., et al. (2013). emcee: the MCMC Hammer. *Astrophys. Source Code Libr.* 125, 306–312. doi:10.1086/670067

Goodman, J., and Weare, J. (2010). Ensemble samplers with affine invariance. *Comm. Appl. Math. Comput. Sci.* 5 (1), 65–80. doi:10.2140/camcos.2010.5.65

Inoue, N., Kitada, N., Shibuya, N., Omata, M., Takahama, T., Tonagi, M., et al. (2020). Probabilistic evaluation of off-fault displacements of the 2016 kumamoto earthquake. *Pure Appl. Geophys.* 177 (5), 2007–2019. doi:10.1007/s00024-019-02345-7

Jin, X. (2019). Study on prediction model of surface permanent displacement of strike-slip faults.(in Chinese). *World Earthq. Eng.* 35 (2), 18–23.

Kirby, E., Harkins, N., Wang, E., Shi, X., Fan, C., and Burbank, D. (2007). Slip rate gradients along the eastern Kunlun fault. *Tectonics* 26 (2). doi:10.1029/2006tc002033

Lee, V. W., and Trifunac, M. D. (1995). Frequency dependent attenuation function and fourier amplitude spectra of strong earthquake ground motion in California. *Soil Biol. and Biochem.* 40 (7), 1646–1653. doi:10.1016/j.soilbio.2008.01.028

Li, C. y., Pang, J. z., and Zhang, Z. q. (2012). Characteristics, geometry, and segmentation of the surface rupture associated with the 14 april 2010 Yushu earthquake, eastern tibet, China. *Bull. Seismol. Soc. Am.* 102 (4), 1618–1638. doi:10.1785/0120110261

Li, H., Pan, J., Lin, A., Sun, Z., Liu, D., Zhang, J., et al. (2016). Coseismic surface ruptures associated with the 2014Mw 6.9 yutian earthquake on the Altyn Tagh fault, Tibetan plateau. *Bull. Seismol. Soc. Am.* 106 (2), 595–608. doi:10.1785/0120150136

Li, K., Tapponnier, P., Xu, X., and Kang, W. (2023). The 2022, Ms 6.9 Menyuan earthquake: surface rupture, Paleozoic suture re-activation, slip-rate and seismic gap along the Haiyuan fault system, NE Tibet. *Earth Planet. Sci. Lett.* 622, 118412. doi:10.1016/j.epsl.2023.118412

Liu-Zeng, J., Liu, Z., Liu, X., Milliner, C., Rodriguez Padilla, A. M., Xu, S., et al. (2024). Fault orientation trumps fault maturity in controlling coseismic rupture characteristics of the 2021 Maduo earthquake. *AGU Adv.* 5 (2), e2023AV001134. doi:10.1029/2023av001134

Liu-Zeng, J., Liu, Z., Liu, X., Milliner, C., Rodriguez Padilla, A. M., Xu, S., et al. (2024). Fault orientation trumps Fault maturity in controlling coseismic rupture characteristics of the 2021 Maduo earthquake. *AGU Adv.* 5 (2), e2023AV001134. doi:10.1029/2023AV001134

Molnar, P., and Tapponnier, P. (1978). Active tectonics of tibet. *J. Geophys. Res. Solid Earth* 83 (B11), 5361–5375. doi:10.1029/jb083ib11p05361

Nurminen, F., Baize, S., Boncio, P., Blumetti, A. M., Cinti, F. R., Civico, R., et al. (2022). SURE 2.0–New release of the worldwide database of surface ruptures for fault displacement hazard analyses. *Sci. Data* 9 (1), 729. doi:10.1038/s41597-022-01835-z

Nurminen, F., Boncio, P., Visini, F., Pace, B., Valentini, A., Baize, S., et al. (2020). Probability of occurrence and displacement regression of distributed surface rupturing for reverse earthquakes. *Front. Earth Sci.* 8, 581–605. doi:10.3389/feart.2020.581605

Padilla, A. M. R., Quintana, M. A., Prado, R. M., Aguilar, B. J., Shea, T. A., Oskin, M. E., et al. (2022). Near-field high-resolution maps of the ridgecrest earthquakes from aerial imagery. *Seismol. Res. Lett.* 93 (1), 494–499. doi:10.1785/0220210234

Pan, J., Bai, M., Li, C., Liu, F., Li, H., Liu, D., et al. (2021). Coseismic surface rupture and seismogenic structure of the 2021-05-22 Maduo (Qinghai) Ms 7.4 earthquake. *Acta Geol. Sin.* 95 (6), 1655–1670.

Peter, M., and Powers, M. (2010). Distribution of seismicity across strike-slip faults in California. *J. Geophys. Res. Solid Earth.* 115, B05305. doi:10.1029/2008JB006234

Petersen, M. D., Dawson, T. E., Chen, R., Cao, T., Wills, C. J., Schwartz, D. P., et al. (2011). Fault displacement hazard for strike-slip Faults. *Bull. Seismol. Soc. Am.* 101 (2), 805–825. doi:10.1785/0120100035

Ren, J., Xu, X., Yeats, R. S., and Zhang, S. (2013). Millennial slip rates of the Tazang fault, the eastern termination of Kunlun fault: implications for strain partitioning in eastern Tibet. *Tectonophysics* 608, 1180–1200. doi:10.1016/j.tecto.2013.06.026

Ren, J., Xu, X., Yeats, R. S., and Zhang, S. (2013a). Latest Quaternary paleoseismology and slip rates of the Longriba fault zone, eastern Tibet: implications for fault behavior and strain partitioning. *Tectonics* 32 (2), 216–238. doi:10.1002/tect.20029

Ren, J., Xu, X., Zhang, G., Wang, Q., Zhang, Z., Gai, H., et al. (2022). Coseismic surface ruptures, slip distribution, and 3D seismogenic fault for the 2021 Mw 7.3 Maduo earthquake, central Tibetan Plateau, and its tectonic implications. *Tectonophysics* 827, 229275. doi:10.1016/j.tecto.2022.229275

Ren, Z., and Zhang, Z. (2019). Structural analysis of the 1997 Mw 7.5 Manyi earthquake and the kinematics of the Manyi fault, central Tibetan Plateau. *J. Asian earth Sci.* 179 (AUG.1), 149–164. doi:10.1016/j.jseaes.2019.05.003

Rodriguez Padilla, A. M., and Oskin, M. E. (2023). Displacement hazard from distributed ruptures in strike-slip earthquakes. *Bull. Seismol. Soc. Am.* 113 (6), 2730–2745. doi:10.1785/0120230044

Sarmiento, A. M., Danielle, B., Yousef, S., Lavrentiadis, G., Dawson, T., Madugo, C., et al. (2021). Fault displacement hazard initiative database report GIRS-2021-08. doi:10.34948/N36P48

Shan, X., Li, J., and Zhang, G. (2006). The tectonic condition and the feature of surface rupture zone of the Mani earthquake (MS 7.9) in 1997. *Chin. J. Geophys. (in Chinese)* 49 (3), 831–837.

Shaw, B. E. (2023). Magnitude and slip scaling relations for fault-based seismic hazard. *Bulletin of the Seismological Society of America* 113 (3), 924–947. doi:10.1785/0120220144

Sun, X., Xu, X., Chen, L., Tan, X., Yu, G., Li, Z., et al. (2012). Surface rupture features of the 2010 Yushu earthquake and its tectonic implication. *Chinese Journal of Geophysics (in Chinese)* 55 (1), 155–170. doi:10.6038/j.issn.0001-5733.2012.01.015

Takao, M., Tsuchiyama, J., Annaka, T., and Kurita, T. (2013). Application of Probabilistic Fault Displacement hazard analysis in Japan. *Journal of Japan Association for Earthquake Engineering* 13 (1), 17–36. doi:10.5610/jaee.13.17

Tapponnier, P., Zhiqin, X., Roger, F., Meyer, B., Arnaud, N., Wittlinger, G., et al. (2001). Oblique stepwise rise and growth of the Tibet Plateau. *Science* 294 (5547), 1671–1677. doi:10.1126/science.105978

Visage, S., Souloumiac, P., Cubas, N., Maillot, B., Antoine, S., Delorme, A., et al. (2023). Evolution of the off-fault deformation of strike-slip faults in a sand-box experiment. *Tectonophysics* 847, 229704. doi:10.1016/j.tecto.2023.229704

Wells, B. D. L., and Coppersmith, K. J. (1994). New empirical relationships among magnitude, rupture length, rupture width, rupture area, and surface displacement. *Bull.seism.soc.am.* 84 (4), 974–1002. doi:10.1785/BSSA0840040974

Wesnousky, S. G. (2006). Predicting the endpoints of earthquake ruptures. *Nature* 444 (7117), 358–360. doi:10.1038/nature05275

Wesnousky, S. G. (2008). Displacement and geometrical characteristics of earthquake surface ruptures: issues and implications for seismic-hazard analysis and the process of earthquake rupture. *Bull.seismol.soc.am.* 98 (4), 1609–1632. doi:10.1785/0120070111

Xu, X., Wang, F., Zheng, R., Chen, W., Ma, W., Yu, G., et al. (2005). Late Quaternary sinistral slip rate along the Altyn Tagh fault and its structural transformation model. *Science in China Series D Earth Sciences* 48, 384–397. doi:10.1360/02yd0436

Xu, X., Yu, G., Klinger, Y., Tapponnier, P., and Van Der Woerd, J. (2006). Reevaluation of surface rupture parameters and faulting segmentation of the 2001 Kunlunshan earthquake (M_w7.8), northern Tibetan Plateau, China. *Journal of Geophysical Research Solid Earth* 111 (B5). doi:10.1029/2004jb003488

Xue, S., Xie, H., Yuan, D., Li, Z., Shu, R., and Wen, Y. (2022). Seismic disaster characteristics of the surface rupture of Menyuan M S 6.9 earthquake in 2022. *China Earthquake Engineering Journal* 44 (2), 458–467. doi:10.20000/j.1000-0844.20220215001

Yao, W., Liu-Zeng, J., Oskin, M., Wang, W., Li, Z., Prush, V., et al. (2019). Reevaluation of the late pleistocene slip rate of the Haiyuan fault near songshan, gansu province, China. *Journal of Geophysical Research Solid Earth* 124 (5), 5217–5240. doi:10.1029/2018jb016907

Youngs, R. R., Arabasz, W. J., Anderson, R. E., Ramelli, A. R., Toro, G. R., Slemmons, D. B., et al. (2003). A methodology for Probabilistic Fault Displacement hazard analysis (PFDHA). *Earthquake Spectra* 19 (1), 191–219. doi:10.1193/1.1542891

Yuan, Z., Liu, J., Li, X., Xu, J., Yao, W., Han, L., et al. (2021). Detailed mapping of the surface rupture of the 12 February 2014 Yutian M s 7.3 earthquake, Altyn Tagh fault, Xinjiang, China. *Science China Earth Sciences* 64, 127–147. doi:10.1007/s11430-020-9673-6

Zhao, J., Liu, Y., Shi, L., and Wu, J. (2008). A probabilistic approach to evaluate permanent displacement crossing fault by 4th generation seismic zoning map of China. *Journal of Earthquake Engineering and Engineering Vibration* 28 (4), 22–27.

frontiers | Frontiers in Earth Science

TYPE Original Research
PUBLISHED 08 January 2025
DOI 10.3389/feart.2024.1526950

EDITED BY
Chong Xu,
Ministry of Emergency Management, China

REVIEWED BY
Yulong Cui,
Anhui University of Science and Technology, China
Chengyu Xie,
Xiangtan University, China
Hengzhong Zhu,
Shandong University of Science and Technology, China
Hao Jian,
Shandong University of Science and Technology, China
Dongjing Xu,
Shandong University of Science and Technology, China

*CORRESPONDENCE
Pengfei Hou,
✉ 451262216@qq.com

RECEIVED 12 November 2024
ACCEPTED 05 December 2024
PUBLISHED 08 January 2025

CITATION
Hou P, Wang S, Feng D, Xie X and Hou E (2025) Surface movement and crack development laws of super-long working faces in medium-depth coal seam mining. *Front. Earth Sci.* 12:1526950.
doi: 10.3389/feart.2024.1526950

Surface movement and crack development laws of super-long working faces in medium-depth coal seam mining

Pengfei Hou[1,2]*, Shuangming Wang[1,2], Dong Feng[1,2], Xiaoshen Xie[1,2] and Enke Hou[1,2]

[1]College of Geology and Environment, Xi'an University of Science and Technology, Xi'an, China,
[2]Shaanxi Provincial Key Laboratory of Geological Support for Coal Green Exploitation, Xi'an, China

Introduction: With the increased application of super-long working faces in coal mining, the surface movement and crack development laws of super-long working faces present an urgent problem to be studied and solved. This study aimed to determine the surface movement and crack development laws of super-long working faces when mining medium-depth buried coal seams.

Methods: The research area in Xiaobaodang No. 2 coal mine, China, was the adjacent working faces 01, 02 and 03, with inclination widths of 300 m and 450 m, respectively. The laws were determined by applying methods such as manual surface movement observation, GNSS automatic surface movement observation, surface crack observation, and crack morphology tracing.

Results: Compared to the working face with an inclination width of 300 m, the maximum subsidence, maximum horizontal movement value, and maximum subsidence coefficient of the super-long working face with an inclination width of 450 m increased by 15.31%, 4.56%, and 16.13%, respectively. Under the influence of mining the 02 working face, the maximum subsidence of the 01 working face increased by 15% and the surface subsidence patterns of the 01 and 02 working face inclination observation lines showed an asymmetric W shape.

Discussion: The widths of the cracks parallel to the open-off cut followed the dynamic development law of opening first, then closing or semi-closing. The widths of the cracks parallel to grooves followed the dynamic development law of opening first, then remaining open. The study results are important to protect mining buildings and the ecological environment.

KEYWORDS

medium-depth buried coal seam, mining subsidence, super-long working faces, surface movement and deformation, surface cracks

1 Introduction

The lack of gas and oil but comparatively abundant coal in China indicates that coal is the country's primary energy source (Shang et al., 2017). Coal resources in western China account for more than 70% of its total coal resources, and the northern Shaanxi coal mining area has become a billion-ton coal production base

(Bai et al., 2018; Zhang et al., 2023). Coal mining frequently causes ecological and environmental problems such as land destruction, soil erosion, and building and road destruction in coal mining areas to varying degrees (Qiao et al., 2017; Guo Q. L. et al., 2019; Zha and Xu, 2019; Song et al., 2021). Those are due mainly to mining destroying the rock strata overlying the working face and the surface movement above the working face. The primary damage from surface movement and deformation is both surface subsidence and surface cracking. Surface movement and deformation, as well as surface cracks, are caused by the movement and destruction of the rock strata overlying the mined-out area (Yi et al., 2022; Yan et al., 2023). Their laws are influenced by a combination of geological and mining factors (Guo W. B. et al., 2019; Dudek et al., 2022). Determining the laws of surface movement deformation and surface crack development from coal mining has an important theoretical significance and practical application value for preventing and controlling the problems of surface movement destruction.

The degrees of surface movement deformation and surface crack development are affected by various factors, such as the coal mining method, the mine depth and height, the inclination width of the working face, the structure of the rock and soil layers overlying the coal seam, and the mechanical strength of the coal seam. Therefore, it has become important to explore the characteristics, laws, and formation mechanisms of surface movement deformation and surface cracks under the conditions of several factors.

The most basic way to study surface movement and deformation is to establish a surface movement and deformation observation station for continuous on-site observation. Material and numerical simulations are also frequently used (Zhou et al., 2015; Prakash et al., 2018; Zhu et al., 2019). For the surface movement characteristics and laws for coal mining faces with various inclination widths, existing research has focused mainly on the surface movement and deformation above mining faces with inclination widths not more than 350 m. Guo et al. (2010) and Guo et al. (2011) analysed the surface subsidence characteristics of the 11,206 working face with its medium-depth buried thick coal seam and an inclination width of 170 m in Zhaojiazhai coal mine in Henan Province, China. Zhang B. C. et al. (2022) observed the surface subsidence of the 24,213 working face with its shallowly buried inclined coal seam, an inclination width of 180 m, and a mining height of 2 m in the 1930 coal mine in Xinjiang, China. Chen et al. (2019) observed and analysed the surface subsidence characteristics of the 52,305 working face with its deeply buried, thick coal seam, an inclination width of 280 m, and a mining height of 6.7 m in the Daliuta colliery in China's Shendong coalfield. Zou et al. (2023) studied the surface movements of the 22,108 and 42,108 working faces with an inclination width of 300 m in the Buertai coal mine in China's Shendong coalfield through on-site measurement and numerical simulation methods. Fu et al. (2021) monitored the surface subsidence of the S12013 working face with an inclination width of 330 m and a mining height of 4 m in the Ningtiaota coal mine in the northern Shaanxi province of China. Xie et al. (2021) studied the surface movements of the 112,201 working face with a deeply buried, thick coal seam and an inclination width of 350 m in the No.1 Xiaobaodang coal mine in the northern Shanxi province of China. These studies obtained surface movement characteristic parameters such as subsidence amount, subsidence coefficient, subsidence velocity, advance influence distance, and delay distance of maximum subsidence velocity through observation and analysis. Yin et al. (2022) analysed and predicted the surface movement characteristics of deeply buried Jurassic coal seam mining in the Hujierte mining area in western China and concluded that there was a certain positive correlation between the ratio of mining width to mining depth and the coefficients of subsidence.

On-site observation and mapping of surface cracks are standard methods for studying surface cracks. In recent years, UAV remote sensing technology has also been applied to surface crack research (Yang et al., 2022; Fu et al., 2023). Zhang Y. J. et al. (2022) observed surface cracks above the working face with its deeply buried coal seam, an inclination width of 180 m, and a mining height of 10 m in the gully terrain of a coal mine in the southern Shanxi province of China. Li et al. (2017) and Xu et al. (2017), Xu et al. (2019) observed surface cracks above the working face of the Bulianta coal mine in China's Shendong coalfield, which had a medium-depth buried coal seam and an inclination width of 300 m. Feng et al. (2022) and Feng et al. (2023) observed characteristics of surface cracks width variation above the 125,203 working face in the gully terrain of Anshan coal mine in northern Shaanxi province of China, which had a shallow-depth buried coal seam and an inclination width of 270 m. Hou et al. (2021) observed surface cracks in the working face of the No.1 Xiaobaodang coal mine in China's northern Shaanxi province, which had a medium-depth coal seam, an inclination width of 350 m, and a mining height of 5.8 m. These studies found that surface cracks caused by coal mining mainly included cracks inside the working face and cracks at the boundary of the working face. The width of cracks within the working face showed a characteristic of opening first, then closing, while the width of cracks at the working face boundary showed a characteristic of only opening and not closing. The width of surface cracks including its dynamic change in the loess gully region was greatly influenced by terrain, and the degree of surface cracks development was relatively strong. When the mining height of the medium-depth buried coal seam was 5.8 m, the depth of surface cracks development in the blown-sand region would not exceed 3.5 m.

In recent years, there have been many studies on the laws of surface movement deformation and surface crack development above working faces with inclination widths of less than 350 m. However, research is lacking on the laws of surface movement deformation and surface crack development in super-long working faces with inclination widths greater than 350 m. Since August 2021, a 450 m super-long working face was successfully mined in the No.2 Xiaobaodang coal mine, which improved coal production and economic benefits. The developers of many other coal mines have begun experimenting with super-long working face mining. The present study was done on the No. 2 Xiaobaodang coal mine in the aeolian (wind deposited) sand area of northern Shaanxi Province, China. It focused on the 01 working face with an inclination width of 300 m, the 02 super-long working face with an inclination width of 450 m and the 03 super-long working faces with an inclination width of 450 m. It explored the laws of surface movement deformation and surface crack development above the super-long working faces caused by mining medium-depth coal seams.

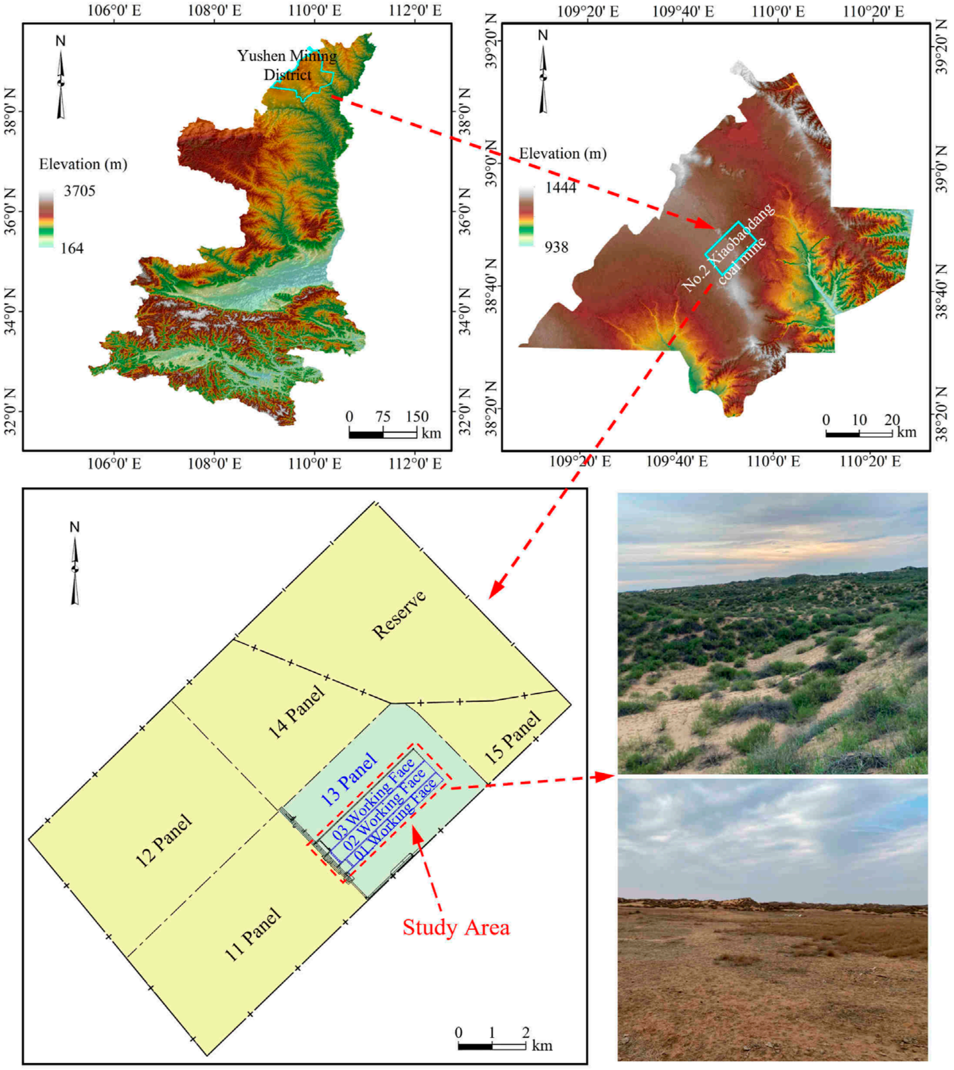

FIGURE 1
Location of study area.

2 Study area and method

2.1 Study area

The study area was at the 01, 02 and 03 working faces of the 13 panel area of the Xiaobaodang No. 2 coal mine in the Yushen mining district in northern Shaanxi Province, China (Figure 1). Those working faces were adjacent, and their surface was covered by an aeolian sand layer. Based on borehole exploration data and stratigraphic maps, the stratigraphy of the study area from old to new groups was as follows: Jurassic Yan'an, Zhiluo, Anding, Neogene Pliocene Baode, and Quaternary. The attitude of strata in the study area was nearly horizontal, and the structure was simple without faults.

The 01, 02 and 03 working faces adopted a longwall retreating mining method, and the roof was managed by the all-caving mining method. The 01 working face was the first mining face in the 13 panel area, with an inclination width of 300 m and a strike length of 4,002 m. The 2^{-2} coal seam in that face was 311 m deep. Its thickness ranged from 1.60 to 2.60 m; the average thickness was 2.14 m. The 01 working face started mining at a mining height of 2.60 m from July 2020 to August 2021.

The 02 super-long working face was on the northwest side of the 01 working face, with an inclination width of 450 m and a strike length of 3,868 m. The 2^{-2} coal seam in that face was 312 m deep. Its thickness ranged from 1.70 to 3.60 m; the average thickness was 2.50 m. The 02 working face started mining at a mining height of 2.60 m from August 2021 to July 2022. The northwest side of the 02 working face was the 03 super-long working face with an inclination width of 450 m, which has the same geological and mining conditions as the 02 working face.

The burial depth of medium-depth coal seams was generally greater than 150 m and less than 600 m. The 2^{-2} coal seam mined in the study area was a medium-depth buried coal seam. In the 01, 02 and 03 working face, the coal seams were horizontally mined, with the mining characteristics of low mining height, medium mining depth and a mining depth to height ratio of approximately 120.

2.2 Methods

2.2.1 Design of manual surface movement observation stations

Manual observation comprises independent overall observation before mining, daily observation during mining, and observation of surface stabilisation after mining. First, the control points of the mining area and the observation line are connected so that measurement can determine the benchmark for surface subsidence and horizontal displacement observation. Then, independent overall observations are made, and the results are used as the benchmark for data processing. After that, daily observations and surface stability monitoring are done from the start of mining until the ground surface stabilises. In observation of surface movement, the instrument of real-time kinematic (RTK) was used for planar observation, and the instrument of electronic level was used for elevation observation. The error of plane measurement was controlled within 10 mm, and the error of elevation measurement was controlled within 3 mm. Surface movement observation stations are arranged in the form of strike observation lines and inclination observation lines.

The strike observation line of the 01 working face was 900 m long, comprising 540 m on the inner side of the open-off cut and 360 m on its outer side. Along the strike observation line of the 01 working face, a total of 46 observation points numbered Z01 to Z46 were set up with a spacing of 20 m, and three control points numbered KZ01 to KZ03 were set up with a spacing of 100 m. The strike observation line of the 02 working face was 900 m long, comprising 550 m on the inner side of the open-off cut and 350 m on its outer side. Along the strike observation line of the 02 working face, a total of 37 observation points numbered Z01 to Z37 were set up with a spacing of 25 m, and three control points numbered KZ01 to KZ03 were set up with a spacing of 100 m. A same inclination observation line with a length of 1,420 m was used on the surface of working faces 01 and 02. That line was 500 m away from the open-off cut of the 01 and 02 working faces and perpendicular to the strike observation lines. Along the inclination observation line, 74 observation points were set up with a spacing of 20 m, including Q1 to Q72 points, Z44 point of the 01 strike observation line and Z35 point of the 02 strike observation line point. On the inclination observation line, there were four control points numbered KQ1 to KQ4 with a spacing of 100 m. The Q1 to Q50 points and Z44 point of the 01 strike observation line were used to observe the 01 working face surface movement in the inclination direction; the observation line composed of them was 1,000 m long. The Q1 to Q35 points, Q51 to Q72 points, Z44 point of the 01 strike observation line, and Z37 point (closed to Q6) of the 02 strike observation line were used to observe the 02 working face surface movement in the inclination direction; the observation line composed of them was 1,140 m long (Figure 2).

Before and after mining of the 01 working face, two independent overall observations and 52 daily observations and surface stability observations were made. Among them were included observations of the secondary surface movement affected by the mining of the 02 working face. Before and after mining of the 02 working face, two independent overall observations and 16 daily observations and surface stability observations were made (Supplementary Table S1).

2.2.2 Design of GNSS automatic surface movement observation stations

Global Navigation Satellite System (GNSS) automatic surface movement observation stations were based on the measurement principle of calculating the 3D coordinates of observation points by receiving signals from multiple satellites and using the time differences of the signals. Unlike manual observation stations, GNSS observation stations have the advantages of high frequency, many data collected, and greater accuracy in analysing the dynamic change characteristics of surface subsidence. The GNSS observation stations numbered ZK2 and ZK3 were installed in the centres of the 02 and 03 working faces surface respectively. The observation stations were 1,800 m away from the open-off cut and were set to obtain one set of surface movement data every 10 min (Figure 3).

2.2.3 Surface crack investigation methods

To study the development characteristics of surface cracks caused by super-long working face coal mining, manual on-site investigation, observation of surface crack width and drop changes, and excavation observations of surface crack development depths were adopted. The manual on-site investigation involved mainly investigating and mapping surface cracks' location, length, width, and drop. The location of surface cracks was determined by real-time kinematic instruments. The length, width, and drop of surface cracks were measured using a small steel ruler. The steps to measure the dynamic changes in the width and drop of crack development were to spray-paint markings on crack monitoring points and measure them once a day. The steps to measure the depth of crack development included first injecting a mixed slurry of putty powder and water along the crack for tracing, then excavating manually or using an excavator, and finally observing and measuring.

The surfaces of working faces 01 and 02 were covered by aeolian sand, and the widths of the surface cracks were small. The actions of wind and rainwater erosion quickly buried them. Consequently, complete data of the dynamic evolution of surface crack widths of the 01 and 02 working faces were not obtained. Afterwards, surface crack observations were made near the open-off cut of the 03 working face. The development width and drop changes of 18 surface cracks were monitored, and relevant data on them were obtained. Among them, 11 surface cracks were grouted, traced, excavated, and observed, and their development depth data were obtained (Figure 4).

3 Results

3.1 Surface movement characteristic parameters and laws of the 01 working face mining

3.1.1 Changes of subsidence along surface strike and inclination observation lines

Along the strike observation line, when the 01 working face was mined to 87 m, the surface above it began to be affected. Within the

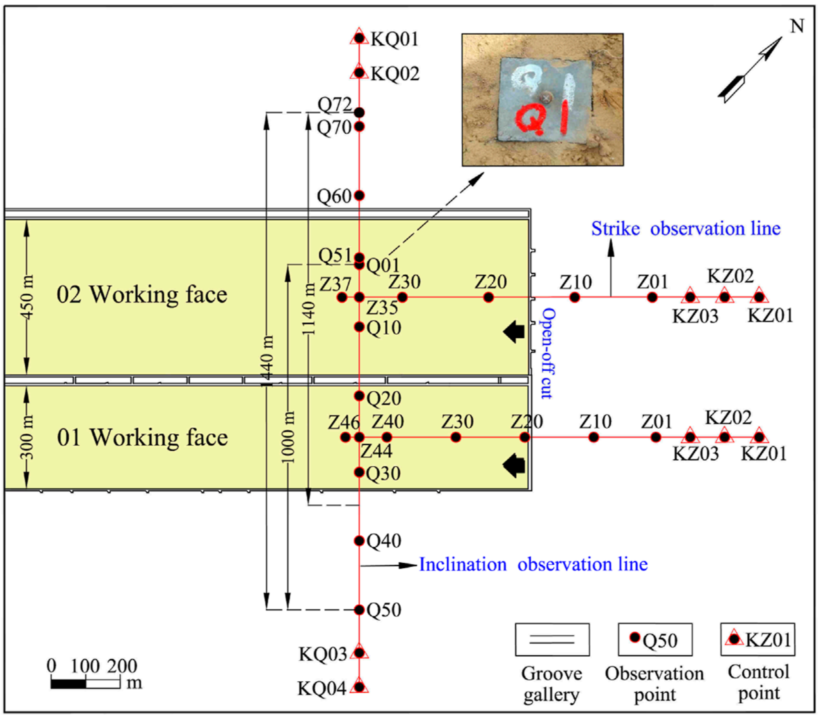

FIGURE 2
Design of surface movement observation lines for working faces 01 and 02.

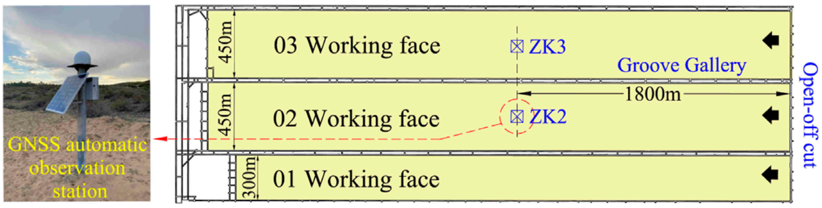

FIGURE 3
Design of GNSS surface movement automatic observation stations for working faces 02 and 03.

range of 40–100 m inside the open-off cut, namely from observation points Z21 to Z24, the surface subsidence reached 10 mm. When the face was mined to 540 m, point Z28 at 180 m inside the open-off cut was the maximum surface subsidence point. Its maximum subsidence was 1,570 mm, and it lagged behind the mining position by 360 m. With continuous mining of the working face, a surface subsidence basin gradually formed and eventually stabilised. After 6 months of mining the face, when the 01 working face was mined to 1,182 m, point Z28 on the surface had a subsidence value of 1,613 mm (Figure 5A). The maximum coefficient of surface subsidence was 0.62.

The gray shadow represented the unmined coal seam in Figure 5B. When the 01 working face was mined to 355 m, the mining position was 167 m away from the surface inclination observation line, and the maximum surface subsidence of the inclination observation line was 18 mm. When the face was mined to 540 m, the mining position exceeded the inclination observation line by 30 m, and the maximum subsidence point of the inclination observation line was Z44 at 180 mm. Point Z44 was at the centre position in the inclination direction of the working face, and the face's surface subsidence curve had a V shape. When the mining of the face was completed, its surface subsidence was generally stable. Point Z44's maximum subsidence was 1,528 mm. The surface subsidence curve in the inclination direction of the face had a V shape, and its symmetrical centre was located at the mine-out area (Figure 5B).

3.1.2 Surface horizontal strain and displacement

The surface horizontal movement in the strike line of the 01 working face was mainly towards the centre of the subsidence basin. Along the mining direction, the surface horizontal displacement fluctuation increased from the outer side to the vicinity of the open-off cut. The surface horizontal displacement on the inner side of the open-off cut initially increased, then decreased, and finally tended

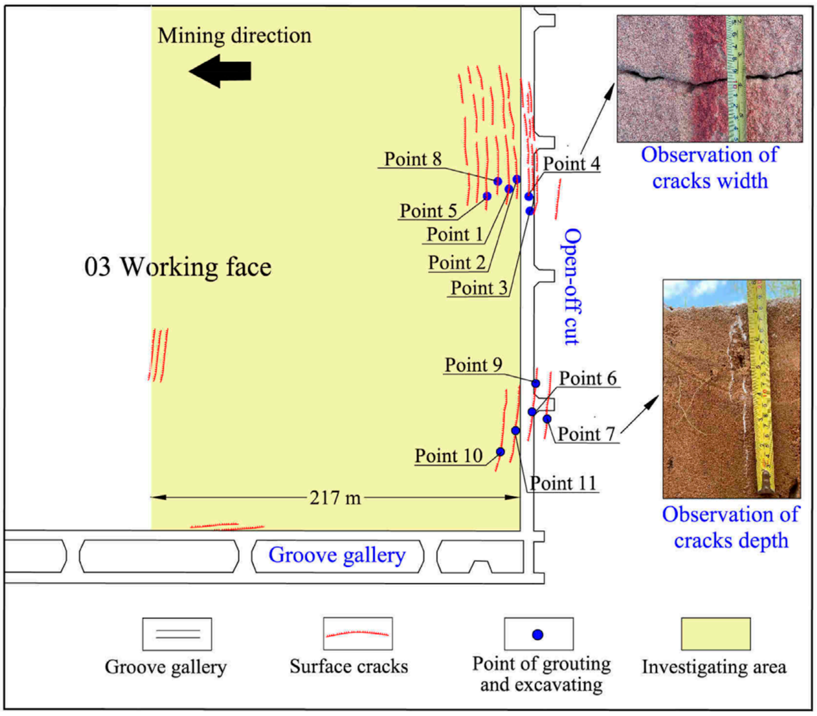

FIGURE 4
Distribution of observation points for surface crack width and depth near the open-off cut above the 03 working face.

to be relatively stable. The horizontal displacement near the open-off cut was generally large and peaked at 414.1 mm at 100 m medial to the open-off cut. The surface horizontal strain value ranged from −11.62 to +11.75 mm/m. The proportions of tensile and compressive deformations on the outer side of the open-off cut were similar, whereas compressive deformation was the main deformation on the inner side of the open-off cut (Figure 6).

3.1.3 Durations of phases of surface movement and deformation

The duration phases of surface movement and deformation were start-up, active, and decline. During the start-up phase of surface movement, the value and speed of surface subsidence slowly increased. The surface subsidence and deformation activities were intense, with surface subsidence of 1,551 mm accounting for approximately 96.15% of the total cumulative subsidence of 1,613 mm (Figure 7).

During the decline phase, the velocity of surface subsidence slowly decayed until the surface movement and deformation stabilised. The total surface movement and deformation duration averaged approximately 185 d, including the start-up phase of 6 d, the active phase of 54 d, and the decline phase of 125 d (Supplementary Table S2). Therefore, the surface movement and deformation of the 01 working face mining had a short start-up phase, a short active phase, and a long decline phase.

3.1.4 Maximum surface subsidence velocity

The maximum subsidence velocity curves at different periods all had a similar "unimodal" shape. As the working face mining continued to advance, the maximum subsidence velocity of the surface at each period along the strike observation line increased from low to high, then decreased again, and finally stabilised. The maximum subsidence velocity reached approximately 103.3 mm/d (Figure 8).

3.1.5 Delay distance and angle of maximum subsidence velocity

The average delay distance of the maximum subsidence velocity of the 01 working face was 102.14 m. According to the Equation 1 for calculating the delay angle of maximum subsidence velocity, its average value was 71.8° (Table 1).

$$\varphi = \operatorname{arccot}\frac{L}{H} \tag{1}$$

where φ was the delay angle of maximum subsidence velocity, L was the delay distance of maximum subsidence velocity, H was the mining depth.

3.1.6 Distance and angle of advance influence

The average distance of the advance influence of the 01 working face was 128 m. According to the Equation 2 for calculating the angle of advance influence, its average angle was 67.6° (Table 2).

$$\omega = \operatorname{arccot}\frac{l}{H} \tag{2}$$

where ω was the angle of advance influence, l was the distance of advance influence, H was the mining depth.

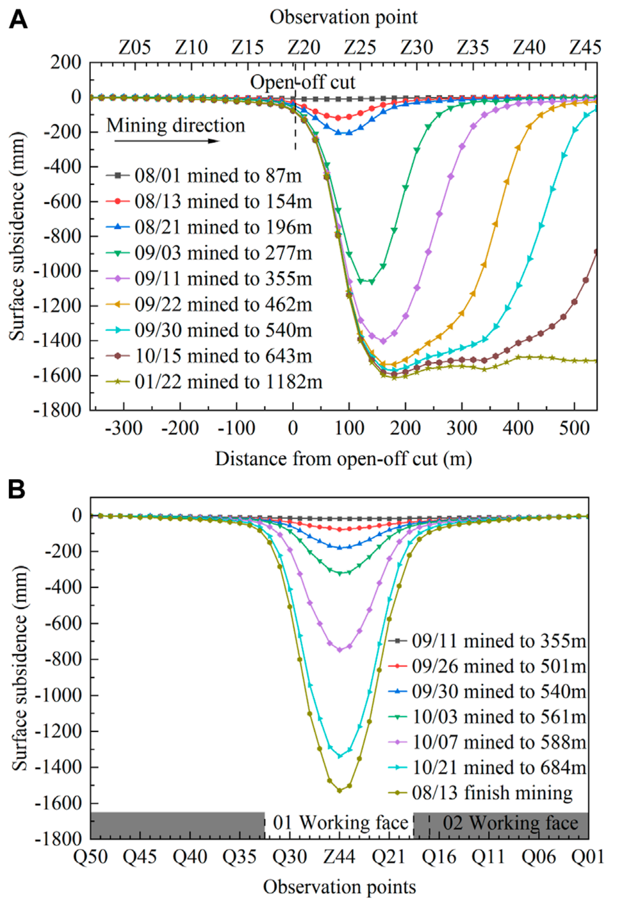

FIGURE 5
Surface subsidence curve of 01 working face. **(A)** in strike direction **(B)** in inclination direction.

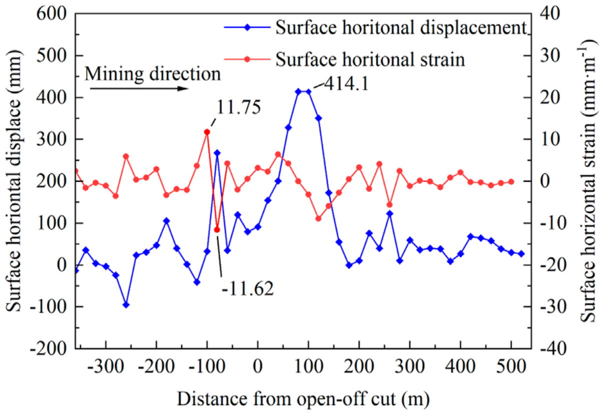

FIGURE 6
Surface horizontal displacement and strain curve in strike direction of 01 working face.

3.1.7 Characteristic parameters of surface movement after stability

The angular characteristic parameters of the ground surface movement after stability were calculated in accordance with the measured data and related formulas, as shown in Table 3. The angle of draw in the strike direction was 57.2°. The angle in the inclination direction was 49.7°. The angle of critical deformation in the strike direction was 80.8°. The angle in the inclination direction was 86.8°. The angle of crack in the strike direction was 86.7°. The angle in the inclination direction was 86.8°. The subsidence limit angle was 90°, and the angle of full subsidence was 59.9°.

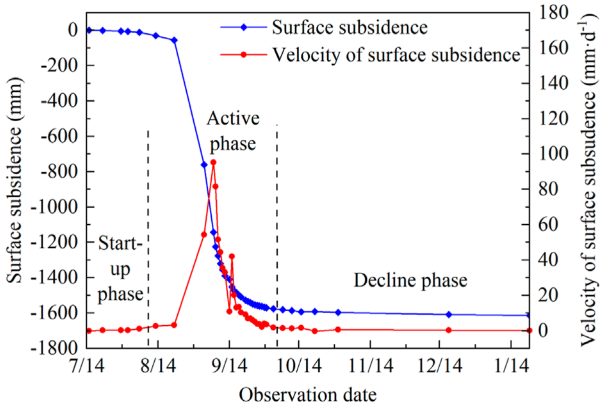

FIGURE 7
Duration curve of surface movement in the strike direction of 01 working face.

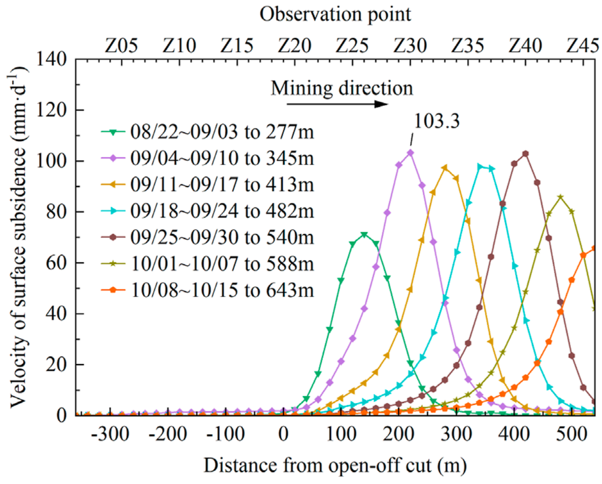

FIGURE 8
Maximum subsidence velocity curve in the strike direction of 01 working face.

3.2 Surface movement characteristic parameters and laws of the 02 working face mining

3.2.1 Changes of subsidence along surface strike and inclination lines

Along the strike observation line, when the 02 working face was mined to 103 m, its surface subsidence exceeded 10 mm, and its

TABLE 1 Calculation result of delay distance and delay angle of maximum subsidence velocity in the 01 working face.

Mining distance of the 01 working face/m	Observation points of maximum subsidence	Distance from maximum subsidence point to open-off cut/m	Delay distance of maximum subsidence velocity/m	Delay angle of maximum subsidence velocity/°
154	Z23	80	74	76.6
196	Z24	100	96	72.8
288	Z26	140	148	64.6
316	Z29	200	116	69.5
336	Z31	240	96	72.8
413	Z35	320	93	73.3
492	Z39	400	92	73.5
Average	—	—	102.14	71.8

TABLE 2 Calculation result of distance and angle of advance influence in the 01 working face.

Observation points of initial surface movement	Mining distance of the 01 working face/m	Distance from initial surface movement point to open-off cut/m	Distance of advance influence/m	Angle of advance influence/°
Z36	196	340	144	65.2
Z39	277	400	123	68.4
Z42	343	460	117	69.4
Average	—	—	128	67.6

surface began to be affected by the mining. When the working face was mined to 653 m, the maximum subsidence point on the surface was Z25 at 250 m inside the open-off cut. Its maximum subsidence was 1,802 mm, and it lagged behind the mining position by 403 m. When the 02 working face was mined to 3,665 m, the surface of the observation range had formed a stable subsidence basin. By June 2022, 10 months after the 02 working face was mined, the maximum subsidence point Z25 on the surface had a subsidence value of 1,860 mm, and the maximum coefficient of surface subsidence was 0.72 (Figure 9A).

When the 02 working face was mined to 330 m, the mining position was 170 m away from the surface inclination observation line, and the maximum surface subsidence of the line was 10 mm. Afterwards, as the working face continued to be mined, the inclination observation line continued to subside. Compared to the area near the solid coal body of the 03 working face, which had not yet been mined, the surface subsidence in the area near the mine-out of the 01 working face was larger. By June 2022, 10 months after the 02 working face was mined, the surface subsidence on the inclination observation line of that face was generally stable. The maximum subsidence point Z35 was at the centre position in the inclination direction of the 02 working face with a maximum subsidence value of 1,758 mm. The surface subsidence curve of the 02 working face had a U shape, with its symmetrical centre located at the mine-out area. The surface subsidence on the side of the area near the mine-out of the 01 working face was relatively large, and the subsidence curve was relatively flat. However, the subsidence on the side of the area near the 03 working face, which had not been mined, was relatively small, and the subsidence curve was steep (Figure 9B).

Affected by the 01 working face mining, the 02 working face surface had already experienced varying degrees of subsidence before mining. Its surface subsidence ranged from 3 to 91 mm on the inclination observation line from Q01 to Q17. During the mining of the 02 working face, the 01 working face surface had a secondary subsidence whose maximum was 875 mm at point Q18 at the boundary between working faces 01 and 02. Affected by the secondary subsidence, the maximum subsidence point of the 01 working face moved from Z44 to Q25. The secondary subsidence value of Q25 was 185 mm, which increased by 12.3% compared to the first subsidence value. The cumulative surface subsidence at the coal pillar section (Q17 to Q18) were 1,005 to 1,019 mm. The surface subsidence curve on the

TABLE 3 Calculation result of surface movement characteristic parameters in the 01 working face.

Direction	Angle of advance influence/°	Angle of draw/°	Angle of critical deformation/°	Angle of crack/°	Subsidence limit angle/°	Angle of full subsidence/°	Delay angle of maximum subsidence velocity/°
Strike	67.6	57.2	80.8	86.7	—	59.9	71.8
Inclination	—	49.7	86.8	86.8	90	—	—

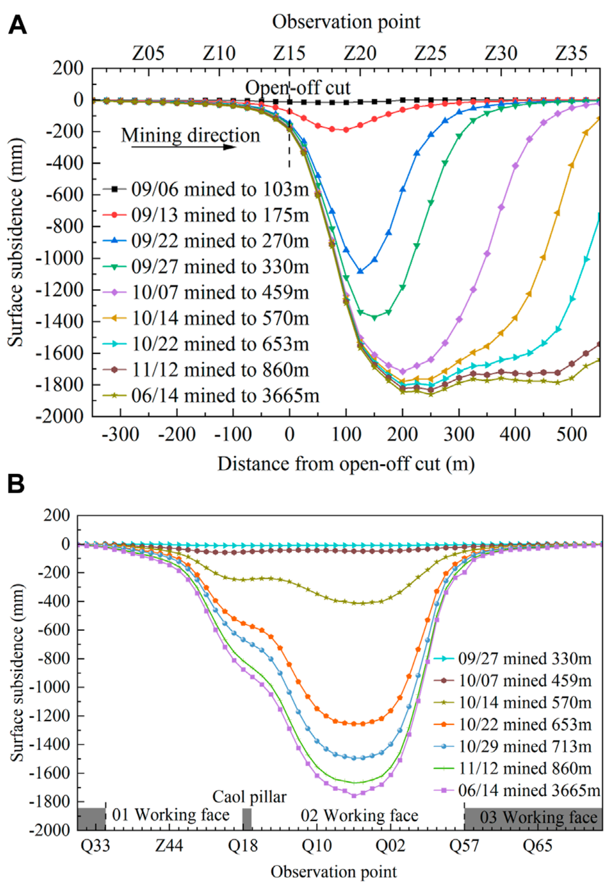

FIGURE 9
Surface subsidence curve of 02 working face in mining period of 02 working face. **(A)** in strike direction. **(B)** in inclination direction.

inclination observation line had an asymmetric W shape as a whole (Figure 10).

3.2.2 Surface horizontal strain and displacement

The surface horizontal displacement in the strike line of the 02 working face was mainly towards the centre of the subsidence basin. Along the mining direction, the surface horizontal displacement of the strike direction first increased, then decreased, and finally stabilised within a certain range. The horizontal displacement near the open-off cut was relatively large, with a peak of 433 mm at a distance of 50 m on the inner side of the open-off cut. The horizontal strain of the surface ranged from −2.64 to 4.64 mm/m (Figure 11).

3.2.3 Durations of surface movement and deformation phases

The total duration of surface movement and deformation was on average approximately 243 d, including a start-up phase of approximately 4 d, an active phase of approximately 53 d, and a decline phase of approximately 186 d (Supplementary Table S3). During the active phase, the surface subsidence of 1798 mm was severe, accounting for 96.66% of the total subsidence of 1860 mm. During that period, the

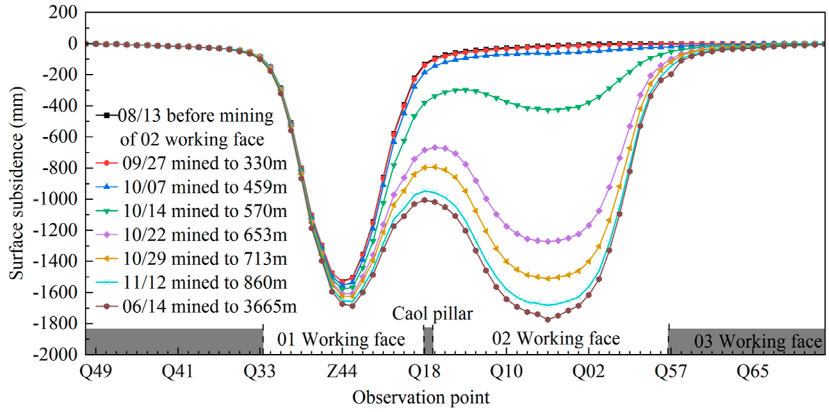

FIGURE 10
Accumulated surface subsidence curve of inclination direction in the working faces 01 and 02.

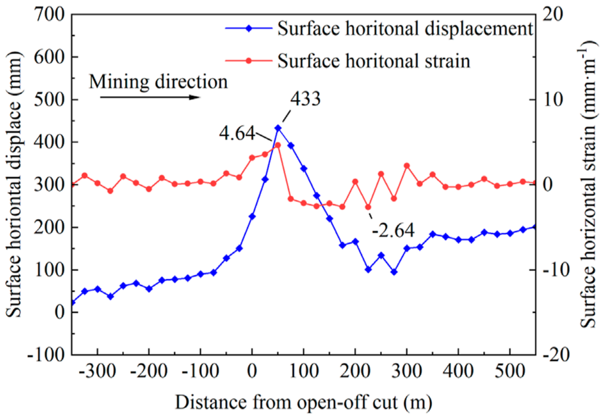

FIGURE 11
Surface horizontal displacement and strain curve in strike direction of 02 working face.

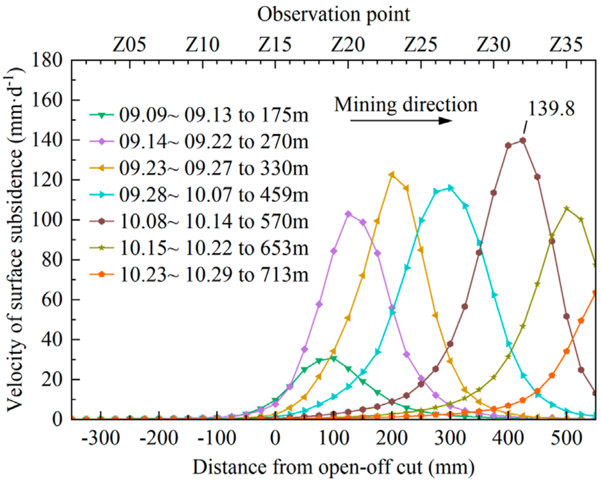

FIGURE 13
Maximum subsidence velocity curve in the strike direction of 02 working face.

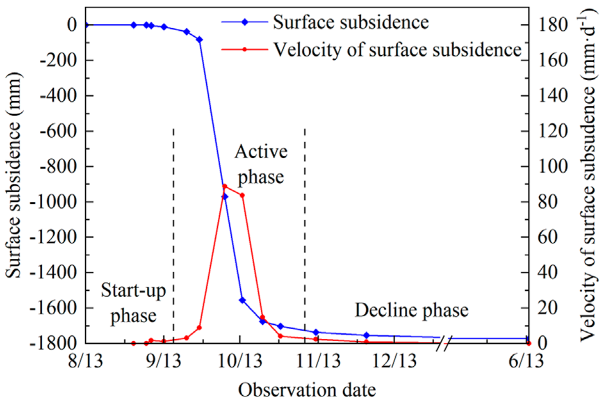

FIGURE 12
Duration curve of surface movement in the strike direction of 02 working face.

surface subsidence's speed increased rapidly, then decreased rapidly (Figure 12).

3.2.4 Maximum surface subsidence velocity

As the 02 working face continued to be mined, the maximum subsidence velocity of the surface in each period along the observation line had a trend of increasing from low to high, then decreasing and tending towards stability. The maximum subsidence velocity was 139.8 mm/d (Figure 13).

3.2.5 Delay distance and angle of maximum subsidence velocity

The average delay distance of the maximum subsidence velocity of the 02 working face was 112.8 m. According to the Equation 1 for calculating the delay angle of maximum subsidence velocity, its average value was 70.1° (Table 4).

TABLE 4 Calculation result of delay distance and delay angle of maximum subsidence velocity in the 02 working face.

Mining distance of the 02 working face/m	Observation point of maximum subsidence	Distance from maximum subsidence point to open-off cut/m	Delay distance of maximum subsidence velocity/m	Delay angle of maximum subsidence velocity/°
237	Z20	122	115	64.5
300	Z23	197	103	71.7
413	Z27	297	116	69.6
521	Z32	422	99	72.4
628	Z35	497	131	67.2
Average	—	—	112.8	70.1

TABLE 5 Calculation result of distance and angle of advance influence in the 02 working face.

Observation point of initial surface movement	Mining distance of the 02 working face/m	Distance from initial surface movement point to open-off cut/m	Distance of advance influence/m	Angle of advance influence/°
Z26	123	272	149	64.5
Z29	175	347	172	61.1
Z33	270	447	177	60.4
Z34	330	472	142	65.5
Average	—	—	160	62.9

3.2.6 Distance and angle of advance influence

The average distance of advance influence of the 02 working face was 160 m. According to the Equation 2 for calculating the angle of advance influence, its average angle was 62.9° (Table 5).

3.2.7 Characteristic parameters of surface movement after stability

The angular characteristic parameters of the ground surface movement after stability were calculated in accordance with the measured data and related formulas, as shown in Table 6. The 02 working face's draw angle in the strike direction was 46.1°. The draw angle near the 03 face in the inclination direction was 49.2°. The draw angle near the 01 face in the inclination direction was 39.8°. The 02 working face's critical deformation angle in the strike direction was 80.8°. The critical deformation angle near the 03 face in the inclination direction was 82.7°. The critical deformation angle near the 01 face in the inclination direction was 83.6°. For the 02 working face, the crack angle in the strike direction was 86.3°, the average of crack angle in the inclination direction was 86.8°, the subsidence limit angle was 90°, and the angle of full subsidence was 52.4°.

3.2.8 Result of GNSS automatic surface movement observation stations for the 02 working face

The ZK2 point of the GNSS automatic surface movement observation station was at the centre of the 02 working face. According to the observation data, the surface began to subside with a value of 12.3 mm when the working face was mined to a distance of 201 m before ZK2. When the 02 working face was mined 668 m beyond the ZK2 point, the surface subsidence at that observation point was basically stable, with a maximum subsidence value of approximately 1,700.0 mm. As of the completion of mining of the 02 working face, the maximum subsidence of the ZK2 observation point stabilised at about 1,720.0 mm with a subsidence coefficient of 0.66 (Figure 14A).

The overall trend of the surface subsidence velocity was a slow increase, then a rapid increase, then a rapid decrease, then a slow decrease, and finally approaching zero. After the surface subsidence velocity approached zero, the surface subsidence value remained basically stable. When the mining of the 02 working face exceeded 115 m after ZK2, the surface subsidence velocity of ZK2 peaked at 153.6 mm/d (Figure 14B). The total duration of surface movement and deformation at the ZK2 GNSS observation averaged approximately

TABLE 6 Calculation result of surface movement characteristic parameters in the 02 working face.

Direction	Angle of advance influence/°	Angle of draw/°	Angle of critical deformation/°	Angle of crack/°	Subsidence limit angle/°	Angle of full subsidence/°	Delay angle of maximum subsidence velocity/°
Strike	62.9	46.1	80.8	86.3	—	52.4	70.1
Inclination (near 03 side)	—	49.2	82.7	86.3	90	—	—
Inclination (near 01 side)	—	39.8	83.6	87.2	90	—	—

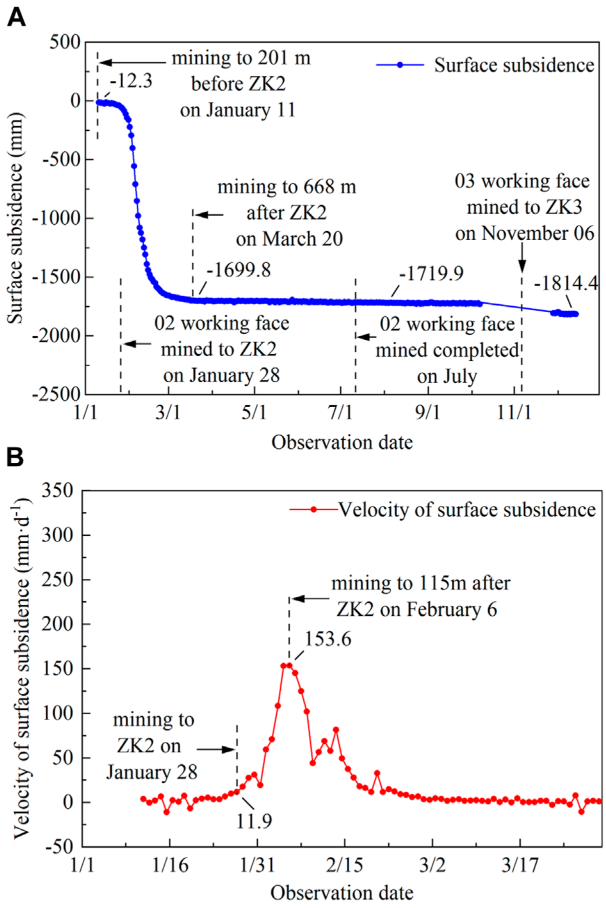

FIGURE 14
Surface subsidence characteristics curve of ZK2 point in the 02 working face. **(A)** surface subsidence. **(B)** velocity of surface subsidence.

246 d, including a start-up phase of approximately 10 d, an active phase of approximately 56 d, and a decline phase of approximately 180 d. During the active phase, the surface subsidence velocity of the ZK2 GNSS observation was high, and its duration was short. When the adjacent working face 03 was mined before and after the ZK3 observation point, the surface subsidence value of the ZK2 GNSS observation point, which was on the surface of the mine-out in the 02 working face, increased from 1,720.0 mm to 1,814.4 mm. The secondary surface subsidence of the ZK2 GNSS observation point was approximately 94.4 mm. In accordance with the observation data of the ZK2 GNSS observation station, it could be calculated that the distance of advance influence was 247 m, the angle of advance influence was 51.6°, and the delay distance and angle of the maximum subsidence velocity were 15 m and 69.8° respectively.

3.3 Development characteristics and laws of surface cracks caused by mining

In the study area including the 01, 02, and 03 working faces, the mining height was relatively small, and the ratio of mining depth to mining height was relatively large. The surface of the study area was

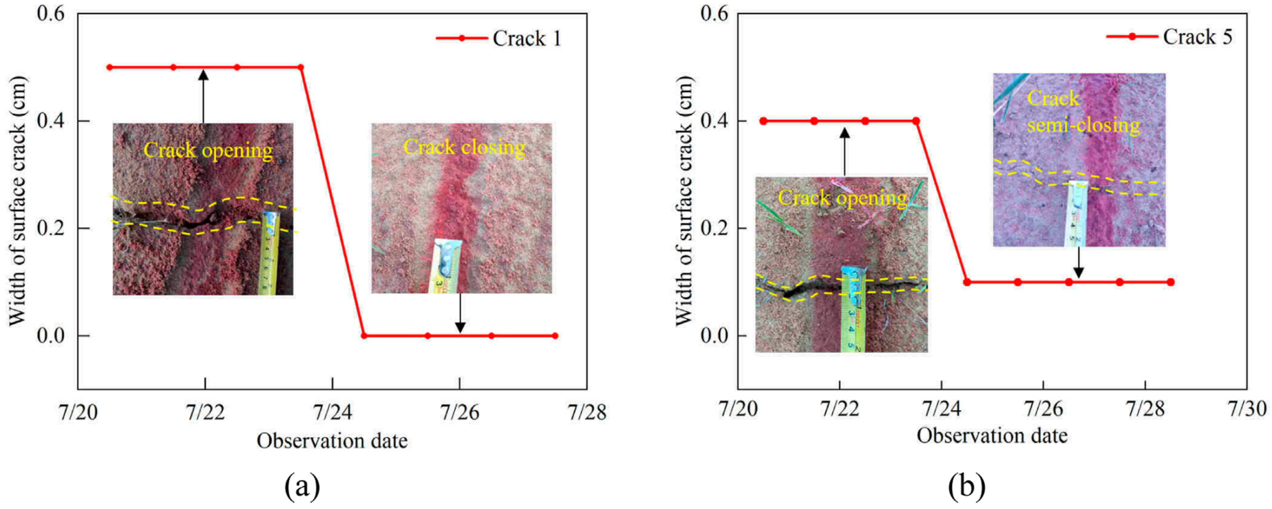

FIGURE 15
Dynamic evolution curve of width of cracks parallel to the open-off cut. **(A)** Width of crack 1. **(B)** Width of crack 5.

covered mainly by an aeolian sand layer. The mining surface cracks in the study area were generally weak and buried by aeolian sand soon after mining. Based on the observation results of surface cracks in the 02 and 03 working faces, it was found that the main types of surface cracks developed during mining were cracks with the mining direction parallel to the open-off cut and cracks with the spreading direction of parallel grooves. In the area around the open-off cut, the width of surface cracks parallel to the open-off cut was relatively large, in the 0.1–0.5 cm range. In the area within the working face, the width of surface cracks parallel to the open-off cut was relatively small, in the 0.05–0.2 cm range. The distance between the surface cracks was mostly between 3 and 5 m, and they had almost no drop. The surface crack widths of the parallel grooves were slightly larger than those parallel to the open-off cut inside the working face and slightly smaller than those parallel to the open-off cut near the open-off cut area.

The width of surface cracks parallel to the open-off cut had a dynamic evolution law pattern of opening first, then closing over time. That specifically showed that the width of the surface cracks was basically unchanged within 3–4 d after they were generated, then the cracks were completely closed or semi-closed within 1 d (Figure 15). The width of the surface crack parallel grooves had a dynamic evolution law pattern of only opening first and not matching over time. Over time, both types of surface cracks were buried by aeolian sand and lost their traces.

Based on the observation results of grouting and excavating for 11 surface cracks near the open-off cut on the 03 working face, the depth of surface crack development ranged from 4 to 68 cm, most of which ranged from 20 to 40 cm. The profile morphology of surface cracks included mainly “falling wedge” and “associated bifurcation” types (Figure 16).

4 Discussion

Determining the characteristics and laws of surface movement and surface crack development caused by coal mining is the scientific basis for protecting surface buildings, land resources, and ecological environments in coal mining areas. Some coal mining enterprises have begun to adopt super-long working faces with an inclination width greater than 350 m. To acquire their characteristics and laws of surface movement deformation and surface crack development, this study took the adjacent mining working faces 01 and 02 of the No. 2 Xiaobaodang coal mine as an example, which had the same mining heights, depths, and methods, nearly horizontal coal seams, and a similar geotechnical structure of the coal seam overburden. Through applying methods of manual observation of surface movement deformation, GNSS automatic observation of surface movement deformation, manual observation of surface cracks, and tracing excavation of surface cracks, the characteristics and laws of surface movement and surface crack development of working faces with inclination widths of 300 m and 450 m were studied.

Table 7 compares surface movement and deformation observation results in the strike direction of the 01 and 02 working faces. The inclination widths of the 01 and 02 workings, whose mining depths and heights were basically the same, were 300 m and 450 m respectively. The average mining speed of the 02 working face, 12.2 m/d, was faster than that of the 01 face with 6.4 m/d. Compared with the 01 working face, the maximum subsidence point of surface movement deformation in the strike direction of the 02 workface was 70 m farther away from the open-off cut, with an increase ratio of 39%. Its maximum subsidence was 247 mm larger with an increase ratio of 15.31%, the maximum coefficient of subsidence was 0.10 larger with an increase ratio of 16.13%, and the maximum horizontal displacement was 18.9 mm larger with an increase ratio of 4.56%. The increases in maximum subsidence, coefficient of subsidence, and maximum horizontal displacement were related mainly to the fact that the inclination width of the 02 working face exceeded that of the 01 working face. Compared with the 01 working face, the angles of advance influence, draw, and full subsidence, and the delay angle of maximum subsidence velocity of the 02 working face, decreased by 4.7°, 11.1°, 7.5°, and 1.7° respectively.

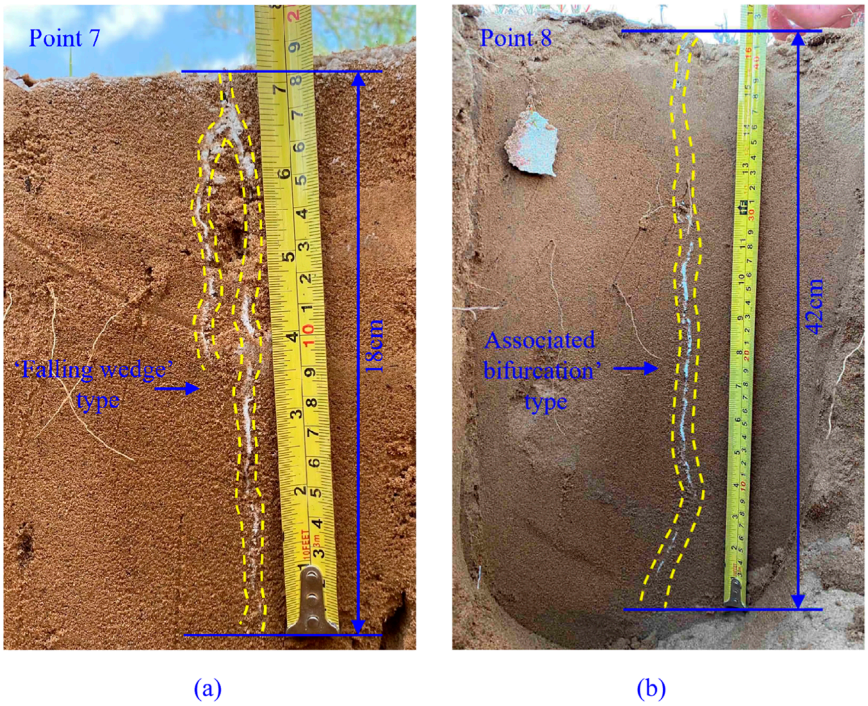

FIGURE 16
Development depth and profile morphology of cracks parallel to the open-off cut. **(A)** Point 7. **(B)** Point 8.

TABLE 7 Comparison of surface movement observation results in the strike direction between working faces 01 and 02.

Parameters	01 working face	02 working face
Length of inclination line/m	300	450
Height mining/m	2.5	2.6
Position of maximum surface subsidence point	180 m inside the open-off cut	250 m inside the open-off cut
Value of maximum surface subsidence/mm	1,613	1,860
Efficient of maximum surface subsidence	0.62	0.72
Position of maximum surface horizontal movement point	100 m inside the open-off cut	50 m inside the open-off cut
Value of maximum surface horizontal displacement/mm	414.1	433.0
Angle of advance influence/°	67.6	62.9
Angle of draw/°	57.2	46.1
Angle of critical deformation/°	80.8	80.8
Angle of crack/°	86.7	86.3
Subsidence limit angle/°	—	—
Angle of full subsidence/°	59.9	52.4
Delay angle of maximum surface subsidence velocity/°	71.8	70.1

The decreases in the angle of advance influence and the delay angle of the maximum subsidence velocity were related mainly to the fact that the mining speed of the 02 working face was faster than that of the 01 working face, and the decreases in the angles of draw and full subsidence might have been related to the larger inclination width of the 02 working face. Critical deformation and crack angles were essentially the same for working faces 01 and 02. Therefore, the inclination width of a coal mining face has some influence on the surface movement deformation of the working face under similar conditions of geology and mining. When the inclination width of the working face increased from 300 m to 450 m, the maximum subsidence, subsidence coefficient, and maximum horizontal displacement of the ground surface increased, the angles of the draw and full subsidence decreased, and the range and depth of the moving basin increased. Because 450 m super-long faces were developed in only recent years, there are no research reports on its surface movement characteristics and laws or its differences from conventional faces. This study determined the surface movement characteristics and laws of 450 m super-long working faces by observing and comparing the surface movement of conventional working faces with an inclination width of 300 m to those of super-long working faces with inclination widths of 450 m. That was important to understanding the influence of the inclination width of the working face on surface movement deformation to prevent and control subsidence disasters of super-long working faces.

As shown in Table 8 and Figure 17, under the influence of the adjacent 02 working face mining, the surface above the mined-out area of the 01 working face underwent obvious secondary subsidence from points Q27 to Q18, with a secondary subsidence value exceeding 100 mm. The maximum subsidence point Z44 in the inclination observation line centre of the 01 working face shifted to the direction of the adjacent 02 working face with an offset distance of 20 m. In the area of the coal pillar surface between the two working faces and its surrounding surface, the secondary subsidence of the surface was notable, with a maximum of 875 mm. Relative to the solid coal seam side of the 02 working face, the surface subsidence amplitude increased obviously, and its curve of cumulative surface subsidence was relatively gentle, so the cumulative subsidence curves of the two working faces were in an asymmetric W shape. That indicated that the coal seam's overlying rock and soil mass had undergone secondary fracturing and movement in the area of the coal pillar between the two working faces and its vicinity, but those activities of secondary breaking and movement were limited. After mining, the subsidence curve of the 01 working face was close to a V shape. Due to the influence of the mining of the 02 working face, the bottom of the subsidence curve of the 01 working face became flatter when the face was approaching full extraction. The maximum subsidence point of the 02 working face was at the centre of the working face, and the bottom of the subsidence curve was close to flat within a range of approximately 100 m. That indicates that the centre and its vicinity of the super-long working face with an inclination width of 450 m reached full extraction in the inclination direction. In the study area, it could be concluded that the inclination width of the full extraction for the working face in the inclination direction was slightly greater than 300 m, while the mining depth-to-height ratio was approximately 120. Previous studies focused mainly on the surface movement deformation of a single working face caused by coal mining (Guo et al., 2010; 2011; Chen et al., 2019; Fu et al., 2021; Xie et al., 2021; Yin et al., 2022; Zhang B. C. et al., 2022; Zou et al., 2023). There have been fewer studies on the surface subsidence changes of working faces and the characteristics of subsidence curves in the inclination direction caused by adjacent working face mining. From this study, based on the analysis of surface subsidence observations in the inclination direction of. From this study, based on the analysis of surface subsidence observations in the inclination direction of working faces 01 and 02, the surface cumulative subsidence curve of the adjacent faces had an asymmetric W shape. The study found that the rock surrounding the coal pillar and its vicinity experienced secondary fractures and movement and provided evidence that the centre area of the super-long working face with an inclination width of 450 m had reached full mining. Those findings have important reference value for preventing and controlling surface subsidence disasters caused by coal mining of working faces.

In the study area, medium-depth coal seams with thick, loose layers were mined in the upper part of the overlying strata. The mining heights were low at 2.6 m, and the mining depth-to-height ratio reached 120. Two types of surface cracks were caused by mining on the working face: those with a spreading direction parallel to the open-off cut and those with a spreading direction parallel to grooves. The crack development width was less than 0.5 cm without a drop, and the depth was less than 1 m. After mining of the working face, the surface cracks could be closed quickly by aeolian sand. The surface cracks in the study area were developed in unconsolidated loose sand layers. This loose sand layer was mainly subjected to plastic deformation, which was not conducive to stress transmission and crack propagation. Therefore, under the same level of stress, the depth of crack development was smaller on the surface covered by unconsolidated loose sand layers, while the depth of crack development was larger on the surface of loess with relatively better consolidation and fully consolidated rock layers. The widths of surface cracks near the working face's open-off cut and groove had a dynamic change characteristic of opening first, then remaining open, whereas the widths inside the working face opened first, then closed. Xiaobaodang No.1 coal mine adjacent to the study area had geological conditions similar to those of the study area, but its working face had a relatively large mining height of 5.8 m, with a mining depth-to-height ratio of 52. In that mine's area, the maximum width and drop of surface cracks were 15 cm and 20 cm respectively (Xie et al., 2021). It was evident that, for working faces with similar geological conditions, higher depth-to-height ratios and lower mining heights result in smaller surface crack development widths and weaker surface crack development degrees. Unlike previous research, this study found that the surface cracks of a coal mining face with a mining depth-to-height ratio of 120 were weakly damaging and could self-repair. That provides a basis for evaluating the degree of surface destruction faced by coal mining working faces.

The surface movement and deformation caused by coal seam mining were influenced by various factors such as topographic features, coal seam depth, overlying rock and soil structure, rock mechanical strength, inclination length of working face, mining height. The 01 conventional working face and

TABLE 8 Accumulated surface subsidence of inclination observation points in working faces 01 and 02.

Observation point	Surface subsidence after completion of 01 working face mining/mm	Surface subsidence after completion of 02 working face mining/mm
Left boundary point Q33 of 01 working face	83	100
Center point Z44 of 01 working face	1,528	1,674
Point Q25, 20 m away from the center of 01working face	1,502	1,686
Right boundary point Q18 of 01 working face	130	1,005
Left boundary point Q17 of 02 working face	92	1,018
Center point Z35 of 02 working face	15	1,773
Right boundary point Q57 of 02 working face	0	235

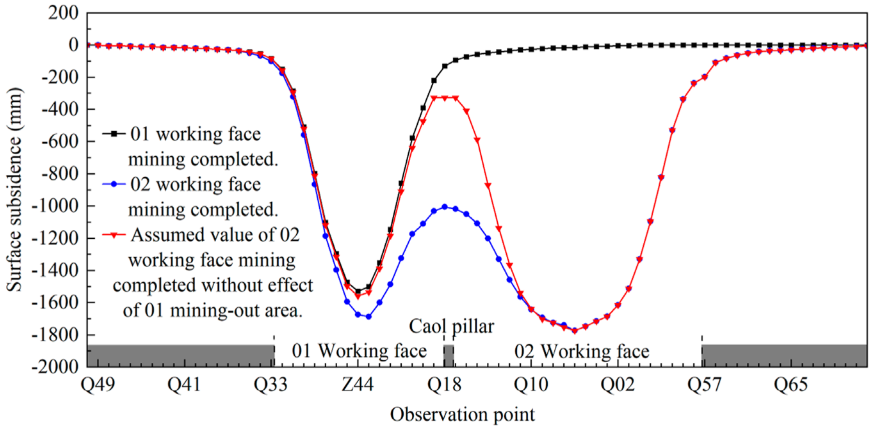

FIGURE 17
Cumulative surface subsidence curve of inclination observation line in working faces 01 and 02.

02 super-long working face observed in this research could not represent all situations. Therefore, with the promotion and application of super-long working faces, further research was needed on the surface movement and surface cracks development laws of super-long working faces under different topographic features, mining heights and overlying rock structures in the future.

5 Conclusion

(1) Through on-site measurement and calculation, the parameters and characteristics of surface movement and deformation of working faces with different inclination widths, the same geological conditions and the same mining height were obtained. The 01 working face, with an inclination width of 300 m, had a maximum surface subsidence of 1,613 mm, a maximum horizontal displacement of 414.1 mm, a maximum surface subsidence coefficient of 0.62, and a surface subsidence active phase of 54 d. The 02 working face, with an inclination width of 450 m, had a maximum surface subsidence of 1,860 mm, a maximum horizontal displacement of 433 mm, a maximum surface subsidence coefficient of 0.72, and a surface subsidence active phase of 53 d. Compared to the 01 working face, the maximum subsidence, maximum horizontal movement value, and maximum subsidence coefficient of the 02 super-long working face increased by 15.31%, 4.56%, and 16.13%, which indicated that the inclination width of the coal mining working face had some effect on its surface movement and deformation.

(2) Affected by the mining of the 02 working face, the 01 working face experienced secondary subsidence with a maximum increase of 12.3%. Along the direction of the inclination observation line, the surface subsidence curve of the 01 working face had a V shape after the mining, and the overall surface subsidence curve of working faces 01 and 02 had an asymmetric W shape after the mining of the 02 working face. The middle of the 02 working face surface subsidence curve was approximately flat bottomed, and a short distance at the bottom of the 01 working face surface subsidence curve

became flat when it was affected by the mining of the 02 working face. That indicated that a super-long working face could achieve full extraction in the inclination direction, and the full extraction's mining depth-to-height ratio was slightly greater than 120.

(3) Surface cracks caused by mining of the two main types included cracks with a spreading direction parallel to the open-off cut and cracks with a spreading direction parallel to grooves. The crack widths ranged from 0.1 to 0.5 cm, and their depths were less than 1 m. The width dynamic evolution law of surface cracks with a spreading direction parallel to the open-off cut was opening first, then closing over time. The width dynamic evolution law of surface cracks with the spreading direction parallel to grooves was opening first, then remaining open. The greater the mining depth-to-height ratio, the weaker the development degree of surface cracks. The development degree of surface cracks was very weak in the coal mining face whose mining depth-to-height ratio was 120, and those cracks could be closed quickly by aeolian sand.

Data availability statement

The original contributions presented in the study are included in the article/Supplementary Material, further inquiries can be directed to the corresponding author.

Author contributions

PH: Conceptualization, Data curation, Formal Analysis, Investigation, Methodology, Resources, Validation, Writing–original draft, Writing–review and editing. SW: Conceptualization, Supervision, Writing–review and editing. DF: Data curation, Investigation, Writing–review and editing. XX: Validation, Writing–review and editing. EH: Conceptualization, Funding acquisition, Methodology, Project administration, Supervision, Writing–review and editing.

Funding

The author(s) declare that financial support was received for the research, authorship, and/or publication of this article. This research was funded by the National Natural Science Foundation of China (No. 42177174), the Basic Research Program of Natural Science of Shaanxi Province (2020ZY-JC-03), and the Shaanxi Province Joint Fund Project (2021JLM-09).

Acknowledgments

The authors would like to sincerely thank Pei Xu and Xicheng Bai from Shaanxi Xiaobaodang Mining Co., Ltd. for their help in basic data collection and field survey work, and Liu Feng from Shaanxi 185 Coal Field Geology Co., Ltd. for his help in surface movement observation.

Conflict of interest

The authors declare that the research was conducted in the absence of any commercial or financial relationships that could be construed as a potential conflict of interest.

Generative AI statement

The author(s) declare that no Generative AI was used in the creation of this manuscript.

Publisher's note

Supplementary material

The Supplementary Material for this article can be found online at: https://www.frontiersin.org/articles/10.3389/feart.2024.1526950/full#supplementary-material

References

Bai, X. F., Ding, H., Lian, J. J., Ma, D., Yang, X. Y., Sun, N. X., et al. (2018). Coal production in China: past, present, and future projections. *Int. Geol. Rev.* 60 (5-6), 535–547. doi:10.1080/00206814.2017.1301226

Chen, C., Hu, Z. Q., Wang, J., and Jia, J. T. (2019). Dynamic surface subsidence characteristics due to super-large working face in fragile-ecological mining areas: a case study in Shendong coalfield, China. *Adv. Civ. Eng.* 2019. doi:10.1155/2019/8658753

Dudek, M., Sroka, A., Tajdus, K., Misa, R., and Mrochen, D. (2022). Assessment and duration of the surface subsidence after the end of mining operations. *Energies* 15 (22), 8711. doi:10.3390/en15228711

Feng, D., Hou, E. K., Xie, X. S., Che, X. Y., Hou, P. F., and Long, T. W. (2022). Prediction and treatment of water leakage risk caused by the dynamic evolution of ground fissures in gully terrain. *Front. Earth Sci.* 9. doi:10.3389/feart.2021.803721

Feng, D., Hou, E. K., Xie, X. S., Wei, J. B., and Hou, P. F. (2023). Differences in the dynamic evolution of surface crack widths at different locations in the trench slope area and the mechanisms: a case study. *Environ. Geochem. And Health* 45 (10), 7161–7182. doi:10.1007/s10653-022-01452-0

Fu, Y. K., Shang, J. X., Hu, Z. Q., Li, P. Y., Yang, K., Chen, C., et al. (2021). Ground fracture development and surface fracture evolution in N00 method shallowly buried thick coal seam mining in an arid windy and sandy area: a case study of the Ningtiaota mine (China). *Energies* 14 (22), 7712. doi:10.3390/en14227712

Fu, Y. K., Wu, Y. Z., Yin, X. W., and Zhang, Y. J. (2023). Mapping mining-induced ground fissures and their evolution using UAV photogrammetry. *Front. Earth Sci.* 11. doi:10.3389/feart.2023.1260913

Guo, Q. L., Han, Y. Y., Yang, Y. S., Fu, G. B., and Li, J. L. (2019a). Quantifying the impacts of climate change, coal mining and soil and water conservation on streamflow in a coal mining concentrated watershed on the loess plateau, China. *Water* 11 (5), 1054. doi:10.3390/w11051054

Guo, W. B., Guo, M. J., Tan, Y., Bai, E. H., and Zhao, G. B. (2019b). Sustainable development of resources and the environment: mining-induced eco-geological environmental damage and mitigation measures-A case study in the henan coal mining area, China. *Sustainability* 11 (16), 4366. doi:10.3390/su11164366

Guo, W. B., Huang, C. F., and Chen, J. J. (2010). The dynamic surface movement characteristics of fully mechanized caving mining under thick hydrous collapsed loess (in Chinese). *J. Of China Coal Soc.* 35 (S1), 38–43. doi:10.13225/j.cnki.jccs.2010.s1.014

Guo, W. B., Huang, C. F., and Chen, J. J. (2011). Observation and study on surface ground subsidence speed of fully mechanized top coal caving mining in thick seam (in Chinese). *Coal Sci. Technol.* 39 (04), 114–117. doi:10.13199/j.cst.2011.04.119.guowb.030

Hou, E. K., Xie, X. S., Wang, S. M., Cong, T., Feng, D., and Chen, Z. (2021). Development law of ground cracks induced by fully-mechanized mining of medium-buried coal seams (in Chinese). *J. Min. and Saf. Eng.* 38 (06), 1178–1188. doi:10.13545/j.cnki.jmse.2020.0293

Li, L., Wu, K., Hu, Z. Q., Xu, Y. K., and Zhou, D. W. (2017). Analysis of developmental features and causes of the ground cracks induced by oversized working face mining in an aeolian sand area. *Environ. Earth Sci.* 76 (3), 135. doi:10.1007/s12665-017-6452-9

Prakash, A., Kumar, N., Kumbhakar, D., Singh, A. K., and Paul, A. (2018). A safe depillaring design for shallow depth of cover with influence of surface ground movements: a study in Jharia Coalfield. *Arabian J. Of Geosciences* 11 (8), 164. doi:10.1007/s12517-018-3508-4

Qiao, W., Li, W. P., Li, T., Chang, J. Y., and Wang, Q. Q. (2017). Effects of coal mining on shallow water resources in semiarid regions: a case study in the shennan mining area, Shaanxi, China. *Mine Water And Environ.* 36 (1), 104–113. doi:10.1007/s10230-016-0414-4

Shang, Y. Z., Lu, S. B., Li, X. F., Hei, P. F., Lei, X. H., Gong, J. G., et al. (2017). Balancing development of major coal bases with available water resources in China through 2020. *Appl. Energy* 194, 735–750. doi:10.1016/j.apenergy.2016.07.002

Song, J. X., Yang, Z. Y., Xia, J., and Cheng, D. D. (2021). The impact of mining-related human activities on runoff in northern Shaanxi, China. *J. Of Hydrology* 598, 126235. doi:10.1016/j.jhydrol.2021.126235

Xie, X. S., Hou, E. K., Wang, S. M., Liu, F., Xie, Y. L., Chen, Z., et al. (2021). Study on surface movement and deformation law of the middle deep buried thick seam in sandy region (in Chinese). *Saf. Coal Mines* 52 (12), 199–206. doi:10.13347/j.cnki.mkaq.2021.12.034

Xu, Y. K., Wu, K., Bai, Z. H., and Hu, Z. Q. (2017). Theoretical analysis of the secondary development of mining-induced surface cracks in the Ordos region. *Environ. Earth Sci.* 76 (20), 703. doi:10.1007/s12665-017-7050-6

Xu, Y. K., Wu, K., Li, L., Zhou, D. W., and Hu, Z. Q. (2019). Ground cracks development and characteristics of strata movement under fast excavation: a case study at Bulianta coal mine, China. *Bull. Of Eng. Geol. And Environ.* 78 (1), 325–340. doi:10.1007/s10064-017-1047-y

Yan, W. T., Guo, J. T., and Yan, S. G. (2023). Difference in surface damage between deep and shallow mining of underground coal resources in China. *Sustainability* 15 (9), 7296. doi:10.3390/su15097296

Yang, K., Hu, Z. Q., Liang, Y. S., Fu, Y. K., Yuan, D. Z., Guo, J. X., et al. (2022). Automated extraction of ground fissures due to coal mining subsidence based on UAV photogrammetry. *Remote Sens.* 14 (5), 1071. doi:10.3390/rs14051071

Yi, S. H., Zhang, Y., Yi, H. Y., Li, X. L., Wang, X., Wang, Y., et al. (2022). Study on the instability activation mechanism and deformation law of surrounding rock affected by water immersion in goafs. *Water* 14 (20), 3250. doi:10.3390/w14203250

Yin, H. J., Guo, G. L., Li, H. Z., Wang, T. N., and Yuan, Y. F. (2022). Prediction method and research on characteristics of surface subsidence due to mining deeply buried Jurassic coal seams. *Bull. Of Eng. Geol. And Environ.* 81 (10), 449. doi:10.1007/s10064-022-02946-y

Zha, J. F., and Xu, M. Q. (2019). High-grade highways deformation and failure laws in mining area - a case in Nantun Coal Mine, China. *Int. J. Of Pavement Eng.* 20 (11), 1251–1263. doi:10.1080/10298436.2017.1402592

Zhang, B. C., Liang, Y. P., Zou, Q. L., Chen, Z. H., Kong, F. J., and Ding, L. Q. (2022a). Evaluation of surface subsidence due to inclined coal seam mining: a case study in the 1930 coal mine, China. *Nat. Resour. Res.* 31 (6), 3303–3317. doi:10.1007/s11053-022-10117-9

Zhang, C., Wang, P., Wang, E., Chen, D., and Li, C. (2023). Characteristics of coal resources in China and statistical analysis and preventive measures for coal mine accidents. *Int. J. coal Sci. and Technol.* 10 (1), 22. doi:10.1007/s40789-023-00582-9

Zhang, Y. J., Lian, X. G., Yan, Y. G., Zhu, Y. H., and Dai, H. Y. (2022b). Study on the development law of mining-induced ground cracks under gully terrain. *Remote Sens.* 14 (23), 5985. doi:10.3390/rs14235985

Zhou, D. W., Wu, K., Cheng, G. L., and Li, L. (2015). Mechanism of mining subsidence in coal mining area with thick alluvium soil in China. *Arabian J. Of Geosciences* 8 (4), 1855–1867. doi:10.1007/s12517-014-1382-2

Zhu, X. J., Guo, G. L., Liu, H., and Yang, X. Y. (2019). Surface subsidence prediction method of backfill-strip mining in coal mining. *Bull. Of Eng. Geol. And Environ.* 78 (8), 6235–6248. doi:10.1007/s10064-019-01485-3

Zou, J. P., Wang, M., Bai, L., and Yan, C. W. (2023). Numerical study on migration of overlying strata and propogation of cracks during multi-coal seams mining. *Front. Earth Sci.* 11. doi:10.3389/feart.2023.1326597

frontiers | Frontiers in Earth Science

TYPE Original Research
PUBLISHED 10 January 2025
DOI 10.3389/feart.2024.1518377

Check for updates

OPEN ACCESS

EDITED BY
Rui Yong,
Ningbo University, China

REVIEWED BY
Yong Nie,
Chinese Academy of Sciences (CAS), China
Yankun Wang,
Yangtze University, China

*CORRESPONDENCE
Chong Xu,
✉ xc11111111@126.com

RECEIVED 28 October 2024
ACCEPTED 26 December 2024
PUBLISHED 10 January 2025

CITATION
Xue Z, Xu C, Zhang Z, Feng L, Li H, Zhang H, Zhu D, Sun J, Wang P, Li L and Chen J (2025) Inventory of landslide relics in Zhenxiong County based on human-machine interactive visual interpretation, Yunnan Province, China. *Front. Earth Sci.* 12:1518377. doi: 10.3389/feart.2024.1518377

Inventory of landslide relics in Zhenxiong County based on human-machine interactive visual interpretation, Yunnan Province, China

Zhiwen Xue[1,2,3], Chong Xu[2,3]*, Zhiqiang Zhang[4], Liye Feng[5], Hao Li[6], Hourong Zhang[4], Dengjie Zhu[4], Jingjing Sun[7], Peng Wang[8], Lei Li[9] and Jingyu Chen[10]

[1]School of Emergency Management Science and Engineering, University of Chinese Academy of Sciences, Beijing, China, [2]National Institute of Natural Hazards, Ministry of Emergency Management of China, Beijing, China, [3]Key Laboratory of Compound and Chained Natural Hazards Dynamics, Ministry of Emergency Management of China, Beijing, China, [4]Research Institute of China Southern Power Grid Co., Ltd., Guangzhou, Guangdong, China, [5]Jiangsu World Group, Danyang, Jiangsu, China, [6]Electric Power Research Institute, Yunnan Power Grid Co., Ltd., Kunming, Yunnan, China, [7]Zhejiang Metallurgical Survey and Design Co., Ltd., Hangzhou, Zhejiang, China, [8]Beijing Engineering Corporation Limited, Beijing, China, [9]Institute of Geology and Geophysics, Chinese Academy of Sciences, Beijing, China, [10]Geological Research Institute, Shougang Geological Exploration Institute, Beijing, China

Introduction: Landslides occur frequently in Zhenxiong County, posing significant threats to residents' lives and property. A comprehensive understanding of the development patterns of landslide disasters in this region is crucial for disaster prevention, land-use planning, and risk assessment.

Methods: This study utilized high-resolution satellite imagery from the Google Earth Pro platform and employed a human-machine interactive visual interpretation approach to investigate landslide occurrences. A comprehensive landslide inventory comprising 3,979 landslide outlines was established through extensive literature review and data cleaning techniques. The spatial distribution characteristics and statistical patterns of landslides were analyzed.

Results: The total landslide-affected area is 319.20 km^2, with the largest landslide covering 4.55 km^2 and the smallest measuring 1,779 m^2. The average landslide area is 80,215 m^2, with the majority (73.54%) classified as medium-sized landslides. The landslide area percentage (LAP) is 8.64%, and the landslide number density (LND) is 1.077 landslides per km^2, with the highest recorded landslide density being 3.380 landslides per km^2. Landslides are predominantly concentrated in four key areas: the confluence of the Baishui River and Yanxi River, Dashuigou Reservoir, both sides of the valley from Heitang Village to Hongyan Village, and Xiaogou Village. These areas are characterized by well-developed water systems, middle and low mountains, and heavily dissected landscapes.

Discussion: The landslide database established in this study provides essential scientific data for analyzing the spatial distribution of landslide disasters in Zhenxiong County. It offers valuable insights for local governments and relevant authorities in disaster prevention, land-use planning, and risk assessment. The findings highlight the significant impact of complex terrain and developed water systems in middle and low mountain regions on landslide disasters. Future studies should further integrate geological and meteorological factors for deeper analysis.

KEYWORDS

geological disasters, landslide inventory, visual interpretation, disaster prevention and control, Zhenxiong County

1 Introduction

Landslides, as a common geological hazard (Huang et al., 2023b; Feng et al., 2024b), are widespread globally and occur with particular frequency in mountainous and hilly regions. These events pose significant threats to human life and property while also adversely impacting transportation, infrastructure, agriculture, and ecological systems. According to the United Global Landslide Database (UGLD), from 1903 to 2020, 37,946 severe landslide events were recorded across 161 countries, resulting in 185,753 fatalities (Gómez et al., 2023). In China alone, landslides claimed 28,139 lives between 1950 and 2016. Notably, in recent decades, the frequency and intensity of landslides have been increasing due to the exacerbation of climate change and intensified human activities (Frodella et al., 2018; Coviello et al., 2024). This rising trend presents significant challenges for disaster forecasting, mitigation, and management (Hwang and Lall, 2024).

Fortunately, the critical issue of landslides has garnered extensive attention over the past decade, leading to a steady growth in landslide research (Xu and Li, 2021; Huang et al., 2022; Chicas et al., 2024; Hosseini et al., 2024; Huu et al., 2024; Jallayu et al., 2024). Landslide inventories have emerged as invaluable resources for advancing our understanding of these hazards. These inventories are crucial for studying landslide processes, types, and triggers, while also providing insights into spatial distribution patterns and risk assessment (McGovern et al., 2024). Many countries have developed detailed landslide inventories (Conforti et al., 2014; Posner and Georgakakos, 2015; Sepúlveda and Petley, 2015; Rosser et al., 2017; Barella et al., 2019; Sultana, 2020). For example, Aristizábal and Sánchez compiled a comprehensive landslide inventory for Colombia, documenting 30,730 landslides between 1900 and 2018 and analyzing their spatiotemporal patterns and socioeconomic impacts (Aristizábal and Sánchez, 2020). Similarly, Bueechi et al. created an inventory of shallow landslides in Peru's Cordillera Blanca, identifying 254 landslides from 2013 to 2017 using Google Earth imagery and developing a regional-scale susceptibility model (Bueechi et al., 2019). In Nicaragua, the Nicaraguan Institute for Earth Sciences (INETER) documented approximately 17,000 landslides from 1826 to 2003 in mountainous and volcanic terrains. This database has been instrumental for hazard assessment, emergency management, land-use planning, early warning systems, and policy implementation (Devoli et al., 2007). Italy's national IFFI project, initiated in 1999, has mapped over 620,808 landslides, providing critical data for managing this pervasive hazard (Trigila et al., 2010).

China, with its diverse landforms—including mountains, hills, basins, plains, and plateaus—offers a geological environment highly conducive to landslides. Consequently, substantial research has been dedicated to developing landslide inventories (Li et al., 2021; Cui et al., 2023; Huang et al., 2023a; Li et al., 2024d; Sun et al., 2024b; Wang W. et al., 2024; Zhang et al., 2024; Zhao et al., 2024). For instance, Xu et al. leveraged high-resolution satellite imagery to create a detailed inventory of landslide relics on the Loess Plateau, identifying approximately 80,000 landslides (Xu et al., 2020). Wang et al. mapped 605 landslides covering a total area of 24.53 km^2 in Jiyuan City, Henan Province, using Google Earth imagery (Wang et al., 2022). In Shaanxi Province, Chen et al. compiled a comprehensive database of landslide relics in Xianyang, analyzing their spatial distribution (Liu et al., 2023). In the Qinling region, Feng et al. developed an extensive inventory of landslide relics, providing key data for this mountainous area (Feng et al., 2024a; Feng et al., 2024b). Furthermore, Zhao et al. documented 1,073 landslides along the Sichuan-Tibet Engineering Corridor, validating their findings through a two-month field survey (Zhao et al., 2023). Similarly, Shao et al. constructed a database of paleo-landslides for the Wudongde Hydropower Station area, applying the data for hazard assessments (Shao et al., 2024b). These efforts underscore the critical role that landslide inventories play in mitigating risks and enhancing our understanding of this complex geological phenomenon.

Although China has developed numerous landslide inventories, county-level data often lack the necessary detail and comprehensiveness. This shortfall impedes a thorough understanding of regional landslide dynamics, diminishes the accuracy of risk assessments, and undermines the effectiveness of disaster prevention, mitigation, and response efforts. These challenges are particularly pronounced in southwestern China, a region highly prone to geological hazards (Shen et al., 2022; Shu et al., 2022). For instance, on 22 January 2024, a catastrophic landslide in Zhenxiong County, Yunnan Province, resulted in significant casualties and severe economic losses. Addressing this gap, our study employed a human-computer interactive visual interpretation approach to construct a detailed inventory of landslide relics within Zhenxiong County. Furthermore, we conducted a preliminary analysis of their spatial distribution patterns. The findings of this research provide a solid scientific foundation for future investigations and offer valuable data to support disaster prevention, mitigation, and response strategies in the region.

2 Study area

Zhenxiong County is situated in the northeastern part of Yunnan Province, at the junction of Yunnan, Guizhou, and Sichuan Provinces. It borders Xuyong County, Sichuan, along the Chishui River to the east; Bijie and Hezhang in Guizhou to the south; Yiliang to the west; and Weixin to the north. Geographically, the county lies between 104°10′ to 104°45′E and 27°13′ to 27°45′N, characterized by a rugged terrain of intersecting mountain ranges and valleys. The area features significant topographical relief and deep dissection, forming multi-level stepped landforms and deeply incised valleys (Figure 1). Elevation generally increases from northeast to southwest, with typical altitudes ranging between 1,000 and 2,000 m, creating a karst-erosion mid-mountain landscape (Yin et al., 2013; Yin et al., 2015). Geologically, Zhenxiong County features a complex structure as part of the Yunnan-Guizhou Plateau, shaped primarily by the convergence of the Yangtze and Kang-Dian tectonic blocks. Long-term tectonic activity has resulted in multiple stratigraphic overlays and intricate fault systems. The county is dominated by Huaxia-type structural features, characterized by a series of northeast-southwest trending folds of varying scales, accompanied by compressional-shear faults that run nearly parallel to these folds. Additionally, east-west and north-south trending structures, along with smaller torsional features, are present. Key tectonic elements include the Zhenxiong-Tangfang fault, Yuhe-Tanglangba wrench fault, Shanlin fault, and Guanmenshan fault, while seismic activity remains generally low. The region exhibits relatively complete stratigraphic sequences, with the oldest formations dating back to the Lower Cambrian. The most widespread lithologies include terrestrial-dominated, coal-bearing sandstones and shales of the Upper Permian, with interspersed marine layers, as well as Lower Triassic shallow marine sandstones and shales, limited carbonate rocks, and Quaternary deposits (Figure 2). Stratigraphically, the Upper Permian Longtan Formation, comprising shales, siltstones, fine sandstones, and coal seams, is primarily found downstream of the Hekou dam site near Poji Town, with limited outcrops near Tangfang Town at the reservoir tail. Overlying this, the Upper Permian Changxing Formation features shale interbedded with bioclastic limestone. The Lower Triassic Feixianguan Formation includes siltstone, fine sandstone, shale interbedded with limestone, and oolitic limestone, while Quaternary deposits are composed of sand, gravel, angular fragments, silt, and clay. The Upper Permian Emeishan Basalt Formation, extensively distributed in the area, is notable for its weak interlayers, which soften significantly upon water exposure, reducing strength and increasing the likelihood of soil layer slippage. Furthermore, sandstone, mudstone, shale, and coal-bearing strata with transitional marine-terrestrial facies exhibit strong permeability, facilitating water infiltration and softening of interbedded shales and mudstones, which in turn promote landslides. The sand-shale formations, interspersed with coal layers, possess low strength and high weathering susceptibility, further amplifying the region's vulnerability to landslides (Zheng et al., 2021).

Zhenxiong County has a subtropical plateau monsoon climate, characterized by distinct altitudinal variations. Due to its topography, with higher elevations in the south and lower elevations in the north, the mountain ranges predominantly run north-south or southwest-northeast. Cold air masses from the northwest are forced upward, resulting in frequent fog and fewer sunny days. The average annual temperature is around 15°C, with moderate summers and relatively cold winters. The county's diverse terrain and significant altitude differences create distinct climate zones: high-altitude areas are cool and humid, while lower elevations are warmer. Rainfall is concentrated during the rainy season from June to August, accounting for 47%–76% of the annual precipitation, and the region experiences an average of 130 rainy days per year, making it one of the wettest areas in China. The combination of complex geology, steep terrain, abundant rainfall, and intense human activities—such as widespread coal mining and rapid infrastructure development—has led to considerable environmental degradation. As a result, Zhenxiong County is highly susceptible to geological hazards.

3 Methods

To construct the landslide disaster database, we primarily utilize human-computer interactive visual interpretation, supplemented by 3S technologies (GIS, RS, GPS) and literature-based validation methods for landslide identification and cataloging. This process involves two key steps: (1) digitizing landslide identification graphical data to establish a graphical database and (2) inputting associated attribute data to form an attribute database. Through calibration, processing, editing, and verification, a comprehensive and accurate landslide catalog database is ultimately created. The method's workflow is illustrated in Figure 3.

3.1 Construction method of graphic database

The graphical construction method primarily employs human-computer interactive visual interpretation, a technique that combines expert observation with computer-based image processing to enhance accuracy and efficiency in geological hazard identification, particularly for landslides. This approach effectively leverages human expertise alongside the computational power of modern image processing tools. Unlike traditional visual interpretation methods, it integrates real-time analysis software, such as GIS, which provides immediate statistical feedback on identified results. This capability allows operators to monitor overarching landslide trends dynamically during the identification process. Recent advancements in machine learning-based image recognition have further supported landslide detection (Yang and Xu, 2022; Saha et al., 2024; Sharma et al., 2024; Yang et al., 2024). However, compared to these machine learning techniques, human-computer interactive visual interpretation retains a key advantage: the incorporation of expert judgment. This method enables users to interact with the system, guiding it to refine identification parameters for greater accuracy. Additionally, it facilitates deeper insights by allowing experts to interpret and expand on computer-generated data. This iterative feedback loop between expertise and computational analysis significantly enhances both precision and efficiency.

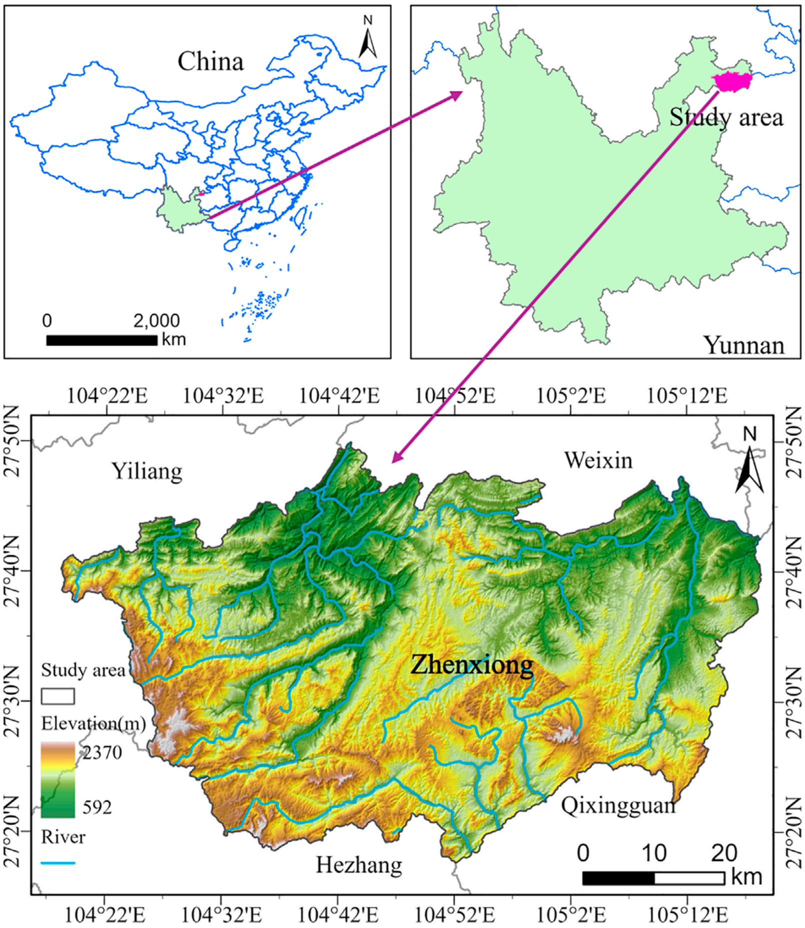

FIGURE 1
Location of the study area.

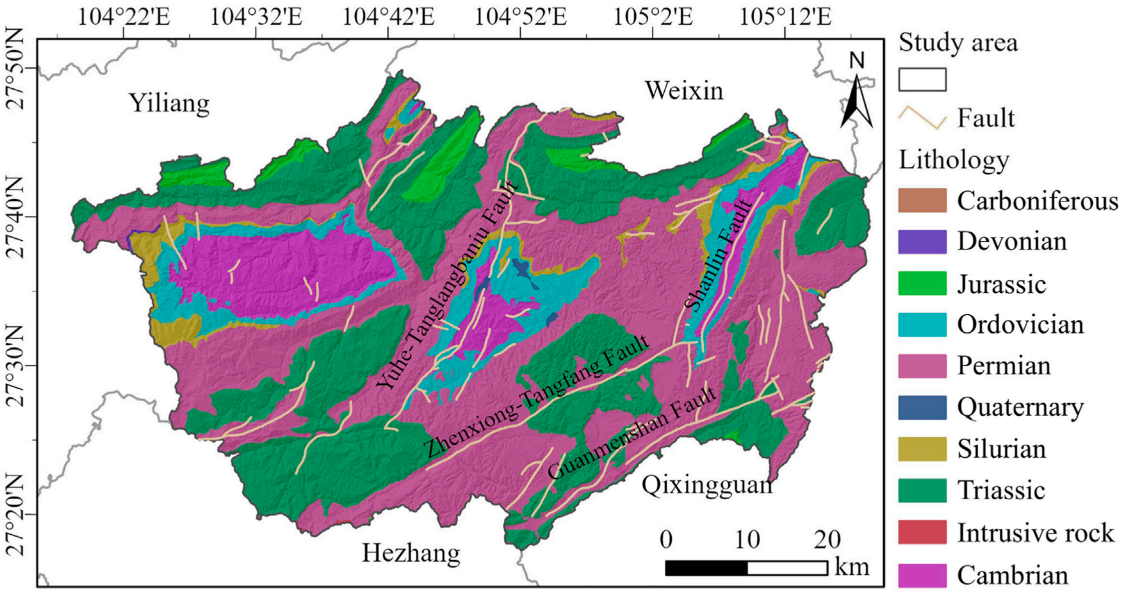

FIGURE 2
Geological map of the study area.

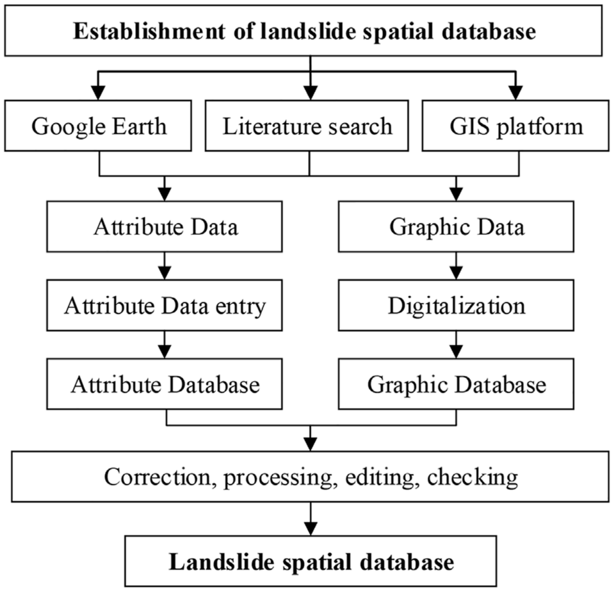

FIGURE 3
Flow chart of landslide database construction.

This work primarily utilizes high-resolution, three-dimensional optical remote sensing imagery provided by the Google Earth Pro platform. The satellite imagery is an integration of multisource remote sensing data, including SPOT5 (2.5 m resolution imagery), QuickBird commercial satellite (0.6 m resolution), IKONOS (1 m resolution), Landsat8, WorldView-1 and WorldView-2 satellites (0.5 m resolution), WorldView-3 (0.3 m resolution), WorldView-4 (panchromatic resolution 0.3 m), and GeoEye-1 (0.5 m resolution). Google Earth continuously expands its imagery database and employs advanced data-mining techniques to reduce the effects of cloud cover and atmospheric interference, thereby improving image clarity and usability for analysis. This platform enables multi-angle, comprehensive observation of regional terrain features and landform characteristics (Yu et al., 2024), providing advantageous conditions for human-computer interactive visual interpretation (Yu et al., 2022). In this study, the research area is defined and divided into multiple sub-regions to ensure no areas are missed during the interpretation process. Occasionally, cloud cover obscures some sections; however, Google Earth Pro's historical imagery function allows us to review these regions over time, enabling more accurate and complete landslide identification across the entire study area.

Landslide identification primarily depends on human visual judgment, requiring personnel to have specialized knowledge of landslide characteristics and assessment criteria. The process relies on identifying discrepancies in color, shape, and texture between the landslide mass and the surrounding geological context, such as landforms and rivers. Key morphological features, including the back scarp, perimeter, and accumulation body, serve as fundamental criteria. Special attention is given to areas with abrupt topographic changes, where regions showing landslide characteristics are accurately delineated using vector polygons. A fully developed landslide should include the following components: the landslide mass, landslide bed, slip surface, back scarp, landslide tongue, landslide steps, and landslide depression, as shown in Table 1. However, not all landslides possess all of these features; nonetheless, the landslide mass and back scarp are present in all cases.

The direct interpretation indicators of landslides primarily focus on the characteristics of the landslide itself in remote sensing images, such as shape, tone, and texture. Shape characteristics: Due to the downward movement of the landslide body, the terrain in the three directions (left, right, and rear) of the landslide tends to be slightly higher, giving it an overall shape resembling a horseshoe, circular chair, bullhorn, or tongue, with the rear wall opening towards the slope base. Tone characteristics: Newly occurred landslides often appear in light tones such as grayish-white or bluish-white due to the destruction of surface vegetation and soil fragmentation. The tone distribution is uneven. Landslide scars tend to appear lighter in tone because they reflect more light, while landslide depressions may appear darker, especially when water accumulates. For older landslides, the recovery of surface vegetation diminishes these color features, but they can still be differentiated from the surrounding tones. Texture characteristics: The original stratigraphic integrity is disrupted, resulting in exposed soil, overturned vegetation, and a fragmented surface. This leads to a rough texture with patchy shadow effects visible in the imagery. The indirect interpretation indicators of landslides primarily focus on environmental factors around the landslide, such as vegetation distribution, topography, geological structure, hydrological information, and ecological landscapes. Vegetation characteristics: For slow-moving or old landslides, the continuous downward movement of the landslide body, combined with the upward growth of trees, results in phenomena like "scythe trees" and "drunken forest" on the landslide surface, which are particularly evident in high-resolution aerial imagery. Hydrological characteristics: Irregular water system patterns on the landslide body, sudden changes in river flow directions at the base of the slope, or narrowing of river channels can indirectly indicate the presence of a landslide. Topographical features: Poor continuity of the landform often results in unique "steep slope + gentle slope" landforms, and the area below the landslide body may exhibit uneven terrain due to the pressure exerted by the sliding mass.

Frequent operations during the identification process may lead to geometric self-intersection issues. Although apparent errors can often be detected manually, smaller discrepancies may evade visual inspection, making algorithmic identification necessary. Unresolved self-intersection issues can hinder the conversion of features into the required GIS format, causing complications in subsequent analyses. Verification is therefore essential after data construction to ensure database integrity and accuracy. This involves using topology checking tools in GIS software to detect self-intersections in polygon features. Identified geometric issues are then corrected to maintain data quality.

3.2 Construction method of attributing database

Collected information is structured into a database, where each landslide point corresponds to a unique attribute record,

TABLE 1 Landslide elements and their meanings.

Landslide elements	Meaning
Landslide body	The mass of rock and soil sliding downward along the slope surface
Landslide base	The stationary rock and soil mass to which the landslide body is attached during its downward movement
Landslide surface	The interface between the landslide body and the landslide base
Landslide scarp	The exposed interface at the rear edge of the landslide body, resembling a circular chair, where it separates from the stationary slope
Landslide toe	The tongue-shaped protrusion at the front end of the landslide body
Landslide step	Displaced steps formed due to inconsistent sliding times and speeds of different parts of the landslide body
Landslide depression	A closed depression with a low center and higher surrounding areas, formed due to the collapse of the landslide body part connecting to the landslide scarp

ensuring precise matching between graphical and attribute data. This includes details such as location, area size, geometric perimeter, and associated geographical factors like elevation, slope, curvature, lithology, and proximity to faults. After data entry, the attribute data undergoes verification and correction to ensure accuracy and completeness. Different experts independently interpret landslide areas using identical satellite imagery and topographic data, recording key characteristics such as location, area size, and boundaries. Their results are compared to calculate consistency indices that quantify the accuracy and reliability of interpretations. Discrepancies are collectively reviewed to identify error sources and refine unified interpretation standards. The final database is stored in shapefile format, comprising the main (.shp), index (.shx), and attribute (.dbf) files, which enable standardized management of geological disaster data. Statistical analysis of attribute data reveals patterns and characteristics of disaster occurrences. For instance, analyzing disaster frequency and regional distribution helps identify high-risk areas and temporal-spatial patterns, providing critical support for disaster early warning and prevention.

4 Results

4.1 The result of landslide identification

Based on the high-resolution optical remote sensing images provided by the Google Earth Pro platform, a detailed interpretation of landslides in the Zhenxiong County area (covering 3,696 km^2) was conducted using a human-computer interaction visual interpretation method. A total of 3,979 landslides were identified, encompassing a combined area of 319.20 km^2. The largest landslide, measuring 4.55 km^2, represents a significant ancient slide that diverted a river by filling a valley. In contrast, the smallest landslide covered just 1,779 m^2, while the average landslide area across the study area was 80,215 m^2 (Figure 4A). Statistical analysis revealed that there are 72 landslides larger than 0.5 km^2, accounting for 1.81% of the total number of landslides, with 15 landslides exceeding 1 km^2. Additionally, there are 758 landslides with areas between 0.10 km^2 and 0.5 km^2, 880 landslides between 0.05 km^2 and 0.10 km^2, and 2,046 landslides ranging from 0.01 km^2 to 0.05 km^2. Only 223 landslides have an area smaller than 0.01 km^2, as illustrated in Figure 4B. Landslides were categorized by area into small (<10,000 m^2), medium (10,000 m^2–100,000 m^2), and large (>100,000 m^2) landslides. It was found that the vast majority (73.54%) of landslides in Zhenxiong County are medium-sized landslides, followed by large landslides, which account for 20.86% of the total number. Small landslides constitute only 5.60% of the total landslide count. Several factors contribute to the prevalence of larger landslides: 1) The morphological features and geomorphology of large landslides are more pronounced, making them easier to identify; 2) Smaller landslides tend to lose their characteristics over time due to erosion, making them difficult or even impossible to recognize; 3) Smaller landslides are more susceptible to vegetation cover, which hampers identification. To gain a deeper understanding of the development of landslide relics in Zhenxiong County, GIS software was utilized to calculate the landslide area percentage (LAP) and landslide point density (LND) across the entire study area. The results showed that LAP and LND were 8.64% and 1.077 landslides per km^2, respectively, indicating a significant development of both the number and area of landslides in the county.

4.2 Spatial distribution of landslide

Overlaying the identified landslides on the elevation map reveals that most are distributed between 1,000 and 2,000 m in elevation, as shown in Figure 5. Statistical analysis of the landslide distribution based on geographic coordinates indicates that landslide density is significantly higher between 104°17′E and 104°47′E compared to other longitudinal areas. Similarly, in the latitudinal range of 27°40′N to 27°25′N, landslide density is notably higher than in other latitudes. Consequently, landslides in Zhenxiong County are primarily concentrated in the northwestern and southwestern regions. To clearly identify areas with higher landslide densities, we used the kernel density tool in GIS software to calculate landslide point density, setting the search radius to 5 km. As shown in Figure 6, the highest density reaches 3.38 landslides per km^2. The maximum density is concentrated

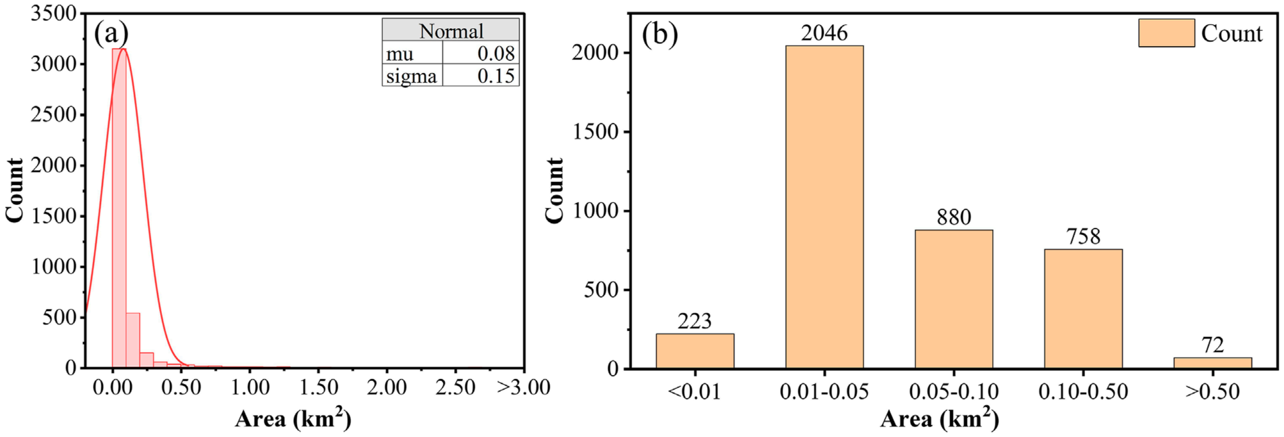

FIGURE 4
Distribution of landslide area scale, **(A)** Area histogram, **(B)** Distribution of landslide area and quantity.

in four specific regions: the confluence of the Baishui River and Yanxi River in the northwest, the Dahuigou Reservoir, the valleys along both sides of the river from Heitang Village to Hongyan Village, and Xiaogou Village. These areas feature well-developed drainage systems and mid-to-low mountainous terrain, with the western canyons being particularly significant for landslide occurrences. In contrast, the eastern part of Zhenxiong County has relatively flat terrain, with a more uniform landslide distribution. The area around Hongjiayuanzi Village shows a concentrated landslide distribution, where higher elevations and significant topographic variations (with a maximum elevation of 2,300 m) make the terrain more susceptible to geological factors contributing to landslides.

4.3 Typical landslide

This database includes several typical landslide morphologies, such as “hoop chair,” tongue-like, oval, and “shovel” shapes. Geomorphologically, the features typically exhibit dual ditches with a common source, cracks and cliff faces at the back of the landslide, a distinct boundary between the landslide mass and surrounding mountains, steep steps or benches on the landslide body, and landslide deposits that obstruct rivers, causing unusual river diversions. Most of the landslide relics are ancient, having undergone long-term geological evolution that often modifies them, making identification challenging. However, the boundaries of the landslides are usually clearly visible, and the deposits are distinctly marked, with color differences that set them apart from the surrounding vegetation and terrain. As shown in Figure 7, the thick white dashed line indicates the overall boundary of the landslide, the white arrows denote the rear edge where material has slid down from the highest point, the yellow arrow shows the direction of landslide movement, and the thin white dashed line represents the landslide deposits.

Figure 7A illustrates a typical landslide located in Zhangzhai Village, covering an area of 0.31 km^2. As shown in the figure, the landslide mass has slid down from the southern mountain, forming deposits below. Upon closer inspection, the length of the deposits on the left side of the landslide is notably greater than on the right side. This discrepancy may be attributed to the heterogeneous nature of the rock masses on the left and right sides during the sliding process. Alternatively, it is possible that the left half of the landslide experienced a secondary sliding event after some time, resulting in a larger deposit area on that side. This has led to a noticeable anomaly in the valley’s orientation. Given the long time since the event, settlements have been constructed on the landslide mass. Figure 7B shows another typical landslide located on the southern mountain of Zhongzhai Village, covering 0.09 km^2. The landslide has an elliptical shape, with a clear boundary between the landslide scarp and the landslide body, as well as a distinct demarcation between the landslide deposits and the surrounding environment. Similar to the previous example, this landslide has caused an abnormal valley orientation. Over time, human activity has resulted in the creation of terraced fields on the landslide mass. Figure 7C depicts a typical landslide situated on the south bank of the Huangshui River, with an area of 0.08 km^2. This landslide is narrow at the top and widens at the bottom, sliding down the mountain at an inclined angle. Moreover, based on the vegetation on the southern bank of the river below, it can be inferred that a small section on the left side of the landslide deposits has also undergone secondary sliding, indicating the instability of the surrounding mountains and their susceptibility to future landslides. Figure 7D depicts a typical landslide located in Fengyan Village, covering an area of 0.30 km^2. This landslide slid northwest from the eastern side of Fengyan Village, with its rear edge still visible. Due to the long time elapsed since the landslide event, settlements have been built on the landslide mass. The landslide has created a significant elevation difference from east to west on the mountain, causing the terraces built by humans to display a discontinuous topography stretching from northeast to southwest. The original southwest-northeast oriented valley was disrupted by the landslide deposits, resulting in the valley shifting approximately 180 m to the northwest. Figure 7E features another typical landslide in Sunjiagou Village, covering an area of 1.21 km^2, classified as a large landslide. Erosion gullies have developed on both sides of the landslide, demonstrating the typical dual-ditch morphology with the

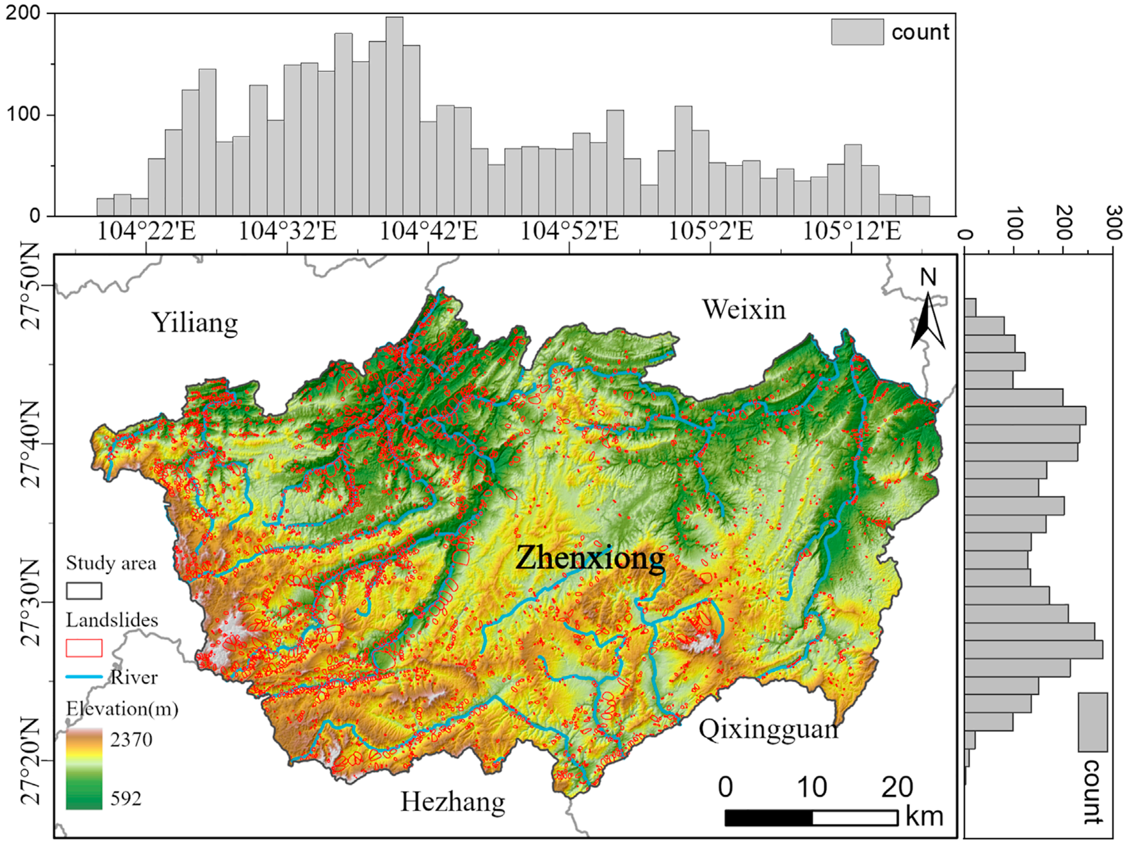

FIGURE 5
Spatial distribution of landslides.

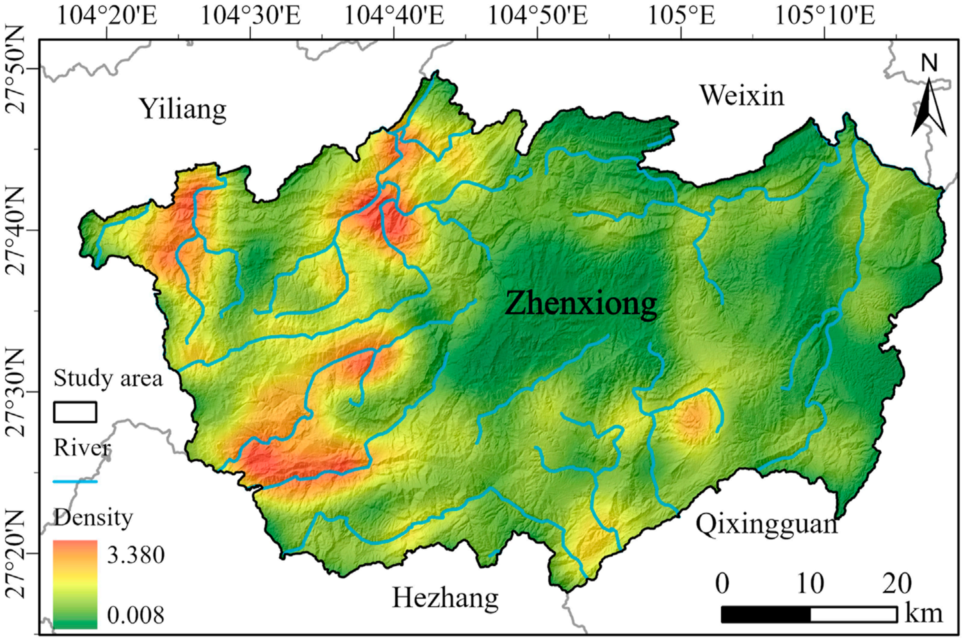

FIGURE 6
Number density map of landslide points.

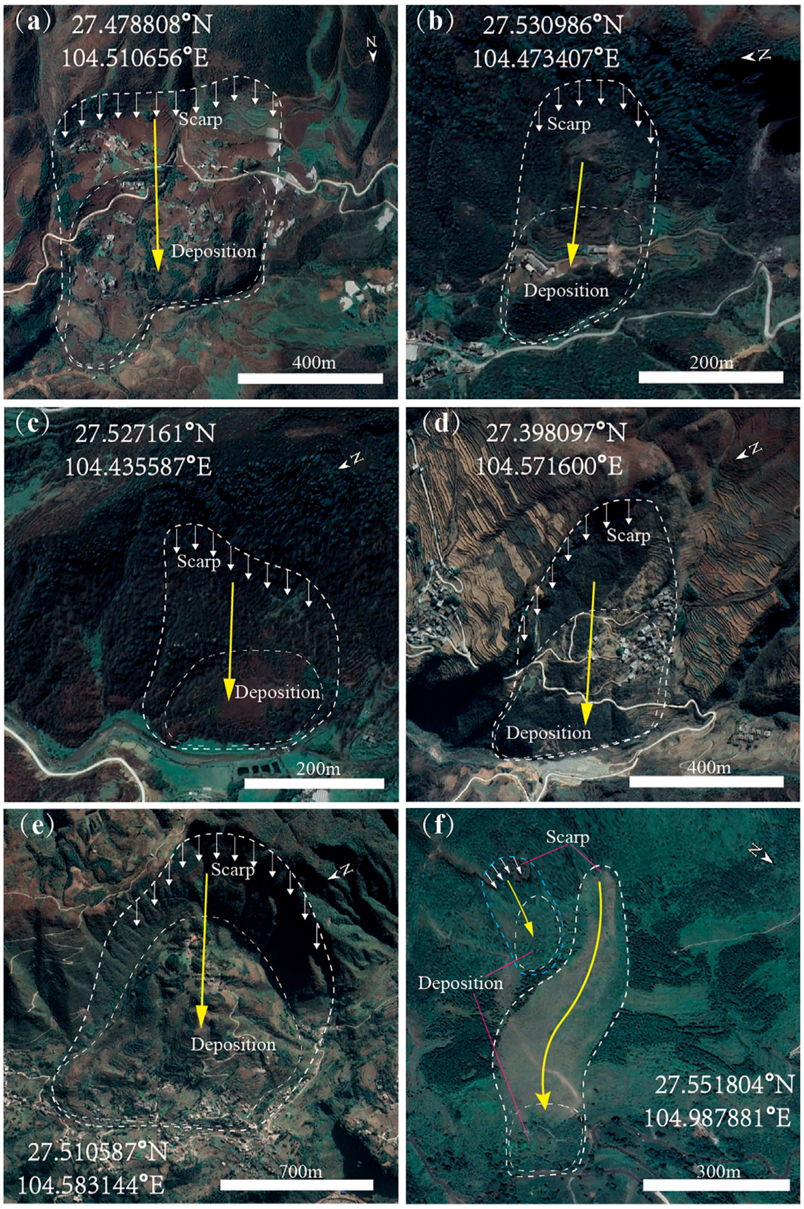

FIGURE 7
Pictures of typical landslides. **(A–F)** are images of landslides with relatively clear morphology from the landslide inventory.

same source. Due to the considerable size of the landslide, numerous settlements and terraced fields have developed on and around the landslide mass. Lastly, Figure 7F illustrates a landslide that occurred on 11 January 2013, in Zhaojiagou Village, with an area of 0.91 km^2. The source, sliding area, and slope morphology of the landslide exhibit a zigzag shape (indicated by the yellow arrows), resembling "boot-shaped terrain." The overall slope of the rear edge ranges from approximately 50°–90°, with the ridge consisting of steep limestone cliffs at an elevation of about 1800–2000 m. Beneath the cliffs lies a gently sloping "bulge" with an elevation of around 1,690–1800 m. Additionally, a smaller landslide, located southeast of the primary landslide, is enclosed by the blue dashed line in Figure 7F, with a height difference of approximately 151 m between the source and deposit areas.

5 Discussion

5.1 Landslide identification technology

In the past decade, landslide identification technology has advanced from traditional field geological survey methods (Wei et al., 2010) to semi-automatic recognition through human-computer interaction, and more recently, to fully automated recognition using machine learning algorithms (Van Den Eeckhaut et al., 2012; Moosavi et al., 2014; Wang Y. et al., 2024). These new landslide identification methods offer several advantages over traditional techniques, such as faster processing and lower costs (Xun et al., 2019; Pang et al., 2022). However, despite these advances, landslide relic identification still primarily relies on semi-automated methods, particularly human-computer interaction visual interpretation. Machine learning technologies have become widely applied in landslide identification due to continuous improvements in algorithm performance (Wang et al., 2023; Bhuvaneswari et al., 2024; Yang et al., 2024). Nonetheless, the accuracy of identification remains inconsistent (Moosavi et al., 2014). For example, when geological environment data are used as training samples, machine learning algorithms may mistakenly classify non-landslide areas as landslides due to similarities in environmental features, which reduces identification accuracy. Additionally, automatic recognition technologies based on image or pixel comparison may merge multiple adjacent landslides into a single large landslide, compromising the accuracy of area size and impact assessments. Furthermore, landslide recognition methods based on visible remote sensing imagery can erroneously identify cultivated land or deforested areas as landslides due to color differences (Li C. et al., 2024). This issue is especially problematic for ancient landslides, whose characteristics may have gradually faded due to vegetation changes and human engineering activities, significantly reducing the effectiveness of automatic landslide identification.

Human-computer interaction visual interpretation technology can partially compensate for the limitations of automatic identification methods, offering significant advantages in the accuracy and completeness of landslide relic identification (Li et al., 2021; Huang et al., 2023a; Wang W. et al., 2024). However, this technology also faces several challenges. For example, optical remote sensing relies on favorable optical conditions, making it difficult to capture clear surface images in foggy or cloudy weather. Additionally, this method requires human experts to have substantial geological and geomorphological knowledge to effectively guide the system's analysis and decision-making. Furthermore, current technology cannot identify landslides in the initial sliding stage or those experiencing minor deformations, requiring the integration of other techniques, such as InSAR, for more comprehensive identification and analysis (Antonielli et al., 2019; Li N. et al., 2024). Moreover, this identification method still incurs significant labor and time costs. In terms of objectivity, past experiences often necessitate field surveys for validation. However, the areas accessible to humans and the perspectives available during on-site investigations are frequently limited. To address this, researchers often use small devices like drones for observation (Yavuz et al., 2023), which offers advantages similar to satellite imagery. As a result, the application of human-computer interaction visual interpretation on satellite images is nearly indistinguishable from field surveys, and this method has been validated in other studies (Li et al., 2021; Liu et al., 2023; Wang W. et al., 2024; Zhang et al., 2024), fully meeting the requirements for identifying landslide relics. However, enhancing the precision of landslide recognition while maximizing automation remains an area of ongoing research. With the advancement of deep learning technology, future landslide identification techniques will likely increasingly rely on artificial intelligence algorithms, such as Convolutional Neural Networks (CNN) and Generative Adversarial Networks (GAN), to improve both the automation and accuracy of identification. As the quality of landslide data continues to improve, the accuracy of automatic landslide recognition will also increase. This highlights the importance of high-quality basic landslide data, suggesting that future automatic landslide recognition technologies and the quality of existing data will be mutually reinforcing.

5.2 Application of landslide data

A highly accurate, complete, and detailed landslide data inventory is playing an increasingly important role in the field of landslide geological hazard research. Firstly, the establishment of the landslide inventory will fill the gap in the basic data on landslide disasters in the study area, providing solid data support for disaster prediction and risk assessment. The landslide inventory is a core foundational dataset for landslide disaster management. It includes key information such as the location and size of landslides, providing a reliable basis for governments and relevant departments to develop precise disaster prevention and reduction strategies. For example, the inventory can help identify high-frequency landslide areas and potential hazard zones, supporting disaster risk zonation and management.

Secondly, the landslide inventory provides essential parameter inputs for landslide susceptibility assessment. Based on the landslide inventory, regional landslide susceptibility models can be developed, especially as recent studies increasingly focus on using landslide databases to establish regional landslide susceptibility, hazard assessment, and risk evaluation (Miao et al., 2023; Abdo and Richi, 2024; Chicas et al., 2024; Guo et al., 2024; Kassa, 2024; Kaur et al., 2024). Such studies require substantial data as the foundational basis for model development (Huang et al., 2024; Ma et al., 2024a; Ma et al., 2024b; Shao et al., 2024a; Sun et al., 2024a; Wu et al., 2024), particularly for training samples in machine learning algorithms (Tang et al., 2023; Zhuo et al., 2023; Singh et al., 2024). These data are crucial for determining the reliability and accuracy of the models. For instance, due to the inability to obtain a complete landslide database for the high-altitude regions of the Himalayas, Du et al. developed a quantitative method that combines heuristic and multi-class statistical models to assess landslide susceptibility in areas with incomplete inventory data and high uncertainty in landslide interpretation (Du et al., 2020). While this method somewhat mitigates the issue of sparse landslide data, it still faces challenges in verifying model accuracy. With a relatively complete landslide inventory, there would be enough samples to validate the accuracy of model methods and further enhance model precision. Sahrane et al. found that studying landslide susceptibility in homogeneous and heterogeneous environments requires the use of different datasets (Sahrane et al., 2023). Landslide inventories with limited data may be reliable in monotonous and repetitive areas, but they often prove unreliable in regions with significant geological and geomorphological diversity (Fu et al., 2020). In contrast, this study effectively addresses the issue of inaccurate risk assessment models by conducting detailed identification of landslide geological hazards in Zhenxiong County.

Finally, the establishment of the landslide inventory provides a data foundation for optimizing monitoring and early warning systems. The inventory data enables the identification of key monitoring areas, optimization of monitoring point layouts, and improvement in the accuracy and efficiency of disaster monitoring. For example, deploying comprehensive monitoring

TABLE 2 Study on identification of landslide relics in relevant areas of Zhenxiong County.

No.	Location	Landslide acquisition methods	Landslide number	Quantity density (/km^2)	Source
1	Dongchuan District, Yunnan Province	Satellite image + visual interpretation	106	0.0570	Zhu et al. (2023)
2	Funing County, Yunnan Province	UAV imagery + field investigation + previous reports	122	0.0228	Wu et al. (2023)
3	Yuanyang County, Yunnan Province	Field investigation	228	0.1031	Liu et al. (2022)
4	Daguan County, Yunnan Province	UAV imagery + field investigation + previous reports	194	0.1127	Gao and Wang (2016)
5	Jinping County, Yunnan Province	Field investigation	361	0.0982	Hu et al. (2021)
6	Qiaojia County and Ludian County in Yunnan Province	Satellite image+field investigation	1818	0.3885	Cheng et al. (2021)
7	Yunnan Province	Field investigation	3,242	0.0082	Wang et al. (2014)
8	Yunnan Province	Satellite image+field investigation	11,327	0.0287	Wu (2015)
9	Bijie City, Guizhou Province	Satellite image + visual interpretation	770	0.0287	Ji et al. (2020)
10	Zhenxiong County, Yunnan Province	Satellite image + visual interpretation	**3,979**	**1.077**	**This work**

The bold type indicates that the results of this study have the highest database integrity compared to other work.

equipment such as surface displacement sensors, rain gauges, and groundwater level meters in high-risk landslide zones can significantly enhance early warning capabilities. Moreover, the inventory can serve as calibration data for landslide simulations. By analyzing historical landslide events, it helps improve the accuracy and reliability of numerical simulations, supporting research on dynamic evolution and triggering mechanisms of landslides.

5.3 Compared with previous studies

Research on regional landslide disasters has been increasingly prevalent, leading to the establishment of numerous landslide inventories across various regions (Shen et al., 2023; Rüther et al., 2024; Shi et al., 2024). Most of these inventories have been created for the purpose of training machine-learning models or investigating landslide disasters in specific scenarios (Gao et al., 2024; Li et al., 2024c; Yingze et al., 2024). As a result, the completeness of the landslide data in these inventories may not be fully representative of the areas in question. Table 2 presents previous studies related to landslide disasters in the vicinity of Zhenxiong County, all of which include landslide relic inventories. To evaluate the completeness and detail of these inventories, the authors used landslide density (i.e., the number of landslides per unit area) as a metric. Since Zhenxiong County is located in the northeastern part of Yunnan Province, the sources of these studies were selectively drawn from this region whenever possible. In total, the authors reviewed ten research outcomes, nine of which were conducted within Yunnan Province, with two covering the entire province. Additionally, one study was from Bijie City in neighboring Guizhou Province, which borders Zhenxiong. This approach ensures the comparability of the landslide inventories.

A comparative analysis of landslide inventories from Zhenxiong County and surrounding areas reveals deficiencies in detail and completeness in inventories from other regions. These deficiencies are mainly reflected in the following aspects: (1) Differences in the purposes of landslide inventory compilation have led to varying levels of data completeness. Some landslide inventories were created primarily for machine learning training or specific geological phenomena studies (Gao and Wang, 2016; Ji et al., 2020; Cheng et al., 2021). In such cases, data collection often emphasizes the representativeness of landslide features rather than the comprehensiveness of landslide events. (2) The scope of the study area influences the detail of landslide records. Certain studies encompass broad areas, which limits detailed records of landslide disasters within smaller, specific areas. Compared with Wang et al. and Wu's research, inventories covering the entire Yunnan Province provide broad coverage but often overlook landslide events in localized areas like Zhenxiong County, thus failing to fully capture landslide distribution and frequency in such regions (Wang et al., 2014; Wu, 2015). (3) The methods of landslide data collection also impact inventory detail. Studies that incorporate high-resolution satellite imagery and drone data tend to achieve more comprehensive landslide information compared to those relying solely on field surveys or historical records. (4) Variations in inventory standards and data processing approaches lead to discrepancies. Some studies apply differing landslide definitions or data filtering methods, resulting in biases in landslide density calculations. For instance, certain inventories record only large-scale or high-impact landslides, omitting smaller or non-lethal events. These landslide lists cannot fully reflect the actual situation of regional landslides, especially in mountainous areas with frequent landslides but small scale. This study aims to achieve a comprehensive identification of historical landslide relics to accurately reflect the landslide hazards in the study area. Consequently, the landslide inventory presented here shows a higher density (1.077 landslides per km^2) than those in previous studies.

5.4 Research prospects

Zhenxiong County, located in northeastern Yunnan Province, is characterized by a complex geological environment and frequently experiences landslide disasters. The severe landslide event in Liangshui Village, Tangfang Town, on 22 January 2024, has underscored the urgent need for landslide research and early warning systems in the region. This study primarily focuses on establishing a comprehensive and accurate inventory of landslide relics within Zhenxiong County and provides a preliminary analysis of landslide size and spatial distribution. Moving forward, we plan to conduct a more detailed analysis of landslide distribution in relation to various environmental factors, including elevation, slope, aspect, proximity to rivers, and lithology. Based on this understanding of landslide spatial distribution, the study will then assess landslide susceptibility across Zhenxiong County. Additionally, by incorporating local rainfall and seismic activity data, we will conduct an analysis of landslide hazards to develop a comprehensive risk assessment model. This model aims to evaluate the potential risks of landslides in the study area, providing critical technical support for the prevention and mitigation of regional landslide disasters.

6 Conclusion

This study utilizes a human-computer interactive visual interpretation method on the Google Earth Pro platform to conduct a detailed identification of landslides in Zhenxiong County, Yunnan Province. As a result, the most comprehensive landslide relic inventory to date for Zhenxiong County has been developed. Findings indicate that, within Zhenxiong's 3,696 km^2 area, at least 3,979 landslide relics have occurred. Landslide-affected areas total approximately 319.20 km^2, with the largest single landslide covering 4.55 km^2 and the smallest extending over 1,779 m^2. The average landslide area across the study region is 80,215 m^2. Statistical analysis reveals that the majority (73.54%) of landslides in Zhenxiong County are classified as medium-sized landslides, followed by large landslides, accounting for 20.86% of total landslide occurrences, while small landslides constitute only 5.60% of the total. Landslides in Zhenxiong County are primarily concentrated in four areas: the confluence of the Baishui River and Yanxi River in the northwest, Dashuigou Reservoir, the valley along both sides from Heitang Village to Hongyan Village, and the Xiaogou Village area. The water systems in these areas are generally well-developed, and the landforms are mostly middle and low mountains. The landslide relic inventory developed in this study at the county scale for Zhenxiong County provides a reliable dataset for future landslide geological hazard research and offers a scientific basis for comprehensive disaster prevention and mitigation efforts in the region.

Data availability statement

The raw data supporting the conclusions of this article will be made available by the authors, without undue reservation.

Author contributions

ZX: Data curation, Formal Analysis, Investigation, Methodology, Writing–original draft, Writing–review and editing. CX: Project administration, Writing–review and editing. ZZ: Funding acquisition, Writing–review and editing. LF: Data curation, Writing–review and editing. HL: Funding acquisition, Writing–review and editing. HZ: Funding acquisition, Writing–review and editing. DZ: Funding acquisition, Writing–review and editing. JS: Data curation, Writing–review and editing. PW: Data curation, Writing–review and editing. LL: Data curation, Writing–review and editing. JC: Data curation, Writing–review and editing.

Funding

The author(s) declare that financial support was received for the research, authorship, and/or publication of this article. This work was supported by a grant from the Science and Technology Project of China Southern Power Grid (SEPRI-K23A018), Research Institute of China Southern Power Grid Co., Ltd. [1500002024030103SJ000003 (CG1500062001647685-001)], Research Institute of China Southern Power Grid Co., Ltd. [1500002024030103SJ00009 (CG1500062001634723-001)], and the National Institute of Natural Hazards, Ministry of Emergency Management of China (2023-JBKY-57). The authors declare that this study received funding from China Southern Power Grid Co., Ltd. The funder was not involved in the study design, collection, analysis, interpretation of data, the writing of this article, or the decision to submit it for publication.

Conflict of interest

Authors ZZ, HZ, and DZ were Research Institute of China Southern Power Grid Co., Ltd.

Author LF was employed by Jiangsu World Group.

Author HL was employed by Yunnan Power Grid Co., Ltd.

Author JS was employed by Zhejiang Metallurgical Survey and Design Co., Ltd.

Author PW was employed by Beijing Engineering Corporation Limited.

The remaining authors declare that the research was conducted in the absence of any commercial or financial relationships that could be construed as a potential conflict of interest.

The author(s) declared that they were an editorial board member of Frontiers, at the time of submission. This had no impact on the peer review process and the final decision.

Generative AI statement

The author(s) declare that no Generative AI was used in the creation of this manuscript.

Publisher's note

References

Abdo, H. G., and Richi, S. M. (2024). Application of machine learning in the assessment of landslide susceptibility: a case study of mountainous eastern Mediterranean region, Syria. *J. King Saud University-Science* 36, 103174. doi:10.1016/j.jksus.2024.103174

Antonielli, B., Mazzanti, P., Rocca, A., Bozzano, F., and Dei Cas, L. (2019). A-DInSAR performance for updating landslide inventory in mountain areas: an example from Lombardy region (Italy). *Geosciences* 9, 364. doi:10.3390/geosciences9090364

Aristizábal, E., and Sánchez, O. (2020). Spatial and temporal patterns and the socioeconomic impacts of landslides in the tropical and mountainous Colombian Andes. *Disasters* 44, 596–618. doi:10.1111/disa.12391

Barella, C. F., Sobreira, F. G., and Zêzere, J. L. (2019). A comparative analysis of statistical landslide susceptibility mapping in the southeast region of Minas Gerais state, Brazil. *Bull. Eng. Geol. Environ.* 78, 3205–3221. doi:10.1007/s10064-018-1341-3

Bhuvaneswari, T., Sekar, R. C. G., Selvi, M. C., Rubavathi, J. J., and Kaviyaa, V. (2024). Robust deep learning for accurate landslide identification and prediction. *Dokl. Earth Sci.* 518, 1700–1708. doi:10.1134/S1028334X23602961

Bueechi, E., Klimeš, J., Frey, H., Huggel, C., Strozzi, T., and Cochachin, A. (2019). Regional-scale landslide susceptibility modelling in the Cordillera Blanca, Peru—a comparison of different approaches. *Landslides* 16, 395–407. doi:10.1007/s10346-018-1090-1

Cheng, L., Li, J., Duan, P., and Wang, M. (2021). A small attentional YOLO model for landslide detection from satellite remote sensing images. *Landslides* 18, 2751–2765. doi:10.1007/s10346-021-01694-6

Chicas, S. D., Li, H., Mizoue, N., Ota, T., Du, Y., and Somogyvári, M. (2024). Landslide susceptibility mapping core-base factors and models' performance variability: a systematic review. *Nat. Hazards* 120, 12573–12593. doi:10.1007/s11069-024-06697-9

Conforti, M., Muto, F., Rago, V., and Critelli, S. (2014). Landslide inventory map of north-eastern Calabria (South Italy). *J. Maps* 10, 90–102. doi:10.1080/17445647.2013.852142

Coviello, V., Palo, M., Adirosi, E., and Picozzi, M. (2024). Seismic signature of an extreme hydro-meteorological event in Italy. *npj Nat. Hazards* 1, 17. doi:10.1038/s44304-024-00018-7

Cui, Y., Yang, W., Xu, C., and Wu, S. (2023). Distribution of ancient landslides and landslide hazard assessment in the Western Himalayan Syntaxis area. *Front. Earth Sci.* 11, 1135018. doi:10.3389/feart.2023.1135018

Devoli, G., Strauch, W., Chávez, G., and Høeg, K. (2007). A landslide database for Nicaragua: a tool for landslide-hazard management. *Landslides* 4, 163–176. doi:10.1007/s10346-006-0074-8

Du, J., Glade, T., Woldai, T., Chai, B., and Zeng, B. (2020). Landslide susceptibility assessment based on an incomplete landslide inventory in the Jilong Valley, Tibet, Chinese Himalayas. *Eng. Geol.* 270, 105572. doi:10.1016/j.enggeo.2020.105572

Feng, L., Qi, W., Xu, C., Yang, W., Yang, Z., Xiao, Z., et al. (2024a). Landslide research from the perspectives of qinling mountains in China: a critical review. *J. Earth Sci.* 35, 1546–1567. doi:10.1007/s12583-023-1935-9

Feng, L., Xu, C., Tian, Y., Li, L., Sun, J., Huang, Y., et al. (2024b). Landslides of China's qinling. *Geoscience Data J.* 11, 725–741. doi:10.1002/gdj3.246

Frodella, W., Ciampalini, A., Bardi, F., Salvatici, T., Di Traglia, F., Basile, G., et al. (2018). A method for assessing and managing landslide residual hazard in urban areas. *Landslides* 15, 183–197. doi:10.1007/s10346-017-0875-y

Fu, S., Chen, L., Woldai, T., Yin, K., Gui, L., Li, D., et al. (2020). Landslide hazard probability and risk assessment at the community level: a case of western Hubei, China. *Nat. Hazards Earth Syst. Sci.* 20, 581–601. doi:10.5194/nhess-20-581-2020

Gao, H., Xu, C., Xie, C., Ma, J., and Xiao, Z. (2024). Landslides triggered by the july 2023 extreme rainstorm in the haihe river basin, China. *Landslides* 21, 2885–2890. doi:10.1007/s10346-024-02322-9

Gao, J., and Wang, Q. (2016). Application of analytical hierarchy process method for landslide susceptibility mapping using GIS. *Electron. J. Geotechnical Eng.* 21, 6615–6627.

Gómez, D., García, E. F., and Aristizábal, E. (2023). Spatial and temporal landslide distributions using global and open landslide databases. *Nat. Hazards* 117, 25–55. doi:10.1007/s11069-023-05848-8

Guo, J., Xi, W., Yang, Z., Shi, Z., Huang, G., Yang, Z., et al. (2024). Landslide hazard susceptibility evaluation based on SBAS-InSAR technology and SSA-BP neural network algorithm: a case study of Baihetan Reservoir Area. *J. Mt. Sci.* 21, 952–972. doi:10.1007/s11629-023-8083-9

Hosseini, K., Reindl, L., Raffl, L., Wiedemann, W., and Holst, C. (2024). 3D landslide monitoring in high spatial resolution by feature tracking and histogram analyses using laser scanners. *Remote Sens.* 16, 138. doi:10.3390/rs16010138

Hu, X., Mei, H., Zhang, H., Li, Y., and Li, M. (2021). Performance evaluation of ensemble learning techniques for landslide susceptibility mapping at the Jinping county, Southwest China. *Nat. Hazards* 105, 1663–1689. doi:10.1007/s11069-020-04371-4

Huang, Y., Xu, C., He, X., Cheng, J., Huang, Y., Wu, L., et al. (2024). Distribution characteristics and cumulative effects of landslides triggered by multiple moderate-magnitude earthquakes: a case study of the comprehensive seismic impact area in Yibin, Sichuan, China. *Landslides* 21, 2927–2943. doi:10.1007/s10346-024-02351-4

Huang, Y., Xu, C., Li, L., He, X., Cheng, J., Xu, X., et al. (2023a). Inventory and spatial distribution of ancient landslides in Hualong County, China. *Land* 12, 136. doi:10.3390/land12010136

Huang, Y., Xu, C., Zhang, X., and Li, L. (2022). Bibliometric analysis of landslide research based on the WOS database. *Nat. Hazards Res.* 2, 49–61. doi:10.1016/j.nhres.2022.02.001

Huang, Y., Xu, C., Zhang, X., Li, L., and Xu, X. (2023b). Research in the field of natural hazards based on bibliometric analysis. *Nat. hazards Rev.* 24, 04023012. doi:10.1061/nhrefo.nheng-1739

Huu, D. N., Cong, T. V., Bretcan, P., and Petrisor, A.-I. (2024). Assessing the relationship between landslide susceptibility and land cover change using machine learning. *Vietnam J. Earth Sci.* 46, 339–359. doi:10.15625/2615-9783/20706

Hwang, J., and Lall, U. (2024). Increasing dam failure risk in the USA due to compound rainfall clusters as climate changes. *npj Nat. Hazards* 1, 27. doi:10.1038/s44304-024-00027-6

Jallayu, P. T., Sharma, A., and Singh, K. (2024). Vulnerability of highways to landslide using landslide susceptibility zonation in GIS: mandi district, India. *Innov. Infrastruct. Solutions* 9, 354. doi:10.1007/s41062-024-01653-9

Ji, S., Yu, D., Shen, C., Li, W., and Xu, Q. (2020). Landslide detection from an open satellite imagery and digital elevation model dataset using attention boosted convolutional neural networks. *Landslides* 17, 1337–1352. doi:10.1007/s10346-020-01353-2

Kassa, S. M. (2024). A Systematic review of machine learning based landslide susceptibility mapping. *J. Road Traffic Eng.* 70, 23–30. doi:10.31075/pis.70.02.03

Kaur, R., Gupta, V., and Chaudhary, B. (2024). Landslide susceptibility mapping and sensitivity analysis using various machine learning models: a case study of Beas valley, Indian Himalaya. *Bull. Eng. Geol. Environ.* 83, 228. doi:10.1007/s10064-024-03712-y

Li, C., Feng, P., Jiang, X., Zhang, S., Meng, J., and Li, B. (2024a). Extensive identification of landslide boundaries using remote sensing images and deep learning method. *China Geol.* 7, 277–290. doi:10.31035/cg2023148

Li, L., Xu, C., Xu, X., Zhang, Z., and Cheng, J. (2021). Inventory and distribution characteristics of large-scale landslides in Baoji city, Shaanxi province, China. *ISPRS Int. J. Geo-Information* 11, 10. doi:10.3390/ijgi11010010

Li, N., Feng, G., Zhao, Y., Xiong, Z., He, L., Wang, X., et al. (2024b). A deep-learning-Based algorithm for landslide detection over wide areas using InSAR images considering topographic features. *Sensors* 24, 4583. doi:10.3390/s24144583

Li, T., Xie, C., Xu, C., Qi, W., Huang, Y., and Li, L. (2024c). Automated machine learning for rainfall-induced landslide hazard mapping in Luhe County of Guangdong Province, China. *China Geol.* 7, 315–329. doi:10.31035/cg2024064

Li, T., Xu, C., Li, L., and Xu, J. (2024d). The landslide traces inventory in the transition zone between the Qinghai-Tibet Plateau and the Loess Plateau: a case study of Jianzha County, China. *Front. Earth Sci.* 12, 1–9. doi:10.3389/feart.2024.1370992

Liu, S., Zhu, J., Yang, D., and Ma, B. (2022). Comparative study of geological hazard evaluation systems using grid units and slope units under different rainfall conditions. *Sustainability* 14, 16153. doi:10.3390/su142316153

Liu, X., Su, P., Li, Y., Xia, Z., Ma, S., Xu, R., et al. (2023). Spatial distribution of landslide shape induced by Luding Ms 6.8 earthquake, Sichuan, China: case study of the Moxi Town. *Landslides* 20, 1667–1678. doi:10.1007/s10346-023-02070-2

Ma, S., Shao, X., Li, K., and Xu, C. (2024a). Landslides triggered by the 30th June 2012 Ms6.6 hejing earthquake, xinjiang province, China. *Bull. Eng. Geol. Environ.* 83, 256. doi:10.1007/s10064-024-03727-5

Ma, S., Shao, X., Xu, C., Chen, X., Lu, Y., Xia, C., et al. (2024b). Distribution pattern, geometric characteristics and tectonic significance of landslides triggered by the strike-slip faulting 2022 Ms 6.8 Luding earthquake. *Geomorphology* 453, 109138. doi:10.1016/j.geomorph.2024.109138

Mcgovern, A., Demuth, J., Bostrom, A., Wirz, C. D., Tissot, P. E., Cains, M. G., et al. (2024). The value of convergence research for developing trustworthy AI for weather, climate, and ocean hazards. *npj Nat. Hazards* 1, 13. doi:10.1038/s44304-024-00014-x

Miao, F., Ruan, Q., Wu, Y., Qian, Z., Kong, Z., and Qin, Z. (2023). Landslide dynamic susceptibility mapping base on machine learning and the PS-InSAR coupling model. *Remote Sens.* 15, 5427. doi:10.3390/rs15225427

Moosavi, V., Talebi, A., and Shirmohammadi, B. (2014). Producing a landslide inventory map using pixel-based and object-oriented approaches optimized by Taguchi method. *Geomorphology* 204, 646–656. doi:10.1016/j.geomorph.2013.09.012

Pang, D., Liu, G., He, J., Li, W., and Fu, R. (2022). Automatic remote sensing identification of co-seismic landslides using deep learning methods. *Forests* 13, 1213. doi:10.3390/f13081213

Posner, A. J., and Georgakakos, K. P. (2015). Soil moisture and precipitation thresholds for real-time landslide prediction in El Salvador. *Landslides* 12, 1179–1196. doi:10.1007/s10346-015-0618-x

Rosser, B., Dellow, S., Haubrock, S., and Glassey, P. (2017). New Zealand's national landslide database. *Landslides* 14, 1949–1959. doi:10.1007/s10346-017-0843-6

Rüther, D. C., Lindsay, E., and Slåtten, M. S. (2024). Landslide inventory: 'Hans' storm southern Norway, August 7–9, 2023. *Landslides* 21, 1155–1159. doi:10.1007/s10346-024-02222-y

Saha, A., Tripathi, L., Villuri, V. G. K., and Bhardwaj, A. (2024). Exploring machine learning and statistical approach techniques for landslide susceptibility mapping in Siwalik Himalayan Region using geospatial technology. *Environ. Sci. Pollut. Res.* 31, 10443–10459. doi:10.1007/s11356-023-31670-7

Sahrane, R., Bounab, A., and El Kharim, Y. (2023). Investigating the effects of landslides inventory completeness on susceptibility mapping and frequency-area distributions: case of Taounate province, Northern Morocco. *Catena* 220, 106737. doi:10.1016/j.catena.2022.106737

Sepúlveda, S. A., and Petley, D. N. (2015). Regional trends and controlling factors of fatal landslides in Latin America and the Caribbean. *Nat. Hazards Earth Syst. Sci.* 15, 1821–1833. doi:10.5194/nhess-15-1821-2015

Shao, X., Ma, S., Xu, C., Xie, C., Li, T., Huang, Y., et al. (2024a). Landslides triggered by the 2022 Ms. 6.8 Luding strike-slip earthquake: an update. *Eng. Geol.* 335, 107536. doi:10.1016/j.enggeo.2024.107536

Shao, X., Xu, C., Li, L., Yang, Z., Yao, X., Shao, B., et al. (2024b). Spatial analysis and hazard assessment of large-scale ancient landslides around the reservoir area of Wudongde hydropower station, China. *Nat. Hazards* 120, 87–105. doi:10.1007/s11069-023-06201-9

Sharma, N., Saharia, M., and Ramana, G. (2024). High resolution landslide susceptibility mapping using ensemble machine learning and geospatial big data. *Catena* 235, 107653. doi:10.1016/j.catena.2023.107653

Shen, C., Zhou, S., Luo, X., Zhang, Y., and Liu, H. (2023). Using DInSAR to inventory landslide geological disaster in Bijie, Guizhou, China. *Front. Earth Sci.* 10, 1–15. doi:10.3389/feart.2022.1024710

Shen, Z., Zhang, Q., Wu, W., and Song, C. (2022). Spatial pattern and attribution analysis of the regions with frequent geological disasters in the Tibetan Plateau and Hengduan Mountains. *Acta Geogr. Sin.* 77, 1211–1224. doi:10.11821/dlxb202205012

Shi, X., Chen, D., Wang, J., Wang, P., Wu, Y., Zhang, S., et al. (2024). Refined landslide inventory and susceptibility of Weining County, China, inferred from machine learning and Sentinel-1 InSAR analysis. *Trans. GIS* 28, 1594–1616. doi:10.1111/tgis.13202

Shu, B., Chen, Y., Amani-Beni, M., and Zhang, R. (2022). Spatial distribution and influencing factors of mountainous geological disasters in southwest China: a fine-scale multi-type assessment. *Front. Environ. Sci.* 10, 1–15. doi:10.3389/fenvs.2022.1049333

Singh, A., Dhiman, N., Kc, N., and Shukla, D. P. (2024). Improving ML-based landslide susceptibility using ensemble method for sample selection: a case study of Kangra district in Himachal Pradesh, India. *Environ. Sci. Pollut. Res.*, 1–24. doi:10.1007/s11356-024-34726-4

Sultana, N. (2020). Analysis of landslide-induced fatalities and injuries in Bangladesh: 2000-2018. *Cogent Soc. Sci.* 6, 1737402. doi:10.1080/23311886.2020.1737402

Sun, J., Shao, X., Feng, L., Xu, C., Huang, Y., and Yang, W. (2024a). An essential update on the inventory of landslides triggered by the Jiuzhaigou Mw6.5 earthquake in China on 8 August 2017, with their spatial distribution analyses. *Heliyon* 10, e24787. doi:10.1016/j.heliyon.2024.e24787

Sun, J., Xu, C., Feng, L., Li, L., Zhang, X., and Yang, W. (2024b). The yinshan mountains record over 10,000 landslides. *Data* 9, 31. doi:10.3390/data9020031

Tang, L., Yu, X., Jiang, W., and Zhou, J. (2023). Comparative study on landslide susceptibility mapping based on unbalanced sample ratio. *Sci. Rep.* 13, 5823. doi:10.1038/s41598-023-33186-z

Trigila, A., Iadanza, C., and Spizzichino, D. (2010). Quality assessment of the Italian landslide inventory using GIS processing. *Landslides* 7, 455–470. doi:10.1007/s10346-010-0213-0

Van Den Eeckhaut, M., Kerle, N., Poesen, J., and Hervás, J. (2012). Object-oriented identification of forested landslides with derivatives of single pulse LiDAR data. *Geomorphology* 173-174, 30–42. doi:10.1016/j.geomorph.2012.05.024

Wang, P., Li, L., Xu, C., Zhang, Z., and Xu, X. (2022). An open source inventory and spatial distribution of landslides in Jiyuan City, Henan Province, China. *Nat. Hazards Res.* 2, 325–330. doi:10.1016/j.nhres.2022.10.004

Wang, W., Huang, Y., Xu, C., Shao, X., Li, L., Feng, L., et al. (2024a). Identification and distribution of 13003 landslides in the northwest margin of Qinghai-Tibet Plateau based on human-computer interaction remote sensing interpretation. *China Geol.* 7, 171–187. doi:10.31035/cg2023140

Wang, X., Wang, D., Sun, T., Dong, J., Xu, L., Li, W., et al. (2023). Dual path attention network (DPANet) for intelligent identification of wenchuan landslides. *Remote Sens.* 15, 5213. doi:10.3390/rs15215213

Wang, X., Zhang, L., Wang, S., and Lari, S. (2014). Regional landslide susceptibility zoning with considering the aggregation of landslide points and the weights of factors. *Landslides* 11, 399–409. doi:10.1007/s10346-013-0392-6

Wang, Y., Gao, H., Liu, S., Yang, D., Liu, A., and Mei, G. (2024b). Landslide detection based on deep learning and remote sensing imagery: a case study in Linzhi City. *Nat. Hazards Res.* doi:10.1016/j.nhres.2024.07.001

Wei, F., Chernomorets, S., Aristov, K., Petrakov, D., Tutubalina, O., Su, P., et al. (2010). A Seismically triggered landslide in the Niujuan valley near the epicenter of the 2008 Wenchuan earthquake. *J. Earth Sci.* 21, 901–909. doi:10.1007/s12583-010-0143-8

Wu, X., Xu, X., Yu, G., Ren, J., Yang, X., Chen, G., et al. (2024). The China active faults database (CAFD) and its web system. *Earth Syst. Sci. Data* 16, 3391–3417. doi:10.5194/essd-16-3391-2024

Wu, Y., A, F., Yang, C., Yan, S., and Kang, X. (2023). Accuracy improvement of different landslide susceptibility evaluation models through K-Means clustering: a case study on China's Funing county. *Math. Problems Eng.* 2023, 2913890. doi:10.1155/2023/2913890

Wu, Z. (2015). *Analysis of Cause and Study on liability assessment of landslides and debris flow hazards in Yunnan province. Master Degree*. Beijing: China University of Geosciences.

Xu, C., and Li, K. (2021). "Inventory of landslides triggered by the hejing Ms6.6 earthquake, China, on 30 June 2012," in *Understanding and reducing landslide disaster risk: volume 5 catastrophic landslides and Frontiers of landslide science*. Editors V. Vilímek, F. Wang, A. Strom, K. Sassa, P. T. Bobrowsky, and K. Takara (Cham: Springer International Publishing), 73–80.

Xu, Y., Allen, M. B., Zhang, W., Li, W., and He, H. (2020). Landslide characteristics in the Loess Plateau, northern China. *Geomorphology* 359, 107150. doi:10.1016/j.geomorph.2020.107150

Xun, Z., Zhao, C., Liu, X., and Liu, Y. (2019). "Automatic identification of potential landslides by integrating remote sensing, DEM and deformation map," in *Igarss 2019 - 2019 IEEE international geoscience and remote sensing symposium*.

Yang, Z., Qi, W., Xu, C., and Shao, X. (2024). Exploring deep learning for landslide mapping: a comprehensive review. *China Geol.* 7, 330–350. doi:10.31035/cg2024032

Yang, Z., and Xu, C. (2022). Efficient detection of earthquake-triggered landslides based on U-Net++: an example of the 2018 hokkaido eastern iburi (Japan) mw = 6.6 earthquake. *Remote Sens.* 14, 2826. doi:10.3390/rs14122826

Yavuz, M., Koutalakis, P., Diaconu, D. C., Gkiatas, G., Zaimes, G. N., Tufekcioglu, M., et al. (2023). Identification of streamside landslides with the use of unmanned aerial vehicles (UAVs) in Greece, Romania, and Turkey. *Remote Sens.* 15, 1006. doi:10.3390/rs15041006

Yin, Y., Liu, C., Chen, H., Ren, J., and Zhu, C. (2013). Investigation on catastrophic landslide of january 11,2013 at Zhaojiagou, Zhenxiong county, yunnan province. *J. Eng. Geol.* 21, 6–15.

Yin, Z., Xu, Y., and Jiang, X. (2015). The key triggering factor and its mitigation implication of Zhaojiagou catastrophic landslide in Zhenxiong County, Yunnan province. *Chin. J. Geol. Hazard Control* 26, 36–42. doi:10.16031/j.cnki.issn.1003-8035.2015.02.07

Yingze, S., Yingxu, S., Xin, Z., Jie, Z., and Degang, Y. (2024). Comparative analysis of the TabNet algorithm and traditional machine learning algorithms for landslide susceptibility assessment in the Wanzhou Region of China. *Nat. Hazards* 120, 7627–7652. doi:10.1007/s11069-024-06521-4

Yu, B., Wang, N., Xu, C., Chen, F., and Wang, L. (2022). A network for landslide detection using large-area remote sensing images with multiple spatial resolutions. *Remote Sens.* 14, 5759. doi:10.3390/rs14225759

Yu, X., Hu, X., Song, Y., Xu, S., Li, X., Song, X., et al. (2024). Intelligent assessment of building damage of 2023 Turkey-Syria Earthquake by multiple remote sensing approaches. *npj Nat. Hazards* 1, 3. doi:10.1038/s44304-024-00003-0

Zhang, X., Xu, C., Li, L., Feng, L., and Yang, W. (2024). Inventory of landslides in the northern half of the taihang mountain range, China. *Geosciences* 14, 74. doi:10.3390/geosciences14030074

Zhao, J., Xu, C., and Huang, X. (2024). Detailed landslide traces database of hancheng county, China, based on high-resolution satellite images available on the Google Earth platform. *Data* 9, 63. doi:10.3390/data9050063

Zhao, S., Dai, F., Deng, J., Wen, H., Li, H., and Chen, F. (2023). Insights into landslide development and susceptibility in extremely complex alpine geoenvironments along the western Sichuan-Tibet Engineering Corridor, China. *Catena* 227, 107105. doi:10.1016/j.catena.2023.107105

Zheng, Y., Chen, M., Yang, D., Long, Y., and Luo, J. (2021). Analysis on the causes and early warning and forecasting of frequent geological disasters in Zhenxiong, Yunnan province. *Industrial Saf. Environ.* 47, 35–38.

Zhu, Z., Yuan, X., Gan, S., Zhang, J., and Zhang, X. (2023). A research on a new mapping method for landslide susceptibility based on SBAS-InSAR technology. *Egypt. J. Remote Sens. Space Sci.* 26, 1046–1056. doi:10.1016/j.ejrs.2023.11.009

Zhuo, L., Huang, Y., Zheng, J., Cao, J., and Guo, D. (2023). Landslide susceptibility mapping in Guangdong province, China, using random forest model and considering sample type and balance. *Sustainability* 15, 9024. doi:10.3390/su15119024

frontiers | Frontiers in Earth Science

TYPE Original Research
PUBLISHED 19 February 2025
DOI 10.3389/feart.2025.1523076

OPEN ACCESS

EDITED BY
Qi Yao,
China Earthquake Administration, China

REVIEWED BY
Luyuan Huang,
China Earthquake Administration, China
Yanshuang Guo,
China Earthquake Administration, China
Suran Wang,
University of Shanghai for Science and Technology, China

*CORRESPONDENCE
Jing Wu,
✉ baihua212@163.com
Yanxin Yang,
✉ yanxinyangswjtu@foxmail.com

RECEIVED 05 November 2024
ACCEPTED 27 January 2025
PUBLISHED 19 February 2025

CITATION
Wu D, Yi Y, Chen Q, Wu J, Yang Y, Wu J and Amin R (2025) Experimental study of geotextiles for karst subgrade collapse under static and dynamic loads.
Front. Earth Sci. 13:1523076.
doi: 10.3389/feart.2025.1523076

Experimental study of geotextiles for karst subgrade collapse under static and dynamic loads

Di Wu[1], Yang Yi[1], Qingshu Chen[2], Jing Wu[3]*, Yanxin Yang[4]*, Jianjian Wu[1] and Ruhul Amin[1]

[1]School of Architecture and Transportation Engineering, Guilin University of Electronic Technology, Guilin, Guangxi, China, [2]Guangxi Institute of Geological Survey, Nanning, Guangxi, China, [3]Natural Resources Ecological Restoration Center of Guangxi Zhuang Autonomous Region, Nanning, Guangxi, China, [4]School of Civil Engineering, Sichuan University of Science and Engineering, Zigong, Sichuan, China

Introduction: Karst subgrade collapse has the characteristics of suddenness and concealment, which poses a major challenge to the stability of infrastructure.

Methods: A scale model test was designed to investigate the effects of different reinforcing conditions and different loading modes on the load transfer and distribute of reinforced cushions, with emphasis on monitoring the vertical pressure, internal fill and surface displacements in the subsided area and the stable area during the collapse process.

Results: The results show that during subsidence, vertical stresses decrease in the subsidence area and increase in the stable area. The load affects the soil arch effect, with dynamic loads having a greater impact on soil stability compared to static load and unloaded conditions. Geotextile reinforcement enhances the soil arch and tensile membrane effects, reducing vertical displacement by 5.58%–10.95% under dynamic loads and by 34.76%–66.56% under static load and unloaded.

Discussion: This research provides theoretical and experimental support for geotextile reinforcement design in karst subsidence, helping to prevent karst collapse.

KEYWORDS

karst subgrade collapse, geotextiles, mode tests, static and dynamic loading, earth pressure

1 Introduction

Karst subsidence is a problem that cannot be ignored when developing roads, railways, motorways and other engineering projects in karst areas. Karst subgrade collapse often occurs without warning, with sudden and hidden characteristics, seriously affecting the safety of human life and property in karst areas, and hindering regional engineering construction and economic development (Guo et al., 2020; Jiang et al., 2024; Yao et al., 2023; Shi et al., 2019). Previous studies have shown that the occurrence of karst collapse is influenced by various factors, including soil characteristics, external loads, changes in geological conditions, and alterations to the water environment (Li et al., 2023; Gao et al., 2023; Yin et al., 2018; Al Heib et al., 2021). Consequently, to ensure the safety of engineering projects in karst areas, researchers must carefully consider the mechanisms, specific causes, and treatment methods of karst collapse.

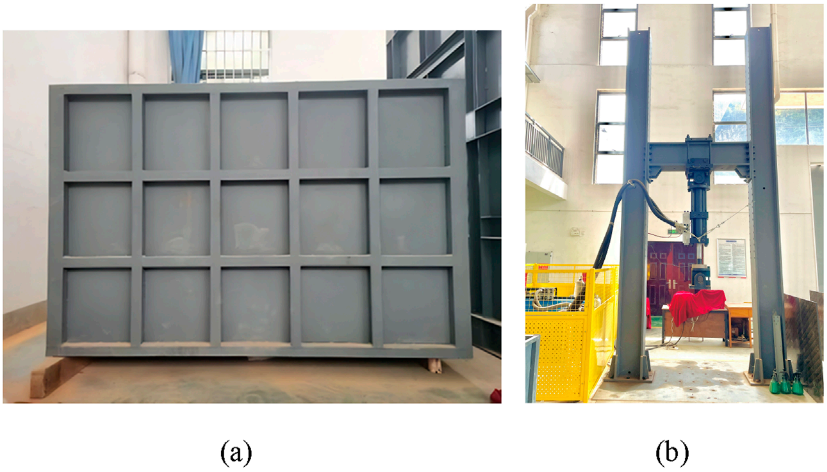

FIGURE 1
Test equipment. **(A)** Test chamber, **(B)** Electro-hydraulic servo fatigue testing machine.

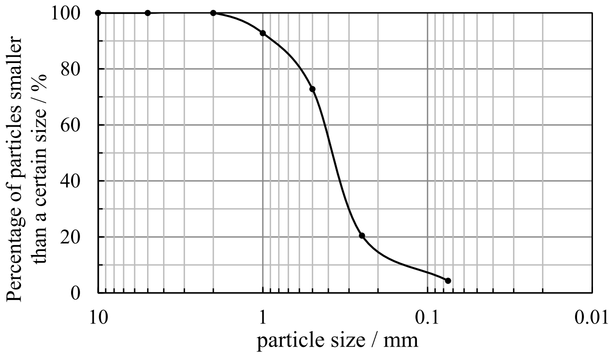

FIGURE 2
Particle grading curve of test sand.

At present, the research into the causes and mechanisms of karst collapse is primarily driven by indoor model tests or numerical simulation methods. Baryakh and Fedoseev (2011) used the discrete element method to analyze the correlation between the final span and depth of the karst cave, and simulated the process of karst collapse using iterative methods. Wang et al. (2022) proposed an equivalent numerical simulation method for karst collapse, and the calculation results show that the karst collapse of the overlying sand layer has a significant impact on the surrounding strata and engineering structures. Islam et al. (2024) analyzed the impact of karst collapse on railway disasters and found that the presence of karst caves in railway embankments significantly increased vertical dynamic displacement, especially in soil layers, which increased by 72%. In some cases, karst areas are not only subjected to static loads, but also to dynamic loads, such as vehicle loads, earthquake and vibrations generated by the process of produce and construct. Bi et al. (2020) carried out the test under cyclic loading, and study the displacement and morphology of soil arch during collapse, found that vertical stress redistributed to stable areas and resulted in a triangular soil arch morphology. Jiang et al. (2015) found that the influence depth of vehicle load on soil can reach 10 m, and the longitudinal tensile stress can increase by 15 times. Wen et al. (2025) conducted a series of physical model experiments and numerical simulations of karst collapse. Their findings revealed that the width of karst channels exerts a substantial influence on the velocity and magnitude of collapse, and the presence of dynamic loads was found to exacerbate these effects. It can be seen that karst collapse is a highly destructive process, with an occurrence mechanism that is extremely complex and difficult to monitor. Research on karst collapse is predominantly limited to single cases, i.e., unloaded and static loads are considered, with a paucity of research on the influence of dynamic loads on karst collapse. Due to the varying loading conditions, the formation of karst subsidence and the corresponding treatment effect also vary. It is imperative to devise a novel experimental methodology to elucidate the mechanism of karst subsidence under unloaded, static and dynamic loads.

The use of geosynthetics to prevent karst subgrade collapse offers significant advantages over traditional methods such as backfill compaction method and grouting method, which are often associated with issues like secondary collapse, high costs, and substantial environmental impacts (Hou et al., 2024; Zheng et al., 2024; Wu D. et al., 2022; Zheng et al., 2023). Based on the results of experimental and numerical simulation studies, many scholars have conducted in-depth studies on the mechanism of geotextiles reinforced cushion under collapse as well as the design method. Rui et al. (2021) investigated the earth pressure distribution and surface subsidence through multi-group model tests, revealing that differential subsidence leads to an increase in upper earth pressure and a decrease in lower earth pressure, with the maximum surface subsidence occurring at the center and increasing as the collapse width expands. Wu Y. et al. (2022) classified the load evolution process into four stages, and proposed a simplified foundation reaction curve. Pham et al. (2018) analyzed the load transfer mechanism based on the experimental results, focusing on the effect of geometric and physical parameters on load transfer, and obtained the conclusion that the vertical stress of soil increases after collapse

TABLE 1 Geotextile mechanical properties.

Material	Mass per unit area/g·m^{-2}	Tensile strength/kN·m^{-1}		Ultimate elongation/%		Thicknesses/mm
		Radial direction (≥)	Latitude direction (≥)	Radial direction	Latitude direction	
Geotextile	200	50	35–50	35	30	2

TABLE 2 Model test similarity constants.

Physical quantity	Quality systems	Similar constant	Physical quantity	Quality systems	Similar constant
Accelerations/g	LT^{-2}	$C_g = 1$	Stresses/σ	$ML^{-1}T^{-2}$	$C_\sigma = 5$
Densities/ρ	ML^{-3}	$C_\rho = 1$	Modulus of elasticity/E	$ML^{-1}T^{-2}$	$C_\sigma = 5$
Cohesive force/c	$ML^{-1}T^{-2}$	$C_c = 5$	Area/A	L^2	$C_A = 25$
Poisson ratio/μ	1	$C_\mu = 1$	Geometric size/l	L	$C_l = 5$
Internal friction angle/ϕ	1	$C_\phi = 1$	Strains/ν	1	$C_\nu = 1$
Force/F	MLT^{-2}	$C_F = 125$	—	—	—

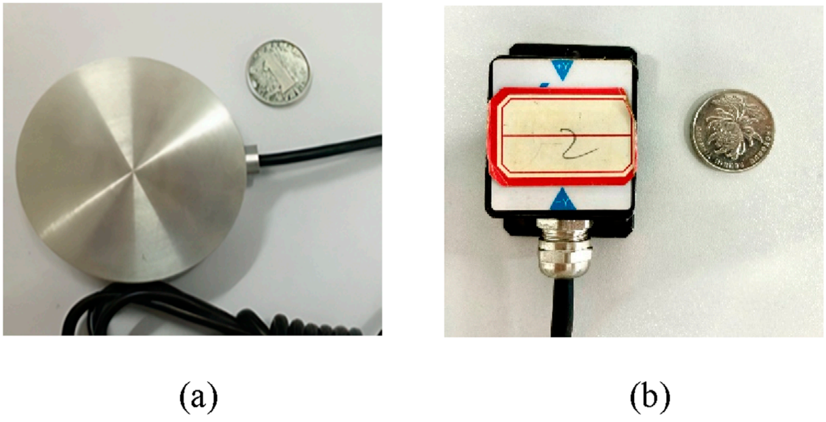

FIGURE 3
Measurement equipment. **(A)** Micro earth pressure box, **(B)** MEMS sensor.

and decreases with the increase of the distance from the center of collapse. Eskişar et al. (2012) showed the arch formation process of soil arches intuitively and efficiently through CT scanning and investigated the load transfer mechanism of the reinforced subgrade with geogrids. Villard and Laurent (2008) examined the relative sliding between reinforcement and soil, and the corresponding increase in reinforcement stress under a uniformly distributed load applied to the upper portion of the reinforced cushion layer, leading to an improved design approach for reinforced subgrades. It can be acknowledged that the presence of differential subsidence in karst collapse leads to an earth arching effect, where part of the load in the collapsed area is able to be transferred to the stable area. The present study demonstrates that the load transfer above the geosynthetics-reinforced bedding is predominantly concentrated in the subsided area, particularly in the case of multi-layer reinforcement. However, the load sharing and transfer efficiency for the stable area remains to be elucidated, underscoring the necessity for a more profound investigation into the load transfer mechanism of geosynthetics reinforcement.

In this paper, the effects of varying reinforcement (reinforced and unreinforced) and loading modes (unloaded, static and dynamic) on the performance of geotextiles in karst subsidence treatment was investigated by means of scaled-down models, focusing on monitoring the vertical stresses, internal and surface displacements of the fill in subsided and stable areas, as well as the distribution of the loads, and the efficiency of the load transfer in the subsided areas during the collapse process.

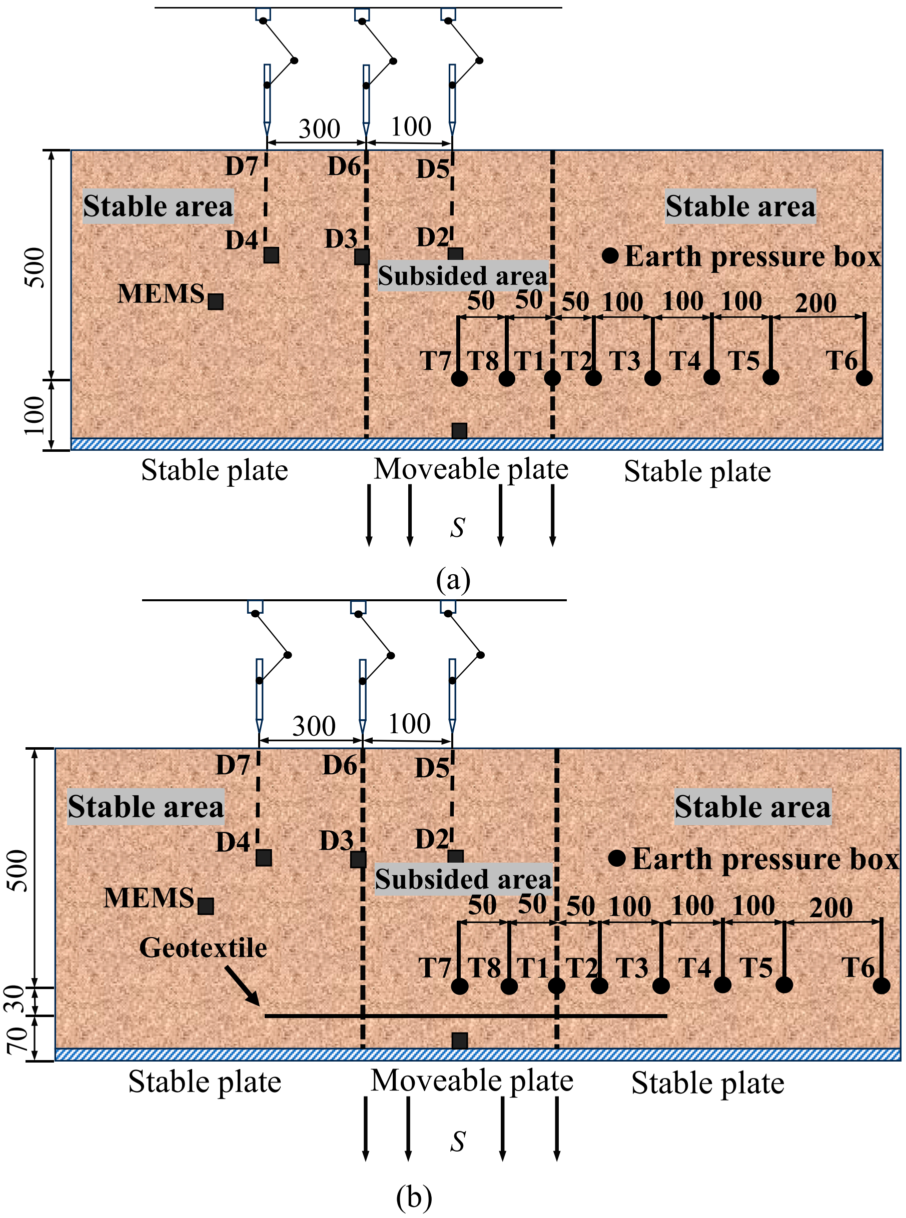

FIGURE 4
Arrangement of measuring instruments (mm). **(A)** Unreinforced condition. **(B)** Reinforcement condition.

2 Scale model test

2.1 Test equipment

The external framework of this scale model test box is welded by square tube and steel plate, and the dimensions of the test chamber are as follows, The test chamber has dimensions of 1,500 mm in length (L), 1,000 mm in width (W), and 1,000 mm in height (H), as shown in Figure 1A. With 18 mm thick density board to separate the test box into two parts, the actual test space dimensions are, L*W*H = 1,500 mm*500 mm*600 mm. The subsided area is 200 mm wide, while the stable areas on both sides measure 650 mm in width. The sinking plate is securely attached through screws and a lifter flange connector, with axial movement controlled by a three-phase motor to simulate subgrade collapse. An electro-hydraulic servo fatigue testing machine with a total stroke of 200 mm is used, with a test frequency range of 0.001–50 Hz and a dynamic/static test force measurement range of 2.0–500 kN, as shown in Figure 1B. Once the load has been applied, a square plate is positioned on the surface of the soil. The top indenter of the testing machine then makes direct contact with the plate, ensuring that the load applied to the soil is uniform. Under static loading conditions, the top indenter applies continuous downward pressure, whereas under dynamic loading, the indenter exerts intermittent pressure at a specified frequency. This setup is designed to simulate various causes of loading during karst collapse and to investigate the load

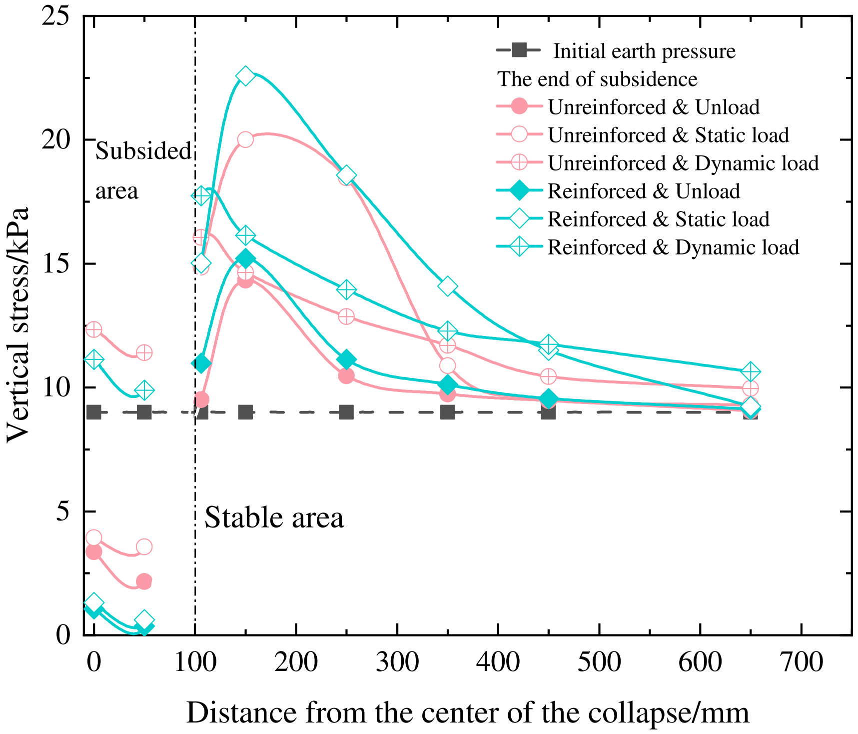

FIGURE 5
Vertical stress distribution on reinforced cushion.

sharing and transfer efficiency of the soil under different loading conditions.

2.2 Test material

The test fill soil was made of Guilin Lijiang River sand, which was sieved with 2 mm sieve after natural drying and indoor drying, and the effective particle size of sand and soil was obtained by sieving method is d_{10} = 0.08 mm, the median particle size is d_{30} = 0.13 mm, and the limiting particle size is d_{60} = 0.22 mm, and its coefficient of inhomogeneity is C_u = 2.75, and coefficient of curvature is C_c = 0.96, which was poorly graded silt, and the gradation curve was as shown in Figure 2.

The filament woven geotextile was selected as the reinforcing material for the test. The total length of the test geotextile reinforcement is 800 mm, the anchorage length on both sides is 300 mm, and the width is 500 mm. Other technical specifications of the geotextile are shown in Table 1 below.

2.3 Experimental and measurement procedure

This test simulates the collapse event at a site on Guilin Road, Heping District, Tianjin, with a collapse length of about 3 m, a width of about 1 m, and a depth of about 2 m. Based on similarity theory, the geometrical similarity constant C_l = 5, so the model similarity ratio of 1:5 is selected (Pai and Wu, 2021). The similarity constants for physical quantities such as gravity acceleration, cohesion, and other related parameters are presented in Table 2. The design of geotextiles to prevent karst subgrade collapse was carried out under the condition of 200 mm collapse width, 500-mm fill height and 1.5 times anchorage length. The primary focus of this study was to examine the effects of different reinforced conditions (reinforced, unreinforced) and different loading modes (unloaded, static, dynamic) on the load transfer and sharing of reinforced cushion. Key parameters monitored included vertical stresses in both subsided and stable areas, as well as displacements within the soil and at its surface. The study also analyzed how reinforced and unreinforced conditions affect the subgrade under both static and dynamic loading, with particular attention to the distribution of vertical stresses and vertical displacements. The static load applied was 2.5 kN, while the dynamic load consisted of a sinusoidal wave with an amplitude of 2 kN, a frequency of 5 Hz, and a repetition rate of 1,000 cycles (Gao, 2021).

Vertical stresses were monitored by a strain micro-earth pressure box, internal displacements were recorded with MEMS sensors, and surface displacements of the fill were measured with a displacement sensor. The MEMS sensors employ high-performance microprocessors to monitor internal displacement of soil, utilizing dynamic solution algorithms and Kalman filter techniques for data processing (Han et al., 2023). The earth pressure box, displacement sensor, and MEMS sensor were integrated with a strain gauge system and connected to a computer for real-time data acquisition. Data was collected at a frequency of one sample per second through dedicated data acquisition and analysis software. The equipment is shown in Figure 3.

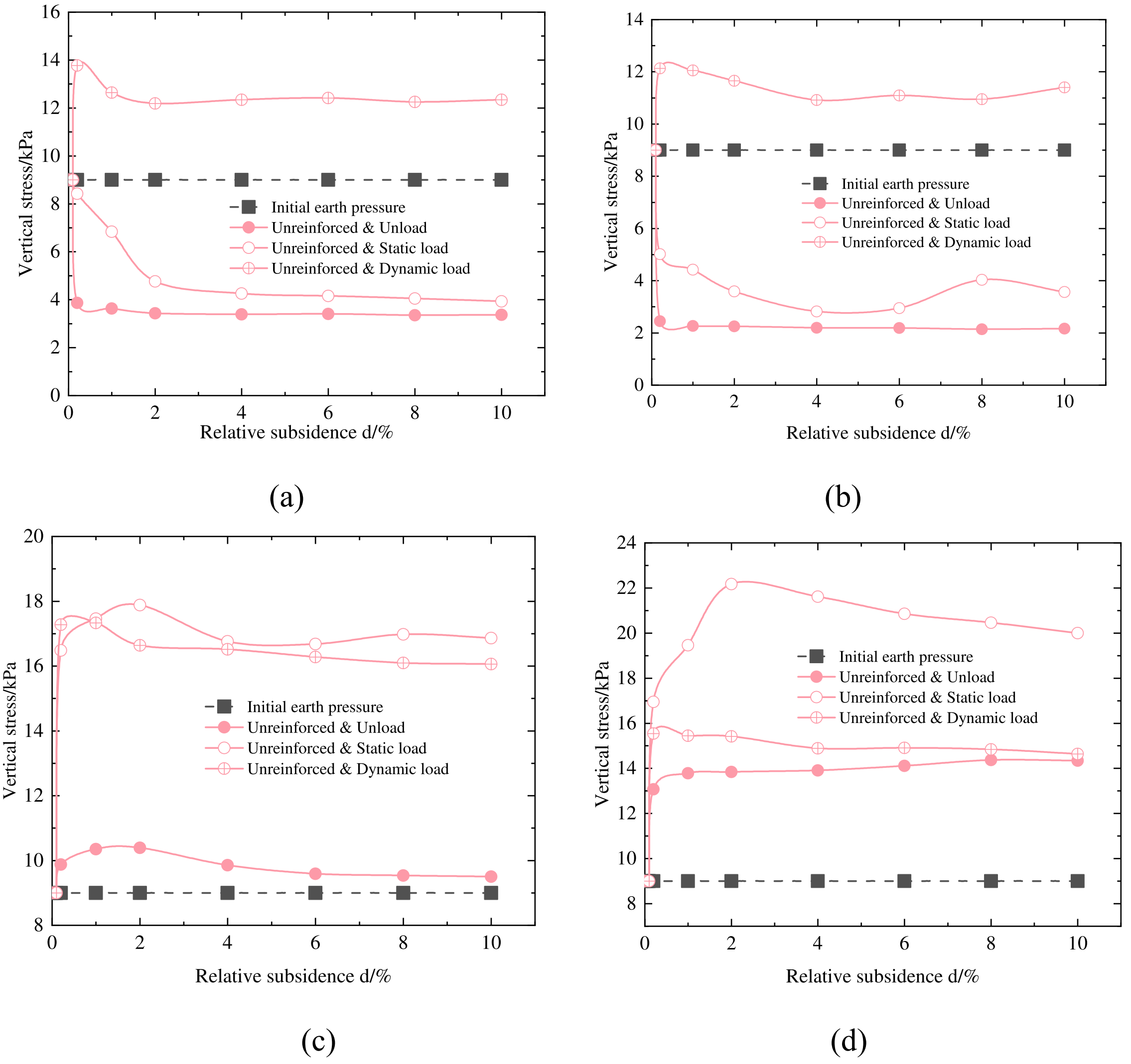

FIGURE 6
Vertical stresses in unreinforced condition. **(A)** Position T7 **(B)** Position T8 **(C)** Position T1 **(D)** Position T2.

The reinforced and unreinforced conditions in model test are shown in Figure 4. The test simulated the karst collapse process through the lower fall of the movable plate structure in the lower part of the model box. In the reinforced condition, 70 mm of sand was utilized to the soil, followed by the placement of a geotextile measuring 800 mm in length and 500 mm in width. This geotextile was then filled with 30 mm in thick of sand and compacted, resulting in an overall thickness of 60 mm for the reinforced bedding (Zhang et al., 2021). In contrast, under unreinforced test conditions, no geotextile was employed. The monitoring devices were installed in the same position in both cases, with the earth pressure box positioned at 100 mm and the three MEMS sensors installed at 350 mm at positions designated as D4, D3 and D2 to monitor the internal displacement of the soil. After the completion of the fill, three displacement gauges were installed on the fill surface at locations noted as D7, D6 and D5 to monitor subsidence on the fill surface.

3 Analysis of test result

3.1 Analysis of load distribution under static and dynamic loads

Figure 5 demonstrates the vertical stress distribution on the reinforced cushion at the end of subsidence (Chen et al., 2020). The end-of-subsidence phase of the test is defined as the relative subsidence $d = \text{subsidence/collapse width}^{*}100\% = 10\%$. The vertical stresses of the fill soil in the subsided area and the stable area are not uniformly distributed. Instead, there is a tendency for the center of the subsided area to have a larger vertical stress, while the edges have a smaller vertical stress. As the distance from the collapse center increases, the vertical stress of the fill soil in the stable area initially rises steeply, then declines steeply, and finally levels off. The decrease of vertical stress shows roughly exponential trend.

A comparison of the vertical stress distribution under dynamic and static loading reveals distinct differences. In the subsided area,

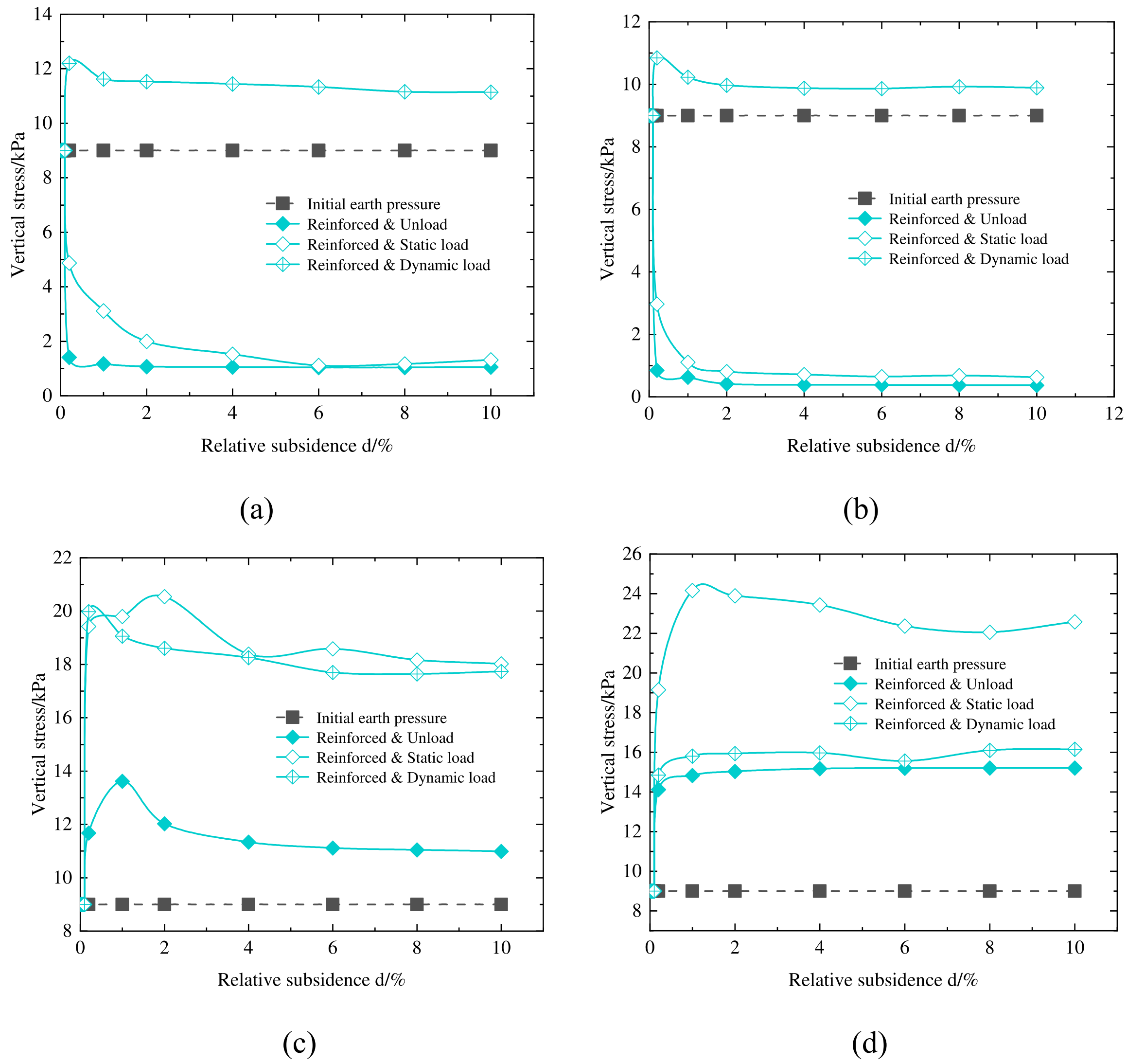

FIGURE 7
Vertical stresses under reinforced condition. **(A)** Position T7 **(B)** Position T8 **(C)** Position T1 **(D)** Position T2.

the vertical stress under dynamic loading is higher than that under static loading, while in the stable area, the vertical stress under static loading is greater. For example, at measurement point T8 in subsided area, the vertical stress is 3.57 kPa under static load and 11.40 kPa under dynamic load, with a difference of 68.68%. Conversely, at point T2 in the stable area, the maximum vertical stress under static loading is 20 kPa, while under dynamic loading, it is 16.06 kPa at point T1, showing a 19.7% difference. This discrepancy can be attributed to the shorter application time of dynamic loads compared to static loads, which results in a more immediate impact. Additionally, dynamic loading exacerbates the instability of the fill, causing adjacent soil particles to shift towards the subsided area. Consequently, dynamic loading exerts a more pronounced weakening effect on the geotechnical arch mechanism in the collapse zone than static loading.

The variation in vertical stress with subsidence at locations T7 and T8 in the subsided areas, and T1 and T2 in the stable areas under unreinforced conditions is shown in Figure 6. In the figure, the grey squares represent the initial earth pressure, the pink solid circles indicate the unloaded condition, the hollow circles correspond to static loading, and the central crosses denote dynamic loading. As seen in Figures 6A, B, the vertical stresses at positions T7 and T8 in static load and unload conditions initially decrease during the early stages of subsidence, falling below the initial earth pressure. In contrast, under dynamic loading, the vertical stresses at these locations exceed the initial earth pressure. For example, at measurement point T7, the initial earth pressure was 9 kPa. At the onset of subsidence, the vertical stress decreased to 3.37 kPa under the unloaded condition, 3.93 kPa under static loading, and increased to 12.34 kPa under dynamic loading. This behavior can be attributed to the interaction between the fill at the edge of the subsided area and the stable fill on both sides. During subsidence, part of the vertical stress is transferred into friction with the edges. Additionally, the primary stress within the fill is redirected due to the constraints imposed by the edges, resulting in a more significant reduction

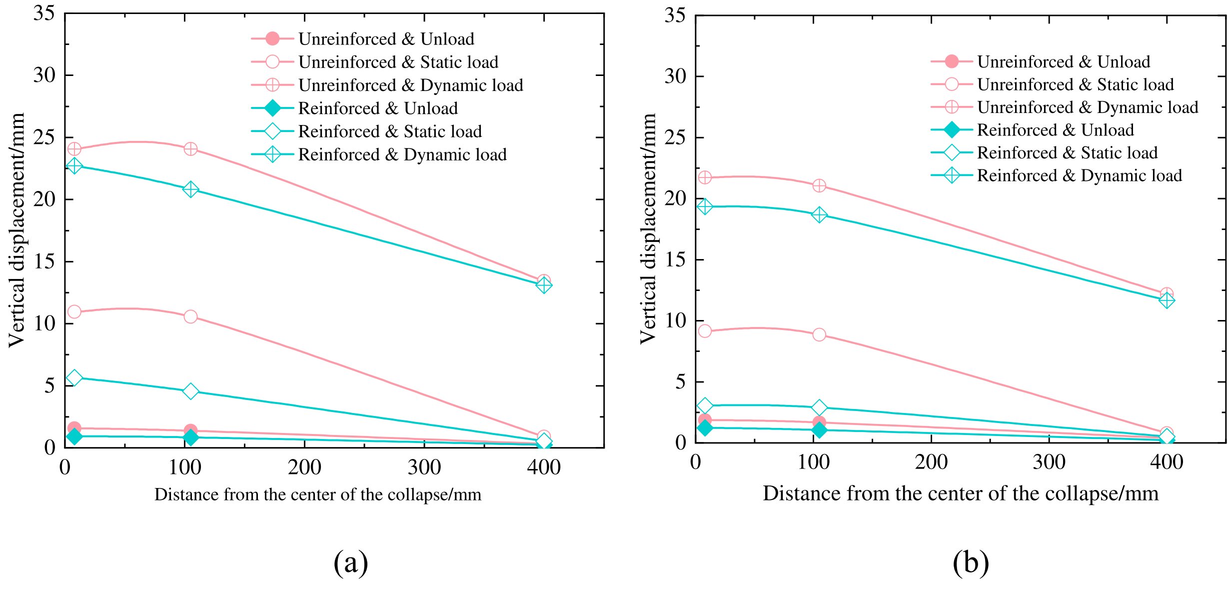

FIGURE 8
Vertical displacements at different fill heights. **(A)** Vertical displacement of soil surface **(B)** Vertical displacement in the middle of the soil.

in earth pressure near the edge compared to the center of the subsidence area (Chen et al., 2019).

From Figures 6C, D, the vertical stresses at T1 and T2 in the stable area are greater than the initial earth pressure, with vertical stresses under static loading being greater than those under dynamic loading. Take T1 as an example, its initial earth pressure is 9 kPa, the vertical stress rises to 10.39 kPa and then slowly decreases to 9.50 kPa under unloaded condition, first rises to 17.88 kPa and then decreases to 16.86 kPa under static loaded condition, and rises to 17.33 kPa and then slowly decreases to 16.06 kPa under dynamic loaded condition. These observations indicate that, under static loading, the soil arch effect rapidly distributes the load from the onset of loading, enhancing load transfer. In contrast, under dynamic loading, the soil arch effect is weakened, preventing effective load sharing, including the self-weight of the fill. As a result, the vertical stress under dynamic loading initially increases and then decreases. Additionally, the primary locations of load transfer differ between static and dynamic loading conditions.

Figure 7 presents the vertical stress curves of the subsided areas T7 and T8 and the stable areas T1 and T2 with relative subsidence under the reinforced condition at the end of subsidence. Under the reinforced condition, the vertical stress change curves of each position in the subsided area and stable area have basically the same trend as that of the vertical stress curve in the unreinforced condition. In the subsided area, for example, at point T7, the vertical stresses under unload, static, and dynamic load are 1.06kPa, 1.31kPa, and 11.14kPa, respectively. The reductions in vertical stress without reinforcement for the three loading scenarios is 68.55%, 69.21% and 9.72% respectively. In the stable area, for example, at point T1, the vertical stresses under unload, static load, and dynamic load are 10.98kPa, 18.02kPa, and 17.74kPa, respectively. The vertical stresses increased by 15.09%, 6.88% and 10.46% respectively.

By analyzing Figures 6, 7, it is evident that under unloaded and static loading conditions, load sharing and transfer in the stable area primarily occur at location T2. However, the introduction of dynamic loading disrupts this balance. Under dynamic loading, the soil arch effect is weakened, and the tensile membrane effect comes into play, causing the load transfer in the stable area to shift from T2 to T1. Additionally, when considering the impact of reinforcement, a significant change in the vertical stress distribution is observed. Under the reinforced condition, the vertical stresses at T7 and T8 in the subsided area are smaller than those in the unreinforced condition, and the vertical stresses at T1 and T2 in the stable area are larger than those in the unreinforced condition, which indicates that the reinforcement of geotextiles can reduce the load on the unstable soil in the subsided area and enhance the stability of the soil. Furthermore, the tensile membrane effect facilitates effective load transfer to the stable area.

3.2 Analysis of soil deformation under static and dynamic loads

Figure 8 illustrates the vertical displacements of the fill surface and the midsection of the fill under various reinforcement conditions and loading scenarios at the end of subsidence (relative subsidence $d = 10\%$). As shown in Figure 8, at the end of subsidence, the vertical displacement of the fill soil within the subsided area and the fill soil in the stable area near a certain range of the subsided area is larger, the vertical displacement of the fill soil in other areas of the stable area is obviously reduced, and the vertical displacement of the fill soil without loading and under static loading is nearly zero.

Under unloaded condition, the vertical displacement of the soil under the unreinforced and reinforced conditions exhibits a trend where the displacement is larger at the midsection of the soil compared to the surface. Furthermore, the displacement

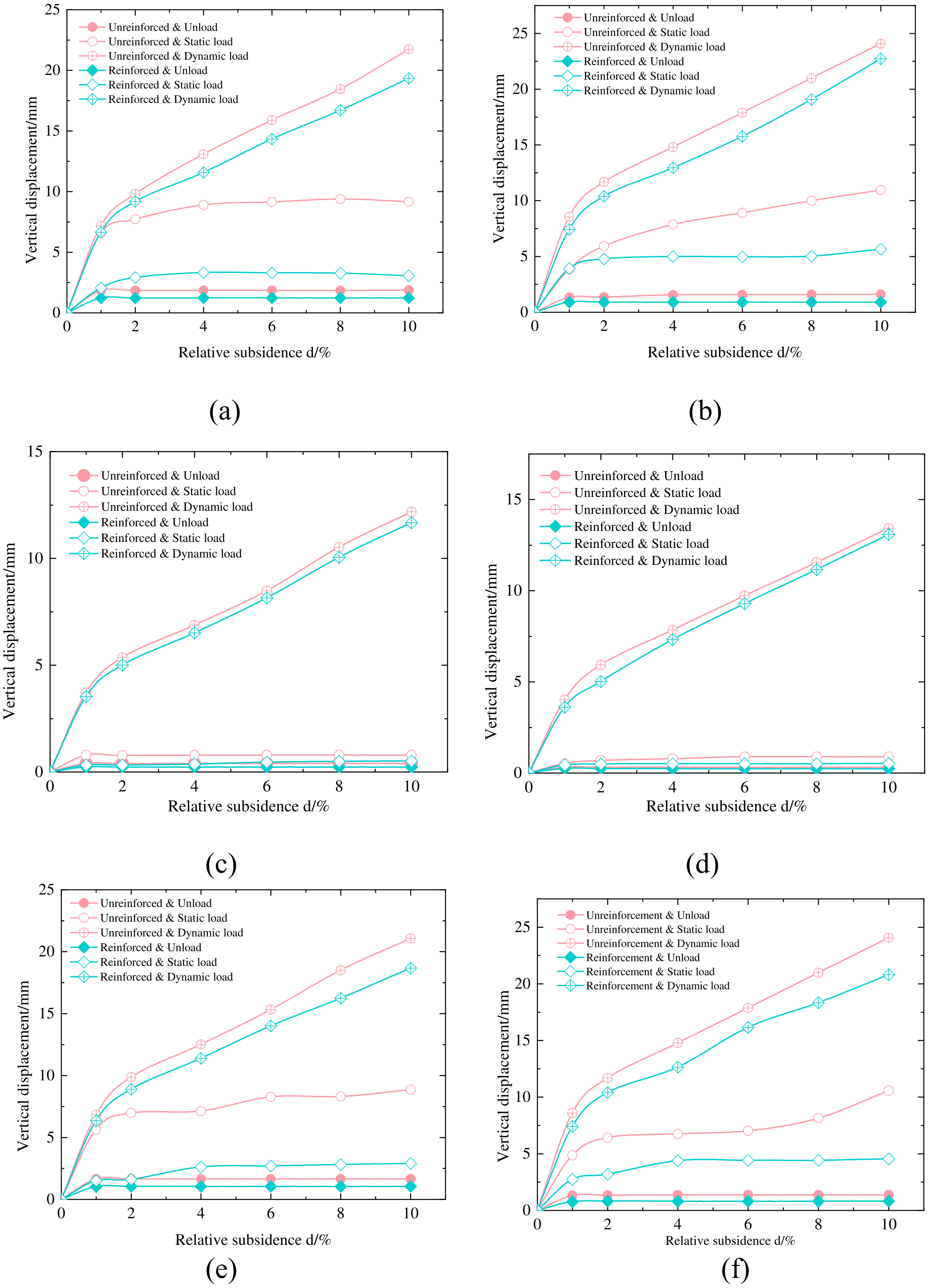

FIGURE 9
Vertical displacements of the fill surface and the location of each measurement point in the center. **(A)** Position D2 **(B)** Position D5 **(C)** Position D4 **(D)** Position D7 **(E)** Position D3 **(F)** Position D6.

increases with decreasing height within the soil. Under both static and dynamic loading conditions, the vertical displacement of the soil, for both unreinforced and reinforced conditions, is greater at the surface than at the midsection, indicating that the loads are primarily applied to the soil surface. The vertical displacement of the fill soil under loading is most pronounced at the surface and in the surrounding areas of the applied load, with dynamic loading resulting in notably higher displacements compared to static

TABLE 3 Load sharing and transfer efficiency in the stable area under different conditions.

Group		Vertical loads at start of subsidence/kPa	Transfer efficiency/%	Vertical loads at the end of subsidence/kPa	Transfer efficiency/%
Initial state		9	—	9	—
Unreinforced-unloaded	T1	9.88	9.78	9.50	**5.56**
	T2	13.07	45.22	14.34	59.33
Unreinforced-static load	T1	16.48	83.11	16.86	87.33
	T2	16.95	88.33	20.00	122.22
Unreinforced-dynamic load	T1	17.27	91.89	16.06	78.44
	T2	15.54	72.67	14.64	62.67
Reinforced-unloaded	T1	11.67	29.67	10.94	21.56
	T2	14.12	56.89	15.20	68.89
Reinforcement-static load	T1	19.43	115.89	18.03	100.33
	T2	19.15	112.78	22.58	**150.89**
Reinforcement-dynamic load	T1	19.98	122.00	17.74	97.11
	T2	14.85	65.00	16.15	79.44

Note: Bold values represent maximum and minimum transfer efficiencies.

TABLE 4 Load sharing and transfer efficiency of soil arching effect and tensile membrane effect.

Test conditions		T1	T2
Soil arching effect	Unloaded	5.60%	59.33%
	Static load	87.33%	122.22%
	Dynamic load	78.44%	62.67%
Tensile membrane effect	Unloaded	16.00%	9.56%
	Static load	13.00%	28.67%
	Dynamic load	18.67%	16.77%

loading. Additionally, it is evident that the geotextile-reinforced cushion significantly restricts vertical displacement. Compared to the unreinforced condition, the vertical displacement at all measured locations is substantially reduced under the reinforced condition.

Figure 9 shows the vertical displacement of the fill at the surface and the center of the fill soil under different loading conditions. The vertical displacement is greatest under dynamic loading, followed by static loading, with the smallest displacement observed under unloaded conditions. In the relative subsidence range of 0%–1%, the vertical displacement at each measurement point increases approximately linearly with relative subsidence. In the 1%–10% relative subsidence range, the vertical displacement under dynamic loading continues to increase roughly linearly with subsidence, though at different rates. Conversely, under both unloaded and static loading conditions, the vertical displacement increases with subsidence, but the change is less pronounced. The vertical displacement of D2 is measured at 24.07 mm in the case of an unreinforced-dynamic load, and 22.73 mm in the case of a reinforced-dynamic load, exhibiting a reduction ratio of 5.58%. The vertical displacement of D5 is 21.73 mm in the case of unreinforced-dynamic load and 19.35 mm in the case of reinforced-dynamic load, resulting in a reduction ratio of 10.95%. It is evident that soil damage is more severe under dynamic load conditions and geotextile reinforcement can also reduce the vertical displacement of the soil. Compared with the unloaded and static load case, the reduction in vertical displacement is not as apparent. The vertical displacement of the soil under the reinforced condition is smaller than that under the unreinforced condition in difference load conditions, indicating that the reinforcement of geotextiles can effectively limit the soil and reduce the vertical displacement of the soil.

3.3 Load transfer efficiency analysis under static and dynamic loads

In order to quantify the load transfer efficiency by the soil arch effect and the tensile membrane effect, the load transfer efficiency is introduced, which is obtained by the ratio of the load increment in the stable area to the initial earth pressure (Wu et al., 2021), as shown in Equation 1.

$$n = \frac{\sigma_0 - \sigma}{\sigma} \times 100\% \tag{1}$$

where σ_0 denotes the vertical stress (kPa) at each location in the stable area and σ denotes the initial earth pressure (kPa).

The load transfer efficiencies obtained from the calculation of the vertical stresses at the beginning of subsidence (0.2% relative subsidence) and the end of subsidence (10% relative subsidence) phases in the selected stable areas T1 and T2 locations are shown in Table 3.

As shown in Table 3, the load sharing and transfer efficiency under reinforced conditions is higher than that under unreinforced conditions. The maximum efficiency is observed under the reinforced-static loading condition, with a value of 150.89%, while the minimum efficiency occurs under the unreinforced-unloaded condition, at 5.56%.

Under unreinforced conditions, the load transfer efficiency is solely attributed to the soil arch effect. In contrast, under reinforced conditions, the load transfer efficiency consists of two components: the soil arch effect and the tensile membrane effect. When disregarding the limiting influence of geotextile reinforcement on the soil arch effect, the load transfer efficiency due to the tensile membrane effect is represented by Equation 2 (Van Eekelen et al., 2013).

$$n_L = n - n_T \tag{2}$$

Where n is the load transfer efficiency under reinforced condition, n_T is the soil arch effect load transfer efficiency under reinforced condition and n_L is the membrane effect load transfer efficiency.

Table 4 presents a comparison of the load sharing effect of the soil arch effect and the load transfer efficiency of the tensile membrane effect. As shown in Table 4, the load sharing efficiency of soil arch effect is basically greater than the load transfer efficiency of fabric tensile membrane effect, which indicates that the load sharing and transfer mainly rely on the stress redistribution under the action of soil arch effect, and the tensile membrane effect of fabric also plays its role in load transfer, but it is much smaller than that of soil arch effect.

4 Conclusion

Based on a practical case study of a subgrade collapse project, six model test schemes were designed to investigate the load transfer and sharing performance of reinforced cushions under various reinforcement and loading conditions. The main conclusions are as follows.

(1) During the subsidence process, vertical stresses in the subsided area decrease, while those in the stable area increase. The load applied influences the soil arch effect, with dynamic loads having a more significant impact on soil stability in the subsided area compared to unloaded and static loading conditions. It is recommended to use higher reinforcement strengths in karst areas subjected to dynamic loads.

(2) The synergy between the soil arch effect and the tensile membrane effect, resulting from geotextile reinforcement, leads to a reduction in vertical soil displacement. Under dynamic loading, vertical displacement is reduced by 5.58%–10.95%, while under unloaded and static loading conditions, displacement is reduced by 34.76%–66.56%. These findings demonstrate that geotextiles are highly effective in treating karst subsidence when the anchorage length is 1.5 times the width of the subsided area.

(3) This study provides both theoretical insights and experimental data to support the design of geotextile reinforcement in karst subsided areas, contributing to the effective prevention of karst collapse.

Data availability statement

The original contributions presented in the study are included in the article/supplementary material, further inquiries can be directed to the corresponding authors.

Author contributions

DW: Conceptualization, Investigation, Methodology, Writing–original draft, Writing–review and editing. YYi: Formal Analysis, Software, Writing–original draft, Writing–review and editing. QC: Data curation, Investigation, Software, Writing–original draft, Writing–review and editing. JnW: Formal Analysis, Investigation, Project administration, Writing–review and editing. YYa: Methodology, Writing–review and editing. JaW: Data curation, Formal Analysis, Investigation, Methodology, Writing–review and editing. RA: Software, Supervision, Writing–review and editing.

Funding

The author(s) declare that financial support was received for the research, authorship, and/or publication of this article. Financial support for this work is gratefully acknowledged from the Natural Science Foundation of China Grant No. 42067044 and Guangxi Science and Technology Major Program Grant No. AB23026028. All the supports are greatly appreciated.

Conflict of interest

The authors declare that the research was conducted in the absence of any commercial or financial relationships that could be construed as a potential conflict of interest.

Generative AI statement

The author(s) declare that no Generative AI was used in the creation of this manuscript.

Publisher's note

References

Al Heib, M., Hassoun, M., Emeriault, F., Villard, P., and Farhat, A. (2021). Predicting subsidence of cohesive and granular soil layers reinforced by geosynthetic. *Environ. Earth Sci.* 80, 70. doi:10.1007/s12665-020-09350-3

Baryakh, A. A., and Fedoseev, A. K. (2011). Sinkhole Formation mechanism. *Joumal Min. Sci.* 47 (4), 404–412. doi:10.1134/S1062739147040022

Bi, Z., Gong, Q., Zhou, S., and Cheng, X. (2020). Experimental study of the evolution law of vertical soil arch under cyclic loading. *Rock Soil Mech.* 41 (03), 886–894+932. doi:10.16285/jrsm.2019.0483

Chen, F., Lin, Y., and Chen, S. (2020). Analytical solutions for geosynthetic-reinforced cohesive subgrade spanning trench voids. *Geotext. Geomembranes* 48 (6), 854–866. doi:10.1016/j.geotexmem.2020.06.004

Chen, Q., Guo, S., Xu, C., Liang, L., and Liu, X. (2019). Trapdoor model tests on loosening earth pressure and failure mode of loosening zone in sand. *J. Central South Univ. Sci. Technol.* 50 (01), 108–117. doi:10.11817/i.issn.1672-7207.2019.01.015

Eskişar, T., Otani, J., and Hironaka, J. (2012). Visualization of soil arching on reinforced embankment with rigid pile foundation using X-ray CT. *Geotext. Geomembranes* 46 (5), 611–624. doi:10.1016/i.geotexmem.2011.12.002

Gao, C. (2021). Model tests of road subsidence progress with underground cavities caused by cyclic dynamic load. *Hydrogeology Eng. Geol.* 48 (01), 70–77. doi:10.16030/j.cnki.issn.1000-3665.202003002

Gao, X., Li, Z., Lin, J., Song, Y., Qing, S., Cui, X., et al. (2023). Grouting technology for surface soft soil in coastal tidal karst area and its application. *J. Zhejiang Univ. Eng. Sci.* 57 (03), 552–561. doi:10.3785/i.issn.1008-973X.2023.03.013

Guo, L., Wang, S., Sun, L., Kang, Z., and Zhao, C. (2020). Numerical simulation and experimental studies of karst caves collapse mechanism in fractured-vuggy reservoirs. *Geofluids* 2020, 1–21. doi:10.1155/2020/8817104

Han, S., Ni, C., and Lu, J. (2023). An optimal estimation approach for MEMS INS performance improvements based on single-FOG monitoring. *IEEE Sensors J.* 23, 7199–7206. doi:10.1109/JSEN.2023.3242962

Hou, J., Chu, C., Li, J., Copeland, T., Chen, J., and Nam, B. H. (2024). An analytical model of horizontal-vertical geogrid reinforced foundation. *Ksce J. Civ. Eng.* 28 (7), 2673–2680. doi:10.1007/s12205-024-0354-7

Islam, N., Linrong, X., Usman, A. B., Raza, B., Yongwei, L., and Shengxiang, L. (2024). Study on field and numerical analysis of karst collapse as railway hazard. *Proc. Institution Civ. Eng. - Geotechnical Eng.*, 1–15. doi:10.1680/jgeen.24.00242

Jiang, H., Bian, X., Chen, Y., and Jiang, J. (2015). Full-scale accelerated testing for simulation of train moving loads in track-subgrade system of high-speed railways. *China Civ. Eng. J.* 48, 85–95. doi:10.15951/j.tmgcxb.2015.09.010

Jiang, X., Dai, J., Zheng, Z., Li, X. J., Ma, X., Zhou, W., et al. (2024). An overview on karst collapse mechanism in China. *Carbonates Evaporites* 39, 71. doi:10.1007/s13146-024-00986-x

Li, P., Wu, J., Zhou, W., and LaMoreaux, J. W. (2023). Karst collapse and its management. *Hazard Hydrogeol.*, 105–141. doi:10.1007/978-3-031-48427-8_5

Pai, L., and Wu, H. (2021). Shaking table test study on dynamic responses of underpass tunnels under earthquake. *Chin. J. Rock Mech. Eng.* 40 (01), 88–100. doi:10.13722/j.cnki.jrme.2020.0353

Pham, M. T., Briancon, L., Dias, D., and Abdelouhab, A. (2018). Investigation of load transfer mechanisms in granular platforms reinforced by geosynthetics above cavities. *Geotext. Geomembranes* 46 (5), 611–624. doi:10.1016/j.geotexmem.2018.04.015

Rui, R., Zhai, Y., Xu, Y., and He, Q. (2021). Experimental investigations on influences of ground loss on earth pressure and settlement of adiecent underground retaining structures. *Chin. J. Geotechnical Eng.* 43 (04), 644–652. doi:10.11779/CJGE202104006

Shi, H., Li, Q., Zhang, Q., Yu, Y., Xing, Y., and Yu, K. (2019). Mechanism of shallow soil cave-type karst collapse induced by water inrush in underground engineering construction. *J. Perform. Constr. Facil.* 34 (1), 04019091. doi:10.1061/(asce)cf.1943-5509.0001353

Van Eekelen, S. J. M., Bezuijen, A., and Van Tol, A. F. (2013). An analytical model for arching in piled embankments. *Geotext. Geomembranes* 39, 78–102. doi:10.1016/j.geotexmem.2013.07.005

Villard, P., and Laurent, B. (2008). Design of geosynthetic reinforcements for platforms subjected to localized sinkholes. *Can. Geotechnical J.* 45 (02), 196–209. doi:10.1139/T07-083

Wang, X., Wang, S., Peng, X., Ma, T., and Chen, B. (2022). Equivalent numerical simulation method and application in karst-induced collapse of overlying sandy stratum. *Eng. Fail. Anal.* 137, 106280. doi:10.1016/j.engfailanal.2022.106280

Wen, H., Fang, Z., Tan, F., Qi, X., Zeng, H., and Tao, L. (2025). Disaster mechanisms of hourglass-type karst ground collapse. *Carbonates Evaporites* 40, 5. doi:10.1007/s13146-024-01041-5

Wu, D., Liang, Y., Yang, Y., and Wu, J. (2022a). Study of the subsidence width influence on the geotextile control of a subgrade collapse based on a half-symmetric model test. *Appl. Sciences-Basel* 12 (19), 9504. doi:10.3390/app12199504

Wu, D., Luo, C., Li, Y., Yang, Y., Liang, Y., and Wu, J. (2021). Application of a geotextile in the treatment of post-subsidence in karst areas. *Appl. Sci.* 11, 11826. doi:10.3390/app112411826

Wu, Y., Zhao, Y., Gong, Q., Zornberg, J. G., Zhou, S., and Wang, B. (2022b). Alternant active and passive trapdoor problem: from experimental investigation to mathematical modeling. *Acta Geotech.* 17 (7), 2971–2994. doi:10.1007/s11440-021-01426-Z

Yao, Y., Li, A., Zhou, B., Xiao, Z., and Chu, Y. (2023). Analysis on Key technologies of high - speed railway subgrade in karst foundation. *J. Of Railw. Eng. Soc.* 40 (08), 35–39. doi:10.16285/j.rsm.2021.0352

Yin, H., Shi, Y., Niu, H., Ma, C., Liu, G., Zhai, P., et al. (2018). Characteristics, detection, and prevention of karst sinkholes: a case study in Laiwu iron ore mine areas, Shandong Province, China. *Environ. Earth Sci.* 77, 136. doi:10.1007/s12665-018-7310-0

Zhang, L., Ou, Q., Zhao, M., Ding, X., and Liu, J. (2021). Numerical analysis on dynamic response characteristics of geosynthetic reinforced embankment under moving load. *Rock Soil Mech.* 42 (10), 2865–2874. doi:10.16285/jrsm.2021.0352

Zheng, G., Xia, B., Zhou, H., Yu, X., and Diao, Y. (2023). Influence of deep-cement-mixing column rows on the performance of geosynthetics-reinforced column-supported railway embankment. *Transp. Geotech.* 41, 101012. doi:10.1016/j.trgeo.2023.101012

Zheng, G., Xia, B., Zhou, H., Yu, X., and Diao, Y. (2024). Investigation of load transfer mechanisms in reinforced cohesive soil embankments in case of subsidence using DEM. *Geotext. Geomembranes* 52, 912–924. doi:10.1016/j.geotexmem.2024.05.004

frontiers | Frontiers in Earth Science

TYPE Original Research
PUBLISHED 17 March 2025
DOI 10.3389/feart.2025.1541217

OPEN ACCESS

EDITED BY
Chong Xu,
Ministry of Emergency Management, China

REVIEWED BY
Pengju An,
Ningbo University, China
Jiao Chenlei,
Tianjin University, China

*CORRESPONDENCE
Yanxin Yang,
✉ yanxinyangswjtu@foxmail.com

RECEIVED 07 December 2024
ACCEPTED 16 January 2025
PUBLISHED 17 March 2025

CITATION
Wu D, Liang T, Yang Y, Pei Q, Yi Y, Wu J and Li D (2025) Experimental study on displacement monitoring of instable highway slope based on MEMS sensors.
Front. Earth Sci. 13:1541217.
doi: 10.3389/feart.2025.1541217

Experimental study on displacement monitoring of instable highway slope based on MEMS sensors

Di Wu[1], Taiming Liang[1], Yanxin Yang[3]*, Qingpeng Pei[4], Yang Yi[1], Jianjian Wu[1] and Dan Li[1]

[1]School of Architecture and Transportation Engineering, Guilin University of Electronic Technology, Guilin, Guangxi, China, [2]Natural Resources Ecological Restoration Center of Guangxi Zhuang Autonomous Region, Nanning, Guangxi, China, [3]School of Civil Engineering, Sichuan University of Science and Engineering, Zigong, Sichuan, China, [4]Guangxi Guiguan Electric Power Co., Ltd., Nanning, China

Introduction: The monitoring of soil displacement during highway slope instability currently faces challenges such as poor stability, low accuracy, and high costs. In this study, a Micro-Electro-Mechanical System (MEMS) sensor is proposed for measuring internal soil displacement during slope movement. A method for converting MEMS-based acceleration signals into displacement data is also developed.

Methods: To evaluate the applicability of MEMS technology for deep displacement monitoring, an indoor model test was conducted using a highway slope composed of gravelly soil from Jiangxi Province as a case study. Three slope models with varying gravel contents (20%, 40%, and 60%) were designed to simulate displacement caused by slope instability. Displacement data obtained from the MEMS sensors were analyzed and compared with Particle Image Velocimetry (PIV) data.

Results and Discussion: The results showed that the average relative errors of vertical displacement for the MEMS sensor compared to PIV at three measurement points in the sliding area were 5.79%, 5.54%, and 5.89% for slopes with 20%, 40%, and 60% gravel content, respectively. Similarly, the average relative errors of horizontal displacement were 6.11%, 5.21%, and 4.73%. These findings indicate that the trends in soil movement within the sliding area correspond to changes in gravel content. Furthermore, the relatively small average relative errors of the MEMS sensor demonstrate its feasibility and potential for deep soil displacement monitoring in slope stability studies.

KEYWORDS

MEMS sensors, slope with gravelly soil, gravel content, model test, deep soil displacement

1 Introduction

Among the various types of road hazards (Li et al., 2016; Wen and Jiang, 2017; Liao et al., 2018), the destabilization of highway cut slopes poses a particularly significant risk (Ren et al., 2021; Zhang et al., 2022; Zhou et al., 2023; Ren et al., 2024; Guthrie et al., 2009).

In practical engineering scenarios, highway slopes are often composed predominantly of gravelly soils, characterized by the presence of lumps and gravels with inter-particle disorder. Key external factors contributing to slope destabilization include rainfall, seismic activity, blasting operations, and excavation at the slope base. Among these, gravel content plays a critical role in influencing the stability of gravelly soil slopes, significantly impacting their physical and mechanical properties as well as their deformation characteristics.

In studies on the influence of gravel on slope stability, Fang (Fang et al., 2024; Fang et al., 2023a) used particle image velocimetry (PIV) to conduct physical model tests, the analysis revealed that soil arches expand and elongate during excavation. The inverse velocity method proved effective for predicting slope failure time. Li and Hu (Li et al., 2024) using the Zaharnur open-pit coal mine in China as a prototype, investigated the arching effect unique to soft rocks. Based on the deformation characteristics of the slope, they proposed that the optimal ratio ranges of slope excavation width to the height and width of the outermost crack are 0.36–0.49 and 0.72–1.00, respectively. Bai and Wang (Wang et al., 2024a) investigated confluence flow generation on slopes with varying gradients and gravel cover conditions. Their results showed that gravel cover effectively reduces runoff under low rainfall intensities. Additionally, the lattice Boltzmann model accurately simulated soil flow formation. Bian and Wang (Bian et al., 2024) conducted consolidated undrained triaxial shear tests on modified gravel soil specimens and observed that gravel soil exhibits greater compactness and higher load-bearing capacity compared to homogeneous soil of equivalent volume. Numerical simulations further revealed that a threshold gravel content of 30% significantly influences the mechanical properties and deformation characteristics of the soil. In model test studies on slope displacement monitoring, Park and Lim (Park et al., 2019) integrated sensors with an Internet of Things (IoT) system to monitor slope damage using modeled slope cutting tests. Their proposed instrumentation standard relies on cumulative and inverse displacement trends. Wang and Peng (Wang et al., 2024b) developed a multi-degree-of-freedom method for monitoring slope displacement and conducted experiments to evaluate its accuracy and stability. Experimental results demonstrated that the measurement error was less than 1 mm for distances under 40 m and less than 5 mm for a distance of 90 m. Numerous studies (Liu et al., 2018; Wang et al., 2022a; Sheng et al., 2024; Wang et al., 2022b) have highlighted the significant impact of gravel content on the shear strength of gravelly soil slopes, which directly influences slope displacement during instability. Understanding the internal deformation characteristics of slopes is therefore critical for analyzing highway cut slope instability. Current methods for monitoring deep slope displacements include optical fiber sensing, ground-penetrating radar (GPR), and time domain reflectometry (TDR). Optical fiber sensors (Wu et al., 2019) measure surface deformation by detecting strain within embedded fibers, offering high accuracy but limited effectiveness in detecting large deformations in deep soils. GPR (Liu et al., 2024; Pajewski and Benedetto, 2012) provides high-precision subsurface imaging using electromagnetic radiation but is cost-prohibitive for widespread adoption. TDR (Guan et al., 2013; Ho et al., 2019), which relies on electrical pulse signals to detect deformation, offers convenience but lacks the ability to accurately determine displacement depth and is prone to measurement errors. These limitations indicate the need for a novel, reliable technique for monitoring deep slope displacements.

In recent years, advancements in MEMS technology have inspired novel applications proposed by researchers (Algamili et al., 2021; Gutierrez et al., 2023; Ge et al., 2024; Victor, 2023; Barzegar et al., 2022). The core principle of MEMS accelerometers is to capture acceleration signals from soil bodies. By applying dynamic solution algorithms combined with Kalman filtering for dynamic estimation, displacement information can be accurately derived from acceleration data, enabling precise soil movement monitoring. Li and Song (Li et al., 2023) introduced a method for real-time monitoring of reservoir bank slope deformation using MEMS inertial sensors. Their approach extended traditional displacement measurement by incorporating rotational angle analysis. Using inertial navigation principles, linear acceleration and angular velocity were converted into motion velocity and displacement at observation points, facilitating early slope failure detection. Tao and Yang (Tao et al., 2021) developed a novel dam stability sensing system utilizing a dual MEMS sensor structure embedded within the dam. This system converted spatial deflection and torsion angle outputs into endpoint coordinates of the sensor array, which were then used to calculate dam settlement displacement values. Additionally, numerous researchers (Freddi et al., 2023; Shentu et al., 2020; Ge et al., 2021; Abraham et al., 2022; Najafabadi et al., 2024; Jiao et al., 2023) have designed a variety of MEMS-based deep displacement sensing devices for flexible geotechnical structures. These devices have been successfully applied in engineering projects, including slopes and excavation pits. In summary, MEMS inertial sensors demonstrate exceptional performance in monitoring various geotechnical structures, offering significant potential for practical applications.

This study investigates the feasibility of using MEMS technology for monitoring displacement data under highway slope instability. Based on a real gravelly soil slope project, three slope instability tests were designed with varying gravel contents (20%, 40%, 60%) (Zhang et al., 2023). The displacement data captured by MEMS sensors were compared with those obtained through Particle Image Velocimetry (PIV). Additionally, the study evaluates the effectiveness of MEMS in slope displacement monitoring and explores the influence of gravel content variations on slope displacement during failure events.

2 Deep soil displacement sensing algorithm

2.1 Preprocessing of acceleration signals

The processing of deep soil displacement signals primarily focuses on the precise acquisition of linear acceleration from the moving soil. Before further analysis, the acceleration signal from the sensor must undergo several preprocessing steps. The first step involves eliminating zero-bias and random errors. To correct for zero-bias error in the acceleration signal, the de-mean method is applied (Zhang et al., 2020). Consider the X-axis as an example. After embedding the sensor module in the soil and initiating accelerometer calibration via the host computer's software, the sensor's default navigation coordinate system is transformed into the carrier coordinate system, aligned with the target measurement point. In this setup, the coordinate system is centered at the sensor measurement point, and the X-axis ideally outputs 0 m/s^2, though occasional zero-bias errors may occur. To address these errors, the sensor is left stationary for a duration of t minutes, during which n acceleration data points are collected and averaged. The average of the sampled acceleration data and individual sampled acceleration values as shown in Equations 1, 2.

$$\bar{a} = \frac{1}{N}\sum_{k-1}^{N} a_k \tag{1}$$

$$a'_k = a_k - \bar{a}(k = 1,2,3,4...N) \tag{2}$$

$\bar{a}$ -Average of the sampled acceleration data, a_k-Individual sampled acceleration values, a'_k-Individual acceleration values after preliminary de-meaning.

To eliminate random errors, a wavelet threshold denoising function (Hu et al., 2023) was applied to remove the noise component from the signal. Additionally, a least squares method was employed to correct for baseline drift during sensor displacement.

The acquired acceleration values are adjusted by subtracting the components of gravitational acceleration (g_x, g_y, g_z) along each axis of the carrier coordinate system, thereby filtering out the gravity component. Taking the X-axis linear acceleration as an example, it is expressed by the following equation, with similar expressions for the Y-axis and Z-axis. The sampled linear acceleration as shown in Equation 3.

$$a_{xlinear} = a'_x - g_x \tag{3}$$

$\bar{a}$ - Sampled linear acceleration along the X-axis, with the gravity component removed, a_k- Preprocessed sampled acceleration along the X-axis, a'_k-Sampled gravitational component along the X-axis.

Following the preprocessing of the acceleration signal, the three-axis linear acceleration can be derived. This linear acceleration is then numerically integrated to obtain the sensor's linear velocity, and a second integration provides the three-axis linear displacement of the sensor. In this study, Simpson's rule is employed for the integration of both linear acceleration and velocity. This method has been shown to offer superior stability compared to the Newton-Cotes formula and greater precision than the trapezoidal rule. The velocity and displacement are obtained from Equations 4, 5.

$$v_{linear}(t) = v_{linear}(t-1) + \frac{a_{linear}(t-1) + 4a_{linear}(t) + a_{linear}(t+1)}{6} \times \Delta t \tag{4}$$

$$s_{linear}(t) = s_{linear}(t-1) + \frac{v_{linear}(t-1) + 4a_{linear}(t) + v_{linear}(t+1)}{6} \times \Delta t \tag{5}$$

t = *0,1,2, N-1*, Δt represents the sampling time. By applying the aforementioned equation, we can obtain S_{linear}, which is the processed MEMS displacement signal.

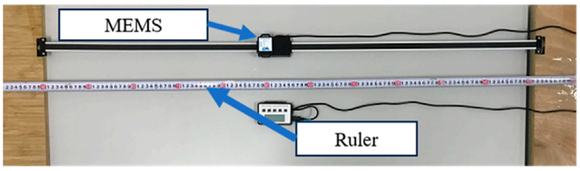

FIGURE 1
Fixed-distance sliding rail test.

2.2 Validation of displacement sensing algorithm based on fixed-distance sliding rail test

The objective of this study is to validate the effectiveness of the time-domain integration algorithm in processing the original acceleration signal and assess the accuracy of the resulting displacement signal. To achieve this, a sliding rail test is designed for verification. The test setup consists of a linear track, 1 m in length, with a slider attached. Before initiating the test, the sensor is securely bonded to the slider to ensure that the sensor's motion is synchronized with that of the slider. The entire test process is documented via video. A schematic diagram of the fixed-distance sliding rail test is provided in Figure 1.

The experimental design consisted of ten distinct groups. The aggregate results from these ten sets of fixed-distance sliding rail tests are summarized in Table 1 To further assess the distribution of the algorithmic displacement values, the Quantile-Quantile (Q-Q) and error bar plot were examined. As shown in Figures 2, 3, the algorithmic displacement values are predominantly clustered around the reference line, thereby supporting the hypothesis that the fixed-distance sliding rail test results obtained from the algorithm are normally distributed.

Given the limited sample size, the displacement values from the ten groups were subjected to a normality test. The Shapiro-Wilk (S-W) test was applied, yielding a p-value of 0.179 ($p > 0.05$), indicating that the data follow a normal distribution. The fixed-distance sliding rail test algorithm displacement values were found to follow a normal distribution. Therefore, a T-test was conducted to evaluate whether any significant systematic errors were present in the data. The formula for the T-test is as shown in Equation 6.

$$t = (\bar{x} - u_0)\frac{\sqrt{n}}{s} \tag{6}$$

$\bar{x}$ represents the mean value of the fixed-distance sliding rail test displacement, and u_0 denotes the standard value. The displacement data from the 10 groups of fixed-distance sliding rail tests are individually substituted into the formula to perform a two-sided T-test. The two-sided T-test formula as shown in Equation 7.

$$|t| < \frac{t_a}{2} \tag{7}$$

Using a two-sided T-test, the obtained p-value is 0.665 < $t_{0.025}$ = 2.262. This finding indicates the absence of significant systematic error in the 10 sets of fixed-distance sliding rail test displacement data. Thus, the accuracy and feasibility of the method proposed in this study for converting MEMS acceleration signals into displacement signals are confirmed.

TABLE 1 Fixed-distance sliding rail test results reference table.

Number of test groups	Actual displacement (mm)	Algorithm displacement (mm)	Relative error (absolute value)
1	1,000	1,037.2	3.72%
2	1,000	968.6	3.14%
3	1,000	1,022.6	2.26%
4	1,000	1,069.7	6.97%
5	1,000	956.2	4.38%
6	1,000	947.9	5.21%
7	1,000	1,056.1	5.61%
8	1,000	963.2	3.68%
9	1,000	935.6	6.44%
10	1,000	975.2	2.48%

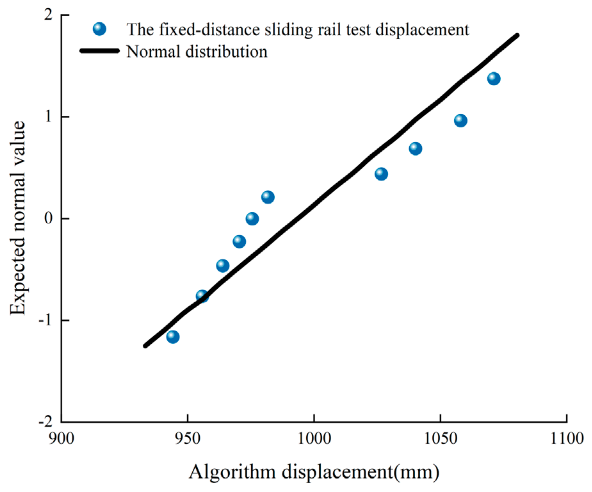

FIGURE 2
Quantile-Quantile plot of the fixed-distance sliding rail test.

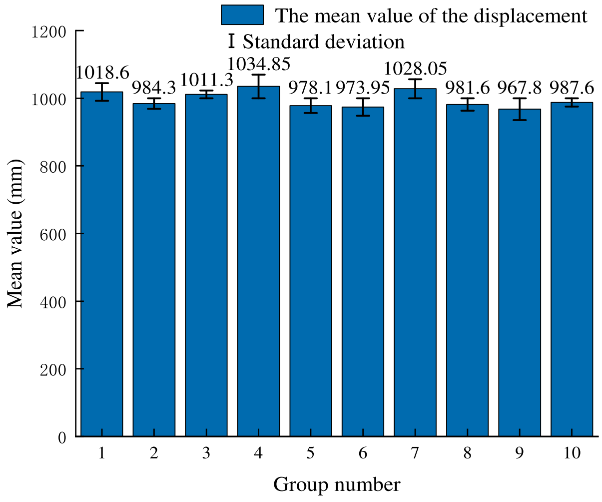

FIGURE 3
Error bar of the fixed-distance sliding rail test.

3 Model test

The actual slope with gravelly soil is shown in Figure 4. The model slopes featured a gradient of 45° and a 1:1 slope ratio, primarily composed of weathered sandstone and gravelly soils. A model box was used to form the slope, inducing an unstable, sliding configuration. MEMS sensors were strategically placed in both the unstable and slip-prone areas to monitor slope displacement. The displacement data recorded by the MEMS sensors were then compared to those obtained via Particle Image Velocimetry (PIV). Furthermore, as the test is based on an actual gravelly soil slope, gravel content was varied as a parameter. To investigate the impact of gravel content on slope displacement during instability, three groups of MEMS-based slope monitoring tests were conducted, each with different gravel contents.

In accordance with the principles outlined in the Buckingham π-theorem, the design of the gravel-soil slope model test was conducted to ensure the accurate determination of the similarity index. The key parameters considered in the soil-gravel mixture slope model test include, slope angle (θ), gravel content (ω), soil unit weight (γ), elastic modulus of the gravel-soil mixture (E), Poisson's ratio (μ), cohesion (c), and the angle of internal friction (φ). The similarity ratio was determined using the magnitude analysis method, resulting in a geometric similarity constant of n = 31.25. Based on this, the prototype slope was found to be 25,000 mm in height, while the model slope was scaled to a height of 800 mm.

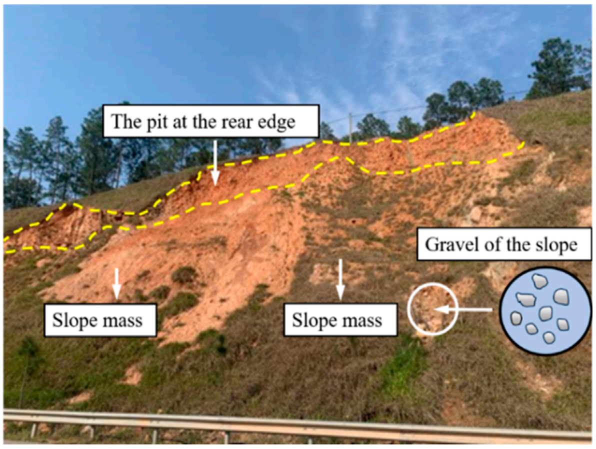

FIGURE 4
Photograph of slope destabilization on a highway in Jiangxi Province.

3.1 Model box

The model box dimensions are 1,500 mm in length, 600 mm in width, and 1,500 mm in height. To observe lateral movement of the fill material, a 25 mm thick glass surface was used at the front of the model box. The physical and schematic diagrams of the model box are shown in Figure 5. The lower part of the model box is designed with a movable base plate, which can be manually lowered to allow the bottom plate to shift downward by 50 mm. The sliding device facilitates soil movement within the designated sliding and unstable areas, simulating slope destabilization. This process mimics the scenario where upper soil layers lose support from underlying soils, either through excavation at the slope toe or sliding of the lower layers. The sliding base plate has a width of 300 mm, with the upper area designated as the sliding-causing area, and the unstable area situated 600 mm above it.

The surface roughness of the test model box is a primary source of friction, which can significantly affect the results. To mitigate this, the lateral boundaries of the model box are smoothed to reduce frictional effects. To further minimize the influence of boundary conditions on the test outcomes, pre-testing and model calibration are conducted. These steps ensure the necessity of any further adjustments to the boundary conditions, thereby enhancing the reliability of the test results. Additionally, the model box is reinforced with steel bars along its perimeter to reduce lateral deformation and maintain structural integrity during testing.

3.2 Test materials

The sand and gravel used in the experimental setup were sourced from the Lijiang River in Guilin. In accordance with the definition of gravelly soil from relevant studies (Design of building foundation, 2013), particles larger than 2 mm must constitute more than 50% of the total weight. During preparation, gravel sieved in the ranges of 10–19 mm and 5–10 mm was uniformly mixed in a 1:1 mass ratio, while particles sieved in the range of 2–5 mm were blended with soil at a 1:1 mass ratio. This mixing procedure ensures that particles larger than 2 mm make up more than 50% of the total mass. The resulting soil-gravel mixture was then used to prepare the necessary amount of raw materials for the model slopes. The slope model was constructed with three gravel content levels (20%, 40%, and 60%) for the first layer, utilizing a combination of soil, river sand, and gravelly soil. The second layer of the model slope was composed solely of gravel.

A vibrating sieve machine with a 4-mesh screen was used to obtain sufficient soil and gravel materials. A series of large-scale comprehensive direct shear tests were conducted to determine the physical properties of soils with varying gravel contents. The physical parameters obtained from these tests are presented in Table 2.

3.3 MEMS and PIV

The MEMS sensor utilized in this experimental evaluation is the HWT901B nine-axis sensor, manufactured by a Chinese company, as shown in Figure 6. This sensor offers a data output frequency of up to 200 Hz, with an attitude angle measurement accuracy of 0.05°, a precision of 0.05° for the X and Y-axes, and 1° for the Z-axis. In the experimental setup of this study, considering the prolonged duration of the test, the sensor's sampling frequency was configured to 1 Hz.

The Particle Image Velocimetry (PIV) diagram used in the test is presented in Figure 7. PIV enables the determination of point displacements within the observation area by analyzing time intervals and displacement rates derived from successive images. Once the commissioning of the PIV equipment is completed, the lifting and sliding screw in the sliding area is rotated to induce a uniform downward movement of the slope's foot. Simultaneously, the CCD camera begins capturing sequential images of the slope, while the PIV host system receives and processes the image data in real time.

3.4 Testing and monitoring procedures

To effectively collect displacement data from the deep soil layer during soil movement in the slip-inducing area of the slope, MEMS sensors in this experiment were strategically deployed in accordance with the slope's layered construction. Initially, sensors were placed at designated points A5, A1, and A2 on the second layer. Subsequently, as the gravel soil slope was modeled, additional sensors were positioned at points A3, A4, A6, A7, A8, and A9. Sufficient slack was provided in the connecting wires to allow the MEMS sensors adequate displacement space, ensuring minimal interference from the wires. The tests were categorized based on gravel content, 20% gravel content was designated as Test A, 40% as Test B, and 60% as Test C. Each test category was conducted twice, resulting in a total of six tests. The sensor configuration for Test A is illustrated in Figures 8A–C, while the configurations for Tests B and C are identical to that of Test A. The test number of different gravel content as shown in Table 3.

The sliding device of the model box was operated to ensure a uniform descent of the sliding base plate. During this operation, the upper computer systems for the MEMS sensors and the PIV system simultaneously received data in parallel. Once the sliding base plate reached its maximum displacement of 50 mm, the operation of the

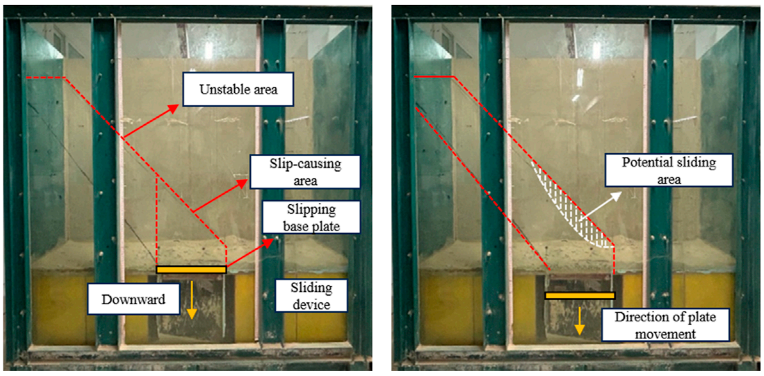

(a) Composition of the model box (b) Downward sliding induced by the slip device

FIGURE 5
Indoor model test device for slope. **(A)** Composition of the model box **(B)** Downward sliding induced by the slip device.

TABLE 2 Physical properties of gravelly soil.

Soil-gravel ratio	Density g/cm^3	Maximum dry density g/cm^3	Optimum moisture content %	Internal friction angle °
80:20	2.14	1.91	12.1%	30.59
60:40	2.20	2.11	9.7%	33.22
40:60	2.37	2.29	8.8%	35.40

settling device was terminated, marking the conclusion of the test. After the test, the gravel soil and gravel were separately extracted, and the MEMS sensors embedded in the slope mass were carefully removed. Following the complete excavation of the gravel soil and gravel, a subsequent series of sub-tests was conducted in accordance with the predefined experimental procedures.

4 Analysis of test results

4.1 Vertical displacement analysis

The modeled slopes with varying gravel contents, both before and after testing, are shown in Figure 9. It was observed that the destabilized area of the slope decreases as the gravel content increases. During the test, the front of the slope exhibited sliding behavior caused by destabilization, with the rate of displacement growth positively correlated with the distance from the source of destabilization. The sensors at A3, A4, and A7 recorded the most significant vertical displacements, whereas A6 and A8 showed relatively minor vertical displacements. The data indicate that the impact of slope failure on the unstable area diminishes gradually with increasing height. This is attributed to the descent of the movable plate, which induces a downward displacement of the soil in the slip-causing area. As a result, the soil in the unstable area partially fills the upper part of the slip-causing area. Consequently, as the vertical displacement in the slip-causing area decreases, the soil in the unstable area becomes increasingly stable. Additionally, the slopes with 40% and 60% gravel content showed reduced vertical displacement due to the higher gravel content, further enhancing slope stability.

Figure 10A illustrates the displacement data from slope sensors for the 20% gravel content test. Points A1, A2, and A5 recorded no displacement (0 mm), while the maximum displacement was observed at point A3, reaching 47.97 mm. Notably, point A3 exhibited a significant displacement at the beginning of the test. This behavior can be attributed to the minimal gravitational influence at the slope's summit, which had little effect on displacement. In contrast, the gravitational forces at the slope's base were substantial, leading to displacement influenced by the pressure and thrust of the overlying soil mass. As a result, the maximum vertical displacement occurred at A3. During the initial 10 s of the test, notable displacement reductions were observed at points A7, A6, and A8. After this period, the displacement curves at these points began to stabilize and decrease gradually. This behavior is explained by the gravel soil at A3 sliding first, creating a void that was subsequently filled by the soil from points A7, A6, and A8. As the slope continued to slide, the frictional forces increased, causing a progressive smoothing of the displacement curves at these locations.

Figures 10B, C illustrate the slope sensor displacements for 40% and 60% gravel content. Significant displacements were detected at sensors B3, B4, and B7, concentrated in the slip-causing area. The maximum vertical displacement occurred at B3 (42.15 mm), comparable to A3 in the 20% gravel test. However, the overall

FIGURE 6
MEMS sensor.

displacements at 40% and 60% gravel content were notably smaller, attributed to increased gravel content, which enhanced friction and shear strength, reducing slope instability. At 60% gravel content, the maximum displacement at C3 was 37.03 mm, slightly lower than at 40% gravel content. The greater gravel content further improved particle interlocking and solidification, enhancing the structural integrity of the gravel skeleton. As the mechanical properties approached those of a rock mass, vertical displacement in deeper soil layers exhibited a significant decline, stabilizing the slope further during sliding.

The study aims to evaluate the influence of varying gravel contents on slope displacement, as well as the displacement characteristics at different locations. Additionally, it seeks to validate the effectiveness of MEMS sensors in monitoring slope displacement by comparing displacement data obtained from PIV and MEMS systems. To achieve this, five measurement points were selected from the PIV system as reference points for vertical displacement in the slope with 20% gravel content. These PIV-derived vertical displacement values served as the true reference values, while the displacement data recorded by MEMS sensors during the model tests were considered the test values. A comparison of the vertical displacement data from MEMS sensors and PIV measurements is presented in Figure 11. Furthermore, the mean relative error between MEMS and PIV vertical displacement data was calculated using the formula as shown in Equation 8.

$$\delta = \frac{\sum \left| \frac{S_{MEMS}-S_{PIV}}{S_{PIV}} \right| \times 100}{N} \tag{8}$$

The parameter δ represents the mean relative error, where S_{MEMS} denotes the vertical displacement endpoint value measured by the MEMS sensor, S_{PIV} represents the vertical displacement endpoint value measured by the PIV system, and N is the total number of sensors used for data acquisition. Table 4 summarizes the vertical displacement values obtained from both the MEMS and PIV systems. In the primary displacement zones of slopes with gravel contents of 20%, 40%, and 60%, the calculated mean relative errors between the MEMS and PIV vertical displacement data are 5.79%, 5.54%, and 5.89%, respectively.

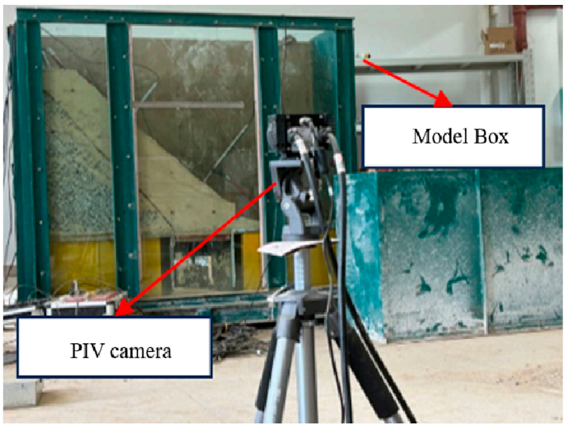

FIGURE 7
Diagram of slope with gravelly soil in PIV system.

4.2 Horizontal displacement analysis

During the test, in the slip-causing area, the horizontal displacements of A3 and A4, both buried at a depth of 100 mm, were the largest within the first 90 s, exhibiting similar movement trends. In contrast, the horizontal displacement of A7, buried at a depth of 300 mm, was smaller than that of A3 and A4 prior to 90 s but increased rapidly thereafter. Sensors A6 and A8, located in the unstable area, experienced displacement due to insufficient support from the underlying soil, which was mobilized by movement in the slip-causing area. Sensors A4 and A7 were positioned at the same horizontal location (L = 600 mm), as were A6 and A8 (L = 400 mm). A comparative analysis of horizontal displacement data from sensors at the same horizontal positions but different burial depths revealed that sensors at shallower depths (A7 and A8) recorded larger horizontal displacements than those at deeper depths (A4 and A6). This indicates that during the descent of the

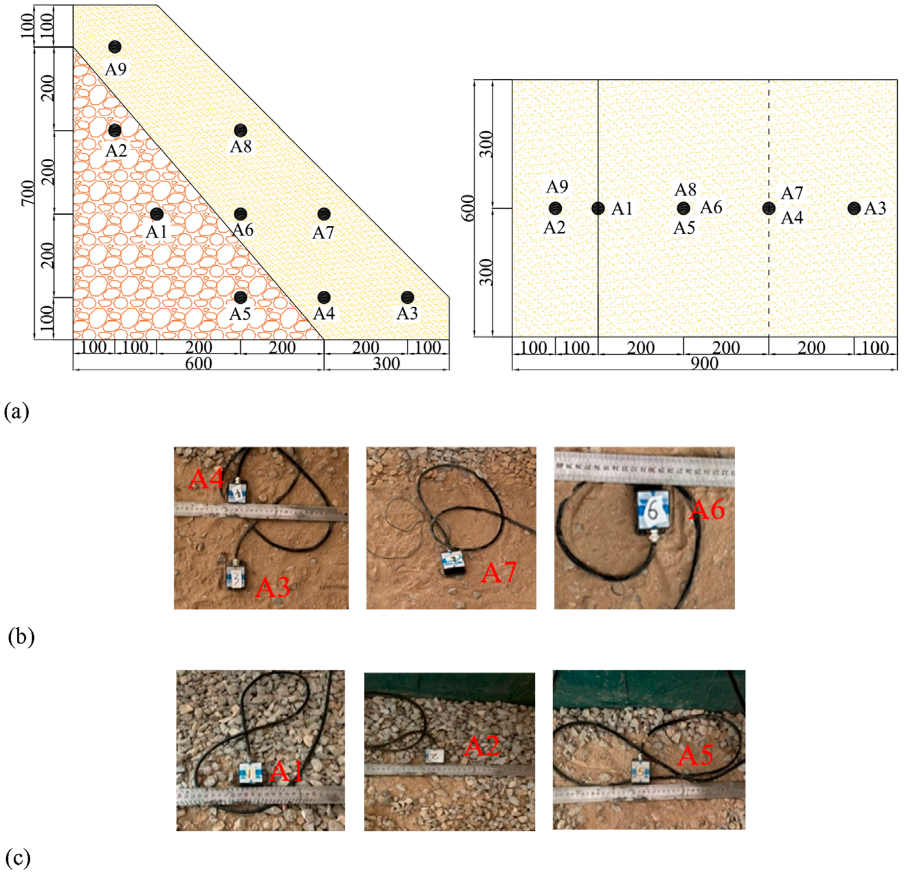

FIGURE 8
The layout of sensor for Test A 4. **(A)** Schematic diagram of sensor layout for Test A (unit: mm, schematic diagram of sensor layout for Test B and Test C is identical to that of Test A. **(B)** Layout of sensors on the first layer of Test A. **(C)** Layout of sensors on the second layer of Test A.

TABLE 3 Test number of different gravel content.

Test name	Soil-gravel ratio	Sensor number
A	20%	A1, A2, A3, A4, A5, A6, A7, A8, A9
B	40%	B1, B2, B3, B4, B5, B6, B7, B8, B9
C	60%	C1, C2, C3, C4, C5, C6, C7, C8, C9

sliding device, the horizontal displacement in the unstable area predominantly affects the shallow soil layer rather than the deeper soil mass. Additionally, the horizontal displacements at A6 and A8 were greater than at A9, confirming that the bottom of the unstable area exhibited the largest horizontal displacement over time. This finding aligns with the hypothesis that sliding of the lower soil layers in highway slopes triggers subsequent movement of the overlying upper soil layers.

Figure 12A illustrates the slope sensor displacements for 20% gravel content, with the maximum horizontal displacement recorded at point A7 (35.12 mm). During the first 90 s, A7 exhibited smaller displacement compared to A3 and A4. However, after 90 s, A7's displacement increased significantly. This behavior reflects typical traction slope instability, where the lower soil mass slides first, triggering movement in the upper layers. Sensors A6 and A8 in the stabilization area recorded displacements of 5.94 mm and 18.58 mm, respectively. Their movement resulted from a lack of support caused by soil displacement in the slip-causing area. Comparing displacement data at the same horizontal position but varying burial depths, A7 and A8 (shallow sensors) exhibited greater horizontal displacement than A4 and A6 (deeper sensors), indicating that the shallow soil experienced more pronounced horizontal movement. Additionally, sensors at different horizontal positions but the same depth revealed higher displacements at A4 and A7 in the slip-causing and unstable junction areas compared to A8 and A6 in the upper unstable area. Displacement at A8 and A6 also exceeded that at A9 in the stabilized upper zone. These observations confirm that initial movement in the lower slope induces a pushing force, propagating displacement to the upper soil layers.

Figure 12B illustrates the horizontal displacement of slope sensors for the 40% gravel content test. Initially, the horizontal displacements at points B3 and B4 were greater than that of B7. However, after 50 s, the displacement at B7 increased significantly,

(a) 20% gravel content

(b) 40% gravel content

(c) 60% gravel content

FIGURE 9
Comparison diagram of slope before and after the test. **(A)** 20% gravel content. **(B)** 40% gravel content. **(C)** 60% gravel content.

reaching a maximum of 34.31 mm, while the displacements at B3 and B4 were comparatively smaller, at 9.88 mm and 9.36 mm, respectively. A similar trend was observed in the 60% gravel content test, as shown in Figure 12C. At the outset, the horizontal displacements at C3 and C4 exceeded that of C7. After 30 s, however, the displacement at C7 escalated sharply, peaking at 28.21 mm, compared to 6.75 mm and 6.28 mm for C3 and C4, respectively. Among the three tests with varying gravel contents, point 7 consistently exhibited the highest horizontal displacement, underscoring its susceptibility to significant movement during slope destabilization.

A comparative analysis was performed on the horizontal displacement of points A4, B4, and C4 versus A7, B7, and C7 in slopes with 20%, 40%, and 60% gravel content, respectively. As shown in Figure 12, at equivalent horizontal positions but different vertical depths, the horizontal displacement at point 7 consistently exceeded that at point 4. This can be attributed to the characteristics of shallow soil, which is typically looser and more susceptible to external loads, leading to greater shear deformation and, consequently, larger horizontal displacement. The surface soil generally has a looser structure and lower shear strength, making it more susceptible to displacement under sliding forces. For the slope with 20% gravel content, a comparison between A6 and A8 reveals that A6 exhibits greater horizontal displacement than A8 at equivalent horizontal positions but varying vertical depths. This observation is consistent with the tendency of landslides to initiate destabilization in the central region, where the sliding surface is typically more gradual. The localized instability induces outward horizontal displacement of the gravel soil within this area.

The measurement points from the PIV system were selected as reference values for horizontal displacement in the slope with 20%, 40% and 60% gravel content, based on sensor deployment locations. These reference values were compared with the horizontal displacement data obtained from MEMS sensors during the model test. Figures 13A–C presents the comparison between the horizontal displacement values measured by the MEMS sensors and those recorded by the PIV system. In the primary displacement areas of slopes with gravel contents of 20%, 40%, and 60%, the mean relative errors between the MEMS and PIV horizontal displacement data were 6.11%, 5.21%, and 4.73%, respectively. PIV and MEMS sensor horizontal displacement relative error as shown in Table 5.

4.3 Impact analysis of gravel content on slope stability

Figure 14A illustrates the vertical displacement at point 3 for slopes with varying gravel contents. The slope with 20% gravel content exhibits the highest vertical displacement, while increasing gravel content results in a gradual reduction in displacement. Compared to the A3 curve, which shows the greatest displacement, the slopes with 40% and 60% gravel content demonstrate reductions of 5.83 mm and 10.95 mm, respectively, at the same location. This indicates that higher gravel content at measurement point 3 enhances slope soil stability. Furthermore, a comparison of the time-displacement curves for B3 and C3 reveals similar trends in soil movement, suggesting that the mechanical behavior of the 40% and 60% gravel content slopes closely resembles each other and differs from the 20% gravel content slope. In the 20% gravel content slope, the soil exhibits characteristics akin to sandy soils, whereas the 40% and 60% gravel content slopes demonstrate properties more typical of gravelly soils.

The vertical displacement at points 4 and 7 for slopes with 40% and 60% gravel content was analyzed. After 80 s at point 4 and 90 s at point 7, the 40% gravel content slope exhibited accelerated soil movement, with displacements gradually diverging from those of the 60% gravel content slope. As shown in Figures 14B, C, the progressive descent of the sliding device resulted in greater vertical movement in the 40% gravel content slope compared to the 60% gravel content slope at both measurement points.

Compared to the A3 curve, the slopes with 40% and 60% gravel content exhibited reductions in displacement of 2.69 mm and 5.82 mm, respectively, at the same location. Further analysis reveals that the slow deformation phase at point 3 lasts approximately 30 s for the 20% gravel content slope, 40 s for the 40% gravel content slope, and 50 s for the 60% gravel content slope. This indicates that the transition from the slow deformation stage to the accelerated horizontal displacement stage in deeper soil layers occurs more gradually with higher gravel content, as shown in Figure 15A. Combined with the observed trend of decreasing horizontal

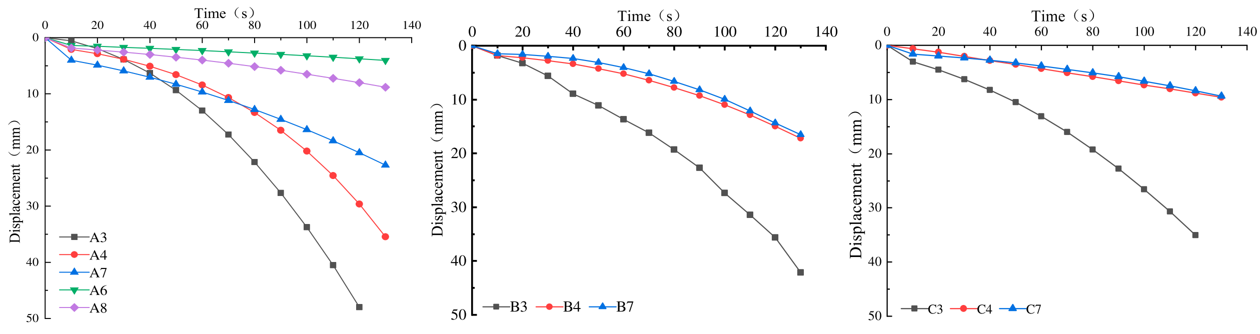

(a) 20% gravel content (b) 40% gravel content (c) 60% gravel content

FIGURE 10
Vertical displacement analysis of measurement points at different locations with the same gravel content. **(A)** 20% gravel content **(B)** 40% gravel content **(C)** 60% gravel content.

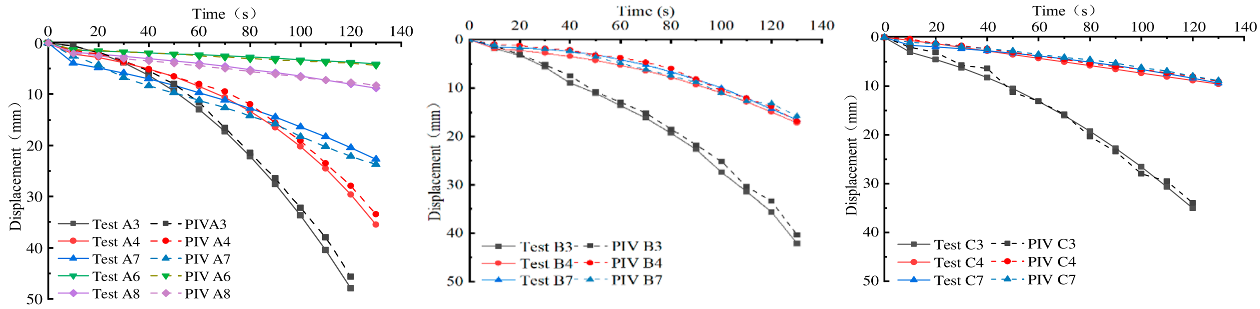

(a) 20% gravel content (b) 40% gravel content (c) 60% gravel content

FIGURE 11
Comparison of vertical displacement test and PIV. **(A)** 20% gravel content **(B)** 40% gravel content **(C)** 60% gravel content.

TABLE 4 PIV and MEMS sensor vertical displacement relative error analysis table.

Soil-gravel ratio	Number of the sensor	MEMS vertical displacement (mm)	PIV vertical displacement (mm)	Relative error/% (absolute value)	Mean relative error/% (absolute value)
80:20	3	47.98	45.74	4.90	5.79
	4	35.47	33.43	6.10	
	7	22.70	23.71	4.26	
	6	4.03	4.3	6.28	
	8	8.84	8.23	7.41	
60:40	3	42.15	39.35	7.12	5.54
	4	17.17	16.34	5.08	
	7	16.52	15.82	4.42	
40:60	3	37.03	34.95	5.95	5.89
	4	9.59	9.02	6.32	
	7	9.37	8.89	5.40	

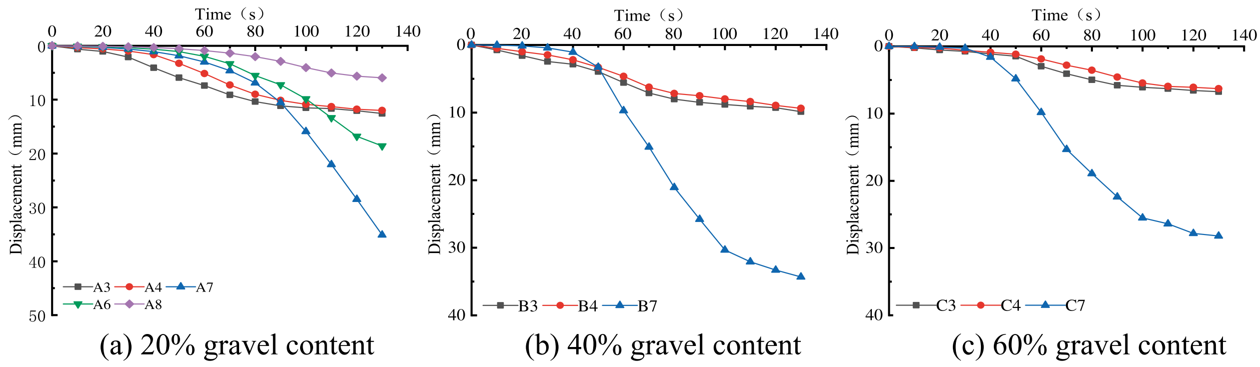

(a) 20% gravel content (b) 40% gravel content (c) 60% gravel content

FIGURE 12
Horizontal displacement analysis of measuring points at different positions on slopes with the same gravel content. **(A)** 20% gravel content **(B)** 40% gravel content **(C)** 60% gravel content.

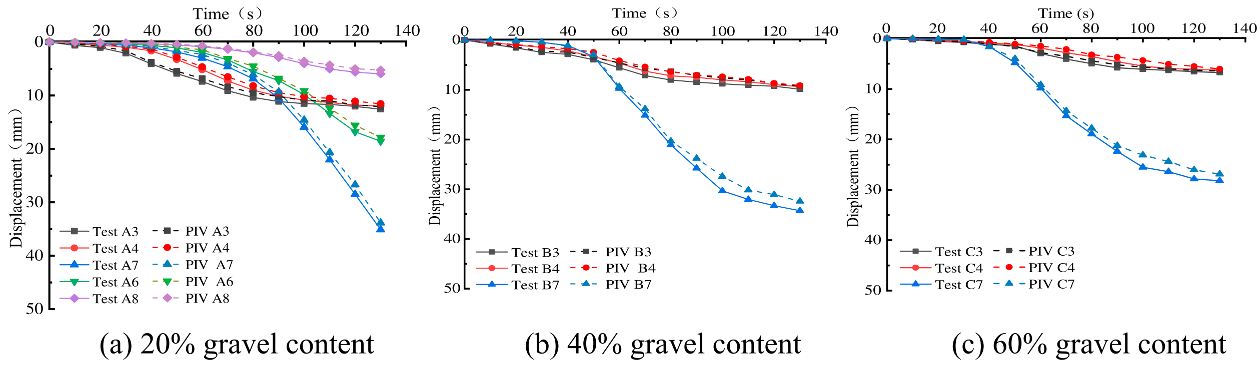

(a) 20% gravel content (b) 40% gravel content (c) 60% gravel content

FIGURE 13
Comparison of horizontal displacement test and PIV. **(A)** 20% gravel content **(B)** 40% gravel content **(C)** 60% gravel content.

TABLE 5 PIV and MEMS sensor horizontal displacement relative error analysis table.

Soil-gravel ratio	Number of the sensor	MEMS horizontal displacement (mm)	PIV horizontal displacement (mm)	Relative error/% (absolute value)	Mean relative error/% (absolute value)
80:20	3	12.57	12.01	4.66	6.11
	4	12.00	11.56	3.81	
	7	35.12	33.54	4.71	
	6	18.58	17.83	4.21	
	8	5.94	5.25	13.14	
60:40	3	9.88	9.22	7.16	5.21
	4	9.36	9.12	2.63	
	7	34.31	32.42	5.83	
40:60	3	6.75	6.42	5.14	4.73
	4	6.28	6.03	4.15	
	7	28.21	26.89	4.91	

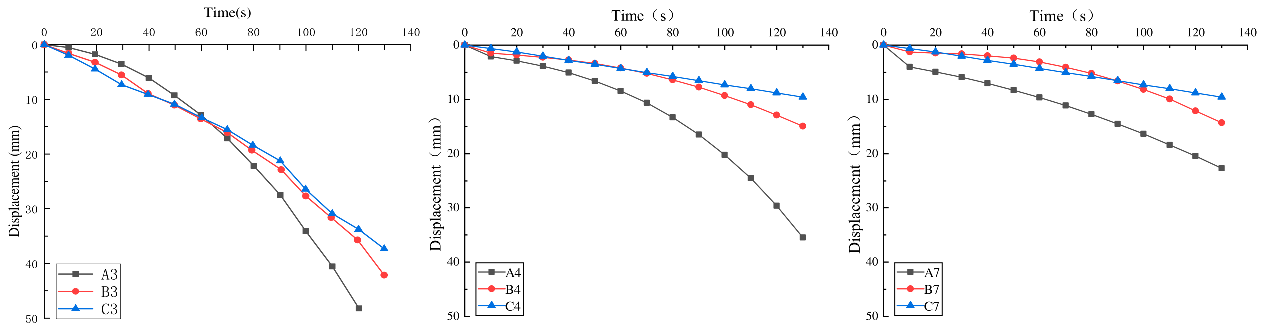

(a) 20% gravel content (b) 40% gravel content (c) 60% gravel content

FIGURE 14
Vertical displacement analysis of measuring points at the same location with different gravel contents. **(A)** 20% gravel content **(B)** 40% gravel content **(C)** 60% gravel content.

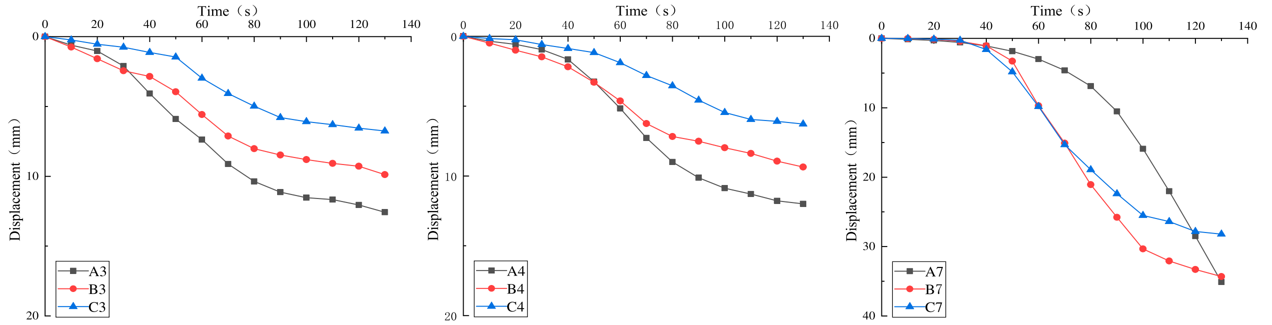

(a) 20% gravel content (b) 40% gravel content (c) 60% gravel content

FIGURE 15
Horizontal displacement analysis of measuring points at the same location with different gravel contents. **(A)** 20% gravel content **(B)** 40% gravel content **(C)** 60% gravel content.

displacement with increasing gravel content, these findings suggest that higher gravel content enhances slope stability at measurement point 3.

The time-displacement curves of A4, B4, and C4 in Figure 15B exhibit a pattern similar to that observed at measurement point 3, indicating that the soil near measurement point 4 undergoes distinct phases of slow deformation, acceleration, and gradual stabilization in horizontal movement. At measurement point 7, the horizontal displacement exceeds 20 mm, as shown in Figure 15C, marking it as the location of maximum horizontal displacement among all measurement points. Notably, this maximum displacement does not occur at the slope foot but rather at the shallow burial position at the junction of the slip-causing area and the stabilization area.

The test results demonstrate a clear correlation between slope stability and gravel content, with stability decreasing as gravel content diminishes. In slopes with 20% gravel content, the rapid expansion of the slip area is attributed to smaller soil particles and reduced cohesive forces, which significantly compromise slope stability. Conversely, slopes with 60% gravel content exhibit high stability due to the higher proportion of gravel, which enhances shear strength and soil stiffness. Slopes with 40% gravel content show moderate stability, further confirming the critical role of gravel content in determining slope stability. Higher gravel content contributes to a robust skeletal structure and increased soil density, which strengthen mechanical properties and improve slope stability. Large gravel particles inhibit the accumulation of fine-grained soils and provide enhanced support. In contrast, slopes with low gravel content exhibit alterations in pore structure, leading to an increased proportion of fine particles that weaken the soil's mechanical properties. Furthermore, in practical applications, the fine particles in low-gravel-content soils are prone to water absorption and swelling, reducing friction and further diminishing slope stability. In conclusion, increasing gravel content enhances slope stability by improving the soil's mechanical properties, thereby reducing vertical and horizontal displacements during slope destabilization.

In slopes with 20%, 40%, and 60% gravel content, the slip-causing area represents the primary region of vertical and horizontal displacement. This study conducts a comparative analysis of the relative errors in vertical and horizontal displacements at measuring points 3, 4, and 7 within the slip-causing area. For slopes with 20%, 40%, and 60% gravel content, the average relative errors in vertical displacement measured by MEMS sensors compared to PIV were 5.79%, 5.54%, and 5.89%, respectively. Similarly, the average relative errors in horizontal displacement for the same slopes were 6.11%, 5.21%, and 4.73%, respectively. While the trends in soil movement within the slip-causing areas of slopes with different

TABLE 6 Summarized protocol for a physical model test.

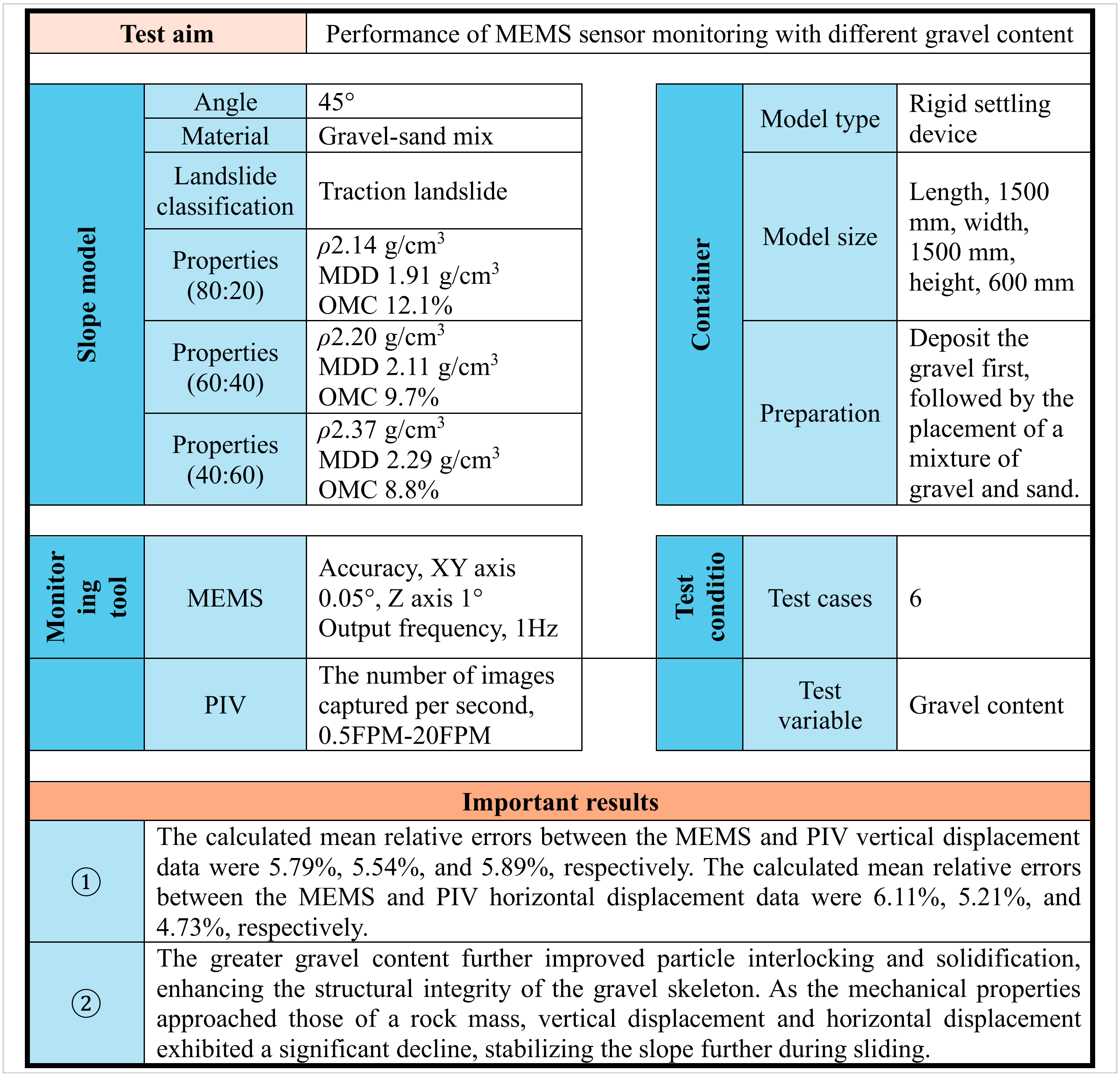

Test aim	Performance of MEMS sensor monitoring with different gravel content

Slope model	Angle	45°	**Container**	Model type	Rigid settling device
	Material	Gravel-sand mix			
	Landslide classification	Traction landslide		Model size	Length, 1500 mm, width, 1500 mm, height, 600 mm
	Properties (80:20)	ρ2.14 g/cm^3 MDD 1.91 g/cm^3 OMC 12.1%			
	Properties (60:40)	ρ2.20 g/cm^3 MDD 2.11 g/cm^3 OMC 9.7%		Preparation	Deposit the gravel first, followed by the placement of a mixture of gravel and sand.
	Properties (40:60)	ρ2.37 g/cm^3 MDD 2.29 g/cm^3 OMC 8.8%			
Monitoring tool	MEMS	Accuracy, XY axis 0.05°, Z axis 1° Output frequency, 1Hz	**Test conditio**	Test cases	6
	PIV	The number of images captured per second, 0.5FPM-20FPM		Test variable	Gravel content

Important results	
①	The calculated mean relative errors between the MEMS and PIV vertical displacement data were 5.79%, 5.54%, and 5.89%, respectively. The calculated mean relative errors between the MEMS and PIV horizontal displacement data were 6.11%, 5.21%, and 4.73%, respectively.
②	The greater gravel content further improved particle interlocking and solidification, enhancing the structural integrity of the gravel skeleton. As the mechanical properties approached those of a rock mass, vertical displacement and horizontal displacement exhibited a significant decline, stabilizing the slope further during sliding.

gravel contents exhibit some variation, the mean relative errors for both vertical and horizontal displacement measurements remain below 1%. This indicates that MEMS sensors provide reliable and accurate measurements of soil movement, demonstrating their effectiveness in monitoring slope stability.

Unlike previous studies that focused on measuring surface displacement, this research investigates internal acceleration signals within the soil during slope failure. By employing MEMS sensors as monitoring tools, acceleration signals are converted into displacement data, enabling direct and intuitive measurements of internal slope displacements. In simulated gravelly soil slope experiments, MEMS sensors demonstrated good monitoring capabilities, suggesting their potential for validation in real-world highway gravelly soil slopes. However, challenges remain with this sensing method. For instance, rotational changes in the sensor's orientation may introduce minor data deviations, and groundwater interference can affect sensor performance. Future experimental optimizations will integrate orientation calculations to achieve precise three-dimensional positioning of sensors within the soil, while also addressing issues related to ensuring the reliable operation of MEMS sensors in subterranean environments. Table 6 presents an example of a standard protocol for a physical model test (Fang et al., 2023b). In this table, a concise summary of the key information for the test is provided, highlighting the essential details rather than including every specific aspect.

5 Conclusion

This study investigates the potential of utilizing MEMS technology to monitor displacements in slope models. Indoor model tests were conducted to collect displacement data from deep measurement points in slopes with varying gravel contents. The primary objective of this research is to analyze the influence of gravel content on the displacement characteristics of deep soil masses in slopes. The accuracy of the displacement data obtained from MEMS sensors in the model tests was validated through PIV, leading to the following key conclusions.

1. This study demonstrates the effectiveness of MEMS sensor technology for deep displacement monitoring in slopes through a series of modeling tests. A comparison between PIV and MEMS displacement data reveals that the vertical and horizontal displacement endpoints calculated by PIV align closely with those measured by MEMS sensors at the same locations. The mean relative error of vertical and horizontal displacements at measurement points within the slip-causing area exhibited a maximum variation of only 1%. These findings validate the accuracy of the algorithmically processed MEMS signals and confirm the reliability of MEMS technology for monitoring slope displacements. However, it is important to acknowledge the limitations of the current experiments, which have not fully addressed the effects of sensor orientation changes, groundwater interference, and large slope displacements on sensor performance. These issues will be incorporated into more advanced and comprehensive future investigations.
2. Additionally, vertical and horizontal displacement values at measurement points with varying gravel contents 20%, 40%, and 60% but identical spatial locations were analyzed. The results indicate a clear trend of decreasing displacement values with increasing gravel content, highlighting the significant influence of gravel content on enhancing slope stability.
3. In practical engineering applications, the composition of highway slopes and the factors contributing to slope instability are often more complex. Future field tests on actual slopes can further investigate these complexities and validate the effectiveness of MEMS technology in diverse conditions. Additionally, integrating MEMS sensors with other monitoring technologies, such as fiber optic sensors and ground-penetrating radar, can form a multi-sensor fusion system. This advanced integration holds significant potential to enhance the accuracy, reliability, and robustness of slope monitoring and early-warning frameworks.

Data availability statement

The original contributions presented in the study are included in the article/supplementary material, further inquiries can be directed to the corresponding authors.

Author contributions

DW: Investigation, Methodology, Project administration, Validation, Writing–review and editing. TL: Software, Writing–original draft, Writing–review and editing. YxY: Writing–review and editing. QP: Software, Writing–review and editing. YgY: Investigation, Writing–review and editing. JW: Investigation, Writing–review and editing. DL: Investigation, Writing–review and editing.

Funding

The author(s) declare that financial support was received for the research, authorship, and/or publication of this article. Financial support for this work is gratefully acknowledged from the Guangxi Science and Technology Major Program Grant No. AB23026028 and Guangxi Science and Technology Major Program Grant No. AB23075096. All the supports are greatly appreciated.

Conflict of interest

Author QP was employed by Guangxi Guiguan Electric Power Co., Ltd.

The remaining authors declare that the research was conducted in the absence of any commercial or financial relationships that could be construed as a potential conflict of interest.

Generative AI statement

The author(s) declare that no Generative AI was used in the creation of this manuscript.

Publisher's note

References

Abraham, M. T., Satyam, N., Pradhan, B., Segoni, S., and Alamri, A. (2022). Developing a prototype landslide early warning system for Darjeeling Himalayas using SIGMA model and real-time field monitoring. *Geosciences J.* 26, 289–301. doi:10.1007/s12303-021-0026-2

Algamili, A. S., Khir, M. H. M., Dennis, J. O., Ahmed, A. Y., Alabsi, S. S., Ba Hashwan, S. S., et al. (2021). A review of actuation and sensing mechanisms in MEMS-based sensor devices. *Nanoscale Res. Lett.* 16, 16. doi:10.1186/s11671-021-03481-7

Barzegar, M., Blanks, S., Sainsbury, B.-A., and Timms, W. (2022). MEMS technology and applications in geotechnical monitoring: a review. *Meas. Sci. Technol.* 33, 052001. doi:10.1088/1361-6501/ac4f00

Bian, H.-G., Wang, S., and Li, D.-Q. (2024). Influence of gravel content on the stability of filling embankment slope. *Eng. Mech.* 2024, 1–11. doi:10.6052/j.issn.1000-4750.2023.08.0638

Design of building foundation (2013). *General administration of quality supervision*.

Fang, K., Miao, M., Tang, H., Jia, S., Dong, A., An, P., et al. (2023a). Insights into the deformation and failure characteristic of a slope due to excavation through multi-field monitoring: a model test. *Acta Geotech.* 18, 1001–1024. doi:10.1007/s11440-022-01627-0

Fang, K., Tang, H., Li, C., Su, X., An, P., and Sun, S. (2023b). Centrifuge modelling of landslides and landslide hazard mitigation: a review. *Geosci. Front.* 14, 101493. doi:10.1016/j.gsf.2022.101493

Fang, K., Jia, S., Tang, H., Zhou, R., Kong, Z., Fu, Y., et al. (2024). Arching effect in slopes under excavation: classification and features. *Eng. Geol.* 337, 107563. doi:10.1016/j.enggeo.2024.107563

Freddi, F., Mingazzi, L., Pozzi, E., and Aresi, N. (2023). Laboratory assessment of an in-place inclinometer chain for structural and geotechnical monitoring. *Sensors* 23, 8379. doi:10.3390/s23208379

Ge, Y., Chen, J., Cao, C., He, J., Sheng, Y., and Zheng, X. (2021). Design and test of a MEMS accelerometer array for submarine landslide displacement monitoring. *Mar. Technol. Soc. J.* 55, 5–16. doi:10.4031/MTSJ.55.1.7

Ge, Y., Zhou, P., Zhou, Q., Ren, X., Fang, Y., Ge, H., et al. (2024). Research and application on *in-situ* monitoring of strata movement in submarine cold seeps area based on three-dimensional MEMS sensor network. *Measurement* 238, 115288. doi:10.1016/j.measurement.2024.115288

Guan, Z., Jiang, X., and Gao, M. (2013). "A calibration test of karst collapse monitoring device by optical time domain reflectometry (BOTDR) technique," in *Full proceedings of the thirteenth multidisciplinary conference on sinkholes and the engineering and environmental impacts of karst* (Carlsbad, New Mexico: National Cave and Karst Research Institute), 71–77. doi:10.5038/9780979542275.1115

Guthrie, R. H., Evans, S. G., Catane, S. G., Zarco, M. A. H., and Saturay, R. M. (2009). The 17 February 2006 rock slide-debris avalanche at Guinsaugon Philippines: a synthesis. *Bull. Eng. Geol. Environ.* 68, 201–213. doi:10.1007/s10064-009-0205-2

Gutierrez, F., Sevil, J., Sevillano, P., Preciado-Garbayo, J., Martinez, J. J., Martin-Lopez, S., et al. (2023). The application of distributed optical fiber sensors (BOTDA) to sinkhole monitoring. Review and the case of a damaging sinkhole in the Ebro Valley evaporite karst (NE Spain). *Eng. Geol.* 325, 107289. doi:10.1016/j.enggeo.2023.107289

Ho, S.-C., Chen, I.-H., Lin, Y.-S., Chen, J.-Y., and Su, M.-B. (2019). Slope deformation monitoring in the Jiufenershan landslide using time domain reflectometry technology. *Landslides* 16, 1141–1151. doi:10.1007/s10346-019-01139-1

Hu, T., Shen, L.-Q., L, P., Zhang, B., Dong, W.-F., and Liu, M.-Y. (2023). Transmission line galloping signal processing technology based on inertial sensor. *J. Vib. shock* 42, 49–57+78. doi:10.13465/j.cnki.jvs.2023.19.007

Jiao, C., Diao, Y., Han, J., and Zheng, G. (2023). Experimental research on a novel soil displacement monitoring system based on measurement unit cells (MUCs). *Measurement* 211, 112605. doi:10.1016/j.measurement.2023.112605

Li, T., He, B., Chen, Z., Zhang, Y., Liang, C., and Wang, R. (2016). Effects of gravel on infiltration, runoff, and sediment yield in landslide deposit slope in Wenchuan earthquake area, China. *Environ. Sci. Pollut. Res.* 23, 12075–12084. doi:10.1007/s11356-016-6394-x

Li, C., Song, S., and Sun, J. (2023). Application and simulation research of MEMS inertial sensor in reservoir bank slope deformation monitoring. *Chin. J. Rock Mech. Eng.* 42, 1248–1258. doi:10.13722/j.cnki.jrme.2022.0632

Li, G., Hu, Z., Wang, D., Wang, L., Wang, Y., Zhao, L., et al. (2024). Instability mechanisms of slope in open-pit coal mines: from physical and numerical modeling. *Int. J. Min. Sci. Technol.* 34, 1509–1528. doi:10.1016/j.ijmst.2024.10.003

Liao, L., Yang, Y., Yang, Z., Zhu, Y., Hu, J., and Zou, D. H. S. (2018). Mechanical state of gravel soil in mobilization of rainfall-induced landslides in the Wenchuan seismic area, Sichuan province, China. *Earth Surf. Dyn.* 6, 637–649. doi:10.5194/esurf-6-637-2018

Liu, S., Huang, X., Zhou, A., Hu, J., and Wang, W. (2018). Soil-rock slope stability analysis by considering the nonuniformity of rocks. *Math. Problems Eng.* 2018, 1–15. doi:10.1155/2018/3121604

Liu, C., Du, Y., Yue, G., Li, Y., Wu, D., and Li, F. (2024). Advances in automatic identification of road subsurface distress using ground penetrating radar: state of the art and future trends. *Autom. Constr.* 158, 105185. doi:10.1016/j.autcon.2023.105185

Najafabadi, H. R., Goto, T. G., Martins, T. C., Tsuzuki, M. S. G., and Barari, A. (2024). Designing MEMS accelerometer for enhanced sensitivity and reduced cross-sensitivity in landslide monitoring. *J. Int. Meas. Confed.* 226, 114092. doi:10.1016/j.measurement.2023.114092

Pajewski, L., and Benedetto, A. (2012). Special issue: civil engineering applications of ground penetrating radar preface. *Nondestruct. Test. Eval.* 27, 187–188. doi:10.1080/10589759.2012.710389

Park, S., Lim, H., Tamang, B., Jin, J., Lee, S., Chang, S., et al. (2019). A study on the slope failure monitoring of a model slope by the application of a displacement sensor. *J. Sensors* 2019, 1–9. doi:10.1155/2019/7570517

Ren, S., Zhang, Y., Xu, N., Wu, R., Liu, X., and Du, G. (2021). Mobilized strength of gravelly sliding zone soil in reactivated landslide: a case study of a giant landslide in the north-eastern margin of Tibet Plateau. *Environ. Earth Sci.* 80, 434. doi:10.1007/s12665-021-09638-y

Ren, S., Zhang, Y., Li, J., Wu, R., and Hao, H. (2024). Response mechanism of the residual strength to the mesostructure of the shear surface in the gravelly slip zone of ancient landslides. *J. Geophys. Research-Earth Surf.* 129, e2023JF007605. doi:10.1029/2023JF007605

Sheng, Y., Zhang, B., Xu, G., Cheng, Z., Shi, Z., and Li, Y. (2024). Mobility forecast of gravel-silty clay landslide using ring shear test and discrete element method in Shaziba, southwestern Hubei Province, China. *Bull. Eng. Geol. Environ.* 83, 488. doi:10.1007/s10064-024-03983-5

Shentu, N., Wang, S., Li, Q., Tong, R., An, S., and Qiu, G. (2020). Research on structure optimization and measurement method of a large-range deep displacement 3D measuring sensor. *Sensors Switz.* 20, 1689. doi:10.3390/s20061689

Tao, T., Yang, J., Wei, W., Wozniak, M., Scherer, R., and Damasevicius, R. (2021). Design of a MEMS sensor array for dam subsidence monitoring based on dual-sensor cooperative measurements. *KSII Trans. Internet Inf. Syst.* 15, 3554–3570. doi:10.3837/tiis.2021.10.005

Victor, R. (2023). "How intelligent monitoring solutions can mitigate slope failure risk," in *Risk, and resilience, conference on geo-risk - advances in theory and innovation in practice* (New York: Amer Soc Civil Engineers), 257–266.

Wang, J.-Y., Song, E.-X., and Zhang, Q.-L. (2022a). DEM analysis of the aggregate shape effect on mechanical properties of rockfill. *Eng. Mech.* 39 (03), 137–146. doi:10.6052/j.issn.1000-4750.2021.01.0061

Wang, W., Wang, P., and Zhang, Z. (2022b). Study on gravel soil strength degradation and its influence on the slope stability in reservoir bank fluctuating zone. *Eng. Fail. Anal.* 134, 105980. doi:10.1016/j.engfailanal.2021.105980

Wang, H., Bai, Y., and Huang, D. (2024a). Study of experimental and numerical simulation on the influence of gravel on the interflow of slope land. *Environ. Sci. Pollut. Res.* 31, 11716–11726. doi:10.1007/s11356-023-31808-7

Wang, W., Peng, J., Hu, W., Wang, J., Xu, X., Zaheer, Q., et al. (2024b). A multi-degree-of-freedom monitoring method for slope displacement based on stereo vision. *Computer-Aided Civ. Infrastructure Eng.* 39, 2010–2027. doi:10.1111/mice.13173

Wen, B.-P., and Jiang, X.-Z. (2017). Effect of gravel content on creep behavior of clayey soil at residual state: implication for its role in slow-moving landslides. *Slopes* 14, 559–576. doi:10.1007/s10346-016-0709-3

Wu, H., Guo, Y., Xiong, L., Liu, W., Li, G., and Zhou, X. (2019). Optical fiber-based sensing, measuring, and implementation methods for slope deformation monitoring: a review. *IEEE Sensors J.* 19, 2786–2800. doi:10.1109/JSEN.2019.2891734

Zhang, Y., Tan, X., and Zhao, C. (2020). UWB/INS integrated pedestrian positioning for robust indoor environments. *IEEE Sensors J.* 20, 14401–14409. doi:10.1109/JSEN.2020.2998815

Zhang, H., Luo, Y., Yuan, S., Zhou, Y., Zhou, Q., Zeng, F., et al. (2022). Shear characteristics of gravel soil with different fillers. *Front. Mater.* 9, 962372. doi:10.3389/fmats.2022.962372

Zhang, Y., Lu, J., Han, W., Xiong, Y., and Qian, J. (2023). Effects of moisture and stone content on the shear strength characteristics of soil-rock mixture. *Materials* 16, 567. doi:10.3390/ma16020567

Zhou, X., Cai, J.-S., Ma, W.-C., and Xiao, H.-W. (2023). Influence of material composition characteristics on the deformation and failure of gravel soil slopes. *Rock Soil Mech.* 44, 531–540. doi:10.16285/j.rsm.2022.0362

frontiers | Frontiers in Earth Science

TYPE Original Research
PUBLISHED 27 March 2025
DOI 10.3389/feart.2025.1501498

OPEN ACCESS

EDITED BY
Eric Josef Ribeiro Parteli,
University of Duisburg-Essen, Germany

REVIEWED BY
Mohammad Azarafza,
University of Tabriz, Iran
Jeffrey Perez,
Philippine Institute of Volcanology and
Seismology, Philippines

*CORRESPONDENCE
Chong Xu,
✉ xc11111111@126.com,
✉ chongxu@ninhm.ac.cn

RECEIVED 25 September 2024
ACCEPTED 05 March 2025
PUBLISHED 27 March 2025

CITATION
Wang Q and Xu C (2025) What are the spatial distribution characteristics of the 4417 landslides in Minhe County, Qinghai Province, China?
Front. Earth Sci. 13:1501498.
doi: 10.3389/feart.2025.1501498

What are the spatial distribution characteristics of the 4417 landslides in Minhe County, Qinghai Province, China?

Qinxia Wang[1] and Chong Xu[1,2]*

[1]National Institute of Natural Hazards, Ministry of Emergency Management of China, Beijing, China,
[2]Key Laboratory of Compound and Chained Natural Hazards Dynamics, Ministry of Emergency Management of China, Beijing, China

Landslide relic inventories serve as essential data for geological disaster investigations and risk assessments. Using a previously developed landslide relic inventory for Minhe County, Qinghai Province, this study employs landslide number density (LND) and landslide area percentage (LAP) to thoroughly investigate the spatial distribution characteristics of landslides in the region. Utilizing a GIS platform, we selected ten factors for in-depth analysis, including elevation, slope aspect, slope gradient, relief degree of land surface, distance to faults, lithology, land use type, distance to rivers, rainfall, and NDVI. The results show that at least 5,517 landslide relics have developed in Minhe County, with a total landslide coverage area of 434.43 km^2. These landslides are mainly distributed in regions with elevations of 2000–2100 m, slope gradients of 15°–25°, Neogene strata, grassland, and within 0–2 km of rivers. Both slope and aspect are the most significant factors influencing the landslide relics in Minhe County. The findings of this study contribute to a better understanding of the development characteristics and spatial distribution of landslides in the Huangshui River Basin and provide valuable data support for future landslide assessments and disaster prevention efforts.

KEYWORDS

huangshui river basin, upper yellow river, landslide inventory, google earth, visual interpretation, spatial analysis

1 Introduction

Landslides are a common geological hazard worldwide (Li et al., 2021a; Petley, 2012; Qiu et al., 2018; Wang et al., 2021; Li et al., 2021b). Many landslides are characterized by large scale, high frequency, and rapid occurrence, often resulting in catastrophic consequences that pose significant threats to human life, property, and socio-economic development (Lin et al., 2008; Wang et al., 2018; Ma et al., 2024c; Shao et al., 2024b; Nanehkaran et al., 2022). China is one of the countries most severely affected by landslides worldwide (Xue et al., 2023; Ma et al., 2023d; Zhao et al., 2024). Between 1950 and 2016, China recorded 1,911 fatal landslides, resulting in 28,139 deaths (Froude and Petley, 2018). These statistics highlight the devastating impact of landslide hazards. Therefore, understanding the mechanisms behind landslides and conducting research on landslide prevention are crucial (Huang et al., 2023). Current research on landslides primarily focuses on landslide inventories (Valenzuela et al., 2017; Wang et al., 2022), spatial distribution patterns (Frattini and Crosta, 2013; Korup, 2005; Shao et al., 2024a), susceptibility assessments

(Cui et al., 2022; Liu et al., 2022; Cemiloglu et al., 2023; Ali et al., 2021), hazard evaluation (Ma et al., 2022; Shao et al., 2023c), numerical simulations (Cui et al., 2021; Xia et al., 2021), stability analysis (Wu et al., 2023), and monitoring and early warning systems (Yin et al., 2010a). Among these, constructing landslide inventories is a fundamental basis for conducting further research (Zhao et al., 2023). Landslide inventories typically provide detailed information on the location, type, and spatial distribution of landslides in a given region (Guzzetti et al., 2012; Piacentini et al., 2018; Wieczorek, 1984; Xu, 2015), which is essential for subsequent studies on their spatial patterns and risk assessment.

Building on the establishment of landslide inventories, scholars both domestically and internationally have conducted extensive studies on the spatial distribution patterns of landslides, utilizing a variety of methods such as field surveys, historical aerial imagery analysis (Kubwimana et al., 2021), satellite imagery and the integration of InSAR technology (Chen et al., 2022). By analyzing these spatial distribution characteristics, we can effectively identify high-risk landslide areas and provide scientific support for disaster prevention efforts. Moreover, to better understand the causes of landslides, researchers often explore vital factors influencing their occurrence. Landslides are typically the result of the combined effects of various factors, including geological, geomorphological, and climatic conditions (Huang et al., 2022). Currently, there is no consensus on the selection of factors that influence landslides in academic research. Most studies use eight common factors: elevation, slope, aspect, lithology, distance to faults, distance to rivers, rainfall, and land use. Additionally, depending on the region and purpose of the study, scholars may introduce additional influencing factors to enrich their findings. For example, in studies of rainfall-induced landslides, researchers have included factors such as the topographic wetness index (TWI) (Xie et al., 2023), the relief degree of land surface (Ma et al., 2023c), the normalized difference vegetation index (NDVI) (Li et al., 2024a). For earthquake-induced landslides, common additional factors include the topographic position index (TPI) (Chen et al., 2023c), peak ground velocity (PGV) (Ma et al., 2023a), peak ground acceleration (PGA) (Ma et al., 2024d; Shao et al., 2022), and earthquake intensity (Shao et al., 2023b; Xiao et al., 2023). In studies on landslide relics, factors such as curvature (Naseer et al., 2021), soil type (Quan et al., 2014), stream power index (SPI) (Chen et al., 2023b), and distance to roads (Bui et al., 2012) have been introduced. Although current research offers valuable insights into the spatial distribution patterns and triggering factors of landslides, studies on landslides in China remain incomplete, and many landslide-prone areas still require further exploration.

The Huangshui River Basin, situated in the upper reaches of the Yellow River, lies in the transition zone between the first and second steps on the northeastern edge of the Qinghai-Tibet Plateau. This region is characterized by intense tectonic activity and complex lithology, with large landslides widely distributed (Zhang et al., 2023). The hilly areas in the middle and lower reaches of the basin are highly prone to geological disasters, both within Qinghai Province and across the country (Cui et al., 2015; Zhou et al., 2002). According to surveys conducted by the Qinghai Hydrology and Environmental Engineering Department, loess landslides in the Huangshui River Basin have caused 26 deaths, destroyed 1,007 houses, and resulted in direct economic losses exceeding 4 million yuan (Zhou et al., 2013). In recent years, significant progress has been made in the study of landslide spatial distribution patterns and causal mechanisms in the upper reaches of the Yellow River (Li Z. et al., 2024; Tu et al., 2023). Existing research has primarily focused on critical parameters such as slope gradient, geotechnical structure, and stratigraphic chronology (Zhang and Liu, 2010; Zhao et al., 2025; Huang et al., 2022; Li Z. et al., 2024), offering in-depth insights into the developmental mechanisms and spatial characteristics of landslides in this region. However, despite substantial advancements, the spatial heterogeneity and evolutionary processes of landslide hazards across different subregions remain insufficiently explored and require further refinement. The Huangshui River, one of the most significant tributaries of the upper Yellow River, flows through a geologically complex and tectonically active landscape. This river basin also constitutes the political, economic, and cultural center of Qinghai Province, where its geographical and environmental conditions exert profound influences on regional socioeconomic development and ecological security. Among the areas within this basin, Minhe County, located in the lower reaches of the basin, has emerged as a high-risk area for landslide hazards due to its highly undulating topography, loosely consolidated geotechnical materials, and the compounded effects of multiple contributing factors. Building upon prior research, this study utilizes a systematically compiled landslide inventory for Minhe County to analyze the spatial distribution characteristics of landslides. Ten key influencing factors were selected, including elevation, aspect, slope gradient, topographic relief, distance to faults, lithology, land use type, distance to rivers, precipitation, and the NDVI. Through a comprehensive spatial analysis, we investigated the relationships between these factors and landslide occurrence, providing preliminary insights into the primary controlling mechanisms of landslide activity in the region. This research not only enhances the understanding of landslide formation processes and evolutionary patterns in Minhe County but also provides a robust scientific foundation for regional disaster risk assessment, infrastructure safety planning, and land-use optimization. Ultimately, the findings contribute to the development of an integrated disaster prevention and mitigation framework, supporting the long-term sustainability and resilience of the region against geohazards.

2 Study area overview

Minhe Hui and Tu Autonomous County (referred to as Minhe County) is located in the eastern part of Haidong City, Qinghai Province, China (coordinates: 102°26′–103°04′E, 35°45′–36°26′N), covering a total area of 1,890 square kilometers (Figure 1). Minhe County lies in the transition zone between the Loess Plateau and the Qinghai-Tibet Plateau, featuring a complex terrain with deep ravines and overlapping mountain ranges. The topography is generally higher in the northwest and lower in the southeast, with the southwestern part dominated by high mountains. The Huangshui and Yellow Rivers flow from west to east through the northern and southern parts of the county, forming the Huangshui and Yellow River valleys. The region experiences a temperate, plateau continental arid climate with an average annual temperature of 9°C.

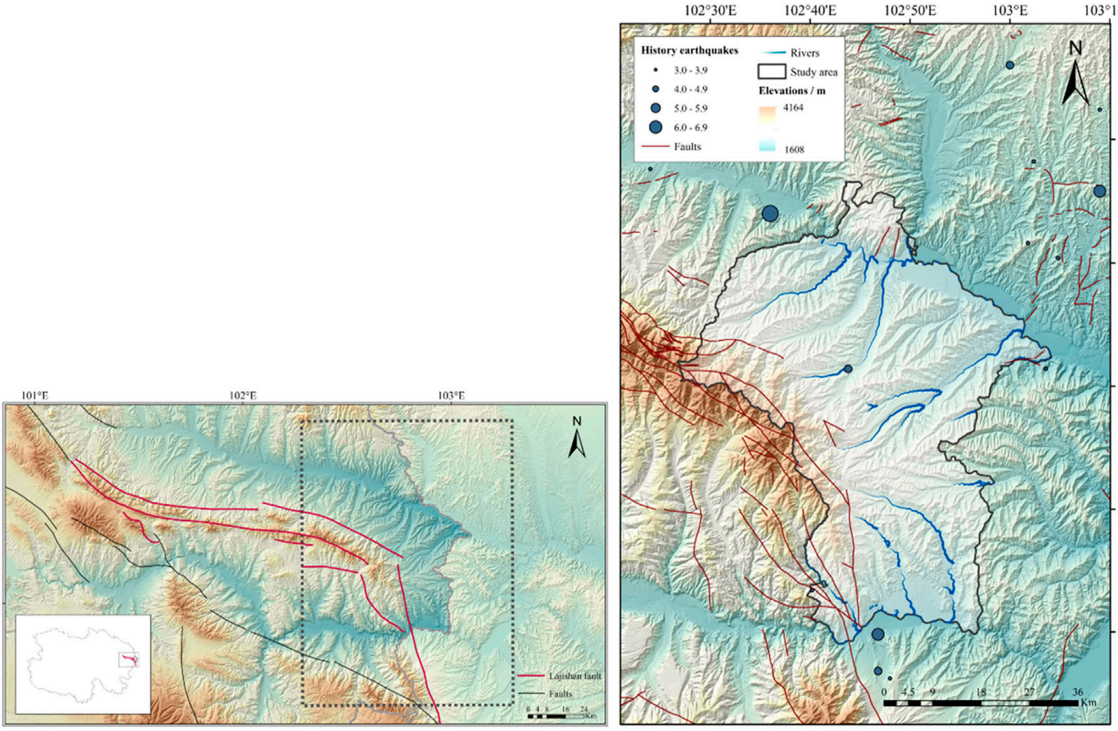

FIGURE 1
Overview of the study area.

Precipitation is unevenly distributed throughout the year, mainly concentrated between May and September, with an average annual rainfall of approximately 292.2 mm.

Minhe County is situated between the South Qilian and North Qilian geosynclinal fold belts and primarily falls within the eastern extension of the Central Qilian fold belt. The main geological structures include the Sangjia-Guantan thrust fault, the Baijiasi-Zhaojia thrust fault, and the Zhaerleng-Keer'ao thrust fault. Stratigraphically, the region is dominated by formations from the Quaternary, Paleogene, Neogene, and Cambrian periods. The Quaternary loess, along with the Paleogene and Neogene red beds, constitutes the main landslide-prone units in the region (Kou et al., 2017).

According to the earthquake catalog published by the China Seismic Network (CSN), the earthquake data for the study area are presented in Supplementary Table S1.

3 Data and methods

3.1 Selection and processing of influencing factors

3.1.1 Selection of influencing factors

To analyze the spatial distribution of landslides in Minhe County, we referenced studies conducted by previous scholars (Wang et al., 2022). Landslide number density (LND) and landslide area percentage (LAP) were selected as key indicators for measuring the spatial distribution of landslides in the study area. LND describes the concentration of landslides, representing the number of landslides per square kilometer (Equation 1). LAP, on the other hand, represents the scale of landslides, expressed as the percentage of the landslide area relative to various influencing factors (Equation 2).

$$LND = \frac{\textit{Landslide number}}{\textit{Classified area of variable I}} \tag{1}$$

$$LAP = \frac{\textit{Landslide area}}{\textit{Classified area of variable I}} \tag{2}$$

By comparing the number of landslides and the areas affected under different influencing factors, we can analyze the spatial distribution patterns of landslides. This method is regarded as the simplest and most fundamental approach for studying landslide spatial distribution (Cui et al., 2024). We used a GIS platform for this analysis. By reclassifying the raster layers of each influencing factor and extracting the values for multiple factors at each landslide point, we determined the number and area of landslides within each factor category. Based on these data, we calculated the LND and LAP values for each category and conducted an in-depth investigation of landslide spatial distribution patterns.

In this study, considering the availability of existing data and drawing on previous research, we selected 10 influencing factors for analysis. These include four topographic factors (elevation, slope aspect, slope gradient, Relief degree of land surface), three geological and geomorphological factors (distance to faults, lithology, land use), and three hydrological and ecological factors (distance to rivers, rainfall, NDVI).

3.1.2 Processing of influencing factors

For the convenience of subsequent calculations in our study, we processed the raw data of the influencing factors to transform them into a format suitable for machine learning model analysis. In this study, two types of factor data need to be processed and converted: continuous factors and categorical factors.

For continuous factors, such as DEM, slope, rainfall, and topographic relief, we discretized the data. Discretization involves dividing the numerical range of continuous factors into several intervals, with each interval representing a specific factor level. For example, for DEM values (which represent the elevation of the region), we typically start with the lowest value in the area and divide it into intervals of 100 m, creating multiple levels. The methods used for discretization include equal interval classification and natural breaks classification. Discretization helps simplify the model analysis process, making the model easier to understand and interpret.

For categorical factors, such as lithology and land type, we convert their attribute information into numerical format by assigning specific values, so that the model can accurately identify and analyze the influence of different categories. For example, the lithology factor contains information about various geological ages, and we can convert this information into numerical values (such as assigning values like 1, 2, 3) to facilitate further analysis in the model.

3.1.3 Correlation of influencing factors

We selected the Pearson Correlation Coefficient (PCC) to further investigate the correlations between the influencing factors. The Pearson Correlation Coefficient is a statistical measure that quantifies the degree of linear correlation between two variables (Ullah et al., 2024). The value of the Pearson Correlation Coefficient ranges from −1 to 1. A positive r_{xy} indicates a positive correlation between the two factors, while a negative r_{xy} indicates a negative correlation. If r_{xy} is close to 0, it suggests that there is almost no linear correlation between the two factors.

When the absolute value of the correlation coefficient between two factors exceeds 0.7, a strong correlation is considered to exist between them (Hong et al., 2020; Qin et al., 2021). By calculating the Pearson Correlation Coefficients between the influencing factors, we can effectively identify factor pairs with strong correlations and selectively retain one factor from such pairs, thereby avoiding interference between factors and addressing multicollinearity issues (Selamat et al., 2024). Specifically, the formula for calculating the Pearson Correlation Coefficient is as follows:

$$r_{xy} = \frac{\sum_{i=1}^{n}\left(X_i - \overline{X}\right)\left(Y_i - \overline{Y}\right)}{\sqrt{\sum_{i=1}^{n}\left(X_i - \overline{X}\right)^2} \times \sqrt{\sum_{i=1}^{n}\left(Y_i - \overline{Y}\right)^2}}$$

Where:

R = Correlation Coefficient.
X_i = Values of x-variable.
$\overline{X}$ = mean of x-variable.
Y_i = Values of y-variable.
$\overline{Y}$ = mean of y-variable.

3.1.4 Importance of influencing factors

Variable Importance Measure (VIM) is a quantitative method used to describe the contribution of each feature to classification or regression tasks. In this study, we utilize the Random Forest (RF) model to calculate the relative importance of influencing factors.

Random Forest is an ensemble learning method introduced by Breiman (2001). It works by constructing multiple decision trees and combining their predictions to improve the accuracy of data analysis and forecasting (Cutler et al., 2012). RF models generally exhibit high predictive accuracy (Chowdhury et al., 2024) and are capable of effectively analyzing data with non-linear relationships, collinearity, and interactions. Additionally, Random Forest not only provides prediction results but also assigns relative importance scores to each variable, making it a widely used and effective tool for evaluating feature importance. In the RF model, feature importance is determined by evaluating the contribution of each feature to the prediction results during the model training process. These importance scores reflect the relative influence of each feature within the model, helping us identify which features have a greater impact on the subsequent susceptibility evaluation results. Therefore, feature importance assessment not only improves the interpretability of the model but also provides a critical basis for further feature selection and model optimization.

3.2 Data sources

The data and sources used in this study are presented in Supplementary Table S2. We clipped the layers of each factor to fit the study area and applied the Universal Transverse Mercator (UTM) projection within the WGS84 coordinate system. The data were resampled to a uniform raster resolution of 12.5 m × 12.5 m. The Digital Elevation Model (DEM), with a resolution of 12.5 m × 12.5 m, was primarily used to extract elevation, slope, aspect, and Relief degree of land surface.

3.3 Landslide data

An accurate and comprehensive landslide inventory is essential for subsequent research, risk assessment, prediction, and disaster management (Du et al., 2020; Wang et al., 2022). In recent years, an increasing number of scholars have focused on constructing landslide relic inventories. For example, using high-resolution remote sensing imagery, scholars have developed landslide inventories for major mountain ranges in China, such as the Yin Mountains (Sun et al., 2024), Taihang Mountains (Zhang et al., 2024), and Qinling Mountains (Feng et al., 2024). Additionally, relatively complete inventories have been created for landslide-prone regions like the Loess Plateau (Peng et al., 2019) and the Qinghai-Tibet Plateau (Wang W. et al., 2024). However, no comprehensive landslide relic inventory has yet been established for Minhe County, the area selected for this study.

In response to this gap, we previously constructed the most comprehensive landslide inventory to date for Minhe County

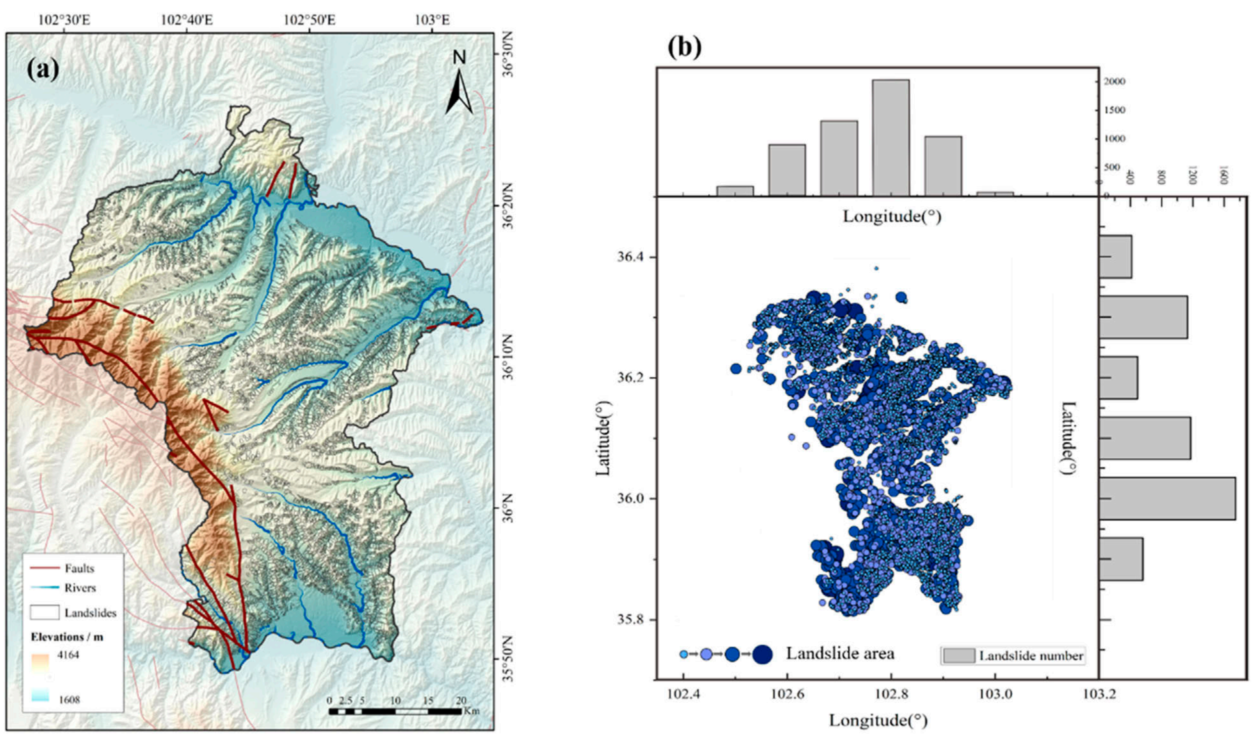

FIGURE 2
(a) Overall spatial distribution of landslides in Minhe County; **(b)** Distribution of landslides of varying magnitudes across different latitudes and longitudes.

(Wang Q. et al., 2024), which serves as the data source for this study. A total of 5,517 landslide relics were identified in the Minhe region, covering a total area of 434.43 km^2, approximately 22.98% of the county's area. The overall distribution of landslides is shown in Figure 2a. The largest single landslide covers an area of 1.62 × 10^6 m^2, while the smallest measures 880.22 m^2, with an average landslide area of 78,743.04 m^2. Statistics indicate that there are 437 landslides with an area smaller than 10,000 m^2, accounting for approximately 7.92% of all landslides. Additionally, 2,547 landslides have an area between 10,000 m^2 and 50,000 m^2, accounting for 46.17% of the total. Moreover, there are 1,318 landslides with an area between 100,000 m^2 and 500,000 m^2, and 1,141 landslides with an area between 500,000 m^2 and 1,000,000 m^2, representing 23.89% and 20.68% of the total, respectively. There are also 74 large landslides with areas exceeding 1 × 10^6 m^2.

As shown in the landslide distribution map, landslide features are widely distributed throughout Minhe County, except in the high-altitude areas in the west and small parts of the northern and southern regions. Additionally, a significant number of landslides are concentrated along the tributaries of the Huangshui and Yellow Rivers, with denser distributions around river bends. Figure 2b illustrates the geographical distribution of landslides of different sizes. The map clearly shows that small landslides are concentrated in the northwest, east, and southeast regions of the county, while larger landslides are primarily located in the northern and southwestern parts.

4 Results

4.1 Spatial distribution of landslides

Using landslide data from previous work, we utilized a GIS platform and applied the Kernel Density method with a 2 km search radius to generate landslide point density and landslide area percentage maps for Minhe County (Figures 3a,b). The results show that the maximum point density in the region is 13.17 km^{-2}, and the maximum area percentage is 87.38%. The spatial distribution of areas with high area percentages largely coincides with those of high point densities, though some regional differences exist. For instance, in the southwestern part of the county, particularly in Xinger Township and Guanting Town, the landslide area percentage is more prominent compared to point density, suggesting that landslides in these areas tend to be larger in scale. In contrast, in the northwestern part of the county, near Xinmin Township and Songshu Township, the landslide point density is more pronounced, indicating a higher number of landslides, though these tend to be smaller in size.

4.2 Analysis of influencing factors

4.2.1 Topographic factors

The elevation of the landslide-affected areas ranges from 1,686 m to 3,565 m. We divided the elevation into 15 intervals, starting from 1,600 m, with each interval spanning 100 m. The statistical results

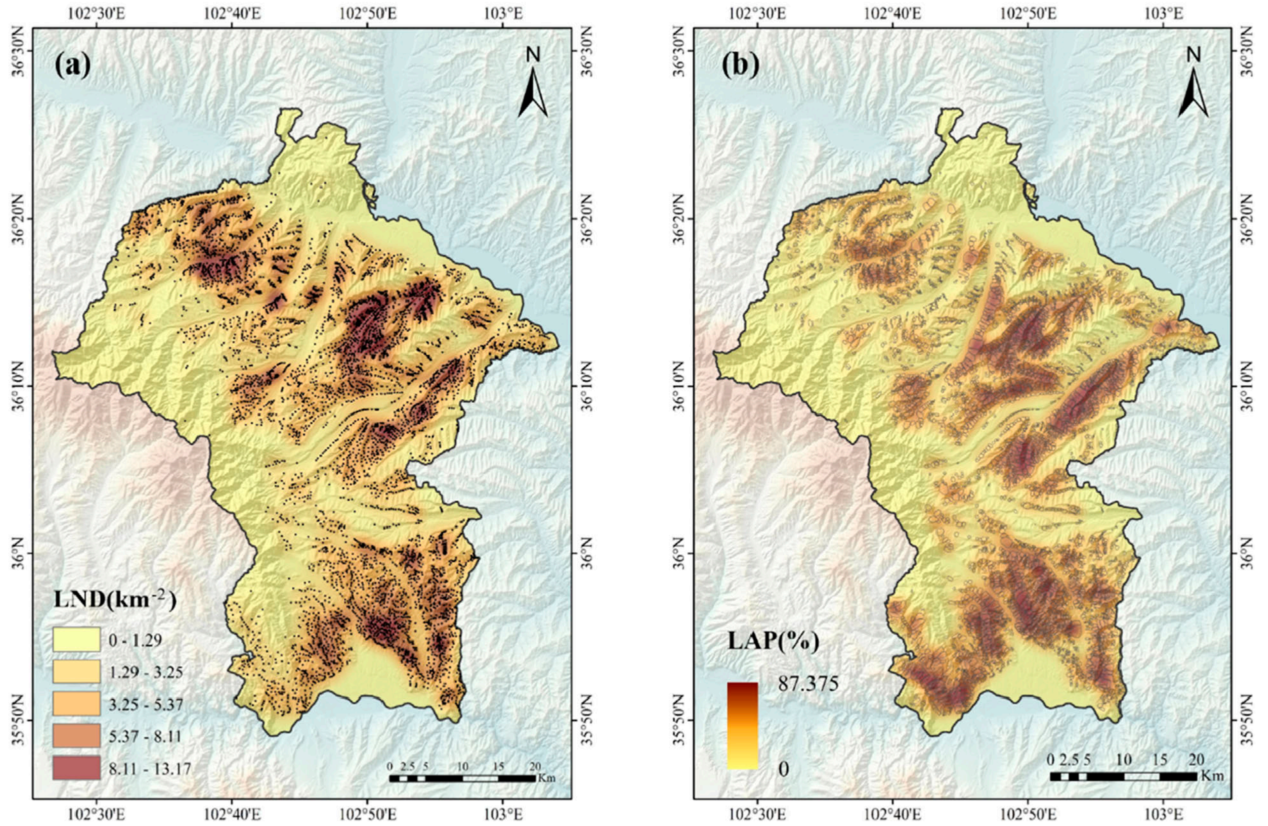

FIGURE 3
Landslide density map. **(a)** Point density map; **(b)** area density map.

are shown in Figure 4. In the 2,000–2,100 m interval, the LND and LAP reach their maximum values of 5.798 km^{-2} and 39.23%, respectively, indicating that both the number of landslides and the total landslide area in this range are significantly greater than in other intervals. A total of 1,122 landslides occurred in this interval, covering an area of 75.91 km^2, accounting for 20.35% of the total number of landslides and 39.23% of the total landslide area.

The slope range of the study area is 0°–78.59°, but the maximum slope within the landslide-affected areas is 59.86°. Therefore, we only considered slopes in the 0°–60° range, divided into intervals of 5°. The results are shown in Figure 5. In the 15°–20° slope range, LAP peaks at 29.84%, while LND reaches its secondary peak at 3.45 km^{-2}. Conversely, in the 20°–25° slope range, LND reaches its peak at 3.88 km^{-2}, while LAP reaches its secondary peak at 28.94%.

Slopes with different orientations receive varying amounts of solar radiation, leading to significant differences in vegetation cover, soil conditions, and evaporation rates (Ma et al., 2024a). In areas with stronger solar radiation, higher evaporation reduces soil moisture, making the soil more prone to weathering, which increases the risk of landslides. The results (Figure 6) indicate that landslides in Minhe County are predominantly concentrated on slopes facing northeast, northwest, west, east, and north, with the northeast-facing slopes covering an area of 54.17 km^2. Both LND and LAP reach their peak values on west-facing slopes, at 3.77 km^{-2} and 30.78%, respectively. On northwest-facing slopes, LND and LAP reach secondary peak values, at 3.39 km^{-2} and 27.88%, respectively.

Relief degree is one of the key parameters in geomorphology, used to describe and reflect the macro features of a region's surface topography. It refers to the difference in elevation between the highest and lowest points within a specific area. Previous studies have shown that the greater the relief degree, the higher the likelihood of landslide occurrence (Wang et al., 2010). The relief degree in Minhe County ranges from 4 to 530, but in the landslide-affected areas, the minimum value is 51 and the maximum value is 453. Therefore, we divided the relief degree into intervals of 50, starting from 50. Due to the smaller number of data points above 250, values between 250 and 413 were merged into a single interval, resulting in five total relief degree intervals. The spatial and numerical distribution of these intervals is shown in Figure 7. As can be seen from the figure, most landslides are distributed in the 100–150 relief degree interval, covering an area of 173.29 km^2, accounting for 41.22% of the total landslide area. The second largest landslide distribution occurs in the 150–200 interval, but the LND and LAP values reach their peak in this interval, at 5.05 km^{-2} and 33.96%, respectively.

4.2.2 Geological and geomorphological factors

The distance between landslide occurrence points and faults in the study area ranges from 0 to 21,204 m. Considering that faults located more than 18 km away have a limited impact on landslides, we combined all distances beyond 18 km into one category, while setting intervals of 3 km for the remaining distances. The statistical results are shown in Figure 8. It is evident that although the landslide

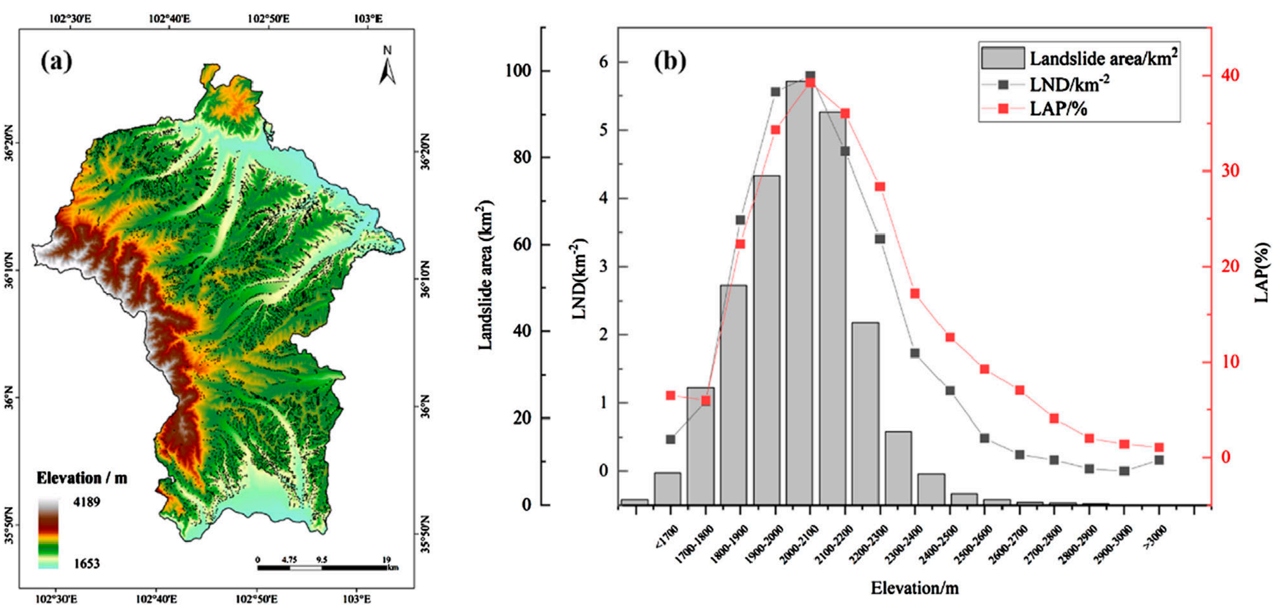

FIGURE 4
Relationship between elevation and landslide distribution. **(a)** Elevation distribution in the study area. **(b)** Statistics of landslide indicators in the elevation intervals.

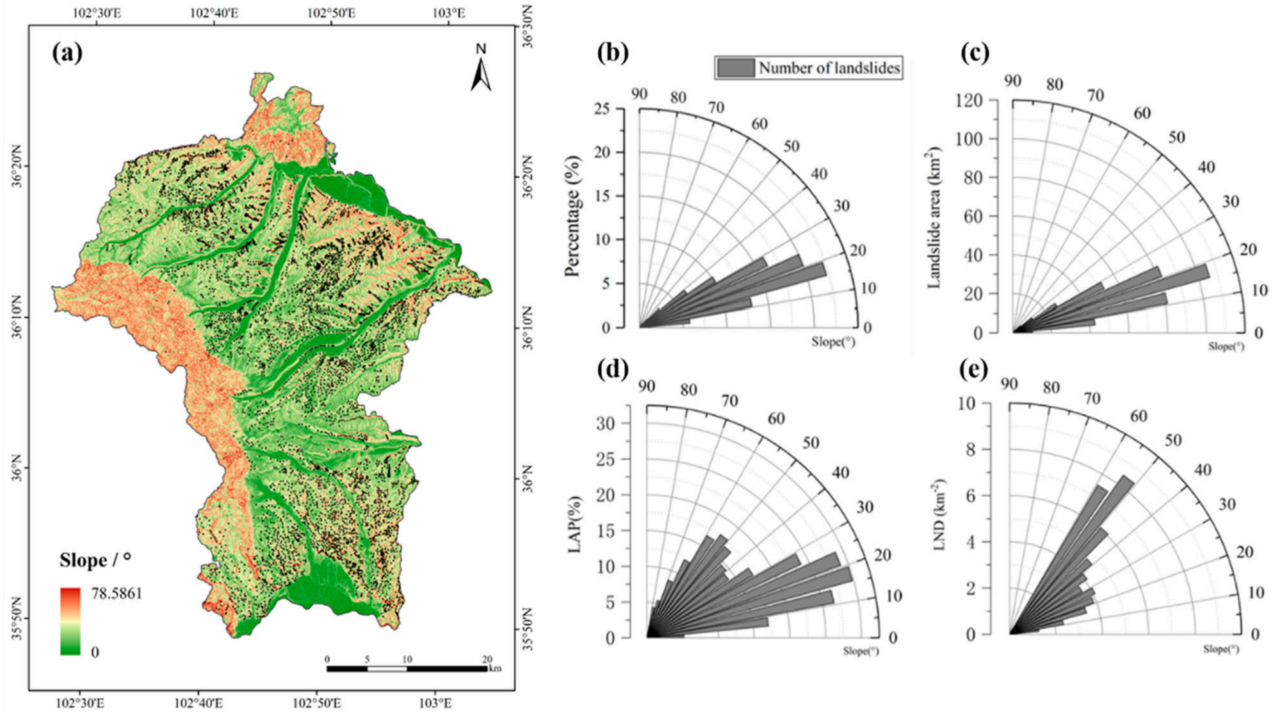

FIGURE 5
Relationship between slope and landslide distribution. **(a)** Slope distribution in the study area. **(b–e)** Statistics of landslide indicators in the slope intervals.

area percentage is highest within the 0–3 km range from faults, the LAP and LND values are the lowest, at only 1.04 km^{-2} and 2.23%, respectively. The LAP and LND values reach their peak in the 12–15 km range, at 4.88 km^{-2} and 6.29%, respectively.

The oldest stratigraphic units in the study area date back to the Early Paleozoic Cambrian period, while the youngest units consist of Quaternary Holocene alluvium and Late Pleistocene glacial deposits, along with other types of sedimentary deposits. Due to the

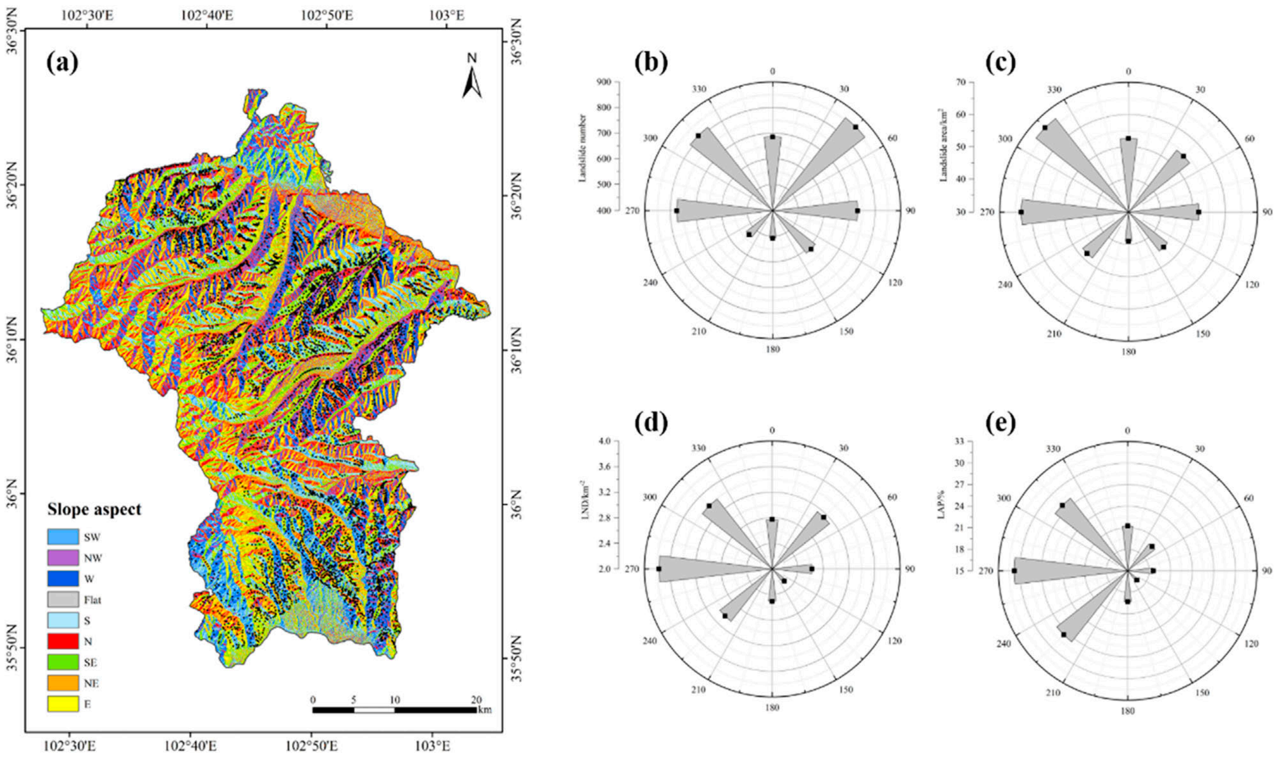

FIGURE 6
Relationship between aspect and landslide distribution. **(a)** Aspect distribution in the study area. **(b–e)** Statistics of landslide indicators in the aspect intervals.

complex lithology, the stratigraphic sections were categorized based on geological age. The statistical results are presented in Figure 9. These results show that the Neogene (N) and Paleogene (E) units exhibit significantly higher LAP and LND values compared to other strata. The Neogene units display the highest LND and LAP values, reaching 4.74 km^{-2} and 42.89%, respectively, while the Paleogene units rank second, with LND at 4.20 km^{-2} and LAP at 32.02%.

The study area has diverse land types, including cropland, grassland, forest land (evergreen broadleaf forest, deciduous broadleaf forest, evergreen coniferous forest), shrubs, grasslands, wetlands, bare land, artificial surfaces, water bodies, and glaciers/snow. However, landslides only occur in seven types of land cover: cropland, grassland, forest land (deciduous broadleaf forest and evergreen coniferous forest), bare land, herbaceous-covered areas, and sparsely vegetated areas. The land use summary is presented in Figure 10. Notably, compared to other land use types, grassland shows the highest LND and LAP values, at 4.23 km^{-2} and 27.39%, respectively. Cropland follows with LND and LAP values of 2.58 km^{-2} and 22.95%, respectively.

4.2.3 Hydrological and ecological factors

The study area is located in the Huangshui Valley, with the Yellow River and Huangshui River flowing through it, making rivers widely distributed. The farthest landslide from a river in the study area occurred at a distance of 8,128 m. Given that only two landslides occurred more than 8 km from a river, we divided the distances into five intervals of 2 km each. The statistical results are shown in Figure 11. As seen from the figure, the area of each interval decreases with increasing distance from the river. Simultaneously, both the LND and LAP values decrease as the distance from the river increases, with both reaching their peak in the 0–2 km interval at 2.55 km^{-2} and 21.62%, respectively.

The maximum annual average rainfall in the study area is 482.9 mm, while the minimum is 151.4 mm. In landslide-affected areas, the maximum annual average rainfall is 324.3 mm. Therefore, starting from 150 mm, we divided the rainfall into intervals of 50 mm, resulting in four categories. The statistical results are shown in Figure 12. The figure clearly indicates that landslide areas are primarily concentrated in the 150–200 mm rainfall interval, followed by the 300–350 mm interval. However, the LND and LAP peak in the 250–300 mm interval, at 4.03 km^{-2} and 27.28%, respectively. Both values show an increasing trend before this interval, followed by a decline.

The NDVI index in the study area ranges from −0.2006 to 0.9989, while the NDVI values within the landslide-affected areas fall between 0.1313 and 0.959. Based on this, we set 0 as the starting point, with an interval increment of 0.2, resulting in five categories. The statistical results are shown in Figure 13. In the 0.4–0.6 interval, LND and LAP reach their peak values at 3.62 km^{-2} and 27.16%, respectively. The second highest values for LND and LAP occur in the 0.2–0.4 interval, at 3.29 km^{-2} and 25.20%, respectively.

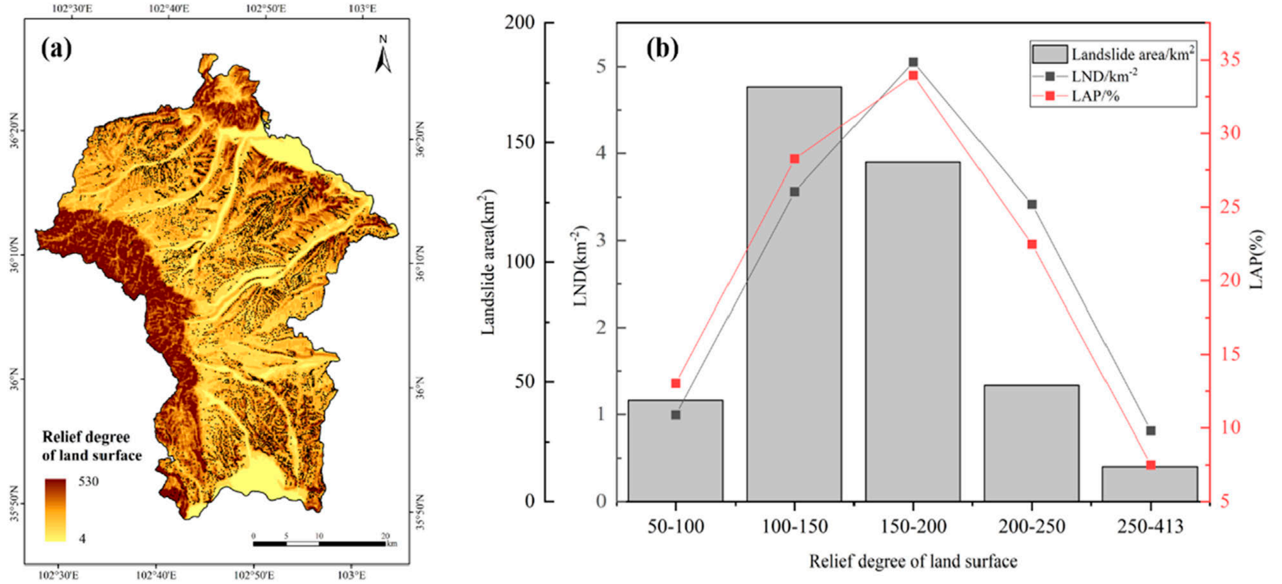

FIGURE 7
Relationship between relief degree and landslide distribution. **(a)** Distribution of relief degree in the study area;**(b)** Statistics of landslide indicators in the relief degree intervals.

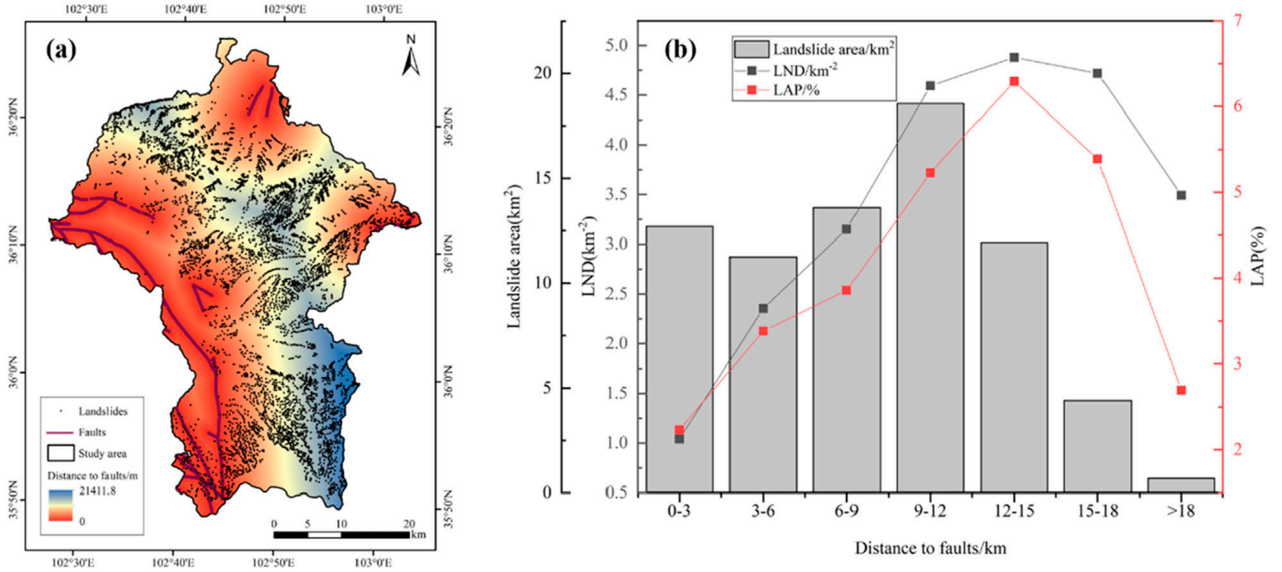

FIGURE 8
Relationship between fault distance and landslide distribution. **(a)** Spatial distribution of faults and landslides within the study area. **(b)** Statistical distribution of landslide occurrences across different distance intervals from faults.

4.3 Correlation and importance analysis of influencing factors

To avoid collinearity issues among the factors, this study conducted a correlation analysis of the 10 factors using the Pearson correlation coefficient. As shown in Figure 14, the absolute values of the correlations between all factors are below 0.7, indicating that there is no collinearity among them. Therefore, the factors are suitable for input into the model for further training.

Based on the analysis results from the Random Forest model, this study systematically ranks the importance of the influencing factors. The results show that slope (0.43428) and aspect (0.38838) have the most significant impact on the landslide relics in Minhe County (Figure 15). In addition, DEM (0.06263), topographic relief (0.03861), and NDVI (0.02697) also exhibit significant statistical correlations. These factors interact through various physical processes such as tectonic movements, human engineering activities, and climate change, collectively affecting surface stability.

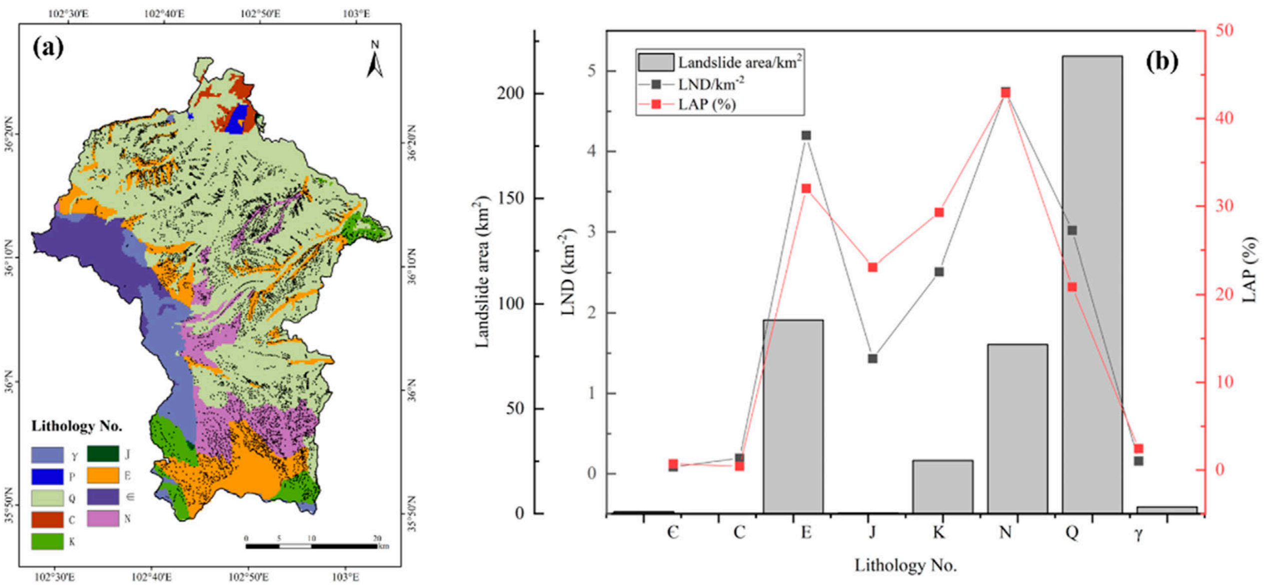

FIGURE 9
Relationship between lithology and landslide distribution. **(a)** Lithology distribution in the study area. **(b)** Statistics of landslide indicators in the lithology intervals. (Strata:Є-Cambrian,C-Carboniferous,E-Paleogene,J-Jurassic,K-Cretaceous,N-Neogene,O-Ordovician,P-Permian,Q-Quaternary,S-Silurian,γ-Intrusive rock).

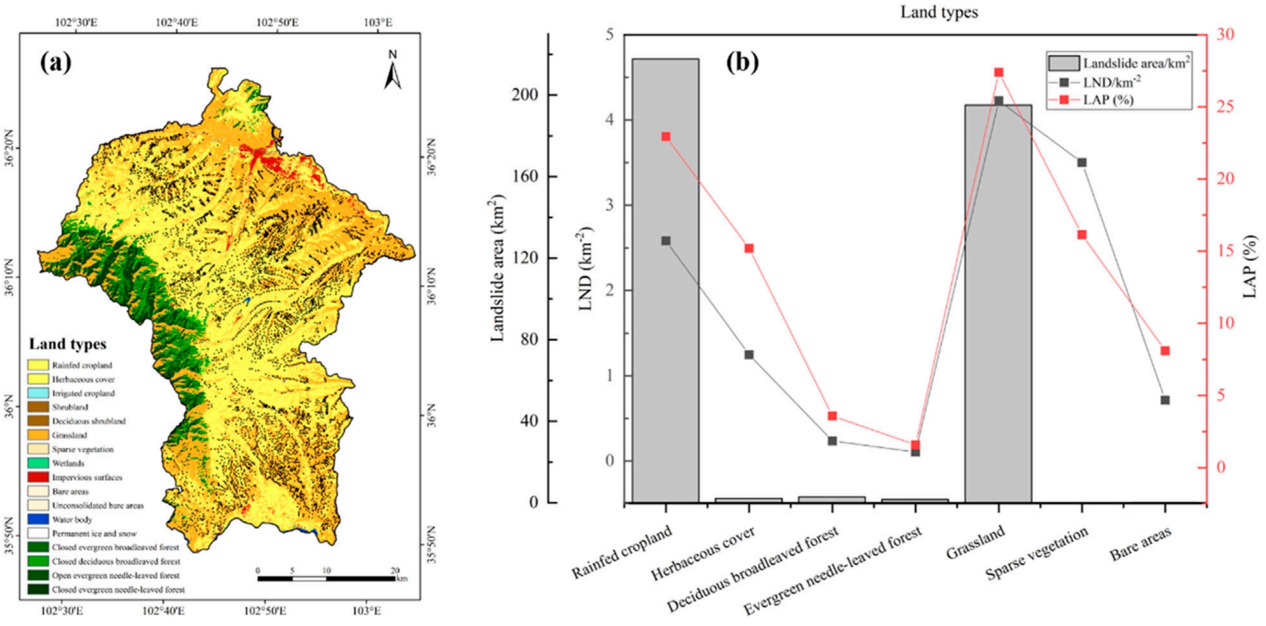

FIGURE 10
Relationship between land use type and landslide distribution. **(a)** Land use type distribution in the study area. **(b)** Statistics of landslide indicators in the land use type intervals.

Slope, as an important intrinsic condition for landslide occurrence (particularly shallow landslides), is one of the primary controlling factors for landslide development (Guo et al., 2013). Generally, the steeper the slope, the stronger the gravitational forces acting on the soil and rock masses, which reduces shear strength and makes landslides more likely (Mao et al., 2024). Aspect, on the other hand, influences the degree of solar radiation and precipitation received by a slope, further adjusting the degree of weathering and moisture content in the soil, thus significantly affecting slope stability. Additionally, aspect affects vegetation growth on the slope;

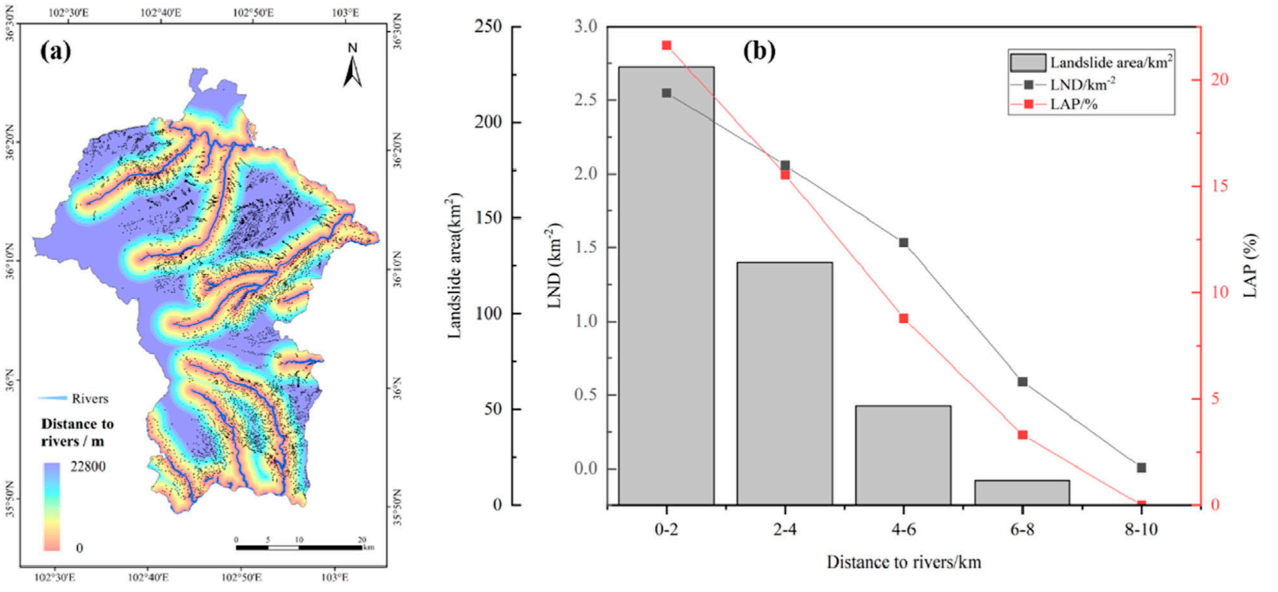

FIGURE 11
Relationship between the distance from rivers and the landslide distribution. **(a)** The distribution of the distance from rivers in the study area. **(b)** Statistics of landslide indicators in the intervals of the distance from rivers.

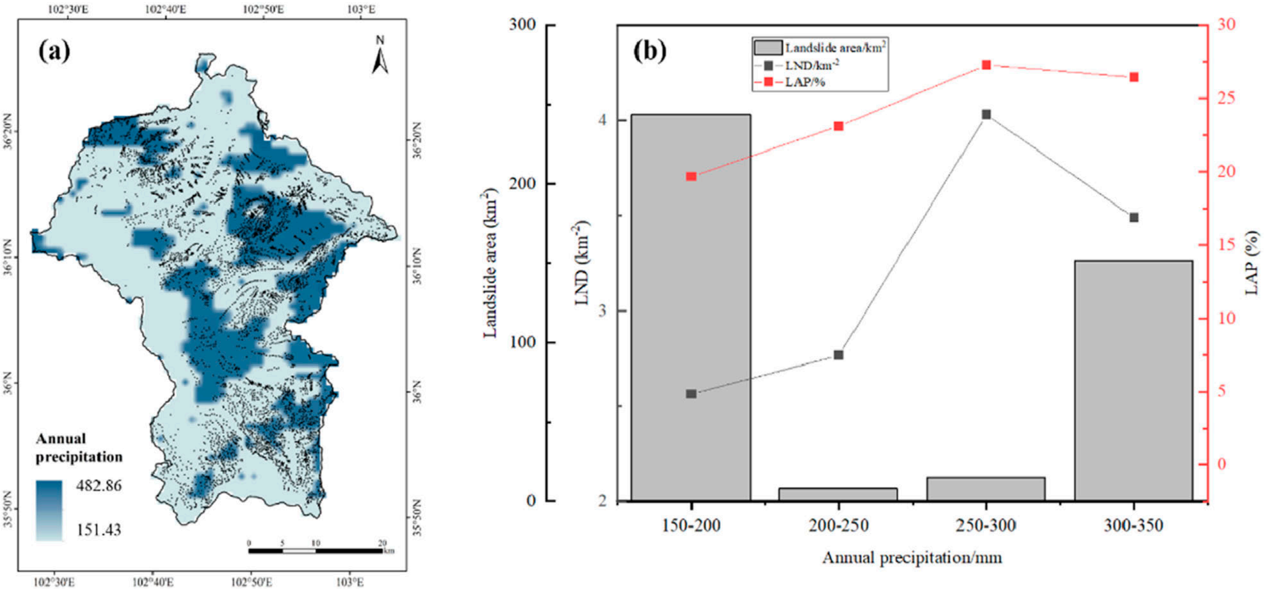

FIGURE 12
Relationship between average precipitation and landslide distribution. **(a)** Average precipitation distribution in the study area. **(b)** Statistics of landslide indicators in the average precipitation intervals.

sunny slopes typically have sparse vegetation and weaker erosion resistance, while shady slopes have denser vegetation but accumulate more moisture, potentially leading to shallow landslides.

In contrast, the influence of lithology (0.0048) and land use (0.0051) on the landslide relics in this region is relatively small. We hypothesize that the lower weight of lithology's impact may be related to several factors: first, the significant topographic relief in the study area makes the influence of gravity on slope stability more direct, overshadowing the effect of lithological differences on landslide formation. Second, the weathering degree of different lithological layers within the region may be relatively similar, which weakens the control of lithology on landslides. As for land use, its limited influence on landslides may be attributed to the fact that most of Minhe County is located in mountainous areas, where extensive natural vegetation is likely present, and land use changes are minimal. In such areas, vegetation plays a role in reinforcing slopes and conserving soil and water, thus reducing the direct impact of land use changes on landslide occurrence.

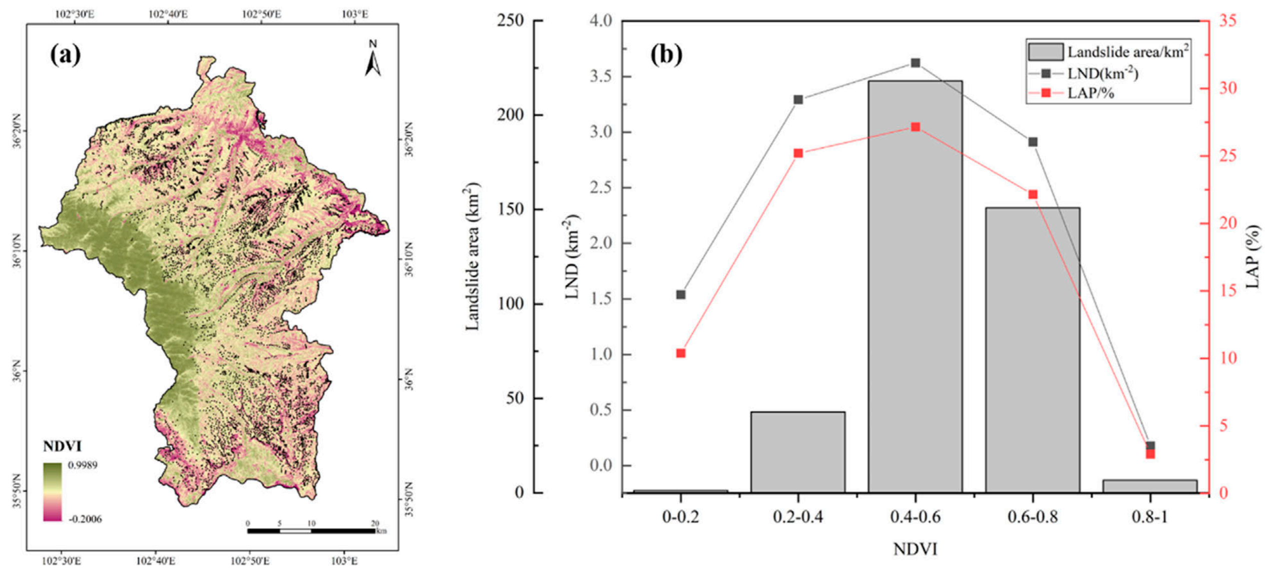

FIGURE 13
Relationship between NDVI and landslide distribution. **(a)** NDVI distribution in the study area. **(b)** Statistics of landslide indicators in the NDVI intervals.

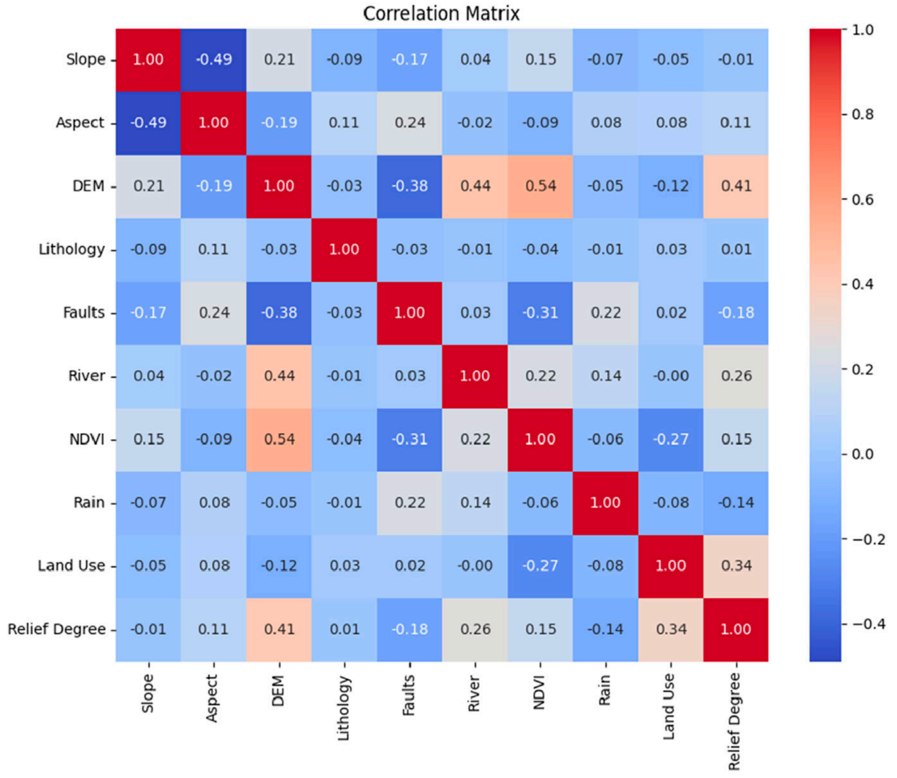

	Slope	Aspect	DEM	Lithology	Faults	River	NDVI	Rain	Land Use	Relief Degree
Slope	1.00	-0.49	0.21	-0.09	-0.17	0.04	0.15	-0.07	-0.05	-0.01
Aspect	-0.49	1.00	-0.19	0.11	0.24	-0.02	-0.09	0.08	0.08	0.11
DEM	0.21	-0.19	1.00	-0.03	-0.38	0.44	0.54	-0.05	-0.12	0.41
Lithology	-0.09	0.11	-0.03	1.00	-0.03	-0.01	-0.04	-0.01	0.03	0.01
Faults	-0.17	0.24	-0.38	-0.03	1.00	0.03	-0.31	0.22	0.02	-0.18
River	0.04	-0.02	0.44	-0.01	0.03	1.00	0.22	0.14	-0.00	0.26
NDVI	0.15	-0.09	0.54	-0.04	-0.31	0.22	1.00	-0.06	-0.27	0.15
Rain	-0.07	0.08	-0.05	-0.01	0.22	0.14	-0.06	1.00	-0.08	-0.14
Land Use	-0.05	0.08	-0.12	0.03	0.02	-0.00	-0.27	-0.08	1.00	0.34
Relief Degree	-0.01	0.11	0.41	0.01	-0.18	0.26	0.15	-0.14	0.34	1.00

FIGURE 14
Pearson correlation coefficient analysis of influencing factors.

5 Discussion

5.1 Landslide inventory

A landslide inventory refers to the systematic organization of landslide characteristic information for a specific region, forming a database. The completeness of such an inventory is crucial to the accuracy of disaster assessments (Guo et al., 2024). Landslide inventories can be divided into event-based landslide inventories and historical landslide inventories. Event-based inventories record landslides triggered by a single event, such as earthquakes (Dai et al., 2011; Xu et al., 2014; Ma et al., 2024b; Shao et al., 2023a) or

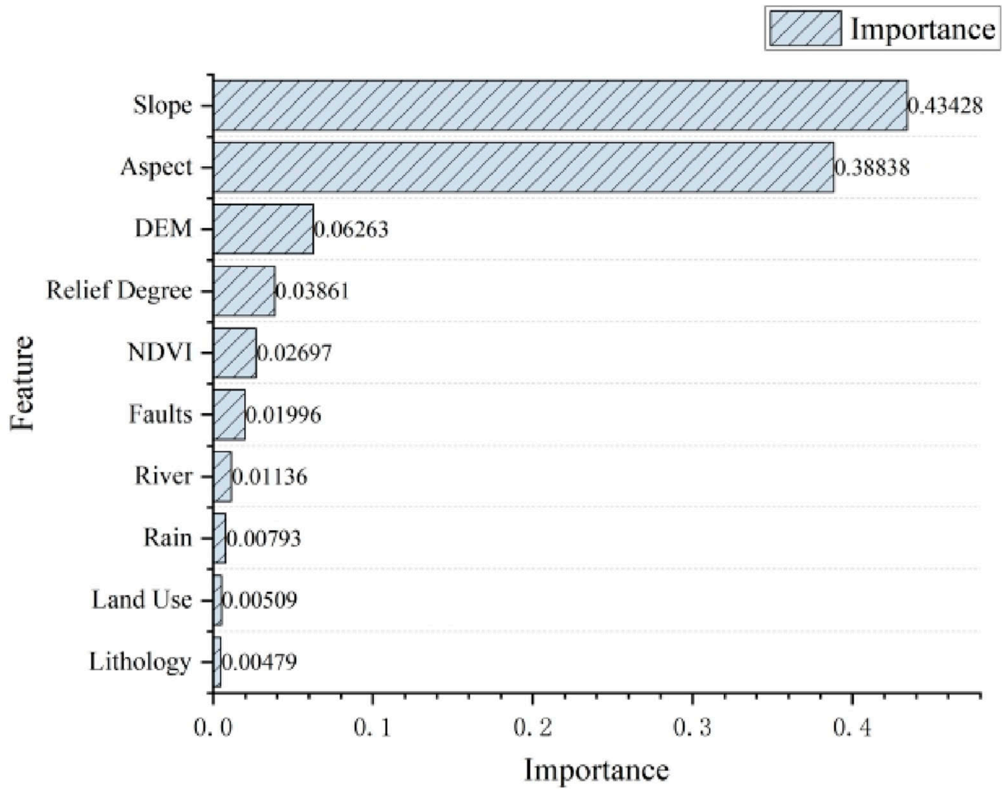

FIGURE 15
Importance of influencing factors.

rainfall (Ma et al., 2023c; Xie et al., 2023; Gao et al., 2024; Shao et al., 2023d). Historical landslide inventories, on the other hand, encompass landslide events accumulated over hundreds or even thousands of years (Chen J. et al., 2023; Li et al., 2022a; Li et al., 2022b; Shao et al., 2020). In our previous work, we focused on historical landslides and, using high-resolution satellite remote sensing imagery for interpretation, created the most comprehensive landslide relic inventory for Minhe County to date.

However, existing landslide surveys in Minhe County still need further refinement. Most current research in this region has focused on individual landslides (Mu et al., 2020), clustered landslides (Cui et al., 2008), or landslides triggered by single events. Only a few scholars have studied landslide distribution and disaster assessments in Minhe County. For instance, Kou et al. in their geological hazard investigation and zoning project, identified 224 landslide disasters in Minhe County (Kou et al., 2017). Zhao et al. used historical geological disaster data provided by the Qinghai Provincial Geological Environment Monitoring Station and found 569 landslide traces in Minhe (Zhao et al., 2021). Additionally, Peng et al. focused on the Loess Plateau region, conducting landslide interpretation and analysis of triggering mechanisms. They identified 14,544 landslides across the entire Loess Plateau, with 1,823 landslides located in the Haidong-Lanzhou-Tongwei area (HLTZ), covering a total area of 3,530 km^2 (Peng et al., 2019). Meng et al. using InSAR technology, created a comprehensive landslide inventory for the Huangshui River region, identifying 31 landslide traces in the 16,000 km^2 area (Meng et al., 2020). While these studies provided valuable references for our interpretation and cross-verification, the number of landslides identified in previous studies is far lower than the 5,517 landslide relics we identified.

Additionally, the southern Guanting Basin in Minhe County, located along the Longyangxia-Liujiaxia section of the upper Yellow River, is a region with frequent landslide disasters. In recent years, many scholars have studied the characteristics and mechanisms of landslides in this area. For example, Yin et al. identified 205 landslides of various sizes along this river section, with seven landslides located in the Guanting Basin, primarily mudstone landslides (Yin Z. et al., 2010). He et al. also obtained similar results (He et al., 2017). Among the landslide relics we identified, 260 are located in the Guanting Basin, far exceeding the number reported in existing studies.

In conclusion, the landslide inventory we developed in previous work is the most comprehensive and high-quality landslide database for Minhe County and its surrounding regions to date. Using this inventory, we analyzed the spatial distribution and possible controlling factors of landslides in Minhe, providing valuable insights. However, there are some limitations to our study. The method we used is based on human-assisted visual interpretation. For smaller landslides, due to the resolution limitations of satellite imagery or subjective interpretation, some landslides may have been missed. However, these omissions have a relatively small impact on the overall accuracy of the inventory. In future research, we will consider integrating additional methods to address this limitation.

5.2 Spatial distribution of landslides

The areas with high point density and high area density of landslide relics in Minhe County generally exhibit similar spatial distributions, although some differences still exist. In the southwestern part of the county, the area density of landslides is more prominent compared to the point density, suggesting that the landslides in this region tend to be larger in scale. Conversely, in the northwestern part of the county, the point density of landslides is more significant.

The higher area density of landslides in the southwestern part of the county indicates that the region experiences more large-scale landslides. Our preliminary analysis suggests that the frequent occurrence of large-scale landslides in this area is the result of multiple geological, geomorphological, and environmental factors. The relatively steep slopes and topographic relief lead to the accumulation of gravitational potential energy, while fault structures cause rock fragmentation and weakening. The easily weathered Paleogene strata provide abundant landslide material, and river erosion continually undermines slope stability. Additionally, the abundant precipitation increases pore water pressure, and sparse vegetation exacerbates slope instability. These factors interact spatially, reinforcing one another, making large-scale, long-runout, and far-reaching landslides more likely to occur in this region.

In contrast, the more significant point density of landslides in the northwestern part of the county suggests a higher frequency of landslides, but the landslides are relatively smaller in scale. We believe this is mainly due to the relatively gentle slopes, stable geological structures, and widespread loose deposits in this region. While local topographic relief and rainfall conditions may trigger landslides, the lack of fault zones, weaker erosion at the slope toes, and limited thickness of loose materials contribute to the prevalence of shallow, small-scale landslides. Furthermore, the low vegetation coverage further reduces slope stability, increasing the frequency of landslides, though it does not significantly affect the scale of the landslides.

In addition, as noted by Kou et al. (2017), landslides in the study area show a certain degree of clustering, with high-risk landslide zones in Minhe County mainly distributed along the middle and lower reaches of the Huangshui River and the tributaries of the Yellow River. Our findings are consistent with this pattern. Wei et al. (2021) summarized the spatial distribution patterns of landslide hazards in Qinghai Province, taking into account administrative regions, geomorphology, agricultural and pastoral zones, and watershed divisions. Their study demonstrated that landslides are predominantly concentrated in the agricultural areas of the Huangshui River Basin in eastern Qinghai, further supporting our results.

Additionally, earthquakes, as a typical representation of neotectonic activity, can lead to a “sheet-like” dense distribution of landslides in loose soil (Li et al., 2021b), a phenomenon also reflected in our study. For example, following the 1987 earthquake in Xigou Township, Minhe County (magnitude 4.1), many landslides were densely distributed around the epicentral area (Figure 16). Active faults are potential sources of destructive earthquakes (Wu et al., 2024), and further research is needed to determine whether the landslides triggered by this earthquake are related to active faulting. We will continue to collect detailed geological data from the region to conduct an in-depth analysis of the mechanisms behind these earthquake-induced landslides.

5.3 Correlation between landslides and influencing factors

In terms of topographic factors, the majority of landslides in the study area occurred at elevations between 1,900 and 2,400 m, mostly in mid-high altitude, moderately rugged mountainous terrain, accounting for about 85.6% of the total. Other researchers have also found similar results (Li et al., 2021b; Qiu et al., 2018), where landslides are concentrated at elevations of 2,000–2,800 m. This range corresponds to mid-low mountain hilly areas, adjacent to river valley alluvial plains. We believe that the dense distribution of landslides in this elevation range is closely related to the well-developed erosion gullies in the area. Additionally, the intensity of human activity in this elevation range plays a significant role in landslide development (Tian et al., 2024; Zhang et al., 2015; Zhao et al., 2021).

Slope gradient is another crucial factor influencing slope stability (Ma et al., 2023b). Our results show that most landslides occurred on slopes with gradients between 10° and 40°, mainly concentrated in the 15°–20° range. This is consistent with previous studies. For example, Li et al. (2024b) found that in the upper reaches of the Yellow River, including the Guanting Basin in Minhe County, landslides are primarily concentrated on slopes between 15° and 40°, with most in the 15°–20° and 35°–40° ranges. Field surveys also revealed that most landslides in the 15°–20° range are relatively stable, with a low likelihood of further movement. However, those in the 35°–40° range are more unstable and may reactivate under heavy or prolonged rainfall. Wang et al. (2015) reached similar conclusions, noting that slopes with a gradient of 15°–30° contribute the most to landslide development, followed by slopes of 10°–15° and 30°–40°, while slopes less than 10° and greater than 40° contribute the least. However, Zhou et al. (2013) presented a different view, suggesting that geological disasters in the Huangshui River Basin, particularly in loess regions, occur mainly on steep slopes of 30°–60°. Variations in slope gradients across different studies are common in landslide research. We believe that, aside from the southwestern mountainous area, the overall terrain in Minhe County is relatively flat, leading to lower overall slope gradients in landslide-affected areas. Furthermore, landslide relics often represent older events, and over time, unstable landslides may move or shift, resulting in a gradual decrease in slope gradients.

The properties of the soil and rock also affect slope stability. In terms of lithostratigraphy, the study area is primarily composed of Quaternary deposits, Paleogene strata, and Neogene strata. Among these, Quaternary deposits have the largest exposed area, covering 54.77% of the total study area and predominantly distributed across the northern, central, and eastern regions of Minhe County. The Paleogene and Neogene formations follow, accounting for 15.13% and 9.87% of the study area, respectively. The occurrence of landslides is closely associated with lithological

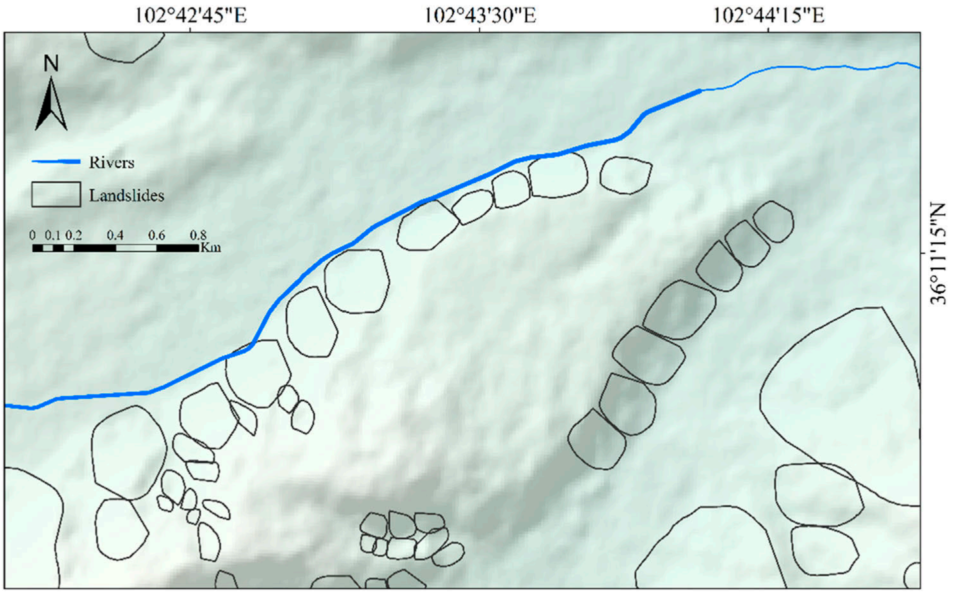

FIGURE 16
Distribution of landslides in the vicinity of the earthquake.

characteristics. Studies have demonstrated that landslides are most prevalent in Quaternary loess deposits, with a total of 3,150 recorded landslides in these formations, a trend consistent with the findings of Li et al. (2021a). Additionally, the primary lithological components of regional slopes include Late Pleistocene loess and Neogene mudstone, both of which significantly influence slope stability due to their unique geotechnical properties. Neogene mudstone is characterized by a high clay mineral content (Xin et al., 2017), making it highly susceptible to softening upon water infiltration. This hydration-induced weakening substantially reduces shear strength, facilitating the formation of sliding zones and increasing the likelihood of slope failure. Similarly, Quaternary loess exhibits large porosity, well-developed vertical joints, and high permeability. These attributes render it particularly prone to softening and slope instability when subjected to prolonged rainfall infiltration (Huang et al., 2022). Collectively, these lithological and hydrogeological characteristics create favorable conditions for landslide initiation and evolution in the region. A deeper understanding of the influence of different lithological units on slope stability is essential for improving landslide susceptibility assessment and providing a scientific foundation for regional geohazard prevention and mitigation strategies.

Land use in Minhe County is predominantly grassland, cropland, and forest. Landslides mainly occur in grassland and cropland areas, likely influenced by human activities and agricultural irrigation (Huang et al., 2022). Agriculture is the main livelihood in the loess regions, and long-term irrigation raises the groundwater level, leading to soil deformation at the base of slopes and slope instability. The frequent landslides in the Heifangtai region of Gansu are a typical example of this (Xu and Yan, 2019).

The Huangshui River is the most important tributary of the upper Yellow River, and its river channel is highly meandering in the study area. In this phase, intense river erosion leads to stress transfer in the valleys, causing slope unloading and fracturing, which increases the instability of rock masses (Zhao et al., 2021). Our results show that most landslides occur within 0–2 km from the river, and both the number and area of landslides decrease as the distance from the river increases. This indicates that river erosion is one of the main factors influencing landslides in the region.

The NDVI reflects the extent of vegetation cover, with higher NDVI values representing denser vegetation. Landslides in the study area are primarily concentrated in areas with NDVI values between 0.4 and 0.8. This result differs from the commonly held view that landslides are more likely to occur in areas with sparse vegetation (Chen et al., 2021). Minhe County is mostly composed of mid-low mountain hilly areas, except for its western highlands. We speculate that most of the area has relatively good vegetation cover, but the root systems are shallow, primarily concentrated in the topsoil layer. The significant difference in soil properties between the root layer and the subsoil makes it easy to trigger large-scale shallow landslides, especially during short periods of heavy rainfall (Xu et al., 2022). Huang Hengwei (Huang, 2017) also supports a similar viewpoint. Additionally, with the implementation of the "Green is Gold" ecological protection policy, vegetation cover in Minhe County has been increasing, which may have affected the NDVI values used in this study, potentially introducing some statistical bias.

In our analysis of fault-related factors, we found no significant correlation between landslide distribution and distance from faults. If we only consider the number and area of landslides, we observe that both decrease as the distance from faults increases. However, this does not necessarily suggest an objective or reliable conclusion. Our analysis shows that LND and LAP peak at a distance of 12–15 km from faults, while the values are lowest at 0–3 km. This suggests that the influence of faults is limited and that landslide causality in the region is highly complex. Further research will be required to explore this in more detail.

5.4 Policy recommendations and future research directions

Based on the spatial distribution characteristics of landslides, the study found that landslide relics in Minhe County are primarily distributed in areas with an elevation of 2,000–2,100 m, slopes of 15°–25°, aspects facing west or northwest, Quaternary strata, and within 0–2 km from rivers. Given these spatial characteristics, future disaster prevention and mitigation efforts should prioritize monitoring and management of areas near riverbanks and those with vulnerable lithology. The government and relevant departments can use these spatial data to scientifically plan monitoring areas, especially in regions with critical infrastructure and high population density, to effectively reduce the potential risks of landslide disasters (Nanehkaran et al., 2023). Moreover, these spatial data provide a solid foundation for subsequent risk prediction and emergency management, enabling rapid identification of high-risk areas and the scientific allocation of disaster prevention resources.

In the quantitative analysis of the overall spatial distribution of landslides, the LND and LAP indices clarified the spatial distribution density of landslides in Minhe County, providing a more precise basis for landslide disaster risk assessment. Through the analysis of these quantitative indicators, the study found that the landslide area density is more significant in the southwestern region, while the landslide point density is higher in the northwestern region. This suggests that, in subsequent geological disaster risk prevention and control efforts, special attention should be given to the larger-scale landslides in the southwestern region, while strengthening the monitoring and prevention of shallow and medium-sized landslides in the northwestern region. Based on these regional risk characteristics, differentiated landslide monitoring and management strategies should be implemented. In areas with high landslide point density, it is essential to strengthen emergency response mechanisms and develop detailed contingency plans to ensure rapid and effective emergency response during disaster events, thereby reducing the harm caused by landslides and protecting public safety.

From the perspective of key influencing factors, slope and aspect are the most important factors affecting landslide occurrence in Minhe County. The study indicates that landslides are frequent in areas with a slope of 15°–25° and a westward or northwestward aspect. Therefore, disaster prevention and mitigation strategies should prioritize addressing these key topographic factors. For example, in areas with steeper slopes, measures such as slope reinforcement and vegetation restoration should be implemented to enhance slope stability. In regions with significant aspects, monitoring of precipitation and water flow should be strengthened to reduce water-induced erosion and prevent slope instability. Additionally, landslide occurrences are typically the result of the interaction of multiple factors (Nikoobakht et al., 2022). For other factors that show significant statistical correlations (e.g., elevation, topographic relief, NDVI), comprehensive mitigation measures should be adopted based on specific regional conditions, such as improving slope drainage systems, reinforcing slope structures, and restoring vegetation, to effectively reduce the risk of landslides.

Overall, the findings of this study not only contribute to a deeper understanding of the triggering factors and distribution patterns of landslide relics in Minhe County, but also provide a scientific basis for subsequent landslide evaluation, early warning, and disaster prevention efforts. Moreover, the analytical methods used in this study are not only applicable to Minhe County but also have strong generalizability. These methods can be widely applied to other regions with similar geological and environmental conditions, providing effective support for landslide disaster risk assessment, monitoring and early warning, and emergency response. Similar research methods have already been successfully applied in several landslide-prone areas, providing valuable insights for disaster prevention in these regions. In future work, we will integrate field investigation data to validate and deepen our findings. We will optimize evaluation models, conduct landslide susceptibility assessments, and comprehensively consider the impact of multiple environmental factors and potential additional influences, thereby achieving a more comprehensive understanding of landslide causality. This will provide a more scientific basis for the prediction and management of geological disasters in Minhe County.

6 Conclusion

Based on the GIS platform, this study conducted an in-depth exploration of the spatial distribution and triggering factors of landslides, using the previously constructed landslide relic inventory of Minhe County, Qinghai Province, China. The earlier work identified 5,517 landslide features in Minhe County, with a total coverage area of 434.43 km^2, accounting for approximately 22.98% of the county's total area. Using landslide number density (LND) and landslide area percentage (LAP) as evaluation indicators, we performed a statistical analysis of the correlation between landslides and influencing factors. The results indicate that the LND and LAP indices for Minhe County are 13.17 km^{-2} and 87.38%, respectively. Furthermore, landslide relics are mainly distributed in the elevation range of 2,000–2,100 m, where the number of landslides and the landslide area account for 20.35% and 39.23% of the total, respectively. The 15°–25° slope gradient range is the most favorable for landslide development in the study area. Due to factors such as solar radiation and soil conditions, landslides are more likely to occur on west and northwest-facing slopes. Relief degree of land surface values between 150 and 200 are favorable for landslide development, and the 12–15 km range from fault lines is where LAP and LND peak, at 4.88 km^{-2} and 6.29%, respectively. Neogene strata are the main geological formations promoting landslide development. Compared to other land types, grasslands exhibit a higher probability of landslide occurrence. LND and LAP values decrease as the distance from rivers increases, with the 0–2 km range being more prone to landslides. The 250–300 mm annual rainfall range is the most favorable for landslide development, while areas with NDVI values of 0.4–0.6 are more susceptible to landslides. Slope and aspect are the most significant factors influencing the landslide relics in Minhe County, while the influence of lithology and land use is relatively low. The results of this study contribute to a better understanding of the triggering factors and spatial distribution patterns of landslide relics in the region, providing crucial support for future landslide risk assessments and local disaster prevention and mitigation efforts.

Data availability statement

The datasets used and/or analyzed during the current study are available from the corresponding author on reasonable request.

Author contributions

QW: Conceptualization, Data curation, Formal Analysis, Investigation, Methodology, Validation, Visualization, Writing–original draft, Writing–review and editing. CX: Conceptualization, Funding acquisition, Resources, Software, Supervision, Writing–review and editing.

Funding

The author(s) declare that financial support was received for the research and/or publication of this article. This research was funded by the National Institute of Natural Hazards, Ministry of Emergency Management of China (2023-JBKY-57) and the National Natural Science Foundation of China (42077259).

Acknowledgments

We would like to express my sincere gratitude to the reviewers for their professional advice and valuable feedback. Their review not only helped to make the content of this paper more accurate and rigorous but also provided important guidance for its quality improvement. I sincerely appreciate their time and effort devoted to the enhancement of this paper.

Conflict of interest

The authors declare that the research was conducted in the absence of any commercial or financial relationships that could be construed as a potential conflict of interest.

The author(s) declared that they were an editorial board member of Frontiers, at the time of submission. This had no impact on the peer review process and the final decision.

Publisher's note

Supplementary material

The Supplementary Material for this article can be found online at: https://www.frontiersin.org/articles/10.3389/feart.2025.1501498/full#supplementary-material

References

Ali, S. A., Parvin, F., Vojteková, J., Costache, R., Linh, N. T. T., Pham, Q. B., et al. (2021). GIS-based landslide susceptibility modeling: a comparison between fuzzy multi-criteria and machine learning algorithms. *Geosci. Front.* 12, 857–876. doi:10.1016/j.gsf.2020.09.004

Breiman, L. (2001). Random forests. *Mach. Learn.* 45, 5–32. doi:10.1023/a:1010933404324

Bui, D. T., Pradhan, B., Lofman, O., Revhaug, I., and Dick, O. B. (2012). Landslide susceptibility mapping at Hoa Binh Province (Vietnam) using an adaptive neuro-fuzzy inference system and GIS. *Comput. and Geosciences* 45, 199–211. doi:10.1016/j.cageo.2011.10.031

Cemiloglu, A., Zhu, L., Mohammednour, A. B., Azarafza, M., and Nanehkaran, Y. A. (2023). Landslide susceptibility assessment for Maragheh County, Iran, using the logistic regression algorithm. *Land* 12, 1397. doi:10.3390/land12071397

Chen, B., Li, Z., Zhang, C., Ding, M., Zhu, W., Zhang, S., et al. (2022). Wide area detection and distribution characteristics of landslides along Sichuan expressways. *Remote Sens.* 14, 3431. doi:10.3390/rs14143431

Chen, J., Li, L., Xu, C., Huang, Y., Luo, Z., Xu, X., et al. (2023a). Freely accessible inventory and spatial distribution of large-scale landslides in Xianyang City, Shaanxi Province, China. *Earthq. Res. Adv.* 3, 100217. doi:10.1016/j.eqrea.2023.100217

Chen, L., Ma, P., Yu, C., Zheng, Y., Zhu, Q., and Ding, Y. (2023b). Landslide susceptibility assessment in multiple urban slope settings with a landslide inventory augmented by InSAR techniques. *Eng. Geol.* 327, 107342. doi:10.1016/j.enggeo.2023.107342

Chen, W., Chen, X., Peng, J., Panahi, M., and Lee, S. (2021). Landslide susceptibility modeling based on ANFIS with teaching-learning-based optimization and Satin bowerbird optimizer. *Geosci. Front.* 12, 93–107. doi:10.1016/j.gsf.2020.07.012

Chen, Z., Huang, Y., He, X., Shao, X., Li, L., Xu, C., et al. (2023c). Landslides triggered by the 10 June 2022 Maerkang earthquake swarm, Sichuan, China: spatial distribution and tectonic significance. *Landslides* 20, 2155–2169. doi:10.1007/s10346-023-02080-0

Chowdhury, M. S., Rahman, M. N., Sheikh, M. S., Sayeid, M. A., Mahmud, K. H., and Hafsa, B. (2024). GIS-based landslide susceptibility mapping using logistic regression, random forest and decision and regression tree models in Chattogram District, Bangladesh. *Heliyon* 10, e23424. doi:10.1016/j.heliyon.2023.e23424

Cui, F., Hu, R., Tan, R., Yang, K., Yu, J., Zhang, M., et al. (2008). Study on formation mechanism and stability evaluation of Badashan landslide group in Qinghai province. *Chin. J. Rock Mech. Eng.* 27, 848–857. (in Chinese)

Cui, F., Xiong, C., Wu, Q., Xu, C., Li, N., Wu, N., et al. (2021). Dynamic response of the Daguangbao landslide triggered by the Wenchuan earthquake with a composite hypocenter. *Geomatics, Nat. Hazards Risk* 12, 2170–2193. doi:10.1080/19475705.2021.1944916

Cui, P., Su, F., Zou, Q., Chen, N., and Zhang, Y. (2015). Risk assessment and disaster reduction strategies for mountainous and meteorological hazards in Tibetan Plateau. *Chin. Sci. Bull.* 60, 3067–3077. doi:10.1360/n972015-00849

Cui, Y., Hu, J., Zheng, J., Fu, G., and Xu, C. (2022). Susceptibility assessment of landslides caused by snowmelt in a typical loess area in the Yining County, Xinjiang, China. *Q. J. Eng. Geol. Hydrogeology* 55, qjegh2021–2024. doi:10.1144/qjegh2021-024

Cui, Y., Yang, L., Xu, C., and Zheng, J. (2024). Spatial distribution of shallow landslides caused by typhoon lekima in 2019 in zhejiang province, China. *J. Mt. Sci.* 21, 1564–1580. doi:10.1007/s11629-023-8377-y

Cutler, A., Cutler, D. R., and Stevens, J. R. (2012). *Random forests*. Ensemble Machine Learning: Methods and Applications, New York, NY: Springer 157–175.

Dai, F. C., Xu, C., Yao, X., Xu, L., Tu, X. B., and Gong, Q. M. (2011). Spatial distribution of landslides triggered by the 2008 Ms 8.0 Wenchuan earthquake, China. *J. Asian Earth Sci.* 40, 883–895. doi:10.1016/j.jseaes.2010.04.010

Du, J., Glade, T., Woldai, T., Chai, B., and Zeng, B. (2020). Landslide susceptibility assessment based on an incomplete landslide inventory in the Jilong Valley, Tibet, Chinese Himalayas. *Eng. Geol.* 270, 105572. doi:10.1016/j.enggeo.2020.105572

Feng, L., Xu, C., Tian, Y., Li, L., Sun, J., Huang, Y., et al. (2024). Landslides of China's qinling. *Geoscience Data J.* doi:10.1002/gdj3.246

Frattini, P., and Crosta, G. B. (2013). The role of material properties and landscape morphology on landslide size distributions. *Earth Planet. Sci. Lett.* 361, 310–319. doi:10.1016/j.epsl.2012.10.029

Froude, M. J., and Petley, D. N. (2018). Global fatal landslide occurrence from 2004 to 2016. *Nat. Hazards Earth Syst. Sci.* 18, 2161–2181. doi:10.5194/nhess-18-2161-2018

Gao, H., Xu, C., Xie, C., Ma, J., and Xiao, Z. (2024). Landslides triggered by the july 2023 extreme rainstorm in the haihe River Basin, China. *Landslides* 21, 2885–2890. doi:10.1007/s10346-024-02322-9

Guo, F., Lai, P., Huang, F., Liu, L., Wang, X., and He, Z. (2024). Literature review and research progress of landslide susceptibility mapping based on knowledge graph. *Earth Sci.* 49, 1584–1606. doi:10.3799/dqkx.2023.058

Guo, G., Chen, Y., Li, M., and Dang, J. (2013). Statistic relationship between slope gradient and landslide probability in soil slopes around reservoir. *J. Eng. Geol.* 21, 0607. (in Chinese). doi:10.3969/j.issn.1004-9665.2013.04.018

Guzzetti, F., Mondini, A. C., Cardinali, M., Fiorucci, F., Santangelo, M., and Chang, K.-T. (2012). Landslide inventory maps: new tools for an old problem. *Earth-Science Rev.* 112, 42–66. doi:10.1016/j.earscirev.2012.02.001

He, Y., Zhang, D., Li, Y., Han, Y., and Xue, B. (2017). The study of landslide characteristics in the mainstream area of the upper Yellow River based on clustering. *Geospatial Inf.* 15, 5. (in Chinese). doi:10.3969/j.issn.1672-4623.2017.11.019

Hong, H., Liu, J., and Zhu, A. X. (2020). Modeling landslide susceptibility using LogitBoost alternating decision trees and forest by penalizing attributes with the bagging ensemble. *Sci. Total Environ.* 718, 137231. doi:10.1016/j.scitotenv.2020.137231

Huang, H. (2017). *The research of relationship between "9.16" mass of shallow landslide in Changning, Yunnan and vegetation type*. Kunming, China: Kunming University of Science and Technology.

Huang, Y., Xu, C., Li, L., He, X., Cheng, J., Xu, X., et al. (2022). Inventory and spatial distribution of ancient landslides in Hualong County, China. *Land* 12, 136. doi:10.3390/land12010136

Huang, Y., Xu, C., Zhang, X., Li, L., and Xu, X. (2023). Research in the field of natural hazards based on bibliometric analysis. *Nat. Hazards Rev.* 24, 04023012. doi:10.1061/nhrefo.nheng-1739

Korup, O. (2005). Distribution of landslides in southwest New Zealand. *Landslides* 2, 43–51. doi:10.1007/s10346-004-0042-0

Kou, L., Bian, J., Zhang, T., Zhao, W., and Wang, H. (2017). The application of GIS-based information method in susceptibility evaluation of regional geological hazards in Minhe County, Qinghai Province. *Northwest. Geol.* 50, 244–248. (in Chinese). doi:10.3969/j.issn.1009-6248.2017.02.025

Kubwimana, D., Ait Brahim, L., Nkurunziza, P., Dille, A., Depicker, A., Nahimana, L., et al. (2021). Characteristics and distribution of landslides in the populated hillslopes of Bujumbura, Burundi. *Geosciences* 11, 259. doi:10.3390/geosciences11060259

Li, L., Xu, C., Xu, X., Zhang, Z., and Cheng, J. (2021a). Inventory and distribution characteristics of large-scale landslides in Baoji city, Shaanxi province, China. *ISPRS Int. J. Geo-Information* 11, 10. doi:10.3390/ijgi11010010

Li, L., Xu, C., Yang, Z., Zhang, Z., and Lv, M. (2022a). An inventory of large-scale landslides in Baoji city, Shaanxi province, China. *Data* 7, 114. doi:10.3390/data7080114

Li, L., Xu, C., Yao, X., Shao, B., Ouyang, J., Zhang, Z., et al. (2022b). Large-scale landslides around the reservoir area of Baihetan hydropower station in Southwest China: analysis of the spatial distribution. *Nat. Hazards Res.* 2, 218–229. doi:10.1016/j.nhres.2022.07.002

Li, L., Xu, C., Zhang, Z., and Huang, Y. (2021b). Spatial distribution and its control factors of landslides in longxi county, Gansu province, China. *IOP Conf. Ser. Earth Environ. Sci.* 861, 052013. doi:10.1088/1755-1315/861/5/052013

Li, T., Xie, C., Xu, C., Qi, W., Huang, Y., and Li, L. (2024a). Automated machine learning for rainfall-induced landslide hazard mapping in Luhe County of Guangdong Province, China China Geology, 7, 315–329. doi:10.31035/cg2024064

Li, Z., Wei, S., Wu, K., Sha, Y., Zhang, X., Li, D., et al. (2024b). Study on temporal and spatial distribution of landslides in the upper reaches of the Yellow River. *Appl. Sci.* 14, 5488. doi:10.3390/app14135488

Lin, W., Chou, W., and Lin, C. (2008). Earthquake-induced landslide hazard and vegetation recovery assessment using remotely sensed data and a neural network-based classifier: a case study in central Taiwan. *Nat. Hazards* 47, 331–347. doi:10.1007/s11069-008-9222-x

Liu, R., Yang, X., Xu, C., Wei, L., and Zeng, X. (2022). Comparative study of convolutional neural network and conventional machine learning methods for landslide susceptibility mapping. *Remote Sens.* 14, 321. doi:10.3390/rs14020321

Ma, S., Chen, J., and Wu, S. e. (2024a). Distribution characteristics and susceptibility assessment of landslide hazards in Yinghu Town, Ankang, Shaanxi. *Geosciences* 38, 437–450. (in Chinese). doi:10.19657/j.geoscience.1000-8527.2023.067

Ma, S., Shao, X., Li, K., and Xu, C. (2024b). Landslides triggered by the 30th june 2012 Ms6. 6 hejing earthquake, xinjiang province, China. *Bull. Eng. Geol. Environ.* 83, 256. doi:10.1007/s10064-024-03727-5

Ma, S., Shao, X., and Xu, C. (2022). Characterizing the distribution pattern and a physically based susceptibility assessment of shallow landslides triggered by the 2019 heavy rainfall event in Longchuan County, Guangdong Province, China. *Remote Sens.* 14, 4257. doi:10.3390/rs14174257

Ma, S., Shao, X., and Xu, C. (2023a). Estimating the quality of the most popular machine learning algorithms for landslide susceptibility mapping in 2018 Mw 7.5 Palu earthquake. *Remote Sens.* 15, 4733. doi:10.3390/rs15194733

Ma, S., Shao, X., and Xu, C. (2023b). Landslide susceptibility mapping in terms of the slope-unit or raster-unit, which is better? *J. Earth Sci.* 34, 386–397. doi:10.1007/s12583-021-1407-1

Ma, S., Shao, X., and Xu, C. (2023c). Landslides triggered by the 2016 heavy rainfall event in Sanming, Fujian Province: distribution pattern analysis and spatio-temporal susceptibility assessment. *Remote Sens.* 15, 2738. doi:10.3390/rs15112738

Ma, S., Shao, X., and Xu, C. (2023d). Physically-based rainfall-induced landslide thresholds for the Tianshui area of Loess Plateau, China by TRIGRS model. *Catena* 233, 107499. doi:10.1016/j.catena.2023.107499

Ma, S., Shao, X., and Xu, C. (2024c). Delineating Non-Susceptible landslide areas in China based on topographic index and quantile Non-Linear model. *Forests* 15, 678. doi:10.3390/f15040678

Ma, S., Shao, X., and Xu, C. (2024d). Potential controlling factors and landslide susceptibility features of the 2022 Ms 6.8 Luding Earthquake. *Remote Sens.* 16, 2861. doi:10.3390/rs16152861

Mao, Y., Li, Y., Teng, F., Sabonchi, A. K., Azarafza, M., and Zhang, M. (2024). Utilizing hybrid machine learning and soft computing techniques for landslide susceptibility mapping in a Drainage Basin. *Water* 16, 380. doi:10.3390/w16030380

Meng, Q., Confuorto, P., Peng, Y., Raspini, F., Bianchini, S., Han, S., et al. (2020). Regional recognition and classification of active loess landslides using two-dimensional deformation derived from Sentinel-1 interferometric radar data. *Remote Sens.* 12, 1541. doi:10.3390/rs12101541

Mu, W., Wu, X., Qian, C., and Wang, K. (2020). Triggering mechanism and reactivation probability of loess-mudstone landslides induced by rainfall infiltration: a case study in Qinghai Province, Northwestern China. *Environ. Earth Sci.* 79, 22. doi:10.1007/s12665-019-8767-1

Nanehkaran, Y. A., Chen, B., Cemiloglu, A., Chen, J., Anwar, S., Azarafza, M., et al. (2023). Riverside landslide susceptibility overview: leveraging artificial neural networks and machine learning in accordance with the United Nations (UN) sustainable development goals. *Water* 15, 2707. doi:10.3390/w15152707

Nanehkaran, Y. A., Licai, Z., Chen, J., Azarafza, M., and Yimin, M. (2022). Application of artificial neural networks and geographic information system to provide hazard susceptibility maps for rockfall failures. *Environ. Earth Sci.* 81, 475. doi:10.1007/s12665-022-10603-6

Naseer, S., Haq, T. U., Khan, A., Tanoli, J. I., Khan, N. G., Qaiser, F.-u.-R., et al. (2021). GIS-based spatial landslide distribution analysis of district Neelum, AJ&K, Pakistan. *Nat. Hazards* 106, 965–989. doi:10.1007/s11069-021-04502-5

Nikoobakht, S., Azarafza, M., Akgün, H., and Derakhshani, R. (2022). Landslide susceptibility assessment by using convolutional neural network. *Appl. Sci.* 12, 5992. doi:10.3390/app12125992

Peng, J., Wang, S., Wang, Q., Zhuang, J., Huang, W., Zhu, X., et al. (2019). Distribution and genetic types of loess landslides in China. *J. Asian Earth Sci.* 170, 329–350. doi:10.1016/j.jseaes.2018.11.015

Petley, D. (2012). Global patterns of loss of life from landslides. *Geology* 40, 927–930. doi:10.1130/g33217.1

Piacentini, D., Troiani, F., Daniele, G., and Pizziolo, M. (2018). Historical geospatial database for landslide analysis: the catalogue of landslide OCcurrences in the emilia-romagna region (CLOCkER). *Landslides* 15, 811–822. doi:10.1007/s10346-018-0962-8

Qin, Y., Yang, G., Lu, K., Sun, Q., Xie, J., and Wu, Y. (2021). Performance evaluation of five GIS-Based models for landslide susceptibility prediction and mapping: a case study of Kaiyang County, China. *Sustainability* 13, 6441. doi:10.3390/su13116441

Qiu, H., Cui, P., Regmi, A. D., Hu, S., Zhang, Y., and He, Y. (2018). Landslide distribution and size versus relative relief (Shaanxi Province, China). *Bull. Eng. Geol. Environ.* 77, 1331–1342. doi:10.1007/s10064-017-1121-5

Quan, H., Moon, H., Jin, G., and Park, S. (2014). Landslide susceptibility analysis in Baekdu Mountain Area using ANN and AHP method. *J. Korean Geo-Environmental Soc.* 15, 79–85. doi:10.14481/jkges.2014.15.12.79

Selamat, S. N., Majid, N. A., and Taha, M. R. (2024). Multicollinearity and spatial correlation analysis of landslide conditioning factors in Langat River Basin, Selangor. *Nat. Hazards* 121, 2665–2684. doi:10.1007/s11069-024-06903-8

Shao, X., Ma, S., and Xu, C. (2023a). Distribution and characteristics of shallow landslides triggered by the 2018 Mw 7.5 Palu earthquake, Indonesia. *Landslides* 20, 157–175. doi:10.1007/s10346-022-01972-x

Shao, X., Ma, S., and Xu, C. (2023b). Hazard assessment modeling and software development of earthquake-triggered landslides in the Sichuan–Yunnan area, China. *Geosci. Model Dev.* 16, 5113–5129. doi:10.5194/gmd-16-5113-2023

Shao, X., Ma, S., Xu, C., Cheng, J., and Xu, X. (2023c). Seismically-induced landslide probabilistic hazard mapping of Aba Prefecture and Chengdu Plain region, Sichuan Province, China for future seismic scenarios. *Geosci. Lett.* 10, 55. doi:10.1186/s40562-023-00307-5

Shao, X., Ma, S., Xu, C., Shen, L., and Lu, Y. (2020). Inventory, distribution and geometric characteristics of landslides in baoshan city, yunnan province, China. *Sustainability* 12, 2433. doi:10.3390/su12062433

Shao, X., Ma, S., Xu, C., Xie, C., Li, T., Huang, Y., et al. (2024a). Landslides triggered by the 2022 Ms. 6.8 Luding strike-slip earthquake: an update. *Eng. Geol.* 335, 107536. doi:10.1016/j.enggeo.2024.107536

Shao, X., Ma, S., Xu, C., and Xu, Y. (2023d). Insight into the characteristics and triggers of loess landslides during the 2013 heavy rainfall event in the Tianshui Area, China. *Remote Sens.* 15, 4304. doi:10.3390/rs15174304

Shao, X., Xu, C., Li, L., Yang, Z., Yao, X., Shao, B., et al. (2024b). Spatial analysis and hazard assessment of Large-scale ancient landslides around the reservoir area of Wudongde Hydropower Station, China. *Nat. Hazards* 120, 87–105. doi:10.1007/s11069-023-06201-9

Shao, X., Xu, C., and Ma, S. (2022). Preliminary analysis of coseismic landslides induced by the 1 June 2022 Ms 6.1 Lushan Earthquake, China. *Sustainability* 14, 16554. doi:10.3390/su142416554

Sun, J., Xu, C., Feng, L., Li, L., Zhang, X., and Yang, W. (2024). The Yinshan Mountains record over 10,000 landslides. *Data* 9, 31. doi:10.3390/data9020031

Tian, N., Lan, H., Li, L., Peng, J., Fu, B., and Clague, J. J. (2024). Human activities are intensifying the spatial variation of landslides in the Yellow River Basin. *Sci. Bull.* 70, 263–272. doi:10.1016/j.scib.2024.07.007

Tu, K., Ye, S., Zou, J., Hua, C., and Guo, J. (2023). InSAR displacement with high-resolution optical remote sensing for the early detection and deformation analysis of active landslides in the upper yellow river. *Water* 15, 769. doi:10.3390/w15040769

Ullah, M., Tang, B., Huangfu, W., Yang, D., Wei, Y., and Qiu, H. (2024). Machine learning-driven landslide susceptibility mapping in the himalayan China–Pakistan economic corridor region. *Land* 13, 1011. doi:10.3390/land13071011

Valenzuela, P., Domínguez-Cuesta, M. J., García, M. A. M., and Jiménez-Sánchez, M. (2017). A spatio-temporal landslide inventory for the NW of Spain: BAPA database. *Geomorphology* 293, 11–23. doi:10.1016/j.geomorph.2017.05.010

Wang, H., Pan, D., and Jin, Y. (2015). Contributing rate of slope gradient to landslide growth in Qianjiang District of Chongqing. *J. Chongqing Jiaot. Univ. Sci.* 33, 81–84. (in Chinese). doi:10.3969/j.issn.1674-0696.2014.05.18

Wang, P., Li, L., Xu, C., Zhang, Z., and Xu, X. (2022). An open source inventory and spatial distribution of landslides in Jiyuan City, Henan Province, China. *Nat. Hazards Res.* 2, 325–330. doi:10.1016/j.nhres.2022.10.004

Wang, Q., Xu, C., and Xu, J. (2024a). Exploration of landslide geomorphology and inventory construction in Minhe county, Qinghai, China, based on Google Earth remote sensing imagery. *Trans. GIS* 29. doi:10.1111/tgis.13281

Wang, T., Wu, S. R., Shi, J. S., Xin, P., and Wu, L. Z. (2018). Assessment of the effects of historical strong earthquakes on large-scale landslide groupings in the Wei River midstream. *Eng. Geol.* 235, 11–19. doi:10.1016/j.enggeo.2018.01.020

Wang, W., Huang, Y., and Li, l. (2021). Development and distribution of ancient landslides in the northwest corner of the Tibetan Plateau. *IOP Conf. Ser. Earth Environ. Sci.* 861, 052034. doi:10.1088/1755-1315/861/5/052034

Wang, W., Huang, Y., Xu, C., Shao, X., Li, L., Feng, L., et al. (2024b). Identification and distribution of 13003 landslides in the northwest margin of Qinghai-Tibet Plateau based on human-computer interaction remote sensing interpretation. *China Geol.* 7, 171–187. doi:10.31035/cg2023140

Wang, Z., Hu, Z., Liu, H., Gong, H., Zhao, W., Yu, M., et al. (2010). "Application of the relief degree of land surface in landslide disasters susceptibility assessment in China," in *2010 18th international conference on geoinformatics*, 1–5.

Wei, Z., Cao, X., Zhang, J., Ying, Z., Yan, H., and Wei, S. (2021). Temporal and spatial characteristics of landslide, rockfall and debris flow disasters in Qinghai Province during the period. *Chin. J. Geol. Hazard Control* 32, 134–142. (in Chinese). doi:10.16031/j.cnki.issn.1003-8035.2021.06-16

Wieczorek, G. F. (1984). Preparing a detailed landslide-inventory map for hazard evaluation and reduction. *Bull. Assoc. Eng. Geol.* 21, 337–342. doi:10.2113/gseegeosci.xxi.3.337

Wu, X., Xu, X., Yu, G., Ren, J., Yang, X., Chen, G., et al. (2024). The China active faults database (CAFD) and its web system. *Earth Syst. Sci. Data* 16, 3391–3417. doi:10.5194/essd-16-3391-2024

Wu, Y., Dong, Y., Wei, Z., Dong, J., Peng, L., Yan, P., et al. (2023). Genetic mechanisms and a stability evaluation of large landslides in Zhangjiawan, Qinghai Province. *Front. Earth Sci.* 11, 1140030. doi:10.3389/feart.2023.1140030

Xia, G., Liu, C., Xu, C., and Le, T. (2021). Dynamic analysis of the high-speed and long-runout landslide movement process based on the discrete element method: a case study of the shuicheng landslide in guizhou, China. *Adv. Civ. Eng.* 2021, 8854194. doi:10.1155/2021/8854194

Xiao, Z., Xu, C., Huang, Y., He, X., Shao, X., Chen, Z., et al. (2023). Analysis of spatial distribution of landslides triggered by the Ms 6.8 Luding earthquake in China on September 5, 2022. *Geoenvironmental Disasters* 10, 3. doi:10.1186/s40677-023-00233-w

Xie, C., Huang, Y., Li, L., Li, T., and Xu, C. (2023). Detailed inventory and spatial distribution analysis of rainfall-induced landslides in Jiexi County, Guangdong Province, China in August 2018. *Sustainability* 15, 13930. doi:10.3390/su151813930

Xin, P., Dong, X., Wu, S., Shi, J., Wang, T., and Liang, C. (2017). The accumulation characteristics and mechanism of rotational-translational landslides in the Neogene basins on the northeastern margin of Tibet Plateau. *Acta Geol. Sin.* 91, 499–509. doi:10.1016/j.enggeo.2018.07.024

Xu, C. (2015). Preparation of earthquake-triggered landslide inventory maps using remote sensing and GIS technologies: principles and case studies. *Geosci. Front.* 6, 825–836. doi:10.1016/j.gsf.2014.03.004

Xu, C., Xu, X., Yao, X., and Dai, F. (2014). Three (nearly) complete inventories of landslides triggered by the May 12, 2008 Wenchuan Mw 7.9 earthquake of China and their spatial distribution statistical analysis. *Landslides* 11, 441–461. doi:10.1007/s10346-013-0404-6

Xu, L., and Yan, D. (2019). The groundwater responses to loess flowslides in the Heifangtai platform. *Bull. Eng. Geol. Environ.* 78, 4931–4944. doi:10.1007/s10064-018-01436-4

Xu, Y., Guo, W., Wang, W., Luo, S., Chen, Z., Lou, Y., et al. (2022). Characteristics of shallow landslides under extreme rainfall and their effects on runoff and sediment on the Loess Plateau. *Acta Ecol. Sin.* 42, 7898–7909. doi:10.5846/stxb202110313052

Xue, Z., Xu, C., Gao, H., and Huang, Y. (2023). Disaster chain thinking improves the capabilities of disaster prevention, mitigation, and relief in China. *Nat. Hazards Res.* 4, 320–323. doi:10.1016/j.nhres.2023.11.013

Yin, Y., Wang, H., Gao, Y., and Li, X. (2010a). Real-time monitoring and early warning of landslides at relocated wushan Town, the three gorges reservoir, China. *Landslides* 7, 339–349. doi:10.1007/s10346-010-0220-1

Yin, Z., Wei, G., Qi, X., and Zhou, C. (2010b). Preliminary study on characteristic and mechanism of super-large landslides in Upper Yellow River since late-pleistocene. *J. Eng. Geol.* 18, 41. (in Chinese). doi:10.3969/j.issn.1004-9665.2010.01.006

Zhang, M., and Liu, J. (2010). Controlling factors of loess landslides in western China. *Environ. Earth Sci.* 59, 1671–1680. doi:10.1007/s12665-009-0149-7

Zhang, S., Sun, P., Li, R., and Wang, F. (2023). Preliminary investigation on a catastrophic loess landslide induced by heavy rainfall on 1 September 2022 in Qinghai, China. *Landslides* 20, 1553–1559. doi:10.1007/s10346-023-02086-8

Zhang, X., Xu, C., Li, L., Feng, L., and Yang, W. (2024). Inventory of landslides in the northern half of the Taihang mountain range, China. *Geosciences* 14, 74. doi:10.3390/geosciences14030074

Zhang, Y., Guo, C., Lan, H., Zhou, N., and Yao, X. (2015). Reactivation mechanism of ancient giant landslides in the tectonically active zone: a case study in Southwest China. *Environ. Earth Sci.* 74, 1719–1729. doi:10.1007/s12665-015-4180-6

Zhao, B., Su, L., Xu, Q., Li, W., Xu, C., and Wang, Y. (2023). A review of recent earthquake-induced landslides on the Tibetan Plateau. *Earth-Science Rev.* 244, 104534. doi:10.1016/j.earscirev.2023.104534

Zhao, D., Lancuo, Z., Hou, G., Xu, C., and Li, W. (2021). Assessment of geological disaster susceptibility in the hehuang valley of Qinghai province. *J. Geomechanics* 27, 83–95. (in Chinese). doi:10.12090/j.issn.1006-6616.2021.27.01.009

Zhao, J., Huang, Q., Peng, J., Wang, Z., Ma, P., Leng, Y., et al. (2025). Typical characteristics and causes of giant landslides in the upper reaches of the Yellow River, China. *Landslides* 22, 313–334. doi:10.1007/s10346-024-02363-0

Zhao, J., Xu, C., and Huang, X. (2024). Detailed landslide traces database of hancheng county, China, based on high-resolution satellite images available on the Google Earth platform. *Data* 9, 63. doi:10.3390/data9050063

Zhou, B., Zhang, Y. X., Sun, Y., and Gan, C. P. (2013). Study on failure mechanism and stability of loess slope in Huangshui River Basin. *Appl. Mech. Mater.* 405, 580–586. doi:10.4028/www.scientific.net/amm.405-408.580

Zhou, J., Zhu, C., Zheng, J., Wang, X., and Liu, Z. (2002). Landslide disaster in the loess area of China. *J. For. Res.* 13, 157–161. doi:10.1007/bf02857244

Frontiers in
Earth Science

Investigates the processes operating within the major spheres of our planet

Advances our understanding across the earth sciences, providing a theoretical background for better use of our planet's resources and equipping us to face major environmental challenges.

Discover the latest Research Topics

See more →

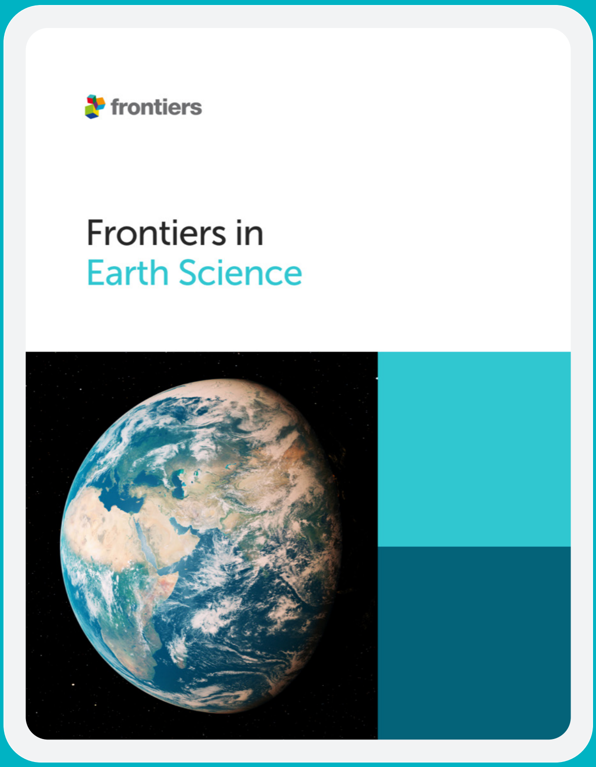

frontiers

Frontiers in
Earth Science

Frontiers

Avenue du Tribunal-Fédéral 34
1005 Lausanne, Switzerland
frontiersin.org

Contact us

+41 (0)21 510 17 00
frontiersin.org/about/contact